Flow of Taylor Bubbles Rising in Stagnant Non-Newtonian Fluids

Renato Luís Gomes de Sousa

A thesis submitted in part fulfilment of the requirement for the degree of Doctor in the Faculty of Engineering, University of Porto, Portugal

Universidade do Porto

Faculdade de Engenharia

FEUP

This thesis was supervised by

Doctor João Bernardo Lares Moreira de Campos, Departamento de Engenharia Química, Faculdade de Engenharia da Universidade do Porto

And co-supervised by

Doctor Alexandra Maria Pinheiro da Silva Ferreira Rodrigues Pinto, Departamento de Engenharia Química, Faculdade de Engenharia da Universidade do Porto

Centro de Estudos de Fenómenos de Transporte
Departamento de Engenharia Química
Faculdade de Engenharia
Universidade do Porto

July, 2005

Abstract

The objective of this thesis is the experimental investigation of the flow of long tubular gas bubbles, also called Taylor bubbles, in non-Newtonian fluids. The flow patterns around isolated bubbles rising in vertical columns of stagnant solutions of Carboxymethylcellulose (CMC) and Polyacrylamide (PAA) in water are studied, using different weight percentages of polymer.

Preliminary visualisation studies are conducted, applying a technique developed by Campos and Guedes de Carvalho (1988), in order to obtain a general idea of the liquid flow in the wake of the bubbles. From these studies, a selection of some key conditions is made. For these conditions the liquid flow around the bubbles is analysed, applying Particle Image Velocimetry (PIV) and Shadowgraphy Technique (ST) simultaneously. This technique was developed for this work, and allows for the simultaneous acquisition of the velocity field and bubble shape, thereby solving optical problems previously encountered and described in applications of PIV to two-phase flows.

The flows around the nose of the bubble, in the annular liquid film and in the bubble wake are described and compared - for the different solutions studied and with the results obtained from simple models.

Coalescence studies are performed with pairs of Taylor bubbles rising simultaneously in some of the solutions analysed with PIV/ST. The distance between bubbles and their velocities are determined with the use of laser diodes and photocells. The interaction between the consecutive bubbles is analysed and related with the velocity fields obtained with PIV/ST.

Keywords: Taylor bubbles, non-Newtonian fluids, Particle Image Velocimetry (PIV), Bubble wake, Coalescence.

Resumo

A presente tese tem como objectivo o estudo experimental do escoamento de bolhas gasosas tubulares, também designadas por bolhas de Taylor, em fluidos não-Newtonianos. Analisa-se o escoamento em torno de bolhas isoladas em ascensão em colunas verticais de soluções estagnadas de Carboximetilcelulose (CMC) e de Poliacrilamida (PAA) em água, com diferentes percentagens mássicas de polímero.

São feitos estudos iniciais de visualização, aplicando uma técnica desenvolvida por Campos e Guedes de Carvalho (1988), com o objectivo de obter uma ideia qualitativa do escoamento do líquido na esteira das bolhas. A partir destes estudos é feita uma selecção de condições chave. Para as condições escolhidas, analisa-se o escoamento do líquido em torno e na esteira das bolhas empregando uma técnica simultânea de Velocimetria por Imagens de Partículas (PIV) e de Ombroscopia. Esta técnica, desenvolvida para este estudo, permite obter simultaneamente o campo de velocidade e a forma da bolha, resolvendo problemas ópticos descritos anteriormente na aplicação de PIV a escoamentos bifásicos.

O escoamento em torno do "nariz"da bolha, na película de líquido em torno da bolha e na esteira é descrito e comparado entre as várias soluções estudadas e com resultados obtidos de modelos simples.

São realizados estudos de coalescência de pares de bolhas de Taylor subindo simultaneamente em algumas das soluções analisadas com PIV/Ombroscopia. A distância entre bolhas e as suas velocidades são determinadas com o auxílio de díodos laser e células fotovoltaicas. É analisada a interacção entre bolhas e relacionada com os campos de escoamento obtidos pela técnica de PIV/Ombroscopia.

Palavras chave: Bolhas de Taylor, Fluidos não-Newtonianos, Velocimetria por Imagem de Partícula (PIV), Esteira de bolhas, Coalescência.

Résumé

L' objectif de cette thèse est l'étude expérimentale de l'écoulement de bulles gazeuses tubulaires (bulles de Taylor), dans des fluides viscoélastiques. On analyse l'écoulement à l'entour des bulles isolées montant dans des tubes verticaux remplis de solutions aqueuses en repos de Carboxyméthyl-cellulose (CMC) et de Polyacrylamide (PAA), avec différents pourcentages de masse de polymère.

Des études initiales de visualisation, sont faites, en appliquant une technique développée par Campos et Guedes de Carvalho (1988), dans le but d'obtenir une idée qualitative de l'écoulement du liquide dans le sillage des bulles. D'après ces études, des conditions clés ont été privilégiées. Dans les conditions choisies on analyse l'écoulement à l'entour et dans le sillage des bulles en utilisant une technique simultanée de Vélocimétrie par Image de Particules (PIV) et d'Ombroscopie. Cette technique, développée pour cette étude, permet l'obtention simultanée du champ de vitesse et de la forme de la bulle, résolvant des problèmes optiques déjà décrits dans l'application du PIV dans les écoulements à deux phases.

L'écoulement à l'entour du nez de la bulle, dans la pellicule de film entourant la bulle et au sillage de celle ci est décrit et comparé par rapport à toutes les solutions étudiées et avec des résultats obtenus par des modèles simples.

Dans certaines des solutions analysées par PIV, des études de coalescence de paires de bulles Taylor montant simultanément sont effectuées. La distance entre les bulles et leurs vitesses sont déterminées à l'aide de diodes laser et de cellules-photo. L'intéraction entre bulles est analysée et rapportée aux champs d'écoulement obtenus avec la technique de PIV/Ombroscopie.

Mots clé: Bulles de Taylor, Fluides viscoélastiques, Vélocimétrie par Images de Particules (PIV), Sillage des bulles, Coalescence.

à Rita
aos meus Pais
aos meus Irmãos
ao meu Avô

Acknowledgements

Upon finishing this thesis I would like to thank everyone that directly or indirectly contributed to the realisation of this work:

I am deeply indebted to my supervisors, Doctor João Campos and Doctor Alexandra Pinto, not only for suggesting this work to me but mainly for their unconditional support during these four years.

Special thanks to Doctor Riethmuller from von Karman Institute for Fluid Dynamics, for his expert support and advice on the work performed in Belgium.

Thanks also to all my fellow Diploma Course students for the great year that we spent together.

My colleague Sofia Nogueira, for her precious help on quickly adapting to life in Brussels and for all her support during the work.

My special gratitude to Doctor Maria do Pilar Gonçalves for her help in the rheological characterisation of the fluids.

Thanks to my colleague Vítor Ferreira, for the precious help during the coalescence experiments.

I am grateful to colleagues in FEUP, for their company and support during these years.

I am indebted to my friends and family, for the great times I spent with them when not thinking of work.

Thanks to Mr. Gordon Grams for his English language revision and suggestions to improve the syntax and readability.

And last but not least, I am truly indebted to Rita, not only for her support during the most difficult times, but also for her patience and understanding, especially during the year I was in Belgium and in the last 'marathon' months of writing this thesis.

This work was supported by Fundação para a Ciência e a Tecnologia, with fellowship SFRH/BD/3389/2000.

Contents

Nomenclature

Roman symbols

a_1, a_2	dimensionless parameters of Carreau-Yasuda viscosity model
A	surface area
$A(i,j)$	grey level of pixel in coordinates (i,j) of frame A
$B(i,j)$	grey level of pixel in coordinates (i,j) of frame B
C	dimensionless parameter in the expression of the bubble velocity in a moving liquid
D	column diameter
D_e	equivalent diameter of a sphere with the same volume of a bubble
F	force measured by the rheometer
g	gravitational acceleration
G'	storage modulus
G''	loss modulus
h	distance to the liquid surface
Δh	distance between photocells
HC	horizontal calibration
l_s	separating distance between bubbles
l_min	distance between bubbles above which there is no interaction
L_b	bubble length
L_w	wake length
k	dimensionless parameter of drift velocity equation
$k_\mathrm{c1} - k_\mathrm{c3}$	dimensionless parameters of bubble shape functions for CMC
$k_\mathrm{p1} - k_\mathrm{p3}$	dimensionless parameters of bubble shape functions for PAA

m_1, m_2	dimensionless parameters of shear stress and first normal stress difference functions of shear rate
n	number of moles
n_{i}	refractive index of medium i
N_{images}	number of images
N_1, N_2	first and second normal stress differences
Δp	window displacement in pixels
$\Delta pixels$	distance in pixels
P	pressure
P_{atm}	atmospheric pressure
$PIVC$	PIV calibration
Q_{exp}	experimental liquid flow rate far ahead of bubble
Q_{A}	liquid flow rate ahead of bubble (moving frame of reference)
Q_{B}	liquid flow rate in the liquid film (moving frame of reference)
r	radial position
r_{box}	radial position in the front face of the optical box
r_{image}	radial position in images neglecting distortion
r_{column}	radial position in mid plane of column
r_∞	maximum bubble radius
R	column radius
R_C	rheometer cone radius
$\Re$	universal gas constant
s_1, s_2	dimensionless parameters in the equations relating the shear stress and first normal stress difference with shear rate
t	time
$t_{\mathrm{A}} - t_{\mathrm{D}}$	laser synchronisation instants
Δt_{f}	time gap between PIV frames
Δt_{i}	time gap between visualisation images
Δt_{pc}	bubble travel time between photocells
t_{Ni}	instant when the nose of ith bubble passes in front of photocell
t_{Ti}	instant when the trailing edge of ith bubble passes in front of photocell
T	temperature
T_R	applied torque in the rheometer

U_0	bubble drift velocity
U_b	bubble velocity
U_L	leading bubble velocity
U_s	superficial liquid velocity
U_T	trailing bubble velocity
V	velocity
$V_1 - V_5$	pneumatic valves
$V_\mathrm{A} - V_\mathrm{D}$	globe valves
VC	vertical calibration
V_exp	axial component of liquid velocity far ahead of bubble
V_i	liquid velocity in i direction
V_r	radial component of liquid velocity
V_z	axial component of liquid velocity
$V_\infty(r)$	axial stabilised velocity in the liquid film
Δx	horizontal window displacement
Δy	vertical window displacement
x, y, z	perpendicular directions in cartesian coordinates
z	axial distance to bubble nose
z_stable	axial distance to the bubble nose where the liquid film becomes fully developed
$z*$	axial distance to bubble trailing edge or distance between consecutive bubbles
$z*_\mathrm{eye}$	axial distance between the wake vortex ring and the bubble trailing edge
Δz	distance travelled by bubble

Greek symbols

α	rheometer cone angle
δ	liquid film thickness
δx	uncertainty associated with the measurement of quantity x
ϕ	normalised cross correlation function
Φ	cross correlation function

$\dot{\gamma}$	shear rate
$\dot{\gamma}_{\mathrm{f}}$	characteristic flow shear rate
γ_0	strain amplitude in oscillatory tests
λ	time constant of Carreau-Yasuda viscosity model
μ	dinamic viscosity
μ_∞	viscosity at infinite shear rate (Carreau-Yasuda viscosity model)
μ_0	viscosity at zero shear rate (Carreau-Yasuda viscosity model)
Ω	angular velocity of rheometer cone
ρ_l	liquid density
ρ_g	gas density
σ	surface tension
$\sigma(x)$	standard deviation of x
τ_{ij}	shear stress in j direction on a plane perpendicular to i direction
θ_{i}	angle between interface and light ray in medium i
θ_{f}	fluid relaxation time
ϑ_b	bubble volume

Acronyms

CMC	carboxymethylcellulose
CCD	charged coupled device
FR	fixed frame of reference
LED	light emitting diode
MR	frame of reference moving with the bubble
Nd	neodymium doped
PAA	polyacrylamide
PC	photocell
PIV	particle image velocimetry
ST	shadowgraphy technique
SNR	signal to noise ratio
TTL	transistor-transistor logic
VKI	von Karman Institute
WIDIM	window distortion iterative multigrid

wt%	weight percentage
YAG	yttrium aluminium garnet

List of Figures

List of Tables

Motivation

Slug flow is a two-phase flow pattern which is observed when gas and liquid flow simultaneously in a column over a determined range of flow rates. In vertical columns it is characterised by a succession of long bubbles, called Taylor bubbles, that almost fill the column cross-section, with liquid flowing around and between them. This flow regime is frequently found in industrial processes, such as absorption columns, air-lift reactors, cooling system of nuclear power plants, oil and gas wells and geothermal processes, among others. Recently, this flow pattern has been used in the depolarisation of membranes, both in ultrafiltration and reverse osmosis processes. Although the slug regime is sometimes to be avoided, it is of extreme importance in some chemical processes where it is used to promote mixing; increasing the rates of mass transfer and chemical reaction.

Typically, the falling liquid film flowing around a Taylor bubble separates at the rear of the bubble to form a wake where intense mixing takes place. When two consecutive bubbles flow in a column, the wake of the leading bubble may affect the velocity of the trailing bubble. If the velocity of the latter increases, coalescence can occur and a single longer bubble is formed. Coalescence greatly reduces the efficiency of the mixing process by reducing the number of mixing regions in the column. In oil and gas wells the unexpected occurrence of long gas bubbles has been the cause of severe accidents.

Slug flow has been studied since the 1940's, mainly with air bubbles flowing in Newtonian liquids. In industry, slug flow is modelled on known correlations that were established for Newtonian liquids. However, there are many industrial processes where the liquid has a non-Newtonian behaviour, as in biological and waste-treatment air-lift reactors and polymer devolatilisation processes. It is well known that some features of non-Newtonian liquids, mainly their viscoelasticity, are responsible for strange phenomena such as the climbing rod, the tubeless siphon and the Ueber effect, among others (Bird *et al.* (1987)). Information on slug flow in non-Newtonian liquids is scarce and so gave impetus to under-

taking this work.

Thesis layout

This thesis has six chapters. In the first chapter, slug flow state-of-the-art of is reviewed and a brief explanation of the behaviour of non-Newtonian fluids is given.

In Chapter 2, the experimental technique used in preliminary visualisation studies is described and the technique of Particle Image Velocimetry with simultaneous shadowgraphy is presented.

In the third and fourth chapters, the description of the visualisation studies and the velocity fields around individual Taylor bubbles is made for the Carboxymethylcellulose and Polyacrylamide solutions respectively. The description of velocity fields is divided into three distinct regions: the bubble nose, the annular liquid film and the wake. These chapters also include the rheological characterisation of the solutions.

In Chapter 5 the results obtained in the coalescence studies are presented. The interaction between two consecutive Taylor bubbles rising in vertical tubes is studied and the results are related with the wake velocity fields obtained in the PIV studies.

Finally, the conclusions of the present work are presented and lines of possible future work are suggested in Chapter 6.

Chapter 1

State of the art

Abstract

This chapter presents a review of the research on slug flow. The work on two-phase flows with non-Newtonian liquids is also reviewed. Finally, the application of Particle Image Velocimetry (PIV) to two-phase flows is briefly described.

1.1 Slug flow

When gas and liquid flow simultaneously in a column, different flow regimes can be found, according to the relative flow rates. In Figure 1.1, five regimes are shown for vertical tubes, with increasing ratios of gas/liquid flow rates.

This figure illustrates that slug flow is characterised by elongated bubbles, with a spheroid "nose" occupying almost the entire cross-section of the tube. Between the gas slugs (also called Taylor bubbles) there are slugs of liquid where small bubbles may be dispersed. According to Davidson and Harrison (1963), gas slugs are bubbles for which $D_e > D/3$, where D_e is the diameter of a sphere with the same volume as the bubble, and D is the column diameter.

A schematic representation of the flow around an individual Taylor bubble is presented in Figure 1.2, in a frame of reference attached to the bubble. The liquid ahead of the bubble, moves away from the axis as the bubble approaches, and forms a free-falling liquid film around the bubble. Below the Taylor bubble the falling liquid film acts as an expanding jet, forming a wake with features that depend on the liquid properties and flow rates.

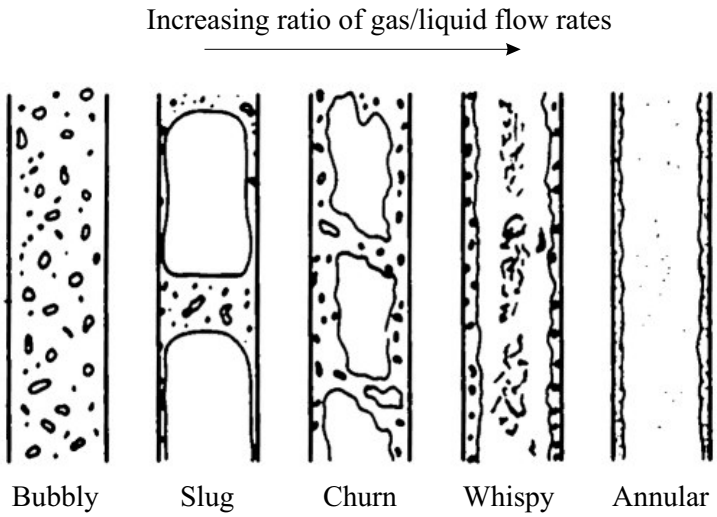

Figure 1.1. Different flow regimes in vertical gas-liquid flow.

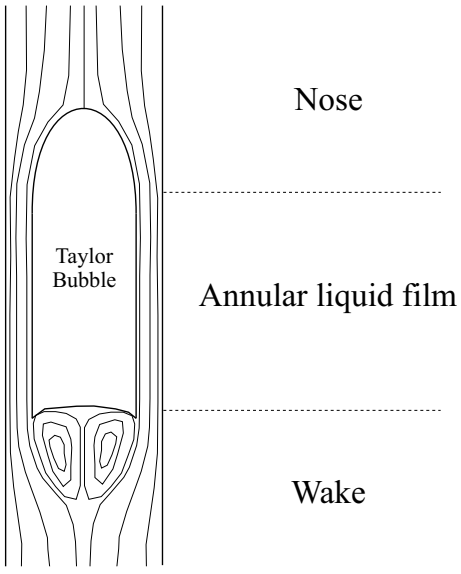

Figure 1.2. Sketch of the flow around an individual Taylor bubble.

Slug flow has been studied in depth since the 1940's and most of this work has focused on air bubbles rising in Newtonian liquids. A more complete review of the work with Newtonian liquids can be found in Nogueira (2005) but the most relevant information will be mentioned here.

Bubble velocity and shape

The velocity of a Taylor bubble rising in stagnant liquid is a function of gravitational acceleration g, column diameter D, liquid viscosity μ, liquid and gas densities, ρ_l and ρ_g, and surface tension σ.

White and Beardmore (1962) applied dimensional analysis to predict the drift velocity, U_0, of a single bubble rising in a stagnant liquid. They concluded that the Froude number, $Fr = U_0/gD^{1/2}$, containing the drift velocity can be expressed as a function of the dimensionless inverse viscosity number, $N_f = D^{3/2}g^{1/2}\rho_l/\mu$ and of a surface-tension-dependent number, $Y = g\mu^4/(\rho_l\sigma^3)$.

For sufficiently large column diameters and moderate liquid viscosities, the drift velocity is independent on the liquid properties, i.e., the Froude number does not depend on N_f and Y, which means that viscous and interfacial effects are negligible. This inertia-controlled regime takes place for $N_f > 300$ and Eötvös number $E_0 = \rho_l g D^2/\sigma = N_f^{4/3}Y^{1/3} > 100$.

Dumitrescu (1943), a pioneer researcher, studied the shape and velocity of Taylor bubbles. Dumitrescu (1943), and later Davies and Taylor (1950), applied potential flow theory to flow around the bubble nose to find that the drift velocity of an elongated bubble rising in a vertical column filled with stagnant water is given by

$$U_0 = k\sqrt{gD} \tag{1.1}$$

For inertia-controlled regime, where the fluid can be considered inviscid and surface tension effects negligible, k is found to be around 0.35. Nicklin *et al.* (1962), experimentally confirmed this value and showed that the velocity of a single Taylor bubble rising in a co-current flowing liquid is given by

$$U_\mathrm{b} = C \cdot U_\mathrm{s} + U_0 \tag{1.2}$$

where $C \cdot U_\mathrm{s}$ is the fluid velocity at the axis of the column ahead of the nose of the bubble

and U_s the superficial liquid velocity. The value of C is generally assumed to depend on the velocity profile in the liquid ahead of the bubble and can be seen as the ratio between the maximum to the mean velocity in the profile. According to this, C should be around 2 for laminar liquid flow and 1.2 for turbulent liquid flow.

Several experimental studies were carried out to test the relation between the bubble velocity and the velocity profile in the liquid ahead of it. Among these are those done by Shemer and Barnea (1987), Polonsky *et al.* (1999), Pinto *et al.* (2001b) and van Hout *et al.* (2002a). These studies covered different flow regimes and applied different techniques, but, in general, the values of the experimental constant C were in agreement with theory.

Theoretical and experimental descriptions of bubble shape were made in different studies. Dumitrescu (1943) was the first to study Taylor bubble shapes using photographs and by applying potential flow theory. Davies and Taylor (1950) also studied bubble shape, describing the bubble nose as perfectly spherical and independent of the bubble length. Layzer (1955) and later Collins (1965, 1966) and Collins *et al.* (1978) gave theoretical support to the results of Dumitrescu (1943) and Davies and Taylor (1950). Brown (1965) measured the rise velocity of Taylor bubbles in liquids with different viscosities and proposed a universal equation for the nose radius of curvature (in a vertical plane containing the axis of the column). Nickens and Yannitell (1987) studied the effect of liquid viscosity and surface tension on the bubble velocity and shape in tubes of various diameters. More recently, Polonsky *et al.* (1999) conducted quantitative measurements of the Taylor bubble shape by image analysis: film thickness, nose and bottom shapes were analysed for gas slugs rising in co-current flowing water at different flow rates. Other studies concerning bubble velocity and shape are summarised in Fabre and Liné (1992).

Both the theoretically predicted bubble shape and the shape determined by image analysis present a similar pattern. The nose of the bubble has a spheroid shape, and the body of the bubble has a cylindrical shape. Between the nose and the body, there is an intermediate region where the bubble radius increases asymptotically. In the literature the bubble shape models typically divide it into these three distinct regions.

Liquid film

The stabilised liquid film region is a critical issue in slug flow studies. Uncertainties persist regarding flow regimes and boundary conditions at the bubble-liquid interface. The

studies present some models to predict constant film thickness; mass balances are used to determine the mean film velocity, and momentum equations with estimated boundary conditions predict the velocity profile.

Dumitrescu (1943) assumed that all the liquid flow around the bubble was inviscid. Brown (1965) modified Dumitrescu's approach to supposing potential flow around the nose and a free falling liquid flow in the developed film, i.e., the liquid weight is supported by the shear stresses developed at the column wall. Based on these assumptions, Brown deduced an equation for the developed velocity profile in the liquid film:

$$V_z(r) = \frac{g\rho_l}{\mu}\left[\frac{R^2 - r^2}{4} - \frac{(R-\delta)^2}{2}\ln\left(\frac{R}{r}\right)\right] \tag{1.3}$$

Brown also stated that the stabilised film thickness could be predicted by

$$\delta = \left[\frac{3\mu U_\mathrm{b}}{2g\rho_l}(R-\delta)\right]^{1/3} \tag{1.4}$$

Fulford (1964) presented a review paper on film flow with reference to the transition from laminar to turbulent flow regime in the liquid film.

Fernandes *et al.* (1983) used Brown's analysis and introduced turbulent flow conditions to obtain a hydrodynamic model for slug flow.

Due to the thin profile of the film (around 1 mm for water), film thickness is difficult to measure accurately, as are the experimental velocity profiles in the film. Mao and Dukler (1990) studied viscosity effects on the liquid film: by increasing the viscosity, the liquid film becomes thicker and stabilises closer to the bubble nose.

DeJesus *et al.* (1995) used a photochromic dye activation technique to obtain two-dimensional velocity profiles around Taylor bubbles. Like Brown, the authors state that the liquid film accelerates downwards from the nose and far downstream, the velocity profile becomes characteristic of developing falling film flow. Ahmad *et al.* (1998) used the same technique to obtain liquid film velocity profiles. Mean liquid velocities agree with those obtained from a mass balance using Dumitrescu's bubble shape. This study was inconclusive on the stabilisation of the liquid film.

More recently, Bugg and Saad (2002) and van Hout *et al.* (2002b) applied Particle Image Velocimetry (PIV) to obtain the velocity field around Taylor bubbles rising in olive oil and water respectively. They described the development of the liquid film profile, with

a maximum velocity approaching the bubble interface as the distance from the bubble nose increases. A fully developed film was observed and the velocity profiles compared well with the predictions of Brown (1965). However, Bugg and Saad stated that PIV measurements were not available close to the gas-liquid interface because of excessive laser light reflected in this region. van Hout *et al.* (2002b) obtained results with a lower resolution. Average film velocity profiles are presented at different distances from the bubble nose. A zero shear stress at the interface is mentioned. The authors note, however, that the falling film does not stabilise due to the relatively short bubble length ($3.6D$).

Bubble wake

The falling liquid film acts as an annular jet in the liquid slug below the Taylor bubble, forming a wake whose characteristics have been studied by several researchers.

Moissis and Griffith (1962) started the investigation of flow in the wake by measuring velocity profiles at different distances from the bottom of a rising bubble in water using a Pitot-tube probe.

Maxworthy (1967), using a very simple visualisation technique, was the first to highlight the occurrence of separated flow wakes behind bubbles. Filla *et al.* (1979), concluded in a detailed study, that the wakes behind Taylor bubbles rising in water are turbulent.

Dukler *et al.* (1985) derived a model to predict the minimum stable liquid slug length, i.e., the distance necessary to redevelop the boundary layer and the velocity profile in the liquid coming from a bubble wake.

Campos and Guedes de Carvalho (1988) studied the wake of gas slugs rising in stagnant mixtures of water and glycerol over a wide range of conditions. Two different techniques were adopted to visualise the flow of the liquid in the wake. One using an inert red dye to observe the liquid transported in the wake, another using small air bubbles to trace the liquid movement and taking images with long exposure times. The authors identified three distinct wake flow regimes: laminar for $N_f < 500$, transition for $500 < N_f < 1500$ and turbulent for $N_f > 1500$. Examples of photographs showing the different types of wakes are presented in Figure 1.3. The authors found a linear correlation between the laminar wake length and N_f:

$$L_w = 0.30 + 1.22 \times 10^{-3} N_f \tag{1.5}$$

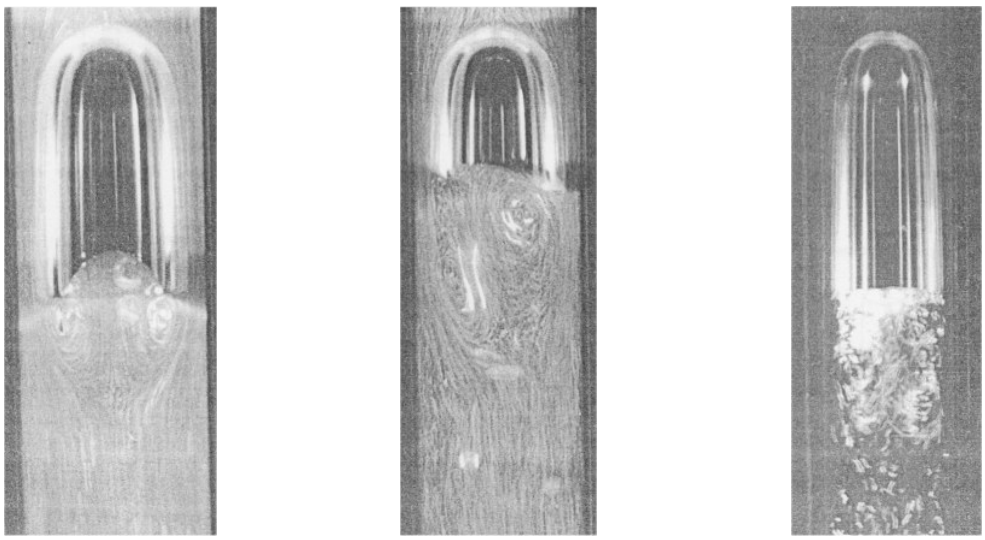

(a) laminar (b) transition (c) turbulent

Figure 1.3. Examples of wake flow patterns found by Campos and Guedes de Carvalho (1988)

Tokuhiro *et al.* (1998) measured the turbulent flow past an air bubble rising in water and a solid ellipsoid by Particle Image Velocimetry (PIV). The differences found between the flow behind the solid and the bubble were restricted to the region up to $2D$. The amplitude of the velocity oscillations were lower for the bubble than for the solid.

Polonsky *et al.* (1999) conducted an investigation on the oscillatory motion of the tail of a Taylor bubble rising in stagnant and upward-flowing water. They observed that the amplitude of the oscillations increases with the bubble length, whereas the frequency remains nearly constant.

van Hout *et al.* (2002a) applied PIV to analyse the velocity field induced by a Taylor bubble rising in stagnant water. Mean velocity fields were calculated from 100 individual bubbles. Ensemble-averaged velocities become negligible at around $12D$ from the bubble tail. However, notable instantaneous velocity fluctuations up to $50D$ were found.

Sotiriadis and Thorpe (2005) used Laser Doppler Velocimetry (LDV) to determine velocity profiles in a turbulent wake behind a cylindrical bluff body and a ventilated cavity, both maintained at a fixed vertical position with counter-current water flow. The time averaged velocities showed a toroidal vortex in both wakes with very similar structures. The axial location, where both the radial and axial velocity are zero, is at $0.72D$ and $0.78D$ below the bluff body and the ventilated cavity respectively. The end of the recirculation

region (stagnation point at the axis of the column) were located at $1.3D$ and $1.35D$ below the objects. These authors also found that the maximum axial recirculation velocity in the centre of the vortex ring was directly proportional to the mean velocity in the bottom of the annular liquid film.

Interaction between consecutive bubbles

When two or more bubbles rise simultaneously in a column, the wake of the leading bubble can affect the velocity of the trailing one, inducing coalescence of bubbles. This bubble interaction has been studied by several authors.

Moissis and Griffith (1962) observed that a trailing bubble separated by a small distance from another bubble ahead travels faster and eventually catches the leading bubble. They also stated that the wake effects were shorter for columns with smaller diameter. A correlation was found relating the rise velocity of a trailing bubble, U_{T}, with the separating distance between bubbles, l_{s}, for plastic bubble models:

$$\frac{U_T}{U_0} = 1 + 8\exp\left(-1.06\frac{l_s}{D}\right) \tag{1.6}$$

where U_0 is the drift velocity. When approaching the leading bubble, the nose of the trailing bubble loses its stable round shape and distorts, occupying alternate eccentric positions in the column cross-section.

Clift *et al.* (1974) studied the coalescence of slug pairs rising in different solutions. The results were not in agreement with the correlation found by Moissis and Griffith (1962) for a plastic bubble, showing that the different conditions at the wall near fixed and freely-rising gas slugs cause different velocity profiles in the wake and hence different behaviour of interacting slugs.

Shemer and Barnea (1987) tried to explain the interaction between bubbles flowing in water by relating the velocity of the trailing bubble to the maximum instantaneous liquid velocity ahead of it. Instantaneous velocity profiles in vertical and horizontal gas-liquid slug flows were recorded using a modified hydrogen bubble technique. Two regions were observed in the development of the velocity profile:

- In the near wake region ($z*/D < 2$), the velocity profile is highly distorted by the plunging of the falling film. A steep decrease in the maximum instantaneous liquid

velocity in a cross-section was observed as the distance to the bubble trailing edge (z*) increases.

- For $z*/D > 2$, a much more gradual decrease of the maximum instantaneous liquid velocity was observed, despite strong flow oscillations. When the nose of the trailing bubble reached this region, a random radial movement of the bubble nose was observed, in accordance to the velocity profiles obtained.

- At $z*/D > 12$, the velocity profile, although still distorted, does not differ much from the fully developed one.

Pinto and Campos (1996) conducted studies on the coalescence of pairs of Taylor bubbles rising in vertical columns, covering a wide range of liquid viscosities in three column diameters. The authors applied a technique based on the signals of differential pressure transducers to determine the distance between bubbles above which there is no interaction, l_{min}, and the approach velocity of the trailing bubble as a function of its distance to the leading one. Relations were found between l_{min} and N_f in different wake regimes:
Laminar

$$\frac{l_{\min}}{D} = 1.46 + 4.75 \times 10^{-3} N_f, \qquad 100 < N_f < 500 \tag{1.7}$$

Transition

$$\frac{l_{\min}}{D} = 6.92 \times 10^{-1} + 7.90 \times 10^{-3} N_f, \qquad 500 < N_f < 1500 \tag{1.8}$$

Turbulent

$$\frac{l_{\min}}{D} = 12.5, \qquad N_f > 1500 \tag{1.9}$$

The authors compared l_{min} with the laminar wake lengths determined by Campos and Guedes de Carvalho (1988), and found a constant ratio between them. The ratio between the velocity of a trailing bubble and the leading bubble velocity is related with the distance between the bubbles, l_s, by:

$$\frac{U_T}{U_0} = -11.4 \frac{l_s}{l_{\min}} + 4.24, \qquad l_s/l_{\min} < 0.24 \tag{1.10}$$

$$\frac{U_T}{U_0} = 2.01 - 1.96 \frac{l_s}{l_{\min}} + 0.95 \left(\frac{l_s}{l_{\min}} \right)^2, \qquad l_s/l_{\min} > 0.24 \tag{1.11}$$

The same authors later (Pinto *et al.*, 1998, 2001a,b) conducted similar studies on coalescence of pairs of Taylor bubbles rising in co-current flowing liquid and in continuous slug flow in vertical tubes of different diameters.

Tudose and Kawaji (1999) conducted studies on the total drag force on a stationary solid model of a Taylor bubble placed in a downward flowing liquid stream. The authors concluded that the drag force decreases when the bubble nose is deformed and the nose tip deviates from the tube axis. Using two solid bubble models they found that the drag force on the second bubble increased gradually over an increasing separation distance up to about two column diameters.

Talvy *et al.* (2000) studied the interaction between two consecutive Taylor bubbles rising in stagnant water using an image processing technique. An acceleration of the trailing bubble in the near wake was observed, despite some instantaneous decelerations. An influence on the trailing bubble velocity was observed (in turbulent water conditions) even at distances exceeding 50 column diameters from the leading bubble trailing edge.

Many other studies have been conducted covering a wide range of subjects not mentioned here, such as the influence on the hydrodynamics of the column inclination (Zukoski, 1966), mass transfer studies (Delfos *et al.*, 2001; Elperin and Fominykh, 1995) or gas holdup (Pinheiro *et al.*, 2000).

The modelling of slug flow, by applying experimental correlations, theoretical models or by CFD simulations has been carried out by several authors (Clift *et al.*, 1974; Taitel *et al.*, 1980; Dukler *et al.*, 1985; Fabre and Liné, 1992; Hasanein *et al.*, 1996; Clarke and Issa, 1997; Bugg *et al.*, 1998)

All the studies mentioned were made with air bubbles flowing in Newtonian liquids, mainly water and water/glycerol mixtures. The research with non-Newtonian liquids is described in the following section.

1.2 Two-phase flow with non-Newtonian liquids

1.2.1 Non-Newtonian liquids

In our daily life, we are in contact mainly with low molecular weight fluids such as air and water, which have Newtonian behaviour. Due to their abundance these fluids are the object of most of the studies in fluid mechanics. They are called Newtonian fluids since

they obey Newton's viscosity law (Eq. 1.12). Consider two plates separated by a liquid (Figure 1.4), the upper plate with surface area $A(\mathrm{m}^2)$ is put into movement by a constant

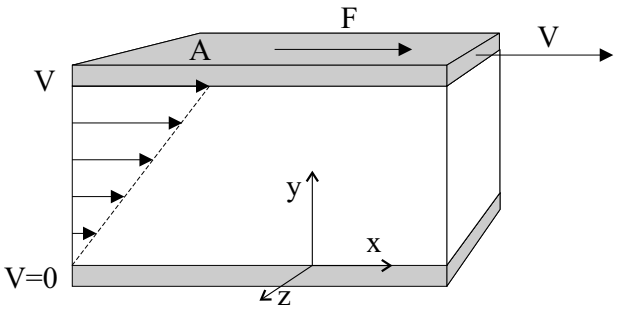

Figure 1.4. Laminar flow between two plates.

force $F(\mathrm{N})$ in the x direction with speed $V(\mathrm{m/s})$ and the lower plate is maintained in a fixed position. If a laminar flow is established in the liquid between the plates, the ratio between the force per unit area, $\tau_{yx} = F/A$ (Pa) and the velocity gradient, $\dot{\gamma} = \partial V_x/\partial y$ (s^{-1}) is constant for a Newtonian fluid:

$$\tau_{yx} = \mu\dot{\gamma} \tag{1.12}$$

being the constant of proportionality, μ, the viscosity of the fluid, τ_{yx} the shear stress exerted in a plane perpendicular to y in the direction of x, and $\dot{\gamma}$ the shear rate.

All fluids in which equation 1.12 is not applicable are called non-Newtonian fluids, and are characterised by an apparent viscosity that depends on the shear rate. Different relations between the shear rate and the shear stress create different categories of non-Newtonian fluids, as illustrated in the examples of Figure 1.5.

Apart from these examples of non-Newtonian fluids there are others that have a yield stress, which means that they only flow if the applied shear stresses are higher than that value. Besides the shear rate-dependent viscosity of non-Newtonian fluids, some of them have other relevant features. Some fluids have a time-dependent viscosity, which might decrease (thixotropy) or increase (rheopexy) with time at a constant applied shear rate. Some also have the ability to partially recover from a deformation once the acting force is removed, which means they have some elasticity.

Another important difference relative to Newtonian fluids is that these can exhibit non zero normal stress differences. It is not possible to measure individual normal stress, but

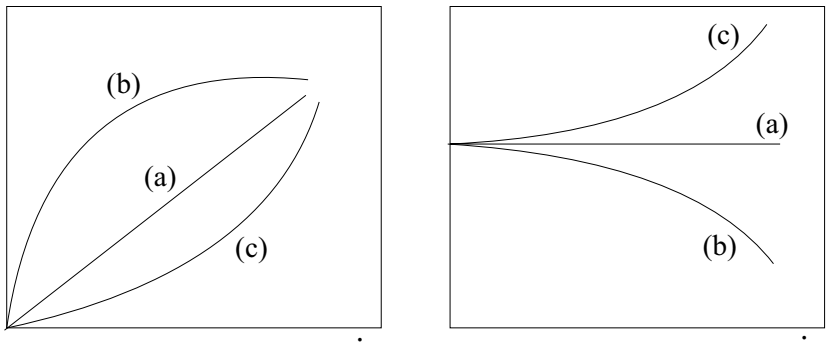

Figure 1.5. Comparison between (a) Newtonian fluid, (b) pseudoplastic or shear thinning fluid and (c) dilatant or shear thickening fluid.

only their differences: $N_1 = \tau_{xx} - \tau_{yy}$ and $N_2 = \tau_{yy} - \tau_{zz}$, being x considered the principal direction of the flow, y and z the other two perpendicular directions. While for Newtonian fluids, the normal stress differences are exactly zero in shearing flow, for polymeric fluids the first normal stress difference is practically always negative and numerically much higher than the second normal stress difference. This means that, in general, polymeric fluids exhibit in addition to the shear stresses, extra stresses in the x direction, behaving as if they were under tension in this direction.

The normal stress differences, extensional stresses and elastic effects are responsible for numerous phenomena not observed in Newtonian liquids, such as those shown in the examples of Figure 1.6. In Figure 1.6(a), a cylinder is rotating, immersed in glycerine (left) and in a non-Newtonian fluid (right). In the glycerine, due to centrifugal forces, the liquid is pushed outwards and a depression is observed in the liquid surface at the middle of the container. In the non-Newtonian liquid, the normal stresses tend to compress the liquid in the direction of the flow, making it rise up the rotating cylinder since the liquid is not compressible. In Figure 1.6(b), liquid is seen coming out of two tubes with small diameters. On the left a Newtonian liquid maintains a stream diameter practically equal to the tube diameter. On the right the fluid expands radially, increasing the stream diameter. In Figure 1.6(c), fluid was initially sucked into an immersed straw. When the straw emerges from the liquid a syphon flow is maintained to the straw due to the large extensional stresses. More detailed information on non-Newtonian fluids and their constitutive equations can be obtained in Bird *et al.* (1987).

In terms of varieties, there are many more non-Newtonian than Newtonian fluids on

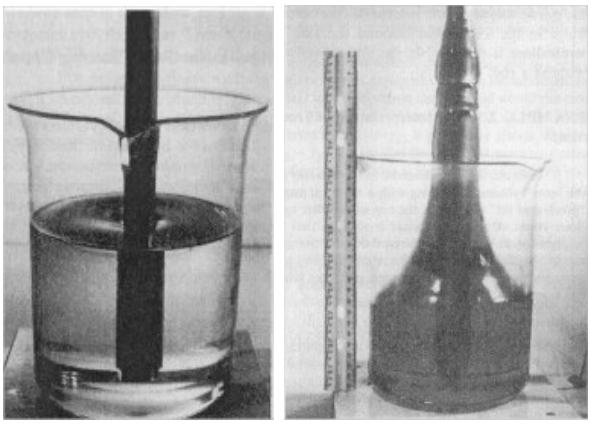

(a)

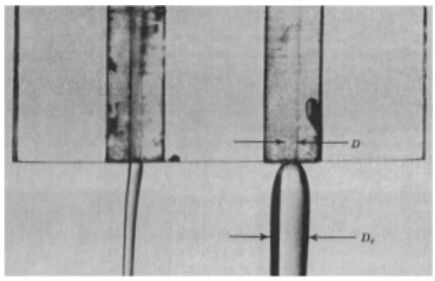

(b)

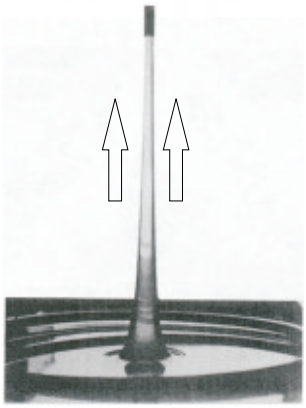

(c)

Figure 1.6. Examples of non-Newtonian flow phenomena (from Bird *et al.* (1987)); (a) normal vortex in glycerine (left), climbing rod in non-Newtonian solution (right) when a cylinder is rotating; (b) behaviour of fluids issuing from orifices: no diameter increase in Newtonian solutions (left), stream diameter increase by a factor of 3 in a non-Newtonian solution; (c) tubeless siphon where a non-Newtonian fluid is being sucked up, indicating a high extensional viscosity.

our planet. Examples of non-Newtonian fluids are human blood, volcano lava, tooth paste, ketchup, resins, paints and polymeric solutions in general and many others.

Since there can be huge differences between the behaviour of Newtonian and non-Newtonian fluids in similar flow conditions, there has been increasing interest in the study of non-Newtonian flows in the last decade.

1.2.2 Bubbly flow in non-Newtonian liquids

The investigation of gas-liquid flows with non-Newtonian liquids has been mainly on bubbly flow, or on the flow around small individual unconfined bubbles.

The first studies reporting on the motion of gas bubbles in non-Newtonian liquids are those of Astarita and Apuzzo (1965). The authors studied the velocity and shape of small gas bubbles rising in Carbopol and Carboxymethylcellulose (CMC) solutions. Discontinuity was seen in the velocity-volume data, where a jump in the velocity occurs above a certain bubble volume. An interpretation of this phenomenon was given, based on a change of flow regime around the bubbles where viscoelasticity is considered to play an important role.

Leal *et al.* (1971) theoretically and experimentally studied the drift velocity jump on bubbles rising in a Separan solution, also stating that viscoelasticity should be taken into account when analysing the problem and that a transition from Stokes to Hadamard regime could be the cause of the discontinuity.

Ting (1975) conducted a theoretical analysis on the effect of viscoelasticity on the growth and collapse of small air bubbles rising in polymeric solutions.

Acharya *et al.* (1977) studied the drag coefficient on isolated gas bubbles moving in low and high Reynolds number regions, bubble shape and the velocity transition and discontinuity. A tear-shaped bubble was found at small Reynolds numbers. With increasing Reynolds numbers the shapes tended to be spherical, oblate spheroidal and finally spherical capped. Later, Acharya and Ulbrecht (1978) studied the effect of viscoelasticity on the coalescence rate of bubbles and drops, concluding that the increase of liquid viscosity enhances the coalescence rate. However, elasticity plays an opposite role. The time that the bubbles take to coalesce after touching is increased due to a higher resistance in the film separating two bubbles before the collapse.

Bhavaraju *et al.* (1978) studied the drag and mass transfer coefficients for a single

bubble moving in power law and Bingham plastic fluids.

Hassager (1979) used a Laser Doppler Anemometry technique to measure the liquid velocity in the wake behind air bubbles rising in Polyacrylamide/Glycerol solutions. The measurements revealed for the first time that the liquid behind the bubbles can flow in a downward direction (opposite to the bubble movement). This liquid, moving in a direction opposed to that usually found in Newtonian liquids, was called a negative wake by the authors. Photographs also revealed that the shape of the bubble at the rear pole is not that of a symmetric cusp but that of a knife edge. Images of the shape of a bubble rising in a polyacrylamide (PAA) solution are presented in Figure 1.7, seen from two perpendicular angles.

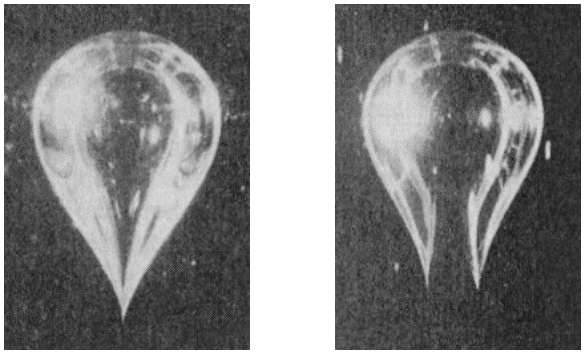

Figure 1.7. Images of a small bubble rising in a polyacrylamide (PAA) solution seen from two perpendicular angles, extracted from Bird *et al.* (1987).

Coutanceau and Hajjam (1982) studied the effects of viscoelasticity on the behaviour of a single air bubble rising in a tube. The authors observed that elasticity does not significantly modify the cross-section and upper part of the bubble. In contrast to a Newtonian liquid, elasticity causes a needle-like tail to appear in the bubble. Regarding the speed of the bubble, elasticity and shear thinning effects cause an increase in bubble velocity compared to a Newtonian liquid with the same reference viscosity. Using long exposure time images to visualise the path of tracer particles confirmed the existence of a negative wake behind bubbles rising in some of the non-Newtonian liquids studied.

Dekée *et al.* (1986) conducted studies on bubble velocity and coalescence in viscoelastic liquids. The velocity-volume data in a CMC solution in water and in a PAA solution in glycerol did not show any discontinuity. There was also no appreciable effect of the time between bubble injections on their drift velocities.

Vatai and Tetik (1987) studied the effect of liquid properties and gas superficial velocity on the local and mean gas hold-up in bubble columns filled with CMC solutions.

Liu *et al.* (1995) describe a two-dimensional cusp at the trailing edge of air bubbles rising in Polyox solutions. No preferred orientation of the cusp was found in circular tubes. Different shapes of the cusp were found, varying from flat like a spade, arched like an axe, pointed like an arrow or flat and tilted like a guillotine.

Li *et al.* (1997a,b, 1998) studied in-line bubble interactions and coalescence in non-Newtonian fluids. A rheological simulation taking into account the experimental time gap between bubble injections and bubble rise velocity showed, for the first time, the accumulation of residual stresses in non-Newtonian fluids after the passage of a chain of bubbles. The relaxation of these residual stresses, closely related with the drag decrease, is therefore the dominant mechanism governing the interactions and coalescence between bubbles. The effect of the time gap between consecutive bubbles was experimentally tested and it was observed that bubble rise velocity increases when shorter time intervals are used.

Rodrigue *et al.* (1998) reviewed the experimental data regarding the abrupt discontinuity in the velocity-volume curves of the gas bubbles rising freely in viscoelastic fluids. The author developed a new criterium based on a modified Capillary number, which takes into account the various characteristic forces in competition in this kind of flow.

Brujan (1999) investigated the theory of dynamical behaviour of a spherical bubble rising in a viscoelastic liquid.

Rodrigue *et al.* (1999) studied the effect of surfactant in non-Newtonian liquids on the drag force of a single gas bubble, concluding that the drag force increases with the presence of contamination, resulting decreased bubble velocity.

Margaritis *et al.* (1999) conducted studies on the rise velocity and drag force coefficient of bubbles in non-Newtonian polysaccharide solutions. They found that bubble velocity reaches a plateau at high bubble volumes. The data analysed from 21 polysaccharide solutions was represented by a single curve relating the drag force coefficient and the Reynolds number.

Wagner (2000) simulated the movement of a bubble rising in a viscoelastic fluid, and was able to reproduce the experimentally observed cusp at the trailing edge of the bubble.

Funfschilling and Li (2001) applied PIV and birefringence visualisation to analyse the flow of non-Newtonian fluids around bubbles rising in PAA solutions. The negative wake behind the bubbles was described. The birefringence visualisations revealed a butterfly-

like spatial distribution of shear stresses between the negative wake and an upward conical flow. These stresses display a temporarily reduced local fluid viscosity which is responsible for the interactions and coalescence between bubbles rising in such media.

Li *et al.* (2001) established a coherent physical picture for the rise of a chain of bubbles in non-Newtonian fluids, using rheological simulation, birefringence visualisation and PIV measurements. The dynamic competition between the stresses created after the passage of bubbles and their relaxation, temporarily forming a corridor of reduced viscosity, is clearly identified as the mechanism governing in-line interactions and coalescence. It means that coalescence is dependent on the relation between the relaxation time of the fluid and the time gap between consecutive bubbles.

De Kee and Chan Man Fong (2002) extended the models developed by Richardson (1968) to a non-Newtonian fluid in order to study the bubble shape.

Herrera-Velarde *et al.* (2003) conducted PIV measurements in the flow around bubbles rising in non-Newtonian fluids. A connection was made between the negative wakes behind the bubbles and the jump discontinuity on the velocity-volume data. The negative wake appears above a certain bubble volume when the bubble becomes cusp-shaped.

Negative wakes were also found behind spheres settling in non-Newtonian liquids, as reported by Joseph and Feng (1995), Arigo and McKinley (1998) and Harlen (2002).

1.2.3 Slug flow in non-Newtonian liquids

Very few studies are found in the literature concerning slug flow in non-Newtonian liquids.

Rosehart *et al.* (1972) carried out studies on horizontal co-current slug flow for the case of a liquid-phase containing small amounts of polyacrylamide. A pressure drop reduction was observed relative to that in a single phase with the same superficial liquid velocities. Later, Rosehart *et al.* (1975) made complementary studies on horizontal co-current slug flow, presenting correlations for void fraction, slug velocity and slug frequency in solutions of Carboxymethylcellulose (CMC), Carbopol and Polyhall.

Otten and Fayed (1976) continued the work of Rosehart conducting studies on pressure drop and drag force in horizontal slug flow.

Carew *et al.* (1995) studied the motion of long bubbles in inclined columns containing Newtonian and non-Newtonian liquids. A physically based correlation was found for the

effects of power law rheology and inclination of the column on the slug bubble rise velocity. Similar studies were made by Sousa *et al.* (1996) in Xanthan gum solutions, where higher bubble velocities were found than in an air-water system when the column inclination was around 45^o.

Kamışlı (2003) derived an one-dimensional flow equation for the motion of a long bubble rising steadily in a vertical or inclined tube filled with a power-law fluid. The theoretical analysis indicates that the liquid film thickness increases with decreasing power-law index. It was also found that, in general, viscoelastic effects tend to reduce the film thickness compared with that predicted by pure viscous theory.

Terasaka and Tsuge (2003) conducted studies on the gas hold-up for slug flow with viscous liquids presenting a yield stress (Carbopol and Xantham gum).

1.3 Experimental techniques - PIV in two-phase flow

In the experimental works conducted in slug flow, a lot of different techniques were used to obtain information about the several flow parameters in analysis.

Concerning the bubble velocity and length, most of the techniques are based on the time the bubble takes to travel a certain distance. This elapsed time has been measured in different ways: using conductive wires, impedance probes, differential pressure transducers, optical fibre sensors and image analysis.

The liquid flow pattern around the Taylor bubbles has also been studied using different techniques. Firstly by intrusive methods such as Pitot-tube probes and conductive wires, which interfere with the flow pattern, then by using tracers; small particles, hydrogen bubbles or coloured liquid.

With the development of laser technology new techniques were applied, such as Laser Doppler Velocimetry, where velocity measurements are taken at a single point in a non-intrusive way.

Increasing memory capacity and processing velocity of computers and video cameras led to the development of Particle Image Velocimetry, with which fluid velocity can be determined simultaneously in a two dimensional measurement plane. This technique consists of acquiring images of seed particles in a two dimensional plane, at consecutive instants. From the correlation between the consecutive images of the particles, the displacement of groups of particles can be determined, which, in the appropriate conditions, should cor-

respond to the liquid displacement. From the known time gap between images, the two dimensional velocity field can be determined. This technique has been developed in recent years and is now commonly used.

A good review of the principles of the PIV technique, its development in the last 20 years and the perspective for future improvement are well summarised in Adrian (1991, 2004).

A model was developed by Keane and Adrian (1990) to analyse and optimise different experimental parameters on Particle Image Velocimetry. The authors recommend several criteria in relation to particle image density, particle image size, out of plane movement, signal to noise ratio threshold and others.

The post-processing methods are also under constant improvement. For this work, the algorithm developed by Scarano and Riethmuller (1999), Window Distortion Iterative Multigrid (WIDIM), was used. The method is based on a cross-correlation, making use of a translation of the interrogation areas. Such a displacement is predicted and corrected by means of an iterative procedure. In addition to iterating, this method allows refinement of the size of the interrogation areas. The quality of the measured vectors is controlled by data validation criteria applied at each intermediate step of the iteration process. The developments in the algorithm enable an enlargement of the measurable dynamic range. The minimum measurable displacement is reduced by about two thirds and the maximum allowable displacement was increased four times in comparison with a previously used method. Scarano (2000a) introduced an intermediate step in the processing, where windows are distorted according to local deformation of the fluid continuum, enlarging the accessible velocity gradient range.

Despite the wide range of applications for the PIV technique, its use in two-phase flow has encountered some difficulties in the interfaces. A review of using PIV-techniques in dispersed two-phase flows is given by Brücker (2000). One problem that arises in two-phase flow is the reflection from the light used to illuminate the particles at the gas-liquid interface. To solve this problem fluorescent particles are used, which emit light at a different wavelength than the laser light. This way, an optical filter can be used to suppress the laser light and allow the passage of the light emitted by the particles. This solution was first applied by Hassan *et al.* (1993) being also described in Philip *et al.* (1994).

Hassan *et al.* (1992) conducted simultaneous velocity measurements of both fluids of a two-phase flow using PIV. The camera resolution was relatively low (256 x 256 pixels^2)

and a point-by-point spatial cross-correlation was used to obtain the velocity fields. Plastic spheres of 70 µm were used as seeding. Since neither fluorescent particles nor a filter were used, large circular halos were found around the bubbles. These circular areas of increased grey level intensity are associated with direct laser light reflection from the surfaces of the bubbles. The individual bubbles could not be distinguished as separate entities by the applied algorithm and a grey level threshold had to be defined to limit the extent of the halos reflection.

Tsuei and Savaş (2000) presented a fist order accurate method of extending the capability of image velocimetry to interfaces. This method uses the velocity information embedded in a pair of PIV flow images. This intrinsic information is used to extend the image data fields across the interface continuously by locally translating and reflecting across the interface and reversing the order of images.

Another problem with two-phase flow is that the interfaces are not static, which means that determining its position is essential. In fixed solid interfaces masks can be used to impose the known zero velocities, which is impossible to do with gas-liquid interfaces where the velocities are unknown. Optical problems at the interface of gas bubbles were observed in bubbly flow by Dias and Riethmuller (1998) and analysed with silicon models by Nogueira *et al.* (2000). The authors describe the reflection and refraction of the light emitted by the particles at the bubble interface, which lead to the processing of erroneous vectors and a wrong identification of the bubble interface.

Tokuhiro *et al.* (1998) applied PIV and shadow-image techniques to analyse the turbulent flow past a bubble and an ellipsoid. Velocity measurements of the flow field around the bubble or solid were made using a CCD (Charged Coupled Device) camera enhanced by Laser Induced Fluorescent (LIF). The shape of the bubble or solid was simultaneously recorded with its velocity using a second CCD camera and an Infrared Shadow Technique (IST). In this way, both the flow-field and the boundary of the bubble were measured. The authors reported problems with reflections at the bubble interface if fluorescent particles and an optical filter were not used. Their images suggest, however, that high reflections are still visible at the bubble interface. It is also mentioned that in the part of the laser plane opposite to the laser source, a higher uncertainty is introduced due to the partial shadow created by the bubble which reduces the laser intensity.

Gui *et al.* (1996) developed a digital mask technique to separate the velocity measurements in both phases of a two-phase flow. The method is based on the significant difference

of the size distribution of the phases. The technique also accounts for differences in the velocity distribution in the phases and for the fact that small particles can be obscured by large particles. A technique combining PIV with fluorescent particles, shadowgraphy and digital phase separation with a masking technique was applied by Lindken and Merzkirch (2002) to bubbly flow to overcome the described optical problems at the interface. The technique consists of placing a background light pulsing simultaneously with the lasers that illuminate the seeding particles, creating a difference between the grey level of the liquid and gas phases (shadowgraphy). This difference in grey levels allows for a clear identification of both phases. Thus, only one CCD camera is needed. This technique applied in bubbly flow was adapted to slug flow in the present work and is described in detail in a following section.

Gouriet *et al.* (2001) analysed the effect of the camera resolution and peak locking in actual measurements. The authors concluded that the processing of synthetic images and real images had shown that lowering the quantisation quality (12 to 8 bits) does not affect the correlation robustness if the most significant bits are preserved. Furthermore, converting images with less significant bits alters the robustness without affecting the measurements quality. However, using a high sensitivity camera can be beneficial in several applications since it improves the margin for blooming and allows lower laser power.

In the studies conducted by Funfschilling and Li (2001) on the flow around small bubbles rising in non-Newtonian liquids, a commercial PIV system from Dantec Inc. was used. Fluorescent particles were used with an optical filter to eliminate the reflections of the laser light on the bubbles. No shadowgraphy was used and so it was difficult to determine the separation between gas and liquid phases from the presented flow fields.

Herrera-Velarde *et al.* (2003) conducted similar studies. Fluorescent particles and an optical filter were also used. No shadowgraphy was used but there are images which seem to be a simple overlapping of bubble photographs with the flow field in an approximate position.

Very few studies were conducted applying PIV in slug flow and none of them used non-Newtonian liquids.

Polonsky *et al.* (1999) applied PIV to study the flow ahead of and in the liquid film of Taylor bubbles rising in stagnant and co-current water. An interlaced image technique was used to perform the PIV measurements around the nose of the bubbles, which was inappropriate to measure higher liquid velocities like the ones in the liquid film due to

the adopted fixed time between frames. A streak length method was used to measure the velocities in the liquid film by leaving the camera open for longer exposure times, so that in each frame the particles produce streaks whose lengths are proportional to the liquid velocity. Fluorescent particles were used with an optical filter to reduce the laser reflections. The shape of the bubbles was determined separately by filming the bubble rising in coloured water illuminated by a 5 W laser. No results are presented close to the bubble interface.

van Hout *et al.* (2002a) continued the studies of Polonsky, conducting studies on the complete flow field around Taylor bubbles rising in stagnant water using PIV. Fluorescent particles and an optical filter were also used and commercially available software from Savant was used to display and capture the images. The bubble shape was also determined separately, which does not allow accurate measurements, especially in the bottom of the bubble due to the random trailing edge oscillations.

Bugg and Saad (2002), studied the flow around a single Taylor bubble rising in stagnant olive oil. No shadow technique was used, and the bubble shape was determined by hand directly from the PIV images. This is inaccurate due to the optical problems already mentioned. Neither fluorescent particles nor an optical filter were used, which created higher reflections at the interface and so no results were available close to the gas-liquid interface. A 3x3 median filter was applied to the vector field to correct erroneous vectors.

As seen from this bibliographic survey, prior to the present work there were very few studies applying PIV to slug flow. None of them used PIV and simultaneous shadowgraphy and none of them was about slug flow in non-Newtonian liquids, which demonstrates the originality of the present work.

Chapter 2

Experimental techniques

Abstract

This chapter describes the experimental techniques used in the preliminary visualisation studies and in the flow field measurements with Particle Image Velocimetry. The experimental procedure and data processing are also presented.

2.1 Visualisation studies

The flow of Taylor bubbles in non-Newtonian liquids is a subject which has not been deeply studied. Therefore, some preliminary visualisation studies were made in order to get an idea of the liquid and gas behaviour in a wide range of conditions. To perform these studies, different non-Newtonian liquids, polymer solutions with different weight percentages, were used.

The technique described by Campos and Guedes de Carvalho (1988) was employed to visualise the wake structure of the Taylor bubbles. This technique involves filling an acrylic tube with a solution, the lower part of which is coloured and the upper part colourless. A closed globe valve prevents initial contact between the solutions. The valve is opened and a Taylor bubble is released at the bottom of the tube, i.e, in the coloured solution. When the bubble reaches the colourless liquid it is possible to see if any liquid is transported in the wake by analysing the colour of the solution behind the bubble. If there is a colour trail it is possible to visualise the wake structure. In the next sections the equipment with which this technique was implemented and the experimental procedure are described.

2.1.1 Experimental setup

The solutions used in the visualisation studies were prepared by continuously stirring the required quantity of polymer in 10 litres of water for 24 hours. Some of this solution was poured into a separate container and an inert red dye was added and uniformly dissolved with a few minutes of stirring, resulting in a coloured liquid.

The visualisation studies were made in an apparatus setup represented in Figure 2.1. It consists of a 32 mm perspex column (internal diameter) divided in two parts by a globe valve: the lower part where the bubble was injected and the upper part where the visualisation took place. The lower part was filled with the coloured solution and, with the globe valve closed to avoid mixing, the upper part was filled with the colourless solution. In the upper part of the column, the test section, an optical box (dimensions, 400 mm x 110 mm x 110 mm) with plane faces was filled with the colourless solution to reduce the optical distortion caused by the column curvature and differences in the refraction indexes (Perspex, air and liquid).

Behind the optical box, two spot-lights (150W each) illuminated a white background paper which reflected and diffused light. To reduce reflections in the bubble interface

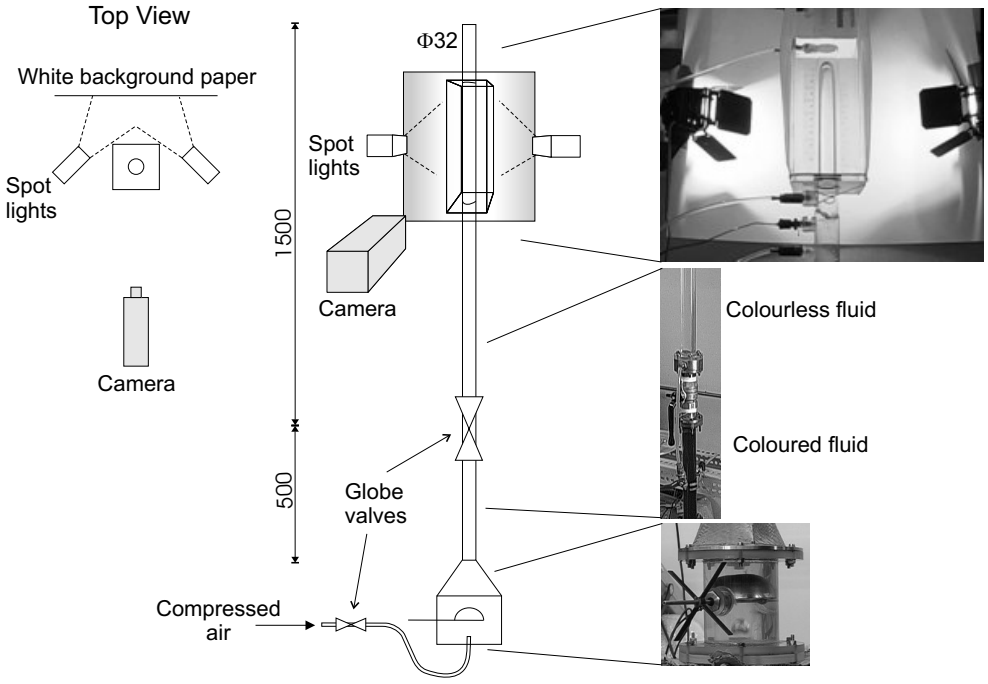

Figure 2.1. Experimental setup used in the visualisation studies (dimensions in mm).

ambient light was kept to a minimum and the box surfaces were covered with opaque paper, except for the front and back faces.

The Taylor bubbles were formed by injecting compressed air into a hemispherical cup at the bottom of the column. With the concavity facing downwards the cup encapsulated the injected air. After the globe valve was opened, rotation of the hemispherical cup released the trapped air in the form of a long Taylor bubble, first passing through a conical section to avoid bubble break up.

A digital camera (3CCD Cannon XM1) was placed perpendicular to the front box face. Bubble images (720×576 pixels^2) were acquired at a 25Hz frequency, with an exposure time of 1/2000 s. Scales were placed on the front and back faces of the optical box, to determine the correspondence between the image pixels and the real dimensions.

The experiments were conducted at ambient temperature and a K-type thermocouple was placed on the column, below the test section, to measure the fluid temperature.

2.1.2 Bubble velocity and length

For each bubble, a small video sequence was taken with the frames separated by 0.04 seconds (25 Hz acquisition frequency). From these frames it is possible to compute the bubble velocity and length.

In Figure 2.2, three frames of a video sequence are represented. In this figure two scales are seen, one on each side of the image and with known horizontal and vertical dimensions. The left and right scales were glued to the front and back faces of the optical

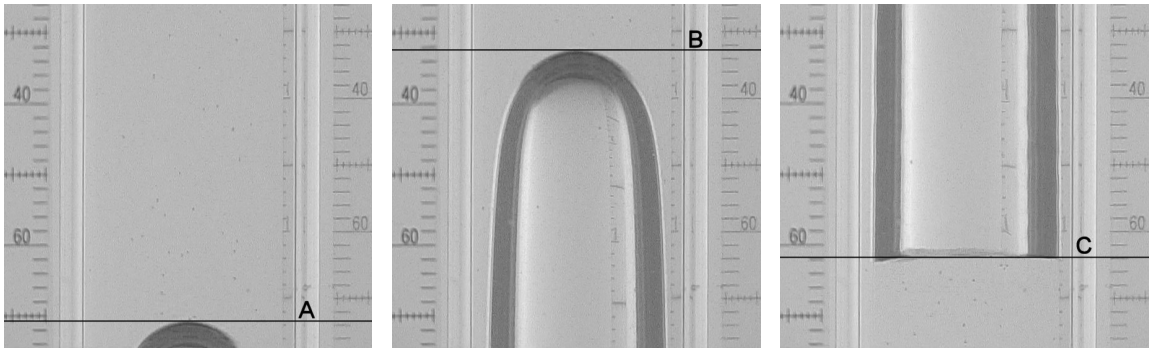

(a) (b) (c)

Figure 2.2. Examples of images extracted from a video sequence; frames 1(a), 6(b) and 16(c).

box respectively. From each scale the relation between the real dimensions of the objects and the number of pixels in the image was obtained; their average gives the corresponding relation at the vertical plane parallel to the paper, containing the axis of the column. In the case shown in Figure 2.2, the relation is $HC = 10.5$ pixels/mm in the horizontal direction and $VC = 11.2$ pixels/mm in the vertical direction. This difference is due to the fact that the pixels in the acquired images are not squared but have a 1.067 ratio between the horizontal and vertical dimension. The horizontal scale was also confirmed by measuring the known internal column diameter.

Bubble velocity can be determined by dividing the distance travelled by the bubble nose between two frames by the time gap between frames. From images (a) and (b) in Figure 2.2, the distance travelled by the bubble is determined by converting the number of pixels between lines A and B with the vertical calibration. In this case,

$$\Delta z = \frac{(513 - 74)(\text{pixels})}{1000(\text{mm/m}) \cdot VC(\text{pixels/mm})} = 0.0392\,\text{m}$$

The elapsed time between the images is equal to the number of frames multiplied by the time between frames, so the bubble velocity is given by

$$U_\text{b} = \frac{\Delta z}{(6 - 1) \cdot 0.04} = 0.196\,\text{m/s}$$

With the known bubble velocity it is possible to determine the bubble length from images of the bubble nose and bottom (Figure 2.2(b) and 2.2(c)). The bubble length is given by the distance travelled by the bubble nose between frames 6 and 16

$$\Delta z' = U_\text{b} \cdot (16 - 6) \cdot 0.04 = 0.0784\,\text{m}$$

plus the distance between lines B and C. The distance between lines B and C is determined in a similar way as the distance between A and B. Therefore, the bubble length is given by

$$L_\text{b} = \Delta z' + \frac{(409 - 74)}{1000 \cdot VC} = 0.108\,\text{m}$$

The uncertainty analysis of the bubble velocity and length determination can be found in Appendix B, where an uncertainty of 0.001 m/s is estimated for the bubble velocity and 0.001 m for the bubble length when there are no oscillations of the bubble trailing edge.

2.1.3 Wake flow pattern

When coloured liquid is transported in the bubble wake, it is possible to visualise the wake structure. In Figure 2.3 an example of the wake of a Taylor bubble rising in a 0.40 wt% CMC solution is presented. In this figure the wake structure, a donut shaped vortex (red

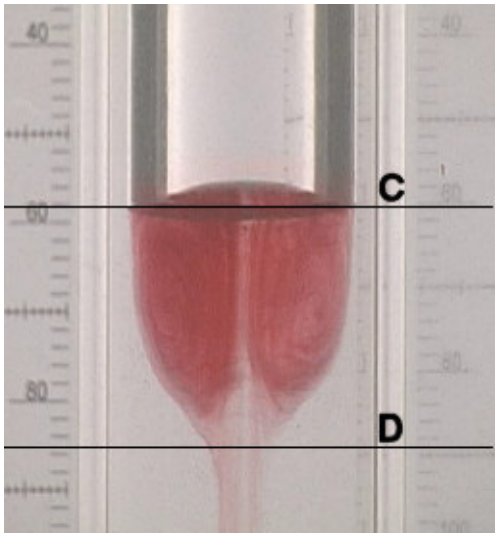

Figure 2.3. Visualisation of the wake of a Taylor bubble rising in a 0.4 wt% CMC solution.

coloured fluid) attached to the bubble, is clearly seen. From the figure it is possible to determine the wake length, by measuring the distance between lines C and D. In this case the wake length is about 0.028 m. Above line C some red fluid is seen, due to the concavity of the bubble trailing edge. This small portion of fluid was not taken into account in measuring the wake length since there is a strong optical distortion in this region caused by the curvature of the bubble interface and by the difference in the refractive indexes of the air and liquid.

For cases in which the wake is closed a program in Visual Basic was developed to calculate the wake volume, and also the bubble velocity and length as described in the previous section. Figure 2.4 shows a screen from this program. After having defined the wake contour (green line), the program determines the wake volume by summing infinitesimal cylindrical volumes (axi-symmetry is assumed).

The visualisation studies were helpful for obtaining information about the wake structure and bubble dynamics in a large range of polymer weight percentages, information which has not been described in previous literature. Concerning the liquid flow pattern,

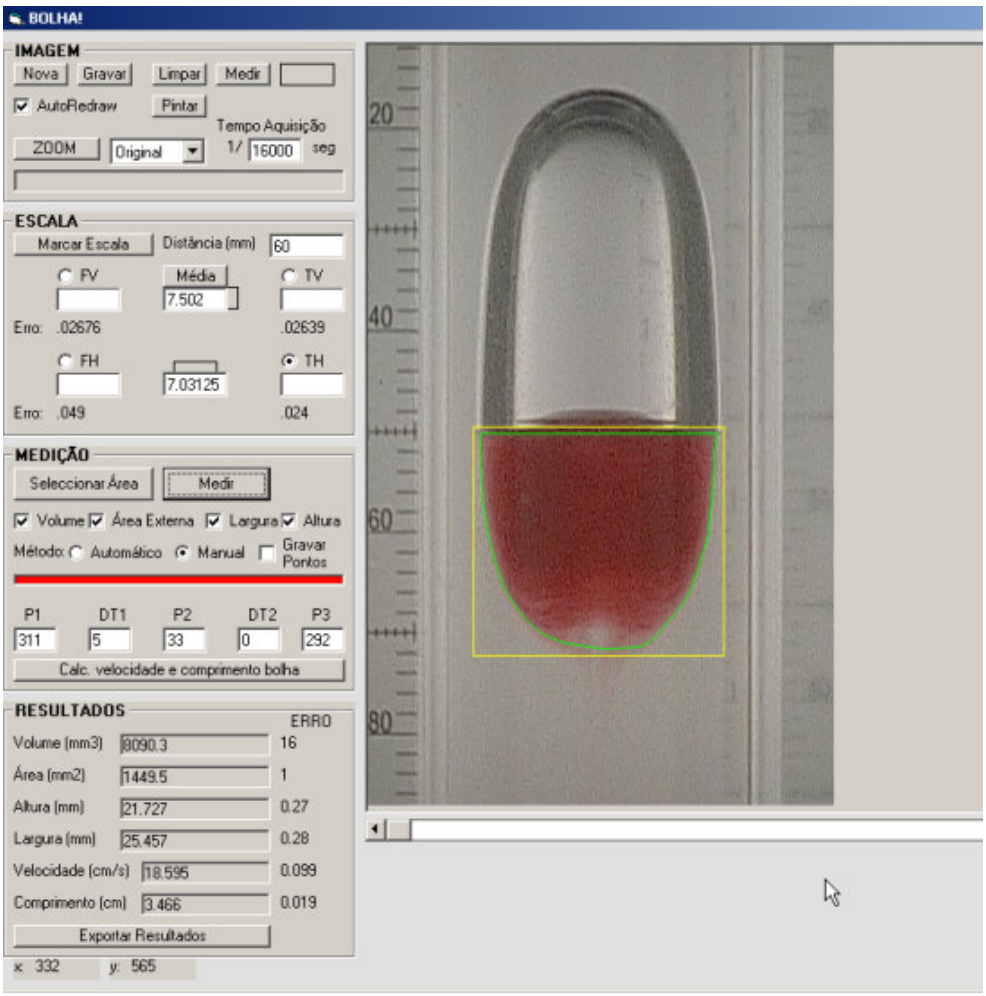

Figure 2.4. Screen of the program developed to determine the wake volume.

only qualitative information was obtained with this technique. However, this research was a necessary step in order to select cases that could be analysed in more detail. This detailed study was made employing the PIV technique described in the next section.

2.2 Particle Image Velocimetry / Shadowgraphy Technique (PIV/ST)

The flow field around Taylor bubbles was obtained using the Particle Image Velocimetry (PIV) technique. This technique involves measuring the displacement of very small particles in suspension in the fluid over a very short time interval. Assuming that the particles faithfully follow the fluid movement, the local fluid velocity can be obtained. Displacement of the particles is determined by acquiring images at a precise time gap. If images of all the particles in a three dimensional region were taken, it would be very difficult to find the position of the same particle in two consecutive images. Even if this was feasible, with only one camera the images would not show more than the two dimensional projection of the actual three dimensional particle displacement.

In this work, as in most applications of PIV, the objective is to determine the velocity field in a certain plane region. By using a single video camera only two dimensional velocity fields can be obtained and so the data processing becomes much easier since only images of particles in a specific plane are recorded. This is done by taking images of the flow in a dark room and illuminating only the particles in a thin plane of interest.

A general description of the experimental setup is presented in the next section, followed by a more detailed explanation of different aspects of the technique.

2.2.1 Experimental setup

The simultaneous PIV and Shadowgraphy technique was developed and applied in The von Karman Institute for Fluid Dynamics. A general view of the experimental setup is represented in Figure 2.5.

The solutions were prepared by stirring the required quantity of polymer in 24 litres of water for more than 12 hours. After addition of the PIV seeding particles, the fluid was placed in tank 1. The perspex column, with a height of 6 m and a 32 mm internal diameter, was filled by pumping the liquid contained in tank 1.

The Taylor bubbles were formed by manipulating the pneumatic valves V_1–V_5. With all valves closed, when V_2 is opened the liquid between valves V_1 and V_2 falls back to tank 1. Closing V_2 and opening V_1 releases the air trapped between these valves to rise up the column, first passing through a conical section to reduce bubble fragmentation and

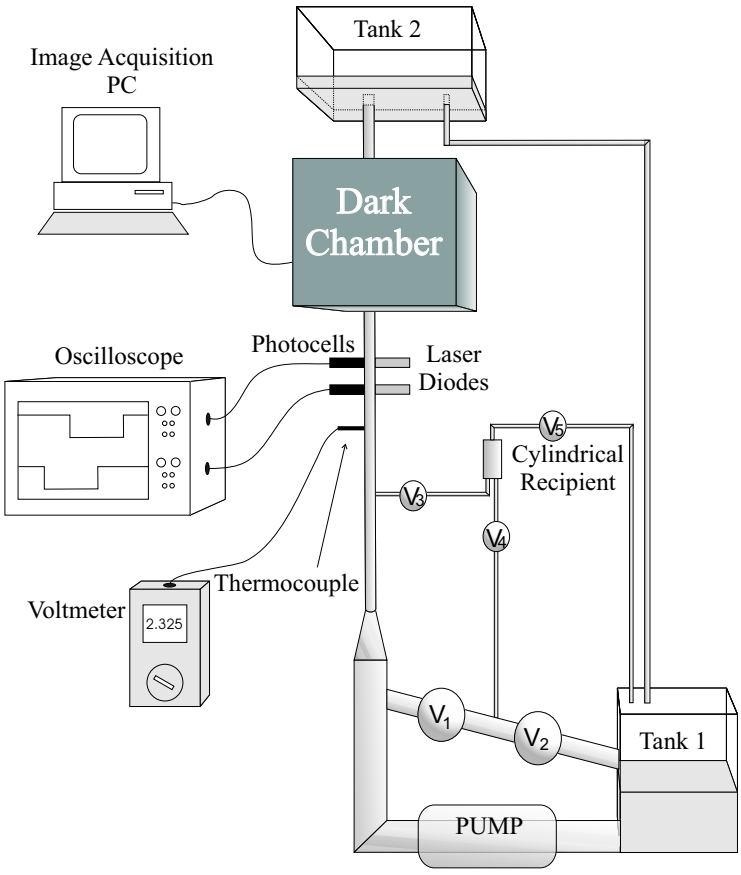

Figure 2.5. General view of the PIV experimental setup.

forming a long tubular bubble (Taylor bubble). To inject smaller bubbles, valves V_3–V_5 can be manipulated to introduce some of the liquid contained in the cylindrical chamber between valves V_1 and V_2. This volume reduction system worked well for low viscosity solutions. For high viscosity solutions it took a long time for the liquid to flow due to the small tube diameters between valves V_3–V_5. For these fluids, the time that valve V_2 is kept open can be used to control the amount of liquid that remains between valves V_1 and V_2.

Another tank, open to the atmosphere, was placed at the top of the column. This was used to avoid flooding by allowing the liquid to return to tank 1 and to maintain a constant liquid level at the height of the return tube.

The experiments were performed at ambient temperature. The liquid temperature was measured by a thermocouple placed inside the column, connected to a voltmeter.

The bubble velocity was measured using an oscilloscope to obtain the signals from

two pairs of laser diode/photocells. The time delay between the signals and the distance between the photocells were used to compute the bubble velocity.

The bubble images were recorded with a PCO SensiCam CCD-camera (from PCO Computer Optics GmbH, Germany) inside the dark chamber, which also contains the test section and the laser optics as represented in Figure 2.6.

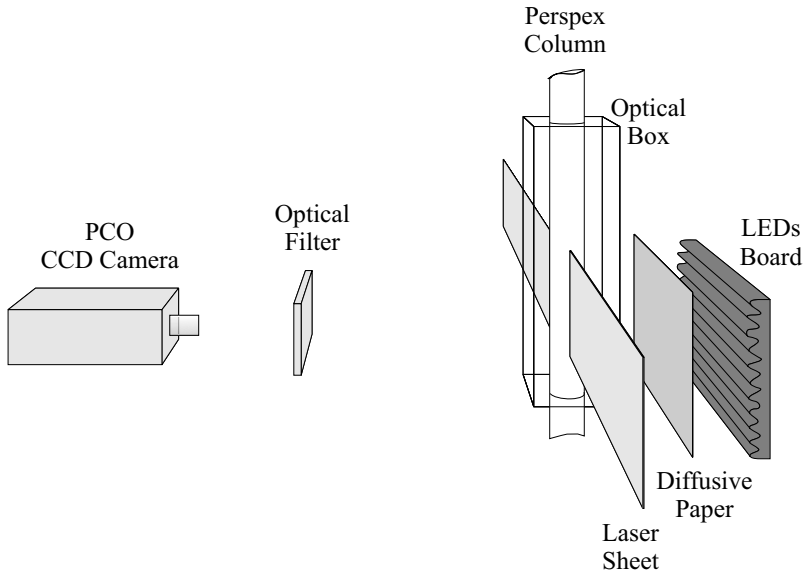

Figure 2.6. Detailed view of the test section inside the dark chamber.

In the test section, an optical box was used to reduce the image distortion caused by the curvature of the column and by the different refractive indexes of air, liquid and perspex. A vertical laser sheet passing through the axis of the column illuminated the two-dimensional flow under study and a LEDs board placed behind the optical box illuminated the background, to create a shadow of the bubble. A paper diffuser was used to disperse the background light uniformly. An optical filter was placed in front of the camera to suppress the laser light so that only the light emitted by the seeding particles and the background light were recorded. A detailed description of the different components of the setup is presented in the next sections.

2.2.2 Laser optics

The illumination of the particles in the measurement plane was done using a laser source. The choice of a laser light is explained by some basic laser characteristics: the

light is emitted in a single direction without spreading and it is possible to have high light intensity with very short duration. The fact that the light is emitted in a single direction allows the illumination of only the particles in a specific plane. The high light intensity is essential for particle imaging by the camera and the very short time duration is crucial to obtaining non-blurred particle images.

For this work a Nd: YAG Laser (Neodymium-doped yttrium aluminium garnet) was used, referenced as SERIES 5000 Nd: YAG Laser, Model, PVL 400/TS from the BMI company. To obtain a particle displacement measurement images of the particle in two different instants is necessary. Normally, due to the relatively high velocities of the flow and the close view of the velocity field, the time gap between the images must be in the order of a few microseconds. After a laser pulse, the laser needs re-charging time before it can pulse again. The laser used here is a double pulse model, which means that two pulses are created from two different power sources, as illustrated in Figure 2.7. With this feature it is possible to reduce the time between pulses below the normal re-charging time.

In Figure 2.7 the laser layout, with two channels is presented. Each part of the laser has a Q-switched oscillator, a frequency doubler (changes the beam from infra-red at 1064 nm

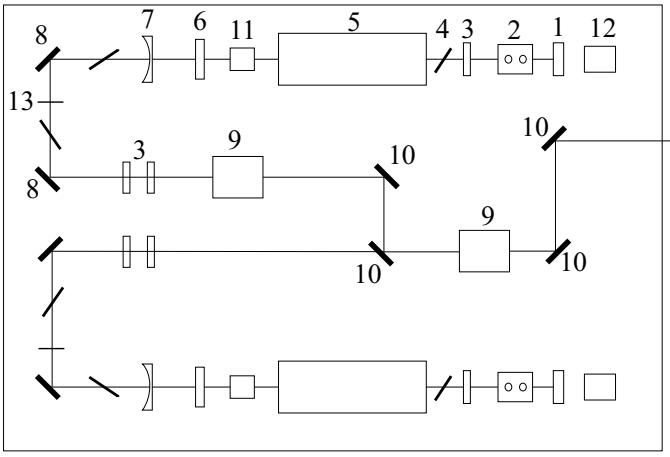

1. High reflection mirror
2. Pockell cell
3. Quaterwave plate
4. Polariser at 1064 nm
5. Q-switched oscillator chamber flashlamp Nd:YAG rod
6. Graded reflectivity output coupler
7. Compensation lens
8. 45-degre mirror at 1064 & 633 nm
9. Doubler crystal (35 degrees)
10. Dichroic mirror at 532 nm
11. Intracavity beamshutter
12. Control photodiode
13. Beam attenuator

Figure 2.7. Diagram of the Nd: YAG laser layout.

to green at 523 nm), and several optic components that form the optical path from the laser rod to the exit. The laser pumping is achieved via the flashlamps in the oscillators. The two pulses are triggered independently by a voltage applied to the Pockell cells. The power of each laser beam can be set by two attenuators. As seen in the laser layout, the design of the mirror arrangement allows both pulses to exit the box at the same point. To assure the laser beams are perfectly aligned, they are independently adjusted to overlap the beam impacts on a thermal paper placed at different distances from the source. A more detailed description of the laser operating principles can be found in Schram (2001). In Table 2.1, some laser specifications are presented. This table shows that the pulse duration is only a

Table 2.1. YAG Laser specifications.

Standard Specifications	
Laser head Material	Nd:YAG
Operating mode	electro-optic Q-switch
Wavelength	532 nm
Repetition frequency	10 Hz
Channel 1 specifications	
Output energy at 532 nm	400 mJ
Pulse duration	4.8 ns at 1064 nm
Channel 2 specifications	
Output energy at 532 nm	375 mJ
Pulse duration	3.5 ns at 1064 nm

few nanoseconds, assuring instantaneous illumination of the particles and avoiding blurred images. The repetition frequency, indicated as 10 Hz, limits the maximum frequency of image acquisitions, but this is not a limiting factor, as will be seen later.

One of the most important parameters to control is the time of each pulse. In Figure 2.8, a scheme of the laser synchronisation time is presented.

The precise instant when the flashlamps begin to charge is set by the laser's internal clock. The delay between the beginning of the flashlamp charge and the firing of the pulse (triggered by the Pockell cell) was optimised for each channel. If t_0 corresponds to the internal clock triggering signal, t_A and t_C correspond to the beginning of the flashlamp charging for each cavity, while t_B and t_D correspond to the opening of the Pockell cells and therefore to the emission of the pulses from each cavity. Fixing the delays of 145 µs and

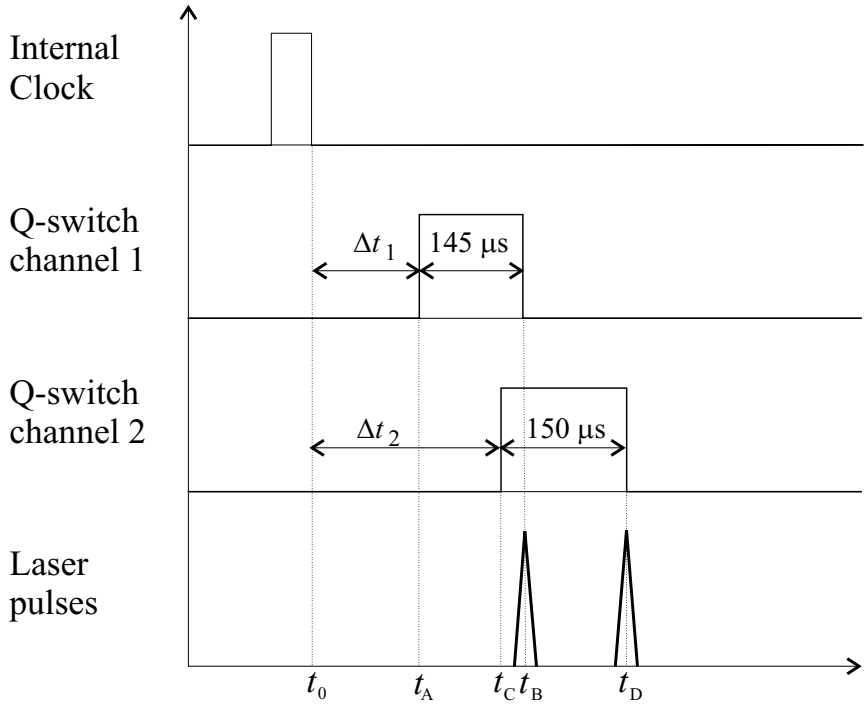

Figure 2.8. Diagram of the time delay between laser pulses.

150 µs (set to optimise the energy delivered by the pulses), t_A, t_B, t_C and t_D are defined by

$$t_A = t_0 + \Delta t_1$$
$$t_B = t_A + 145\,\mu s$$
$$t_C = t_0 + \Delta t_2$$
$$t_D = t_C + 150\,\mu s$$

The delay between the pulses is then equal to

$$\Delta t_f = \Delta t_2 - \Delta t_1 + 5\,\mu s$$

In practice, Δt_1 is normally set to zero, so the time between pulses is Δt_2 plus 5 µs. The laser can operate in four different modes:

- **Automatic Mode - Internal Clock** - Pairs of laser pulses fire at a constant frequency of 10 Hz with no external synchronisation.

- **Automatic Mode - External Clock** - The starting time is imposed by a TTL signal sent to the EXTERNAL SIGNAL BNC connection. This signal must have an amplitude of between 5 V and 15 V and a length of between 10 µs and 500 µs. For maximum laser power the frequency should remain equal to 10 Hz.

- **Single Shot Mode** - Only one pulse from each cavity is released, either by pressing a shot button on the remote control, or by sending a single TTL signal to the SINGLE SHOT BNC connection.

- **Synchronous Mode** - Here also, only one pulse from each cavity is released, but the input of the signal to the laser shot is set by the operator. In this mode, the instant when the flashlamp charging of first channel begins can be precisely controlled.

In this work the **Automatic Mode - External Clock** was used to take images at a constant frequency as the bubble rose. The **Synchronous Mode** was used to study the flow field in one specific region. In this mode the signal by the photocells from the passage of the bubble was used to trigger the laser with a pre-defined delay.

Beams from the Nd: YAG laser have an almost circular cross-section. In order to obtain a laser sheet, two lenses were placed between the laser source and the measurement section. The layout of the laser optical path is schematised in Figure 2.9. First, a cylindrical lens is used to open the beam vertically, then a spherical lens is used to deflect the beams back to the horizontal so as to obtain a thinner laser sheet. A mirror is placed between the laser source and the lenses for easier adjustment of the laser sheet position. The laser sheet had a thickness of about 1 mm in the test section; it was perpendicular to a lateral face of the optical box (parallel to the front face) and enclosed the axis of the column.

2.2.3 Particle image acquisition

As was already mentioned, the principle of the PIV technique is to measure the displacement of small seeding particles assuming that they have the same velocity as the fluid. The displacement is measured by comparing the particle positions in consecutive frames taken within a short time interval. Image acquisition is therefore an essential part of the technique. For better understanding, the distinction between PIV images and frames is given here: a 'PIV image' is composed of two consecutive frames; in the other sections the general term 'image' can be attributed to a single frame.

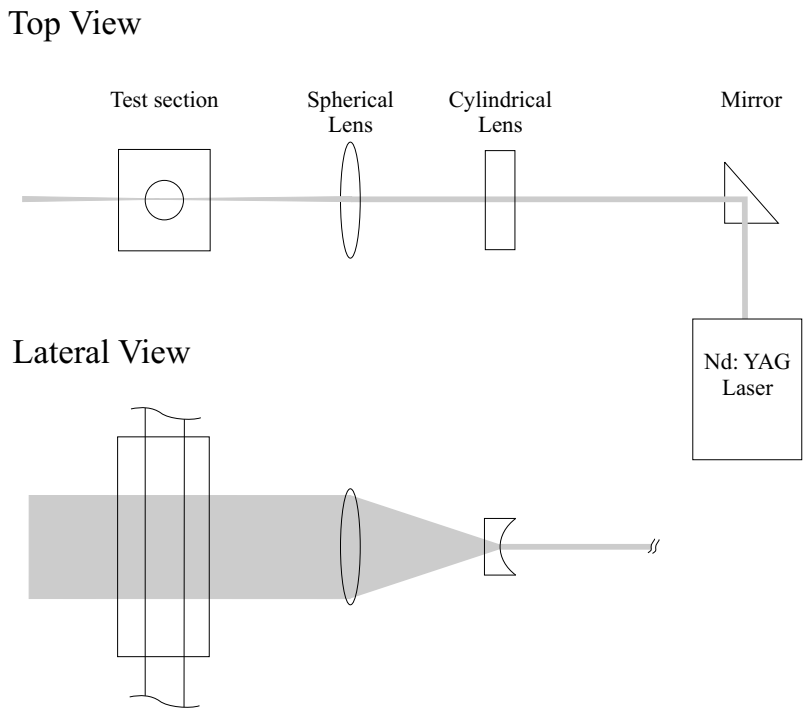

Figure 2.9. Laser optical path layout.

Some criteria have to be taken into account when choosing the seeding particles. Their density should be nearly the same as the fluid density to avoid floating or deposition during the experiments. They should be small enough to follow the fluid flow and large enough to be visible with the camera.

In this work a fluorescent orange vinyl pigment was used as seeding particles. These fluorescent particles emit light at 590 nm. The illumination process is described in the previous section. As mentioned, the particles were illuminated by a 1 mm thick green laser sheet with a wavelength of 532 nm. As the light emitted by the particles and the laser light have a different wavelength, an optical filter was used to suppress the unwanted wavelengths. Therefore, a red filter (model OG-570, Image Optics Components), 95% opaque below 550 nm, was used to block the intense green laser light (532 nm) and to allow passage of the light emitted by the fluorescent particles (590 nm).

These particles have a size of about 10 µm. A sedimentation test was performed by suspending the particles in the fluid and leaving at rest for 24 hours. As no particles were observed settling or floating it was assumed that their density was very close to that of the fluid so the particles should consistently follow the fluid flow.

The particle images were captured using a PCO SensiCam CCD-camera, with a resolution of 1280×1024 pixels and 4096 grey levels. The camera was placed perpendicular to the laser sheet and operated in the Double-Shutter mode. In this mode two full-resolution frames can be taken in a very short time (the minimum time between the frames in this mode is 1 µs). The integration time (time during which the CCD is exposed) for the first frame is user-defined by setting the duration of an external signal. In this case the same signal that triggered the laser Q-switch channel 1 was used. The integration time of the second frame is exclusively determined by the CCD readout time of the first one (the time that the camera takes to record the frame in the memory). This means that the user has no direct influence on the duration of the second integration time. Figure 2.10 represents the triggering of the camera and the exposure times for each frame.

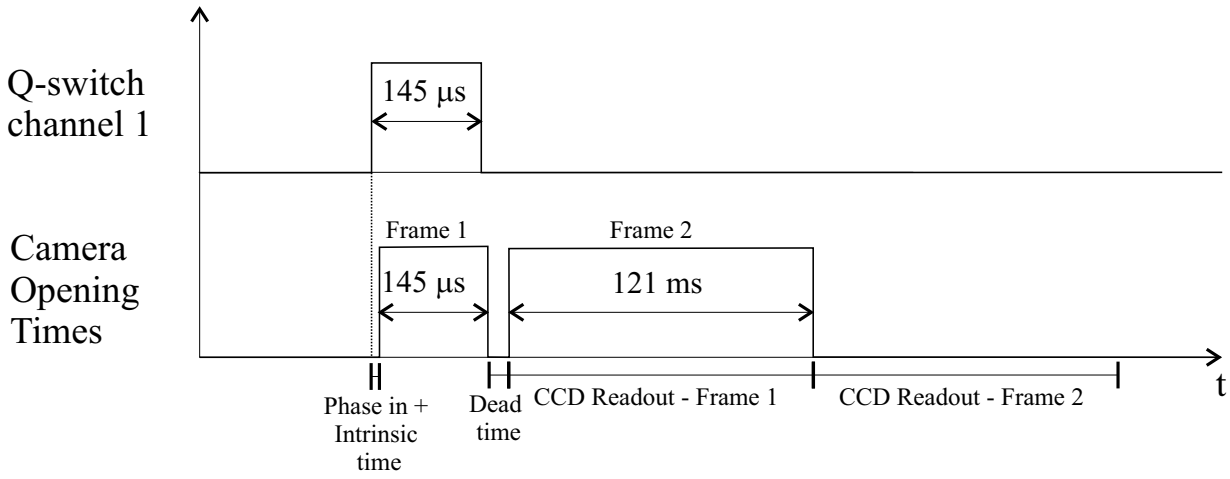

Figure 2.10. Triggering of the camera and exposure times of the two frames (not at scale).

The first frame is acquired at 145 µs and the second at 121 ms. The dead time between the two frames is 1 µs. Although the same signal was used to trigger the camera and the laser, there are also some system times (phase in, intrinsic, CCD readout time) which have an effect on the opening instant of the camera. The elapsed time between the triggering and the true opening time of the camera, for example, is affected by the cable used and is around 1.25 µs.

The exposure time of each frame is not important if the test section is in a dark room. There are two ways of acquiring an instantaneous non-blurred image; if the illumination is constant the image must be recorded over a very short time, and if the recording time is

long the illumination must be instantaneous. In this work, due to the long exposure times of the camera, the second option was taken. The time between the frames is then given by the time between the laser pulses. The camera has a maximum frequency of 4.11 Hz for the cycle described in Figure 2.10. The complete synchronisation scheme will be presented later.

When the whole cross-section of the column was filmed, a 35 mm lens was used to capture a test section of about 0.070 m × 0.055 m. A 50 mm lens was also used, with a 12 mm extension ring to obtain a close view of the liquid film region around the bubble. Examples of PIV frames of the Taylor bubble nose and of the falling liquid film are presented in Figure 2.11. In this figure, the luminosity of the frames was increased for better visualisation and even so, the bubble interface is not well defined. Some reflections are visible in the bubble nose and the liquid film, as well as some other optical effects. This led to using shadowgraphy simultaneously with the PIV technique, as will be described in the next section.

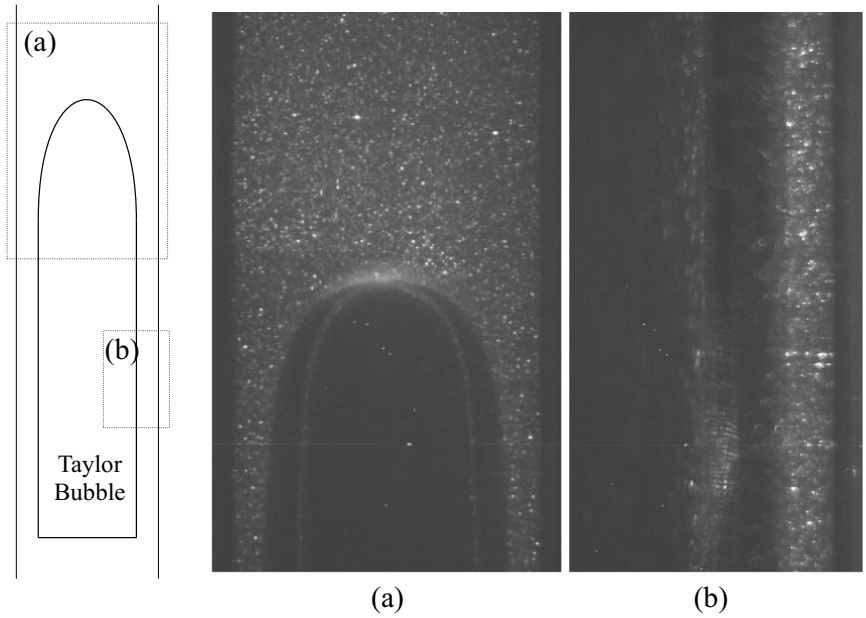

Figure 2.11. Example of a PIV frame in (a) the nose of a Taylor bubble and (b) in the falling liquid film (close view).

2.2.4 Simultaneous shadowgraphy

In preliminary PIV measurements, spurious optical effects were found in the bubble interface due to reflection and refraction of the light emitted by the seeding particles. These false optical effects influence the PIV image processing since erroneous velocity vectors are determined. The bubble interface position was also very difficult to accurately define, due to these virtual particle images. These problems are fully described in Nogueira *et al.* (2000). To overcome these problems a technique, first used by Lindken and Merzkirch (2002) in bubbly flow, was adapted to slug flow (Nogueira *et al.*, 2003). This technique consists of applying shadowgraphy simultaneously with PIV. This technique uses a background light to create a shadow image of the Taylor bubble. With the bubble shadow it is possible to accurately define the bubble interface and eliminate erroneous velocity vectors created by virtual particle images.

Although the principle is very simple, some points have to be considered for applying this technique. The background light should be unidirectional and parallel to the camera so that the bubble shadow corresponds to the bubble shape. The light wavelength must be higher than the high pass optical filter limit so it can be "seen" by the camera. The light pulse duration should be as short as possible to avoid blurred images of the Taylor bubble. The light intensity should be sufficient to be detected by the camera and at the same time, lower than the light reflected by the seeding particles, so that they can be distinguished in the acquired images. Finally, the background illumination should be as uniform as possible.

A background light source that meets the required conditions is a Light Emitting Diode (LED). An LED is a semiconductor chip that converts electrical energy into luminous energy (light). This conversion happens on the quantum level within the molecular makeup of the semiconductor chip. After finding LEDs with the desired characteristics, preliminary tests were performed before construction of the final apparatus.

A first test was performed with a single LED to see if it was possible to create a light pulse with a short duration. The LED was triggered by a TTL signal coming from a signal generator. A photomultiplier, which converts light intensity into voltage, was connected to an oscilloscope to check the duration of the pulses.

In Figure 2.12, the signal output on an oscilloscope shows that a pulse of 8 µs could be generated. The pulse had a delay of 5 µs relatively to the triggering signal. The pulse

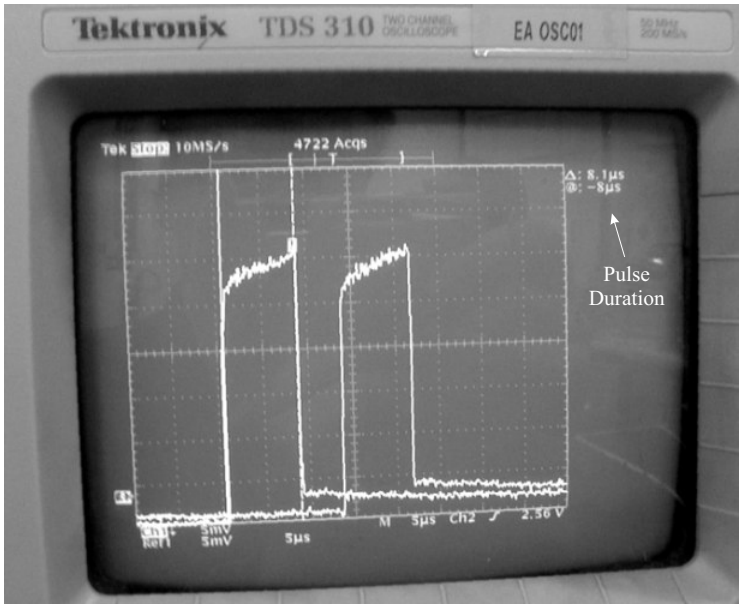

Figure 2.12. Signal of the photomultiplier received by the oscilloscope while testing the LED pulse duration.

duration was ultimately set at 12 µs to optimise the light intensity. This time is short enough since the Taylor bubble moves only about 0.05 pixels in 12 µs, so a non-blurred image could be expected.

A second test was made with the camera. The LED emits light at a wavelength of 650 nm. An oscillating mirror was used to test that the light could be seen by the camera through the optical filter and to confirm that the images would not be blurred. In this test, the camera was focused on an oscillating mirror reflecting the light from the LED. The mirror oscillation simulated the LED movement at a velocity that was double the Taylor bubble velocity. Figure 2.13 shows an image made under these conditions and can be seen that the light passes the optical filter and that the images are not blurred.

In order to have a uniform light, the LED images were taken at different focus distances. The unfocused LED was not diffused enough to obtain a satisfactory uniform background and so a diffuser paper was placed in front of it.

After the preliminary tests an LED board was constructed. The width of the LED board was set wider than the width of the optical box because it had to be located some distance from rear face of the optical box. The optical effects in the column wall, which slightly shorten the background image by distortion were also taken into account when

Figure 2.13. LED images filmed through an optical filter, of an oscillating mirror which simulates movement of the LED.

deciding on the size of the LED board. The final LED board is shown in Figure 2.14, with final dimensions of 180 mm × 120 mm, comprising 594 individual LEDs.

The LED board used a resistance switch to control the light intensity. The LED board was triggered by the same signal as the laser and the camera. The complete synchronisation scheme is presented in the next section.

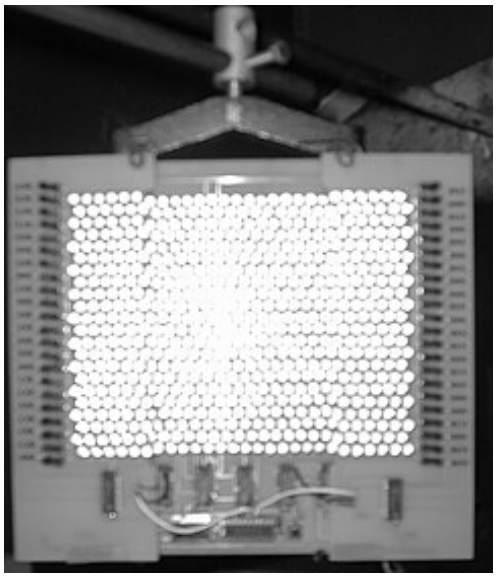

Figure 2.14. Final LED board with 594 LEDs.

2.2.5 Synchronisation

The simultaneous PIV and shadowgraphy technique uses two light sources: a laser source to illuminate the particles and a background light source to create the bubble shadow. This will only work if both light pulses are synchronised with the CCD camera that captures the pairs of frames. The synchronisation scheme between the camera and the light sources is represented in Figure 2.15.

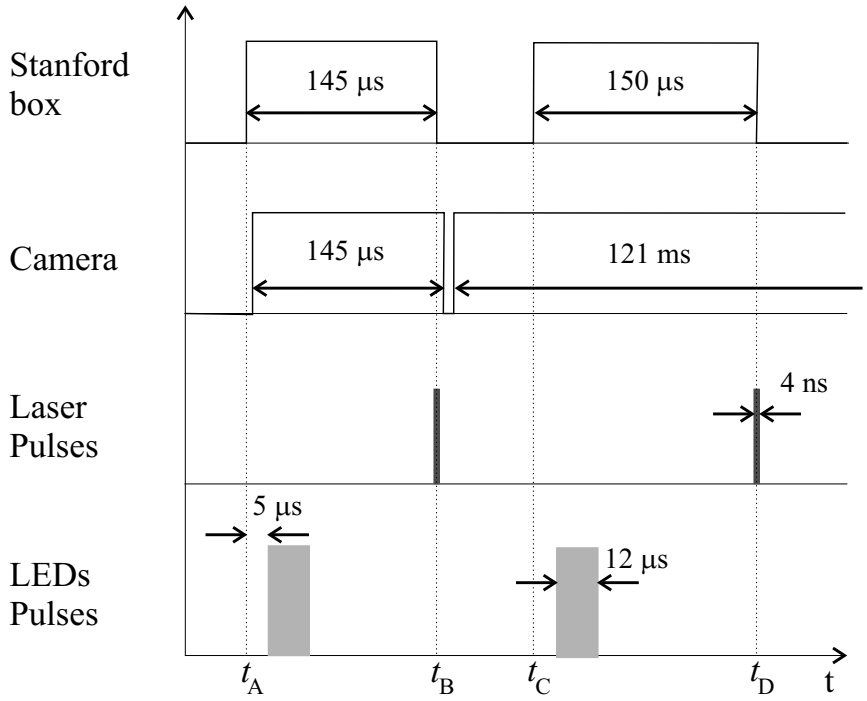

Figure 2.15. Complete synchronisation diagram of camera, laser and LED board.

The synchronisation of all devices was made by a Stanford box, in which points t_A, t_B, t_C and t_D can be set by the user. t_A is normally set to zero, t_B and t_D are set to 145 and 150 µs after t_A and t_C respectively, since these are the optimal values of time during which the Q-switch channels are in charge (§2.2.2). The user only has to set instant t_C which determines the time between the laser pulses and, therefore, the time between the acquired particle images. The time between the frames is defined by t_C plus 5 µs due to the difference in the charging times of the Q-switch channels (as seen in §2.2.2).

The camera is triggered by the first signal of the first Q-switch channel. There is an intrinsic time delay due to cables and electronic devices. For the first frame, the opening

of the camera starts slightly after t_A and finishes slightly after t_B. The second frame of the camera is acquired during 121 ms after 1 µs of dead time.

The laser pulses have a duration of about 4 ns and are triggered by the falling signals of the Stanford box (instants t_B and t_D), after the charging of the Q-switch channels. The intrinsic delay in the camera makes it possible to capture the first laser pulse in the first frame of the PIV images. The second pulse is captured in the second frame, except when the time between the two pulses is greater than 121 ms, which was not the case here.

The LED board is triggered by the initial point of the signals from the Stanford box (instants t_A and t_C). Due to the electric circuit, there is a delay of 5 µs in the LED pulse relative to the triggering signal. The two pulses fall with one in each frame of the PIV images and have a duration of 12 µs. Although the LEDs do not pulse at exactly the same time as the laser pulses, the difference is 145 µs maximum and during that time the Taylor bubble travels less than 1 pixel. In practice this movement is not detectable by the camera and the pulses can be considered to happen at the same instant.

The maximum acquisition frequency of the camera is 4.11 Hz. The laser should work at 10 Hz for the maximum power. In order to acquire images at a constant frequency without loss of frames, the laser was set to 8.22 Hz, double the camera frequency. Therefore, the actual image acquisition frequency is 4.11 Hz, although the synchronisation process described in Figure 2.15 runs at a frequency of 8.22 Hz for the Laser and LEDs board, which means that between each pair of frames there is a pair of pulses that is wasted.

To demonstrate the usefulness of shadowgraphy, images were acquired with only the laser pulse (standard PIV) and with both the laser and the LEDs pulses (simultaneous PIV and shadowgraphy). Figure 2.16 shows the output: frames (a) and (c) with PIV and (b) and (d) with simultaneous shadowgraphy and PIV. In the nose region, the bubble interface and the column wall are difficult to identify accurately when only PIV is used (a), while with shadowgraphy (b) these interfaces become clearly identifiable. However, the main reason for using these techniques simultaneously is exemplified in frames (c) and (d). The problems described by Nogueira *et al.* (2000) concerning the optical effects in the bubble interface are clearly seen in these frames. In frame (c), three pairs of large particle images are seen. With simultaneous shadowgraphy, it becomes clear that only the left pair of particles images corresponds to the real position of the particles. The pair in the middle is due to reflection in the bubble interface and the pair on the right is due to refraction through the bubble. Shadowgraphy allows for elimination of the velocity vectors

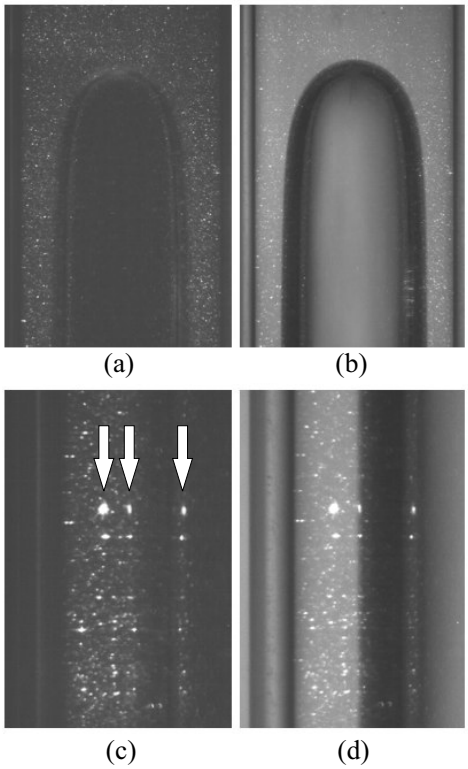

Figure 2.16. Frames with PIV only (a, c) and PIV with simultaneous shadowgraphy (b, d) in the nose and in the liquid film.

positioned inside the bubble *a posteriori*, since the interface position is well defined. The image processing is described in the next section.

2.2.6 Image processing

As seen in Figure 2.16, the images acquired with simultaneous PIV and shadowgraphy techniques contain information both on the particles and on the bubble shadow. The processing of the images has two main steps: the determination of the bubble shadow and the PIV processing to obtain the particle displacements.

Bubble shadow

The attainment of the bubble shadow was tested using different methods, either by simply defining a grey level threshold to establish which part of the image was the bubble

and which part was not, or by determination of grey level gradients, which should be higher in the bubble interface. After analysing the different image processing possibilities, the most efficient method for obtaining the bubble shadow in the studied conditions was chosen, as is described next.

Figure 2.17 represents the different steps followed to obtain the bubble shadow.

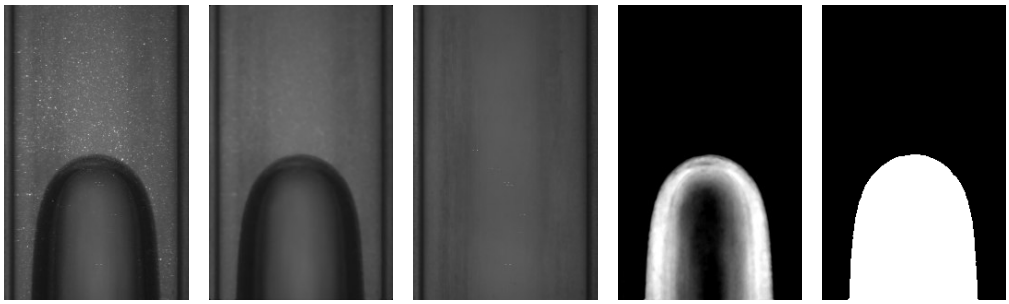

Figure 2.17. Sequential image processing steps to obtain the bubble shadow.

A median filter was applied to the original image (Figure 2.17(a)), which substitutes the grey level of each pixel by the median of the grey levels in a user-defined neighbourhood around that pixel. This step eliminates the particles from the PIV frame since their grey level is of a much smaller quantity than the background light grey level, while maintaining a defined bubble shape (Figure 2.17(b)).

A frame with only LED light was used as background reference (Figure 2.17(c)). The difference between this image (c) and the median filtered original image (b) gives the bubble image (d), with a certain gradient of grey levels. By defining a threshold value for the grey level it is possible to transform the image into a binary notation; zeros and ones respectively below and above that value. The threshold value is iteratively adjusted in order to coincide the position of the bubble interface in the final image with its position in the original image. The final step consists of filling the inner region of the bubble to obtain the complete bubble shadow (Figure 2.17(e)). This procedure was implemented in order to process several PIV images sequentially, using Matlab programs presented in Appendix D.

PIV processing

The processing of each pair of frames to obtain the particle displacements and the velocity field was made using the WIDIM (Window Distortion Iterative Multigrid) code developed by Scarano and Riethmuller (1999). The general principles of the code will be described in this section. A more detailed description can be found in Scarano (2000b) and Nogueira (2005).

As described in §2.2.5, the camera acquires two frames separated by a user-defined time. Depending on the velocities present in the flow field, the time between the frames is adjusted to set the particle displacement sufficiently high in order to minimise the uncertainty of the velocity data, and always below a maximum value due to processing limitations.

Figure 2.18(a) represents an example of an original PIV image composed of two frames. The frames were acquired with the camera rotated 90 degrees in order to obtain maximum

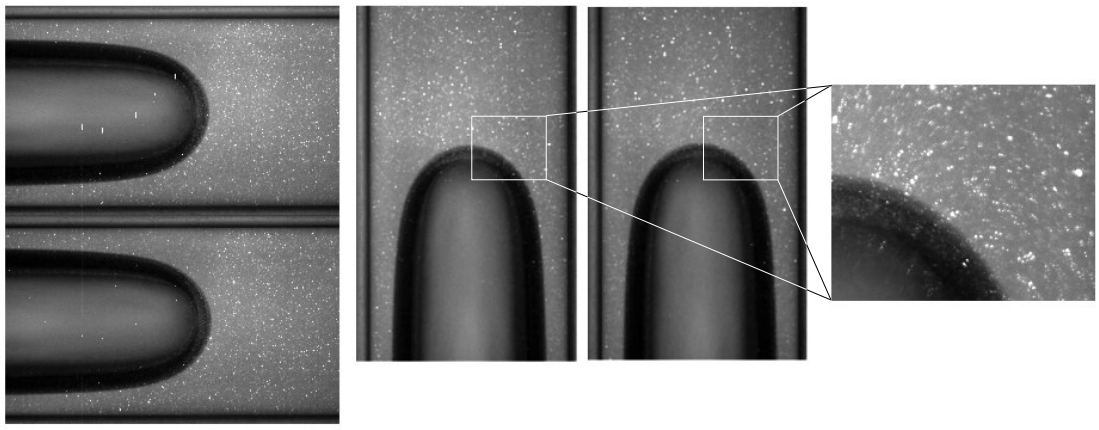

Figure 2.18. (a) PIV image, (b) and (c) separated frames after rotation, (d) overlapping of frames (b) and (c).

column length in the image, since the horizontal dimension of the image is greater than the vertical one. The acquiring software allows cropping some lines of unwanted pixels. This was applied to the regions outside the perspex column which are not needed and would increase the image recording times. The original image is then rotated 90^o and the two frames separated in two images (Figure 2.18(b,c)). At the same time, the burned pixels of the camera (some can be seen in Figure 2.18(a) inside the bubble) are replaced by pixels with random grey levels (within the grey level range of the image). This does not affect the

particle displacement determination and avoids the tendency to create zero displacements in the flow field. The Matlab programs used in this procedure are presented in Appendix D. Figure 2.18(d) shows a close-up of frames (b) and (c) overlapping, which gives a picture of the displacement of the particles. This displacement is particularly visible close to the bubble where the velocities are higher. The PIV processing consists of the determination of the particles displacement from one frame to the other. The displacement of a single particle is not determined (which can be done with the Particle Tracking Velocimetry - PTV technique), but the mean displacement of a window containing a group of particles.

In Figure 2.19, the horizontal and vertical displacement of a group of particles is shown schematically. For simplicity, the whole frame has 10 x 10 pixels^2 and each particle has the dimensions of 1 pixel^2.

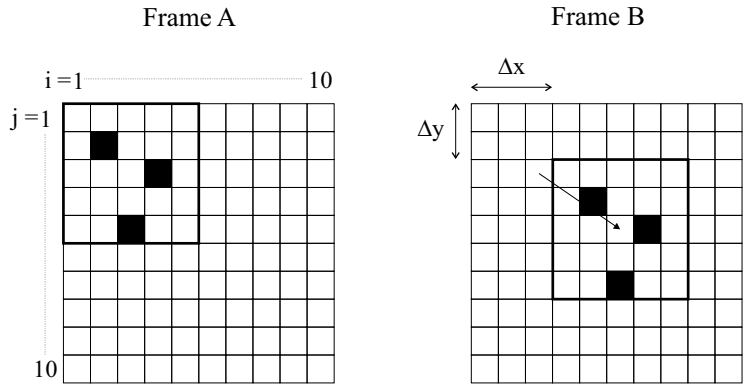

Figure 2.19. Schematic illustration of particle displacement from frame A to frame B.

To determine the displacement of a window with 5 x 5 pixels^2, a cross-correlation function between the two frames, can be used. Let $A(i,j)$ and $B(i,j)$ be the pixels values (measured in grey levels) of frames A and B in coordinates i and j. A cross correlation function can be defined between the search window in frame A (dark line) and an interrogation window with the same size in frame B displaced by Δx and Δy in horizontal and vertical directions respectively:

$$\Phi(\Delta x, \Delta y) = \sum_{i,j=1}^{5} A(i,j) \cdot B(i+\Delta x, j+\Delta y) \tag{2.1}$$

with Δx and Δy expressed in pixels.

If the pixel grey levels values are 1 for a particle and 0 for the background, the cross

correlation function for a given displacement will be zero if there are no particles in the same relative position in the windows, and will be maximum if the positions of all the particles coincide.

Figure 2.20, represents the cross correlation function for the example given in Figure 2.19. Figure 2.20 shows that the maximum value for the cross correlation function occurs

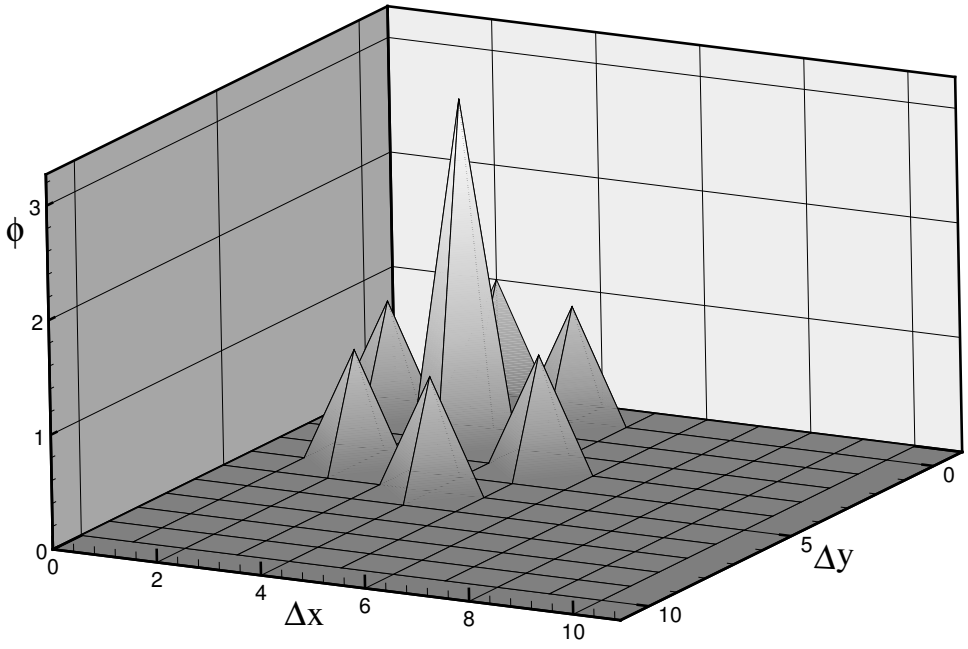

Figure 2.20. Cross correlation function of frames A and B from Figure 2.19.

for the displacement of 3 pixels in the horizontal direction and 2 pixels in the vertical direction. The other peaks correspond to the cases where there are less particles in the same relative position. This example is of a simple and ideal case. Since the particles have an area of only one square pixel the difference between the grey levels of the particle and the background is maximum, and particle movement is a simple translation. Even so, it demonstrates the basic principle for the determination of the displacement of small windows into which the original frame is divided.

When a lot of particles are present, a larger number of peaks is found. The signal to noise ratio (SNR) is defined as the height of the highest peak divided by the height of the second peak. The higher the SNR, the higher is the probability that the correct displacement was found. In standard PIV measurements the displacement vectors are validated if

the SNR is higher than 1.5. This value can be reduced if the operating conditions are not ideal, such as in a very high or low concentration or size of seeding particles, non focused images, etc. In the WIDIM code, when the SNR for a certain window is lower than the threshold value the window displacement is considered invalid and is substituted by the average of the neighbourhood values.

The particles usually have a size larger than 1 pixel and the grey level varies from 0 (black) to 255 (white) in 16 bit images. The cross correlation scheme used is similar to the one represented in equation 2.1, but normalised by an average grey level (Scarano, 2000b):

$$\phi_{AB}(\Delta x, \Delta y) = \frac{\sum_{i,j=1}^{M} A(i,j) * B(i-\Delta x, j-\Delta y)}{\sqrt{\sum_{i,j=1}^{M} (A(i,j))^2 \cdot \sum_{i,j=1}^{M} (B(i,j))^2}} \tag{2.2}$$

where $A(i,j)$ and $B(i,j)$ are the grey levels of the pixels in column i and line j of the first and second frames respectively, Δx and Δy are the horizontal and vertical displacements of the search window relative to the interrogation window.

The determination of the peak position is made by fitting a Gaussian function to the integer values found, in order to find the maximum of the cross correlation function with a sub-pixel accuracy. In standard PIV measurements that use this scheme, an accuracy of 0.1 pixels is obtained in the window displacement. In this work using simultaneous shadowgraphy, tests with known velocity fields showed an error slightly higher, but still below 0.2 pixels.

A problem that may occur in PIV technique is the in-plane loss of pairs, which means that particles that are at instant t in the first frame, the interrogation area, partially escape during time Δt_f between frames and are not present in the second frame, or search area. Adrian (1991) proposes a criterion to minimise this effect: the ratio between the maximum displacement of the particles and the window size must be kept below 0.25 (one-quarter rule), in order to maintain a detection probability above 95%.

The time Δt_f between the frames has to be set according to the fluid velocity: it must be sufficiently high for particle displacement to be detectable, and at the same time not too high, due to the one-quarter rule. If there are large displacements, the windows size must be high and spatial resolution of the velocity field is reduced. With WIDIM, the velocity vectors are determined iteratively. First, large windows are used to get a first estimate of

particle displacement. Then, to increase the spatial resolution, windows dimensions are reduced and the first estimate works as a guide to limit the search area.

Frequently, there are high velocity gradients in the flow field, close to surfaces or inside vortices. In these cases the particles are not only subjected to translational displacement, but also to rotation and shearing. To improve the peak detection accuracy, windows are distorted according to the velocity gradient. Figure 2.21, represents an example where the search window is distorted (b), after a first estimate (a) of the velocity vectors. In this way, the relative movement of the particles inside a window is taken into account and more particles are detected, increasing the SNR.

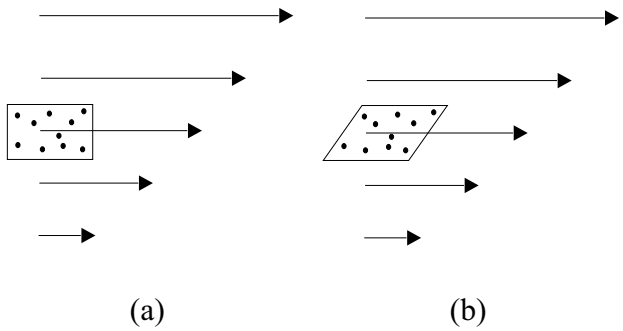

Figure 2.21. Distortion of the search window (a) relative to the interrogation window (b) according to the velocity gradients.

In summary, the general steps for the WIDIM code to obtain the window displacement are:

- division of the first frame into small interrogation windows;
- cross correlation of these interrogation windows with similar search windows in the second frame;
- cross correlation of all interrogation windows with distorted search windows according to the velocity gradients;
- repetition of the previous steps, iteratively reducing window size and using the previous estimate as a guide for the search area

To increase the spatial resolution, the image can be divided in windows with a certain overlapping area. This means that the same particles can be part of two consecutive windows and, therefore, the information of consecutive vectors is not completely independent.

In this work, after checking different window sizes and iterations, non-square windows with an initial size of 20(H)×40(V) pixels were used, which were reduced to half-size after one iteration and a 50% overlapping. The use of non-square windows is due to the main flow direction; the main flow is in the vertical direction so there is no need for a large window size in the horizontal direction (one quarter rule).

By using WIDIM the user can define a mask to indicate the known velocities in the flow field apart from the image size, window sizes, number of iterative steps, overlapping and SNR threshold. This mask is mainly used to indicate a zero velocity in the walls. Figure 2.22 presents an example of a PIV frame (a) of the nose of a Taylor bubble and the respective mask (b) used in WIDIM. The mask must have the same dimensions of the PIV

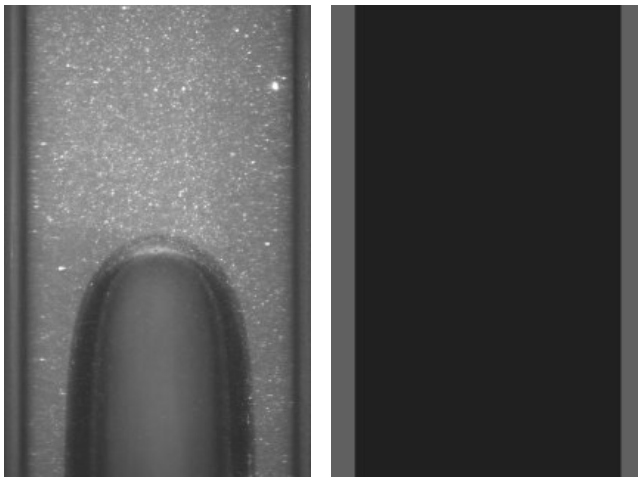

(a) (b)

Figure 2.22. Example of a PIV frame (a) and respective mask (b).

frame and different velocity values can be attributed to different grey levels. In this case, a grey level of 64 was set for the column walls, corresponding to a zero velocity. In the rest of the figure a zero grey level (black) indicates the region where the window displacement should be determined.

After data processing with the WIDIM code, the flow field represented in Figure 2.23(a) is obtained, containing the window displacement and the vector positions in pixels. Only half of the vectors obtained are represented. The bubble shadow allows the elimination of the meaningless vectors inside the bubble by simple multiplication of the vector field by the bubble shadow image containing zeros in the bubble shadow area and ones in the rest

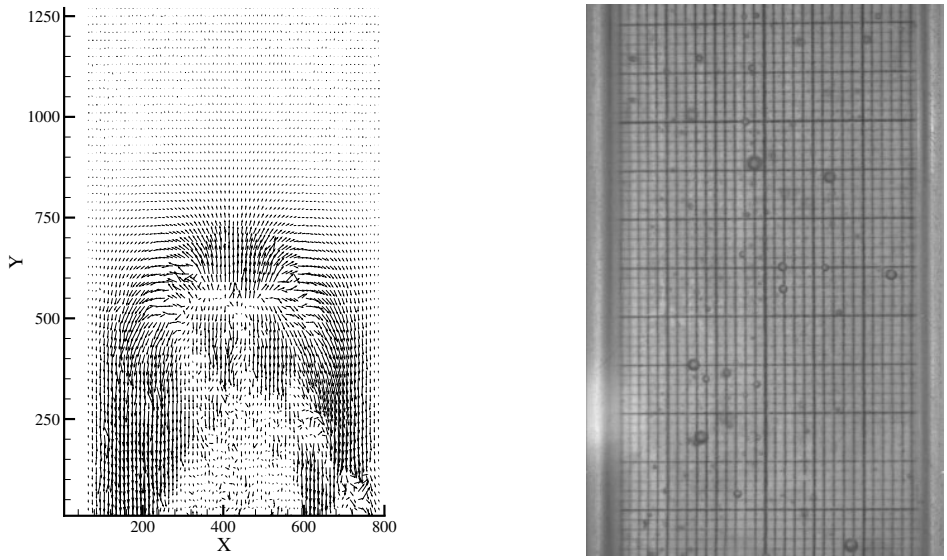

(a) (b)

Figure 2.23. Example of a velocity field obtained with PIV (a) and respective calibration image (b).

of the image.

A calibration image (Figure 2.23(b)) showing a millimetric scale in a vertical plane, containing the axis of the column and perpendicular to the camera angle, is used to establish the correlation between the pixels and the real dimensions. With this correlation, $PIVC$=pixels/m, and the known time gap between the two frames, $\Delta t_f(s)$, the displacements in pixels, Δp(pixels), can be converted into velocities using the following equation:

$$V(m/s) = \frac{\Delta p}{\Delta t_f \cdot PIVC} \tag{2.3}$$

The final vector field is represented in Figure 2.24, after dividing the radial and vertical distances by the column diameter. All the Matlab programs developed to process the images are presented in Appendix D.

2.2.7 Bubble velocity and length

In most cases, the Taylor bubble velocity could not be measured from PIV data. In PIV measurements the frequency of the camera is low and usually only one image of the bubble nose is acquired.

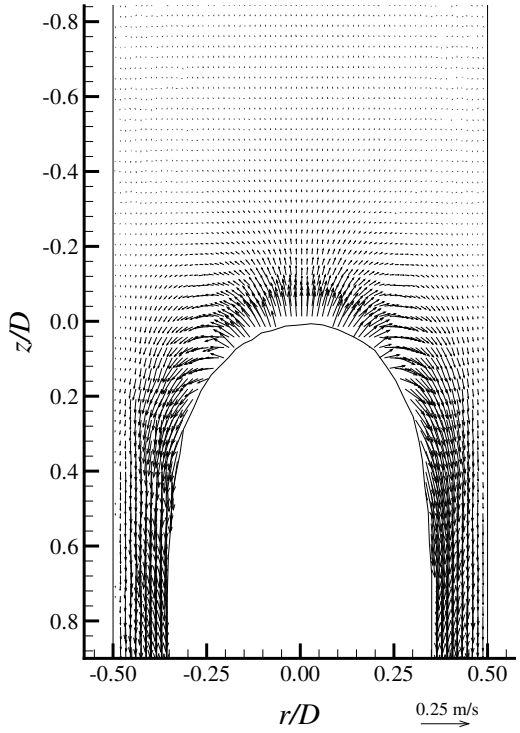

Figure 2.24. Example of the final velocity field obtained with PIV and simultaneous shadowgraphy.

To obtain the bubble velocity, a different technique was used. Two laser diodes were placed close to the column, aimed at two photocells (which convert the laser light into voltage) on the opposite side of the column. Passage of the bubble causes a deflection in the laser beams (Figure 2.25) and the photocell signal drops abruptly. The photocell signals and distance between the two photocells are analysed to compute the bubble velocity and length.

If the laser beam intercepts a transparent surface perpendicularly it will not be deflected. Therefore, if the laser diode is placed perpendicular to the column wall, the beam is not deflected in the developed bubble region where the interface is parallel to the column axis. Only in the nose and bottom of the bubble is the laser light deflected. However, if the laser beam is slightly deviated (Figure 2.26) it is deflected even in the developed region of the bubble because the incident angle is different from zero. This does not introduce any significant error in the bubble velocity reading since a deviation of only 1 mm from the axis of the column is enough to deflect the laser beam from the photocell when the bubble

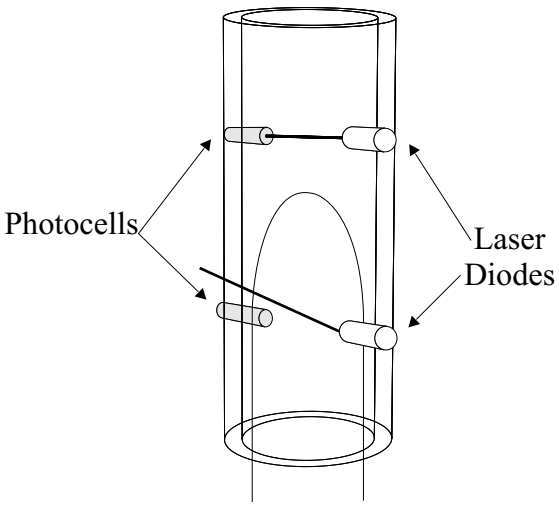

Figure 2.25. Sketch of the laser diodes and photocells used to measure the bubble velocity.

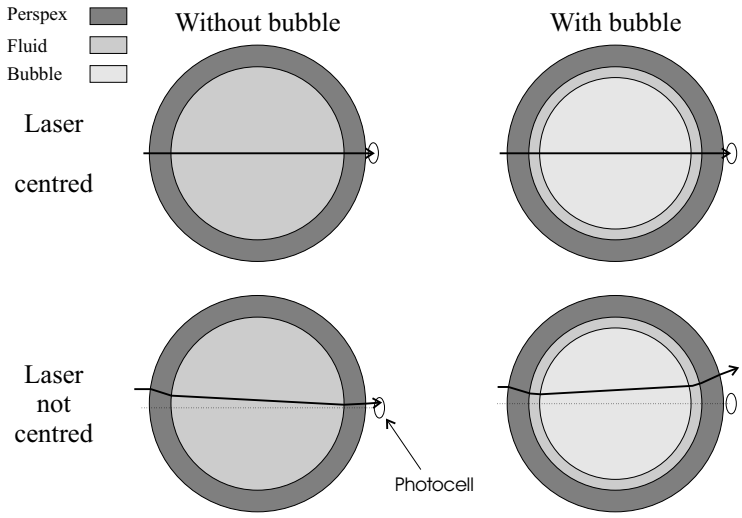

Figure 2.26. Laser beam trajectory through the column, at different positions, with and without the presence of the bubble.

passes. This fact, apart from explaining why the laser beam must be slightly deviated from the axis, also shows that the laser sheet must cross exactly at the axis of the column.

The photocell signals are similar to those represented in Figure 2.27. Moments N and T represent the instants when the nose and the trailing edge of the bubble pass in front of the laser diode, and indexes 1 and 2 refer to the first and second pairs of laser diode/photocell.

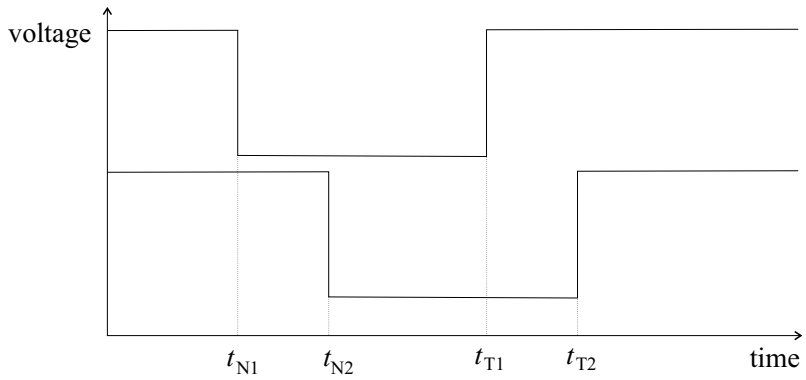

Figure 2.27. Signals acquired from the photocells.

The Taylor bubble velocity and length can be determined by the following equations:

$$U_b = \frac{\Delta z}{t_{N2} - t_{N_1}} \tag{2.4}$$

$$L_b = U_b \cdot (t_{T1} - t_{N1}) \tag{2.5}$$

where Δz is the distance travelled by the bubble (distance between the photocells).

When the column is open to the atmosphere, $t_{T1} - t_{N1}$ is normally shorter than $t_{T2} - t_{N2}$, which shows that the bubble length increases due to gas expansion as it rises in the column. When referring to the bubble length, the average length given by the two photocell signals is used.

2.2.8 Optical distortion checking

In both visualisation studies and PIV measurements, images are acquired inside a circular tube of perspex. The curvature and the difference in refractive indexes of air, perspex and liquid cause a deviation of the light rays passing through the interfaces, so images are distorted. To reduce the optical distortion, a liquid-filled box with plane faces was placed in the measurement section, enclosing the column. However, some optical distortion persists.

Tests were made to check the magnitude of the optical distortion. In Table 2.2 the refractive indexes of perspex and of the fluids used in the experiments are presented. The maximum weight percentage of CMC and PAA polymer in the solutions was 1.0%, so from

Table 2.2 it is seen that there is no significant difference between the refractive indexes of water and the solutions used. Nevertheless, the difference in the perspex refractive index might be important.

Table 2.2. Refractive indexes of perspex and polymer solutions used.

Material	Refractive Index
Air	1.001
Water	1.333
2.0 wt% CMC	1.336
1.0 wt% PAA	1.335
Perspex	1.490

To check if the refractive index differences would distort the images, thin lines separated by 0.3 mm were printed on a transparent paper. This paper, with a width equal to the internal diameter of the perspex column, was immersed in the column and images were taken with and without the optical box. Figure 2.28 shows the effect of the optical box on reducing the distortion.

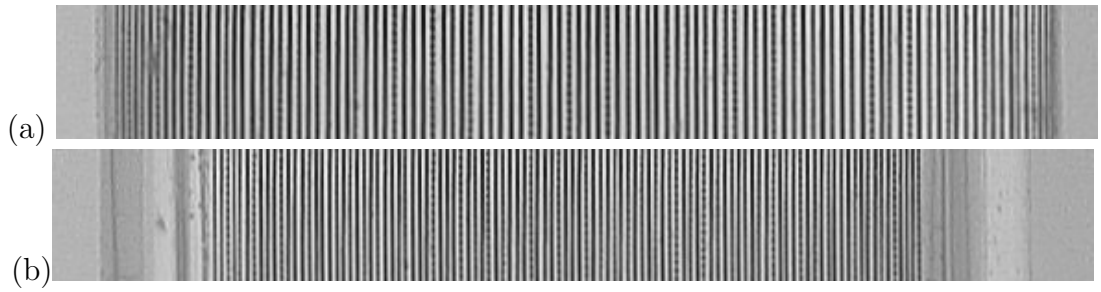

Figure 2.28. Images of vertical lines in the central plan of the column without (a) and with the optical box (b).

From Figure 2.28(a) it is evident that without the optical box the inner wall of the column is not clear and the lines become closer together as the distance from the axis increases. The optical box (Figure 2.28(b)) significantly reduces the distortion, making it possible to identify the inner wall of the column and the lines appear to maintain the same distance apart. To prove this, an image analysis was made, by defining a grey level threshold value that distinguishes the background from the printed lines. The position of each line was then determined along a horizontal line and the distance between consecutive

lines was computed. Figure 2.29 represents the distance between consecutive lines with and without the optical box. From this figure it becomes clear that with the optical box

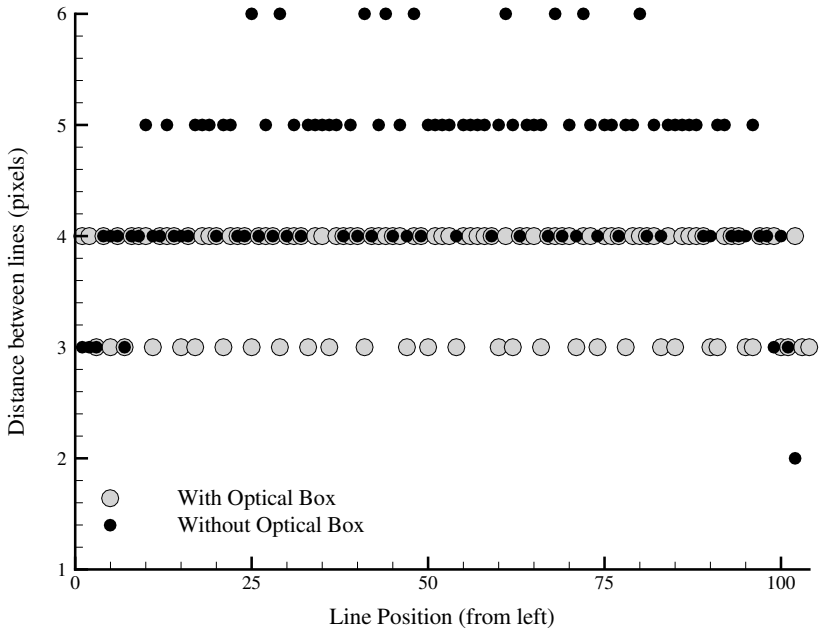

Figure 2.29. Distance between consecutive lines with and without the optical box.

the distance between the lines appears to remain constant (3-4 pixels) along the radial position, while without the box, the distance between lines can be 6 pixels close to the axis of the column, and only 3 pixels close to the column wall. These tests were made with the camera used in the visualisation studies, which has a lower resolution than the CCD camera used in the PIV measurements, so if some distortion remains below the camera resolution it can not be detected by these images. The uncertainty between 3-4 pixels in the distances between the lines led to a more detailed study.

The image analysis with this camera was not sufficiently accurate to quantify the optical distortion. Therefore, the optical path of the light rays between the camera and the vertical plane containing the axis of the column was determined by ray tracing. In Appendix C the procedure used is described in detail. It was found that in the acquired images the distortion in the vertical direction is negligible but the distortion along the radial position is not constant, inducing an error if the radial position is considered to be equally spaced from the axis of the column to the column wall.

Figure 2.30 shows a schematic of the ray tracing technique where the real positions in

the vertical plane containing the axis of the column can be compared with the positions seen by the camera by analysing the ray trajectories through the different interfaces.

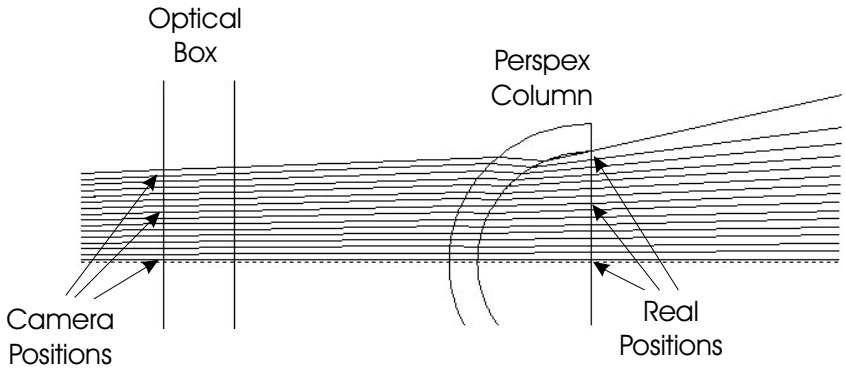

Figure 2.30. Sketch of the ray tracing method used to analyse the optical distortion.

In Table 2.3 are presented the deviations between the real radial positions obtained by ray tracing and the positions in the acquired images (assuming equally spaced positions). The error is higher closer to the column wall reaching a maximum value of 0.25 mm. In the following chapters all the results were corrected according to this small distortion caused by optical effects.

Table 2.3. Real radial position obtained by ray tracing (r_{column}), image radial position (r_{image}) assuming equally spaced positions and error, all in mm.

r_{column}	r_{image}	$error$
16.00	16.00	0.00
14.80	15.00	0.20
13.77	14.00	0.23
12.77	13.00	0.23
11.78	11.99	0.21
10.79	10.99	0.20
9.81	9.99	0.18
8.78	8.95	0.17
7.84	7.99	0.15
6.96	7.10	0.14
5.88	5.99	0.11
4.90	4.99	0.09
3.92	4.00	0.08
2.94	3.00	0.06
1.96	2.00	0.04
0.98	1.00	0.02
0.00	0.00	0.00

Chapter 3

Individual Taylor bubbles in Carboxymethylcellulose (CMC) solutions

Abstract

In this chapter the results obtained with Carboxymethyl Cellulose (CMC) polymer solutions are presented. Preliminary visualisation studies are described. After the visualisation studies, some solutions were selected for a detailed analysis. The rheological characterisation of these CMC solutions is shown and the the flow field around the Taylor bubbles is analysed with the simultaneous Particle Image Velocimetry / Shadowgraphy technique (PIV/ST).

3.1 Visualisation studies

Some preliminary visualisation studies were performed to get an idea of the flow behaviour around the Taylor bubbles rising in non-Newtonian fluids, especially in the wake region, since there was no information available in the literature.

The experimental setup and procedure of the visualisation studies were described in §2.1. The non-Newtonian fluids first tested were different solutions of Carboxymethylcellulose (CMC), a polymer frequently used in industry and in laboratory characterisation of complex fluids (pseudoplastic and viscoelastic properties). Several solutions with different

Table 3.1. Experimental conditions in the visualisation studies with CMC solutions.

CMC wt%	$T(^o\mathrm{C})$	CMC wt%	$T(^o\mathrm{C})$
0.10	24.3	0.50	24.9
0.20	25.3	0.55	24.8
0.30	24.3	0.60	25.5
0.35	24.4	0.80	24.4
0.40	25.8	1.00	26.0

weight percentages (wt%) of CMC in water were studied to cover a wide range of rheologic properties. In Table 3.1 the weight percentages used and the corresponding experimental temperatures are presented. For each of these conditions, between 13 and 19 Taylor bubbles with different volumes were analysed. The bubble volume was limited to the volume of the hemispherical cup, about $1.9 \times 10^{-4}\,\mathrm{m}^3$ (experimental setup of Figure 2.1). The highest solution concentration was the 1.00 wt% CMC solution since above this weight percentage the solution becomes less limpid; small bubbles which form when preparing and manipulating the solution have a practically zero terminal velocity and are therefore difficult to remove.

3.1.1 Bubble velocity and length

The experimental values of the bubble velocity, U_b, and the dimensionless bubble length, L_b/D, obtained in the visualisation studies are represented in Figure 3.1. From the uncertainty analysis in Appendix B, an uncertainty of 0.001 m/s was determined for the bubble velocity and 0.001 m ($0.03D$) for the bubble length.

For a given bubble length, the bubble velocity decreases as the CMC wt% increases. The velocity variation between 0.10 and 1.00 wt% CMC solutions can reach around 20% for a given bubble length. This behaviour is explained by the increase in the viscosity forces as the CMC wt% increases.

Figure 3.1 also shows that for a given CMC solution the bubble velocity increases slightly with the bubble length. The column is open to the atmosphere at the top, and so, as the bubble rises in the column, the hydrostatic pressure decreases, therefore the bubble volume increases due to gas expansion. This expansion induces a displacement of the liquid ahead of the bubble nose. The velocity of this moving liquid is, by continuity, equal to the displacement rate of the nose region due to the expansion. Therefore, the

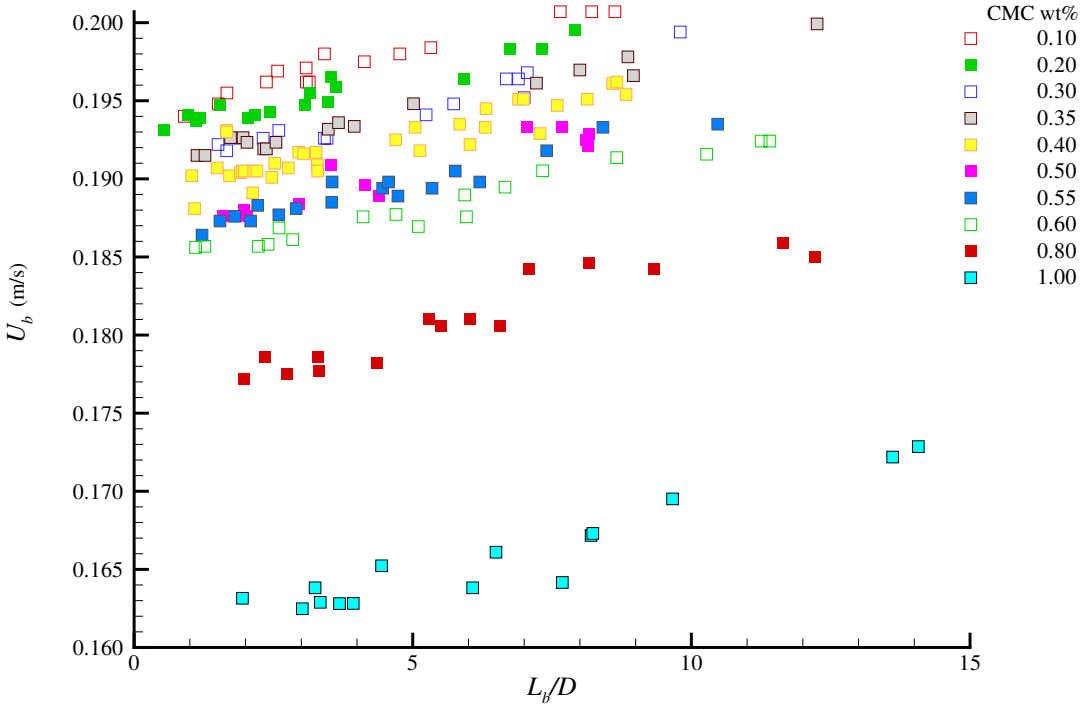

Figure 3.1. Plot of the bubble velocity versus the dimensionless length of the Taylor bubbles obtained from the visualisation studies.

measured velocity of the bubble has two contributions: the drift velocity of the bubble and the velocity of the liquid ahead of the nose (at the axis of the column). The longer the bubble, the higher the variation rate of the gas volume. This induces a higher velocity on the liquid ahead of the bubble, and thus a higher bubble velocity. In the bubble length range studied, the increase in bubble velocity reached 3% in the 0.10 wt% CMC solution and 6% in the 1.00 wt% CMC solution from the shorter to the longer bubbles. As will be seen in the PIV results, if the liquid velocity ahead of the nose (at the axis of the column) is subtracted from the bubble velocity, the Taylor bubble velocity (drift velocity) becomes independent of the bubble length.

3.1.2 Wake flow pattern

The main objective of the visualisation studies is to qualitatively characterise the wake flow pattern. From these studies it is not possible to get information about the liquid flow around the nose of the bubble nor in the annular film, apart from a corresponding increase

in the film thickness with the liquid viscosity. The qualitative analysis of the liquid flow in the wake of the bubbles for the different solutions is described below.

0.10 wt% CMC solution

The lowest CMC weight percentage used in these studies was 0.10 wt%. This solution is very diluted, so the bubble behaviour was not expected to be very different from a Taylor bubble rising in water. The bubble length varied from 1.0 to 8.4D and the bubble velocity from 0.194 to 0.201 m/s.

In Figure 3.2 six consecutive frames of the wake of a Taylor bubble rising in a 0.10 wt% CMC solution are presented. The bubble in this figure is one of the longest bubbles

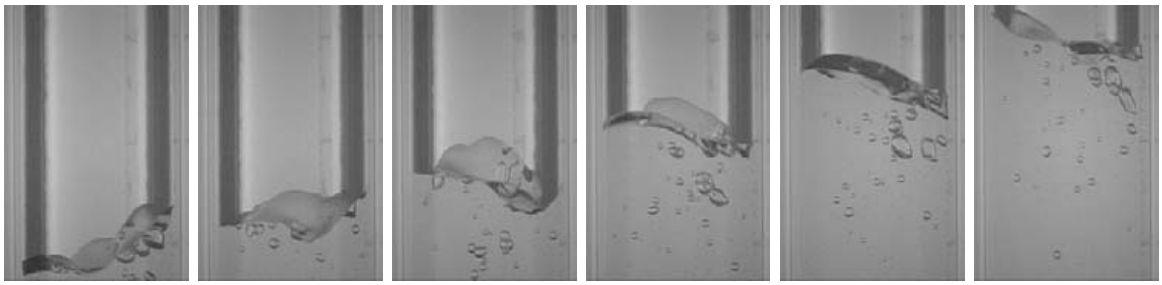

Figure 3.2. Consecutive frames of the wake of a Taylor bubble rising in a 0.10 wt% CMC solution; time between frames 0.04 s.

studied, with a length of 8D. It is evident that the trailing edge of the bubble is not stable, oscillating three dimensionally. This oscillation is due to the high turbulence of the flow in the wake region. The absence of coloured liquid in the images shows that the liquid in the wake is renewed as the bubble rises. This implies that there is no transport of liquid in the wake over long distances.

In the liquid film around the Taylor bubble very small portions of gas can be torn out of the bubble, which then coalesce into larger bubbles. The oscillation of the bubble trailing edge also contributes to the formation of small bubbles in the wake region during the Taylor bubble movement. Turbulence in the wake is responsible for re-collapsing some of these bubbles into the Taylor bubble and for pushing other bubbles downwards. The bubbles which are pushed downwards form a train of small bubbles (about 4 mm diameter) behind the turbulent wake, starting at about 2.5D from the trailing edge and with a length of several column diameters, as shown in Figure 3.3.

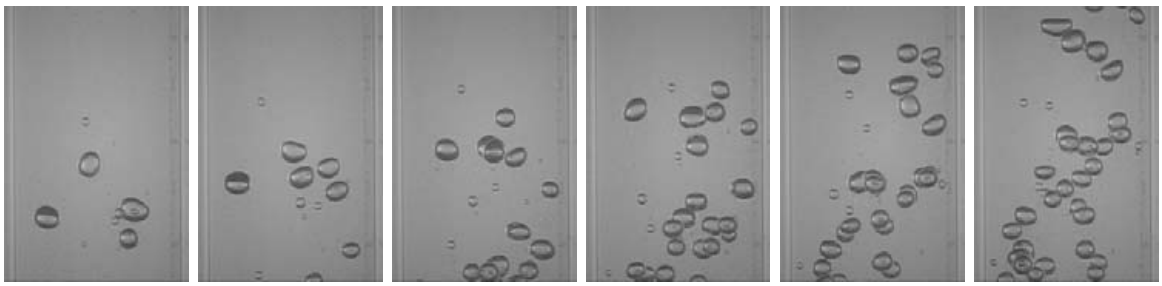

Figure 3.3. Train of small bubbles following a Taylor bubble with $8D$ length; time between frames 0.04 s.

Figure 3.4 shows consecutive frames of the wake of a short Taylor bubble with about a $2.5D$ length. By comparing Figures 3.2 and 3.4 it is clear that the amplitude of the oscillations of the trailing edge is lower for the shorter Taylor bubble. This behaviour can be explained by the lower velocity in the liquid film around the bubble (perhaps not yet stabilised). The velocity of the liquid merging at the bottom of the bubble is lower, inducing less turbulence in the wake. These observations are in agreement with those made by Polonsky *et al.* (1999) which confirmed that the amplitude of the oscillations increases with the bubble length, whereas the frequency remains nearly constant for bubbles rising in water.

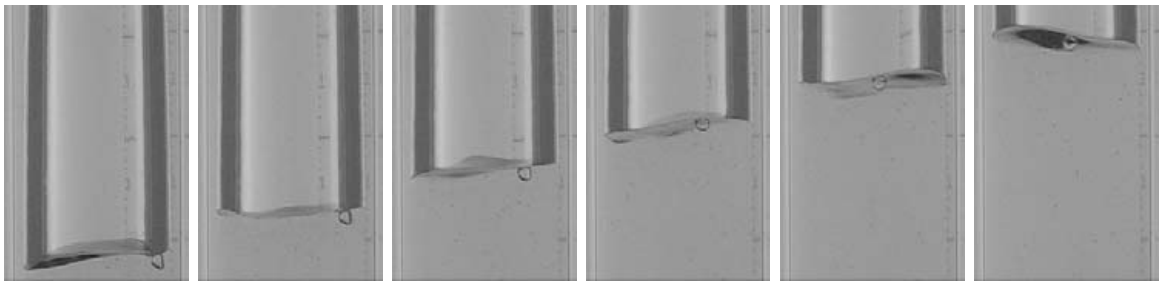

Figure 3.4. Consecutive frames of the wake of a Taylor bubble $2.5D$ in length rising in a 0.10 wt% CMC solution; time between frames 0.04 s.

For the smaller bubbles, although the amplitude of the trailing edge oscillations is reduced, any transport of liquid in the wake is not yet observed. There is, however, a lower number of small bubbles rising behind the Taylor bubble.

0.20 wt% CMC solution

For the 0.20 wt% CMC solution, the bubble length varied between 0.6 and 7.8D, and the bubble velocity between 0.193 and 0.200 m/s.

In this case, even with bubble velocities very close to those in the previous solution, some coloured liquid transported in the wake was observed. Recirculation regions are not clearly seen, however the presence of coloured liquid suggests this internal flow pattern occurs. Figure 3.5 shows sequential frames of the wake of a Taylor bubble rising in a 0.20 wt% CMC solution, with 0.08 s between frames.

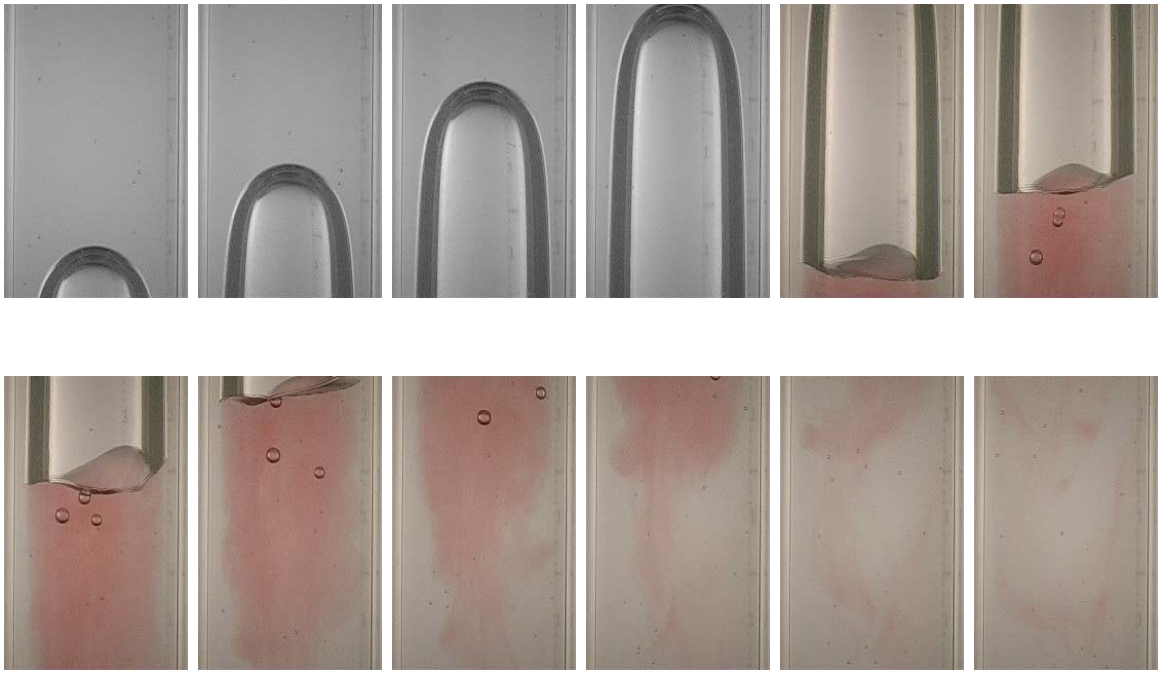

Figure 3.5. Sequential frames of the wake of a Taylor bubble ($L_\mathrm{b} = 2.2D$) rising in a 0.20 wt% CMC solution; time between frames 0.08 s.

The increase in liquid viscosity decreases turbulence in the wake region. Figure 3.5 clearly shows that there is still some oscillation in the trailing edge. The replacement of the liquid in the wake is slower due to the lower frequency of the turbulent eddies. This behaviour allows transport of coloured liquid to the top of the column although some is left behind, as seen in the last frames of Figure 3.5.

Although the wake region is not well defined due to the oscillations, an average length of 1.5D can be estimated. Due to the effect of stronger oscillations in the trailing edge of

large bubbles their wakes loose more fluid, presenting a less intense colour.

0.30 wt% CMC solution

In the 0.30 wt% CMC solution the trailing edge oscillation tends to disappear. In this solution, the bubble length varied from 1.5 to 9.7D and the velocity from 0.192 to 0.199 m/s.

In Figure 3.6 twelve consecutive frames of the wake of a Taylor bubble rising in a 0.30 wt% CMC solution are presented. This figure shows that the liquid colour in the wake

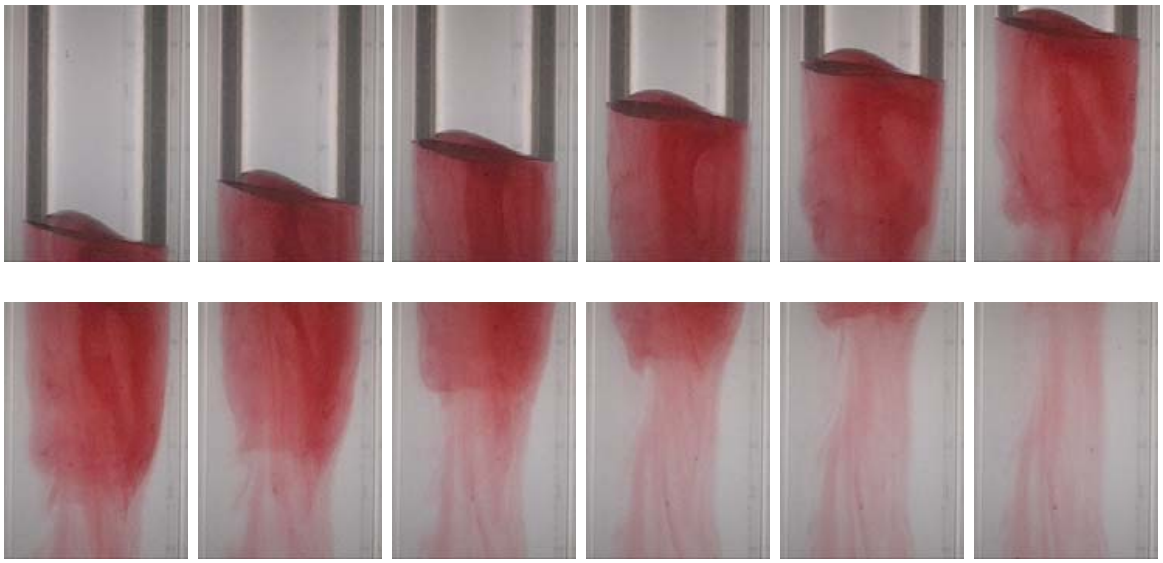

Figure 3.6. Consecutive frames of the wake of a Taylor bubble rising in a 0.30 wt% CMC solution; time between frames 0.04 s.

is now more intense, meaning that less fluid is lost during the bubble rise. The trailing edge maintains a stable inclined position during the rise of the bubble. This asymmetry is probably caused by a a vertical deviation in the column. The column inclination induces an asymmetric flow around the bubble and, consequently, an asymmetric recirculation region forms in the wake as shown in Figure 3.7.

Despite the trailing edge inclination, it can be concluded from the images acquired that the wake structure tends to be more stable than in the previous solutions and that there is no formation of small bubbles. These facts can be explained by a lower liquid film velocity which reduces the turbulence in the wake and incidental separation of small portions of gas. The wake length was now about 1.2D.

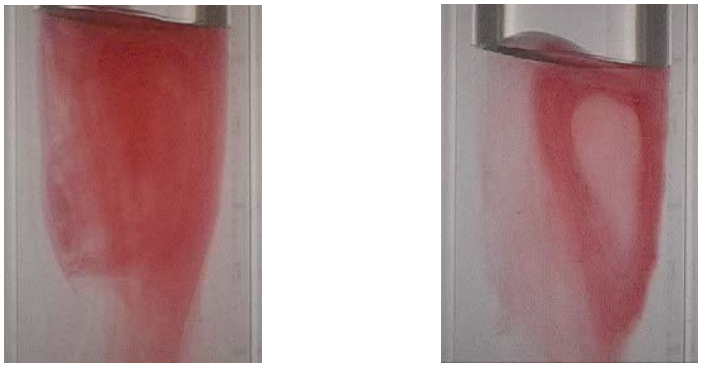

(a) Small vortex ring in the left (b) Large vortex ring in the right

Figure 3.7. Images of the wake of Taylor bubbles rising in a 0.30 wt% CMC solution.

0.35 wt% CMC solution

In the 0.35 wt% CMC solution the wake pattern was very similar to that of the previous solution. The bubble length varied between 0.9 and 12.2D and the velocity between 0.192 and 0.199 m/s. Figure 3.8 shows some consecutive frames of the wake of a bubble rising in a 0.35 wt% CMC solution. Different bubbles had a similar wake structure and the

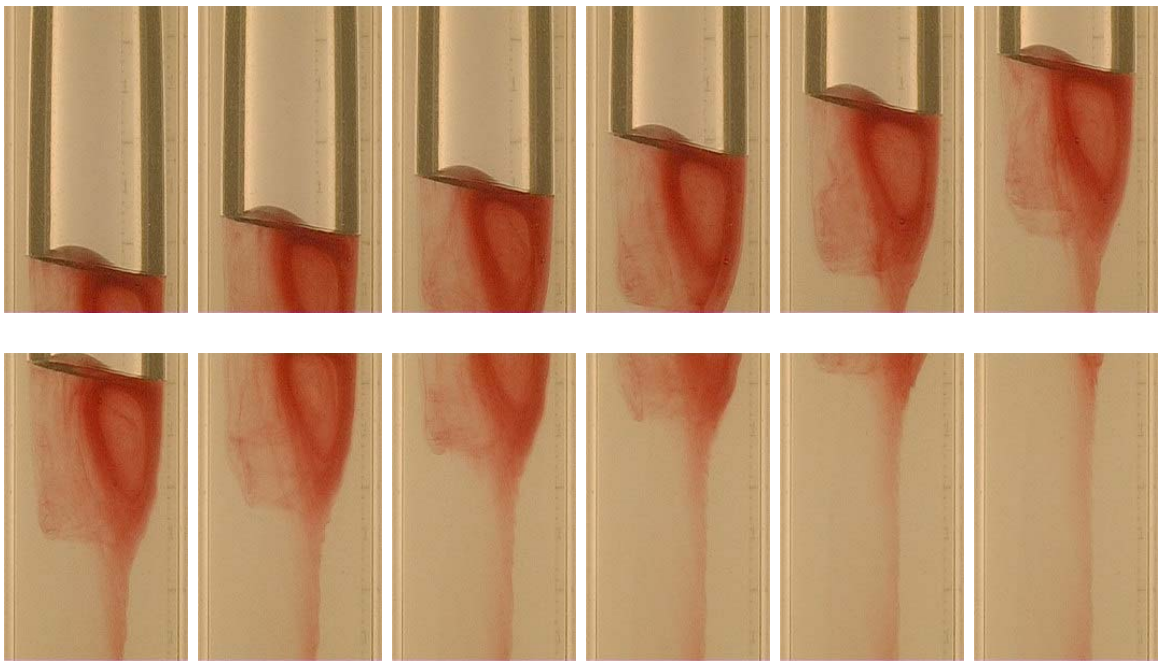

Figure 3.8. Consecutive frames of the wake of a Taylor bubble rising in a 0.35 wt% CMC solution; time between frames 0.04 s.

inclination of the trailing edge still appears, but the colour intensity changes for different bubble lengths.

Figure 3.9 shows the wakes of three bubbles with different length: in (a) a large vortex is seen on the right and an elongated vortex ring is seen on the left, in (b) the large vortex ring is clearly visible on the right and in (c) no coloured liquid is seen. Image (c) is of the longest bubble studied in this solution.

(a) Elongated vortex ring on the left and large vortex on the right, $L_\mathrm{b} = 2.5D$

(b) Large vortex on the right, $L_\mathrm{b} = 5D$

(c) No coloured liquid, $L_\mathrm{b} = 12D$

Figure 3.9. Images of the wake of Taylor bubbles rising in a 0.35 wt% CMC solution.

The absence of coloured liquid in the wake of the longest bubble ($12D$ long) is probably due to some small instabilities in the liquid film flow, which tend to appear preferentially in the longest bubbles. This does not imply a different wake volume, but vortex shedding occurs during the bubble rise, leaving some of the coloured liquid behind. The wake length for the bubbles rising through this fluid is around $1.0D$.

0.40 wt% CMC solution

In the 0.40 wt% CMC solution, no inclination or instability of the trailing edge of the Taylor bubbles was seen. Since between the experiments with different solutions the column has to be removed for cleaning, its orientation might suffer slight changes, below the uncertainty of the instrument used to verify its vertical alignment. The bubble length varied between 0.9 and $8.7D$ with a corresponding velocity variation in the range of 0.188 to 0.196 m/s.

The stability and symmetry of the trailing edge results in a stable and symmetric wake flow pattern. Figure 3.10 shows a sequence of images of the wake of a Taylor bubble rising in a 0.40 wt% CMC solution.

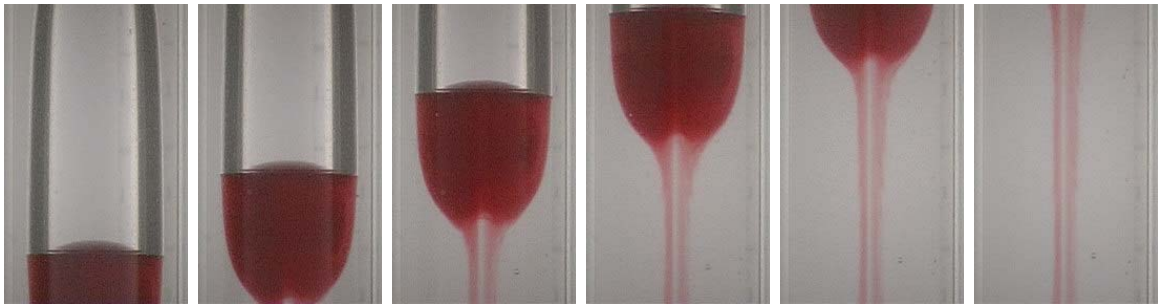

Figure 3.10. Sequential frames of the wake of a Taylor bubble rising in a 0.40 wt% CMC solution; time between frames 0.08 s.

Most of the wakes of the bubbles rising in this solution have a symmetric, donut-like shape. Figure 3.11 shows the wakes of different bubbles rising in a 0.40 wt% CMC solution; the plane projection in frame (a) clearly shows the recirculation regions that characterise these wakes and the symmetric leaking of coloured liquid behind the wake. Figures 3.11(b) and (c) show the result of the disturbance created by a small bubble trapped in the wake, which is responsible for the shedding of part of the wake. Figure 3.11(d) shows the practically closed wake of a shorter Taylor bubble, with insignificant loss of coloured

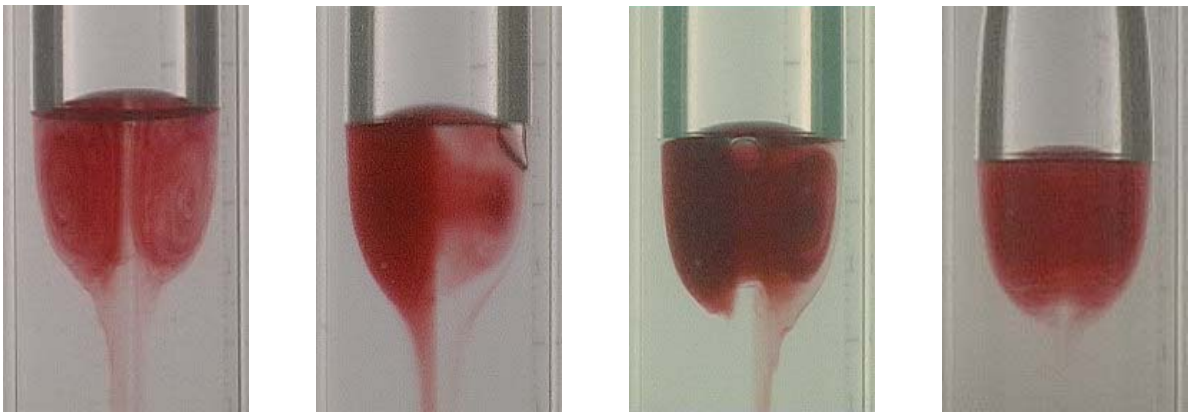

(a) Recirculation with symmetric leaking of fluid

(b) Disturbance of small bubble in the wake

(c) Asymmetric leaking of fluid

(d) Closed wake

Figure 3.11. Images of the wake of Taylor bubbles rising in a 0.40 wt% CMC solution.

liquid.

The wake length of Taylor bubbles rising in a 0.40 wt% CMC solution is around $0.8D$.

0.50 wt% CMC solution

As seen previously, the wake length tends to decrease as the weight percentage of CMC increases. In the 0.50 wt% CMC solution the wake length is around $0.5D$. A sequence of images of the wake of a Taylor bubble rising in this solution is represented in Figure 3.12.

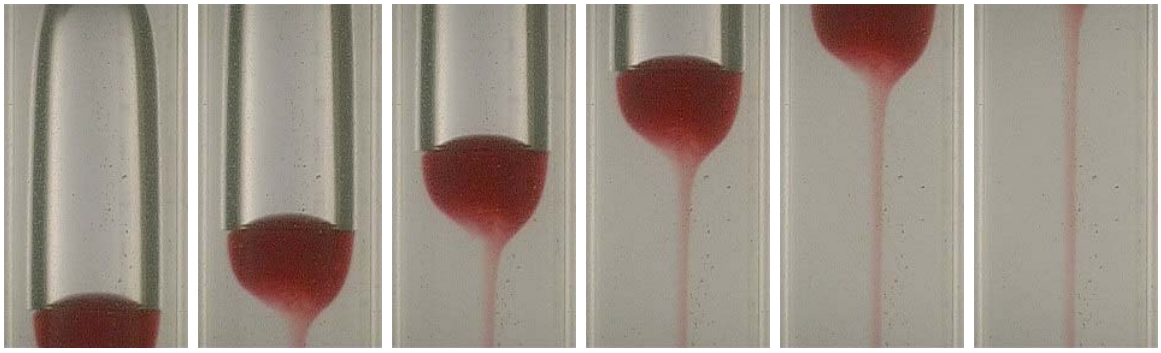

Figure 3.12. Sequential frames of the wake of a Taylor bubble rising in a 0.50 wt% CMC solution; time between frames 0.08 s.

The bubble length varied between 1.5 and $8.1D$ with the bubble velocity varying in the range 0.188-0.193 m/s. The wake flow patterns observed were all similar to the one shown in Figure 3.12, with a stable and slightly asymmetric wake shape and a tendency for a right-sided fluid leakage in the wake (in the two dimensional projection on the paper plane). This asymmetry is unexplained, but might indicate that there is a systematic experimental error, perhaps a slight misalignment of the column.

0.55 wt% CMC solution

In the 0.55 wt% CMC solution, the bubble length varied between 1.2 and $10.3D$, with a corresponding velocity variation between 0.186 and 0.193 m/s.

Figure 3.13 shows the wake of a small $2.5D$-long Taylor bubble rising in this solution. The wake length for this solution is only $0.35D$. For smaller bubbles the trailing edge is stable and the wake is symmetric.

For longer bubbles the wake pattern is not symmetric. In Figure 3.14 some frames acquired during the rise of a Taylor bubble with length of $5.3D$ are presented. In this case

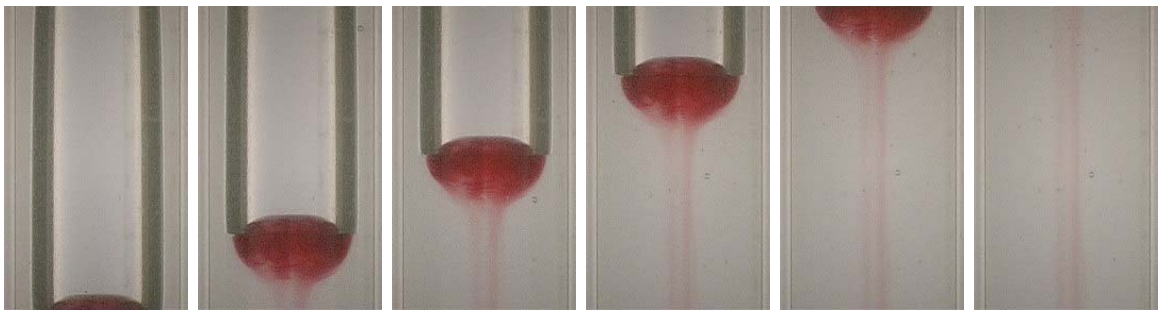

Figure 3.13. Sequential frames of the wake of a Taylor bubble with $2.5D$ in length rising in 0.55 wt% CMC solution; time between frames 0.08 s.

an unusual asymmetric shape is observed, especially in the concave region of the trailing edge, which is not completely filled with coloured fluid. Once again, this asymmetry always had a tendency to occur on the same side.

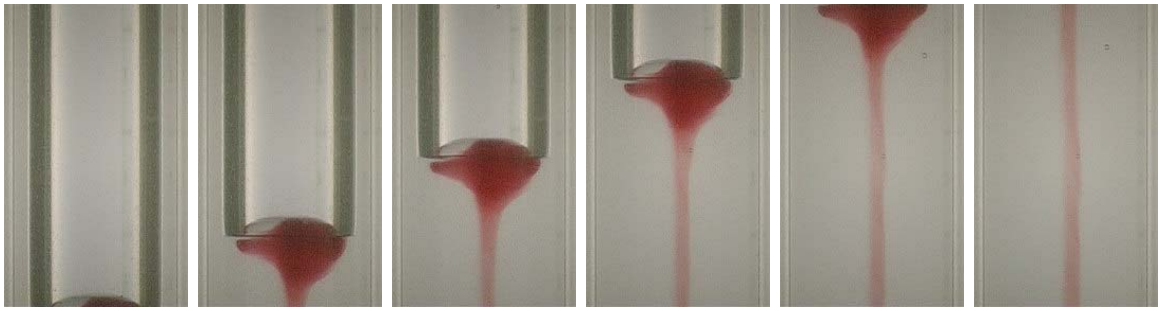

Figure 3.14. Sequential frames of the wake of a Taylor bubble $5.3D$ in length rising in a 0.55 wt% CMC solution; time between frames 0.08 s.

For the longest bubbles studied, with lengths greater than $8.0D$, some instabilities appear in the liquid film as oscillations (ripples) on the bubble body and trailing edge. Consequently, all the coloured fluid in the wake is lost during the rise of the bubble; an example for a bubble with $10.0D$ in length is presented in Figure 3.15.

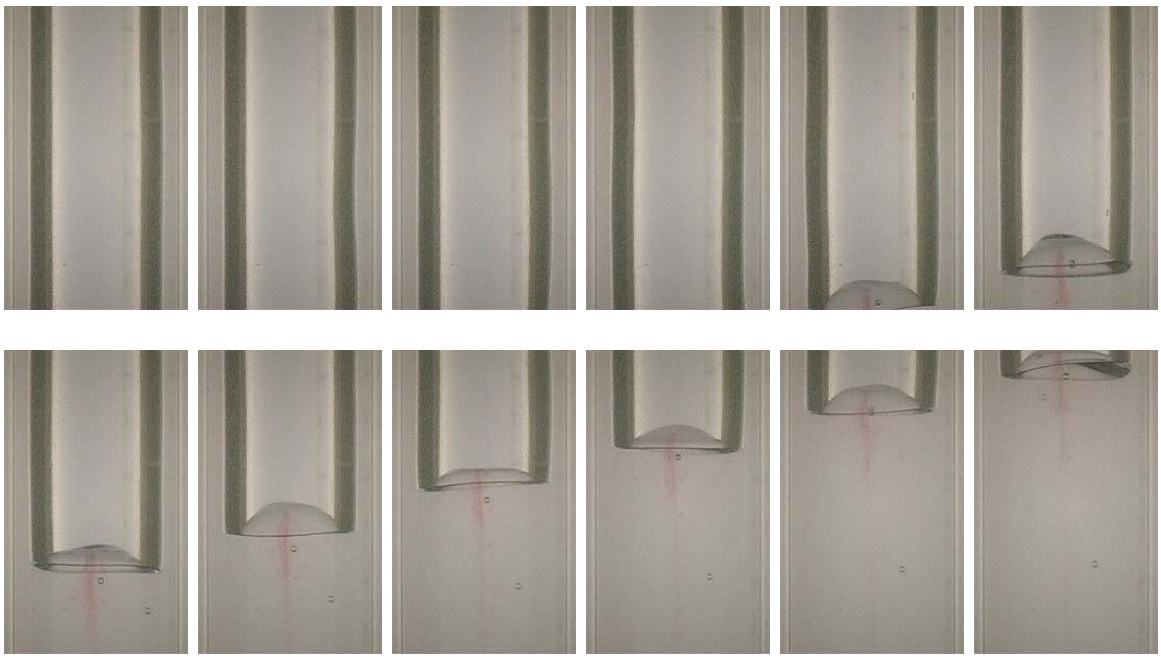

Figure 3.15. Consecutive frames of the rise of a Taylor bubble with $10.0D$ in length in a 0.55 wt% CMC solution; time between frames 0.04 s.

Wake volumes

The volumes of coloured liquid in the closed laminar wakes were determined with Visual Basic program mentioned in §2.1.3. The variation in volumes of coloured liquid related to bubble length is represented in Figure 3.16.

In this figure it is clear that for a given dimensionless bubble length, the coloured liquid volume decreases as the weight percentage of polymer increases. This is due to a decrease in bubble velocity and an increase in liquid film thickness. Both bubble velocity and liquid film thickness contribute to a lower velocity of the liquid at the bottom of the bubble. This low velocity and the high liquid viscosity induce a high rate of momentum diffusion in the radial direction (towards the axis of the column) and the result is an expansion of the liquid film over a shorter distance.

For the 0.40 wt% solution, the coloured liquid volume increases as the bubble length increases, up to a length where the liquid film should stabilise (around $L_\mathrm{b} = 4.0D$). For longer bubbles the coloured liquid volume remains constant to around $12 \times 10^{-6}\,\mathrm{m}^3$, since the merging velocity of the liquid film is the same. As no instabilities are seen in this solution this measured coloured liquid volume should correspond to the wake volume.

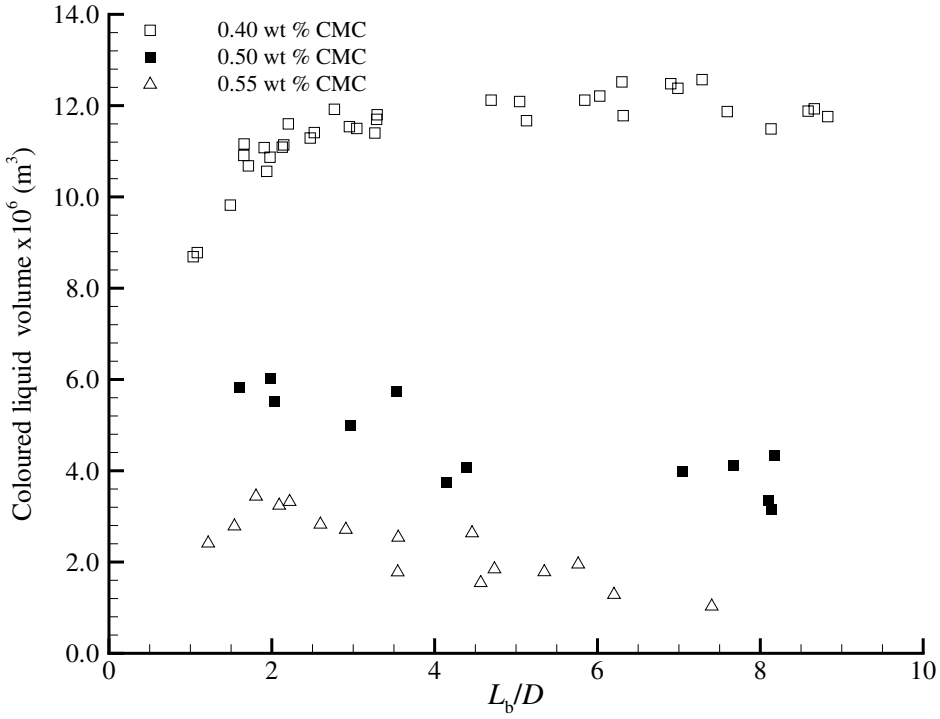

Figure 3.16. Representation of the coloured liquid volume versus the dimensionless bubble length for Taylor bubbles rising in 0.40, 0.50 and 0.55 wt% CMC solutions.

For the 0.50 and 0.55 wt% CMC solutions the instabilities in the longer bubbles are responsible for the loss of some coloured liquid, which is replaced by colourless liquid. The measured coloured liquid volume then appears to decrease for increasing bubble lengths, which does not mean a decrease in the bubble wake volume, which should follow the tendency observed in the 0.40 wt% CMC solution.

0.60 wt% CMC solution

In the 0.60 wt% CMC solution no coloured fluid was observed in the wake of rising Taylor bubbles. In the separation region between coloured and colourless liquid, small quantities of coloured liquid were present in the wake but were lost in a short distance. In this solution the bubble length varied between 0.9 and $10.9D$, and the bubble velocity between 0.185 and 0.192 m/s.

Figure 3.17 shows the trailing edge of a rising Taylor bubble in a 0.60 wt% CMC solution, in a 0.04 s frame sequence. All the bubbles with a length below $10D$ showed the

same behaviour seen in Figure 3.17, with a stable trailing edge and a high concavity.

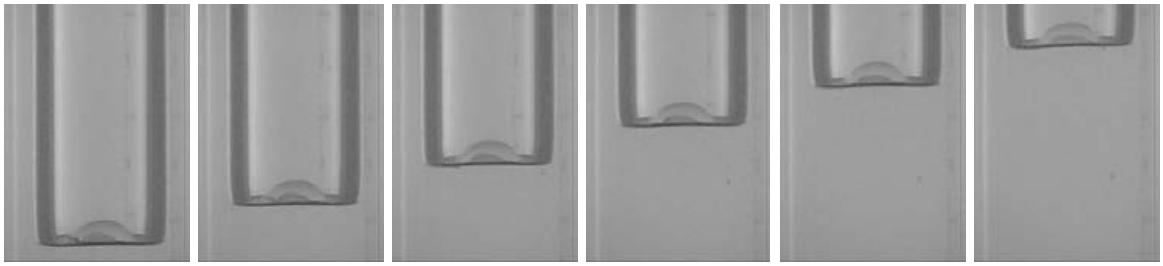

Figure 3.17. Consecutive frames of the trailing edge of a Taylor bubble, $L_b = 6D$, rising in a 0.60 wt% CMC solution; time between frames 0.04 s.

For the longest bubbles the same liquid film instabilities seen in previous solution weights appear, causing an oscillation on the bubble body and, consequently, on the trailing edge. Figure 3.18 shows frames of a rising Taylor bubble with a $11.2D$ length in a 0.60 wt% CMC solution. This figure demonstrates instabilities causing higher amplitude oscillations in the bubble body than in the previous solutions and bubble lengths.

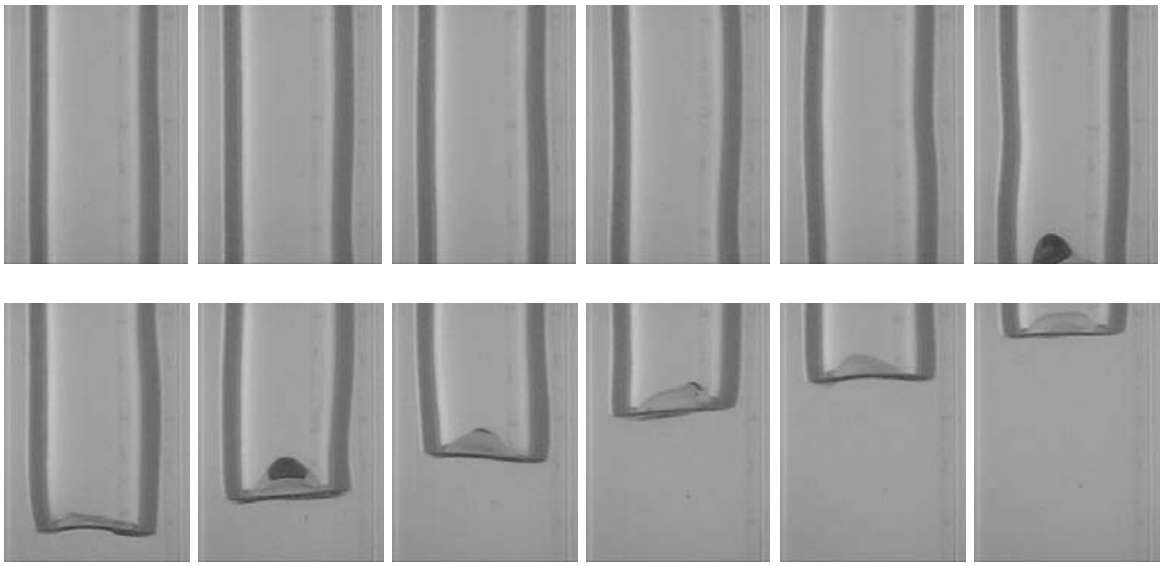

Figure 3.18. Consecutive frames of the trailing edge of a Taylor bubble, $L_b = 11.2D$, rising in a 0.60 wt% CMC solution; time between frames 0.04 s.

0.80 wt% CMC solution

In the 0.80 wt% CMC solution the bubble lengths were in the range of 1.8-12.1D, with bubble velocities varying between 0.177 and 0.186 m/s. As shown in Figure 3.1, the decreasing bubble velocity related with increasing wt% CMC is accentuated for the more concentrated solutions.

In this solution there is a drastic change in the shape of the bubble trailing edge. Figure 3.19 shows a sequence of frames acquired during the rise of a Taylor bubble in a 0.80 wt% CMC solution, where a droop in the profile in the trailing edge is seen. Instead of a concave

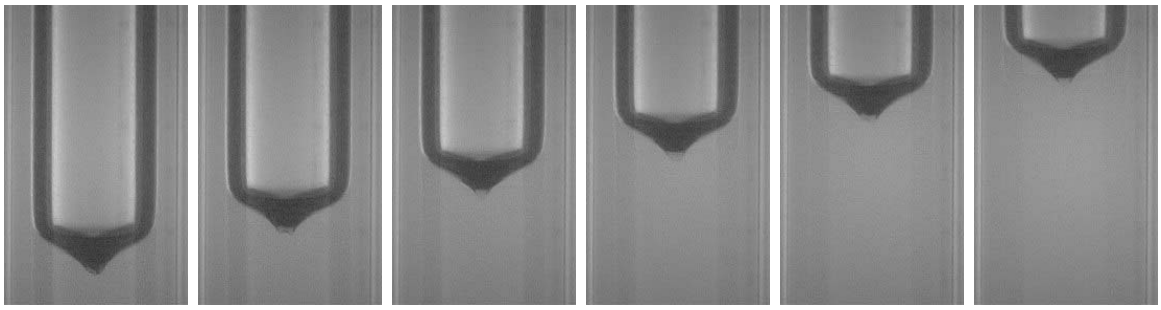

Figure 3.19. Consecutive frames of the trailing edge of a Taylor bubble with 6.5D in length rising in a 0.80 wt% CMC solution; time between frames 0.04 s.

shape (from the liquid side), the trailing edge acquires a lachrymal shape with decreasing radius. Although not very clear from the images, it was observed that the tip of the trailing edge changes slightly in shape during the rise.

Images of a small bubble in the falling liquid film around the Taylor bubble and in the wake are presented in Figure 3.20 suggesting a different wake flow pattern from those observed before.

In the first two frames, the downward movement of a small bubble on the right side of the image is seen. In the third frame, the bubble leaves the falling liquid film. In the fourth frame, the bubble is pushed to the axis of the column, to occupy the space left by the rising Taylor bubble. An interesting action is the downward displacement in the following frames, which implies a downward liquid movement in the axis of the column behind the Taylor bubble. This liquid movement is in the opposite direction to the buoyancy forces and to the Taylor bubble progress, which might indicate that the small bubble is in a negative wake, similar to that described by Hassager (1979) behind small bubbles.

For the largest bubbles, the same instabilities seen in the previous fluids occur but with

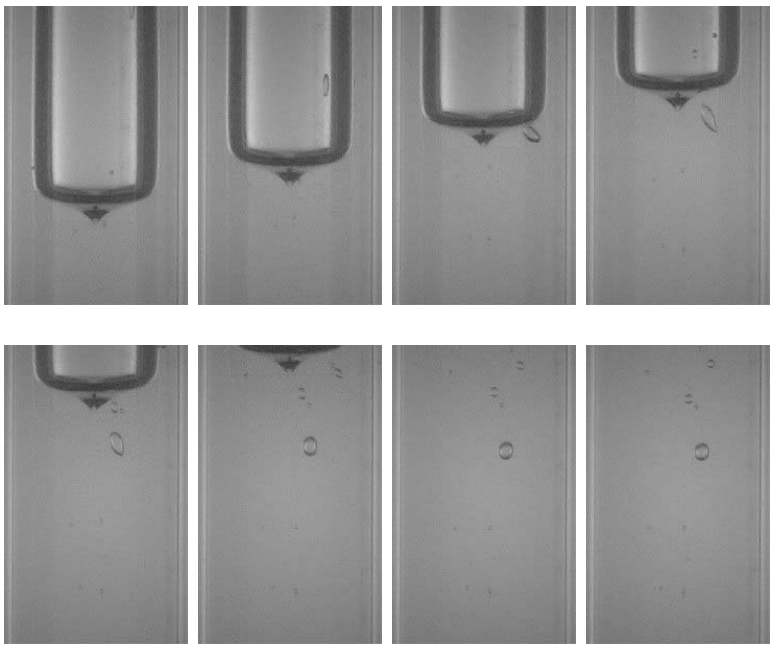

Figure 3.20. Consecutive frames of a small bubble in the wake of a Taylor bubble rising in a 0.80 wt% CMC solution; time between frames 0.04 s.

a higher intensity. Figure 3.21 shows those instabilities in a Taylor bubble with a $12D$ length.

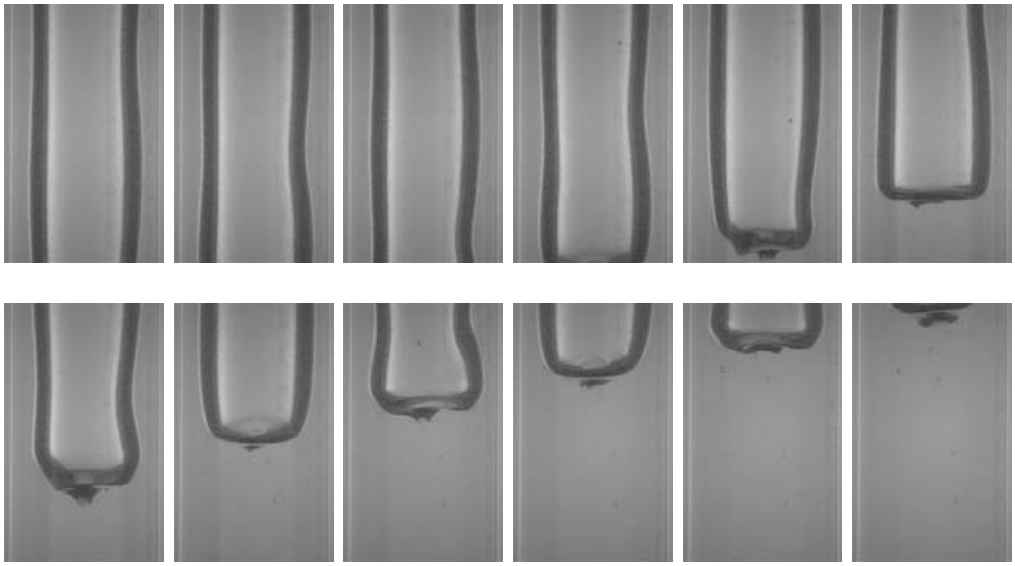

Figure 3.21. Consecutive frames of a Taylor bubble with $12D$ in length rising in a 0.80 wt% CMC solution; time between frames 0.04 s.

1.00 wt% CMC solution

The 1.00 wt% CMC solution was the highest concentration studied. Bubbles with lengths between 1.8 and 14.0D and velocities in the range 0.162-0.173 m/s were analysed. Once again, the bubble velocity was much lower than that in less concentrated solutions (Figure 3.1).

Figure 3.22 shows a sequence of frames of the trailing edge of a Taylor bubble rising in a 1.00 wt% CMC solution. The lachrymal shape becomes more pronounced and the shape of the tip changes slightly with time. In Figure 3.23 a set of enlarged images of the trailing edge tip in consecutive frames is presented. Due to the difficulty in seeing the bubble trailing edge shapes, they have been outlined.

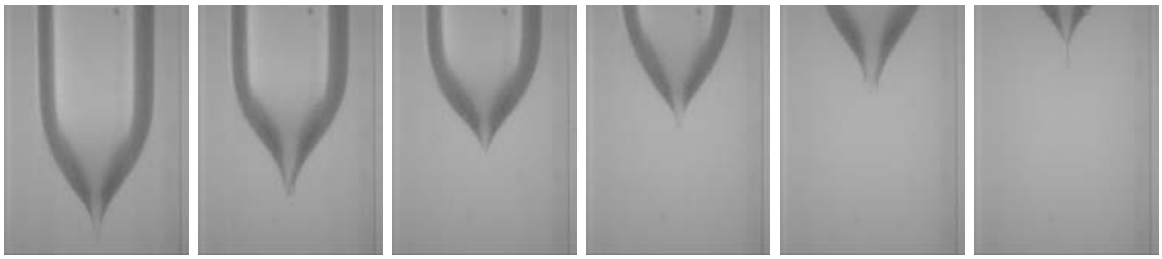

Figure 3.22. Consecutive frames of the trailing edge of a Taylor bubble rising in a 1.00 wt% CMC solution; time between frames 0.04 s.

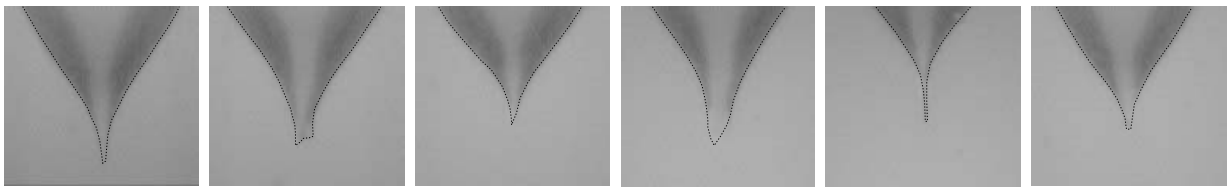

Figure 3.23. Enlargement of consecutive frames of the trailing edge tip of a Taylor bubble rising in a 1.00 wt% CMC solution; time between frames 0.04 s.

These images show that the trailing edge tip is not symmetric, and has a cusp shape. The different positions of the cusped edge in consecutive frames appear to indicate a rotation of the cusped trailing edge.

Similar to in the previous solution weights, in the largest bubbles there are disturbances in the liquid film flowing around the bubble, causing an oscillation on the bubble interface. An example of a Taylor bubble with 14D in length rising in this solution is presented in

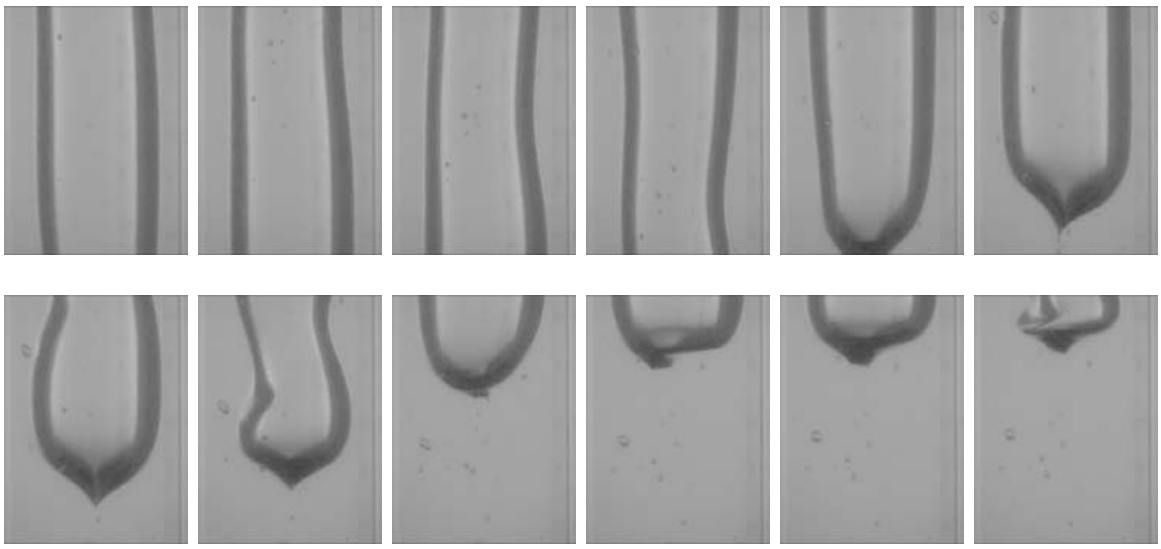

Figure 3.24. Consecutive frames of a Taylor bubble with $14D$ in length rising in 1.00 wt% CMC solution; time between frames 0.04 s.

Figure 3.24.

This was the highest CMC concentration studied because in higher viscosity solutions small bubbles appear during the fluid mixing and manipulation, which are very difficult to remove. Higher concentrations of CMC also lead to less limpid solutions, which are inappropriate for visualisation studies.

Summary of visualisation studies in CMC solutions

As a summary of the typical wake structures seen in all the visualisation studies performed with CMC polymer solutions is presented in Figure 3.25,.

Figure 3.25 shows the changes observed in the wake flow pattern. From a qualitative perspective, it can be said that in case (a) there is a turbulent flow in the wake. The transition from turbulent to laminar occurs in cases (b)-(d). In cases (e)-(g) the wake regime is laminar and the wake is practically a closed recirculation region. In the higher concentration solutions, (h)-(j), there is no coloured liquid seen in the wakes.

These visualisation studies allowed flow characterisation in a large range of polymer weight percentages, facilitating the selection of conditions to be studied in detail with the PIV technique. Due to time limitations it was not possible to study all the conditions observed. Therefore, cases (b), (d), and (g) where excluded from the PIV studies. The

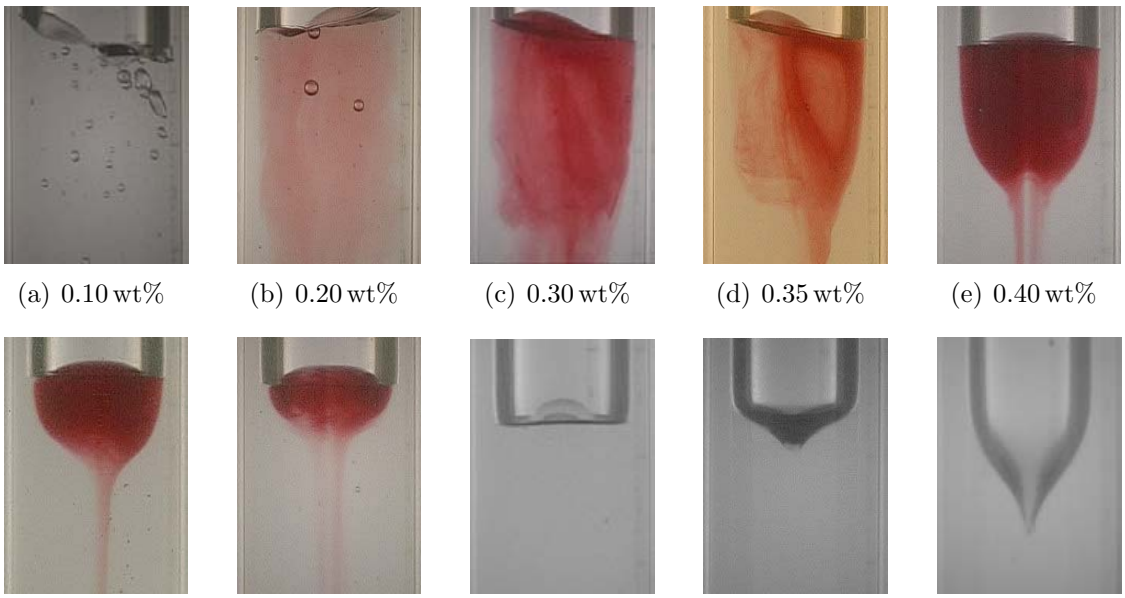

(a) 0.10 wt% (b) 0.20 wt% (c) 0.30 wt% (d) 0.35 wt% (e) 0.40 wt%

(f) 0.50 wt% (g) 0.55 wt% (h) 0.60 wt% (i) 0.80 wt% (j) 1.00 wt%

Figure 3.25. Summary of CMC solutions visualisation studies.

rheology of the solutions used in the PIV studies is presented in the next section.

3.2 Rheological characterisation of CMC solutions

The rheological characterisation of the CMC polymer solutions used in the PIV measurements was made in an AR 2000 DTA Instruments Rheometer. The polymeric solutions used are non-Newtonian fluids, with shear thinning viscosity and moderate elasticity.

In the rheological characterisation of the fluids, a cone-plate geometry, sketched in Figure 3.26, was used to determine the relation between the shear rate and the shear stress, where R_C(m) is the radius of the cone, T_R(Nm) the torque, Ω(rad/s) the angular velocity, $\alpha(^o)$ the cone angle and F(N) the vertical force that is the result of non-zero normal stress differences in non-Newtonian fluids.

The advantage of this geometry is that all the fluid is under the same shear rate, as long as the cone angle is below 4°. In these studies the cone radius was $R_C = 20\,\text{mm}$, and the cone angle $\alpha = 2°$.

With the cone-plate geometry the shear stress, τ(Pa), shear rate, $\dot{\gamma}(\text{s}^{-1})$, and first

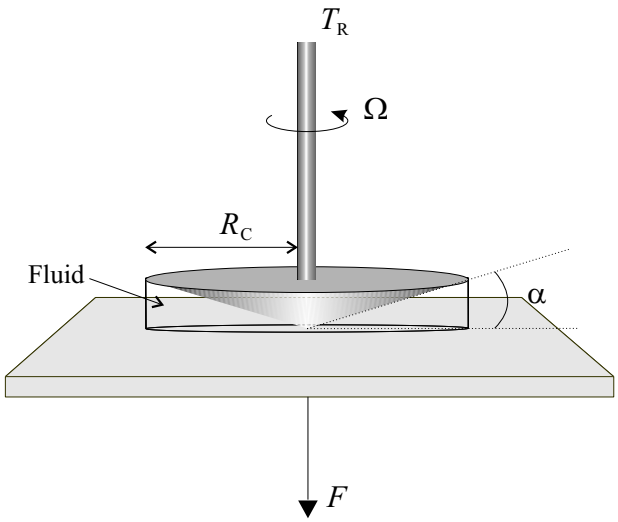

Figure 3.26. Cone-plate geometry used in the rheologic characterisation of the fluids.

normal stress difference, N_1(Pa), are given by equations 3.1, 3.2 and 3.3 respectively.

$$\tau = \frac{3T_R}{2\pi R_C^3} \tag{3.1}$$

$$\dot{\gamma} = \frac{\Omega}{\tan\alpha} \tag{3.2}$$

$$N_1 = \frac{2F}{\pi R_C^2} \tag{3.3}$$

By measuring the torque that has to be applied in order to keep a certain angular velocity it is possible to determine the applied shear stress and the corresponding shear rate. The shear viscosity is given by the ratio between these two quantities. For each fluid the shear viscosity was measured as a function of the shear rate at experimental temperature. All the fluids showed a shear thinning behaviour, with decreasing viscosity for increasing shear rate. The measured viscosity data are well-fitted to the Carreau-Yasuda viscosity model:

$$\mu = \mu_\infty + (\mu_0 - \mu_\infty)(1 + (\lambda \cdot \dot{\gamma})^{a_1})^{\frac{a_2-1}{a_1}} \tag{3.4}$$

where; μ is the measured viscosity, $\dot{\gamma}$ the applied shear rate, μ_0 the viscosity limit when $\dot{\gamma} \to 0$, and μ_∞ the viscosity at infinite shear rate, which was set as the solvent viscosity. The parameter λ has units of time, a_1 and a_2 are dimensionless parameters. The viscosity of the different CMC solutions and the Carreau-Yasuda model curves are represented in

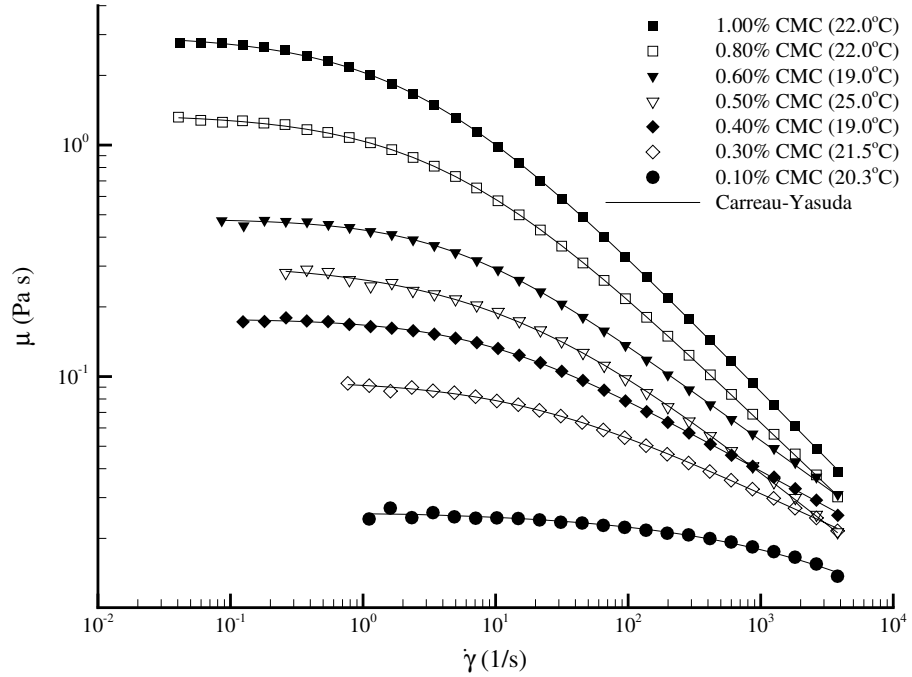

Figure 3.27. Representation of the shear viscosity, μ, as a function of the shear rate, $\dot{\gamma}$, for the CMC solutions studied with PIV.

Figure 3.27.

The values of the Carreau-Yasuda model parameters are listed in Table 3.2.

Table 3.2. Carreau-Yasuda viscosity model parameters for the CMC solutions.

CMC wt%	$T(^o\mathrm{C})$	μ_0 (Pa s)	μ_∞(Pa s)	λ (s)	a_1	a_2	$\dot{\gamma}(\mathrm{s}^{-1})$
0.10	20.3	0.009	0.001	0.021	0.850	0.871	1–4000
0.30	21.5	0.051	0.001	0.057	0.712	0.721	0.7–4000
0.40	19.0	0.110	0.001	0.110	0.809	0.675	0.125–4000
0.50	25.0	0.220	0.001	0.063	0.565	0.509	0.25–4000
0.60	19.0	0.360	0.001	0.183	0.832	0.574	0.08–4000
0.80	22.0	1.050	0.001	0.221	0.661	0.433	0.04–4000
1.00	22.0	2.990	0.001	0.365	0.668	0.400	0.04–4000

The first normal stress difference, N_1, was measured for the more concentrated solutions and is represented in Figure 3.28 versus the shear rate. In order to quantify the viscoelastic effects, the fluid relaxation time was determined for the fluids with measurable first normal

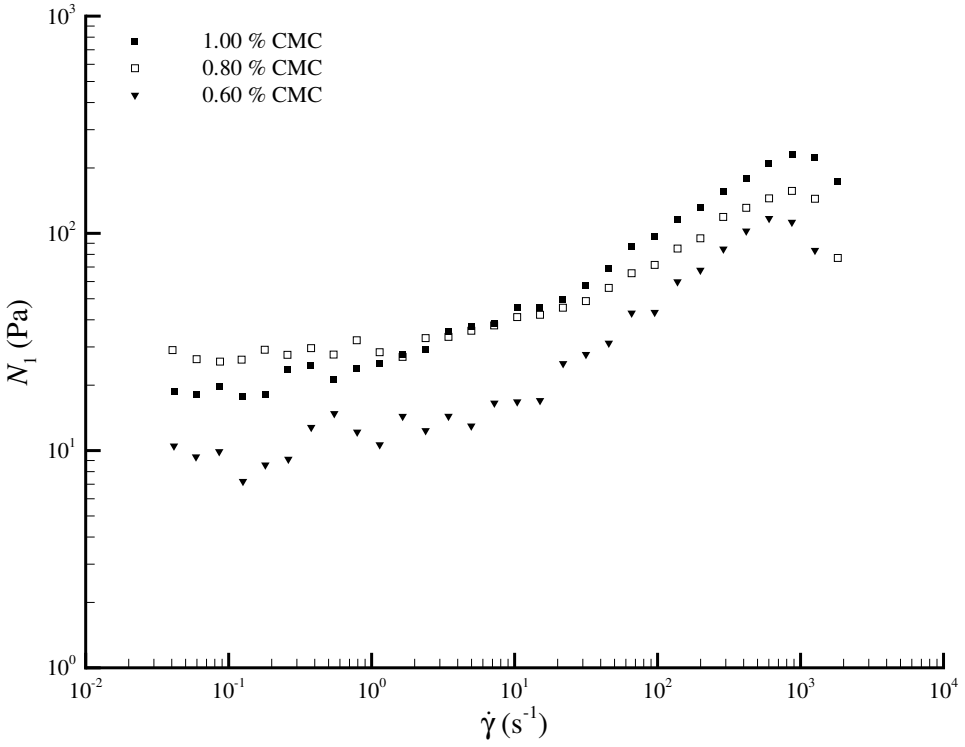

Figure 3.28. Representation of the first normal stress difference versus the shear rate for the more concentrated CMC solutions.

stress difference. Leider and Bird (1974) defined the fluid relaxation time, θ_f, using the fact that both shear stress, τ, and N_1 can be well approximated by power functions of the shear rate over the range of conditions of interest, i.e., $\tau = m_2(\dot{\gamma})^{s_2}$ and $N_1 = m_1(\dot{\gamma})^{s_1}$.

$$\theta_f = \left(\frac{m_1}{2m_2}\right)^{\frac{1}{s_1 - s_2}} \tag{3.5}$$

The characteristic shear rate of the flow, defined as $\dot{\gamma}_f = U_b/D$, is between 5 and 6 s^{-1} for the more concentrated solutions. To obtain the relaxation time, the shear stress and the first normal stress difference were approximated by power functions of the shear rate in the range 0.04–10 s^{-1}. The relaxation time, θ_f, and the corresponding Deborah number, $De = \theta_f \cdot \dot{\gamma}_f$, are presented in Table 3.3 for the more concentrated solutions.

The Deborah number absolute values depend on the proposed definition of relaxation time. However, from Table 3.3 there is a clear change in its order of magnitude from the less to the more concentrated solutions, indicating an increase of the elastic effects.

Table 3.3. Relaxation time and Deborah number for the higher concentration solutions.

CMC wt%	θ_{f} (s)	De
0.60	< 0.001	< 0.001
0.80	0.029	0.166
1.00	0.047	0.236

The Reynolds number, $Re = \rho_l U_{\mathrm{b}} D/\mu$, where ρ_l is the liquid density, was also determined, using the viscosity at the characteristic flow shear rate, $\dot{\gamma}_{\mathrm{f}}$. Values of the experimental temperature, gas bubble velocity and Reynolds number are presented in Table 3.4 for all the solutions studied.

Table 3.4. Experimental temperature, bubble velocity and Reynolds number.

wt%	$T(^{\circ}\mathrm{C})$	$U_{\mathrm{b}}(m/s)$	Re
0.10	20.3	0.199	714
0.30	21.5	0.198	144
0.40	19.0	0.195	70
0.50	25.0	0.192	41
0.60	19.0	0.187	24
0.80	22.0	0.180	10
1.00	22.0	0.160	4

The Taylor bubble shape and the velocity field around the bubbles rising in the different solutions are described in the next sections.

3.3 PIV/ST measurements

The simultaneous Particle Image Velocimetry and Shadowgraphy Technique described in §2.2 were applied to analyse the flow around individual Taylor bubbles rising in the CMC solutions described in the previous section. The flow around the Taylor bubble is described in the next sections, comparing the different velocity fields in each region of the flow: bubble nose, annular liquid film and wake.

During the PIV experiments different bubble sizes were studied. For some of the fluids several bubble lengths were used, while in others only two lengths were used. For all the fluids, the results are focused on bubbles with a fully developed liquid film and without film instabilities (rippling). The instabilities were not part of this investigation since they cause a three dimensional flow in the liquid film which is difficult to analyse with two-dimensional PIV.

In the following sections, the system of coordinates represented in Figure 3.29 was used, with the origin placed at the bubble nose. The positive vertical direction is downwards

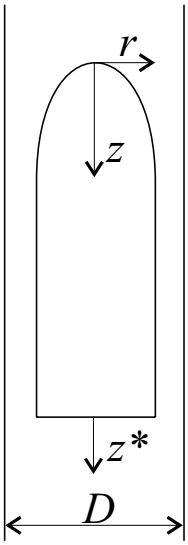

Figure 3.29. Coordinates system used to present the PIV/ST results.

for position and axial velocity. In the wake flow section, the axial distance, $z*$, is relative to the bubble trailing edge and not to the bubble nose. The radial position is positive to the right of the column axis and negative to the left, in the paper plane. The radial velocities are considered to be positive when the direction is outwards and negative when

moving towards the axis of the column. Most of the time the position is presented in a dimensionless form, by dividing the radial and axial distances by the column diameter.

3.3.1 Bubble shape

The shape of a Taylor bubble changes with different weight percentages of polymer. Fluid viscosity increases with polymer concentrations and the falling liquid film becomes thicker, changing the nose curvature slightly.

Taylor bubble shapes were obtained from the bubble shadows, using a simultaneous PIV and shadowgraphy technique as described in §2.2.6. The bubble shapes with better contrast could also have been obtained from the visualisation images, but the shadow images have the advantages of being acquired in the same experimental conditions as the PIV images and have better resolution.

The dimensionless bubble shapes are represented in Figure 3.30 for some of the CMC fluids studied. For better visualisation not all the bubble shapes are represented in this figure since they fall between the presented ones.

From the nose region to the trailing edge the Taylor bubble shapes are very similar. They have a prolate spheroid nose, with a more accentuated curvature in higher viscosities. The radius of the bubble (in a horizontal plane) increases with z/D, until it reaches a maximum value, r_∞, at a certain distance from the nose. The maximum bubble radius for each solution studied is presented in Table 3.5.

Table 3.5. Maximum bubble radius, r_∞ for the different solutions studied.

Re	(r_∞/D)	Re	(r_∞/D)
714	0.455	24	0.406
144	0.438	10	0.393
70	0.427	4	0.353
41	0.418		

Due to the similarity of the bubble shapes in different solutions, an attempt to define a general bubble shape was successful. It was found that the bubble shapes are well described by:

$$r/D = k_{c1} \cdot \tanh(k_{c2} \cdot (z/D)^{k_{c3}}) \tag{3.6}$$

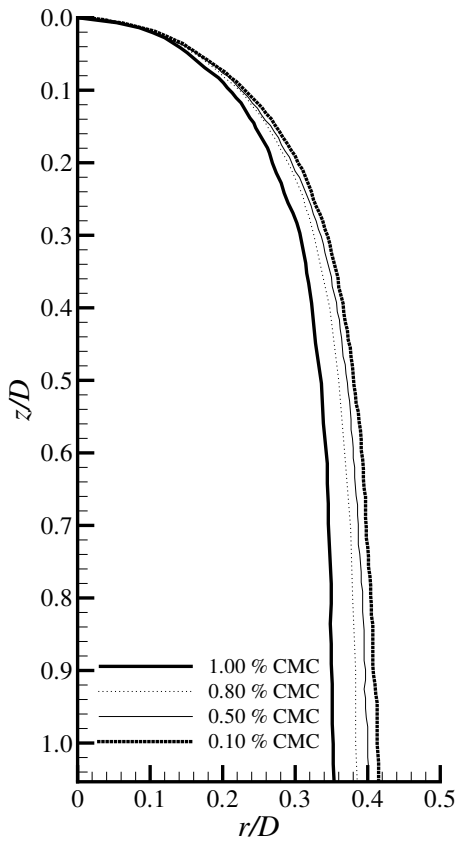

Figure 3.30. Taylor bubble shapes in the form of dimensionless radius, r/D, versus the dimensionless distance to the nose, z/D.

where the parameter k_{c1} coincides with the dimensionless maximum bubble radius presented in Table 3.5, which is function of Reynolds number according to equation 3.7:

$$(r_\infty/D) = k_{c1} = 0.019 \ln(Re) + 0.342 \tag{3.7}$$

and k_{c2}, k_{c3} were obtained by adjustment to the experimental values. These parameters are a function of Reynolds number according to equations 3.8 and 3.9 respectively.

$$k_{c2} = 3.983 \cdot Re^{-0.111} \tag{3.8}$$

$$k_{c3} = 0.648 \cdot Re^{-0.068} \tag{3.9}$$

The bubble shapes obtained with correlation (3.6) have a maximum error of 4%, mainly in the higher and lower viscosity limits. This represents a new approach to modelling Taylor

bubble shapes, since the three different regions in which the bubble shape is usually divided are now described by a single equation.

Using the formula deduced by Brown (1965) (see §1.1) for the prediction of the laminar film thickness based on the characteristic viscosity of the flow at a shear rate of U_b/D, overestimates the film thickness. This is because the characteristic viscosity is higher than that in the liquid film, where the shear rate is much higher. Since the liquid film shear rate is not known, *a priori*, Brown's formula can not be used to estimate the film thickness or maximum bubble radius.

The shape of the bubble trailing edge was already described in §3.1.2, using a higher frequency camera. The PIV camera acquires images at 4.11 Hz, which allows only a single instant view of the bubble and not its evolution over time.

3.3.2 Bubble velocity and length

In section 3.1.1 the bubble velocities and lengths obtained in the visualisation studies were presented. Since the column is open to the atmosphere in the PIV measurements, there is also the effect of bubble expansion in the liquid above the bubble and the consequent effect on the bubble velocity. Figure 3.31 shows the velocity and length of all the bubbles in the PIV studies. Taylor bubble behaviour is the same as in the visualisation studies, but due to differences in the experimental temperature there is a slight shift in the velocities, which tend to be lower in the PIV studies. The explanation for the velocity variation with the bubble length can be experimentally confirmed with the PIV measurements, as shown in the next section.

3.3.3 Flow ahead of Taylor bubble

When the column of liquid is open to the atmosphere the bubbles expand during the rise, due to the hydrostatic pressure gradient. This expansion induces an upward movement in the liquid above the bubble. The liquid velocities are relatively low so the seeding particle displacement can only be detected with large time gaps between PIV frames . To measure the flow above the Taylor bubble only the first frames of consecutive pairs of PIV images were used, the 1/4.11 s time between them being given by the camera frequency.

The volumetric flow rate of the liquid above the bubble should be equal to the bubble volume change rate. To check this, a detailed study of bubbles of different sizes rising in

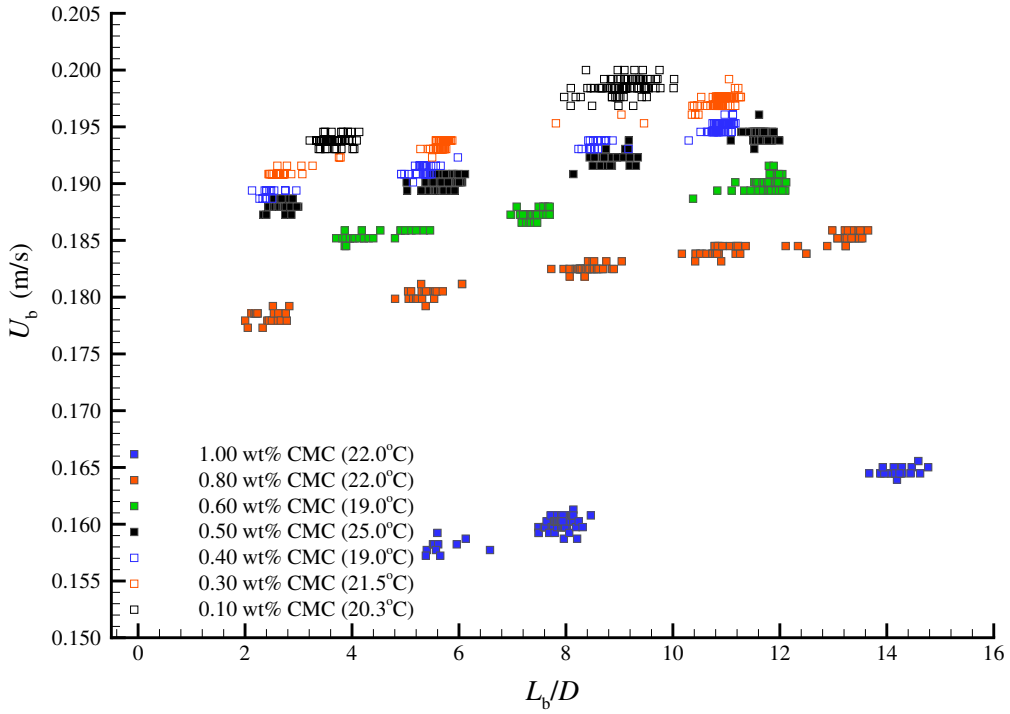

Figure 3.31. Representation of bubble velocity versus bubble length measurements in the PIV studies.

a 0.50 wt% CMC solution was made. This solution was chosen since it approximates the average concentration of the solutions studied. The stability of the trailing edge and the absence of small bubbles in the wake also contributed to a more accurate determination of the gas volume.

The flow field in the liquid far ahead of a bubble with $11.7D$ in length is represented in Figure 3.32, where the flow is fully developed.

Figure 3.33 represents the average velocity profile in the liquid ahead of four bubbles with different lengths. These velocity profiles were taken more than $2D$ ahead of the bubble nose where the flow is not disturbed, as will be seen later. From this figure it is clear that the longer the bubble is, the higher is the velocity in the liquid ahead of it. In this region, due to the low velocity gradients, the maximum shear rate is around $1\,s^{-1}$, which means that the viscosity does not vary significantly, as expected from Figure 3.27. Therefore, the liquid in this region has a practically Newtonian behaviour. The velocity profiles represented in Figure 3.33 practically coincide when represented in the dimensionless form, dividing the local velocities by the maximum velocity at the axis. The same behaviour is found in the

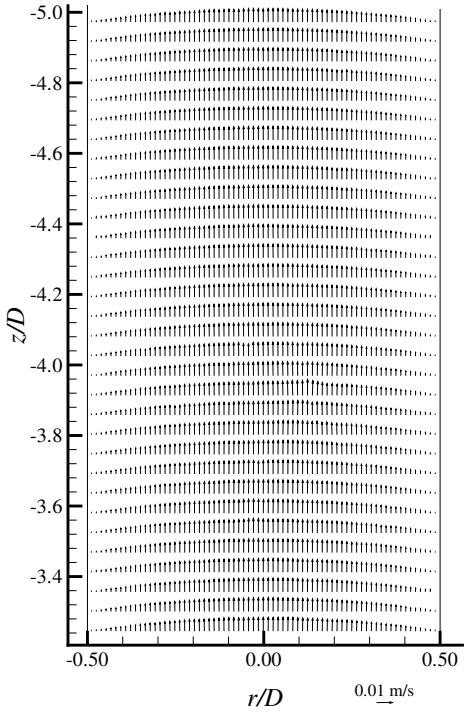

Figure 3.32. Flow field ahead of a bubble with $11.7D$ in length rising in a 0.50 wt% CMC solution.

other CMC solutions. The comparison between the dimensionless velocity profiles in the CMC solutions and the theoretical Newtonian case is shown in Figure 3.34.

The contribution of the bubble expansion to the bubble velocity may be confirmed if the maximum velocity of the liquid above the bubble is subtracted from the bubble velocity, as shown in Figure 3.35. Despite the spread in bubble velocity-length values, Figure 3.35 shows that this subtraction gives an approximately constant bubble velocity value for each solution. This value is close to the tendency observed in Figure 3.31 when $L_\mathrm{b} \to 0$ and should be the drift bubble velocity (independent of bubble length) if the column was closed on both ends, thereby blocking bubble expansion.

By integrating the velocity profile in the cross-sectional area of the column far ahead of the bubble, it is possible to calculate the liquid flow rate, Q_exp. This flow rate will now be compared with the expected gas volume variation rate:

If h is the distance from the bubble nose to the liquid surface at a certain position in

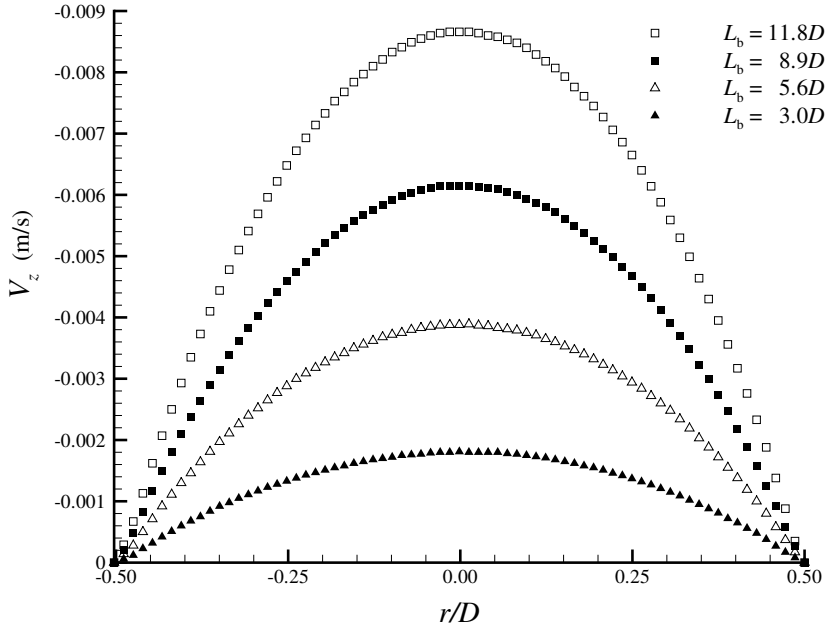

Figure 3.33. Average velocity profiles ahead of bubbles with different lengths (L_b) rising in a 0.50 wt% CMC solution.

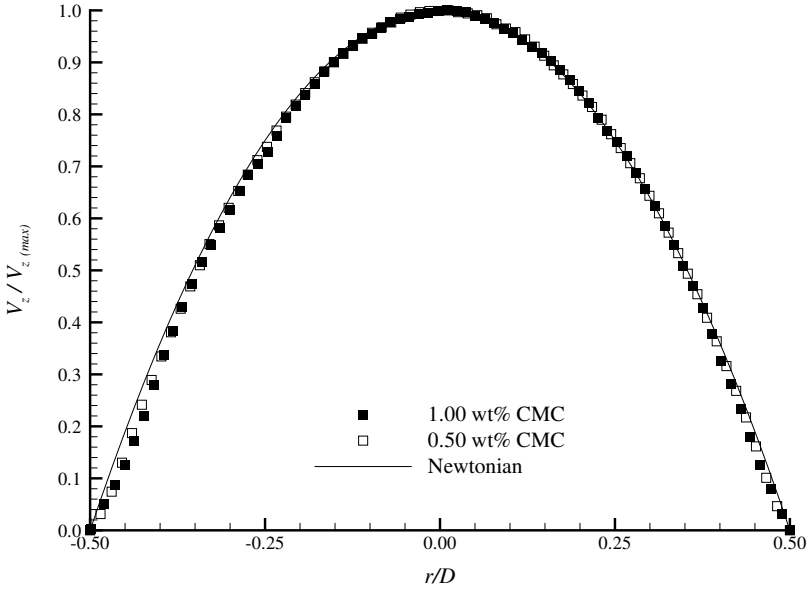

Figure 3.34. Comparison between the dimensionless expansion velocity profiles ahead of bubbles rising in the CMC solutions and the Newtonian velocity profile in a tube.

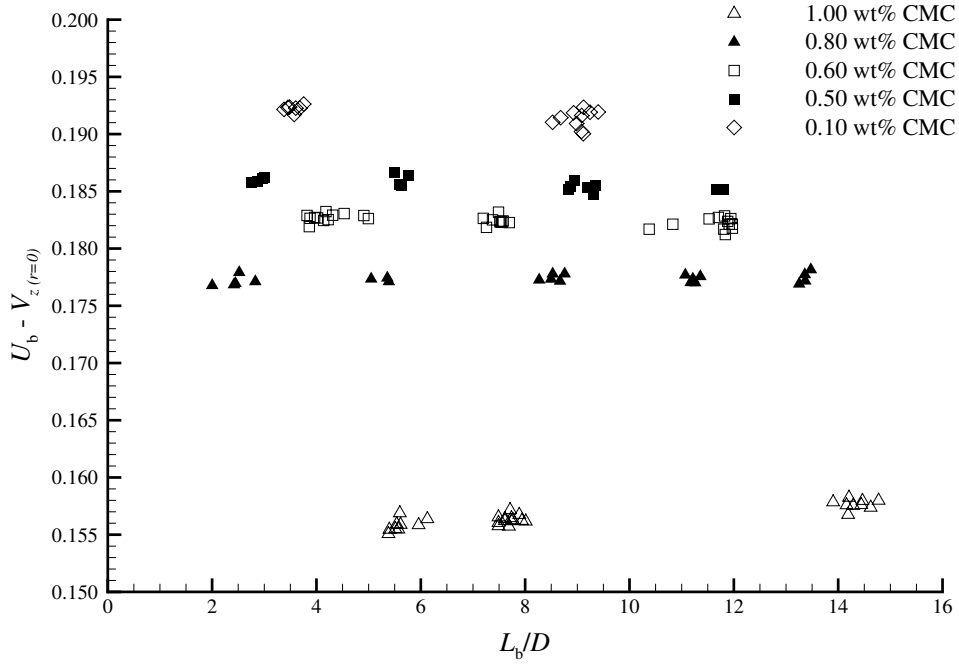

Figure 3.35. Bubble velocity after subtracting the liquid velocity at the axis ahead of the bubble nose, versus the bubble length.

the column, the hydrostatic pressure at the nose is given by

$$P(h) = P_{atm} + \rho g h \tag{3.10}$$

The volume of a Taylor bubble (ϑ_b) is then given by the perfect gas law:

$$\vartheta_{\mathrm{b}} = \frac{n \cdot \Re \cdot T}{P(h)} = \frac{n \cdot \Re \cdot T}{P_{atm} + \rho g h} \tag{3.11}$$

The variation of the bubble volume with the distance to the liquid surface is given by:

$$\frac{\partial \vartheta_{\mathrm{b}}}{\partial h} = -\frac{n \cdot \Re \cdot T}{(P_{atm} + \rho g h)^2} \cdot \rho g = -\frac{\vartheta_{\mathrm{b}}}{P_{atm} + \rho g h} \cdot \rho g \tag{3.12}$$

The variation rate of the bubble volume is:

$$\frac{\partial \vartheta_{\mathrm{b}}}{\partial t} = \frac{\partial \vartheta_{\mathrm{b}}}{\partial h} \cdot \frac{\partial h}{\partial t} = -\frac{\partial \vartheta_{\mathrm{b}}}{\partial h} \cdot U_{\mathrm{b}} \tag{3.13}$$

The liquid flow rate ahead of the bubble should then be equal to the variation rate of

the Taylor bubble volume given by equation 3.13, which can be determined if the distance to the liquid surface and the bubble volume are known. The bubble volume was determined by integrating its shape (see §3.3.1) over the bubble length obtained from the photocell signals (as mentioned in §2.2.7). Since the photocells were positioned below the test section where the velocity profiles were obtained, the distance to the surface was measured from the mean point between the photocells, which was 1.6 m.

After substituting equation 3.12 into equation 3.13, the experimental liquid flow rate ahead of the bubble, should be proportional to $\vartheta_b \cdot U_b$, with the proportionality constant given by $(\rho g)/(P_{atm} + \rho g h) = 0.085\,\mathrm{m}^{-1}$. Figure 3.36 shows the experimental liquid flow rate, $Q_{\exp}$, versus $\vartheta_b \cdot U_b$. The experimental liquid flow rate ahead of the bubble varies

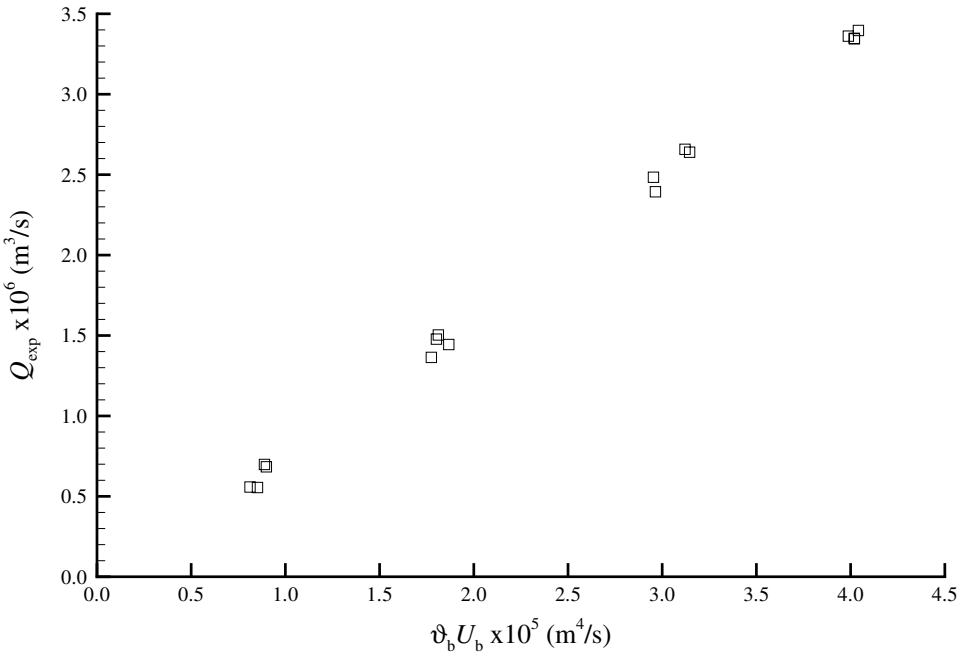

Figure 3.36. Representation of the experimental liquid flow rates versus $\vartheta_b \cdot U_b$.

linearly with $\vartheta_b \cdot U_b$, the proportionality constant being equal to $0.087\,\mathrm{m}^{-1}$ and the origin ordinate $-1.2 \times 10^{-7}\,\mathrm{m}^3/s$. These values are very close to those expected from equation 3.13.

Another proof of bubble expansion is the difference in the duration of the photocells signals, as mentioned in 2.2.7. Since the photocells are separated by 0.25 m, when the bubble passes the second photocell, it has already undergone a slight expansion, which is

the reason for a larger time gap between its nose and its trailing edge. This difference, although small and with an uncertainty of 0.0025 s in the measured times, is enough to compute an estimate of the variation rate of bubble volume during that period. If L_{b_1} and L_{b_2} are the bubble lengths given by photocell 1 and 2 respectively, an estimate of the variation rate of bubble volume can be given by equation 3.14

$$(\frac{\partial \vartheta_b}{\partial t})_{pc} = \frac{\pi \cdot {r_\infty}^2 \cdot (L_{b_2} - L_{b_1})}{\Delta t_{pc}} \tag{3.14}$$

where the subscript pc refers to photocells and Δt_{pc} is the time taken by the bubble to travel between photocells.

Figure 3.37 shows the comparison between the measured liquid flow rate ahead of the bubble and an estimate of variation rate of bubble volume from equation 3.14, for different bubble lengths. Although the uncertainty is higher for the variation rate of bubble volume

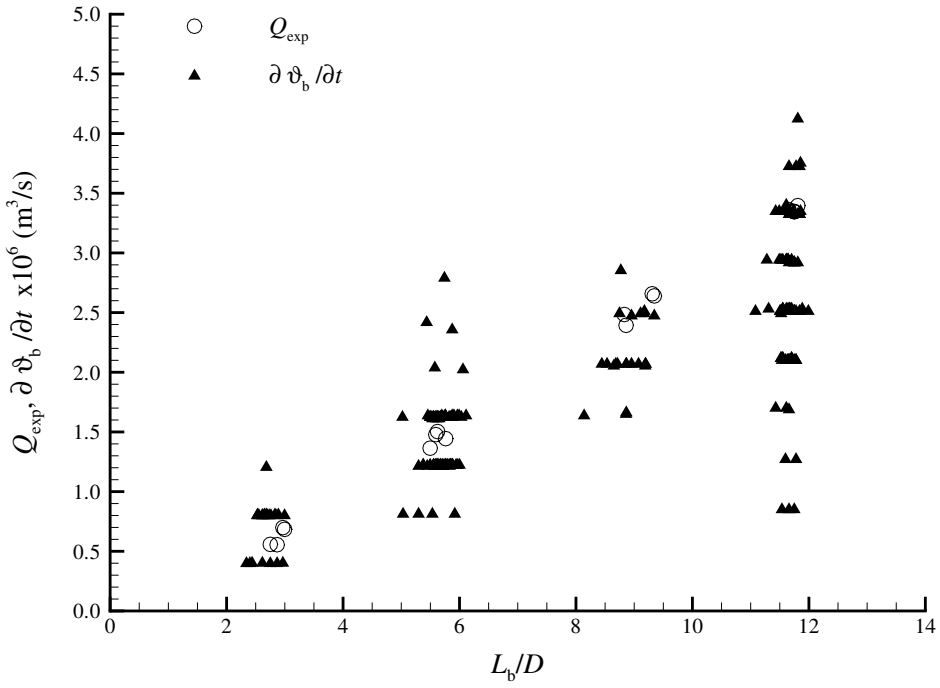

Figure 3.37. Comparison between the liquid flow rate ahead of the bubble, Q_{exp}, and the variation rate of bubble volume, $\partial\vartheta_b/\partial t$, determined by the photocells signal.

given by the photocell signals, the values are in agreement with the liquid flow rates ahead of the bubbles. It is seen that the values of the variation rate of bubble volume have

discrete values due to the resolution of 0.005 s on the photocells signals. The increased scattering for the larger bubbles is due to the appearance of instabilities in the liquid film which cause some oscillations in the bubble trailing edge.

In Figure 3.38, the bubble volume variation for different bubble lengths is represented for both 0.10 and 0.50 wt% CMC solutions. For the 0.10 wt% CMC solution the oscillations of the bubble trailing edge are seen even for the smaller bubbles, which induce a higher scattering of the bubble length values, leading to erroneous (negative) variations of bubble volume.

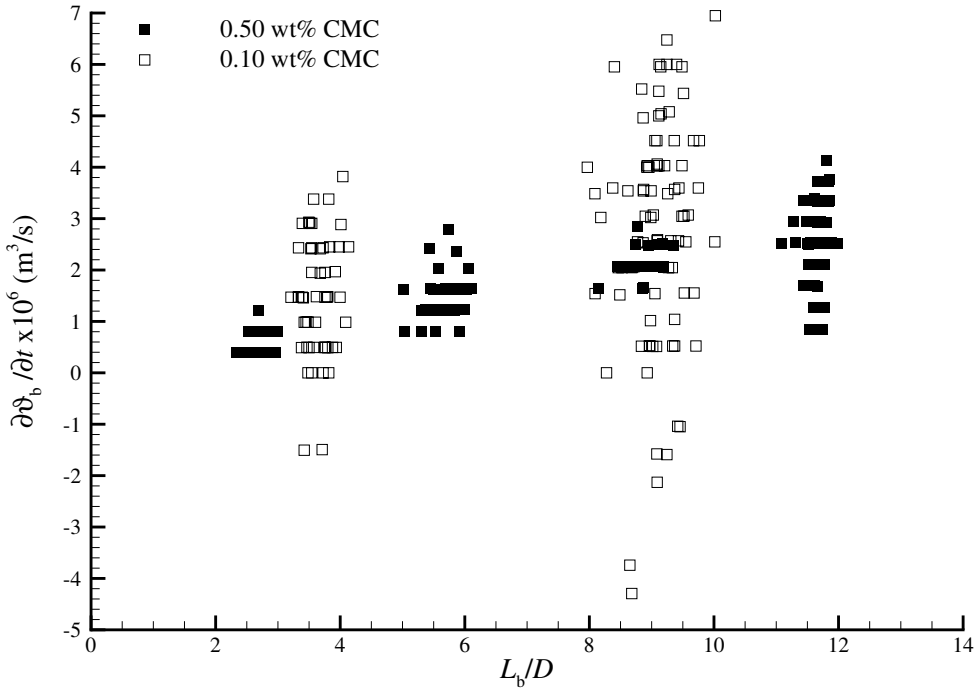

Figure 3.38. Comparison between variation rate of bubble volume determined by the photocell signals for the 0.50 and 0.10 wt% CMC solutions.

3.3.4 Flow around the nose of Taylor bubble

After describing the liquid flow ahead of Taylor bubbles due to the gas expansion, the flow closer to the bubble nose was analysed. Figure 3.39 presents the velocity field around the nose of a bubble rising in a 0.50 wt% CMC solution. Only half of the vectors obtained were represented and they are relative to a fixed frame of reference (indicated by FR in

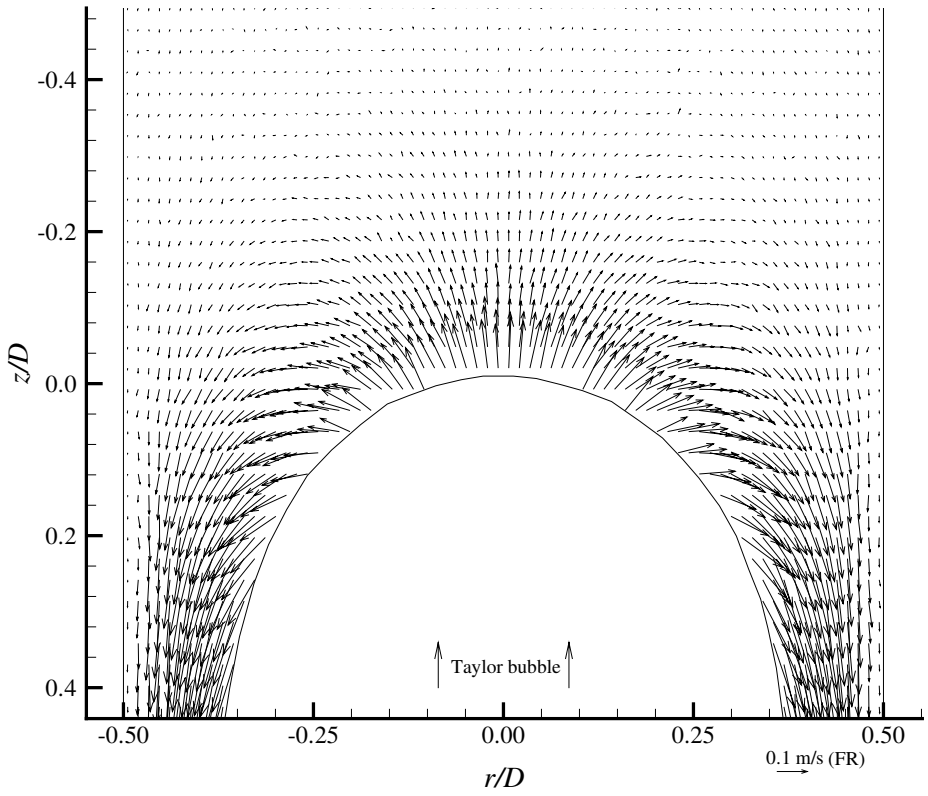

Figure 3.39. Velocity field around the nose of a Taylor bubble rising in a 0.50 wt% CMC solution.

the vector scale) as compared to a reference frame moving with the bubble velocity (MR), which will be presented later.

In all the CMC solutions studied the flow pattern around the Taylor bubble nose was qualitatively the same. Due to the shorter time gaps between the frames in order to obtain the higher velocities close to the bubble nose, the fluid displacement far ahead of the bubble presented in Figure 3.32 is imperceptible in Figure 3.39.

As the bubble rises it pushes fluid up ahead of it, which then moves away from the axis of the column and falls around the Taylor bubble.

To establish the distance from the nose when the flow starts to become disturbed by the bubble passage, the instantaneous values of the axial velocity component, V_z, in the axis of the column ($r = 0$) were represented versus the distance to the bubble nose. Figure 3.40 shows this velocity profile for two bubbles of different size rising in a 0.50 wt% CMC solution. The velocity and the distance to the nose have negative values according to the

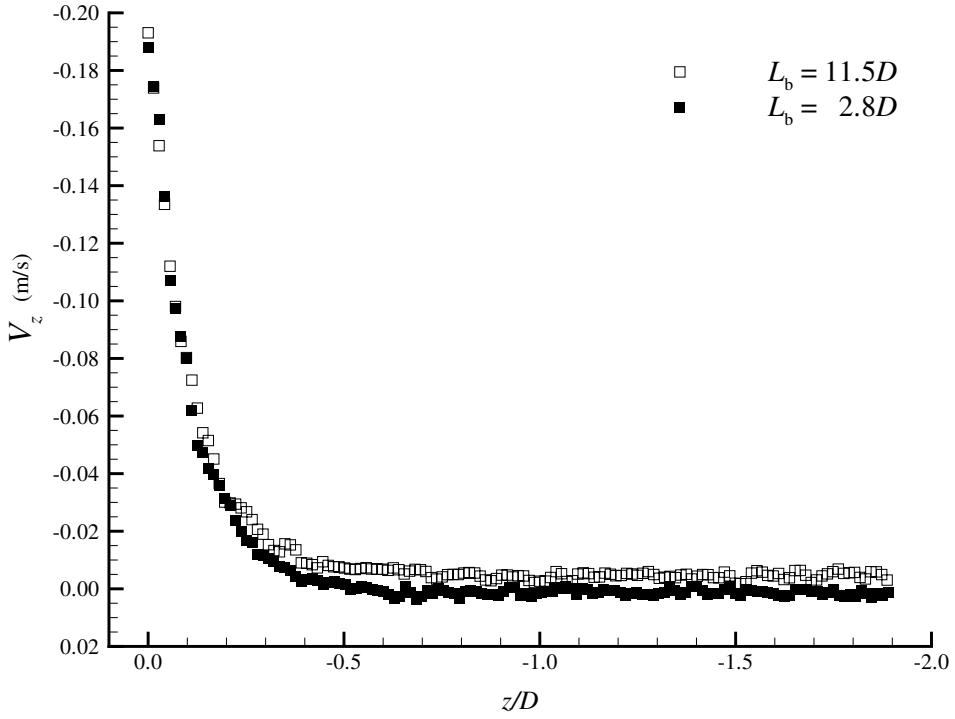

Figure 3.40. Representation of the axial component of the liquid velocity at $r = 0$ versus z/D, for two bubbles with different lengths rising in a 0.50 wt% CMC solution.

coordinate system presented in Figure 3.29. From this figure it is obvious that, for both bubble sizes, at the nose of the bubble ($z = 0$) the liquid has a velocity magnitude equal to the bubble velocity, and as the upward distance from the nose increases the velocity magnitude decreases until reaching a constant value at around $0.7D$ from the bubble nose. The difference between the two cases is only in the final velocity magnitude, which is related with the bubble length as shown in Figure 3.33.

After confirming that bubble length has no influence on the distance ahead of the bubble at which the liquid starts to be disturbed, it was checked whether this distance changes with the fluid properties. The variation of the axial component of the velocity ahead of the nose for the other solutions was found to be very similar to that observed in the 0.50 wt% CMC solution. The difference was only in the magnitude of the velocities. After dividing the liquid velocities by the Taylor bubble velocity, this difference disappears (Figure 3.41). For all the CMC solutions, the upward flow field is disturbed up to about $0.7D$ from the bubble nose. This value is close to the $0.5D$ mentioned by van Hout *et al.*

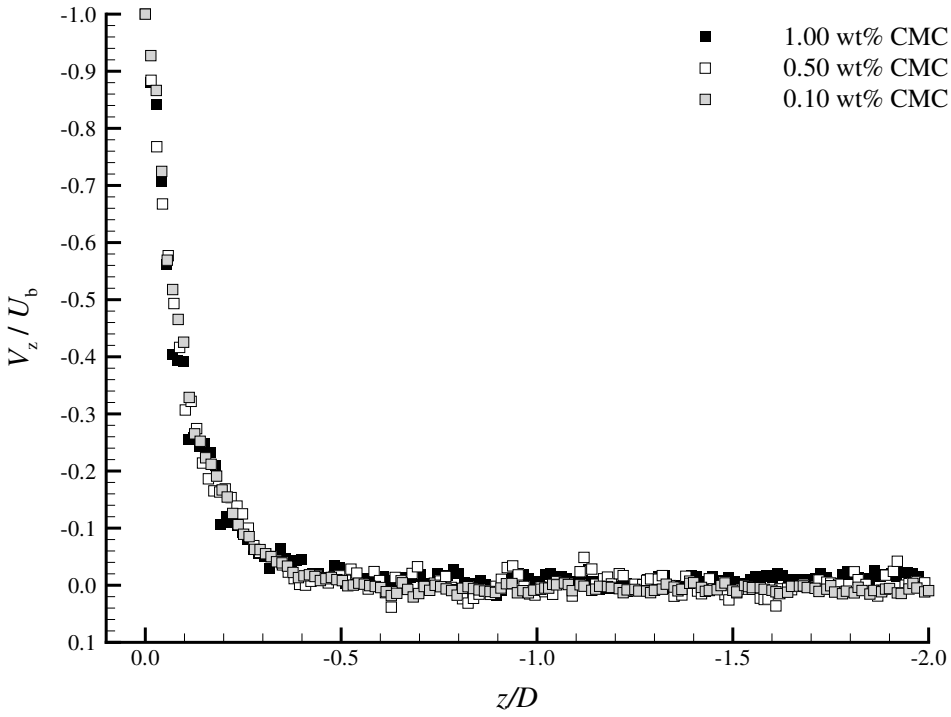

Figure 3.41. Plot of the dimensionless axial component of the liquid velocity at $r = 0$ versus z/D, for different polymer wt%.

(2002b) for bubbles rising in stagnant water in a 0.025 m internal diameter column.

The flow patterns around the bubble nose in all the CMC solutions may also be compared by means of the velocity profiles at $z = 0$. In Figures 3.42 and 3.43, the instantaneous axial, V_z, and radial, V_r, components of the liquid velocity at $z = 0$ are represented along the radial position, for the solutions with the highest and lowest concentration of CMC.

The limit cases studied present very similar behaviour, with slight variations in the velocity magnitudes due to the different bubble velocities. The axial velocity component has its maximum in the axis of the column, which is equal in magnitude to the bubble velocity. Close to the walls it is seen that the fluid is already in a downward movement (positive axial velocity values). The radial velocity component is zero in the axis of the column and increases in magnitude as it moves away from the axis, reaching a maximum value around $r = 0.2D$. Positive values indicate an outward movement of the liquid from the axis of the column.

In the left region of the image there appears to be a little more scattering in the velocity

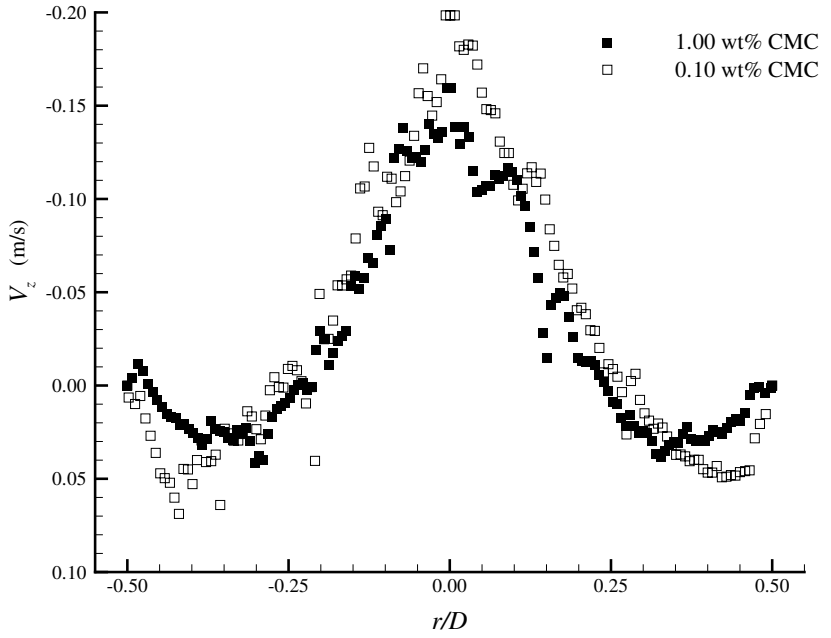

Figure 3.42. Axial component of liquid velocity, V_z, at $z = 0$ along the radial position.

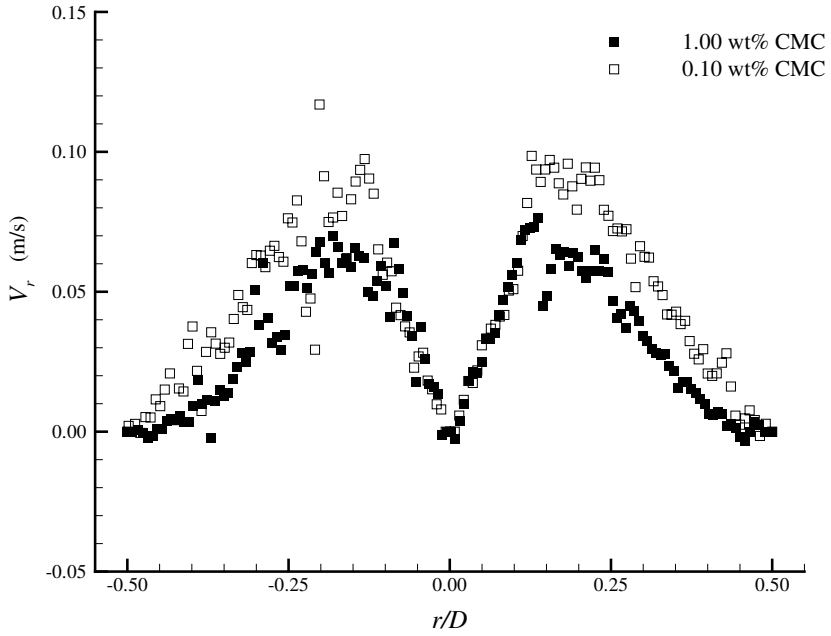

Figure 3.43. Radial component of liquid velocity, V_r, at $z = 0$ along the radial position.

values than in the right region. This is due to a small disturbance that the bubble causes in the laser sheet. Figure 3.44 shows an example of a PIV frame when a small bubble is passing and another PIV frame of the nose region of a Taylor bubble. The laser sheet

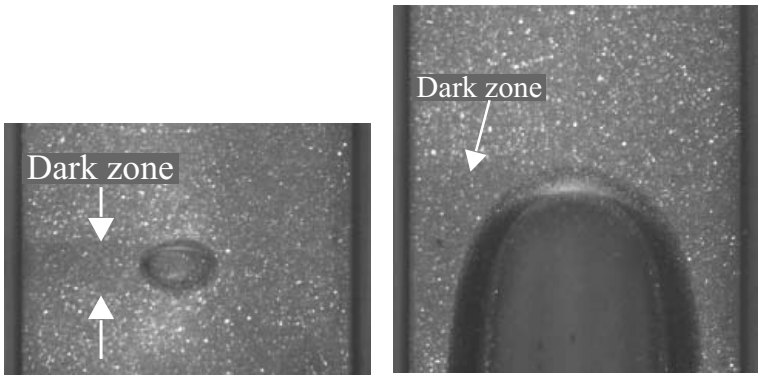

Figure 3.44. Example of a PIV frame while passing a small bubble (a) and of the nose of a Taylor bubble (b).

enters the column from the right side of the image. After passing through the gas bubble the light intensity decreases due to reflections in the bubble interface. In Figure 3.44(a) it is clear that due to the passage of a small bubble there is a shadow in the left side of the image. This also happens during the passage of a Taylor bubble. The reduction in light intensity decreases the image quality in the left region, with consequences on the accuracy of the results.

The presented results show that the flow around the bubble nose is very similar in all the fluids studied. There is an upward velocity profile in the liquid ahead of the Taylor bubble, caused by the bubble volume expansion during the rise. At about $0.7D$ from the bubble nose the fluid starts to be displaced by the bubble passage, increasing in velocity and starting to move radially to flow around the Taylor bubble.

When a frame of reference moving with the bubble is used (Figure 3.45) it is seen that the fluid surrounds the bubble nose tangentially to the bubble interface and starts to accelerate downwards as the bubble radius increases, forming a falling liquid film that is described in the next section.

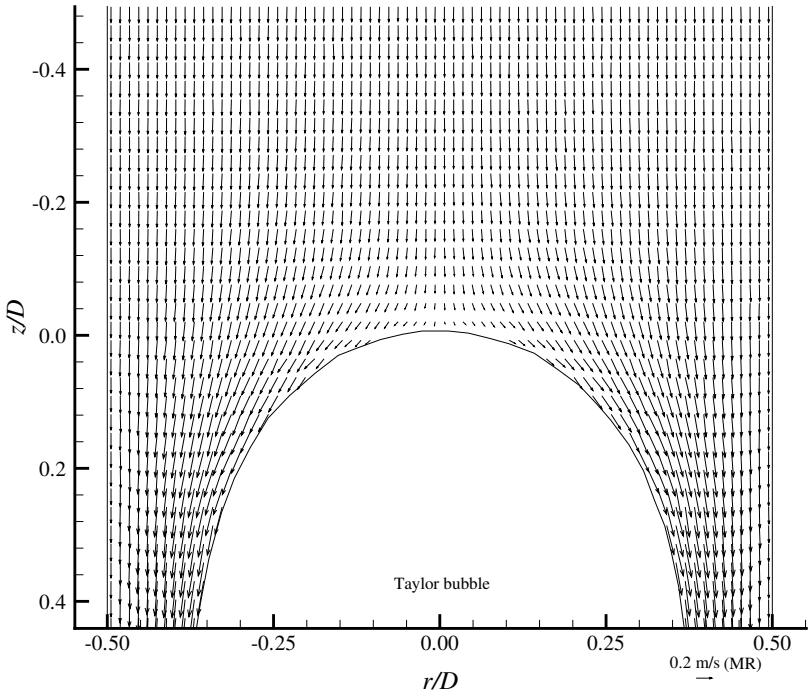

Figure 3.45. Flow field around a Taylor bubble rising in a 0.50 wt% CMC solution, in a frame of reference moving with the bubble.

3.3.5 Liquid film

The liquid flowing around the bubble nose starts accelerating downwards as the distance from the bubble nose increases, due to the increasing bubble radius that leaves less open area for the liquid to flow. Figure 3.46 shows the flow field in the developing film region of a bubble rising in a 0.50 wt% CMC solution. Some of the vectors obtained were not represented, so as to better visualise the velocity profile development in the liquid film. The increasing velocity magnitude can be confirmed by the background colour.

As shown in §3.3.1 at a certain distance from the nose the bubble radius stabilises, reaching its maximum value. To study the liquid velocity evolution along the liquid film, the axial component of the velocity at a fixed radial position is plotted in Figure 3.47 against the distance to the nose for three of the solutions studied. In each case, the fixed radial position corresponds to the middle position between the column wall and the bubble interface. Despite the spread of the values, it is clear that after a certain distance from the nose the liquid film velocity appears to stabilise.

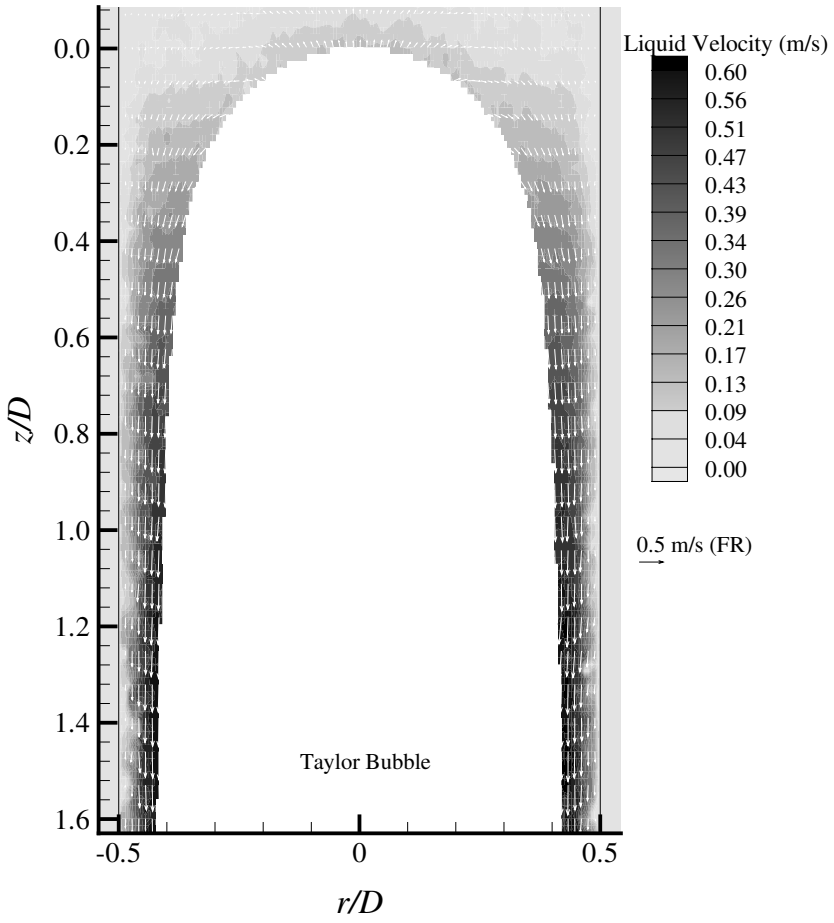

Figure 3.46. .
Liquid film development around a bubble rising in a 0.50 wt% CMC solution.

The next step is to determine whether the point where the maximum bubble radius is reached coincides with the point where the liquid velocity profile is fully developed. The axial component of the liquid velocity and the bubble radius were plotted in the same graph, with both variables in a dimensionless form divided by their stabilised values (at high z/D). Figure 3.48 shows this analysis for the 0.50 wt% CMC solution. The dark square points represent the centred median of 20 neighbouring velocity points, since the original values have a large scattering. This figure shows that in the 0.50 wt% solution both the bubble radius and the liquid velocity stabilise around $z = 3.5D$. This analysis was performed for all the CMC solutions and the approximate values at which the film becomes fully developed are presented in Table 3.6. The more viscous the fluid the shorter is the

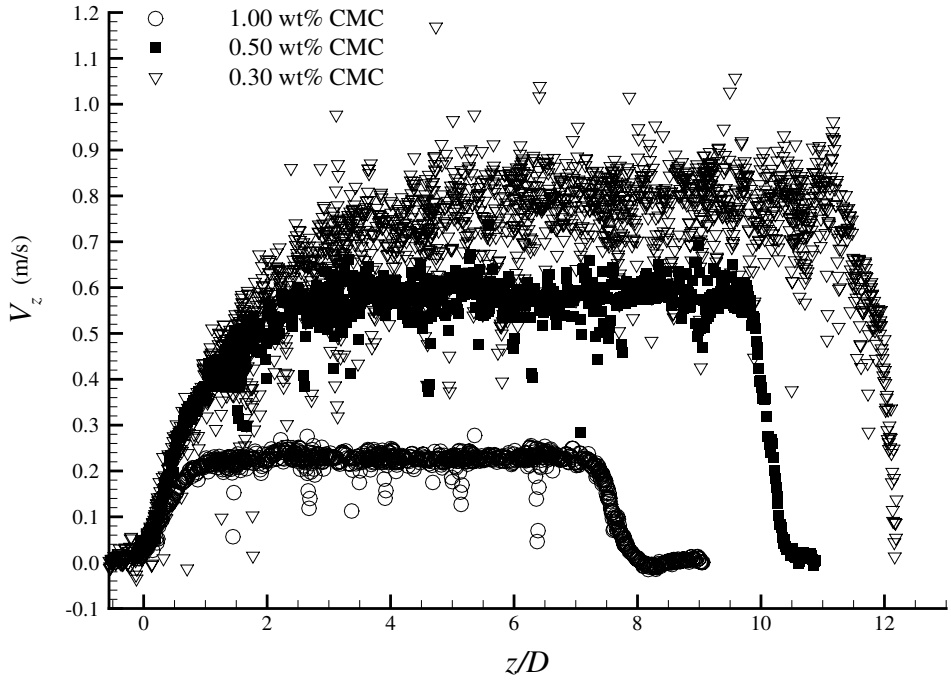

Figure 3.47. Evolution of the liquid axial velocity at a fixed radial position with the distance to the bubble nose for 1.00 wt% ($r = 0.43D$), 0.50 wt% ($r = 0.46D$) and 0.30 wt% ($r = 0.47D$) CMC solutions.

Table 3.6. Approximate distance to the bubble nose where the liquid film becomes fully developed, z_{stable}, in the CMC solutions.

CMC wt%	0.10	0.30	0.40	0.50	0.60	0.80	1.00
z_{stable}/D	8.0	6.0	4.0	3.5	2.4	1.8	1.6

distance that the film flow takes to stabilise, which is in accordance with the observations of Mao and Dukler (1990) in Newtonian viscous solutions.

In the present section, only bubbles with sufficient length to have a stabilised liquid film were analysed. The longer bubbles with instabilities in the liquid film were also excluded from this study.

The acceleration of the liquid film along z/D can be visualised by plotting the axial velocity component along the radial position at different distances from the nose, as shown in Figure 3.49. In this figure it is once again clear that as z/D increases, the axial liquid velocity also increases, until the stabilisation of the liquid film. It seems strange, however, that when the velocity profiles are fully developed there is a decrease in the velocity close to

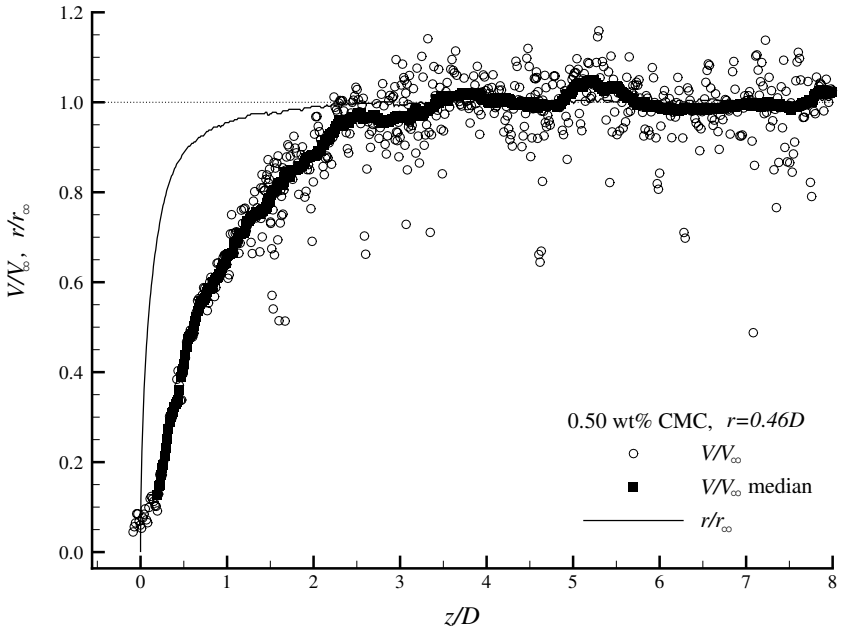

Figure 3.48. Plot of the dimensionless bubble radius and normalised axial velocity (at $r = 0.46D$) versus the distance to the nose of a bubble rising in a 0.50 wt% CMC solution; V_∞ represents the stabilised axial velocity ($r = 0.46D$) and r_∞ the maximum bubble radius.

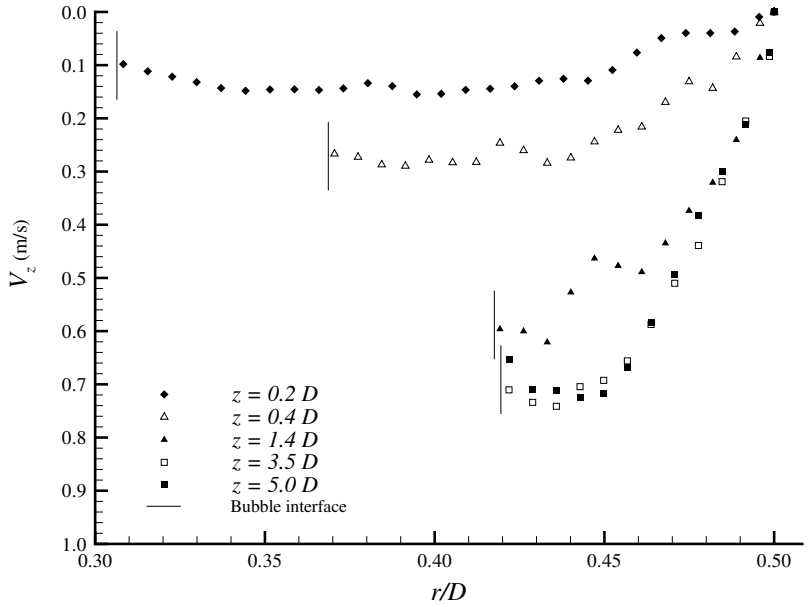

Figure 3.49. Instantaneous axial velocity component along the radial position in the liquid film at different distances from the nose, in a 0.50 wt% CMC solution.

the bubble interface. This phenomenon must be analysed in detail to check whether it is a processing effect or an unexpected fluid behaviour. The liquid film velocity profiles shown until now were obtained from the full view images acquired to characterise the general flow around the Taylor bubbles. To improve the data resolution, a different lens was used to analyse the liquid film in more detail.

The maximum bubble radius varies from $r_\infty/D = 0.455$ to 0.353 from the less to the most viscous fluid. This means a space of only 1.4 to 4.7 mm in width is available for the liquid to flow between the bubble and the column. This tiny measurement area and the exceptionally high velocity gradients make the liquid film region a very challenging task for standard PIV. To overcome these difficulties a 50 mm lens was used, with a 12 mm extension ring to obtain a close-up view of the liquid film region around the bubble. Figure 3.50 shows an example of PIV images for 0.10 and 1.00 wt% CMC solutions acquired with this lens. Only the right side of the image was analysed with the close-up view due to the effects shown in Figure 3.44.

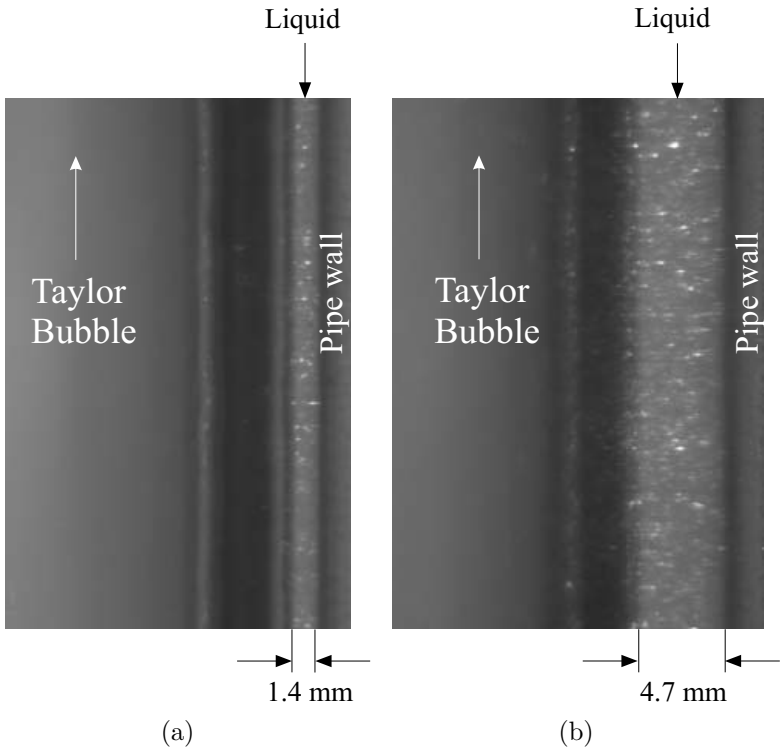

Figure 3.50. Example of PIV images acquired in (a) 0.10 and (b) 1.00 wt% CMC solutions, with a 50 mm lens.

These close-up images were analysed to check if the previously mentioned decrease in the liquid velocity close to the bubble interface was a processing effect or not. During this analysis the window displacement and the coordinate system were maintained in pixels. An image in the stabilised film region was processed without any mask; the average window displacement profile is represented in Figure 3.51. In the column region, due to the non-

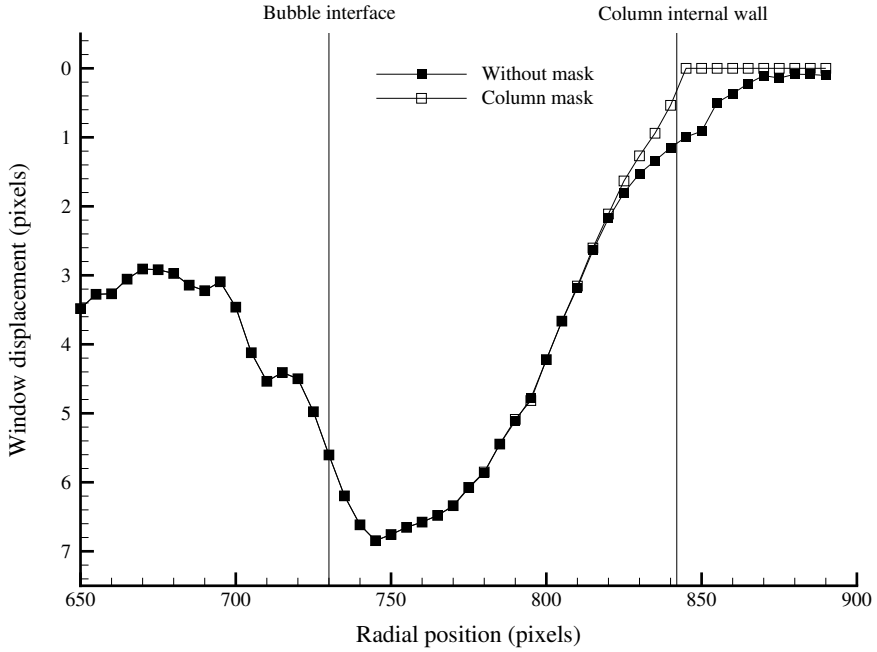

Figure 3.51. Average velocity profile in the stabilised liquid film in a 0.50 wt% CMC solution with and without mask in the column region.

slip condition, the velocities should be zero. However, due to the reflection of the particle images, slightly different intensities of the laser pulses and the absence of particles close to the wall inducing a low SNR, the image processing may place false non-zero values of window displacement in the column region. This is why it was necessary to process the images with a mask, imposing known null velocities at the wall, as mentioned in §2.2.6. Figure 3.51 shows that the use of the mask also slightly changes the values close to the wall, which means that they were also being affected by the wrong values in the column region. This occurs due to a low SNR close to the wall. As mentioned in the data processing description, when the SNR is below a certain threshold value, the window displacement at that point is substituted by an interpolation of the surrounding known values.

However, the liquid film is not only in contact with the column wall but also with

the bubble interface, where the velocity is unknown. Due to a poor SNR and particle reflections and refractions at the bubble interface, the vectors in the liquid region close to the interface are affected in a similar way as those near the column wall. Therefore, the unexpected magnitude of these vectors could be a data processing deception and not the real liquid velocity. The bubble interface was then artificially moved 20 pixels to the right to determine whether the vectors close to this new interface would be affected by this change. Figure 3.52 shows the comparison between the profiles obtained with the real bubble interface and with the displaced interface. This example shows that the bubble

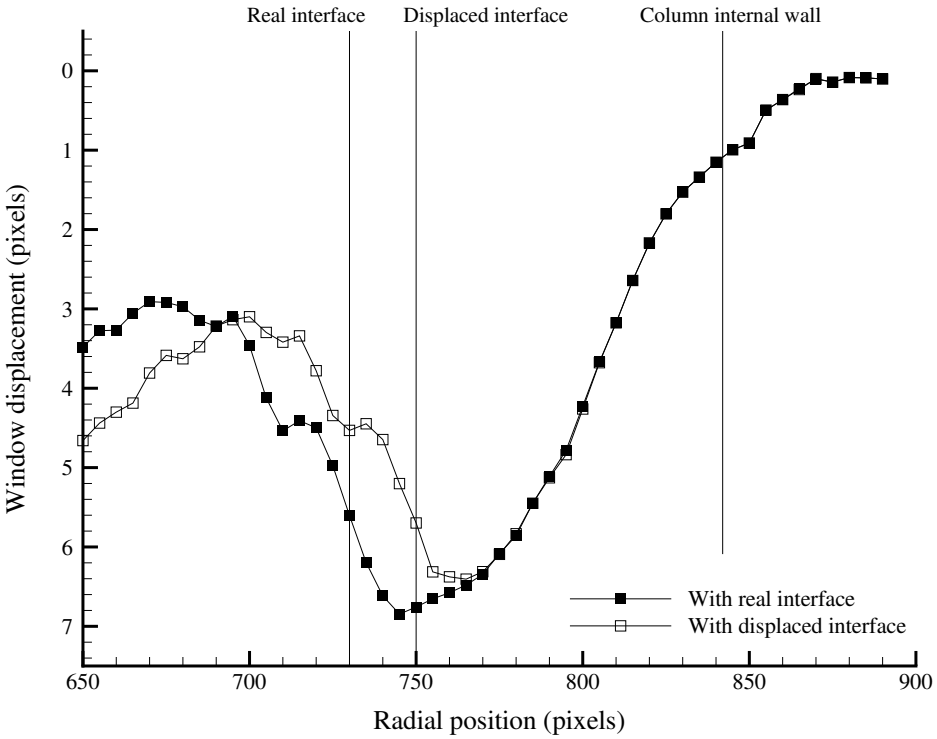

Figure 3.52. Influence of the interface position on the velocity profiles.

interface affects the processing of the closest liquid velocity vectors. The most probable reason for this effect is the reflection of particle images at the bubble interface, as described in §2.2.5. Figure 3.53 shows a sketch to explain this phenomena. The reflected images at the interface might be of any particle in any region of the liquid film, so they always have a velocity lower or equal to the velocity of the particles close to the interface. Due to the light scattering the images of the particles are always larger than the actual particle size,

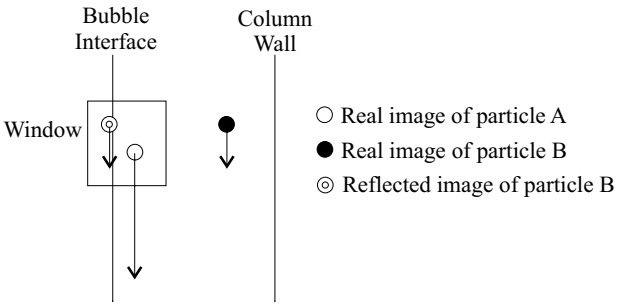

Figure 3.53. Schematic example of the effect of particles image reflection at the bubble interface on the window displacement.

which means that, in most cases, a part of the reflected images lies in the liquid region. Even with a valid SNR, the displacement of a window containing reflected images will always be lower than the displacement of the particles close to the interface. To minimise this effect a mask was also used in the bubble region. In this mask the maximum liquid film velocity obtained from the processing with no mask was imposed.

Figure 3.54 shows the comparison between the velocity profile first obtained without any mask and the final velocity profile obtained with column and bubble masks. The

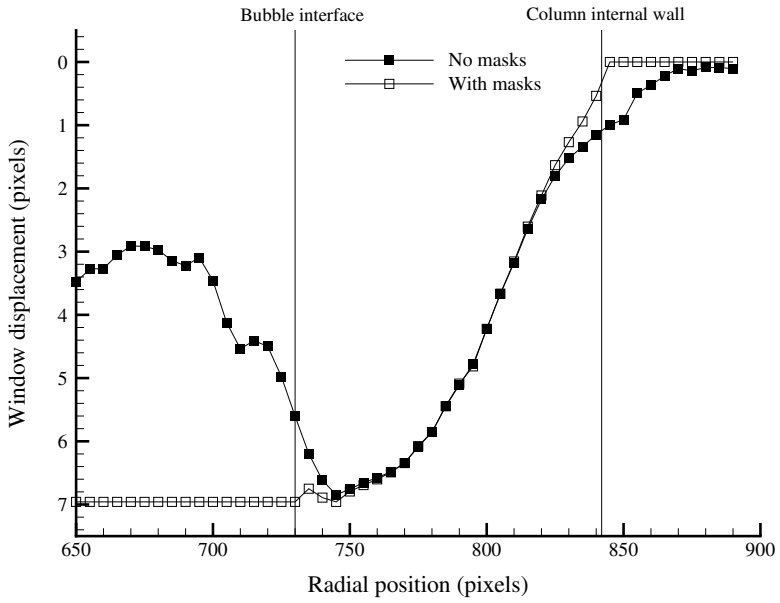

Figure 3.54. Velocity profile in the stabilised liquid film in a 0.50 wt% CMC solution with bubble and column masks.

velocity profiles obtained with the masks have slightly different values in the points close to the interfaces. This region of corrected vectors is small, however, having less than a 0.5 mm thickness. There is no guarantee that these are the exact liquid velocity values but they should be closer to reality, as will be demonstrated by a mass balance. This processing with the bubble mask was only used in the stabilised liquid film region, where the axial velocity should be constant, with a maximum at the interface. In the other regions where the gas-liquid interface is present, the velocity at the interface is unknown and no mask could be used. However, since the liquid thickness there is not so little, the number of erroneous vectors is negligible in the overall flow.

For each CMC solution, several images were processed for bubbles of the same size and velocity (Table 3.7). As mentioned before, only the bubbles with sufficient length to have a developed liquid film and without interface instabilities were analysed.

Table 3.7. Average length and velocity of the bubbles in which the liquid film was analysed.

CMC wt%	L_b/D	U_b (m/s)
0.10	9.4	0.199
0.30	11.1	0.198
0.40	11.0	0.195
0.50	8.8	0.192
0.60	7.3	0.187
0.80	5.2	0.180
1.00	7.9	0.160

The liquid film velocity fields obtained for the 0.10 and 1.00 wt% CMC solutions are shown in Figure 3.55.

From the vector fields in the developed liquid film some small velocity variations are seen. This velocity scattering was already seen in Figure 3.47, where the velocity at a fixed radial position in the liquid film was plotted versus the distance to the nose; the scattering was more intense for the less viscous fluids. This velocity spread was analysed in detail to see if it could be related to turbulence.

For each bubble, between one and three velocity fields, similar to those represented in Figure 3.55, were obtained at consecutive axial positions in the stabilised film region. For each solution, only bubbles of the same velocity and length were analysed. Therefore, in each solution, more than 1000 velocity profiles were averaged in the stabilised region (5 bubbles$\times$ 2 images/bubble $\times$ 127 profiles/image).

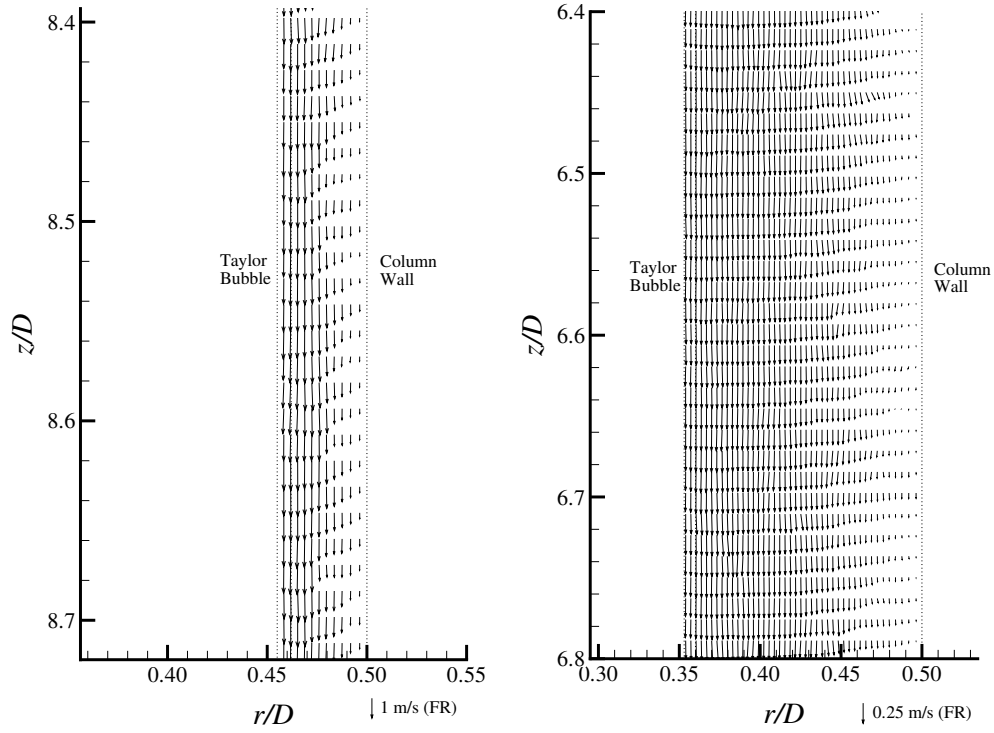

Figure 3.55. Velocity field in the developed liquid film of Taylor bubbles rising in 0.1 (a) and 1.0 (b) wt% CMC solutions.

The average window displacement and standard deviation in the developed liquid film were computed in pixels and are plotted in Figure 3.56 for the 0.10 and 0.80 wt% CMC solutions. The time between the PIV frames was set to 80 µs and 355 µs for the 0.10 and 0.80 wt% CMC solutions respectively. The standard deviations presented in Figure 3.56 are up to four times the estimated PIV error (0.2 pixels) mentioned in §2.2.6 and the same behaviour was found for all the studied conditions. This means that the standard deviation is the same in terms of window displacement, but the standard deviation of the velocity is amplified for the less viscous CMC solutions due to the decreasing time gap between PIV frames.

Several hypotheses can be considered to justify this high scattering in the velocity values. The fact that the standard deviation of the window displacement is independent of the viscosity is a strong argument to conclude that turbulence should not be the cause of the spread. The bubble shape, described in section 3.3.1, contains small disturbances.

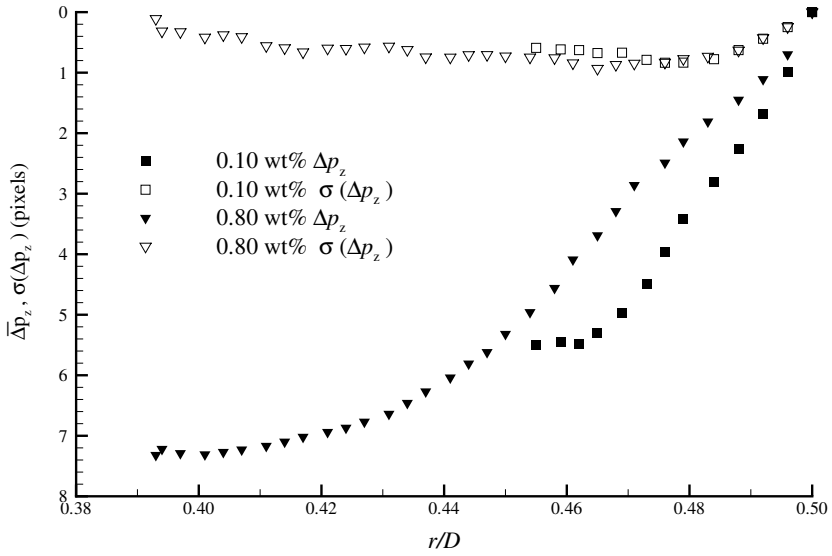

Figure 3.56. Average windows vertical displacement (pixels) in the liquid film and standard deviation(pixels) for the 0.10 and 0.80 wt% CMC solutions.

These disturbances are due to the presence of particle images reflected and refracted at the interface, which interferes in the image processing to obtain the bubble shape. Even so, if these disturbances were caused by bubble interface oscillations they would induce, in the worst case, a maximum variation of 4% in the liquid film thickness. By computing the liquid velocity profiles with 4% thickness variations, these oscillations could be responsible for a maximum scattering of only 8% in the axial liquid film velocity at a certain radial position. This value is still half of the standard deviation obtained in all the cases studied, so this hypothesis is not sustainable. In the processing of liquid film profiles with different windows sizes no change in the standard deviation (0.8 pixels) was observed. Other tests were made. Liquid was pumped in the column at different flow rates without the presence of the Taylor bubble. PIV images with different time gaps where taken and analysed in order to cover a large range of particle displacements. In these tests, the velocity is only a function of the radial position, as in the liquid film. The maximum scattering obtained did not exceed 0.2 pixels even in the region close to the column wall where the liquid film profiles are taken. A comparison between the grey level histograms in the liquid film and in the same region of an image without the bubble shows that there is a slight increase in the grey levels when the bubble is present. One explanation for this might be the reflection

of the laser sheet in the bubble interface back to the liquid film region. Although this reflection of the laser sheet is much less intense than the laser sheet itself, the curvature of the bubble interface makes the reflected laser sheet larger than the original one. This fact, in conjunction with small, undetected misalignments of the laser sheet/ Taylor bubble/ column axis system should inevitably result in the illumination of particles in a plane wider than the original laser sheet, which could be responsible for the decrease in the accuracy of the measurements. This is the most probable reason for the higher velocity scattering in the liquid film, but it is not easy to prove experimentally. According to this analysis, a maximum error of 0.8 pixels in the window displacement should be considered for the liquid film region, which is four times higher than the 0.2 pixels considered for all the other regions.

In Figure 3.57 the average velocity profiles in the developed film region for all the solutions studied are represented. This figure shows the velocity in the liquid film increasing as the viscosity decreases, due to reduced film thickness. For the lower viscosity, the film

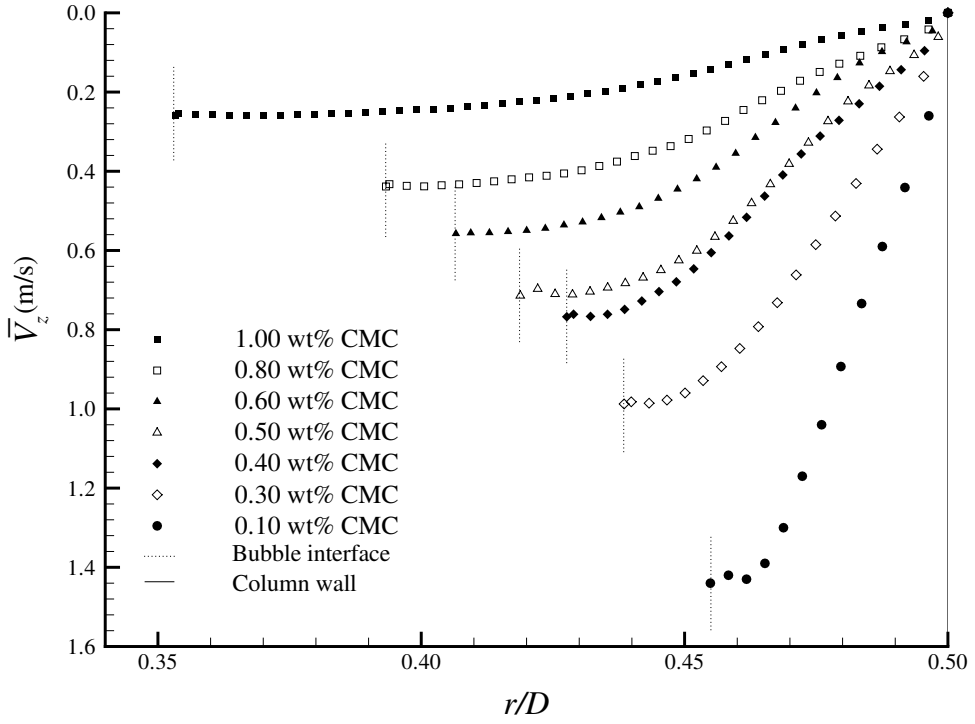

Figure 3.57. Average developed velocity profiles around the Taylor bubbles rising in the CMC solutions studied.

velocity is up to 7 times greater than the bubble velocity. The average velocity profile around the bubbles rising in 0.40 and 0.50 wt% CMC solutions are closer than would be expected. This fact is due to the difference in the experimental temperatures (25^{o}C for 0.50 wt% and 19^{o}C for 0.40 wt%) and to the duration of the 0.40 wt% CMC solution experiments; these experiments took five days, three days more than for the other solutions, and this long period of time might have resulted in some water evaporation. These two facts approximate the fluid viscosities and explain the close velocity profiles.

To have an idea of the spread of the velocity data in the liquid film, in Figure 3.58 the velocity profiles for three solutions are represented with error bars corresponding to the standard deviations. As mentioned before, the apparent increase of data scattering for the

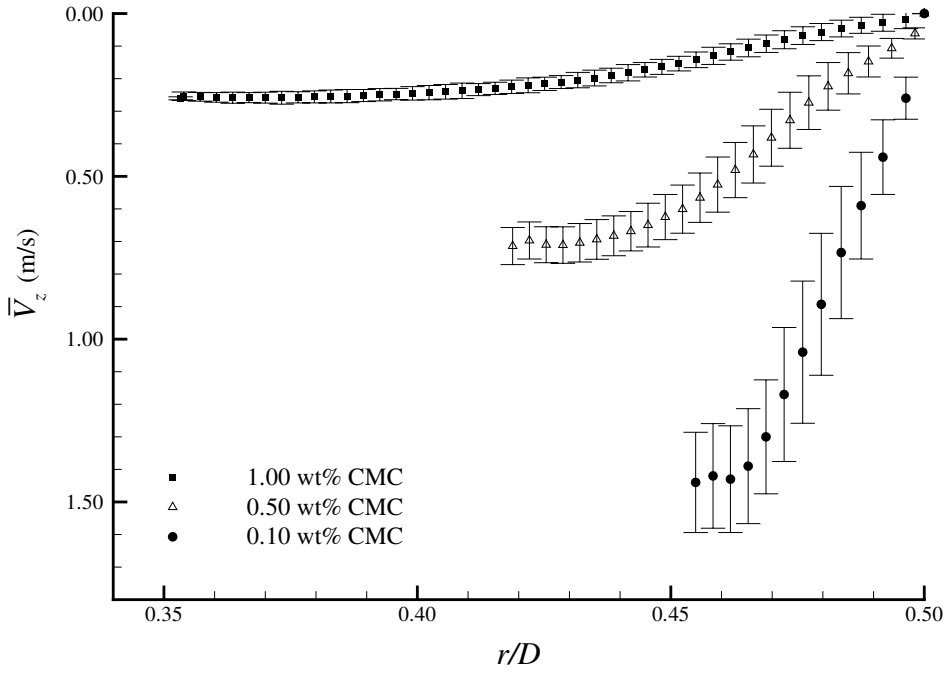

Figure 3.58. Standard deviation of the average velocity profiles in the liquid film around Taylor bubbles rising in CMC solutions.

less viscous fluids is mainly due to the shorter PIV times used between frames. Figure 3.59 shows the relative data scattering, where by dividing the standard deviation by the average velocity a very similar behaviour is found for all solutions. At the same radial position the relative error is slightly higher for the most viscous solutions, which definitely excludes turbulence as a cause of the velocity scattering. This does not mean that there

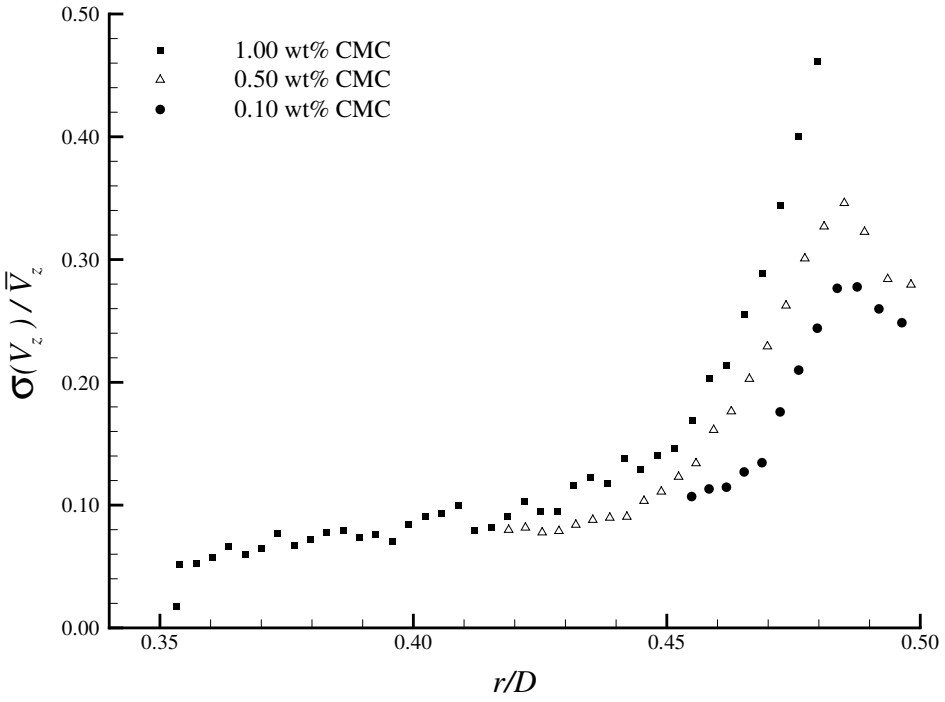

Figure 3.59. Relative deviation of the average velocity profiles in the liquid film around Taylor bubbles rising in CMC solution.

is no turbulence in the liquid film, but if there is, its intensity is below the measurement error in this region.

To check if the average velocity profiles in the film obey mass conservation, a mass balance was performed. Figure 3.60 shows a schematic of the flow around a Taylor bubble in a fixed frame of reference (FR) and in a frame of reference moving with the bubble (MR). The vector field obtained in the experiments is always relative to a fixed frame of reference, since the PIV camera is fixed at the test section and the bubble is moving upwards. If we subtract the bubble velocity from the velocity field, we obtain the velocity field relative to a frame of reference moving with the bubble (MR), which means that we see the flow as if we were moving at the bubble velocity. In this reference (Figure 3.60(b)), the liquid flow rate at cross-section A must be equal to the liquid flow rate at cross-section B, to respect mass conservation.

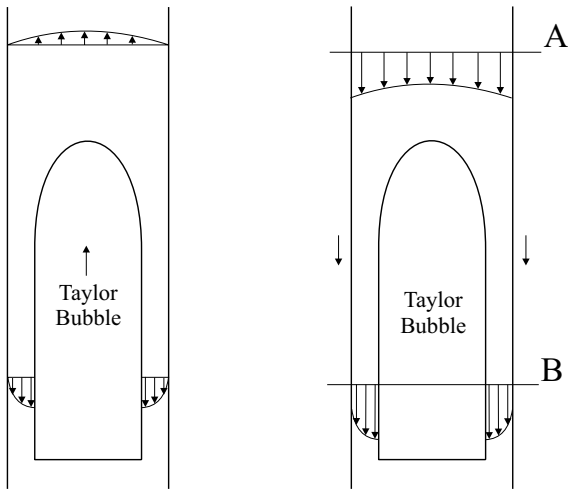

Figure 3.60. Schematic representation of the flow around a Taylor bubble in a fixed frame of reference (a) and in a frame of reference moving with the bubble (b).

The flow rate at cross-section A is given by

$$Q_{\mathrm{A}} = \int_0^R (V_{\mathrm{exp}}(r) - U_{\mathrm{b}}) 2\pi r \, \mathrm{d}r \tag{3.15}$$

where $V_{\mathrm{exp}}(r)$ is the axial velocity of the liquid ahead of the bubble due to bubble expansion (see Figure 3.33) and U_{b} the Taylor bubble velocity, both of which are negative according to the frame of reference shown in Figure 3.29 (the difference between the velocities is then positive since the velocity ahead of the bubble is much lower than the velocity of the bubble). The flow rate in cross-section B is given by

$$Q_{\mathrm{B}} = \int_{R-\delta}^R (V_{\mathrm{z}}(r) - U_{\mathrm{b}}) 2\pi r \, \mathrm{d}r \tag{3.16}$$

where V_z is the axial velocity in the liquid film (Figure 3.57) and δ the liquid film thickness.

Figure 3.61 shows the comparison between Q_{A} and Q_{B} for the 0.50 wt% CMC solution, where each discrete value of Q_{B} corresponds to the average flow rate in the developed film of a bubble (similar to those presented in Figure 3.55). For the 0.50 wt% CMC solution, 26 images from nine bubbles with the same length and velocity were used. This figure

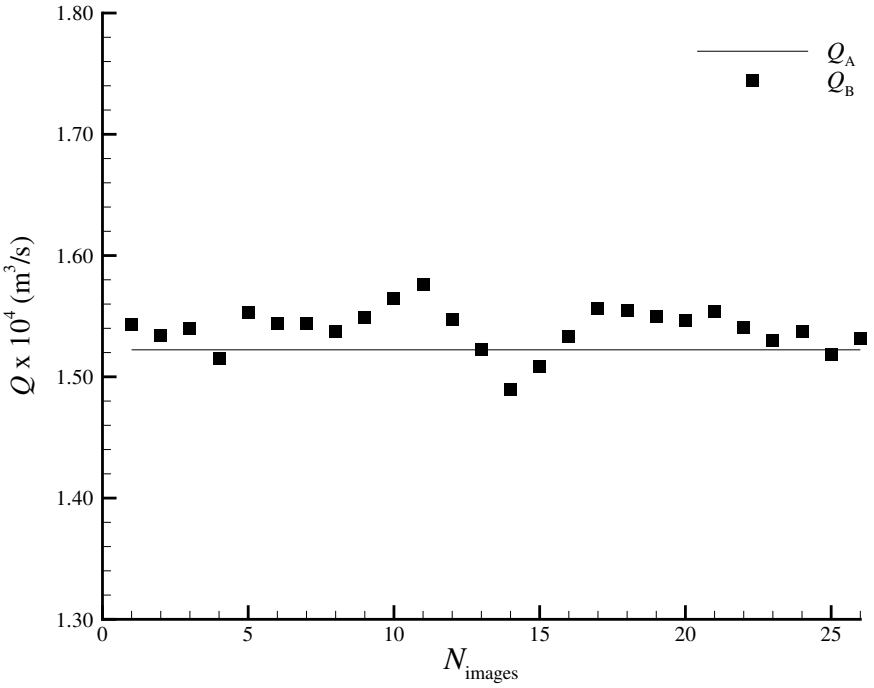

Figure 3.61. Comparison between Q_A and Q_B for the 0.50 wt% CMC solution, where Q_B was determined in every image, N_{images}, analysed in the developed film region.

Table 3.8. Comparison between Q_A and Q_B (average values) for all the CMC solutions.

CMC wt%	$Q_A \times 10^4(m^3/s)$	$Q_B \times 10^4(m^3/s)$	$(Q_B - Q_A)/Q_A\%$
0.10	1.57	1.54	-1.9
0.30	1.55	1.53	-1.3
0.40	1.54	1.39	-9.7
0.50	1.52	1.54	1.3
0.60	1.49	1.45	-2.7
0.80	1.43	1.41	-1.4
1.00	1.27	1.34	5.5

shows that the liquid film flow rate is very close to expected; the average liquid film flow rate is only 3% higher than expected, with a 1.5% standard deviation. The error in Q_A is mainly due to the error associated with bubble velocity, and is around 1%. The same comparison was made for all the CMC solutions and the results are presented in Table 3.8. From this table, it can be concluded that the liquid film flow rates are very close to what was expected. The difference between Q_A and Q_B is always below 10% and only for the

0.40 wt% and 1.00 wt% CMC solutions is it higher than 5%. These differences are quite acceptable, considering the spread of the velocity data and that the liquid flow rate was computed by integrating a velocity profile obtained in a single plane.

After validating the average liquid film profiles a theoretical analysis was performed.

Considering the developed film as a free-falling film with constant pressure at the gas-liquid interface, the momentum equations show that the weight of the fluid is balanced by the shear stresses:

$$\frac{\partial(\tau r)}{\partial r} - \rho g r = 0 \tag{3.17}$$

where τ is the shear stress, r the radial position, ρ the liquid density, g the gravitational acceleration and δ the liquid film thickness. Equation 3.17 was integrated with the boundary condition, $\tau = 0$ at $r = R - \delta$. The shear stress variation with the radial position is then given by:

$$\tau = \frac{\rho g r}{2}\left(r - \frac{(R-\delta)^2}{r}\right) \tag{3.18}$$

Having the shear stress profile, the corresponding shear rate is then obtained from the rheological data, with

$$\tau = \mu(\dot{\gamma}) \cdot \dot{\gamma} \tag{3.19}$$

where $\mu(\dot{\gamma})$ is given by fitting the the Carreau-Yasuda model to the measured viscosities. From this equation the shear rate, $\dot{\gamma}$, can not be explicitly set as a function of the shear stress and must be solved numerically for each radial position.

With the shear rate profile, the velocity profile is then obtained from

$$\frac{\partial V_z}{\partial r} = -\dot{\gamma}(r) \tag{3.20}$$

by integrating between $r = R$ and $r = R - \delta$, with the boundary condition $V_z = 0$ at $r = R$. Since the liquid film thickness is not known *a priori*, it must be iteratively determined in order to obey a mass balance. The value of δ is determined so that the flow rate given by equation 3.16 equals the known flow rate obtained from equation 3.15.

In Figure 3.62 the theoretical velocity profiles are compared with those of the experiment for some of the studied solutions. As this figure shows, the experimental velocity profiles are well predicted from the theoretical analysis. Despite the experimental data

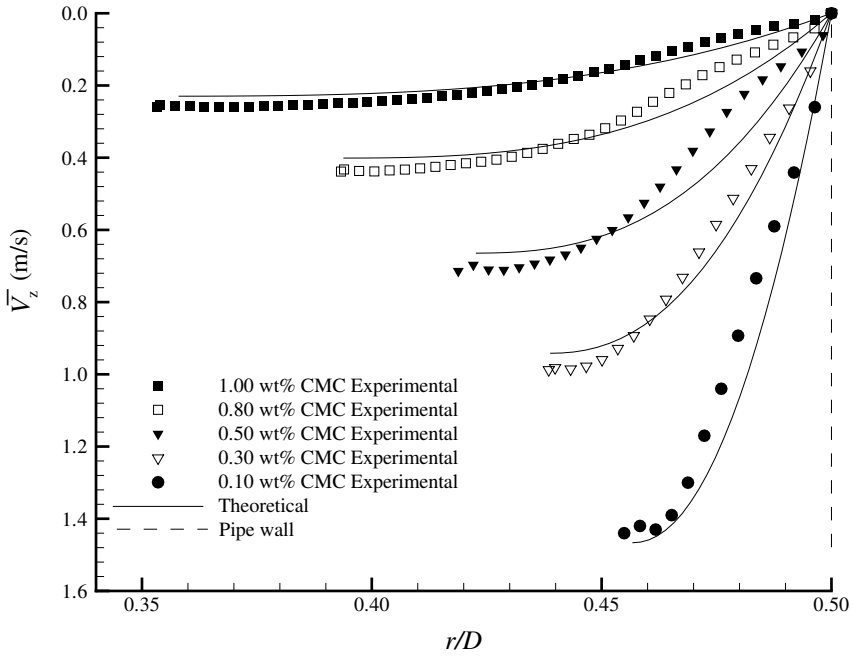

Figure 3.62. Comparison between theoretical and experimental velocity profiles in the liquid film.

uncertainty on the liquid velocity, bubble velocity and rheological data, the theoretical film thickness differs less than 5% from those obtained in the experiment, in all the ranges studied. This analysis shows that the liquid velocity profiles around the Taylor bubble can be theoretically predicted if the bubble velocity and the fluid rheology are known.

Different liquid rheology and velocity of the merging liquid film induce different flow patterns in the wake of the bubbles, which are described in the next section.

3.3.6 Bubble wake

The bubble wake region is where the main differences between the flow patterns in the different solutions are found. The different viscosity and liquid film velocity affect the distance needed for diffusion and attenuation of the linear momentum transported by the liquid at the bottom of the bubble.

The different patterns in the Taylor bubble wakes are described individually, then a final comparison is presented. The more concentrated solutions are presented separately to highlight the different behaviour found due to viscoelastic effects. A new variable, $z*$, is defined as the distance to the bubble trailing edge. When the bubble trailing edge oscillates, $z* = 0$ is considered the average position between the highest and lowest positions of the trailing edge. For the more concentrated solutions, $z* = 0$ is taken at the tip of the trailing edge. Concerning the velocity profiles, and according to the frame of reference of Figure 3.29, the axial velocity component is positive in the downward direction, while the radial velocity component is positive in the outward direction and negative towards the axis of the column. The wakes are those of the bubbles analysed in the liquid film study (Table 3.7).

0.10 wt% CMC

In the visualisation studies presented in §3.1.2, it was shown that in the less concentrated solutions the bubble trailing edge oscillated three-dimensionally while rising in the column. No coloured liquid was found in the wake of the bubbles rising in this solution.

In the visualisation studies, due to the higher frequency of the camera, it was possible to capture several images of the trailing edge of a single bubble and observe its position and orientation changing over time. In the PIV results the camera had a lower frequency (4.11 Hz) and usually only one image of the trailing edge was obtained for each bubble. For this reason, the instantaneous wake flow fields presented in this section were obtained from different bubbles. Even so, for bubbles of the same length, instantaneous positions of the trailing edge of each bubble are representative of the different positions of the trailing edge of a single bubble at different instants.

When using two-dimensional PIV in a three-dimensional flow, only the two-dimensional projection of the velocity vectors in the measurement plane is obtained. Nevertheless, this projection can give some qualitative information about the flow pattern. In Figure 3.63,

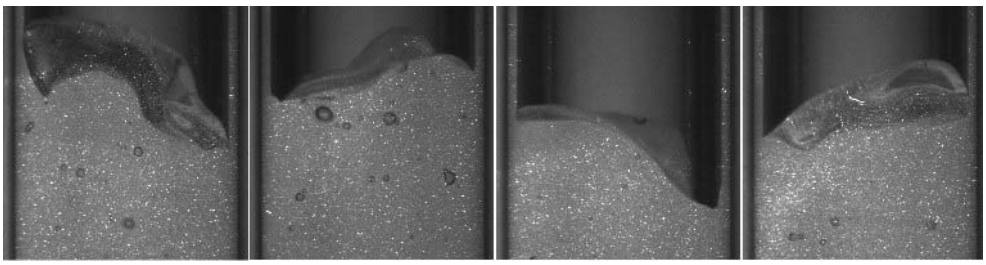

Figure 3.63. Images (PIV) of the trailing edge of Taylor bubbles rising in a 0.10 wt% CMC solution.

some PIV images showing instantaneous trailing edge positions of Taylor bubbles rising in a 0.10 wt% CMC solution are presented.

The different orientations of the bubble trailing edge at consecutive instants induce an oscillating flow field in the wake of the bubble. In Figure 3.64 some examples of the flow field in the wake of bubbles with a $9.2D$ length rising in a 0.10 wt% CMC solution are represented.

Even with only a two-dimensional projection of the velocity field in a central plane of the column, it can be seen that the downward velocity magnitude in the fluid leaving the liquid film is around 1.0 m/s, and in the middle region of the wake the upward velocity vectors reach 0.60 m/s, which is three times higher than the bubble velocity. Several recirculation structures are seen in the wake, changing position according to the trailing edge oscillations. The liquid film expansion in the wake region is also dependent on the trailing edge position. The similarities between these different flow fields are the high velocity magnitude, a falling liquid film that expands up to 1.0-1.2D from the bubble trailing edge and an upward velocity in the middle of the wake with a maximum magnitude of around $z* = 0.5D$.

To better visualise the recirculation structures in the wake, the same velocity fields of Figure 3.64 are represented in Figure 3.65 in a frame of reference moving with the bubble. These velocity fields were obtained by subtracting the bubble velocity from the velocity vectors.

Since most of the liquid velocity magnitude in the flow field is much higher than the bubble velocity, there are only small changes relative to the flow fields represented in a fixed frame of reference. Nonetheless, in a frame of reference attached to the bubble it is possible to have an idea of the trailing edge movement by checking the liquid velocity direction close

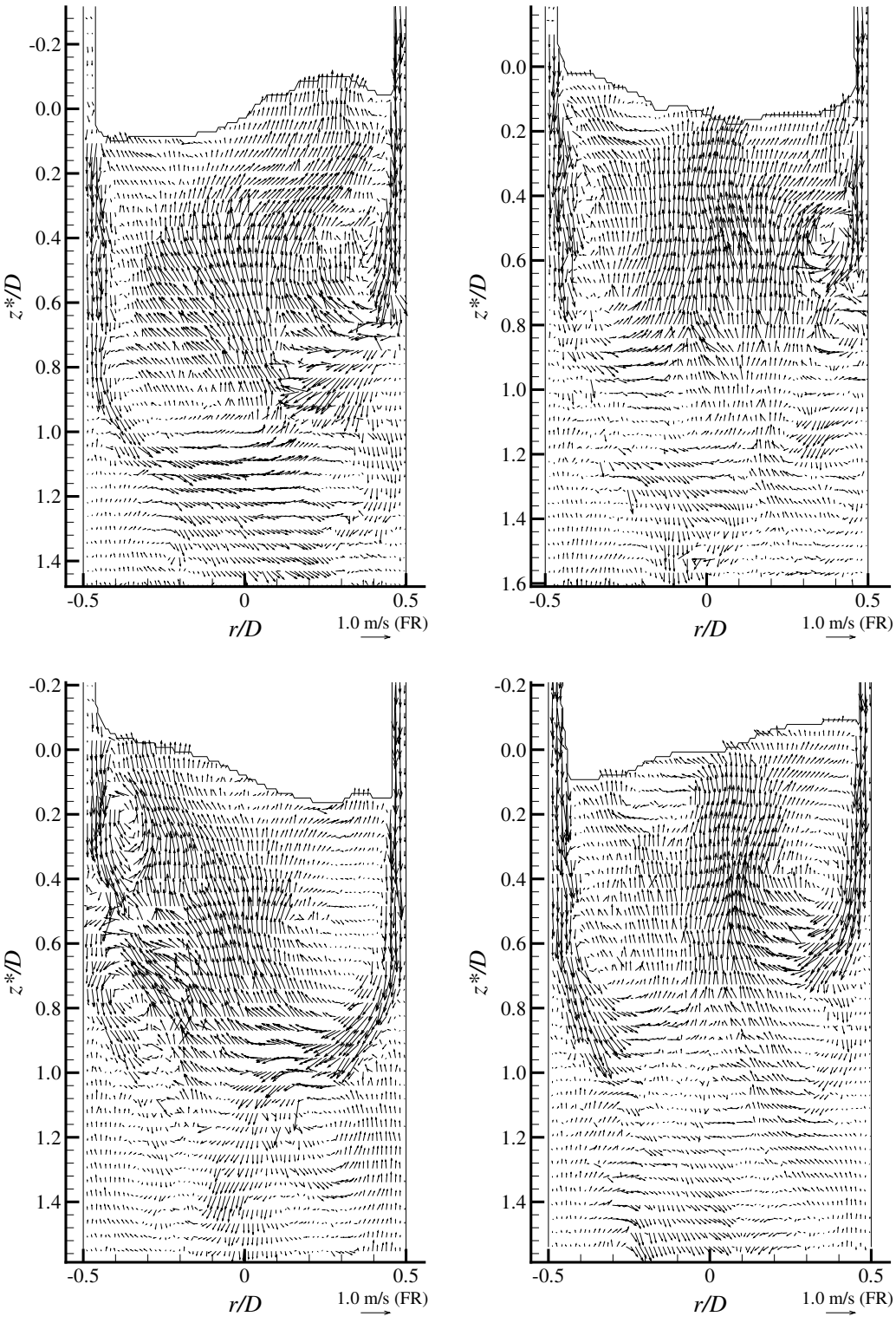

Figure 3.64. Flow fields in the wake of bubbles with $9.2D$ in length rising in a 0.10 wt% CMC solution (FR).

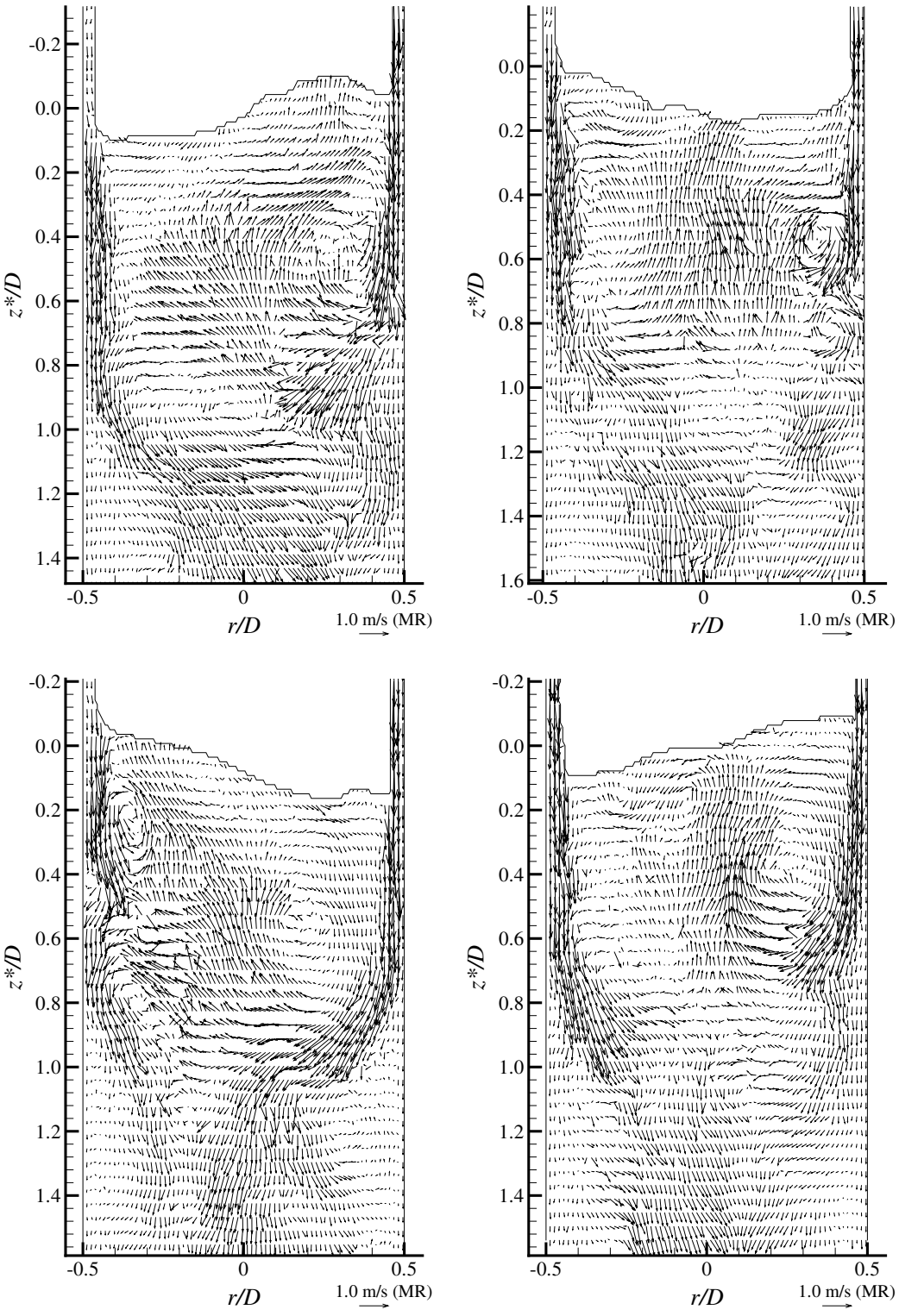

Figure 3.65. Flow fields in the wake of bubbles with $9.2D$ in length rising in a 0.10 wt% CMC solution in a frame of reference moving with the bubble velocity (MR).

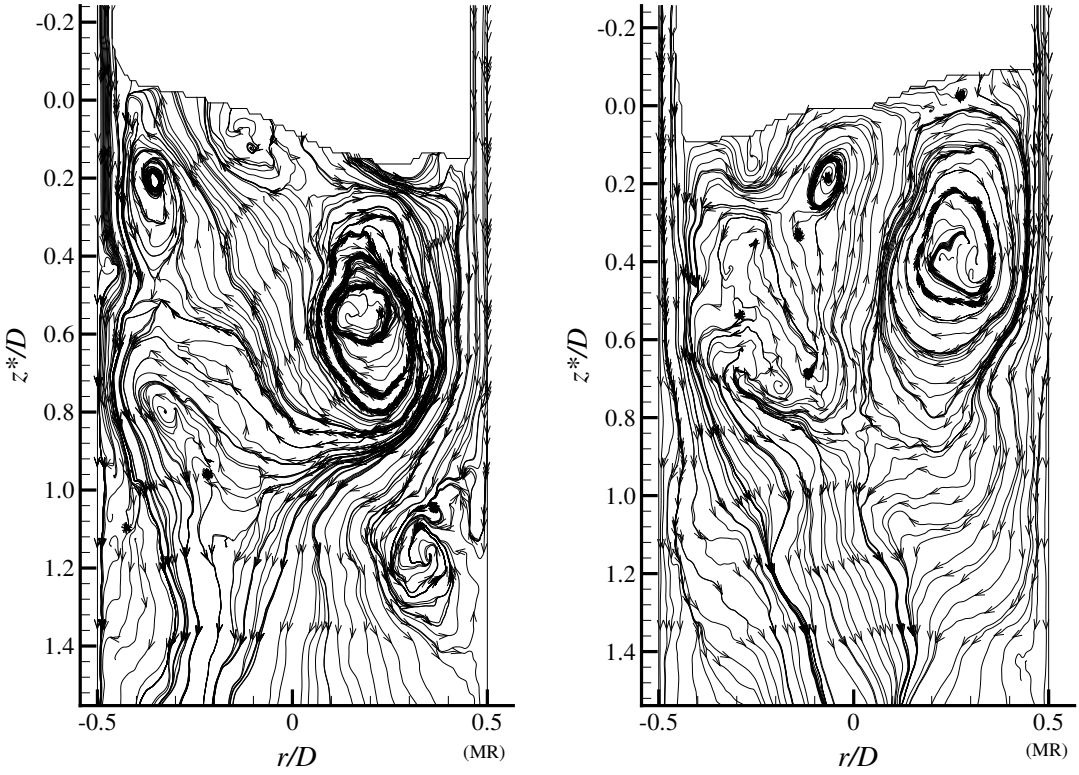

Figure 3.66. Instantaneous liquid trajectories in the wakes of bubbles rising in a 0.10 wt% CMC solution (two-dimensional projection in the measurement plane).

to it. In the images on the left in Figure 3.65 it is clear that the upper part of the trailing edge is moving up, inducing a movement of the liquid in the wake in that direction (to the upper right region in the top image and to the upper left region in the bottom image). In the images on the right in Figure 3.65, the trailing edge oscillation is mainly in the perpendicular direction to the measurement plane, inducing a liquid movement in that direction (into or out of the paper plane), the projected velocity being practically null.

The high upward liquid velocity in the central region of the wake shows that there is transport of liquid in the wake. However, the trailing edge oscillation induces a continuous change in the size and position of the recirculation regions. During this process some liquid is lost and renewed by liquid coming from the falling film, which explains the absence of coloured liquid in the visualisation studies.

Figure 3.66 shows two examples of instantaneous flow patterns in the wake. It should be noticed that the lines presented do not correspond exactly, neither to the trajectories of the

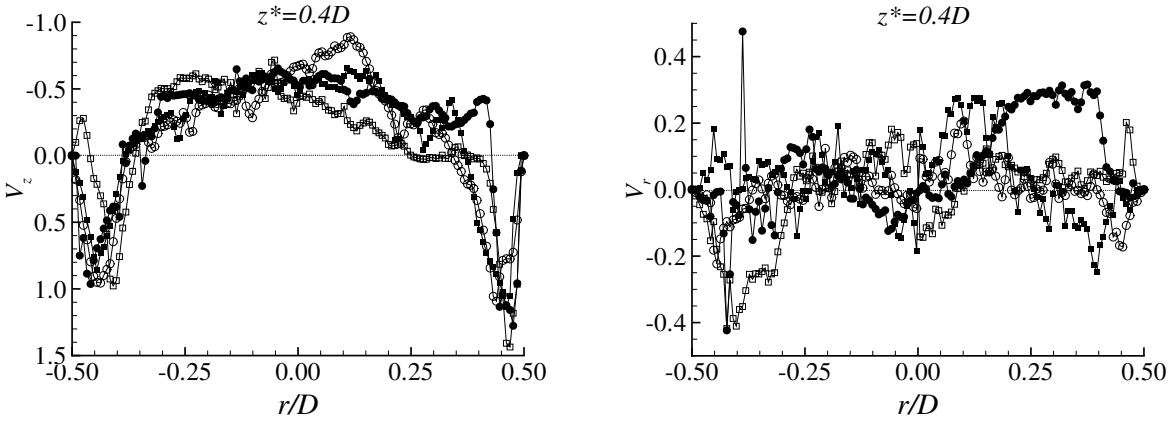

(a) Instantaneous axial velocity profiles

(b) Instantaneous radial velocity profiles

Figure 3.67. Instantaneous velocity profiles at $z* = 0.4D$.

particles nor to streamlines, since the flow is three-dimensional and transient. Even though it helps to visualise some of the recirculation present in the wake of the bubbles and the changes in position and configuration over time, a detailed description of the displacement of the recirculation was not possible due to the low frequency of the images acquisition.

To confirm that the wake flow pattern changes according to the bubble trailing edge orientation, some instantaneous velocity profiles are plotted in Figure 3.67 at $z* = 0.4D$, in a fixed frame of reference. Concerning the axial velocity profiles, liquid moving upwards in the axis of the column and downwards far from the axis can be observed. However, the velocity magnitude at a given radial position varies significantly. In the radial velocity profiles, positive values indicate an outward movement and negative values a movement into the axis of the column. From the instantaneous profiles a defined pattern can not be established, since in a given radial position the velocity direction varies according to the trailing edge position.

Despite the many oscillations in the wake of bubbles rising in a 0.10 wt% CMC solution, several profiles were averaged at the same distance from the bubble trailing edge to determine whether a mean pattern could be defined. For this analysis, 21 images of instantaneous trailing edge configurations were available. To see if the number of images (and therefore the number of instantaneous values) was enough to have meaningful average values the average velocity and the standard deviation at a given coordinate were plotted in Figure 3.68 as a function of the number of images analysed. The coordinates chosen are

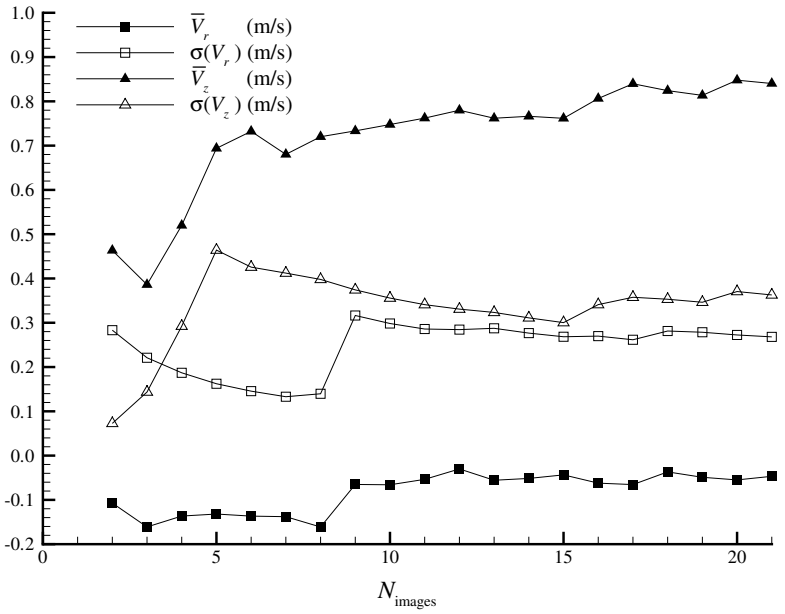

Figure 3.68. Average velocity and standard deviation at fixed coordinates, as a function of the number of images analysed; $r = 0, z* = 0.8D$ for V_r, $r = 0.45D, z* = 0.2D$ for V_z.

those where the maximum standard deviation for the horizontal and vertical components of the velocity was found. Figure 3.68 shows that the number of images was enough to have a representative average and standard deviation of the velocity components, since these values tend to stabilise after about 17 images.

In Figure 3.69 the average axial velocity profiles and standard deviations at different distances from the bubble trailing edge are represented. Positive axial velocities correspond to the downward direction; the vertical scale is inverted for a better perception of the liquid movement. Figure 3.69 shows that despite the oscillations in the velocity fields during the bubble rise the average of more than 20 velocity profiles gives a practically symmetric flow pattern, meaning that the bubble trailing edge oscillation has no preferential direction.

Concerning the axial upward velocity in the middle of the wake, the velocity profiles confirm that the maximum should be located around $z* = 0.5D$, as the velocity fields had suggested. The change in the axial velocity direction in the middle of the wake occurs between $z* = 1.0D$ and $z* = 1.2D$, which is approximately the point where the falling liquid film reattaches.

The fluid coming from the falling liquid film is responsible for the maximum downward velocity located around $r = 0.45D$. The deceleration of the liquid film is clearly seen by

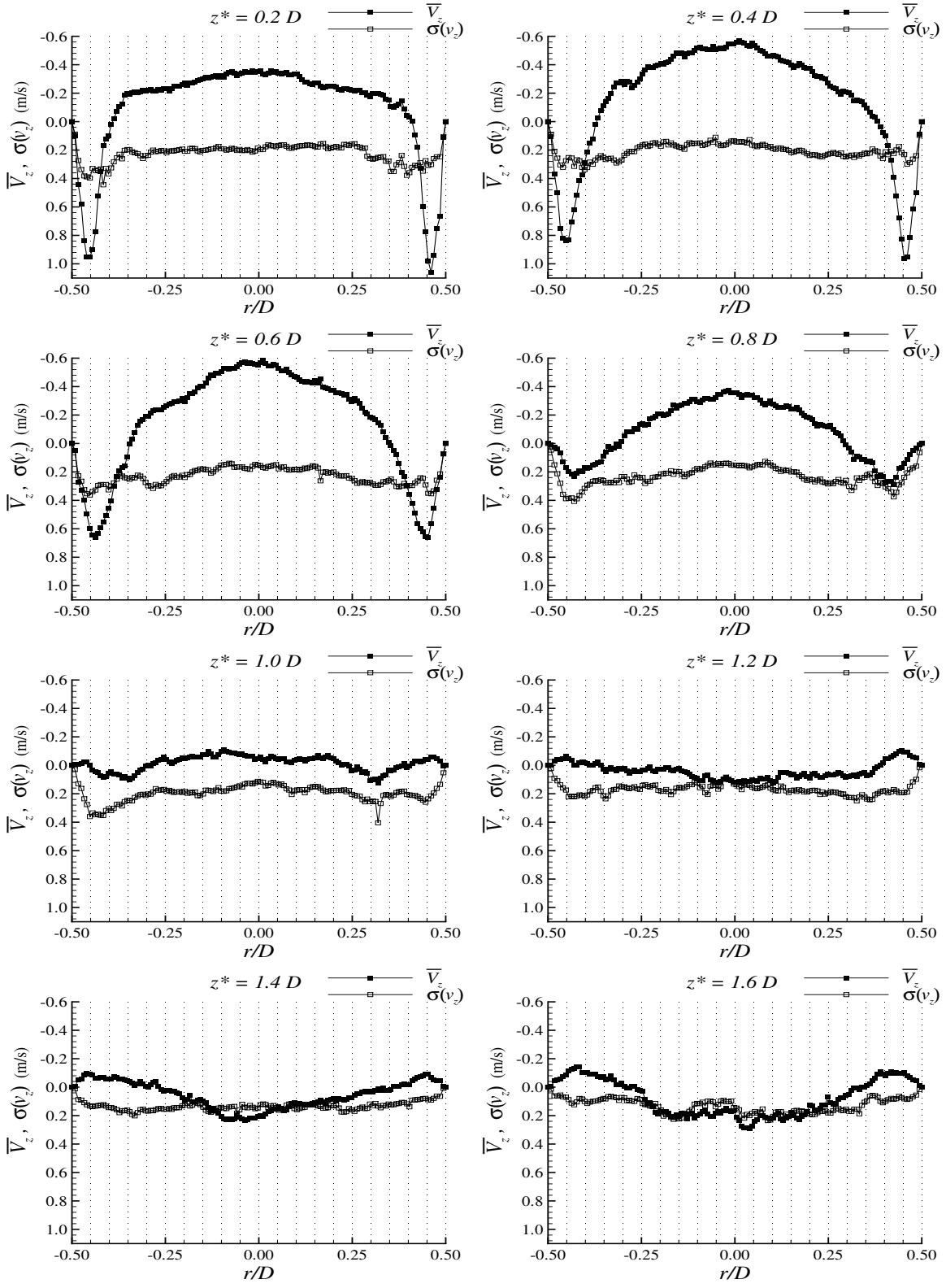

Figure 3.69. Average axial velocity profiles (fixed frame of reference) and standard deviation at different distances from the bubble trailing edge rising in a 0.10 wt% CMC solution.

checking the decrease of this maximum velocity as the distance from the bubble trailing edge increases up to $z* = 1.0D$. From there on there is an inversion of the flow pattern, which starts to move downwards in the axis of the column and upwards at higher radial positions.

Although the velocity profiles were extracted from different images and some scattering is due to the error in defining the bubble trailing edge position, the standard deviation of the velocity is clearly related with the velocity oscillations in the wake. The standard deviation between $z* = 0.2D$ and $z* = 1.0D$ shows a very similar behaviour, with a magnitude around 0.2 m/s in the middle of the wake and a maximum between 0.3 and 0.4 m/s at a radial position close to the maximum downward liquid velocity. This high standard deviation is explained by the displacement of the recirculation regions along the wake according to the trailing edge oscillation. For distances above $z* = 1.0D$ a decrease in the standard deviation is observed.

The average radial velocity profiles and respective standard deviations are represented in Figure 3.70. By analysing the average radial velocity profiles it is possible to conclude that in the region close to the bubble trailing edge the average velocity is positive, meaning that the fluid moves radially from the axis to the walls. Between $z* = 0.4D$ and $z* = 0.6D$ an inversion occurs and the fluid starts to move in the opposite direction, i.e., into the axis of the column. This means that despite the high oscillating flow in the wake, the average flow pattern is similar to the recirculating flow that will be described for laminar wakes: fluid moving upwards close to the axis of the column, and then moving radially outwards close to the bubble trailing edge to start falling close to the liquid film. Above $z* = 1.0D$ the average radial velocity profile starts to flatten.

The standard deviation of the radial velocity is higher than the average radial velocity itself in practically the whole wake region, traducing the high amplitude of the oscillations. The maximum standard deviation occurs close to the axis of the column. For higher radial positions, the fluid velocity direction is mainly vertical due to the liquid coming from the falling film, and less radial oscillations are seen.

To have a better perception of the average flow field, vectors were created from the average velocity profiles and plotted in the corresponding positions relative to the bubble trailing edge. A virtual average flow field is then obtained and is represented in Figure 3.71.

In the visualisation studies, it was noticed that for the smaller bubbles the trailing edge

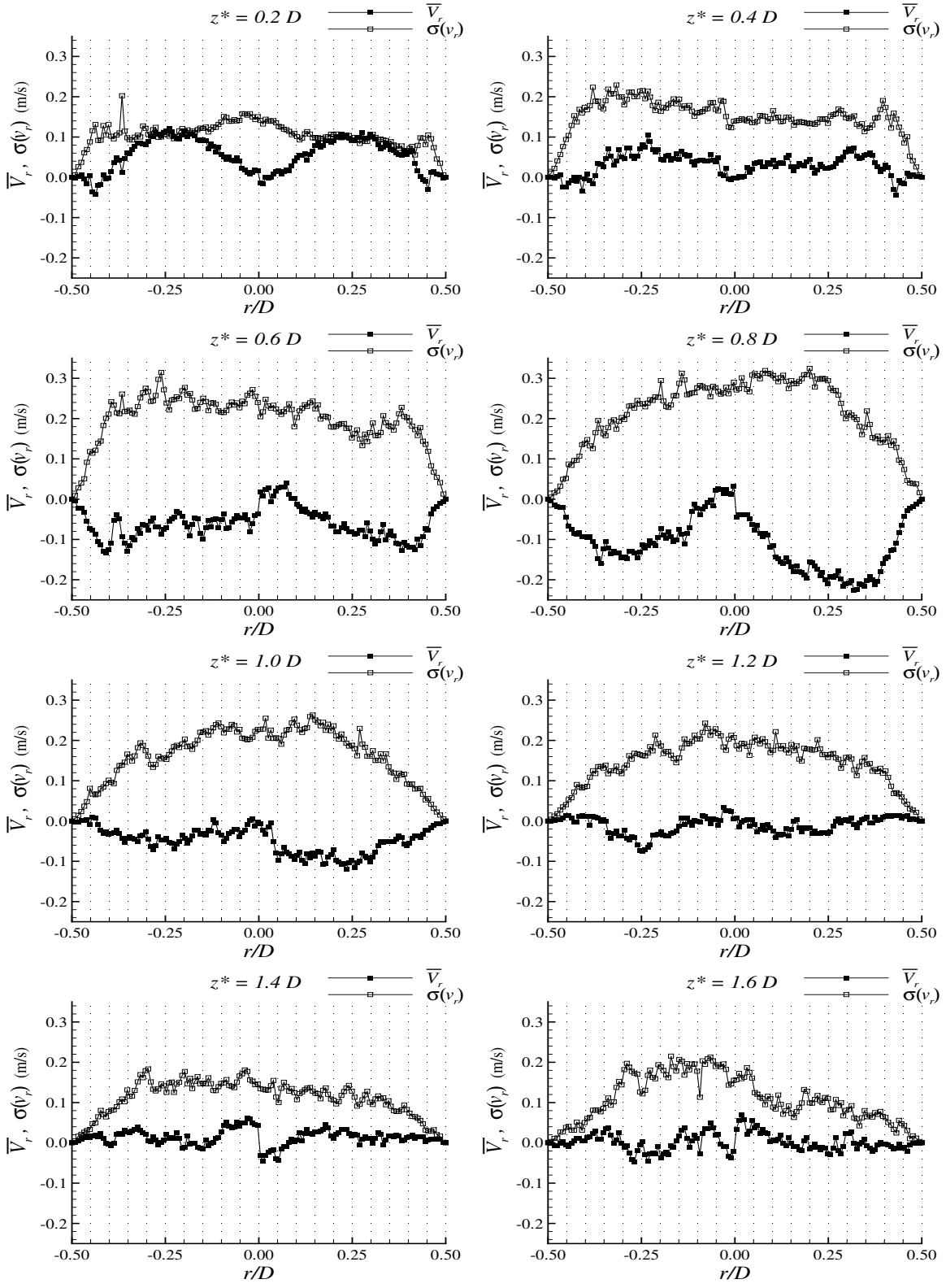

Figure 3.70. Average radial velocity profiles and standard deviation at different distances from the trailing edge, of bubbles rising in a 0.10 wt% CMC solution.

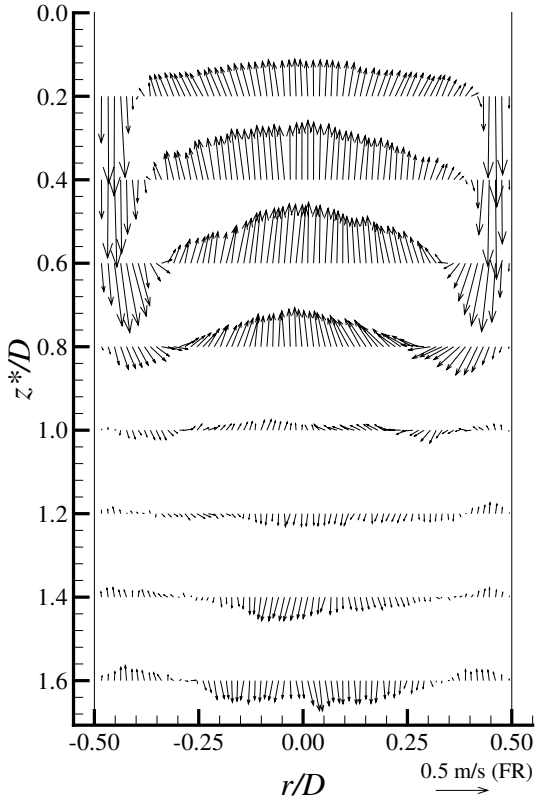

Figure 3.71. Average flow field in the wakes of Taylor bubbles ($L_b = 9.2D$) rising in a 0.10 wt% CMC solutions.

oscillations were not so intense. To compare the velocity field in bubbles of different size, 20 instantaneous velocity profiles in the wake of bubbles with $3.5D$ in length were averaged. Figure 3.72 shows the comparison between the average velocity profiles and the standard deviations at $z* = 0.2D$ for long ($9.2D$ in length) and short ($3.5D$ in length) bubbles. Although for the smaller Taylor bubble the liquid film is still not fully developed (see Table 3.6), the average velocity profiles in the wake do not present significant differences. The main difference is in the standard deviation in the region between the falling liquid film and the upward wake flow. Its magnitude is lower for the smaller bubbles, indicating a decrease in the amplitude of the trailing edge oscillations; behaviour which was expected from the visualisation studies.

It was already mentioned in the visualisation studies that behind the Taylor bubbles rising in 0.10 wt% CMC solution there is a train of small bubbles, formed mainly during the gas injection. During the PIV measurements these bubbles were also present. Figure 3.73

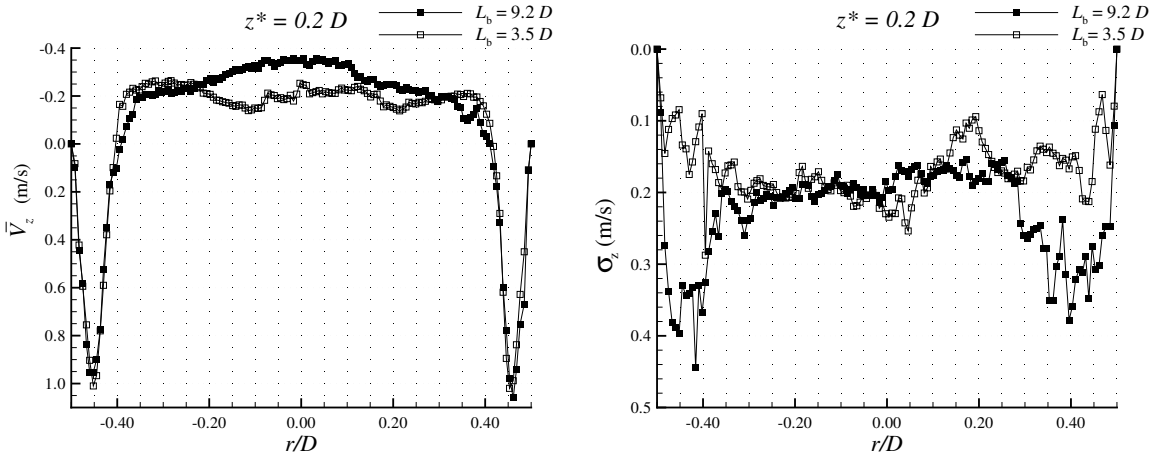

Figure 3.72. Average axial velocity profiles and standard deviation at $z* = 0.2D$ for bubbles of different lengths rising in 0.10 wt% CMC solution.

shows a PIV image with those bubbles behind the Taylor bubble and the corresponding velocity field. In the image processing no vectors were eliminated inside bubble shadows, since the bubbles can be out of the measuring plane. This velocity field is only an example to illustrate the role of these small bubbles in the liquid flow pattern. They induce an

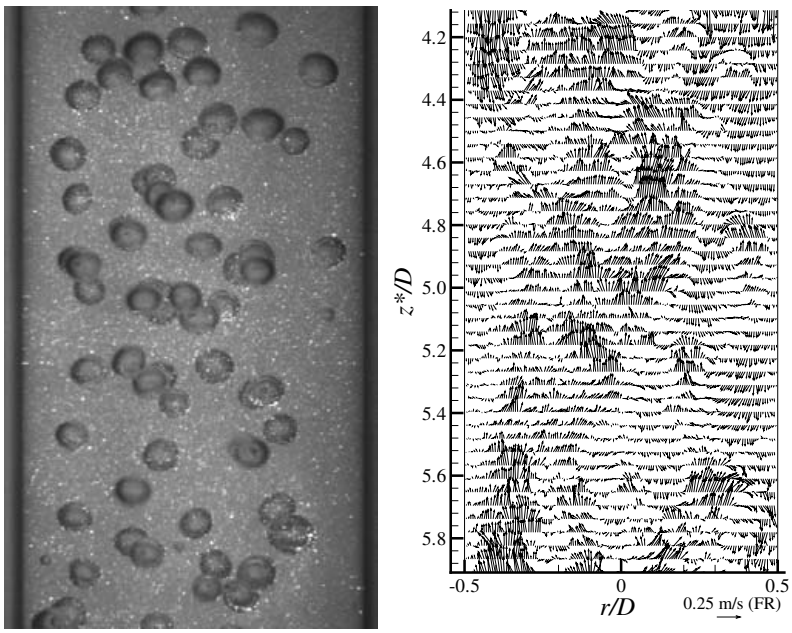

Figure 3.73. PIV image of small bubbles behind a Taylor bubble rising in a 0.10 wt% CMC solution and the corresponding velocity field.

upward liquid displacement in the axis of the column and a downward movement close to the walls. This induced flow should influence the coalescence of Taylor bubbles rising in this solution. This large group of small bubbles starts at about $z* = 2.5D$ and extends to more than $10D$ from the bubble trailing edge.

The axial velocity at $r = 0$ in function of $z*/D$ is plotted in Figure 3.74 by extracting instantaneous velocity profiles in consecutive images of the wake of a Taylor bubble rising in a 0.10 wt% CMC solution. This plot is representative of the velocity field behind a

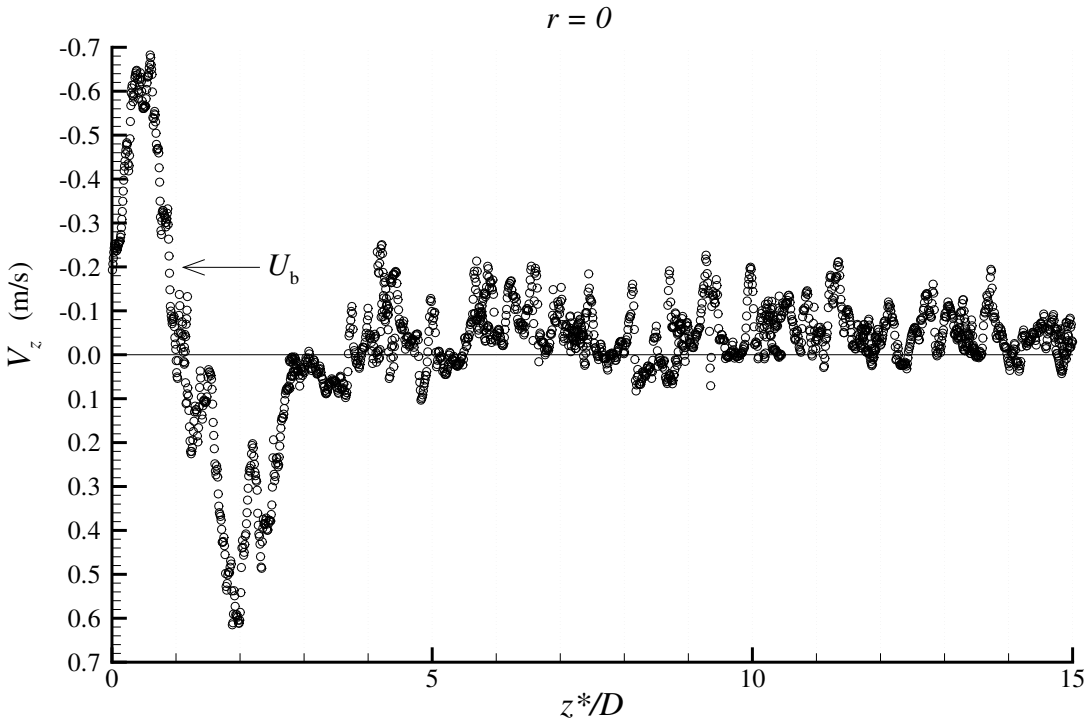

Figure 3.74. Instantaneous axial velocity profile (fixed frame of reference) at $r = 0$ in function of $z*/D$ behind a Taylor bubble rising in a 0.10 wt% CMC solution.

Taylor bubble rising in this solution. There is a central region with liquid moving upwards with high velocity (maximum velocity magnitude at around $z* = 0.5D$), followed by a downward velocity region where the film reattaches below $z* = 1.0D$. The tendency of the fluid to stagnate after the film reattachment is then disturbed by the train of small bubbles following the Taylor bubble, inducing an average upward liquid velocity close to the axis of the column for several column diameters.

van Hout *et al.* (2002a) confirmed that the ensemble averaged velocity profiles behind

Taylor bubbles rising in water become negligible at around $12D$ from the bubble trailing edge, however, notable instantaneous velocity fluctuations were found to exist up to $50D$.

0.30 wt% CMC

From the visualisation studies, §3.1.2, it was seen that in the 0.30 wt% CMC solution there was coloured liquid transported in the wake. The bubble trailing edge was stable but with an inclined position which induced the formation of asymmetric recirculation regions in the wake, with a preferential orientation.

In the PIV measurements the bubble trailing edge was not stable, oscillating during the rise, but with a much lower frequency and amplitude than in the 0.10 wt% CMC solution. Figure 3.75 shows some examples of bubble trailing edge positions found in this solution.

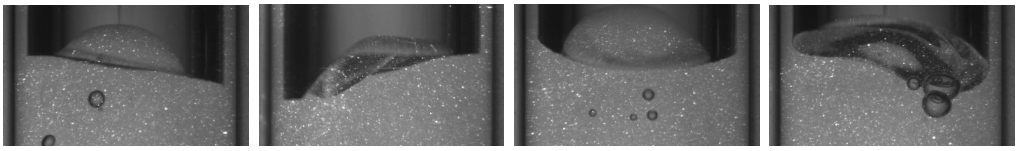

Figure 3.75. Examples of trailing edge positions of Taylor bubbles rising in a 0.30 wt% CMC solution.

The small oscillations of the bubble trailing edge are responsible for asymmetries in the wake flow pattern, as shown in Figure 3.76.

It is clear that, despite some asymmetries, there is some similarity between the different flow fields. The liquid film expands surrounding a central region of upward velocity. Although the velocity magnitude in the central region of the wake is similar to the 0.10 wt% CMC solution, the lower amplitude and frequency of the trailing edge oscillations reduce the out-of-plane movement and it can be seen the formation of large recirculation regions. Figure 3.77 shows the same flow fields in a frame of reference moving at the bubble velocity. In this frame of reference it can be observed that the film reattaches between $z* = 1.2D$ and $z* = 1.4D$. The asymmetries that appear in the wake are clearly seen when the instantaneous streamlines are plotted, as Figure 3.78 shows. While the flow is practically symmetric in the left image, in the other images the recirculation regions appear distorted, similar to the visualisation studies. This is due to the inclination of the bubble trailing edge and to the fact that only a two dimensional projection of the flow field is represented. As in the 0.10 wt% CMC solution, the oscillation of the bubble trailing edge induces chan-

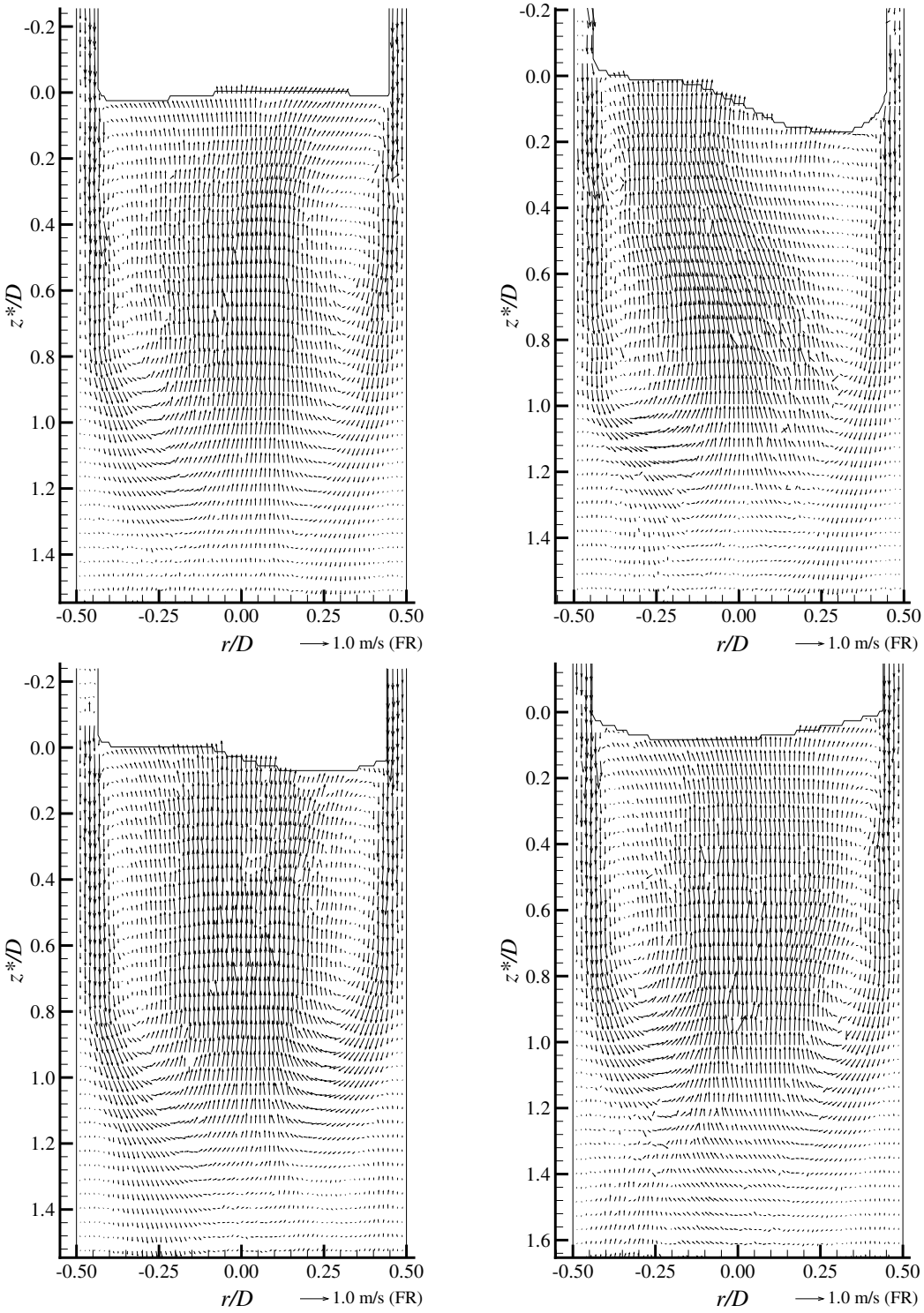

Figure 3.76. Flow fields in the wake of Taylor bubbles rising in a 0.30 wt% CMC solution.

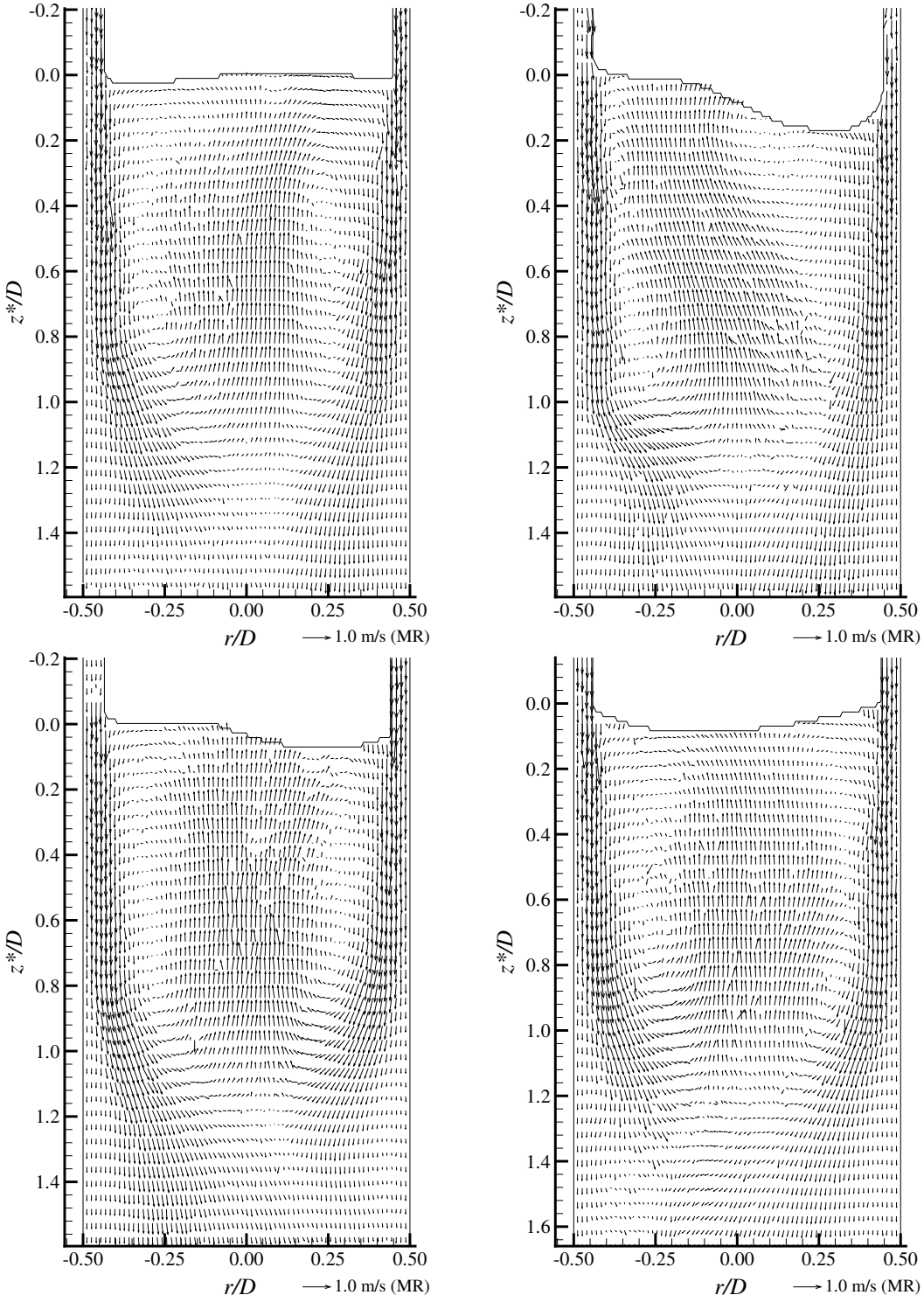

Figure 3.77. Flow fields in the wake of Taylor bubbles rising in a 0.30 wt% CMC solution in a frame of reference moving with the bubble velocity.

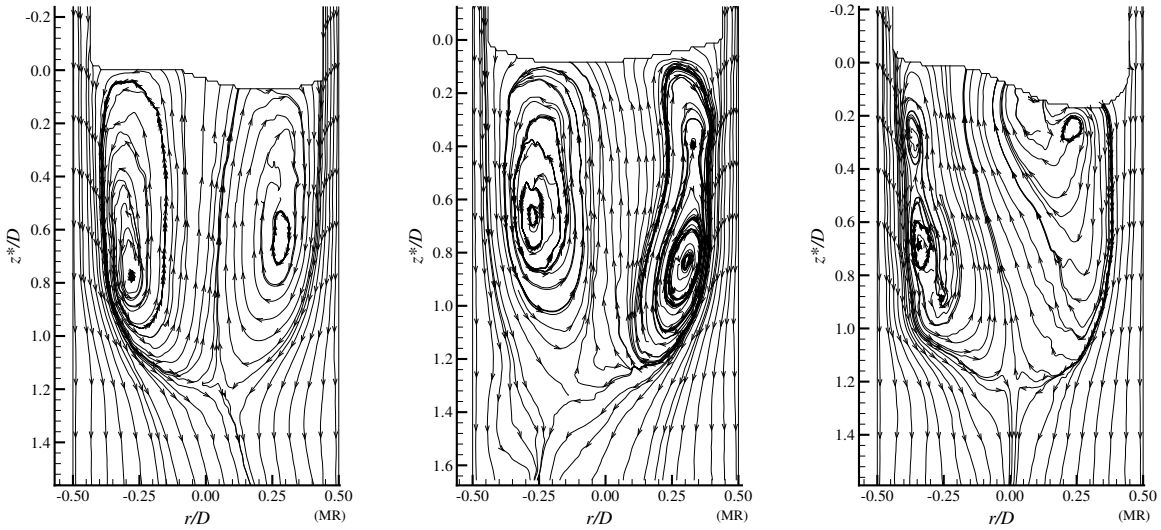

Figure 3.78. Instantaneous streamlines on the wakes of Taylor bubbles rising in a 0.30 wt% CMC solution.

ges in the size and position of the recirculation regions. However, in the 0.30 wt% CMC solution the differences between the flow fields at different instants are not so drastic, and similar flow patterns can be found in a large set of images. The fact that the streamlines coming from the liquid film practically surround the wake region shows that there is a low rate of liquid renewal, which explains the transport of coloured liquid in the visualisation studies.

The average velocity profiles at different distances from the bubble trailing edge were also determined for the flow in the wake of bubbles rising in a 0.30 wt% CMC solution. Twenty-four instantaneous flow fields were available. To check if the number of instantaneous measurements was enough to have meaningful average values, the axial and radial velocity components and the respective standard deviation were represented in Figure 3.79 at fixed coordinates where the maximum standard deviations were found. It is clear that due to less amplitude and frequency of the oscillations, a lower number of images is necessary to stabilise the average velocity components and standard deviations; 20 images were used to obtain the average velocity profiles.

Figure 3.80 shows the average axial velocity profiles and standard deviations in the wake of Taylor bubbles rising in this solution. It can be noticed that there is a slight asymmetry in these profiles since the maximum velocity magnitudes in the central region of the wake are shifted to the left. This shows a preferential oscillation direction which might be due to

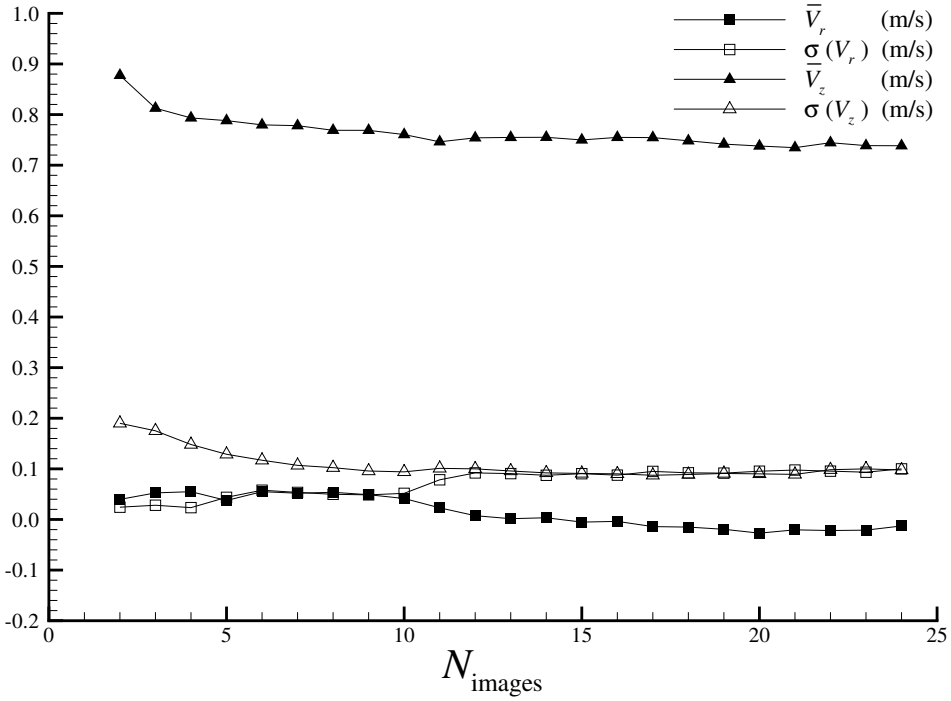

Figure 3.79. Average velocity and standard deviation at a fixed point in function of the number of images used; $r = 0, z* = 1.2D$ for V_r and $r = 0.45D, z* = 0.2D$ for V_z.

some experiment interference. Possibly there was a slight vertical deviation in the column, which induced a slightly asymmetric flow around the bubble.

The average velocity in the central region of the wake is on the same order as the 0.10 wt% CMC solution, despite all the large oscillations in this last case. The maximum axial velocity appears to be located between $z* = 0.6D$ and $z* = 0.8D$ which is slightly more downward from the trailing edge than in the 0.10 wt% CMC solution.

While in the 0.10 wt% CMC solution the average axial velocity profile flattens and inverts direction between $z* = 1.0D$ and $z* = 1.2D$, in the 0.30 wt% CMC solution the inversion of the velocity direction in the axis of the column only occurs between $z* = 1.4D$ and $z* = 1.6D$, indicating a larger wake length.

In regard to the liquid from the film around the Taylor bubble, its deceleration is clearly seen as the distance from the trailing edge increases, up to $z = 1.0D$. For longer distances, the liquid from the film moves towards the axis of the column, inducing an upward movement of the liquid at higher radial positions.

By considering the standard deviation of the velocity profiles a decrease in maximum

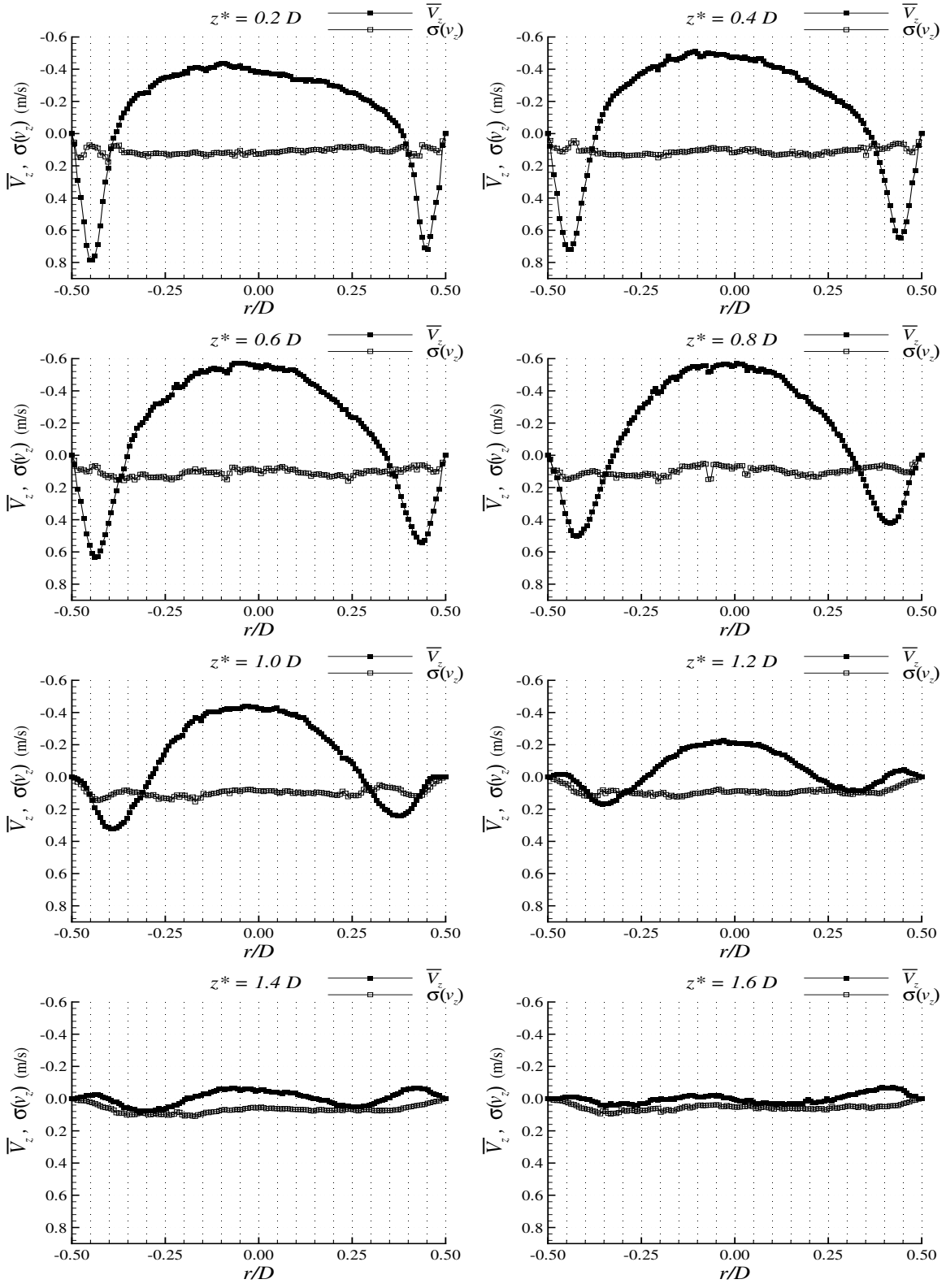

Figure 3.80. Average axial velocity profiles (fixed frame of reference) and standard deviation at different distances from the bubble trailing edge rising in a 0.30 wt% CMC solution.

magnitude is clear; 0.4 m/s in the 0.10 wt% CMC solution, to values below 0.2 m/s in the present case.

The average radial velocity profiles in the wake are represented in Figure 3.81. It is worth remembering here that positive radial velocities correspond to fluid moving in an outward direction and negative velocities are those moving toward the axis of the column. Once again, there is a slight asymmetry since the radial velocity is zero in a position shifted to the right of the column axis until $z* = 0.6D$ and to the left at longer distances. The discontinuity observed at $r = 0$ has to do with the velocity signal definition and with the asymmetric flow. If in the axis of the column the fluid has a radial velocity component, it is negative on one side (flowing towards axis) and positive in the other (flowing away from the axis) and this is an indication of an asymmetric flow. The point where the outward flow is inverted is now between $z* = 0.6D$ and $z* = 0.8D$, indicating the centre of the three-dimensional donut-shaped vortex.

The standard deviation of the radial component is also much lower than in the 0.10 wt% CMC solution, although still higher than the average velocity in most of the wake region. The standard deviation is below 0.1 m/s, with the local maximum at the axis of the column.

The average wake flow field in the wake of the Taylor bubbles rising in 0.30 wt% CMC solution is represented in Figure 3.82. The asymmetry mentioned is identified, as well as the occurrence of the liquid film reattachment at a longer distance from the bubble trailing edge than in the 0.10 wt% CMC solution.

In Figure 3.83, the instantaneous vertical velocity in the axis of the column ($r = 0$) is represented versus $z*/D$. This figure shows the maximum upward axial velocity between $z* = 0.6D$ and $z* = 0.8D$ and the beginning of the central downward flow between $z* = 1.4D$ and $z* = 1.6D$, as suggested by the axial velocity profiles. In this work the wake length is considered to be the distance from where the film reattaches to the bubble trailing edge; at this distance, the axial velocity changes signal in a frame of reference moving with the bubble. In a fixed frame of reference it should correspond to the distance where the upward liquid velocity equals the bubble velocity. In the 0.30 wt% CMC solution the wake length is then around $1.2D$.

The absence of small bubbles behind the Taylor bubble allows the flow to stabilise around $z* = 3.5D$. This value is expected to be approximately the distance above which there will be no interaction between two consecutive Taylor bubbles. Although between $z* = 1.5D$ and $z* = 3.5D$ the liquid flows downwards close to the axis of the column,

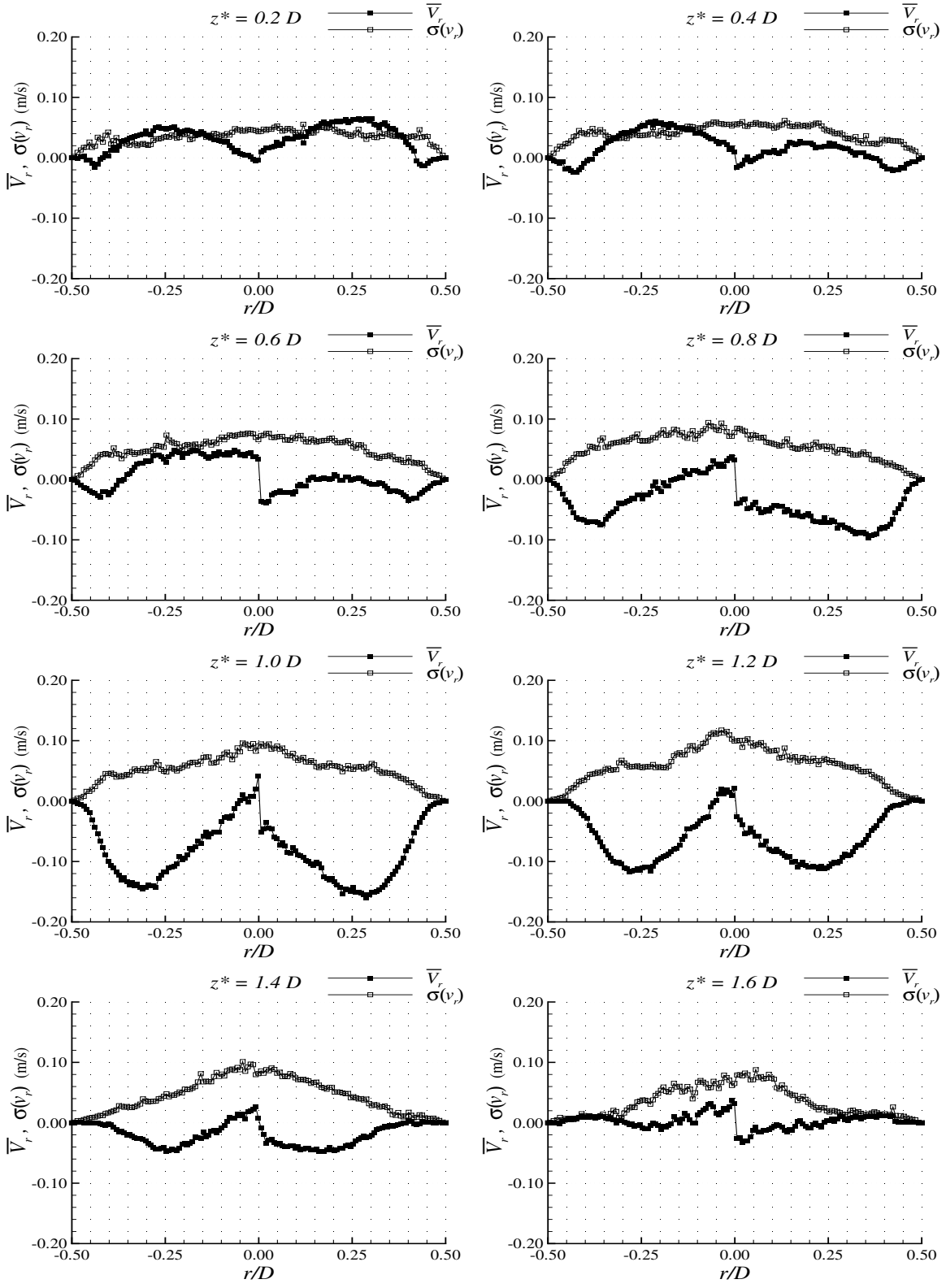

Figure 3.81. Average radial velocity profiles and standard deviation at different distances from the bubble trailing edge rising in a 0.30 wt% CMC solution.

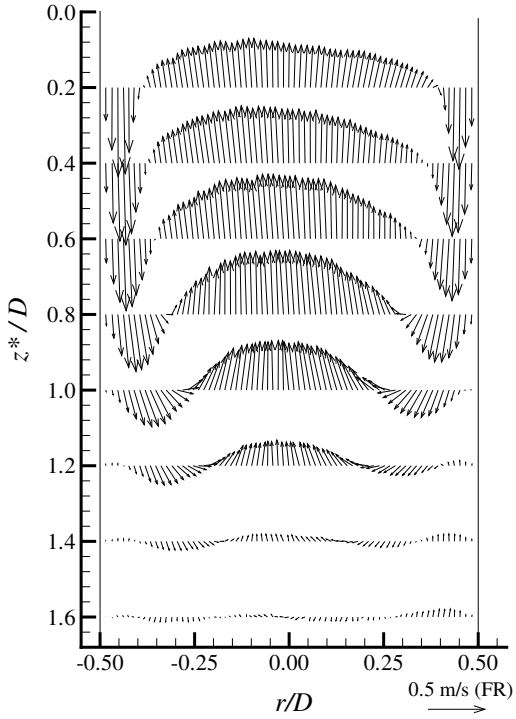

Figure 3.82. Average wake flow field for bubbles rising in a 0.30 wt% CMC solution.

there is an upward flow in the outer regions to obey mass flow continuity, as represented in Figure 3.84. The upward liquid movement in the outer regions at $z* = 2.5D$ might still affect the velocity of a trailing bubble since the bubble nose always follows the liquid with the most upward velocity (the least-resistant path). At $z* = 4.0D$, despite still being in movement, the liquid has very low velocity magnitudes and its effect on the second bubble velocity should be minimum. To understand bubble coalescence, Figure 3.83 by itself gives several useful points of information.

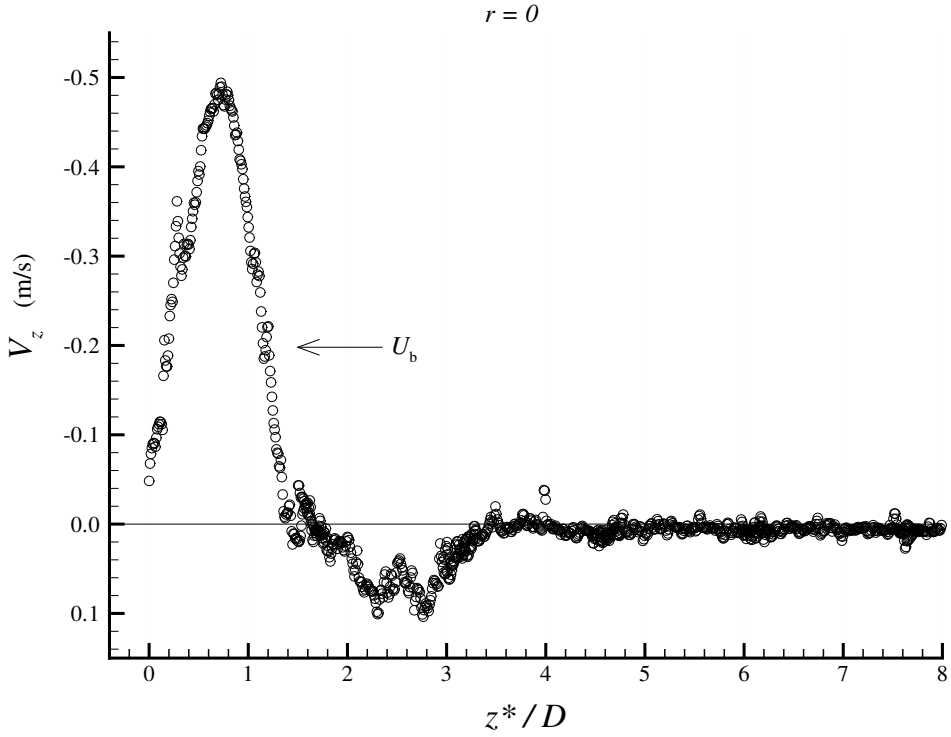

Figure 3.83. Instantaneous axial velocity profile (fixed frame of reference) at $r = 0$ as a function of $z*/D$ in the wake of a Taylor bubble rising in a 0.30 wt% CMC solution.

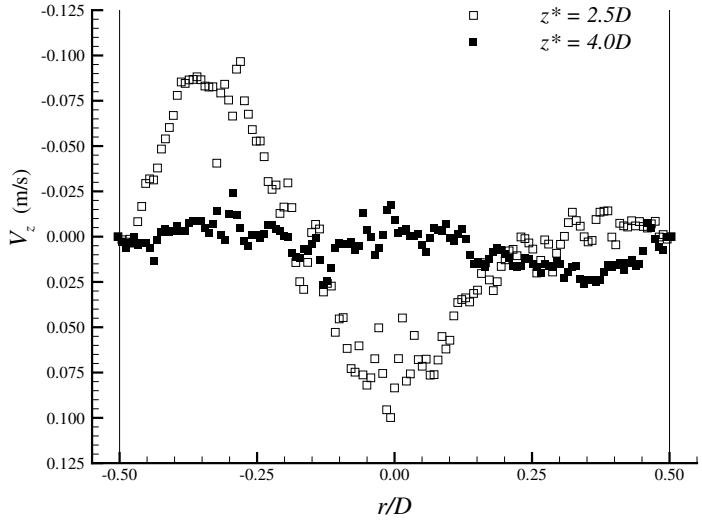

Figure 3.84. Instantaneous axial velocity profiles (fixed frame of reference) at $z* = 2.5D$ and $z* = 4.0D$ in the wake of a Taylor bubble rising in a 0.30 wt% CMC solution.

0.40 wt% CMC

In the visualisation studies for the 0.40 wt% CMC solution no instabilities were seen in the bubble trailing edge. The wake flow pattern was a symmetric closed recirculation region, except in the cases where small bubbles were trapped in the bubble wake.

Chronologically, this was the first solution studied in this work with the PIV technique. Due to some unexpected technical problems, this experiment extended for a longer period of time than the others, which might have led to some degradation of the CMC solution.

In Figure 3.85, some examples of trailing edges of bubbles rising in a 0.40 wt% CMC solution are represented. This figure shows very stable behaviour of the bubble trailing

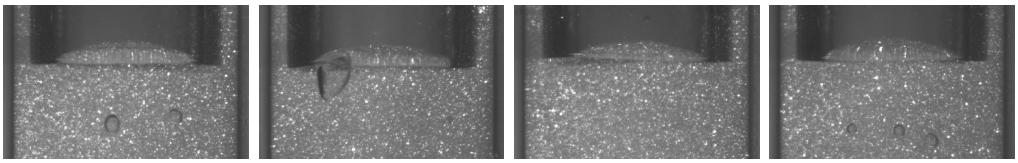

Figure 3.85. Images of the trailing edge of Taylor bubbles rising in a 0.40 wt% CMC solution.

edge, with a basically horizontal position. In some cases, small bubbles trapped in the bubble wake are observed. The bubble trailing edge has a concave shape (from the liquid side), similar to the bottom of a glass bottle, where liquid is in recirculation. The velocity field in this region was not taken into account. Due to the difference between the refractive indexes of air and liquid and the curved surface, erroneous velocity vectors and positions are obtained in that concave region when using the PIV technique.

In Figure 3.86 two examples of velocity fields in the wake of Taylor bubbles rising in a 0.40 wt% CMC solution are represented. It is clear that although they are from different bubbles the flow fields present practically no differences, apart from small disturbances caused by the presence of small bubbles. With a stable trailing edge the wake flow pattern is symmetric, in contrast to the asymmetry in previous solutions, so that this two dimensional flow field is now representative of the flow in any vertical plane containing the column axis.

In comparison with the previous case, it can also be noticed that the liquid film expands and decelerates in a shorter distance.

The stable trailing edge allows the formation of a practically symmetric recirculation region, which is better seen in a frame of reference moving at the bubble velocity, as represented in Figure 3.87 for two flow field examples with the corresponding streamlines.

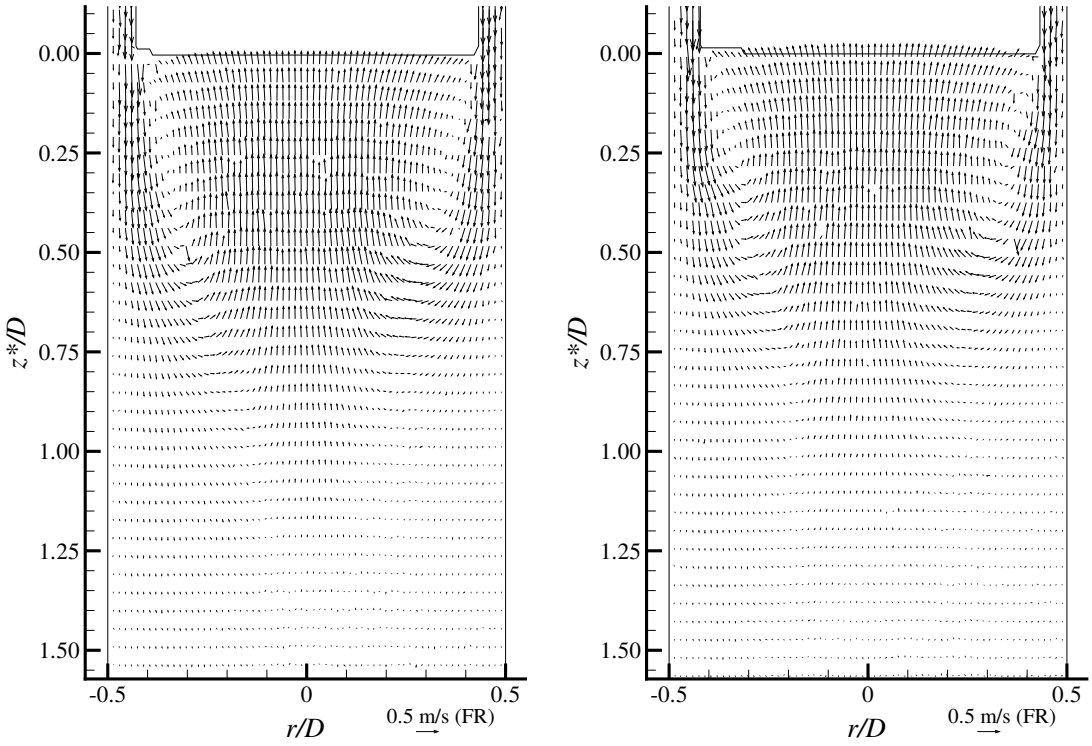

Figure 3.86. Flow fields in the wake of Taylor bubbles rising in a 0.40 wt% CMC solution.

The streamlines were plotted with graphics software at random positions. This was only to get an idea of the fluid particle trajectories, so the distance between them should not be related to any constant mass flow rate. The streamlines, in a frame of reference moving with the bubble, confirm that in the measurement plane the flow is practically symmetric and with closed recirculation regions. This explains the transport of coloured liquid in the visualisation studies. An overlapping of the streamlines obtained from the PIV measurements with an image of the visualisation studies is presented in Figure 3.88. The similarity between them is evident. From this comparison, it can be concluded that the wake length is about $0.8D$, which is the distance from the bubble trailing edge to where the axial velocity changes signal. The wake length should not be confused with the distance above which there is no interaction between two consecutive bubbles, since below the wake there is still a region with liquid in motion.

As in the previous solutions, average axial velocity profiles were determined at different distances from the bubble trailing edge and are presented in Figure 3.89. In the 0.40 wt%

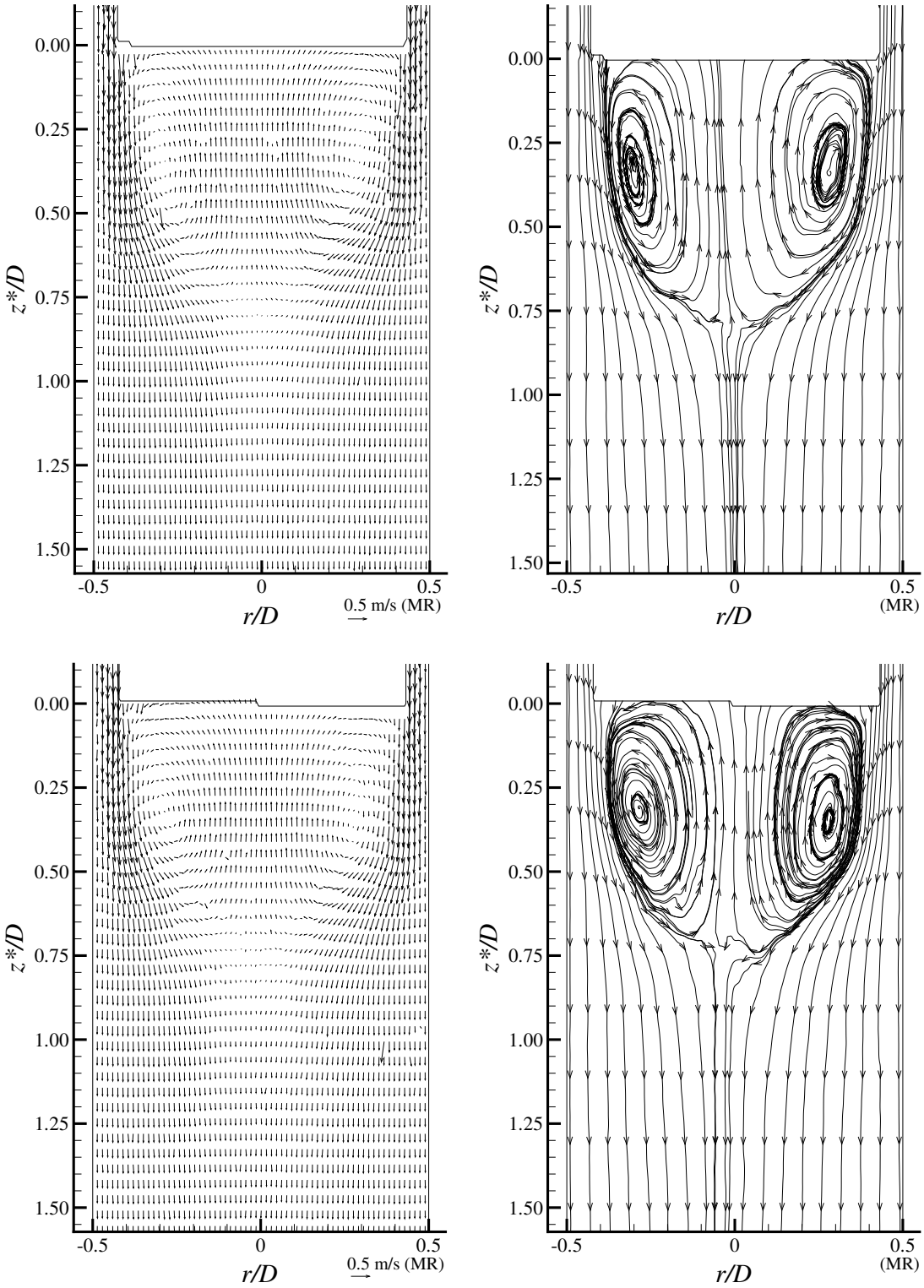

Figure 3.87. Flow fields and streamlines in the wake of Taylor bubbles rising in a 0.40 wt% CMC solution in a frame of reference moving with the bubble.

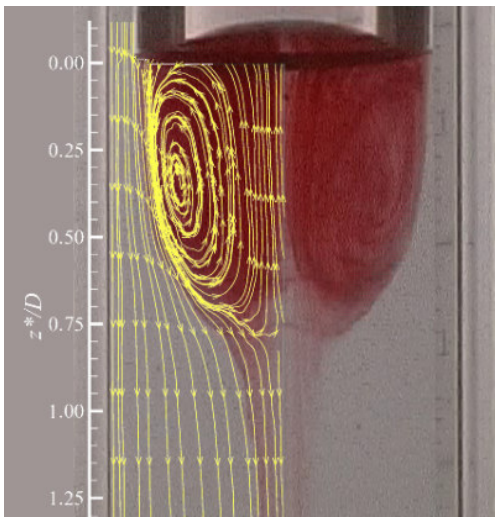

Figure 3.88. Overlapping of streamlines with a visualisation image of the wake of a Taylor bubble rising in a 0.40 wt% CMC solution.

CMC solution, there is a decrease in the maximum upward velocity magnitude in the central region of the wake and its location is now closer to the trailing edge, between $z* = 0.2D$ and $z* = 0.4D$. It is also possible to confirm the wake length around $0.8D$ since it is the region where the axial velocity at $r = 0$ reaches the bubble velocity, which means a zero velocity in a frame of reference moving with the bubble.

In this solution there is no visible inversion of the velocity direction in the axis of the column until $z* = 1.4D$. Due to the higher viscosity, the axial velocity profile maintains the same shape from $z* = 0.1D$ until $z* = 1.4D$, with a smooth decrease in the velocity magnitudes. Inversion of the velocity direction occurs after $z* = 1.4D$, but with residual velocity magnitudes.

The maximum standard deviation of the axial velocity is located close to the bubble trailing edge, mainly due to the presence of small bubbles trapped in that region. For distances above $z* = 0.4D$ the standard deviation decreases to values below 0.1 m/s, showing the stability of the flow.

The radial velocity profiles were also determined and are plotted in Figure 3.90. In the previous solutions, the liquid coming from the falling film had a very low radial velocity in the region close to the bubble trailing edge. In the 0.40 wt% CMC solution at $z* = 0.10D$ the difference is clear in the flow direction, moving outwards near the axis and in the opposite direction in the outer regions where the liquid film is expanding. The inversion

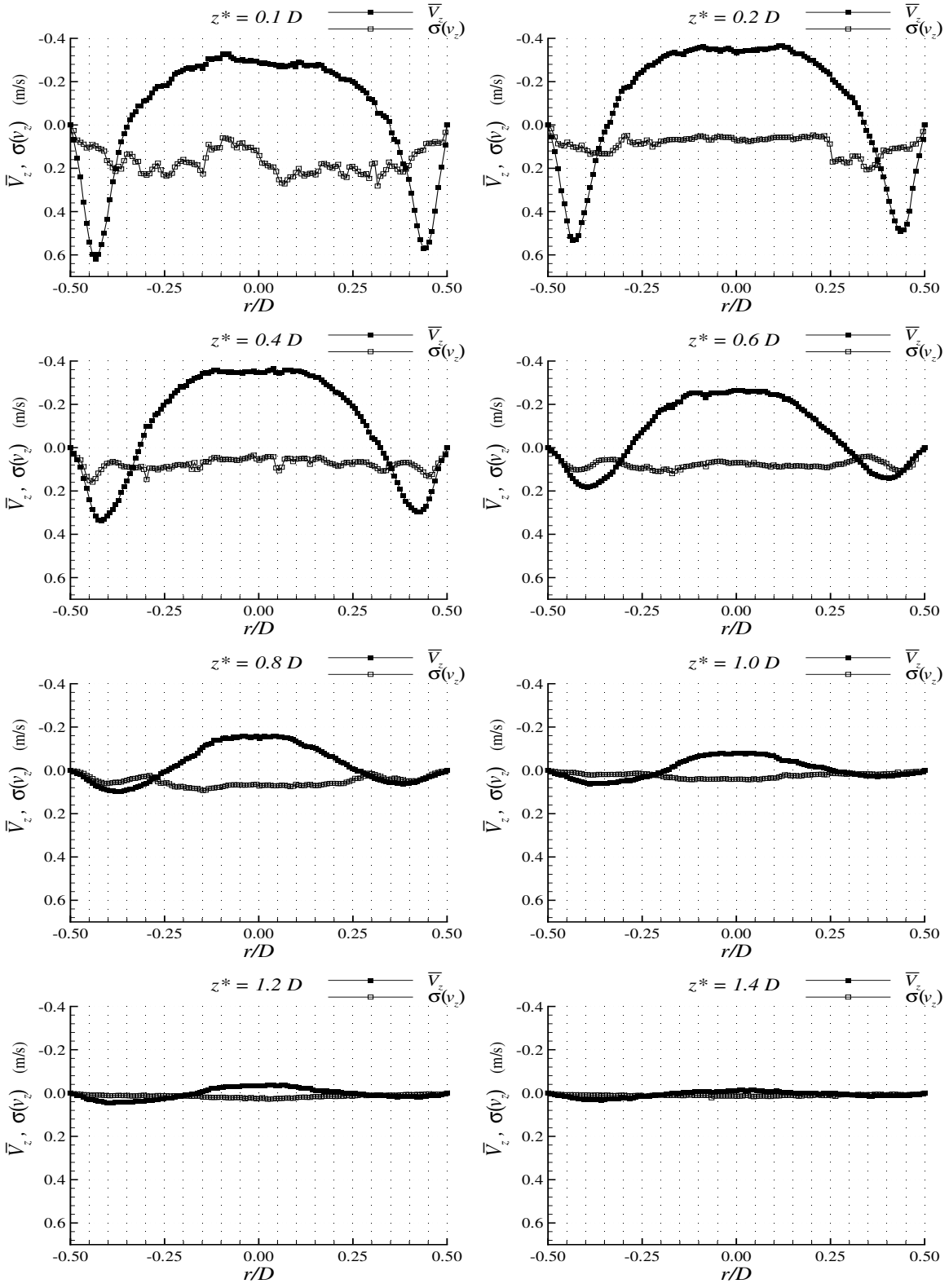

Figure 3.89. Average axial velocity profiles (fixed frame of reference) and standard deviation at different distances from the bubble trailing edge rising in a 0.40 wt% CMC solution.

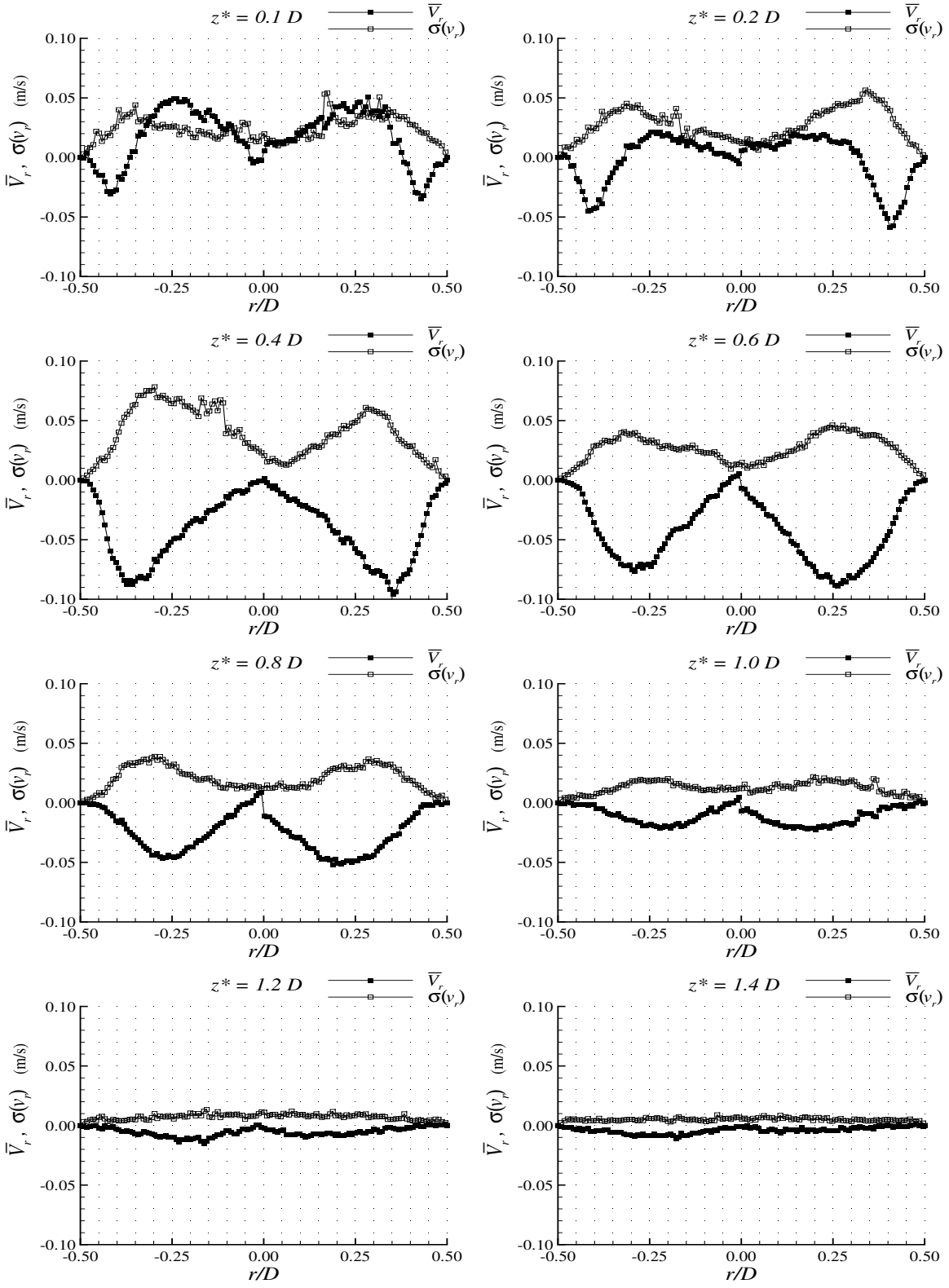

Figure 3.90. Average radial velocity profiles and standard deviation at different distances from the bubble trailing edge rising in a 0.40 wt% CMC solution.

of flow direction inside the wake, and therfore the centre of the donut shaped vortex, now occurs between $z* = 0.2D$ and $z* = 0.4D$, coinciding once again with the maximum in the axial velocity magnitude. The magnitudes of the radial velocity and standard deviation are now low and close to measurement uncertainty, since the previously mentioned uncertainty of 0.2 pixels corresponds to a velocity of 0.014 m/s, with the calibration and time used in these flow fields

As seen from the instantaneous flow fields and from the low standard deviations, the average flow field should not be very different from an instantaneous flow field in the wake of a bubble rising in a 0.40 wt% CMC solution. Nevertheless, the average flow field is represented in Figure 3.91.

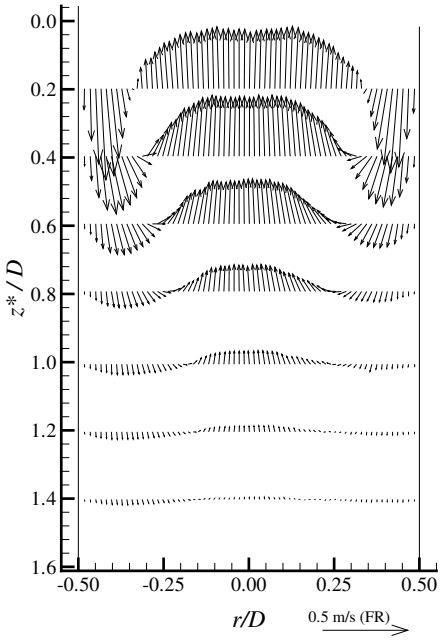

Figure 3.91. Average flow field in the wake of a Taylor bubble rising in a 0.40 wt% CMC solution.

The average axial velocity profile at $r = 0$ as a function of the distance to the bubble trailing edge is represented in Figure 3.92. This figure shows the expected maximum upward velocity at $z* = 0.3D$, with a velocity magnitude around 0.40 m/s. The liquid velocity reaches the bubble velocity magnitude between 0.6 and $0.8D$ from the bubble trailing edge, which is in accordance with the wake length ($0.8D$). Above $z* = 1.4D$ the downward velocity has its maximum around $z* = 2.5D$, but with a much lower magnitude

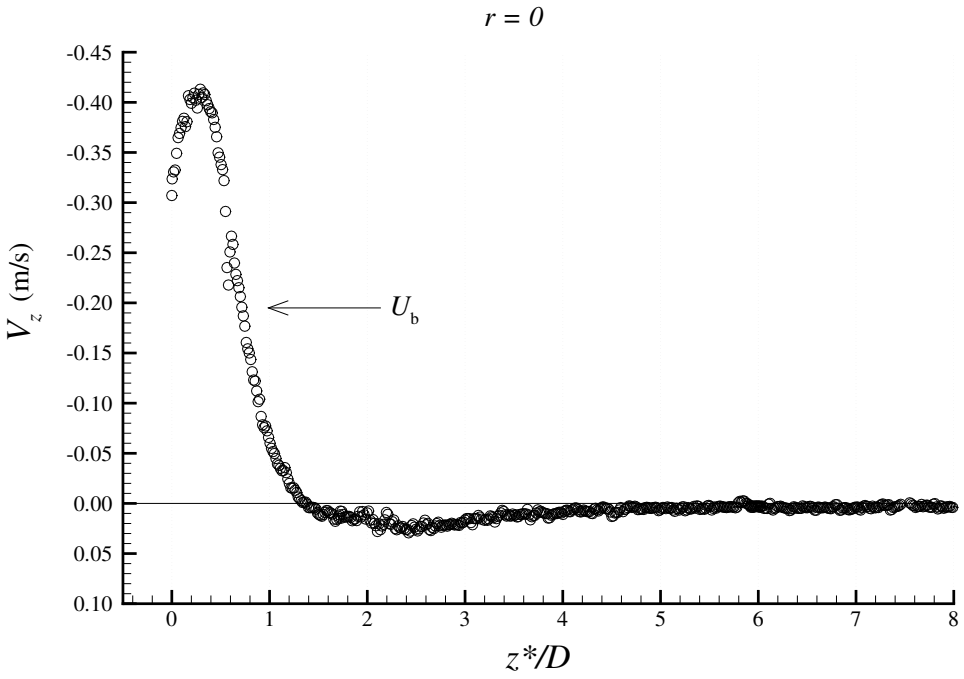

Figure 3.92. Instantaneous axial velocity profile (fixed frame of reference) at $r = 0$ behind a Taylor bubble rising in a 0.40 wt% CMC solution.

than in the previous solutions and smoothly decreasing to zero velocity. Although of very low magnitude, the corresponding upward velocities far from the axis of the column might still affect the velocity of a trailing bubble.

0.50 wt% CMC

In the visualisation studies made with 0.50 wt% CMC solution, the behaviour found was similar to that of the 0.40 wt% CMC solution, but with a decrease in the wake length.

In the PIV measurements the ambient temperature of the 0.50 wt% CMC experiments was about 6^oC higher than for the 0.40 wt% CMC solution, which slightly reduced the viscosity, decreasing the expected difference between the flow patterns in both solutions.

In Figure 3.93, some images of the trailing edge of bubbles rising in a 0.50 wt% CMC solution are presented. Small bubbles are seen trapped in the wake, as in the previous solution. The trailing edge presents a stable position and a concavity similar to that found in the 0.40 wt% CMC solution.

As in the previous solution, the bubble trailing edge is stable and the difference between

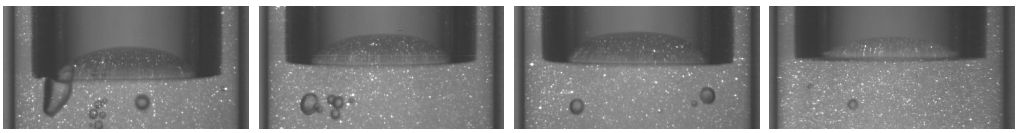

Figure 3.93. Images of the trailing edge of Taylor bubbles rising in a 0.50 wt% CMC solution.

the flow fields in different Taylor bubble wakes is mainly due to slight disturbances induced by the small bubbles trapped in the wake. In Figure 3.94, two velocity fields in the wakes of Taylor bubbles rising in a 0.50 wt% CMC solution are represented. The flow pattern is very similar to that in the wakes of bubbles rising in the 0.40 wt% CMC solution. The differences are in the velocity magnitudes and wake length, which are lower in the 0.50 wt% CMC solution.

In Figure 3.95 the same flow fields from Figure 3.94 are represented, but in a frame of reference moving with the bubble as well as the corresponding streamlines. Figure 3.95

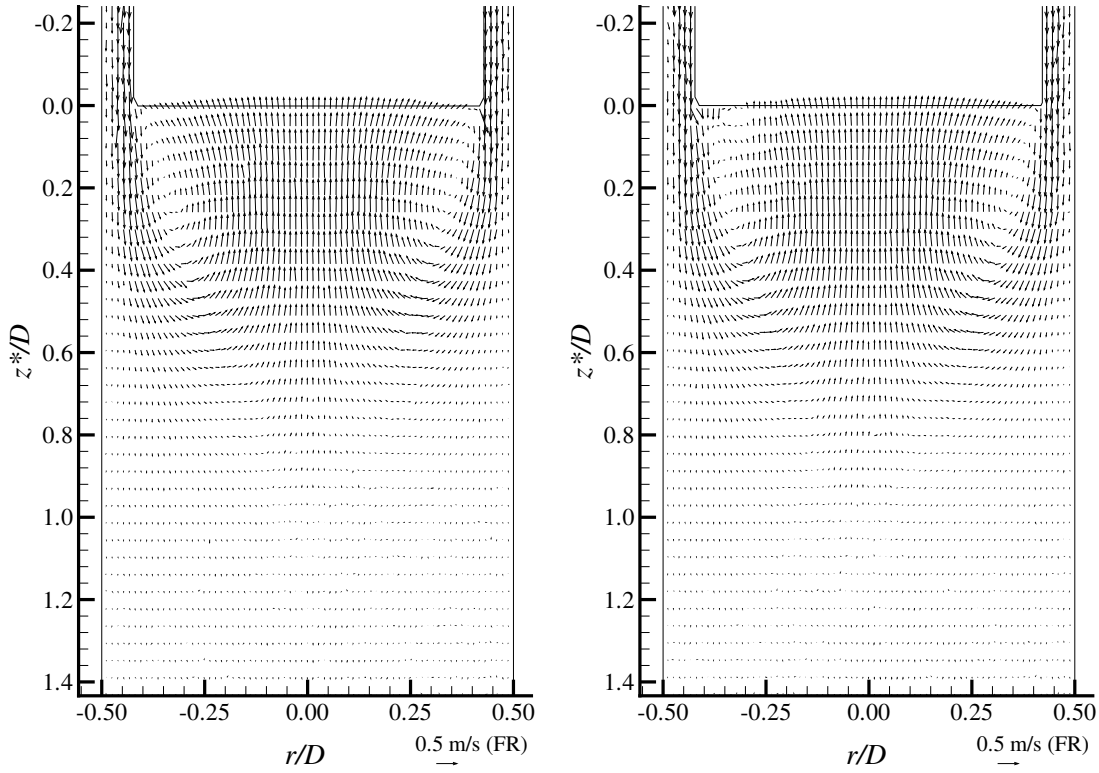

Figure 3.94. Flow fields in the wake of Taylor bubbles rising in a 0.50 wt% CMC solution.

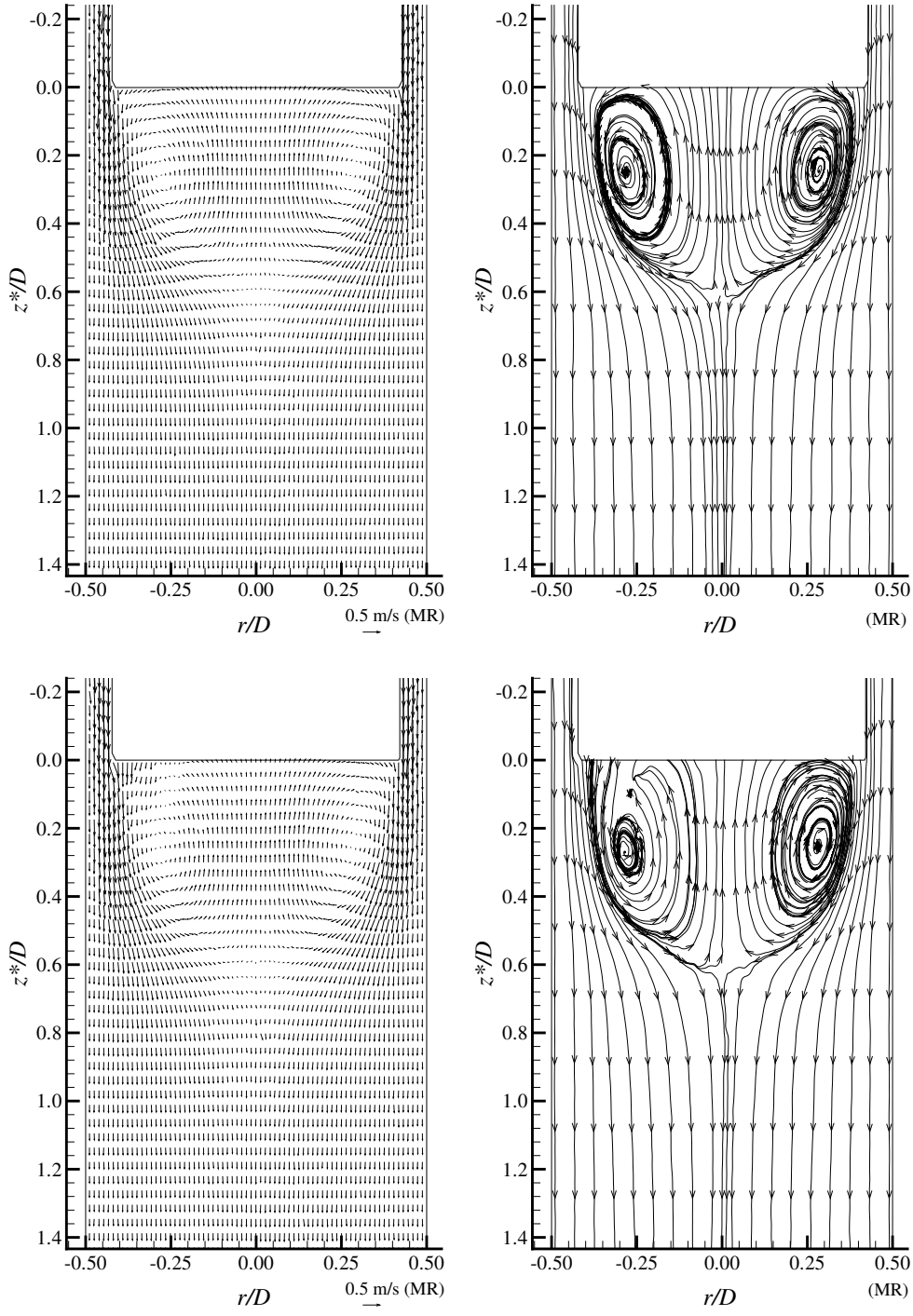

Figure 3.95. Flow fields and streamlines in the wake of Taylor bubbles rising in a 0.50 wt% CMC solution in a frame of reference moving with the bubble.

clearly shows the liquid film expansion around a closed recirculation region behind the bubble trailing edge. Despite the presence of small bubbles in both wakes, there is good symmetry in the wake structure, apart from a small disturbance in the bottom of the wake.

The axial coordinate of the stagnation point in a moving frame of reference indicates the wake length and is now located around $z* = 0.6D$, which is closer to the trailing edge than in the 0.40 wt% CMC solution, as expected.

The average axial velocity profiles in a fixed frame of reference are represented in Figure 3.96 at different distances from the bubble trailing edge. If compared with the velocity profiles obtained for the 0.40 wt% CMC solution, they practically coincide until $z* = 0.6D$. As mentioned, this is due to the experimental temperature, which approximates the fluid viscosities and is responsible for very similar liquid film velocity profiles, as seen in §3.3.5. Above $z* = 0.6D$ a faster decrease is observed in the velocity magnitudes for the 0.50 wt% CMC solution, the velocity magnitudes being practically zero at $z* = 1.2D$.

The standard deviation is also very similar to that of the 0.40 wt% CMC solution; maximum at the liquid film close to the bubble trailing edge, with a value around 0.14 m/s.

The average radial velocity profiles in the wake of Taylor bubbles rising in a 0.50 wt% CMC solution are presented in Figure 3.97. The radial velocity profiles are also very similar to the ones found in a 0.40 wt% CMC solution, apart from slight changes in magnitude. The symmetry of the flow in the wake becomes clear from these velocity profiles. The centre of the three dimensional recirculation region is located between $z* = 0.2D$ and $z* = 0.4D$, similar to the previous solution.

As seen from these velocity profiles, the difference between the wake of bubbles rising in the 0.40 wt% and in 0.50 wt% CMC solutions is only in the downward wake region, where in the heavier solution the velocity decreases faster and is traduced by a shorter wake length.

The average flow field in the wake of Taylor bubbles rising in a 0.50 wt% CMC solution is represented in Figure 3.98.

The axial velocity profile at $r = 0$ as a function of the distance to the bubble trailing edge is represented in Figure 3.99. This figure confirms the similarities found in the wakes of bubbles rising in the 0.40 and 0.50 wt% CMC solutions. There are slight differences in the maximum velocity magnitude, which is slightly lower in the 0.50 wt% CMC solution, and the wake length is reduced from $0.8D$ to $0.6D$. The maximum downward axial velocity is about the same value at around 0.03 m/s, but is located closer to the bubble trailing

edge, between $z* = 1.6D$ and $z* = 1.8D$.

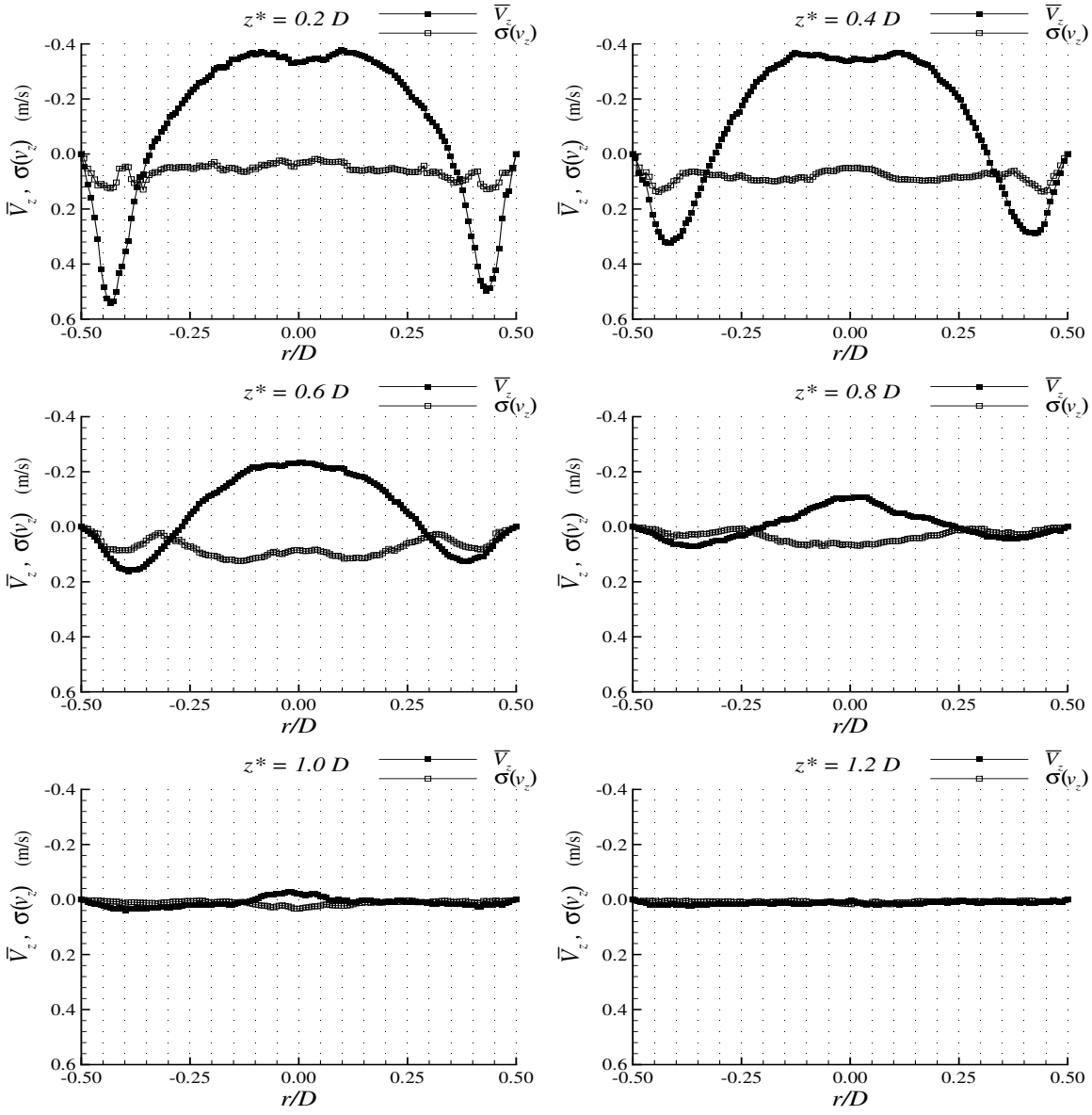

Figure 3.96. Average axial velocity profiles (fixed frame of reference) and standard deviation at different distances from the bubble trailing edge rising in a 0.50 wt% CMC solution.

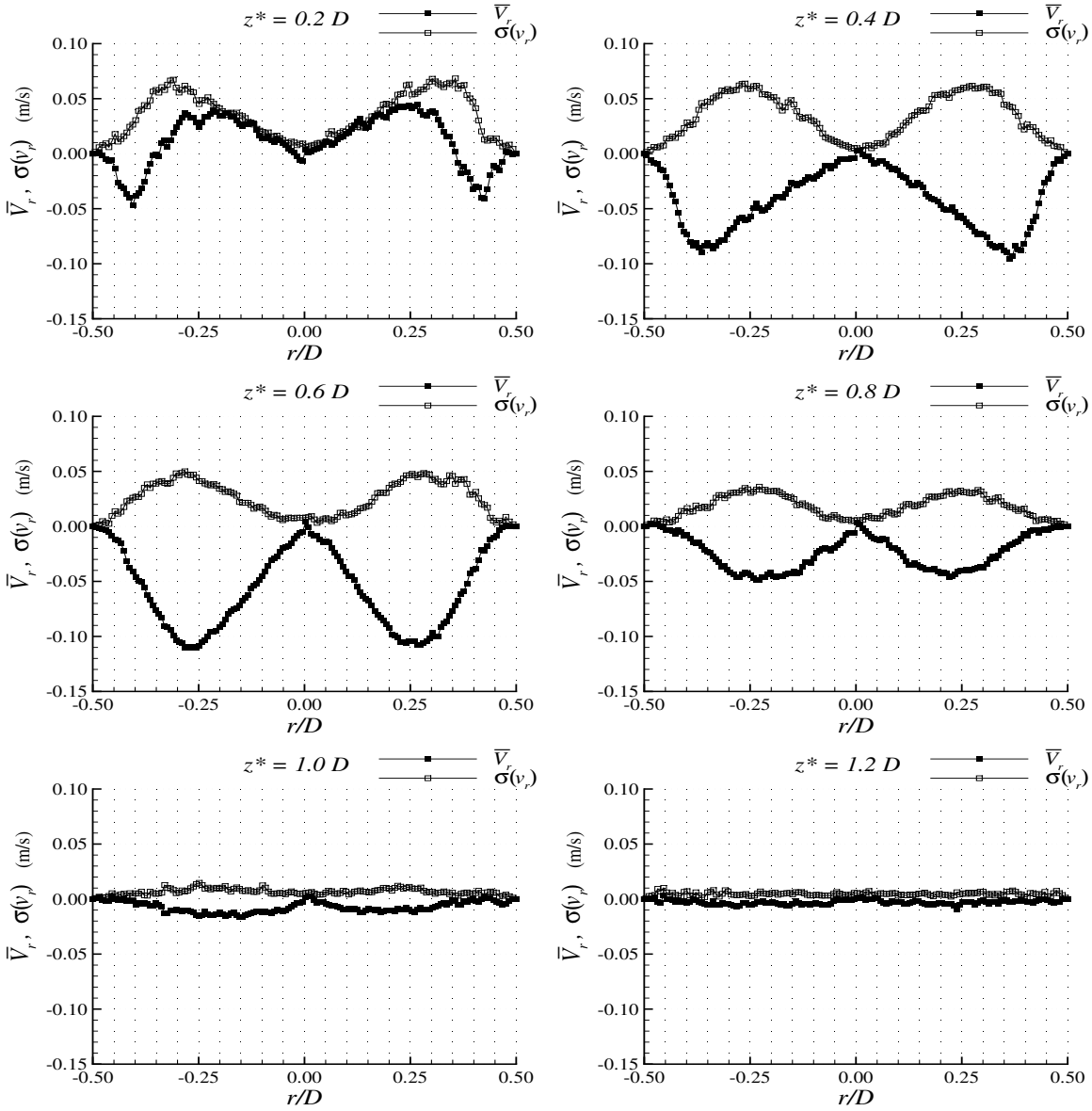

Figure 3.97. Average radial velocity profiles and standard deviation at different distances from the bubble trailing edge rising in a 0.50 wt% CMC solution.

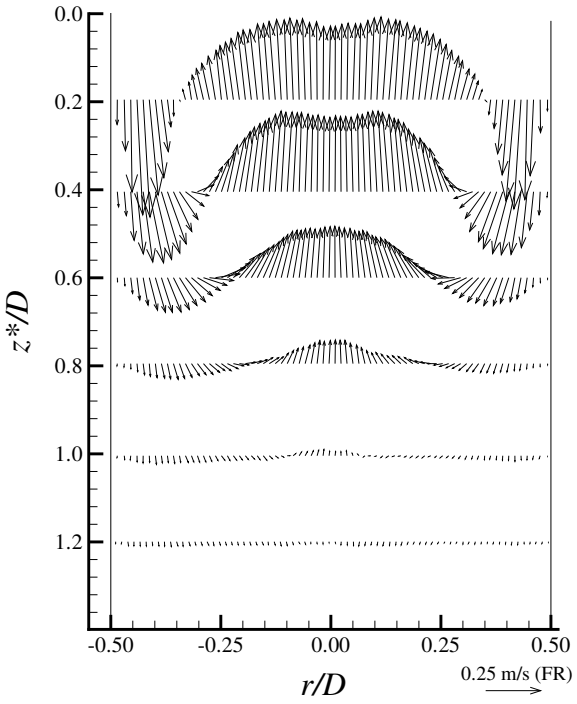

Figure 3.98. Average velocity field in the wake of bubbles rising in a 0.50 wt% CMC solution.

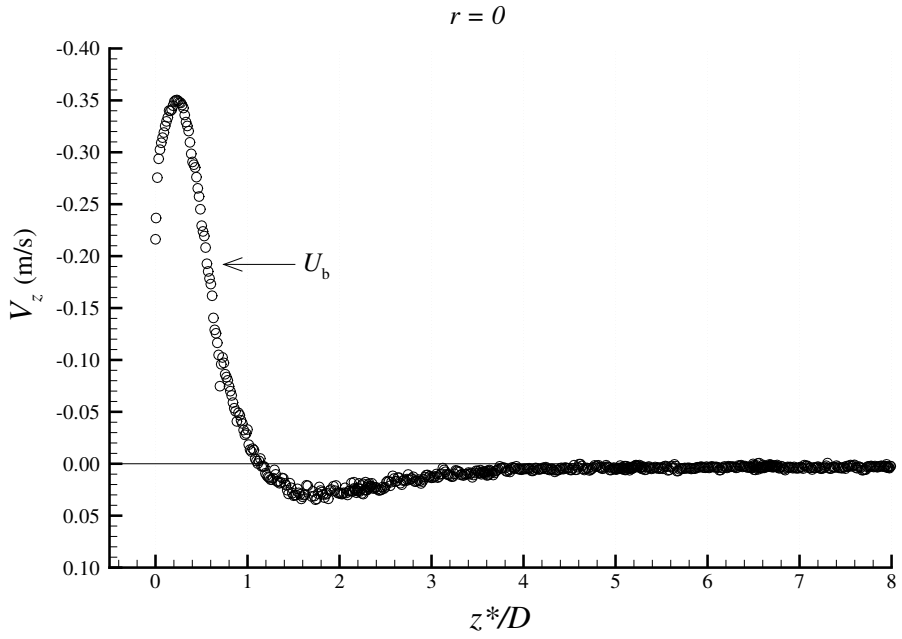

Figure 3.99. Instantaneous axial velocity profile (fixed frame of reference) at $r = 0$ as a function of $z*$ behind a Taylor bubble rising in a 0.50 wt% CMC solution.

0.60 wt% CMC

In the visualisation studies for the 0.60 wt% CMC solution it was observed that the bubble trailing edge was stable and had a higher concavity than in the previous solutions. Very few coloured liquid regions were seen in the wake during the rise in the colourless liquid.

Figure 3.100 shows some examples of PIV images of bubble trailing edges rising in a 0.60 wt% CMC solution. Differences between the trailing edges are now practically

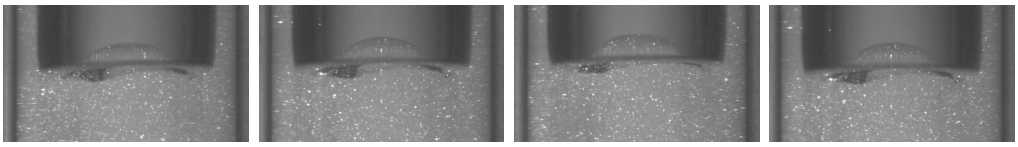

Figure 3.100. Images of the trailing edge of Taylor bubbles rising in a 0.60 wt% CMC solution.

imperceptible, meaning that during the bubble rise the trailing edge maintains a stable position. Compared with the previous solutions a more pronounced concavity is now observed.

The flow fields in the wake of two bubbles rising in a 0.60 wt% CMC solution are presented in Figure 3.101 relative to a fixed frame of reference. As the bubbles have the same length ($L_\mathrm{b} = 7.3D$), the flow fields are representative of the same bubble at different instants. Figure 3.101 confirms that, as shown in the different PIV images of the trailing edge, the flow field in the wake of the Taylor bubbles does not vary significantly along the rise.

The falling liquid film expands just after the bubble trailing edge and for a much shorter distance than in the previous solutions. The liquid velocity is already very close to zero at $z* = 0.5D$.

In the axis of the column an upward liquid flow is seen just behind the trailing edge with a velocity magnitude that is around that of the Taylor bubble velocity, meaning that the liquid should be practically stagnant in a frame of reference moving with the bubble.

Figure 3.102 shows the same flow fields as in Figure 3.101 but in a frame of reference moving with the bubble and the corresponding streamlines. There is only a small region below the bubble trailing edge where the velocity vectors have an upward velocity component, indicating that a small portion of fluid is transported in the wake. Indeed, the

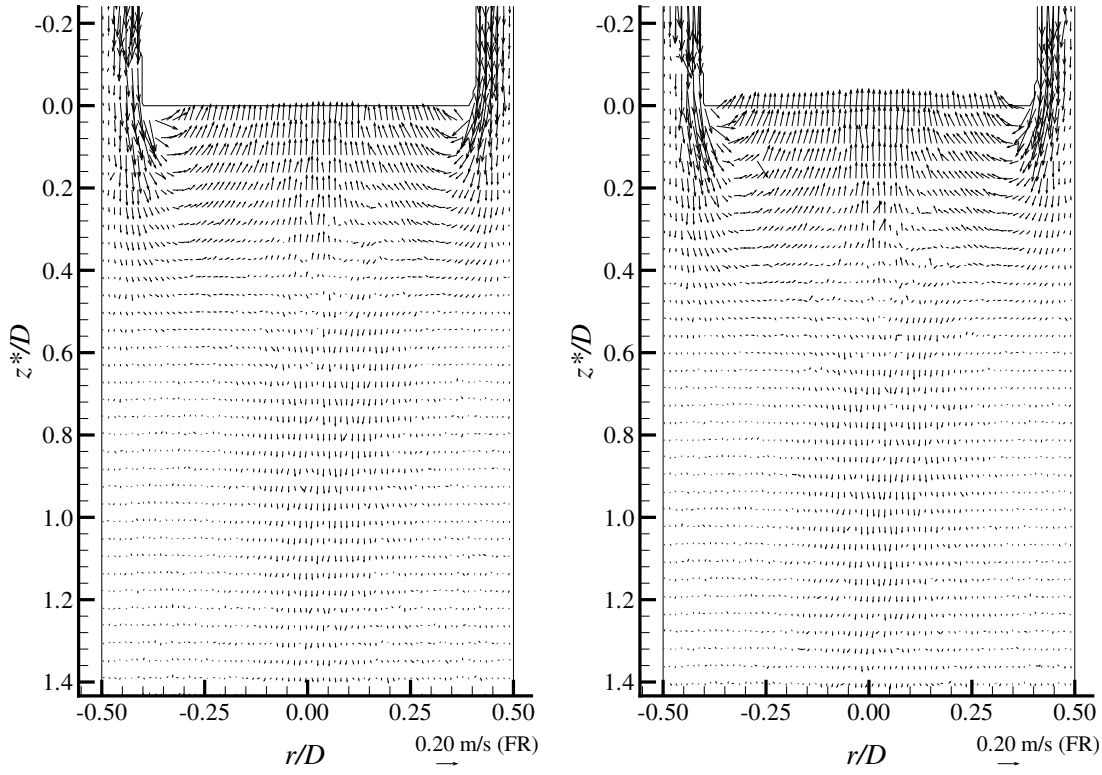

Figure 3.101. Flow fields in the wake of Taylor bubbles rising in a 0.60 wt% CMC solution.

velocity of this liquid is very close to the bubble velocity, i.e., very close to zero in a frame of reference moving with the bubble. Small disturbances in the flow around the bubble during its rise can cause the detachment of this small portion of fluid, which explains the absence of coloured liquid in the test section during the visualisation experiments.

In the moving frame of reference, due to low velocity magnitudes about the same as the measurement error, it is not possible to accurately define the streamlines close to the bubble trailing edge. Nonetheless, it can be seen that the fluid coming from the falling film expands suddenly after the bubble trailing edge, surrounding a small region of fluid that should be in recirculation with very low velocity magnitudes. This recirculation region extends to the concave region of the trailing edge, where the PIV images were not processed due to the strong optical distortion caused by the pronounced curvature and differences in the refractive indexes of the liquid and air. A flow field obtained with the 50 mm lens used for the liquid film, and presented in Figure 3.103, shows the streamlines in the film

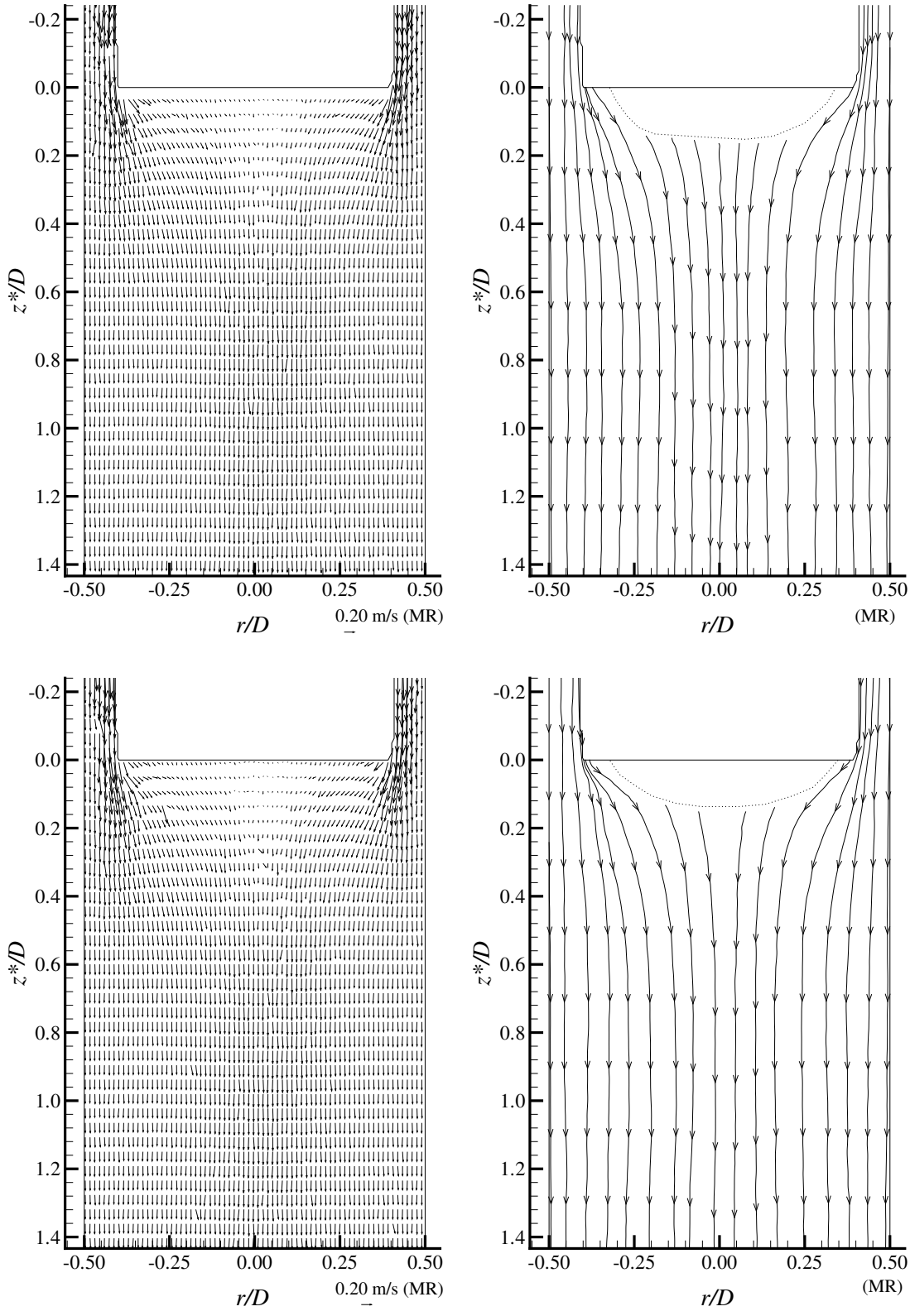

Figure 3.102. Flow fields in the wake of Taylor bubbles rising in a 0.60 wt% CMC solution and respective streamlines; frame of reference moving with the bubble (MR).

expansion region with better definition.

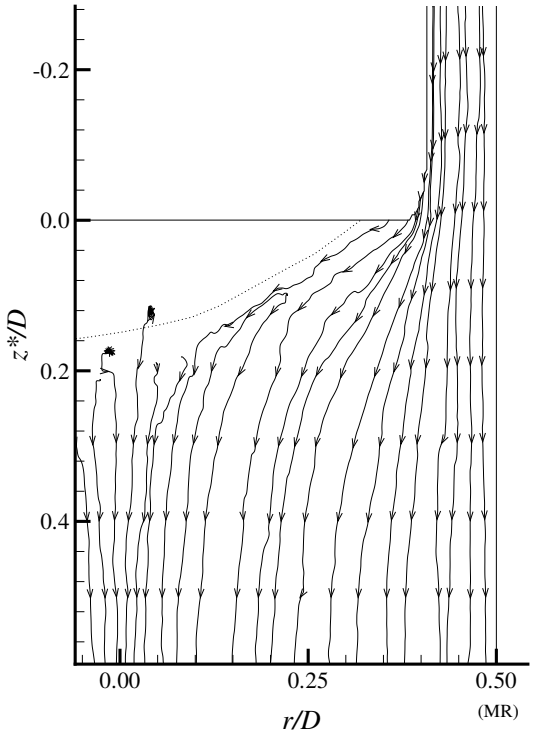

Figure 3.103. Close view of the streamlines in the wake of a Taylor bubble rising in a 0.60 wt% CMC solution in a frame of reference moving with the bubble (MR).

The average axial velocity profiles in a fixed frame of reference at different distances from the bubble trailing edge are represented in Figure 3.104. From the profiles, the rapid deceleration of the liquid coming from the falling film is clearly perceptible. At $0.05D$ from the bubble trailing edge, the maximum downward velocity is practically half of the maximum velocity in the stabilised liquid film. The deceleration continues up to $z* = 0.5D$, where the velocity profile is practically flat.

The liquid velocities are about the bubble velocity only very close to the bubble trailing edge and around the axis of the column, which confirms that just a very small quantity of fluid is transported. The fluid velocity decreases as the distance from the trailing edge increases, until $z* = 0.5D$, where inversion of the velocity direction occurs; a downward flow of low magnitude is seen in the axis of the column.

The very low standard deviation in all the regions of the wake shows negligible differences between the velocity fields at different instants.

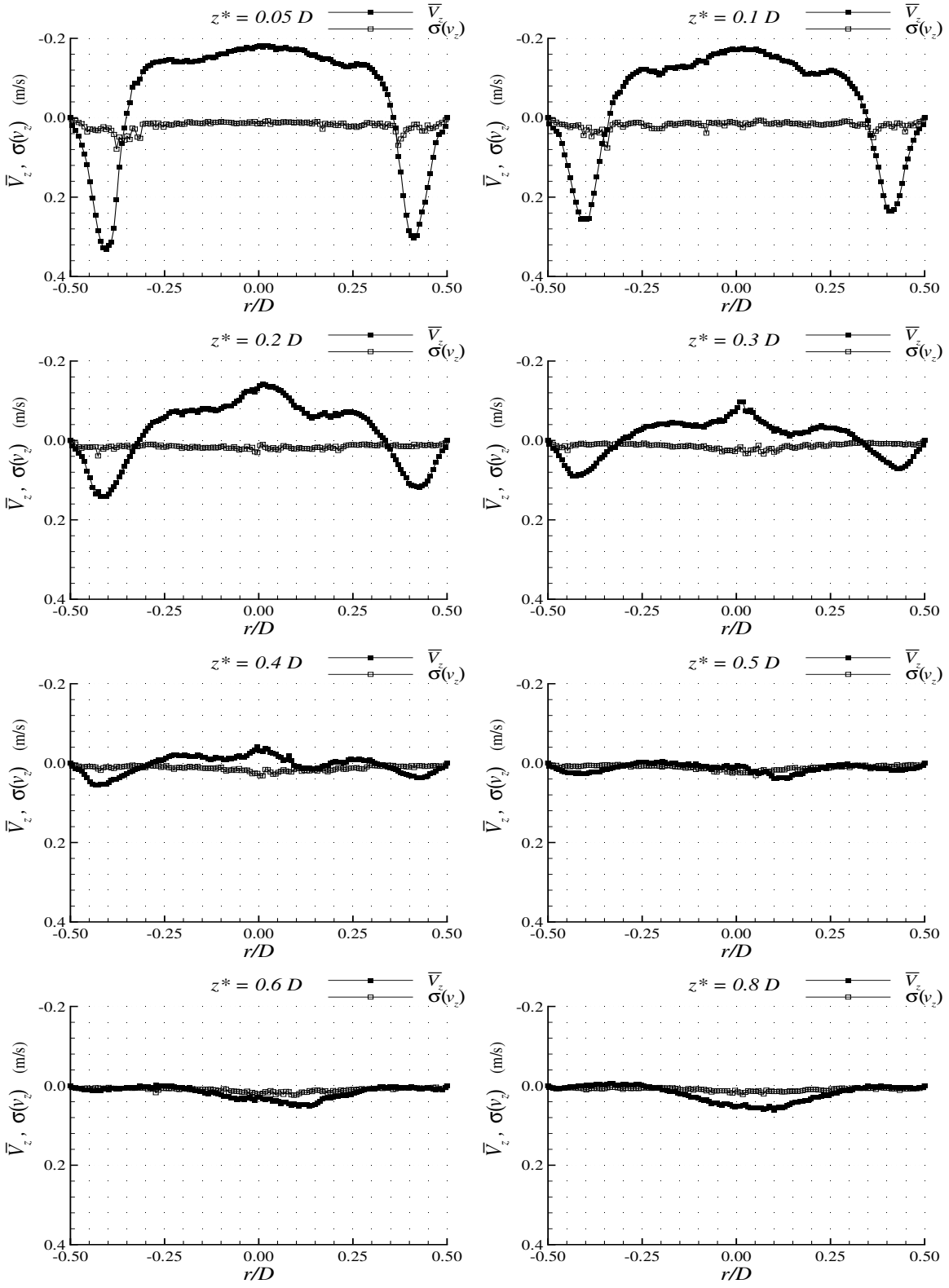

Figure 3.104. Average axial velocity profiles (fixed frame of reference) and standard deviation at different distances from the bubble trailing edge in a 0.60 wt% CMC solution.

The radial velocity profiles at the same distances from the trailing edge are represented in Figure 3.105. The rapid liquid film expansion below the bubble trailing edge is once more in evidence; the maximum radial velocity magnitudes are located close to the bubble trailing edge. Contrary to the previous cases, in the 0.60 wt% CMC solution there is no inversion in the radial velocity direction. Radial velocities are always negative, meaning that the fluid is moving radially toward the axis of the column. The radial liquid movement decreases as the distance from the bubble trailing edge increases, up to $z* = 0.8D$, where the radial velocity component vanishes.

The standard deviation of the radial velocity component is also very low, the deviations being mainly due to the experimental uncertainty, about 0.016 m/s.

The average flow field in the wake of the Taylor bubbles rising in a 0.60 wt% CMC solution is represented in Figure 3.106. A small asymmetry in the downward liquid movement is seen, possibly due to a slight vertical misalignment in the column.

In Figure 3.107, the instantaneous axial velocity profile at $r = 0$ behind a bubble rising in a 0.60 wt% CMC solution is represented. This figure confirms that the maximum upward velocity in the wake is in the same order of magnitude as the bubble velocity, decreasing in magnitude until $z* = 0.5D$. From there on a downward flow is seen in the axis of the column, with the maximum amplitude of around 0.07 m/s, located at $1D$ from the bubble trailing edge. The flow then smoothly slows down to zero velocity. The wake length is now below $0.2D$.

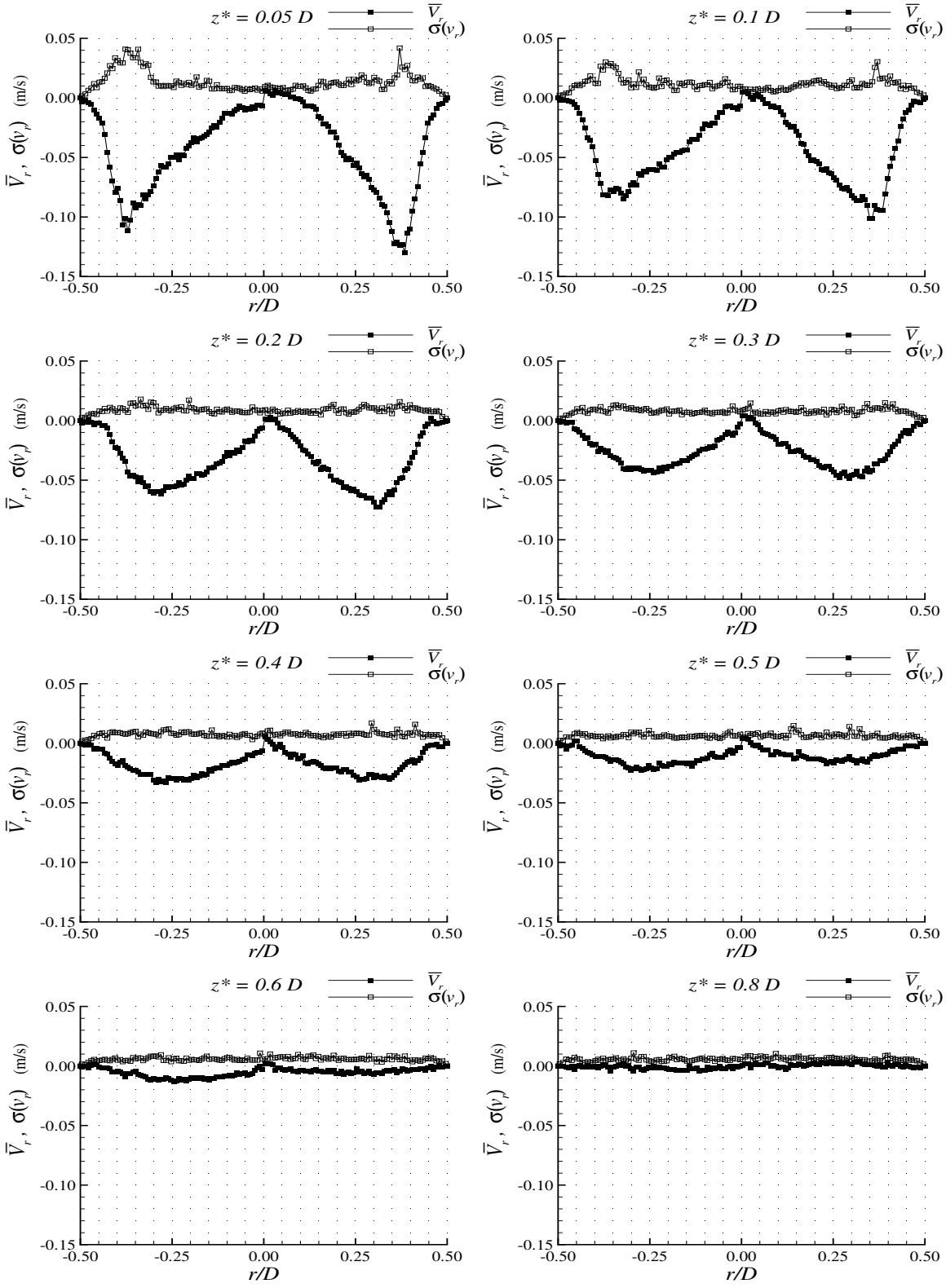

Figure 3.105. Average radial velocity profiles and standard deviation at different distances from the bubble trailing edge in a 0.60 wt% CMC solution.

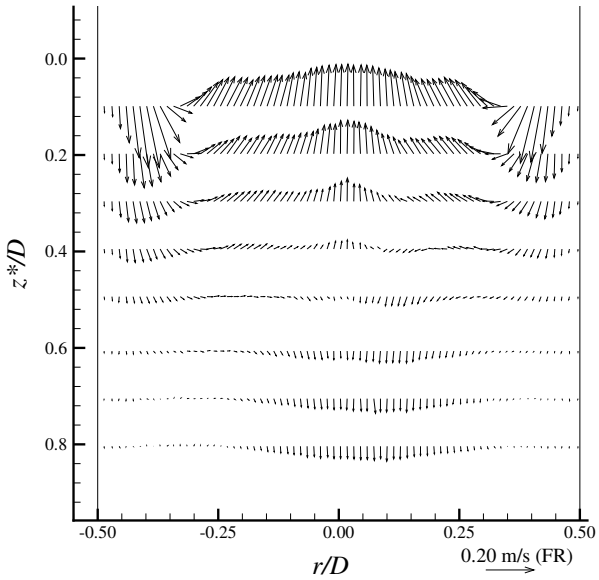

Figure 3.106. Average velocity field in the wake of Taylor bubbles rising in a 0.60 wt% CMC solution.

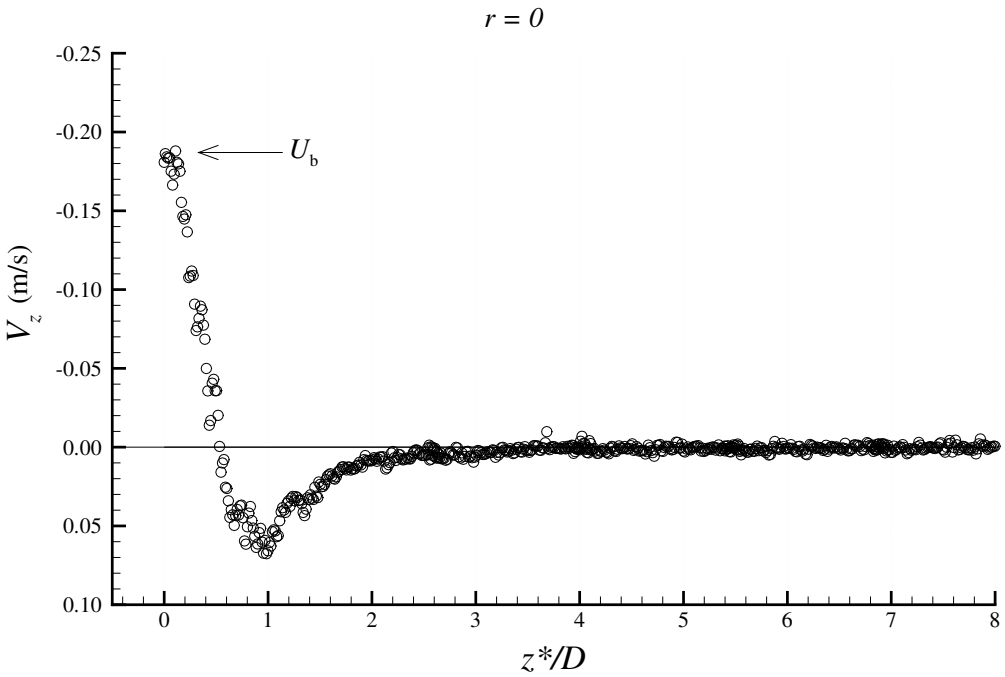

Figure 3.107. Instantaneous axial velocity profile (fixed frame of reference) at $r = 0$ in the wake of a Taylor bubble rising in a 0.60 wt% CMC solution.

Negative wake

For the higher concentrations of CMC, the bubble trailing edge shape and the flow in the wake showed a different behaviour, and they are thus described in a separate section. This behaviour was not found in the wakes of Taylor bubbles rising in Newtonian fluids.

0.80 wt% CMC

In the visualisation studies with the 0.80 wt% CMC solution it was observed that the trailing edge changed from a concave to a lachrymal shape and no coloured liquid was seen in the wake. Images of a small bubble flowing in the expansion region of the falling liquid film seemed to indicate a downward liquid movement behind the bubble trailing edge.

In Figure 3.108 some PIV images of the trailing edge of bubbles rising in a 0.80 wt% CMC solution are presented. This figure shows that the bubble trailing edge is not stable,

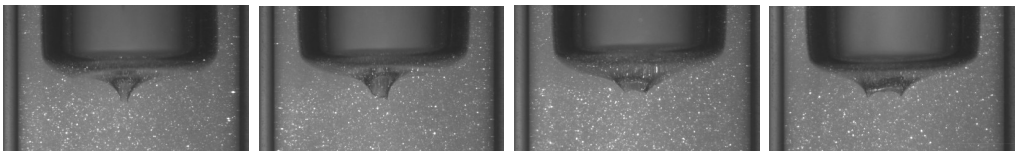

Figure 3.108. Images of the trailing edge of Taylor bubbles rising in a 0.80 wt% CMC solution.

having slight variations on its shape. Due to the low image acquisition frequency, 4.22 Hz, it is not possible to describe the bubble trailing edge movement in detail. However, there appears to be a continuous expansion and contraction of the trailing edge, during the rise of the bubble.

Two flow fields in the wake of Taylor bubbles rising in a 0.80 wt% CMC solution, are presented in Figure 3.109. In this figure, it can be seen that the fluid coming from the liquid film undergoes a sudden deceleration upon reaching the bottom of the Taylor bubble and acquires a radial velocity towards the axis of the column, moving into the space occupied by the bubble the instant before. The radial displacement of the fluid towards the axis of the column induces, by momentum diffusion, movement in the fluid that is immediately below. This fluid initiates a rotational displacement; downwards in the axis of the column and upwards outside the axis. The downward liquid displacement close to the trailing edge does not appear in the wake of bubbles rising in Newtonian liquids, which is why this wake is called a negative wake. This downward liquid movement explains the observed

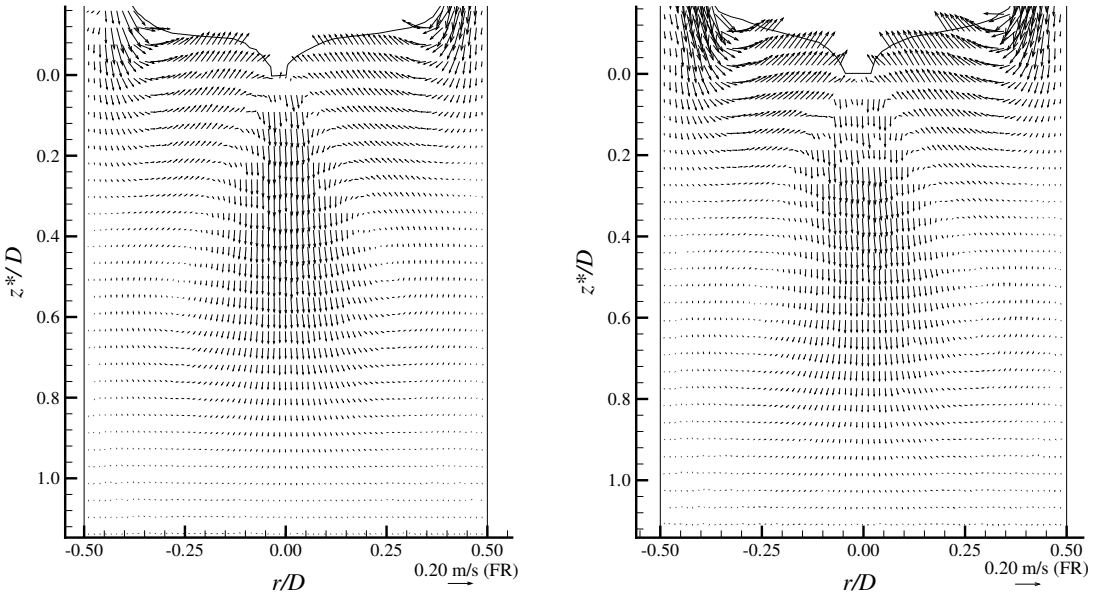

(a) Expanding trailing edge

(b) Contracted trailing edge

Figure 3.109. Flow fields in the wake of Taylor bubbles rising in a 0.80 wt% CMC solution.

behaviour of the small bubble coming from the liquid film in the visualisation studies. An enlargement of Figure 3.109(a) is presented in Figure 3.110, where the described flow pattern is better seen.

While the velocity in the central downward fluid reaches 90% of the Taylor bubble velocity, the maximum upward velocities in the recirculating region far from the tube axis reaches only 10%. The higher velocity magnitude in the axis is due to mass conservation across a cross-sectional area. The downward flow area, a small circle containing the axis of the column, is smaller than the upward flow area between this circle and the pipe wall.

In Figure 3.109 the main difference between both flow fields is the velocity magnitude close to the bubble interface. The upward liquid velocity is lower when the edge is contracted and moving down initiating the expansion, as appears to be the case in Figure 3.109(a). In Figure 3.109(b) the trailing edge is totally expanded and the upward velocity is higher. These flow fields are represented in Figure 3.111. In a frame of reference moving with the bubble the recirculation regions of the flow are not visible and only downward velocities are seen, due to the higher magnitude of the bubble velocity relative to the liquid in recirculation.

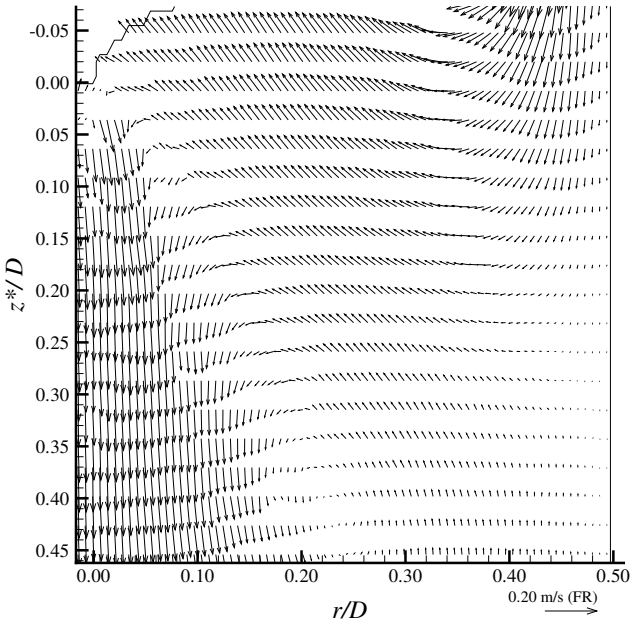

Figure 3.110. Close-up of a part of the wake of a bubble rising in a 0.80 wt% CMC solution.

In the close-up of the flow field around the bubble trailing edge the axial movement can be confirmed. In Figure 3.111(d), the vectors are tangent to the bubble interface, meaning that the edge is moving at the velocity of the bubble; the edge is fully expanded. In Figure 3.111(c), there is a normal outward velocity component relatively to the bubble interface, meaning that the trailing edge is moving down, relatively to the bubble; the contracted edge is expanding, thrusting the fluid downwards.

If the streamlines are plotted, Figure 3.112(a), it is clear that for the expanding edge the liquid in the central region appears to come from the bubble trailing edge, while in Figure 3.112(b) it comes from the falling liquid film, expanding along the bubble trailing edge interface.

The average axial velocity profiles at different distances from the bubble trailing edge are represented in Figure 3.113. Concerning the standard deviation of the velocity, even with very low values its maximum is naturally located close to the bubble trailing edge, due to its constant movement. From Figure 3.113 it can be seen that at $z* = 0.05D$ there is already a downward flow in the axis of the column. In the upper part of the wake there is fluid flowing downwards in high radial positions (fluid coming from the falling liquid film) and in the axis of the column, while between these regions there is fluid moving upwards.

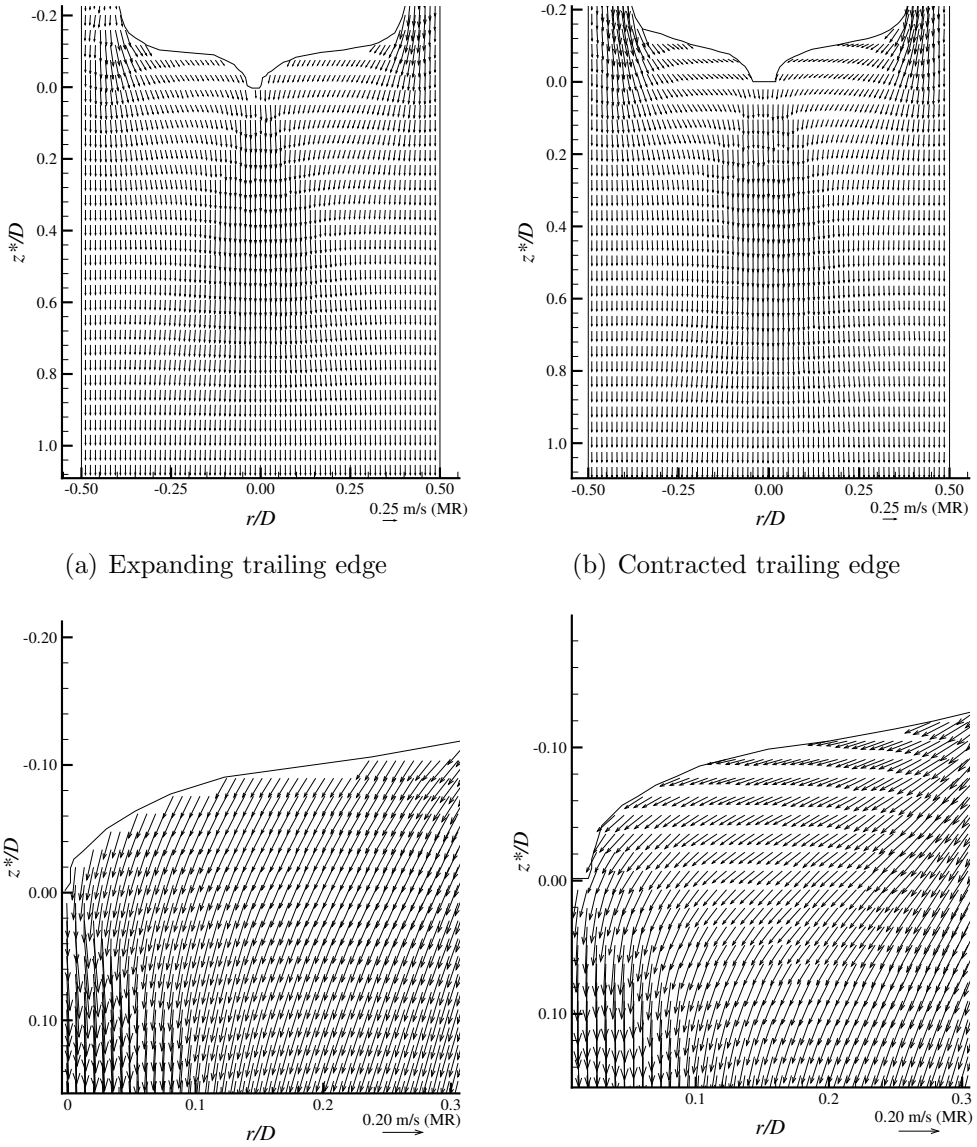

(a) Expanding trailing edge

(b) Contracted trailing edge

(c) Expanding trailing edge (zoom)

(d) Contracted trailing edge (zoom)

Figure 3.111. Flow fields in the wake of Taylor bubbles rising in a 0.80 wt% CMC solution; frame of reference moving with the bubble.

The maximum downward velocity in the axis of the column is located between $z* = 0.2D$ and $z* = 0.4D$, where an inversion of flow direction occurs in the outer regions, changing from downward to upward flow. After $z* = 0.4D$, the velocity magnitude decreases up to $z* = 1.0D$, and at $z* = 1.2D$ there is again an upward liquid movement in the axis of the column. This upward movement is unexpected, but is explained by the formation of

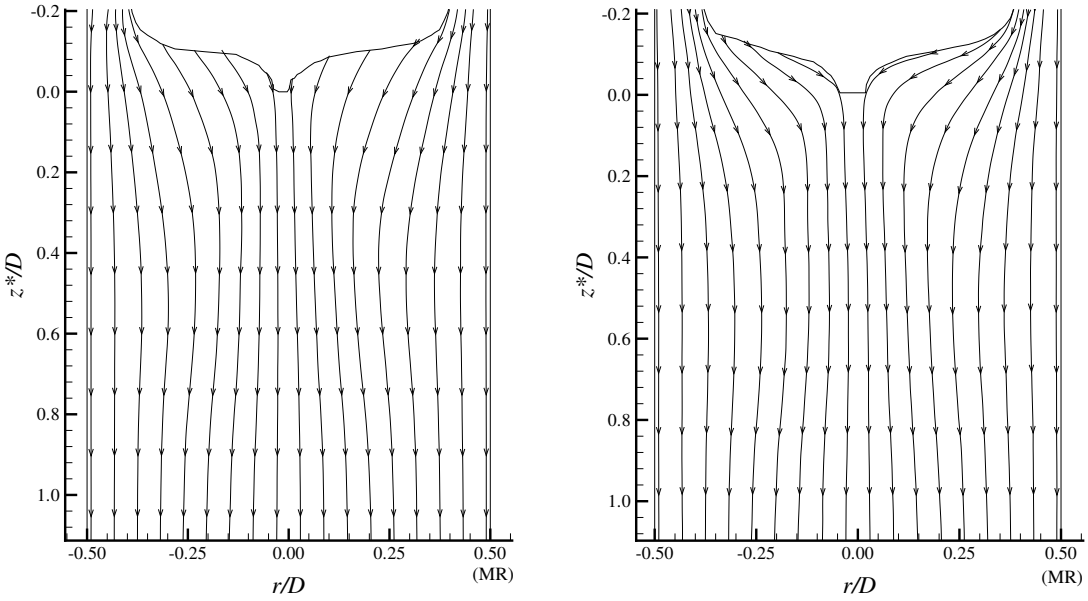

(a) Expanding trailing edge

(b) Contracted trailing edge

Figure 3.112. Streamlines in the wake of Taylor bubbles rising in a 0.80 wt% CMC solution; frame of reference moving with the bubble.

secondary circulating regions below the principal one. As previously explained, the radial liquid movement of the liquid that comes from the falling film induces, by momentum diffusion, a circulating movement in the fluid below; downwards in the axis and upwards flow away from the axis. This circulation, by itself, induces a new circulating movement on the liquid below, which rotates in the opposite direction (upwards in the axis and downwards outside of the column axis) with lower velocity magnitude. The mechanism of these alternating recirculation regions is similar to that in a gear, when a set of wheels with teeth on their edges revolve together. A close-up flow field of the second circulation region is represented in Figure 3.114.

From this figure, a stagnation point can be seen between $z* = 1.1D$ and $z* = 1.2D$. Above the stagnation point is the end of the main circulation region, and below it is the secondary circulation region with fluid rotating in an opposite direction. These flow fields were obtained with the time between frames set to study the main wake flow. For a better description of the secondary region a larger time between frames should have been used, since the velocity magnitudes are very low. Even so, it is still perceptible, and in the 1.00 wt% CMC solution a similar flow pattern will be clearly seen.

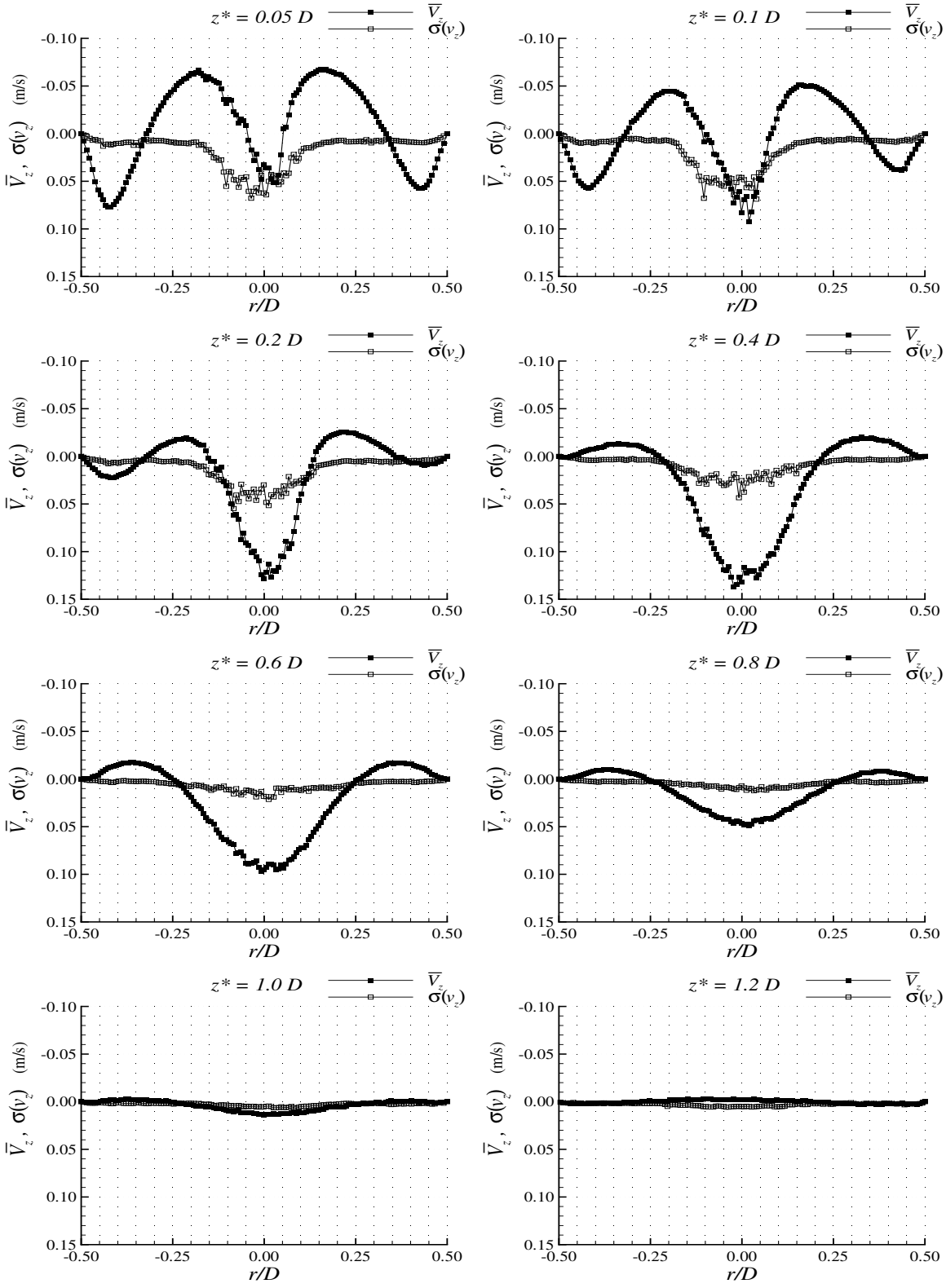

Figure 3.113. Average axial velocity profiles (fixed frame of reference) and standard deviation at different distances from the bubble trailing edge rising in a 0.80 wt% CMC solution.

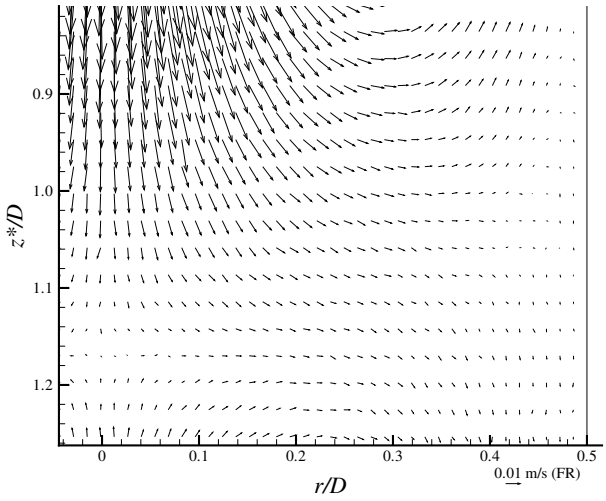

Figure 3.114. Close-up of the flow field between a main and a secondary circulation region in the wake of a Taylor bubble rising in a 0.80 wt% CMC solution.

The average radial velocity profiles at different distances from the bubble trailing edge are represented in Figure 3.115. From this figure, high radial velocities close to the bubble trailing edge are seen in the direction of the column axis (negative). The radial velocity magnitude decreases with increasing distance from the trailing edge, and around $z* = 0.40D$, there is an inversion of the flow direction, starting to move away from the axis. It is also interesting to see that the velocity magnitudes are very similar at $z* = 1.0D$ and $z* = 1.2D$ due to continuity, although there is an inversion in the axial velocity direction while moving from the principal to the secondary circulation region.

In Figure 3.116, the average wake flow in the wake of Taylor bubbles rising in the 0.80 wt% CMC solution is represented.

The instantaneous axial velocity profile at $r = 0$ in function of the distance to the bubble trailing edge is represented in Figure 3.117. This figure shows the downward liquid flow in the axis of the column, behind the bubble trailing edge. The maximum downward velocity magnitude is located at around $z* = 0.30D$, reaching about 90% of the bubble velocity. After the downward liquid movement there is a small-magnitude upward flow in the secondary circulation region, and then the fluid smoothly stagnates.

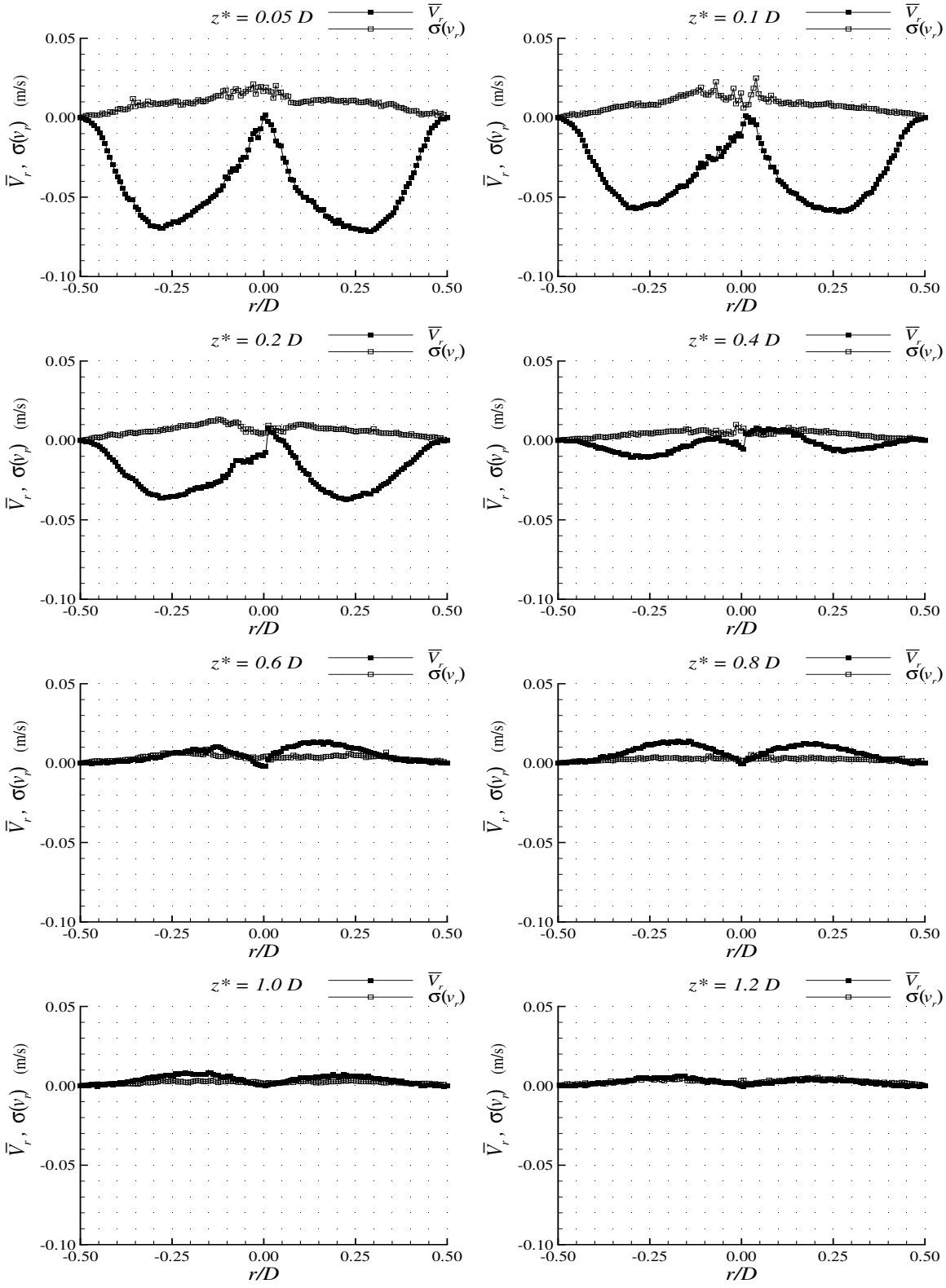

Figure 3.115. Average radial velocity profiles and standard deviation at different distances from the bubble trailing edge rising in a 0.80 wt% CMC solution.

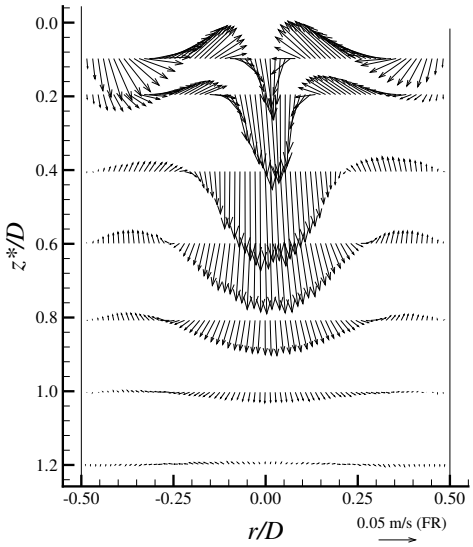

Figure 3.116. Average flow pattern in the wake of Taylor bubbles rising in a 0.80 wt% CMC solution in a fixed frame of reference.

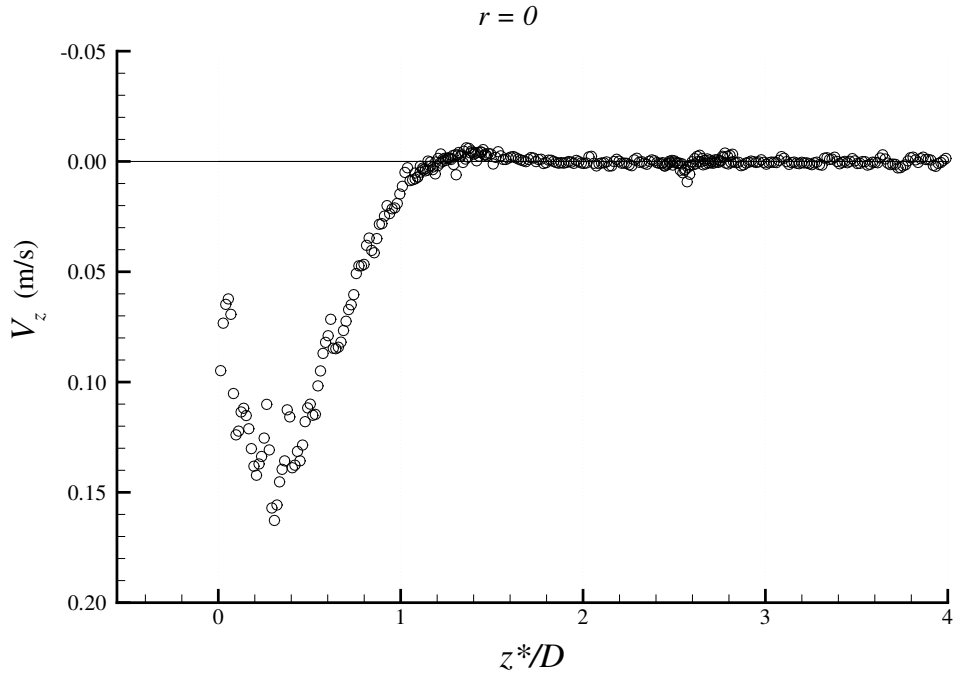

Figure 3.117. Instantaneous axial velocity profile (fixed frame of reference) at $r = 0$ in the wake of a Taylor bubble rising in a 0.80 wt% CMC solution.

1.00 wt% CMC

For the 1.00 wt% CMC solution, the visualisation studies also showed a lachrymal shape in the trailing edge of the Taylor bubbles, although different from that observed in the 0.80 wt% CMC solution. The tip of the trailing edge has a two dimensional cusp shape, similar to that described by Hassager (1979) and by other authors, as referred by Liu *et al.* (1995). The two dimensional cusp has no constant orientation, since it is in different positions on consecutive images of the same bubble. This behaviour indicates a rotational movement of the cusp, similar to that of an air core in a sink drain flow of a viscoelastic liquid (see Liu *et al.* (1995)).

In Figure 3.118, some PIV images of the trailing edge of bubbles rising in a 1.00 wt% CMC solution are shown, with an enlargement of the trailing edge tip. This figure shows

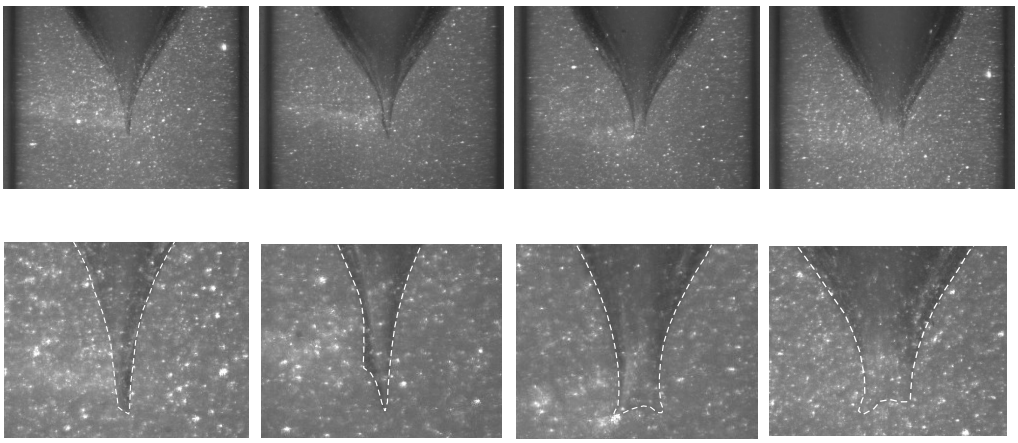

Figure 3.118. Images of the trailing edge of Taylor bubbles rising in a 1.00 wt% CMC solution with an enlargement of the trailing edge tip.

different orientations of the two dimensional cusp. Images (a) and (d) show the cusp in two perpendicular orientations. In (a), the cusp is in a plane perpendicular to the paper and so its projection has a very narrow profile, while in (d) the cusp is in the paper plane so its projection has a wider dimension. The projected dimension in the paper plane of the width of a two-dimensional cusp rotating at a constant velocity must be random, corresponding to a uniform distribution in a large number of samples. A considerable number of images of the cusp in the 1.00 wt% CMC solution were analysed (about 120) and a quasi-uniform distribution of the projected dimension was found (6 classes were considered between the

1-pixel minimum and 60-pixel (about $2.6 \cdot 10^{-3}$ m) maximum values. This distribution, as represented in Figure 3.119, suggests constant dimensions of the cusp and a constant rotational velocity.

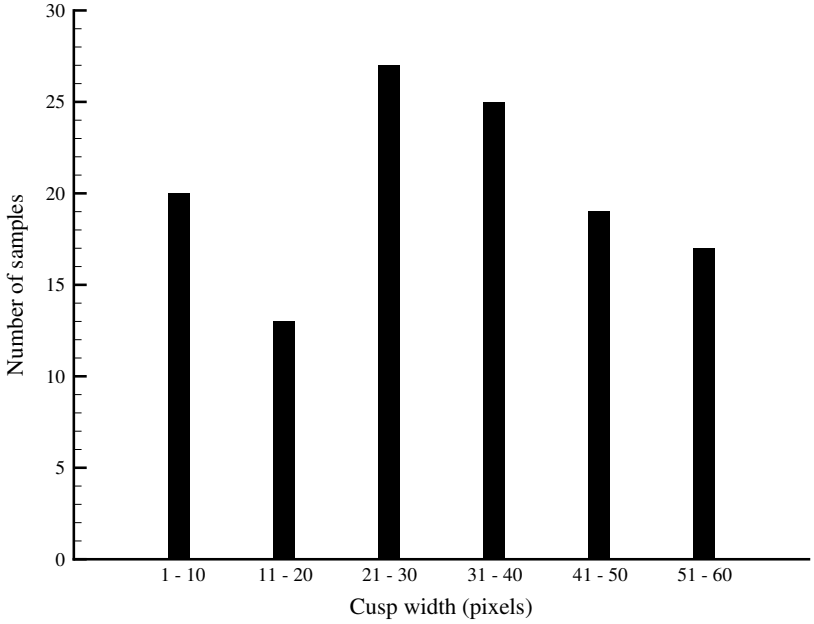

Figure 3.119. Histogram of cusp width projection, obtained from about 120 images.

According to the images we can assume that the rotation frequency must be very high, at least higher than the frequency of the CCD camera used in the visualisation study (25 Hz). It was impossible to detect the direction of the rotation from the images.

Two flow fields corresponding to perpendicular cusp orientations are represented in Figure 3.120. The flow pattern in the wake of the Taylor bubbles rising in 1.00 wt% CMC solution is similar to that of a bubble rising in 0.80 wt% CMC solution, apart from the bubble trailing edge shape and the velocity magnitude. The fluid coming from the liquid film decelerates, acquiring radial velocity towards the axis of the column to occupy the space left by the bubble. This movement also creates a negative wake by inducing a rotational movement on the liquid immediately below, flowing downwards at the axis and upwards farther from the column axis. The downward velocity magnitude now reaches only 45% of the bubble velocity, while the upward velocity far from the tube axis reaches 6% of the bubble velocity.

In Figures 3.120(a) and 3.120(b), the main difference is the provenance of the liquid

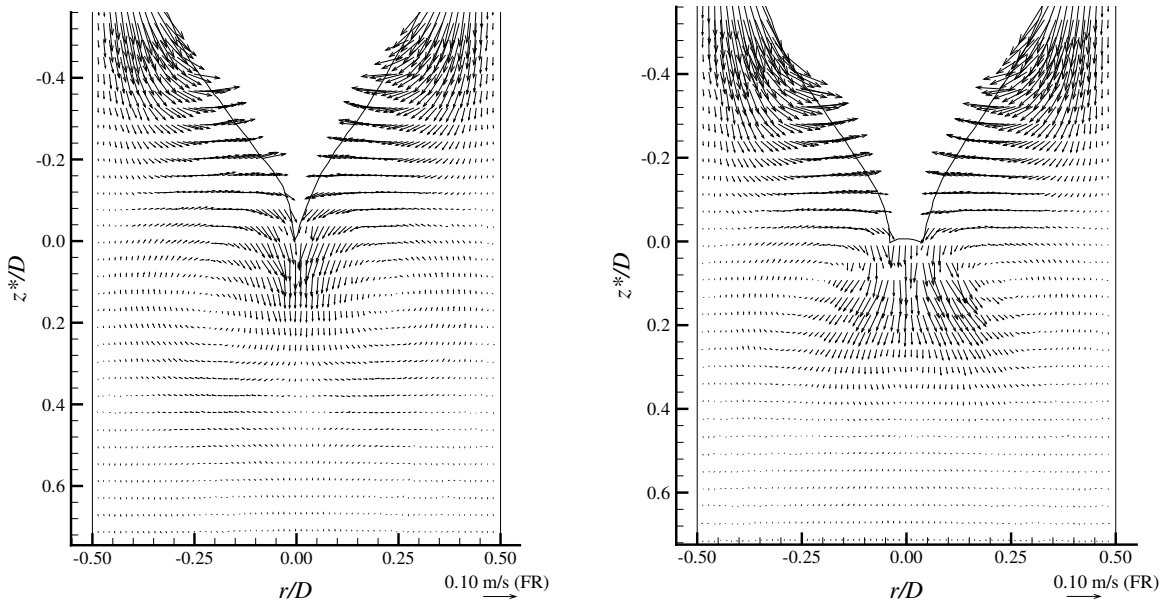

Figure 3.120. Instantaneous velocity fields in the wake of Taylor bubbles rising in a 1.00 wt% CMC solution.

flowing downwards close to the column axis below the bubble trailing edge. In Figure 3.120(a), the wider dimension of the cusp is perpendicular to the laser sheet plane (paper plane) and all the liquid that is going downwards in the axis comes from this laser sheet plane. In Figure 3.120(b), the cusp wider dimension is now in the laser sheet plane and the liquid that is going downwards in the axis comes from other planes including the plane represented in Figure 3.120(a). Therefore, around the axis below the cusp the vectors represented in Figure 3.120(b) should have a velocity component normal to the laser sheet plane, i.e., the flow in the wake region is slightly asymmetric (three-dimensional flow).

From these figures it can be concluded that the asymmetric shape of the trailing edge in the 1.00 wt% CMC solution is responsible for an asymmetric flow in the wake region. Taking into account the small dimension of the cusp, the magnitude of these asymmetries should be low but it must be quantified. According to mass conservation law, the flow through a cross-section of the column must be zero, which implies a zero mean axial velocity. Mean velocities were determined from the axial velocity profiles (supposing axisymmetric flow) at three different distances from the bubble trailing edge and are presented in Table 3.9. This table shows that in case (a) the mean velocity is negative (upwards) and in

Table 3.9. Mean axial velocity (m/s) at different distances from the bubble trailing edge with different orientations (from Figure 3.120).

$z*/D$	$\overline{V_z}$ (a)	$\overline{V_z}$ (b)
0.1	-0.0043	+0.0040
0.2	-0.0059	+0.0068
0.3	-0.0048	+0.0052

case (b) it is positive. Since these mean velocities have a low magnitude, they must be compared with the velocity uncertainty to see if they have any significance. In these flow fields, a time of 3000 µs between frames was used and the calibration of the images was 22.6 pixels/mm. The uncertainty of the window displacement was estimated to be 0.2 pixels (§2.2.6), corresponding to an uncertainty of 0.003 m/s in the velocity. The mean velocities in Table 3.9 are somewhat higher than this value, and so they have some significance.

These velocity values confirm the asymmetric flow. In case (b) there is fluid in the axis coming from other planes and so a mean downward flow is found. This downward flow is compensated in other planes, as in case (a), with an average upward flow in order to maintain a zero flow rate in the cross-section of the column.

Secondary circulation regions were also present in the wakes of bubbles rising in 1.00 wt% CMC solution. In Figure 3.121 an example of this flow pattern is presented. This figure shows that the main circulation (region (a)) close to the bubble trailing edge induces, by momentum diffusion, a movement on the fluid below, which rotates in the opposite direction (region (b)). These rotational movements have different velocity magnitudes, as seen by the reference vectors below each region, hence different times between the PIV frames were used to obtain perceptible flow fields.

The flow fields in a frame of reference moving with the bubble are represented in Figure 3.122. In this frame of reference no circulations are seen and the fluid smoothly surrounds the bubble, the velocity vectors being tangent to the bubble interface. The absence of circulations in this frame of reference is due to their low velocity magnitude relative to the bubble velocity.

The average axial velocity profiles at different distances from the bubble trailing edge are represented in Figure 3.123. From this figure the negative wake behind the trailing edge is evident. Close to the trailing edge there is a downward flow in the axis of the

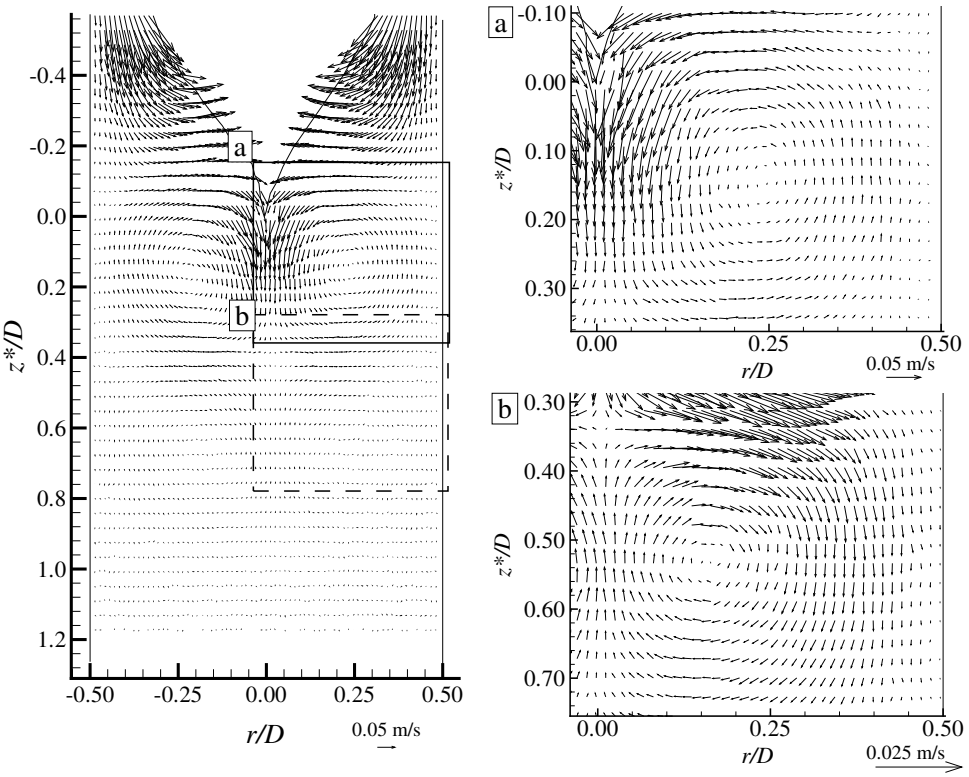

Figure 3.121. Detail of secondary recirculations in the wake of a Taylor bubble rising in a 1.00 wt% CMC solution.

column and an upward flow outside the tube axis region. The velocity magnitude is, however, lower than in the 0.80 wt% CMC solution. The length of the main circulation region is also shorter than in the previous solution; between $z* = 0.3D$ and $z* = 0.4D$. At $z* = 0.4D$, there is practically no axial velocity component, so this must be approximately where the main region separates from the secondary circulation region in which the fluid moves radially outwards. Above $z* = 0.4D$ it is possible to notice the secondary circulation region where the liquid flows upwards in the axis of the column, despite the low velocity magnitude.

The maximum velocity oscillations occur very close to the bubble trailing edge due to its constant rotation, which causes a three-dimensional flow in that region.

From Table 3.9 it was seen that the flow was asymmetric in two instantaneous perpendicular planes since the mean axial velocity through a cross-section at a certain distance from the bubble trailing edge was not zero. The velocity profiles in Figure 3.123 are the average profiles from random trailing edge positions. The mean axial velocities at different

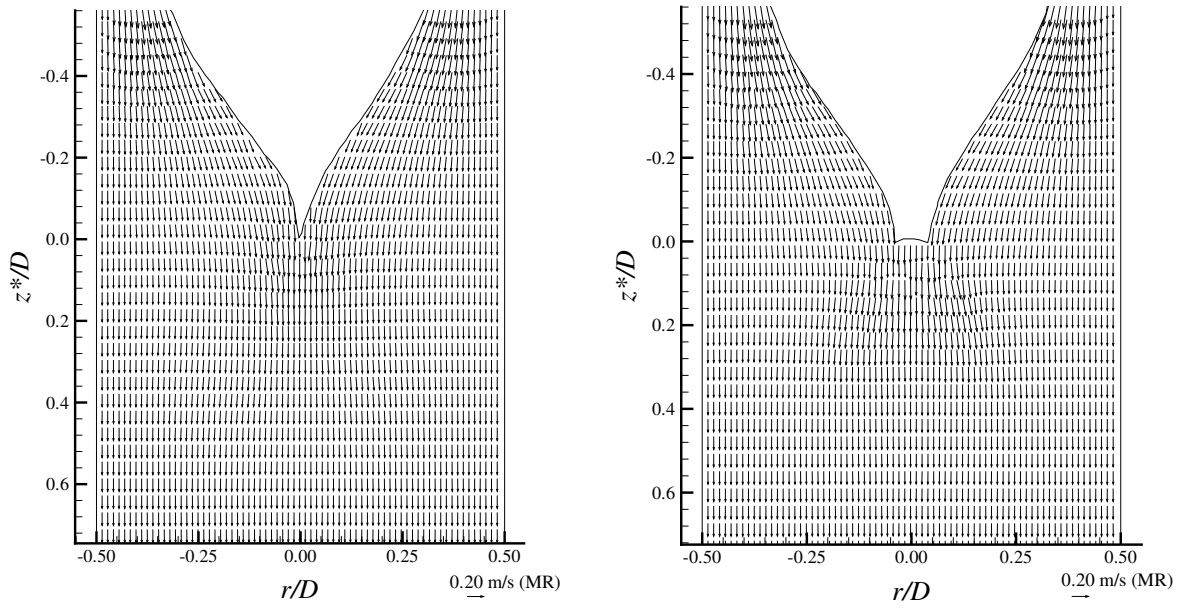

Figure 3.122. Flow fields in the wake of Taylor bubbles rising in a 1.00 wt% CMC solution, in a frame of reference moving with the bubble velocity.

distances from the bubble trailing edge taken from these average profiles are presented in Table 3.10. These values are already below the 0.003 m/s velocity uncertainty, and are

Table 3.10. Mean axial velocity (m/s) at different distances from the bubble trailing edge taken from the average velocity profiles.

$z*/D$	$\overline{V_z}$ (m/s)
0.1	-0.0021
0.2	-0.0006
0.3	+0.0006

thus negligible and highlight the constant rotational frequency of the cusp edge.

The radial velocity profiles at different distances from the bubble trailing edge are represented in Figure 3.124. The radial velocity profiles show that the fluid is moving towards the axis close to the bubble trailing edge and at $z* = 0.1D$ there is already an inversion of direction, indicating the middle plane of the main circulation region (between $z* = 0.05D$ and $z* = 0.1D$). The velocity magnitude decreases over distance from the

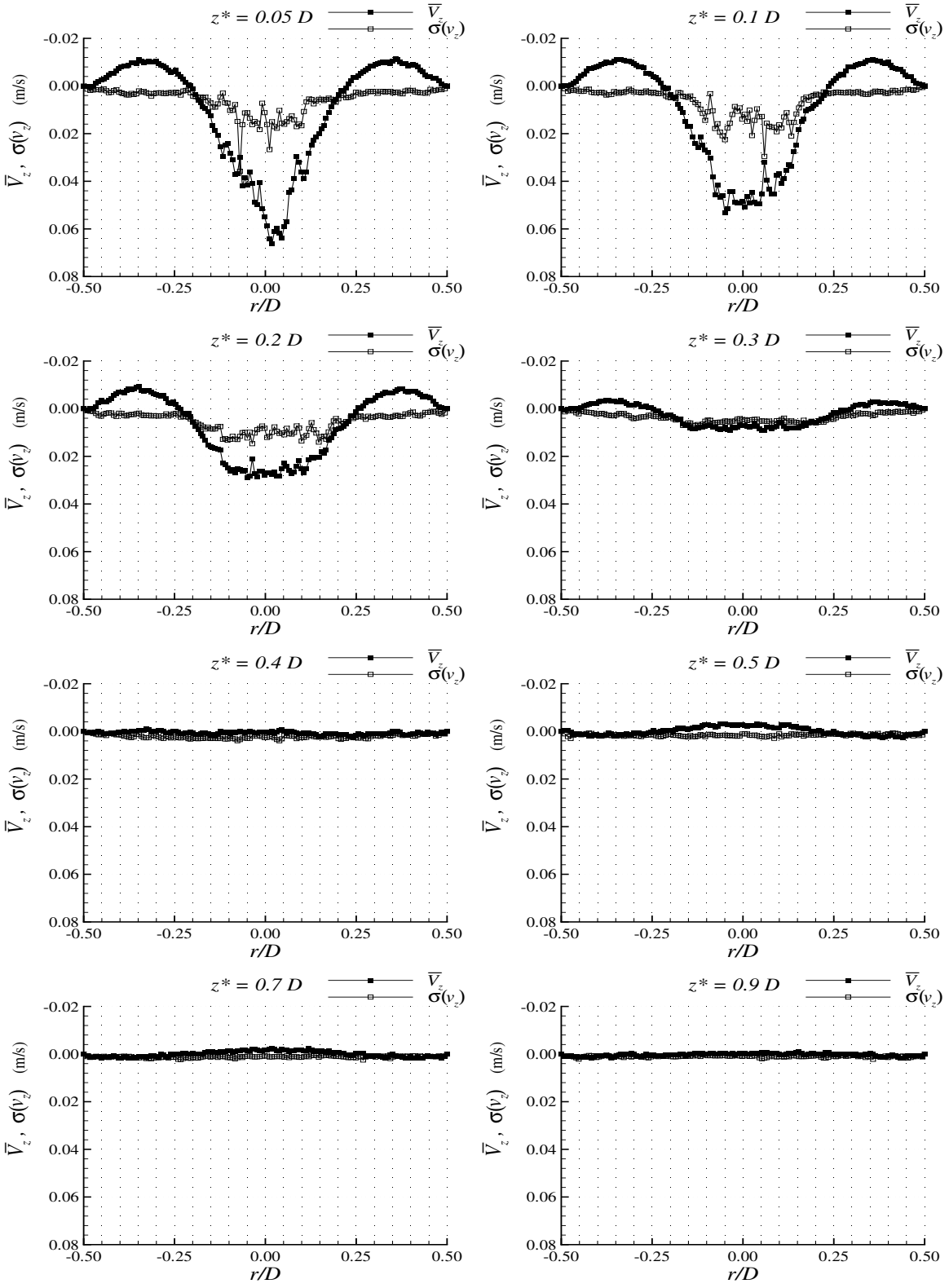

Figure 3.123. Average axial velocity profiles (fixed frame of reference) and standard deviation at different distances from the trailing edge of a bubble rising in a 1.00 wt% CMC solution.

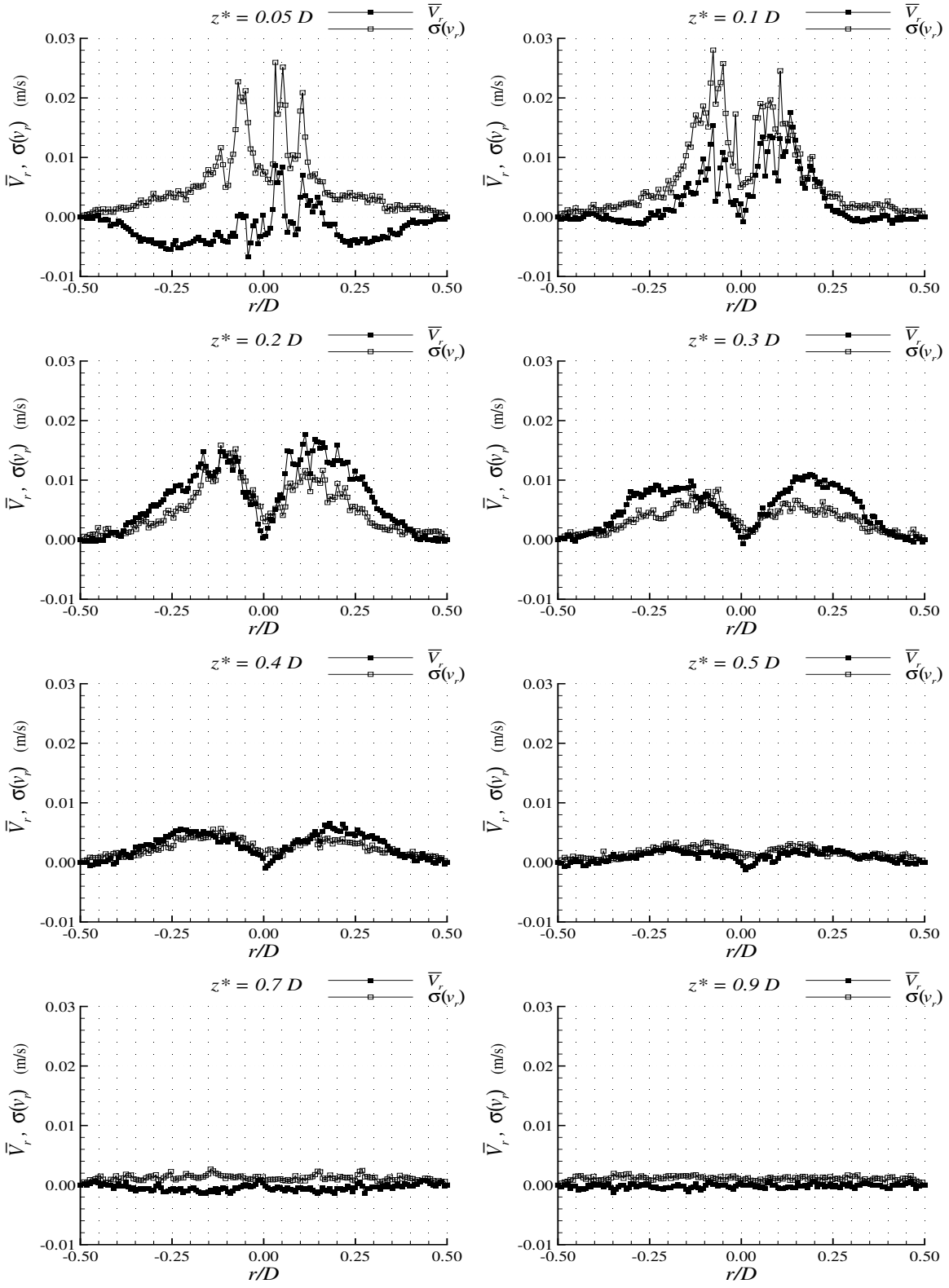

Figure 3.124. Average radial velocity profiles and standard deviation at different distances from the bubble trailing edge rising in a 1.00 wt% CMC solution.

bubble trailing edge, but there is another flow inversion between $z* = 0.5D$ and $z* = 0.7D$, indicating the middle plane of the secondary circulation region. At $z* = 0.9D$ the fluid is practically stagnant.

The average flow field in the wake of Taylor bubbles rising in a 1.00 wt% CMC solution is represented in Figure 3.125, highlighting the different velocity magnitudes in the recirculation regions.

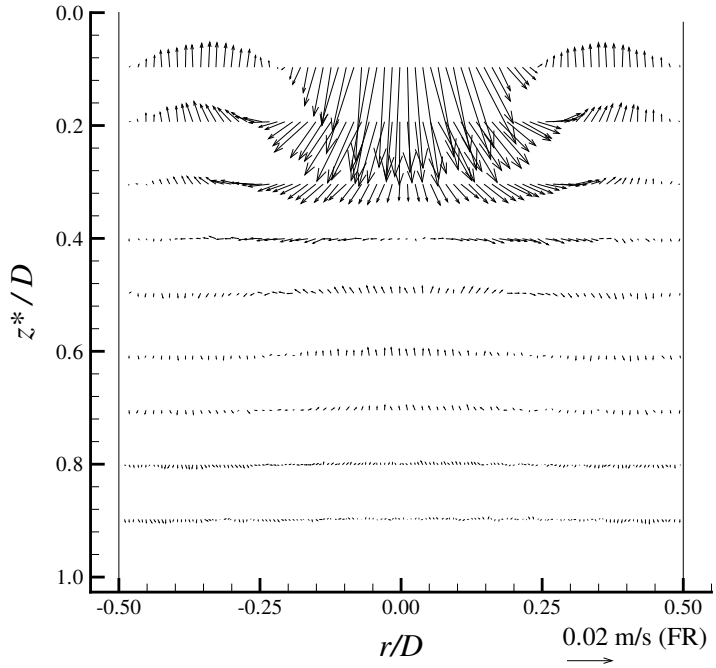

Figure 3.125. Average wake flow pattern in the wake of Taylor bubbles rising in a 1.00 wt% CMC solution.

The axial velocity profile at $r = 0$ as a function of the distance to the bubble trailing edge is represented in Figure 3.126. The negative wake behind a Taylor bubble rising in a 1.00 wt% CMC solution is once again visible in the downward flow behind the trailing edge. The upward flow corresponding to the second circulation region is also visible before the fluid stagnation.

A comparison between the flow patterns in all the wakes is presented in the next section.

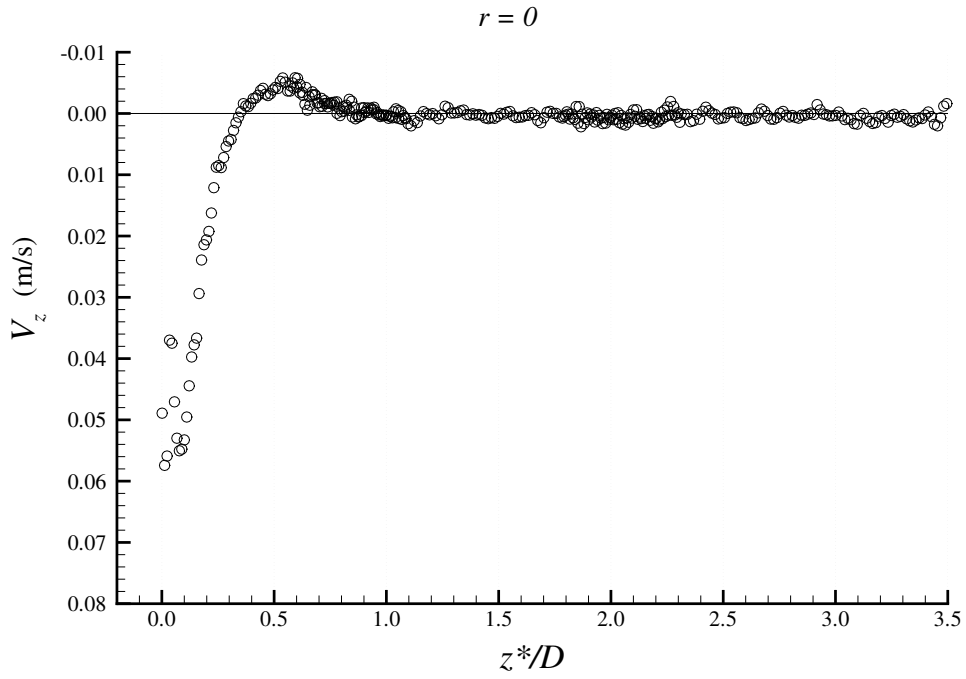

Figure 3.126. Instantaneous axial velocity profile (fixed frame of reference) at $r = 0$ as a function of the distance to the trailing edge of a Taylor bubble rising in a 1.00 wt% CMC solution.

3.3.7 Summary of bubble wakes in CMC solutions

In the previous sections the wakes in the different CMC solutions studied were described. For better comparison between them, some wake characteristics are now summarised and presented together.

In Figure 3.127, the axial velocity profiles at $r = 0$ behind Taylor bubbles rising in CMC solutions of increasing concentration are represented, up to the weight % where the negative wake appears. This figure compares the flow behind the Taylor bubbles rising in the less viscous solutions In the 0.10 wt% CMC solution there are some velocity oscillations which traduce the turbulence in the wake. Small bubbles flowing behind the Taylor bubble perturb the liquid flow, which does not stagnate for a length of several column diameters.

For the solutions in the $0.30 - 0.50$ wt% CMC range there is a stable upward flow with velocity magnitudes higher than the bubble velocity, which means that there is liquid in recirculation transported in the wake. As the viscosity increases there is a decrease in the distance at which there is an upward flow, which means a decrease in the wake length. In the 0.60 wt% CMC solution the upward liquid flow has a velocity magnitude close to the

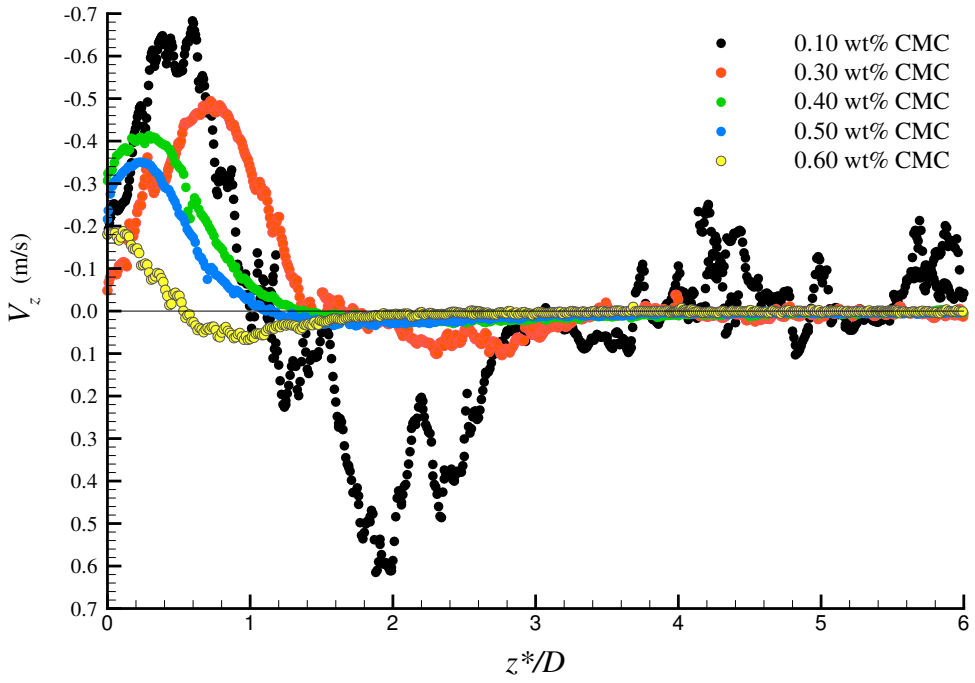

Figure 3.127. Axial velocity profiles at $r = 0$ behind Taylor bubbles rising in solutions with concentrations lower than 0.80 wt% CMC.

bubble velocity and only a small portion of fluid is transported in the wake.

A similar velocity profile is represented in Figure 3.128 for the most viscous solutions studied. For the 0.80 and 1.00 wt% CMC solutions the velocity magnitudes are much lower and there is an inversion in the flow pattern behind the bubble trailing edge, where negative wakes are seen. In the axis of the column the liquid flows downwards in a first circulation region, inducing a secondary circulation region in the liquid below where an upward flow is seen before fluid stagnation.

The comparison between the axial velocity profiles at a $z* = 0.2D$ in the wake of Taylor bubbles rising in the solutions studied is presented in Figure 3.129. The 0.50 wt% CMC solution profile was not plotted since it practically coincides with that of the 0.40 wt% CMC solution. This figure clearly shows that the velocity magnitudes in the liquid coming from the falling film decrease as the viscosity increases. At this distance from the bubble trailing edge, the upward velocity magnitude in the central region of the wake is practically the same for all the less concentrated solutions. For the 0.60 wt% CMC and higher concentration solutions there is a decrease in the central velocity magnitude, becoming downwards for

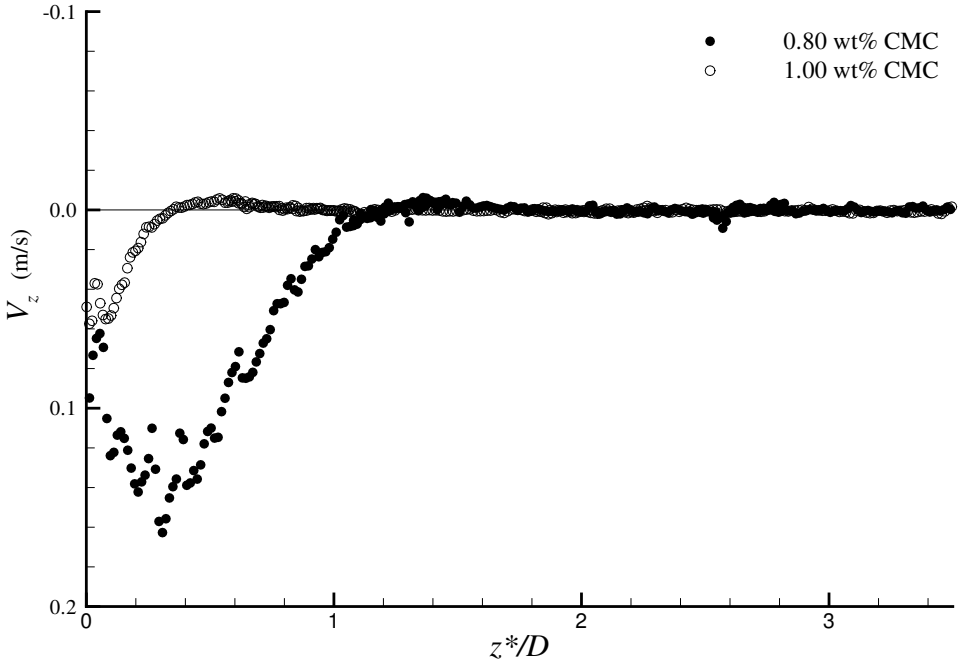

Figure 3.128. Axial velocity profiles at $r = 0$ behind Taylor bubbles rising in 0.80 and 1.00 wt% CMC solutions.

the 0.80 and 1.00 wt% CMC solutions (negative wake).

The wake lengths, L_w, in the solutions where closed recirculations were found behind the Taylor bubble are presented in Table 3.11, defined as the points where the axial liquid velocity is equal to the bubble velocity in a fixed frame of reference, or equal to zero in a frame of reference moving with the bubble.

Table 3.11. Wake lengths of solutions with concentration between 0.30 and 0.60 wt% CMC.

CMC wt%	L_w/D
0.30	1.2
0.40	0.8
0.50	0.6
0.60	<0.2

Sotiriadis and Thorpe (2005) measured velocity profiles in the wake of a solid replica of a Taylor bubble and in the wake of an aerated cavity, with water flowing counter-current in order to maintain the bubble at a fixed position. These authors found that the stagnation

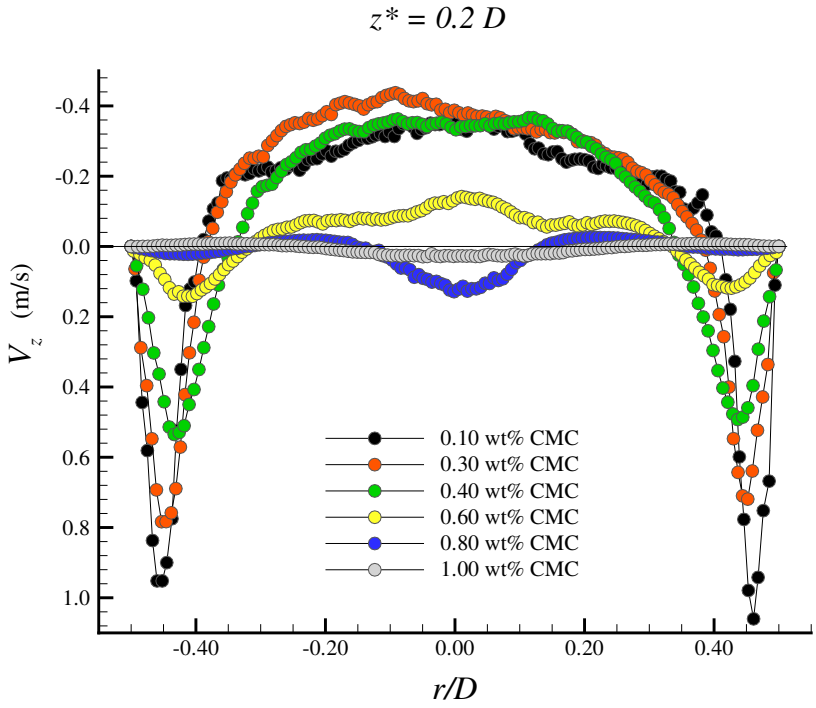

Figure 3.129. Axial velocity profile at $z* = 0.2D$ in the wake of Taylor bubbles rising in the CMC solutions studied.

point in the axis of the column was located at $1.3D$ and $1.35D$ from the solid body and aerated cavity respectively, which are in accordance with the tendency found in the CMC solutions.

In order to compare these results with the data from Campos and Guedes de Carvalho (1988) for Newtonian fluids, the dimensionless parameter $(gD^3)^{1/2}\rho_l/\mu$ was determined for the CMC solutions. Since for the CMC solutions the viscosity is shear rate dependent, a mean viscosity in the liquid film, corresponding to a shear rate of $\overline{V}_{z(film)}/\delta$ was used to compute the dimensionless parameter. The comparison is presented in Figure 3.130. There is a similar tendency for wake length variation with the dimensionless parameter, the differences being mainly due to the shear rate dependence of the viscosity of the CMC solutions.

Another interesting parameter is the axial location of the "eyes of the vortexes" in the wake, i.e., the centre of the recirculation streamlines in the vertical plane. Sotiriadis and Thorpe (2005) observed that in water the "eyes of the vortexes" were located at $0.72D$ and $0.78D$, from the trailing edge of the solid body and of the aerated cavity respectively.

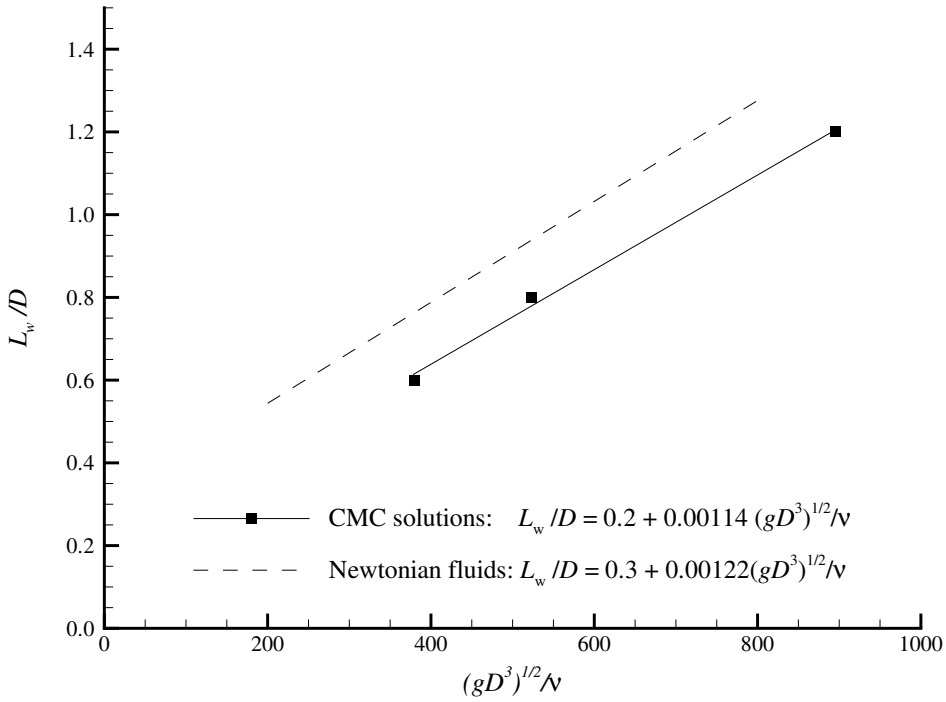

Figure 3.130. Wake length (L_w) dependence on the dimensionless parameter $(gD^3)^{1/2}/\nu$

In Table 3.12, the distance of the eyes of the vortexes relative to the trailing edge of the bubbles rising in the different CMC solutions are presented as determined in a moving frame of reference. The increasing viscosity induces shorter wake lengths, with the respective approach of the vortex eyes to the bubble trailing edge.

Table 3.12. Axial distance of the vortexes eyes, z_eye/D, relative to the bubble trailing edge.

CMC wt%	z_eye/D
0.30	0.70
0.40	0.35
0.50	0.25

Chapter 4

Individual Taylor bubbles in Polyacrylamide (PAA) solutions

Abstract

In this chapter the studies performed with Polyacrylamide (PAA) polymer solutions are presented. The preliminary visualisation studies are described and the selection of the most relevant conditions is made. The selected solutions rheologic characterisation is done before presenting the corresponding flow field measurements with PIV/ST. From the flow field measurements the flows around the bubble nose, in the annular liquid film and in the wake of the Taylor bubbles are described.

4.1 Visualisation studies

As in the CMC solutions, there was no information available in the literature about the flow field around Taylor bubbles rising in Polyacrylamide (PAA) solutions. Preliminary visualisation studies were performed using the same experimental setup designed for the CMC solutions, to get an idea of the flow pattern in the wake of Taylor bubbles.

The choice of the PAA polymer (solutions) was related to its different rheologic properties compared with the CMC (solutions). A more accentuated shear thinning behaviour and higher viscoelasticity than the CMC solutions were found, as will be shown in the rheological characterisation section.

Several solutions with different weight percentages (wt%) of PAA in water were studied to cover a wide range of rheologic properties. The weight percentages and experimental temperatures are presented in Table 4.1. For each condition, between 10 and 30 bubbles of different volumes were analysed.

Table 4.1. Experimental conditions in the visualisation studies with PAA solutions.

PAA wt%	$T(^o\mathrm{C})$	PAA wt%	$T(^o\mathrm{C})$
0.01	29.7	0.30	25.1
0.05	26.0	0.40	26.2
0.10	26.5	0.80	26.0
0.20	25.3		

4.1.1 Bubble velocity and length

The experimental values of bubble velocity, U_b, and the dimensionless bubble length, L_b/D, obtained in the visualisation studies, are represented in Figure 4.1. From the

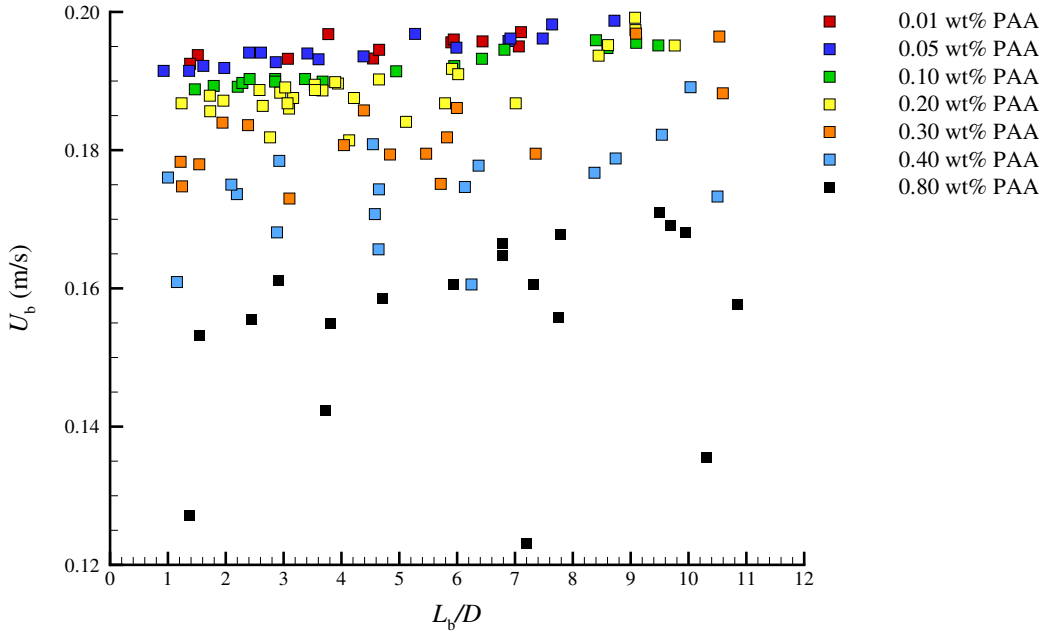

Figure 4.1. Plot of bubble velocity versus dimensionless bubble length of Taylor bubbles in the visualisation studies with PAA solutions.

uncertainty analysis in Appendix B, an uncertainty of 0.001 m/s was determined for the bubble velocity and 0.001 m ($0.03D$) for the bubble length.

As was the case in CMC solutions, for a given bubble length the bubble velocity decreases as the PAA wt% increases. The velocity variation between 0.01 and 0.80 wt% PAA solutions can reach almost 30% for a given bubble length. The aforementioned effect of bubble expansion is also visible in the velocity increase with bubble length for a given PAA solution.

Figure 4.1 shows a high velocity spread for solutions above 0.20 wt% PAA. This behaviour is related with the relaxation time of these solutions. A simple experiment was made in the 0.80 wt% PAA solution by injecting bubbles of the same length and changing the time interval between consecutive bubbles. Figure 4.2 shows the effect of the time parameter on the velocity of the Taylor bubbles. During the passage of a bubble the fluid

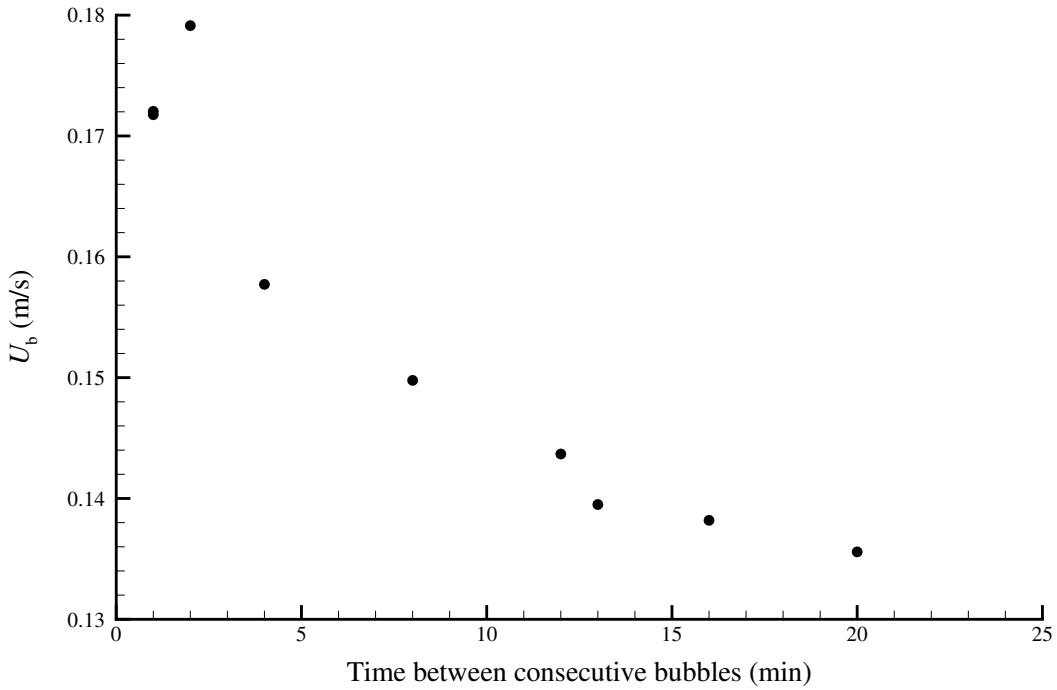

Figure 4.2. Velocity of Taylor bubbles with $8.2D$ length rising in 0.80 wt% PAA solutions as a function of the time between consecutive bubbles.

viscosity decreases and it takes some time to recover its initial viscosity. Therefore, in the higher concentration PAA solutions the bubble velocity is not only dependent on the bubble length but also on the fluid history. In the visualisation studies this parameter was

not controlled, although most of the bubbles were injected with approximately the same time interval. Li *et al.* (1997a,b, 1998) refers to a similar effect the time between bubble injections has on the velocity of small bubbles rising in PAA solutions. The following sections present descriptions of the wake flow patterns in different PAA solution weights.

4.1.2 Wake flow pattern

The qualitative characterisation of the liquid flow in the wake of Taylor bubbles in different PAA solutions is made, beginning with less concentrated solutions.

0.01 wt% PAA solution

The lowest PAA weight percentage used in these studies was 0.01 wt%. The bubble length varied from 1.4 to 7.1D and the bubble velocity from 0.192 to 0.197 m/s.

In Figure 4.3, twelve frames of the wake of a Taylor bubble rising in a 0.01 wt% PAA solution, are represented. The bubble trailing edge oscillates three-dimensionally and small

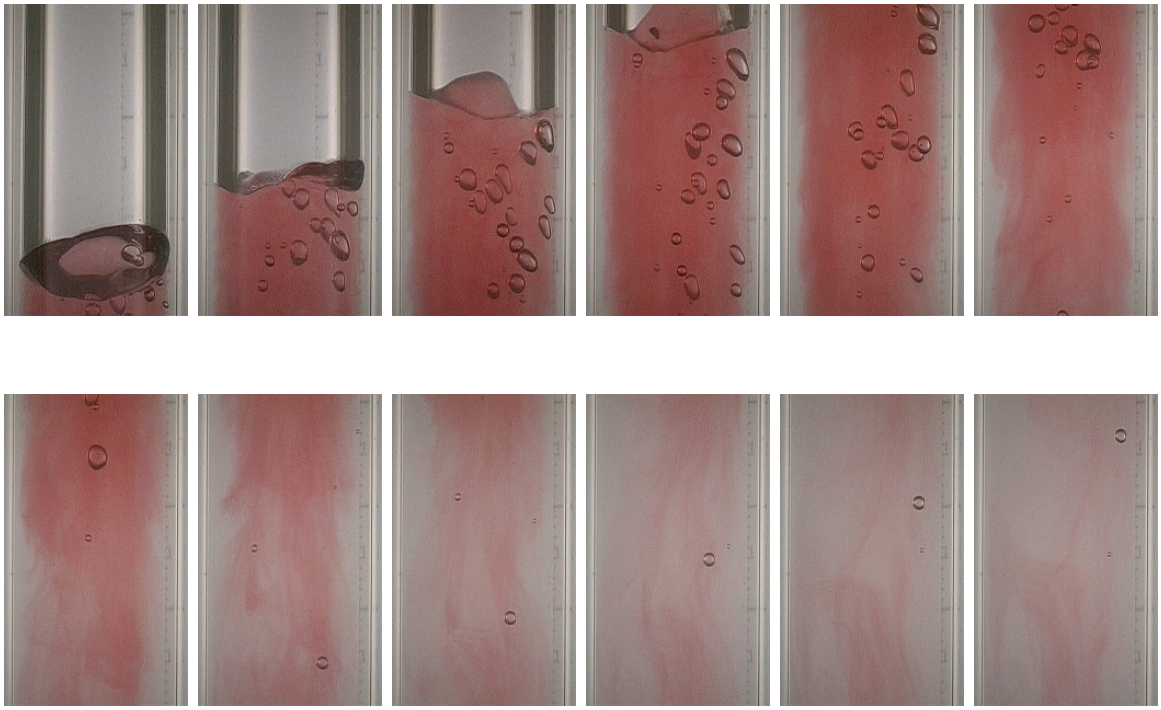

Figure 4.3. Consecutive frames of the wake of a Taylor bubble with a 3.8D length, rising in a 0.01 wt% PAA solution; time between frames 0.08 s.

bubbles are formed, as in the 0.10 wt% CMC solution. Despite being ten times less concentrated than the minimum CMC weight percentage solution studied, it is clear that there is coloured fluid transported in the wake. The wake flow pattern looks similar to those found in the 0.20 wt% CMC solution but have a longer wake length; the wakes are between 2.5 and $3D$ in length and some radial oscillations are seen in the bottom of the wake. The wake length was considered to be the region in which there is coloured liquid moving upwards with the bubble.

The small bubbles that form are mainly trapped in the bubble wake. Even so, some are seen at several column diameters length from the bubble trailing edge, but in smaller numbers than in the 0.10 wt% CMC solution, as shown in Figure 4.4.

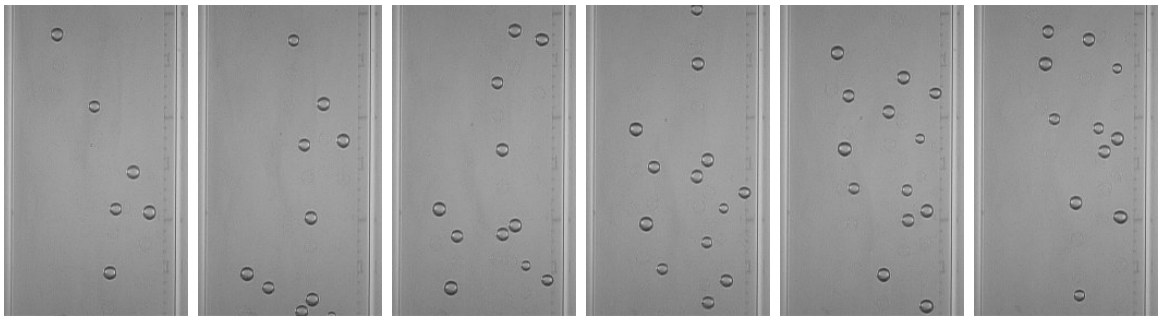

Figure 4.4. Consecutive frames showing small bubbles rising behind a Taylor bubble in a 0.01 wt% PAA solution; time between frames 0.08 s.

In this solution, even for the longer bubbles with a length of about $7D$, the Taylor bubble radius continuously increases until the bottom of the bubble, and a stable maximum radius is not reached.

0.05 wt% PAA solution

In the 0.05 wt% PAA solution, the bubble lengths varied from 1.0 to $8.4D$ and the velocities between 0.191 and 0.199 m/s. In Figure 4.5, twelve sequential frames of the wake of a Taylor bubble rising in this solution, are represented. The bubble trailing edge still oscillates but with less amplitude than in the previous solution. A decrease in the number of small bubbles present in the wake is also evident.

The wake pattern looks very different from those found in the CMC solutions. A clear recirculation region is not visible and the wake pattern is similar to a waving skirt. The

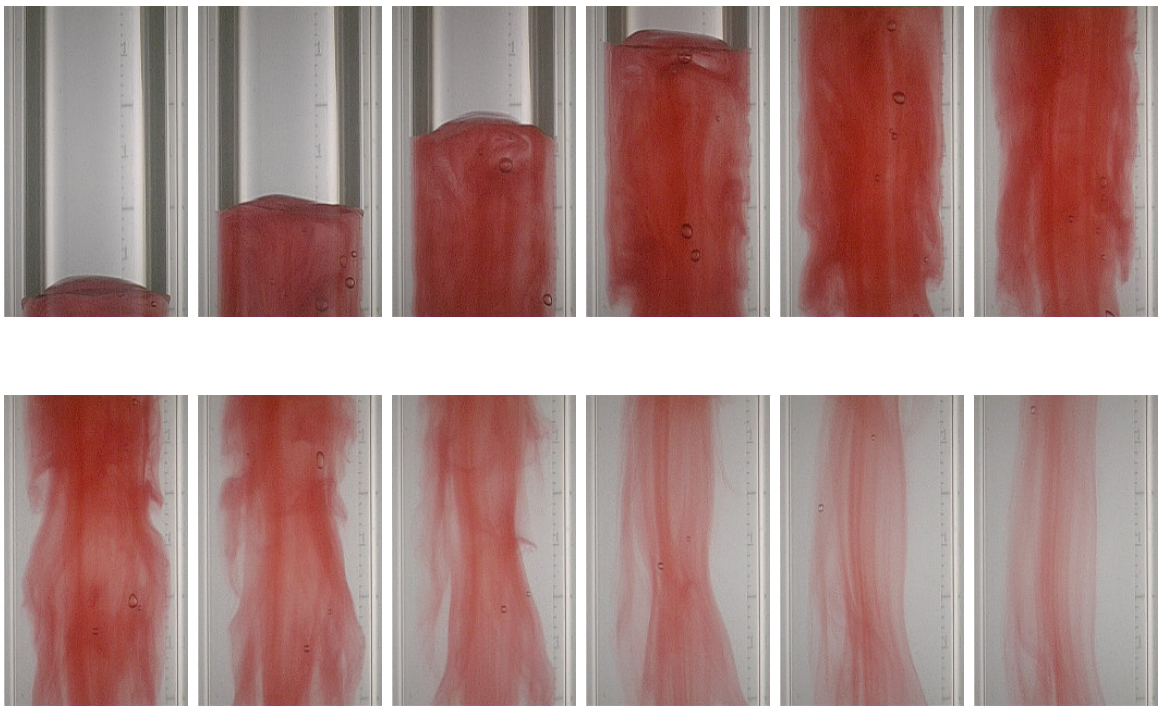

Figure 4.5. Consecutive frames of the wake of a Taylor bubble $4.4D$ in length, rising in a 0.05 wt% PAA solution; time between frames 0.08 s.

liquid film does not expand smoothly, keeping an approximately constant thickness over a certain distance, apart from some wavy movements.

For a better view of the wake length, in Figure 4.6 nine sequential frames of the wake of a bubble are presented with less magnification. The oscillatory movement of the wake is

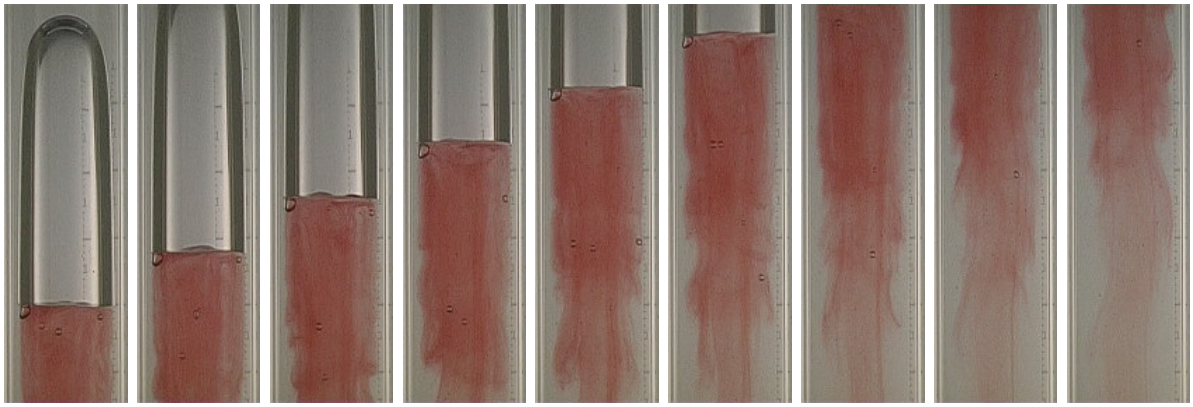

Figure 4.6. Consecutive frames of the wake of a Taylor bubble with a $2.6D$ length, rising in a 0.05 wt% PAA solution; time between frames 0.08 s.

seen up to $3D$ from the bubble trailing edge. After the main region of the wake a central coloured liquid is left behind, and some ascending liquid movement can be observed even at $12D$ from the bubble trailing edge.

These long wakes are also visible for the smaller Taylor bubbles. In Figure 4.7 a Taylor bubble with a $1D$ length is seen, with a wake three times longer than itself.

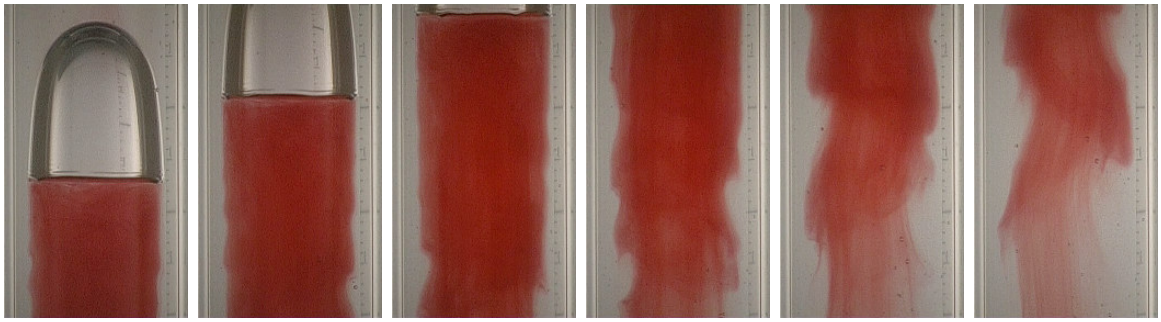

Figure 4.7. Consecutive frames of the wake of a Taylor bubble with a $1.0D$ length, rising in a 0.05 wt% PAA solution; time between frames 0.08 s.

0.10 wt% PAA solution

In the 0.10 wt% PAA solution, the bubble length varied between 1.5 and $9.5D$ and the bubble velocity between 0.189 and 0.197 m/s. The wake flow pattern is very similar to that of the previous solution. In Figure 4.8, eighteen sequential frames of the wake of a Taylor bubble rising in this solution are presented.

In the 0.10 wt% PAA solution the oscillations of the bubble trailing edge are almost imperceptible. Some elongated recirculation regions are visible close to the bubble trailing edge, and the wavy movement is present mainly in the lower region of the wake.

The lower region of the wake has an anemone-like movement. There is a central region of stable coloured liquid that is pushed up, surrounded by a waving skirt of liquid that expands and contracts axially during the bubble rise. An example of this wake region is represented in Figure 4.9.

Although the waving wake is seen up to about $3.5D$ from the bubble trailing edge, the central upward movement of coloured liquid extends up to $6D$ from the bubble trailing edge.

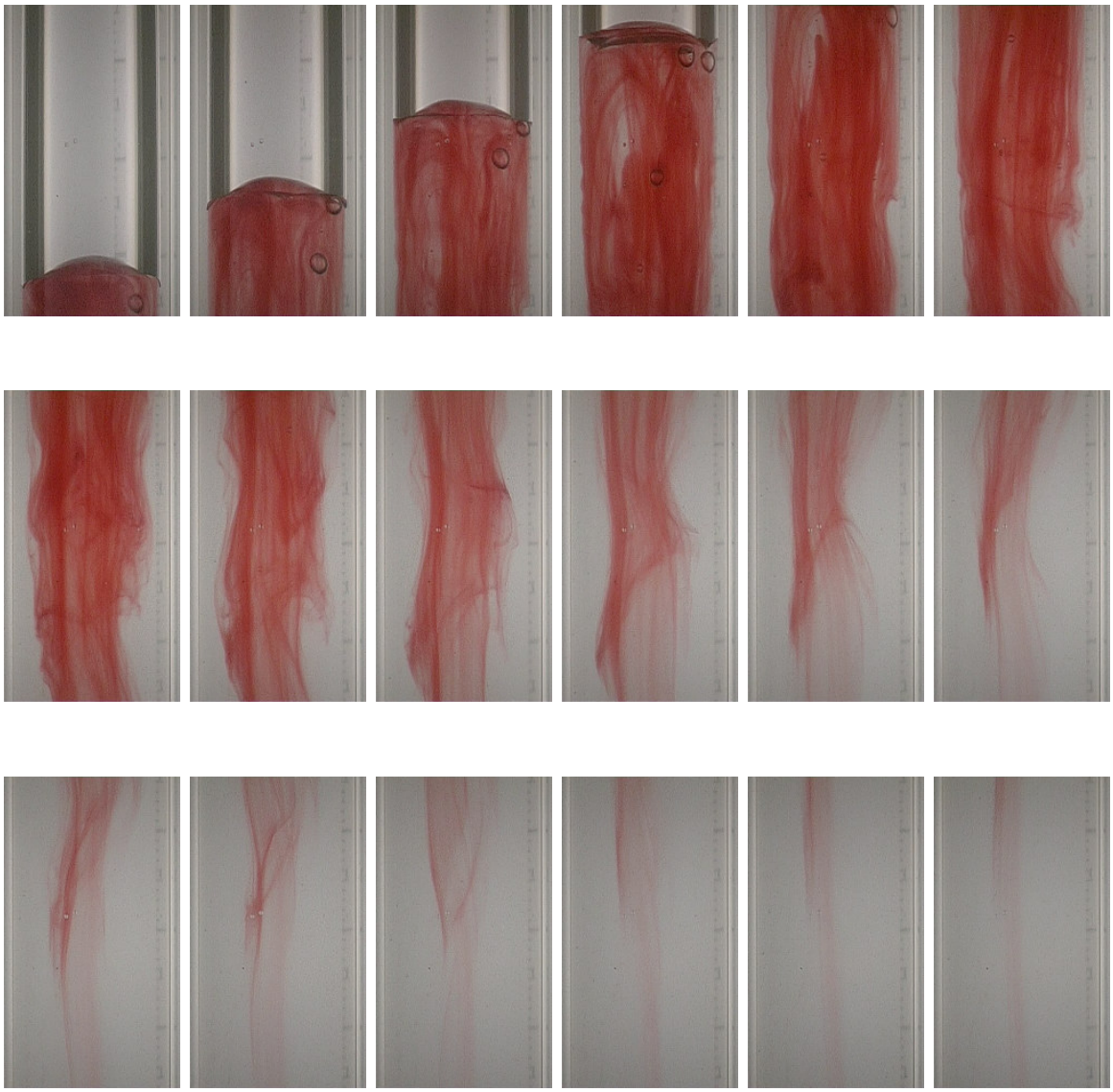

Figure 4.8. Consecutive frames of the wake of a Taylor bubble with a $3.7D$ length, rising in a 0.10 wt% PAA solution; time between frames 0.08 s.

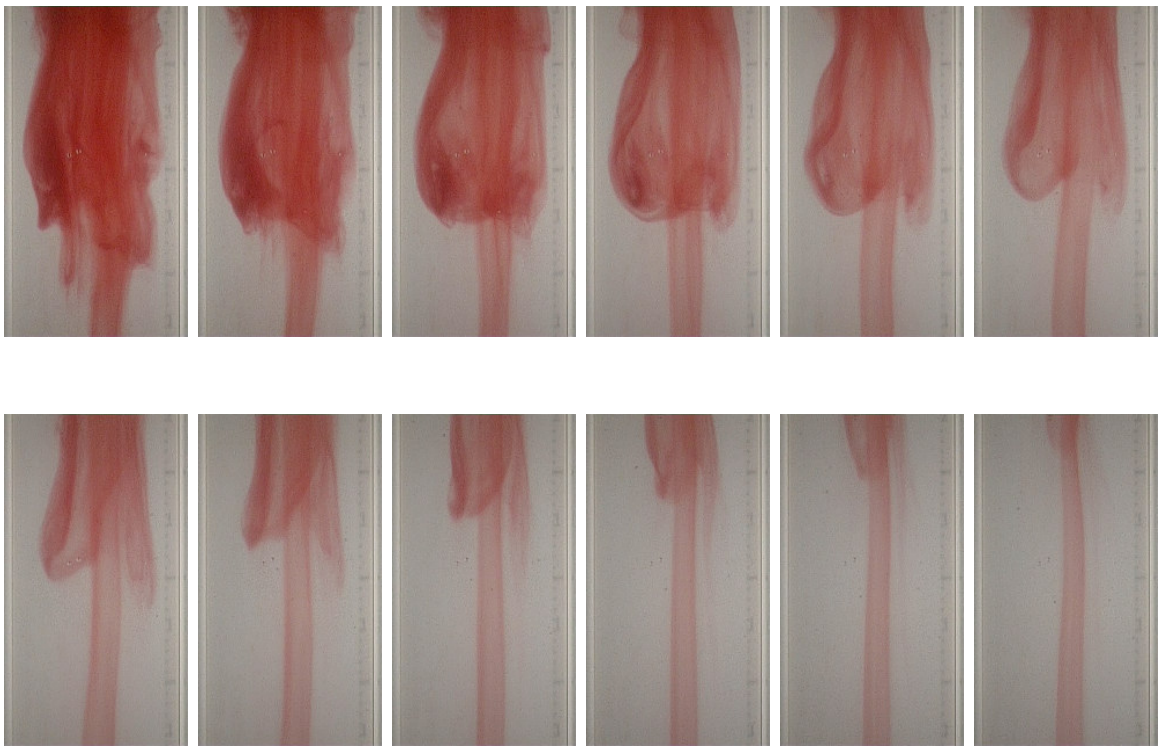

Figure 4.9. Consecutive frames of the wake of a Taylor bubble with a $2.5D$ length, rising in a 0.10 wt% PAA solution; time between frames 0.04 s.

0.20 wt% PAA solution

In the 0.20 wt% PAA solution visualisation studies, the Taylor bubble length varied between 1.2 and $9.8D$ and the bubble velocity between 0.181 and 0.199 m/s.

In this solution the effect of the fluid history started to be noticed. The first bubble studied after placing the liquid in the column did not show any coloured liquid in the wake. In Figure 4.10, consecutive frames of the trailing edge of the first bubble studied in this solution, are presented. Despite the stability of the trailing edge, there are some small bubbles trapped in the wake but no coloured liquid is seen. This behaviour was found in the first two bubbles studied after renewing the column liquid.

Coloured liquid is seen in the wakes of the following bubbles showing an effect of the fluid history. Consecutive frames of the wake of a bubble rising in 0.20 wt% PAA solution are presented in Figure 4.11. This sequence of frames shows a flow pattern where a "skirt" surrounds a central region of fluid that is practically static relative to the bubble. In the upper left region of the "skirt" an elongated closed circular region is seen in the top

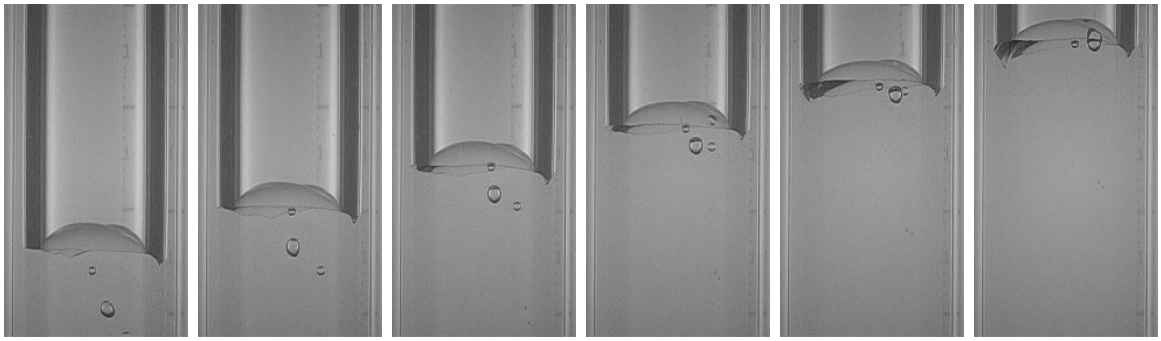

Figure 4.10. Consecutive frames of the trailing edge of the first Taylor bubble ($6.0D$ long) studied in a 0.20 wt% PAA solution; time between frames 0.04 s.

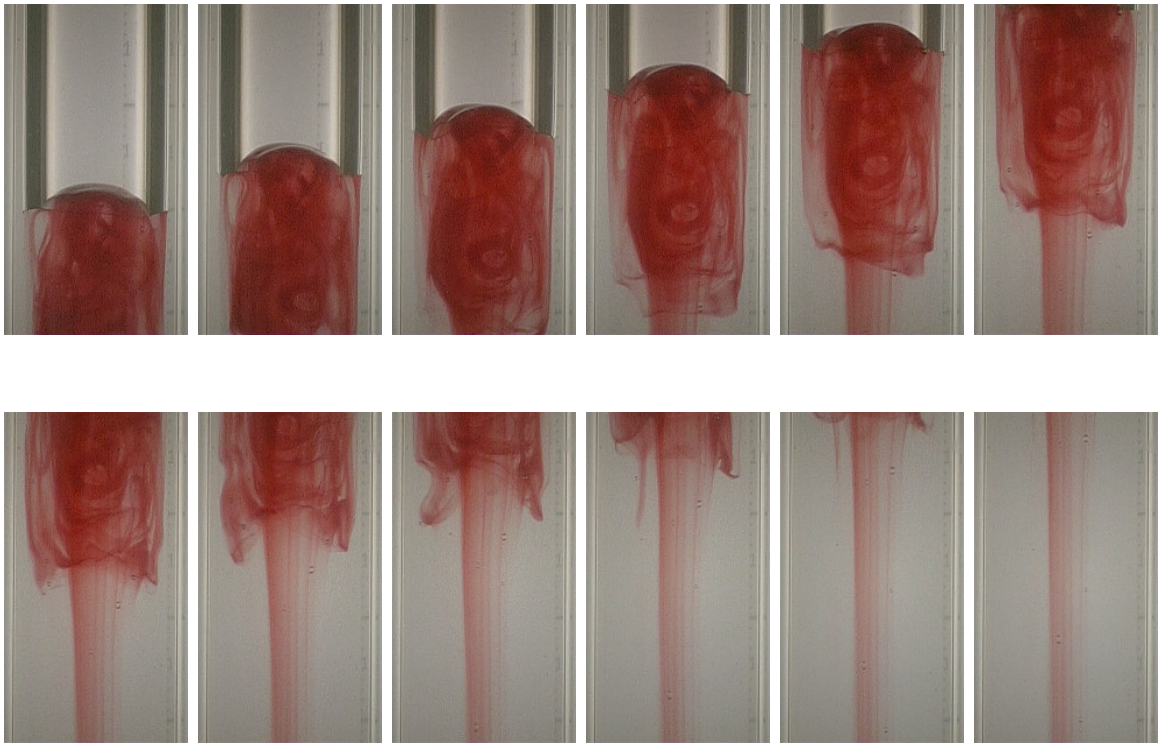

Figure 4.11. Consecutive frames of the wake of a Taylor bubble with a $6D$ length, rising in a 0.20 wt% PAA solution; time between frames 0.04 s.

frames, while a darker circle in the central region of the wake maintains its position under the bubble trailing edge. The length of the main coloured-liquid section is now much shorter than in the previous solutions, having only around $1.4D$.

Some examples of frames acquired in the wake of different Taylor bubbles are presented in Figure 4.12 This figure shows that, depending on the fluid history, there can be more or

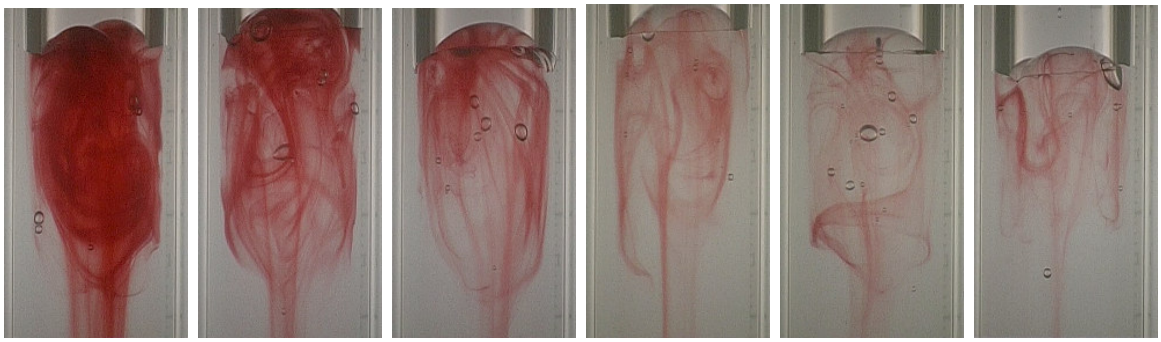

Figure 4.12. Wakes of different Taylor bubbles rising in a 0.20 wt% PAA solution.

less coloured liquid in the wake although the flow pattern is in general the same. The images in this figure were ordered by decreasing quantity of coloured liquid and not necessarily by the time between them which was not measured.

As in the previous solutions there is a region in the axis of the column with an upward coloured liquid movement, seen at distances up to $4D$ from the bubble trailing edge.

0.30 wt% PAA solution

In the 0.30 wt% PAA solution, the Taylor bubble length varied between 1.2 and $10.6D$ and the bubble velocity between 0.173 and 0.197 m/s.

In this solution no coloured liquid was observed in the wake of the Taylor bubbles. The bubble trailing edge was not completely stable, presenting a slight three-dimensional movement. In Figure 4.13, consecutive frames of the trailing edge of a Taylor bubble rising in 0.30 wt% PAA solution are presented.

Due to the absence of coloured liquid no information could be obtained concerning the flow pattern in the wake. It was noticed that for some bubbles there was an asymmetry in the flow around the bubble, since the liquid film thickness was not equal on the left and right sides of the bubble two-dimensional projection. This was probably caused by a slight inclination of the column.

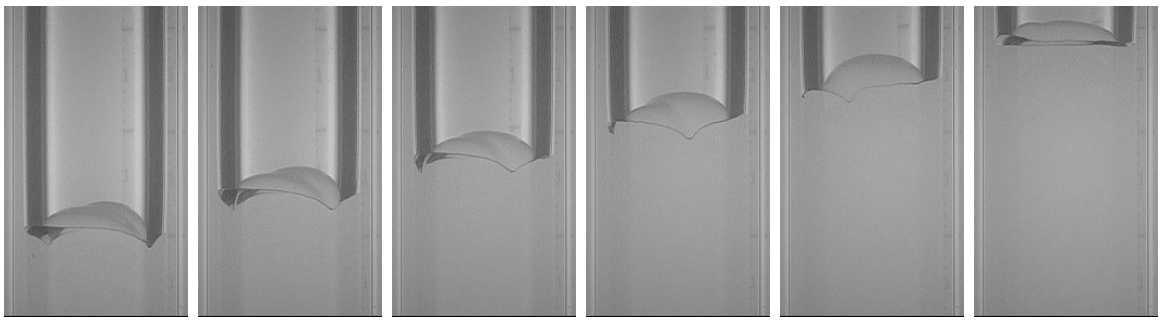

Figure 4.13. Consecutive frames of the trailing edge of a Taylor bubble with a $4.8D$ length, rising in a 0.30 wt% PAA solution; time between frames 0.04 s.

0.40 wt% PAA solution

In the 0.40 wt% PAA solution, the Taylor bubble lengths were in the range 1.0–10.5D and the bubble velocity varied between 0.160 and 0.189 m/s.

As in the previous solution, there was no coloured liquid transported in the wake. The bubble trailing edge also presented some three-dimensional movement as shown in Figure 4.14.

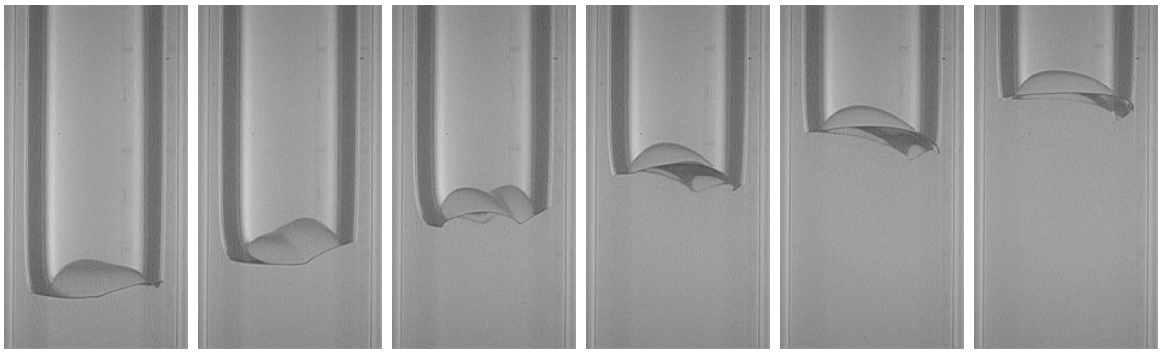

Figure 4.14. Consecutive frames of the trailing edge of a Taylor bubble with a $6.4D$ length, rising in a 0.40 wt% PAA solution; time between frames 0.04 s.

Although there was no coloured liquid in the wake, the movement of a small bubble in the wake can provide an idea of the flow pattern. In Figure 4.15, consecutive frames of the wake of a Taylor bubble rising in 0.40 wt% PAA solution are presented. This figure shows the movement of a small bubble behind a Taylor bubble. In the first frames the small bubble maintains approximately the same distance from the Taylor bubble trailing edge, but after the fifth frame it begins a downward movement lasting for five frames then

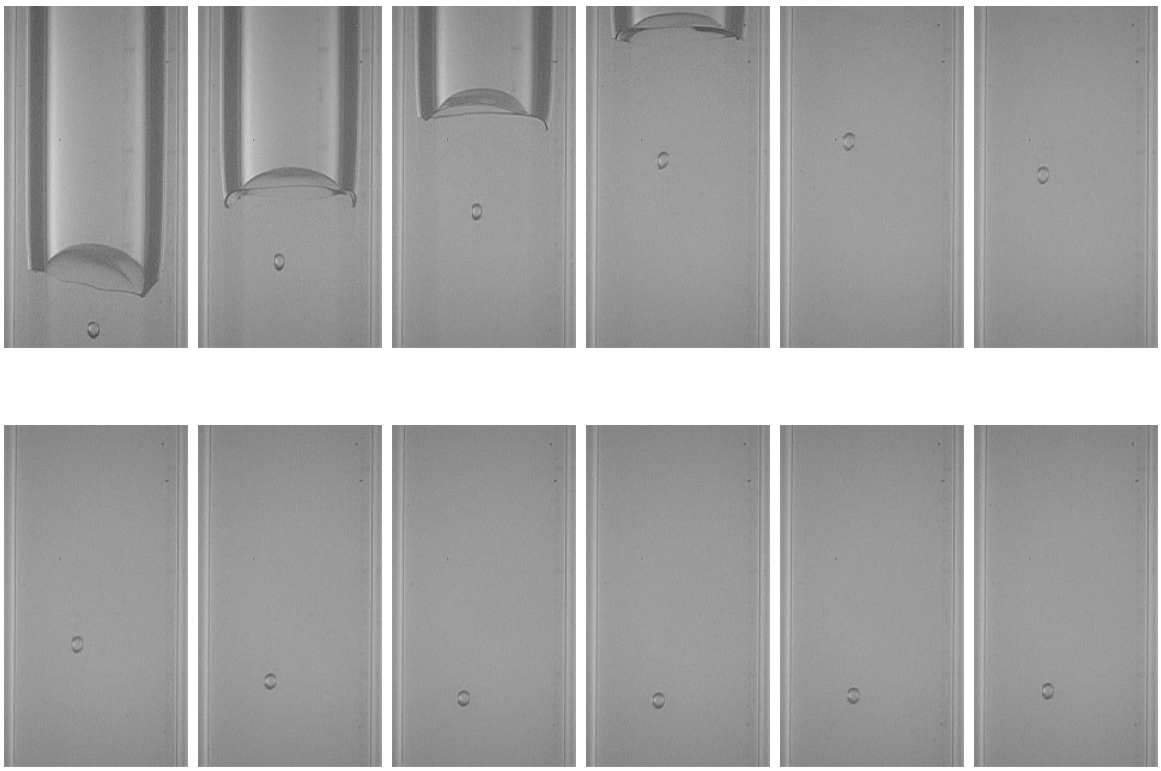

Figure 4.15. Consecutive frames of the wake of a Taylor bubble with $10D$ length, rising in a 0.40 wt% PAA solution; time between frames 0.08 s.

returns to upward movement. The movement of the small bubble shows that there is a downward liquid flow behind the Taylor bubble, at a certain distance from the bubble trailing edge. In some cases a second downward movement of a small bubble in the wake of a Taylor bubble was perceptible, which might indicate secondary recirculation regions similar to those found in the 0.80 and 1.00 wt% CMC solutions.

0.80 wt% PAA solution

In the 0.80 wt% PAA solution, the bubble length varied between 1.2 and $10.8D$ and the bubble velocity between 0.123 and 0.179 m/s. As mentioned in §4.1.1, this large velocity range is mainly due to the effect of the fluid history.

In Figure 4.16, consecutive frames of the trailing edge of a Taylor bubble rising in a 0.80 wt% PAA solution are presented. This figure shows a change in the shape of the bubble trailing edge, similar to the one found in the 1.00 wt% CMC solution. The micro-bubbles seen in the figure were inside the optical box. Due to the high viscosity of the liquid, the

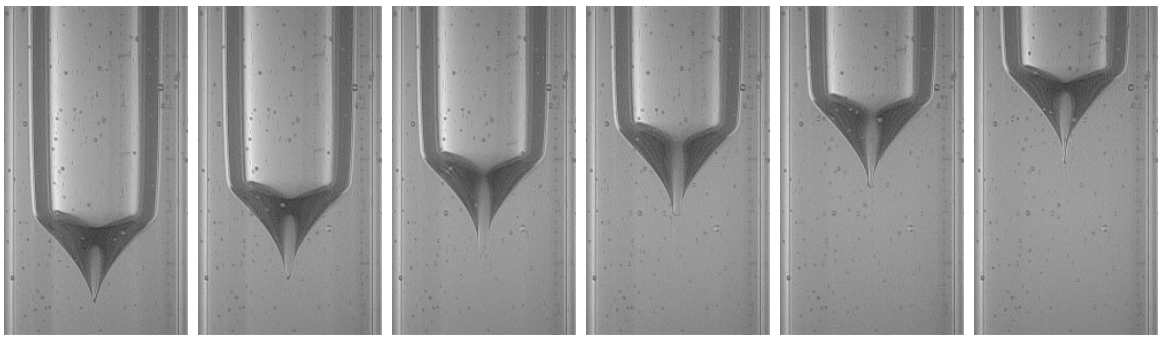

Figure 4.16. Consecutive frames of the trailing edge of a Taylor bubble with $8.2D$ in length, rising in a 0.80 wt% PAA solution after leaving the fluid at rest for 20 minutes; time between frames 0.04 s.

small bubbles are practically static and therefore difficult to remove. The Taylor bubble shown in Figure 4.16 was injected after leaving the fluid at rest for twenty minutes, so the liquid viscosity was very high; the Taylor bubble velocity was 0.136 m/s.

Figure 4.17 shows consecutive frames of the trailing edge of a Taylor bubble after leaving the fluid at rest for only two minutes. Despite being the same length as the bubble

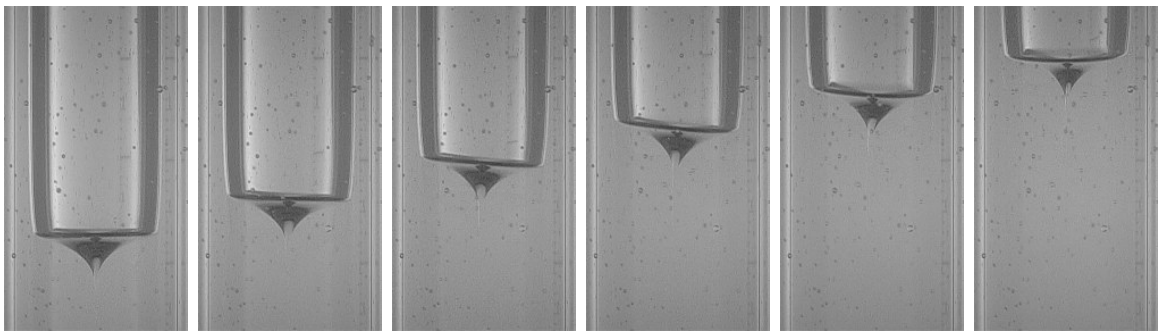

Figure 4.17. Consecutive frames of the trailing edge of a Taylor bubble with a $8.2D$ length, rising in a 0.80 wt% PAA solution after leaving the fluid at rest for 2 minutes; time between frames 0.04 s.

shown in Figure 4.16, this Taylor bubble had a velocity of 0.172 m/s. This demonstrates the effect of fluid history on Taylor bubble behaviour. Due to the shorter resting time, the fluid did not recover the initial viscosity it had before being disturbed by the previous Taylor bubble. This not only affects the bubble velocity but also the bubble trailing edge shape, which is now closer to that described in the 0.80 wt% CMC solution.

Due to the presence of small bubbles in the liquid and to the difficulty of operating

with a liquid of very high viscosity and elasticity, this was the most concentrated solution studied with the PAA polymer. A summary of the visualisation studies performed with Polyacrylamide solutions is presented next.

Summary of visualisation studies in PAA solutions

As a summary of the visualisation studies performed with the Polyacrylamide solutions, Figure 4.18 shows a representative example of each solution studied.

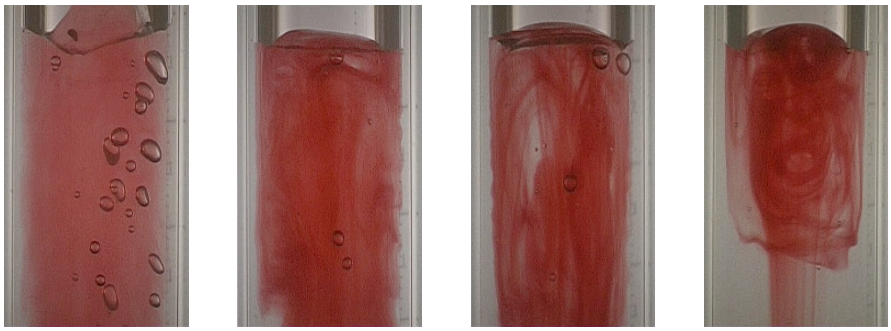

(a) 0.01 wt% (b) 0.05 wt% (c) 0.10 wt% (d) 0.20 wt%

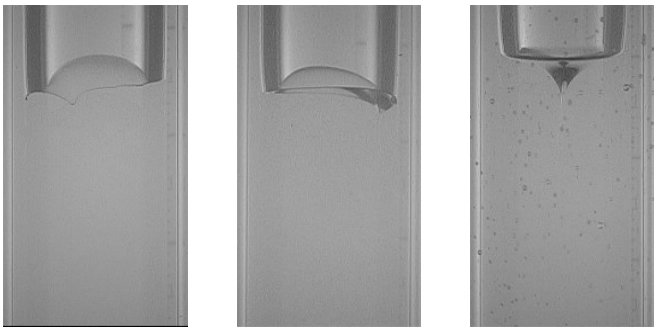

(e) 0.30 wt% (f) 0.40 wt% (g) 0.80 wt%

Figure 4.18. Summary of PAA solutions visualisation studies.

In the 0.01 wt% PAA solution, despite the strong oscillation of the bubble trailing edge there is coloured liquid transported in the wake. Small bubbles are seen, most of them being trapped in the wake and some others behind the wake. The wake is between 2.5 and $3D$ in length.

The 0.05 and 0.10 wt% PAA solutions present a similar wake flow pattern. The wake lengths are around 3.0 and $3.5D$ respectively, although there is a central coloured liquid region which is seen in upward movement even at $6D$ from the bubble trailing edge. There

are no defined recirculation regions like those observed in the CMC solutions. The coloured liquid has some radial oscillations in the upper region, and radial and axial oscillations in the bottom region. The oscillations of the bubble trailing edge are less intense, relative to the 0.01 wt% PAA solution.

In the 0.20 wt% PAA solution the effect of the fluid history starts to affect the wake flow pattern. For the first bubble there is no coloured liquid in the wake. For the following bubbles a central upward-flowing liquid is seen, surrounded by a waving skirt, shorter than in the previous PAA solutions (around $1.4D$ in length). The central coloured liquid is seen moving upwards even at $4D$ from the bubble trailing edge. The bubble trailing edge presents a more stable behaviour than in the previous solutions.

In the more concentrated solutions no coloured liquid is seen in the wake. The 0.30 and 0.40 wt% PAA solutions present similar behaviour, with some instabilities in the trailing edge. The movement of small bubbles in the wake indicate the presence of recirculation regions at a certain distance from the bubble trailing edge.

The Taylor bubbles rising in the 0.80 wt% CMC solution show a drastic change in the bubble trailing edge shape. If there is enough time between two bubbles for the liquid to recover the initial viscosity, the bubble trailing edge becomes a lachrymal shape similar to that observed in the 1.00 wt% CMC solution. When the liquid is left resting for less time, the shape is similar to that observed in the 0.80 wt% CMC solution.

After these visualisation studies it was decided to use PIV to analyse the flow field around Taylor bubbles rising in all the solutions visualised except the 0.05 and 0.30 wt% PAA solutions due to lack of time. The rheological characterisation of the solutions studied with PIV is presented in the next section.

4.2 Rheological characterisation of PAA solutions

The rheological characterisation of the PAA polymer solutions used in the PIV measurements was made with in an AR 2000 DTA Instruments Rheometer, following the same procedure used in the CMC solutions. The PAA solutions studied are also non-Newtonian fluids, with a highly shear thinning viscosity and higher elasticity than the CMC solutions.

The viscosity of the different PAA solutions as a function of the shear rate is represented in Figure 4.19. In this figure the 1.00 wt% CMC solution viscosity is also represented, for a better comparison between the different polymers rheology. From this figure it is seen

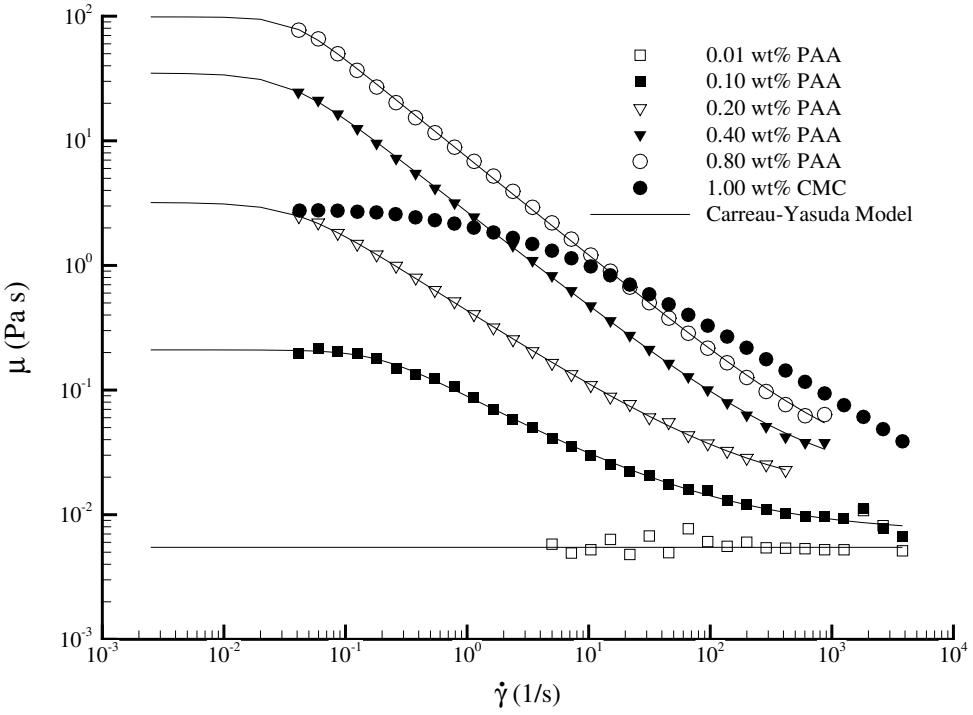

Figure 4.19. Representation of the shear viscosity, μ, as a function of the shear rate, $\dot{\gamma}$, for the PAA solutions studied with PIV/ST.

that the shear thinning behaviour is more pronounced in the PAA solutions, and for the same weight percentages the PAA solutions are more viscous than the CMC solutions, at least for low shear rates. In all the CMC solutions there was a tendency for a constant viscosity at low shear rates. In the PAA solutions, this tendency is only seen in the 0.10 wt% PAA solution. For the less concentrated solution, 0.01 wt% PAA, the viscosity is very low and there is some scattering in the viscosity values since they are close to the measurement uncertainty. In the more concentrated solutions there is no clear tendency for a constant viscosity, which means that the predictions of the Carreau-Yasuda model are only valid in the measured range. The extrapolated viscosity values for low shear rates might be deviated from the real values, affecting the theoretical results as will be seen in a subsequent section.

The values of the Carreau-Yasuda model parameters are listed in Table 4.2 for the PAA solutions studied. The low shear rate viscosities, μ_0, are clearly higher than in the corresponding weight percentages of CMC solutions. Another visible difference is the

Table 4.2. Carreau-Yasuda viscosity model parameters for the PAA solutions.

PAA wt%	$T(^oC)$	μ_0 (Pa s)	μ_∞(Pa s)	λ (s)	a_1	a_2	$\dot{\gamma}(s^{-1})$
0.01	21.4	0.006	0.006	-	-	-	5–3800
0.10	19.8	0.210	0.007	5.321	2.007	0.464	0.04–3800
0.20	20.9	3.201	0.013	24.991	1.795	0.372	0.04–4200
0.40	22.6	34.961	0.018	29.039	1.938	0.237	0.04– 900
0.80	21.7	98.727	0.019	26.698	2.826	0.210	0.04–900

magnitude of the parameter λ, which according to some authors (Bird *et al.* (1987)) is related with the relaxation time of the fluids, which is much higher in the PAA solutions.

The first normal stress difference is represented in Figure 4.20 for the PAA solutions with measurable values. The first normal stress difference for the 1.00 wt% CMC solution is also represented for a better comparison between both polymers. In the PAA solutions a steeper variation of the normal stress difference with increasing shear rate is visible. For the higher shear rate values the normal stress difference is higher for the PAA solutions, while for low shear stresses the opposite occurs.

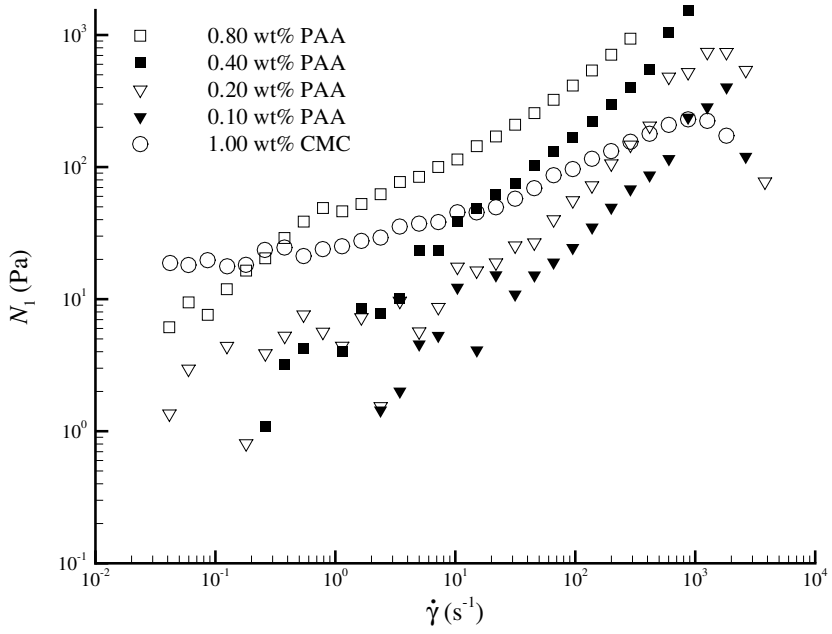

Figure 4.20. First normal stress difference as a function of the shear rate for the PAA solutions.

An attempt was made to determine the relaxation times according to the methodology used in the CMC solutions. The relaxation times are, however, strongly dependent on the shear rate interval. It is known that non-Newtonian liquids can have a spectrum of relaxation times. For the 0.80 wt% PAA solution a maximum relaxation time of around 28 s was found, while for the 0.40 wt% PAA and 0.20 wt% PAA solutions times of around 0.8 s and 2.3 s respectively were found. While the relaxation time for the 0.80 wt% PAA solution is similar to the λ value of the Carreau-Yasuda model, the experimental study on the bubble velocity (Figure 4.2) shows that the fluid needs a much longer time to recover its initial viscosity. A longer relaxation time for the 0.40 wt% PAA than for the 0.20 wt% PAA solution was also expected. This led to undertaking some additional tests in order to obtain values with more physical meaning.

In the rheometer the fluids were initially subject to a high shear rate for twenty seconds, followed by a very low shear rate until stabilisation of the viscosity. In Figure 4.21, the dimensionless viscosity variation with time is represented for the 0.80 wt% PAA solution. In this plot, $t = 0$ is the instant where the shear rate changed from $1000\,\mathrm{s}^{-1}$ to $0.02\,\mathrm{s}^{-1}$.

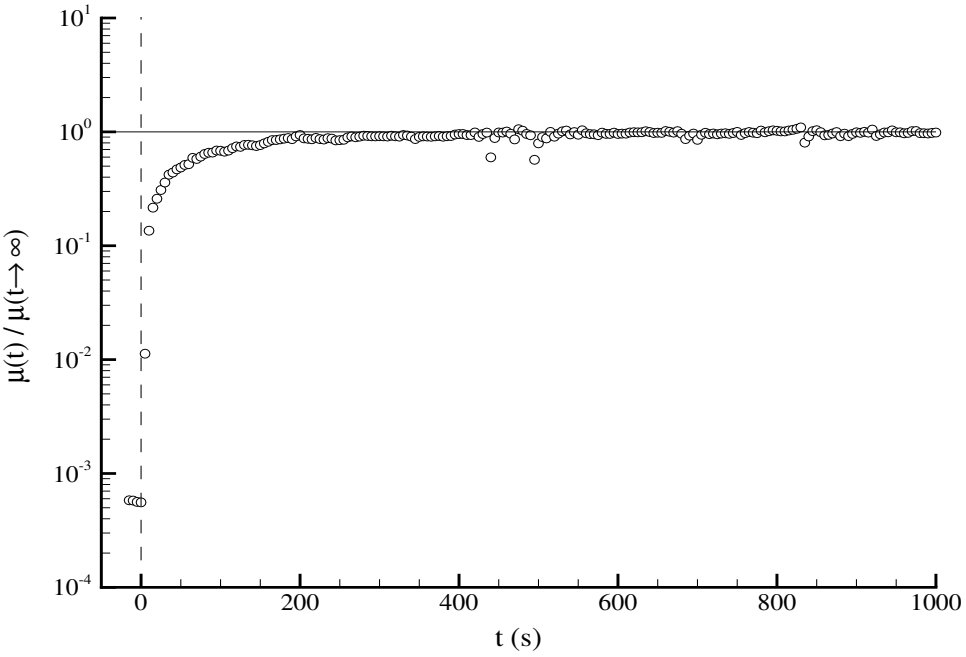

Figure 4.21. Variation of the 0.80 wt% PAA solution viscosity with time at $\dot{\gamma} = 0.02\,\mathrm{s}^{-1}$, after 20 seconds at $\dot{\gamma} = 1000\,\mathrm{s}^{-1}$.

This figure shows that the liquid viscosity varies asymptotically, reaching its maximum only about 500 s after the step decrease of the shear rate. In the test the low shear rate was set at $0.02\,s^{-1}$, since it was the minimum value at which the shear stresses could be measured. The value 500 s is then a sub-estimated relaxation time of the fluid, since the time for the fluid to completely stagnate might be slightly higher.

The same test was performed for the other PAA solutions. In the 0.10 wt% PAA solution this test was not conclusive, since the fluid reaches the stabilised viscosity in a very short time after the shear rate decrease. The same behaviour was found for the more concentrated solution of CMC polymer, as shown in Figure 4.22. These tests show that

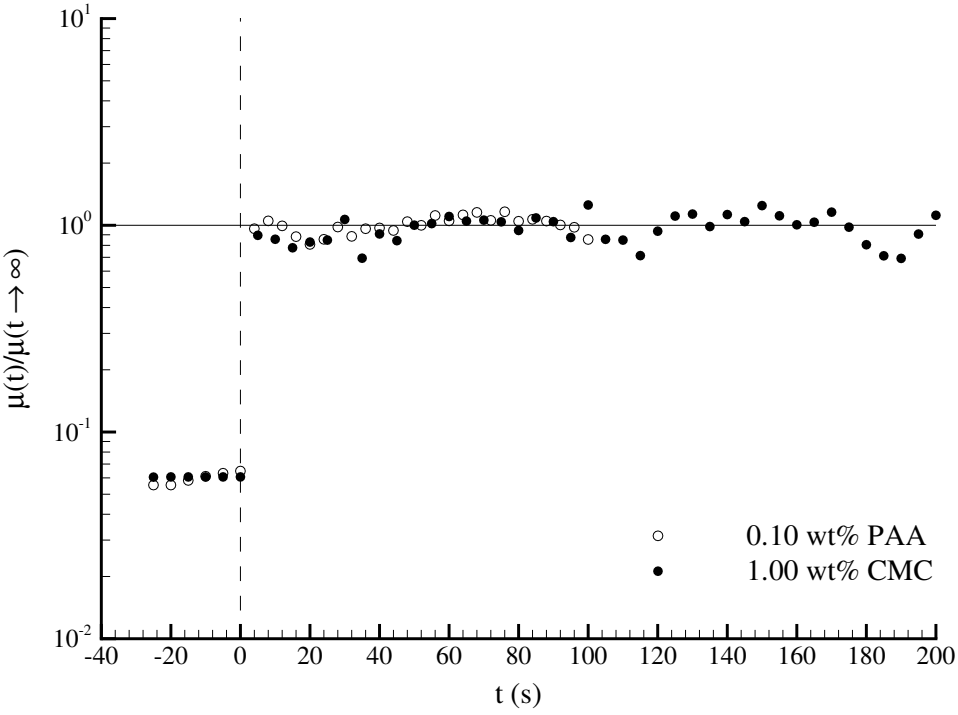

Figure 4.22. Variation of the 0.10 wt% PAA and 1.00 wt% CMC solutions viscosity with time at $\dot{\gamma} = 0.04\,s^{-1}$, after 20 seconds at $\dot{\gamma} = 1000\,s^{-1}$.

for these solutions the relaxation time is very short, at least lower than 5 s (minimum time that the rheometer needs to acquire a value).

The relaxation times of the PAA solutions and the respective Deborah numbers are presented in Table 4.3. The relaxation times of the PAA solutions were determined directly from the viscosity tests, whereas in the CMC solution relaxation times an indirect

Table 4.3. Estimate of relaxation times and Deborah numbers of the PAA solutions from the viscosity tests.

PAA wt%	θ_f (s)	De
0.10	<5	<30
0.20	175	1000
0.40	300	1600
0.80	500	2000

measurement was made. These relaxation times, despite being sub-estimated, are closer to those expected from experiments where the bubble velocity depends markedly on the time between the injection of consecutive bubbles.

The Reynolds number was also determined from the viscosity data using the viscosity at the characteristic flow shear rate, similar to the CMC solutions. The average bubble velocity and the Reynolds number of the flow in the PAA solutions are represented in Table 4.4.

Table 4.4. Average Taylor bubble velocity and flow Reynolds number for the PAA solutions.

PAA wt%	U_b	Re
0.01	0.198	1158
0.10	0.198	162
0.20	0.196	41
0.40	0.171	7
0.80	0.132	2

The rheological characterisation of the PAA solutions showed a steeper variation of the viscosity with shear rate and a higher viscoelasticity, relative to the CMC solutions. The results obtained from the studies of Taylor bubbles rising in these solutions are described in the next sections.

4.3 PIV/ST measurements

The measurements of the flow field around individual Taylor bubbles rising in polyacrylamide (PAA) solutions were performed in the same experimental setup used for the carboxymethylcellulose (CMC) solutions. The experimental procedure and data processing were the same and the results are presented in the same sequence as those of the CMC solutions.

4.3.1 Bubble shape

The Taylor bubble shape was determined from the shadow of the bubbles, as described for the CMC solutions. The shapes of the bubbles rising in the PAA solutions are in general very similar to those found in the CMC solutions. They have a prolate spheroid nose and increasing radius as the distance from the nose tip increases. After a certain distance from the nose, the radius maintains a constant value.

In Figure 4.23, the shapes of the bubbles rising in the lowest and highest PAA concentration solutions are compared with the 0.50 wt% CMC solution bubble shape. This figure

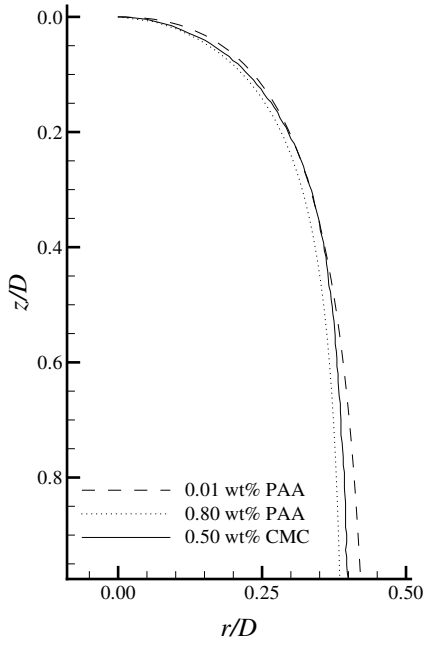

Figure 4.23. Shapes of Taylor bubbles rising in 0.01 and 0.80 wt% PAA solutions in comparison with the shape of bubbles rising in the 0.50 wt% CMC solution.

shows that the shape of the bubbles is very similar, the main difference being the values of the maximum bubble radius.

In the 0.01 wt% PAA solution, stabilisation of the bubble radius was not observed even for the longest bubbles studied ($9.4D$ in length). For the 0.80 wt% PAA solution, after the stabilisation of the bubble radius a slight decrease of its value was observed before the bubble trailing edge. The maximum bubble radius and the distance from the bubble nose at which it is reached are presented in Table 4.5.

Table 4.5. Maximum bubble radius and approximate distance from the bubble nose at which it is reached.

PAA wt%	Re	(r_∞/D)	z_{stable}/D
0.01	1158	>0.461	>10.0
0.10	162	0.450	8.0
0.20	41	0.439	6.0
0.40	7	0.427	4.5
0.80	2	0.396	3.0

The shapes of the Taylor bubbles are well-adjusted by the same type of equation used to describe the CMC bubble shapes, although with different parameters:

$$r/D = k_{\text{p1}} \cdot \tanh(k_{\text{p2}} \cdot (z/D)^{k_{\text{p3}}}) \tag{4.1}$$

The k_{p1} value coincides with the maximum bubble radius and is given by:

$$(r_\infty/D) = k_{\text{p1}} = 0.010 \ln(Re) + 0.400 \tag{4.2}$$

The values of k_{p2} and k_{p3} were obtained by fitting the bubble shape to equation 4.1 and they are function of Reynolds number according to equations 4.3 and 4.4 respectively.

$$k_{\text{p2}} = 2.228 \cdot Re^{-0.056} \tag{4.3}$$

$$k_{\text{p3}} = 0.554 \cdot Re^{-0.035} \tag{4.4}$$

The shape of the bubbles, obtained from equation 4.1 in the form of the bubble radius as a function of the distance to the nose, differs less than 5% from the experimental data.

4.3.2 Bubble velocity and length

In the visualisation studies, it was noticed that the bubble velocity depends on the fluid history. Figure 4.24 represents the bubble velocity and the dimensionless length of all the Taylor bubbles studied in the PIV/ST measurements with PAA solutions. The effect of the bubble length on the bubble expansion and consequently on the bubble velocity was already analysed in the CMC solutions, therefore in the PAA solutions the study is only focused on two bubble lengths.

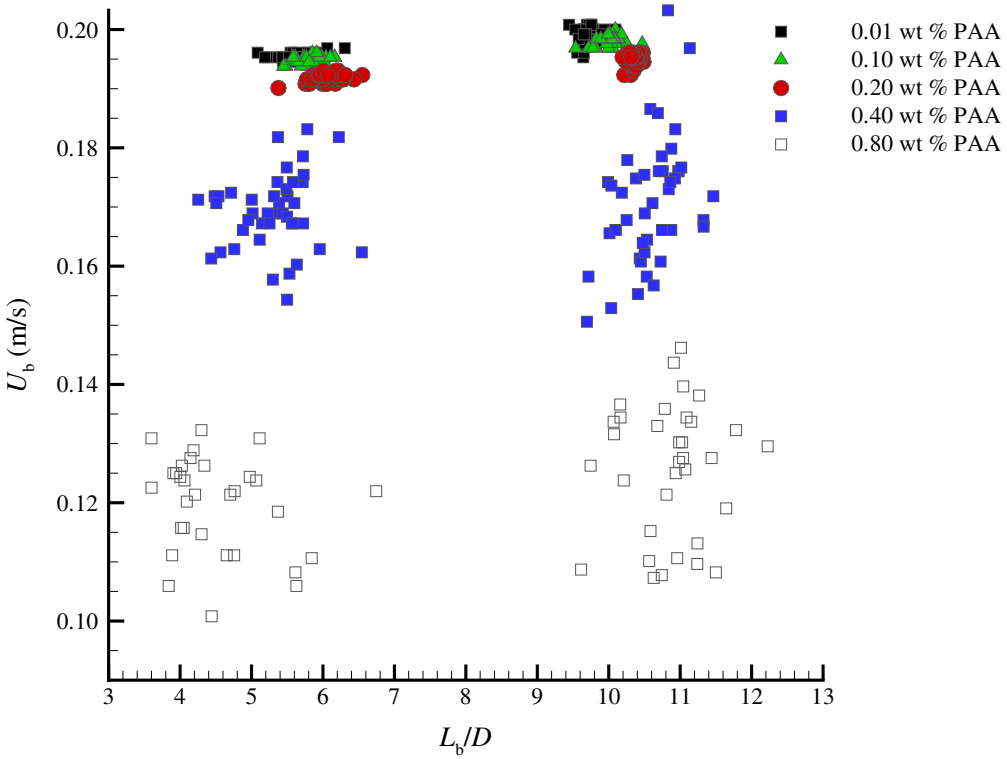

Figure 4.24. Taylor bubble velocity, U_b, as a function of the dimensionless bubble length, L_b/D, in the PIV/ST measurements in PAA solutions.

Figure 4.24 shows, as expected, that the bubble expansion is responsible for a slight increase of the bubble velocity with the bubble length. A large spread in the bubble velocity data for concentrations above 0.20 wt% PAA can also be seen. The time between bubbles injection was approximately the same (around 2 minutes), but it was not enough to assure an equal fluid history for every bubble. To analyse the effect of the fluid history in detail, a deeper study should be made with a larger number of bubbles. To assure

identical fluid history, the time between bubbles should be higher than those observed in the viscosity recovering tests presented in the rheological characterisation of the fluids. In the experiments performed, the statistical description of the flow in relation to the average velocity profiles in the liquid film and in the wake can only be done for solutions up to 0.20 wt% PAA concentration.

For the 0.40 and 0.80 wt% PAA solutions some differences were found relative to the visualisation studies. A clear asymmetry was noticed in the flow around the Taylor bubbles, especially for the 0.80 wt% PAA solution where not only did the liquid film present a different thickness in the left and right sides of the bubble (projection in the paper plane) but the bubble shape projection itself was asymmetric. This fact might be justified by a lower experimental temperature relative to the visualisation studies, which increases the liquid viscosity and also a possible non-homogeneity of the solutions. A larger solution volume is needed for the PIV measurements and despite being stirred for 24 hours, it is not guaranteed that the solutions were completely homogeneous due to their high viscosity and elasticity. Nevertheless, a qualitative description of the flow for the more concentrated solutions is made when possible.

4.3.3 Flow ahead of Taylor bubble

Since the column was open to the atmosphere on top the bubble expansion during the rise in the column caused a movement of the liquid ahead of the bubble, as described for the CMC solutions. In the PAA solutions the behaviour is very similar, despite a stronger effect of the viscoelastic properties on the velocity profiles.

In Figure 4.25, two velocity fields ahead of Taylor bubbles rising in 0.10 and 0.80 wt% PAA solutions are represented. From this figure it is clear that, apart from the different velocity magnitudes, there is also a difference in the velocity profiles shape. In the 0.80 wt% PAA solution, the velocity profile is practically flattened around the axis of the column, contrasting with the parabolic profile of the lower concentration solution. This fact is related with the strong reduction of viscosity with shear rate, even for low shear rates.

As explained in §3.3.3, longer Taylor bubbles have a higher volume expansion rate, inducing a higher liquid flow rate ahead of them. In Figure 4.26, the average velocity profiles ahead of Taylor bubbles with $4.2D$ and $10.8D$ length rising in a 0.80 wt% PAA solution are represented.

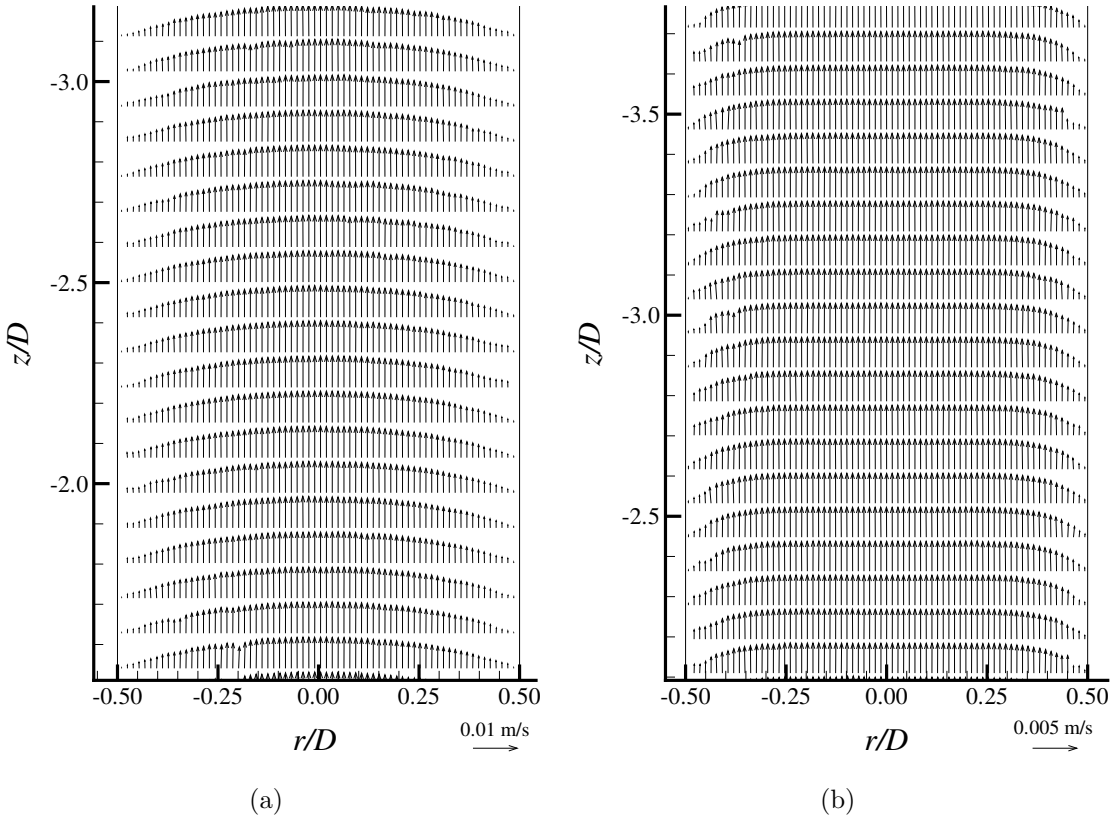

Figure 4.25. Example of flow fields ahead of Taylor bubbles rising in (a) 0.10 wt% PAA and (b) 0.80 wt% PAA solutions.

In the CMC solutions, the dimensionless velocity profiles ahead of the Taylor bubbles were very close to the laminar Newtonian behaviour for all the solutions studied. In the PAA solutions this was not the case. As shown in Figure 4.25, for increasing PAA wt%, the velocity profile is no longer close to the laminar Newtonian behaviour, becoming flat in the central region. Due to the stronger dependence of the viscosity on the shear rate, even for the same solution (at high concentrations), some shape differences are found between the dimensionless velocity profiles ahead of bubbles of different sizes.

The dimensionless velocity profile ahead of the longer bubbles rising in each solution are represented in Figure 4.27. As seen from the plot, above the 0.10 wt% PAA concentration the dimensionless velocity profiles are no longer similar to the laminar Newtonian case. These velocity profiles can be theoretically predicted by knowing the fluid rheology.

Assuming that the flow is driven by a pressure difference that is balanced by the weight

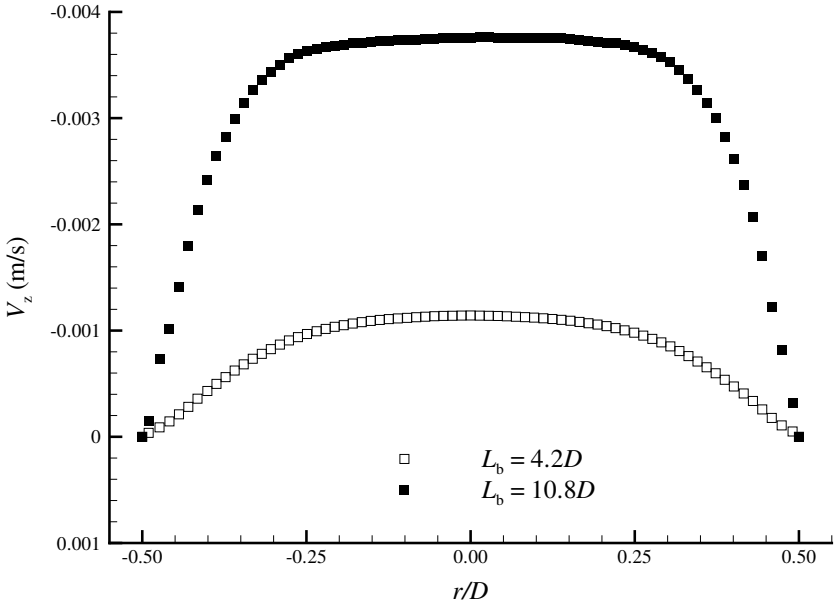

Figure 4.26. Average flow rates ahead of bubbles with $4.2D$ and $10.8D$ in length rising in a 0.80 wt% PAA solution.

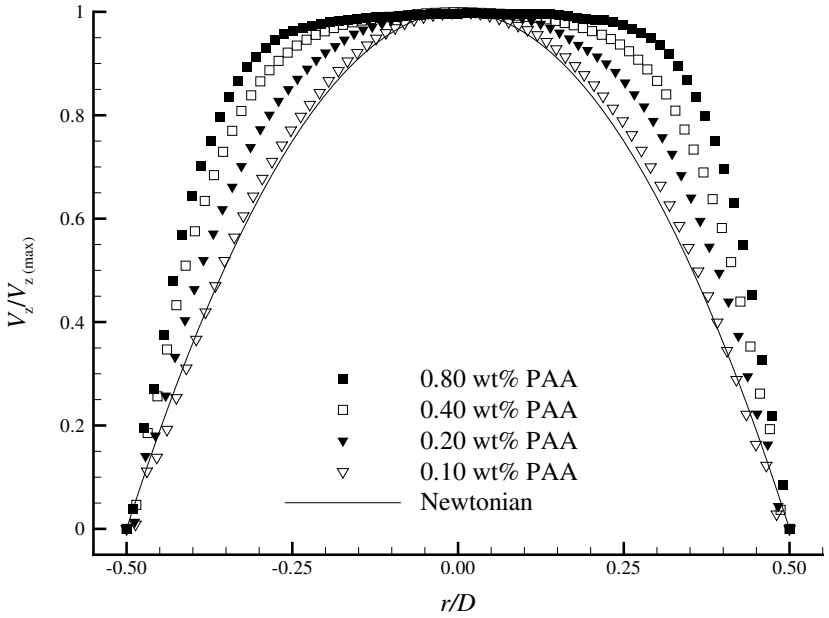

Figure 4.27. Dimensionless velocity profiles ahead of Taylor bubbles rising in PAA solutions.

of the liquid and the shear stress, the following momentum equation is found:

$$\frac{\partial(\tau r)}{\partial r} = \left(\frac{\partial P}{\partial z} - \rho g\right) r \tag{4.5}$$

Integrating equation 4.5 with the boundary condition $\tau = 0$ at $r = 0$, the shear stress profile is given by

$$\tau = \left(\frac{\partial P}{\partial z} - \rho g\right) \frac{r^2}{2} \tag{4.6}$$

For the shear stresses, the correspondent shear rate profile is obtained from the rheological data with the following equation:

$$\tau = \mu(\dot{\gamma}) \cdot \dot{\gamma} \tag{4.7}$$

Depending on the viscosity model used, the shear rate can be determined explicitly or equation 4.7 must be solved numerically.

Finally, the velocity profile is obtained from:

$$\frac{\partial V_z}{\partial r} = -\dot{\gamma}(r) \tag{4.8}$$

by integrating between $r = 0$ and $r = R$, with the boundary condition $V_z = 0$ at $r = R$.

In Figure 4.28, the theoretical velocity profiles ahead of the bubble are compared with the experimental ones. From this figure, it is observed that the theoretical velocity profiles follow the tendency for flattening as the viscosity increases, although they do not exactly match the experimental ones.

The theoretical velocity profiles were obtained from equations 4.5–4.8 using the Carreau-Yasuda model for the viscosity. As mentioned in §4.2, for the PAA rheological data there is no defined tendency for the low shear rates viscosity as was observed for the CMC solutions. In the velocity profiles ahead of the Taylor bubbles the shear rates are very low, as shown in Figure 4.29 for the 0.80 wt%, for example. The maximum shear rate at the wall is between 1 and $2\,s^{-1}$ for all the solutions, with a fast decrease towards the axis of the column to around zero in the central region. To show the importance of the viscosity at low shear rates, Figure 4.30 represents, as an example, the theoretical velocity profiles for a 0.80 wt% PAA solution, determined using both the Carreau-Yasuda and the Power Law models. Both models adjust well to the viscosity in the measured range. The difference is

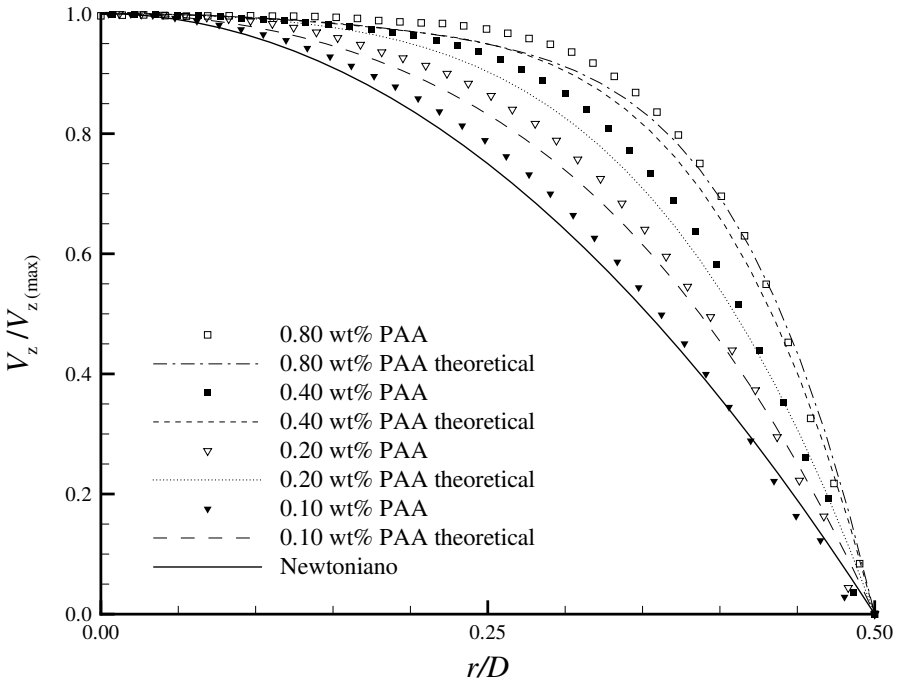

Figure 4.28. Comparison between experimental and theoretical velocity profiles ahead of Taylor bubbles rising in PAA solutions.

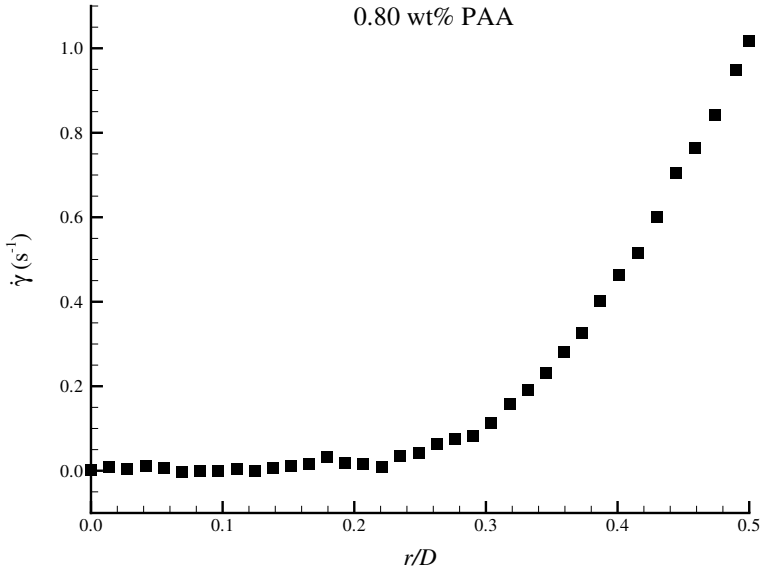

Figure 4.29. Shear rate profile ahead of a Taylor bubble rising in a 0.80 wt% PAA solution.

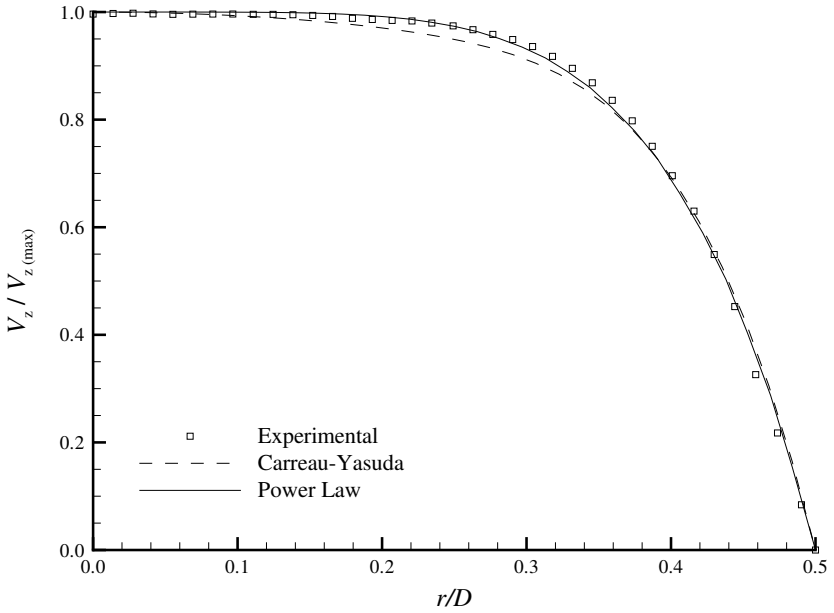

Figure 4.30. Theoretical velocity profiles ahead of a Taylor bubble rising in a 0.80 wt% PAA solution determined from different viscosity models.

in the extrapolation of the viscosity at low shear rates, as shown in Figure 4.31. While in the Carreau-Yasuda model the viscosity tends towards a constant value at low shear rates, in the Power Law model the viscosity continues increasing with decreasing shear rate.

As seen in the example of Figure 4.30, this difference in the prediction of the low shear rate viscosity affects the determination of the theoretical velocity profile. In the 0.80 wt% PAA solution, the Power Law model seems more adequate to predict the low shear rate velocity profiles than the Carreau-Yasuda model. However, this is not the case for the lower viscosity solutions. Whether the observed differences between the theoretical and experimental velocity profiles are due to the rheological properties of the liquids at low shear rates or not can only be checked with a different sensitivity rheometer.

Despite the different liquid velocity profiles ahead of the Taylor bubbles, when the maximum liquid velocity ahead of the bubble is subtracted from the bubble velocity the result is a size independent bubble velocity. For the more concentrated solutions this result is not so clear due to the high data scattering related to the fluid history, as shown in Figure 4.32.

Even with the bubble velocity dependence on the fluid history for the more concentrated

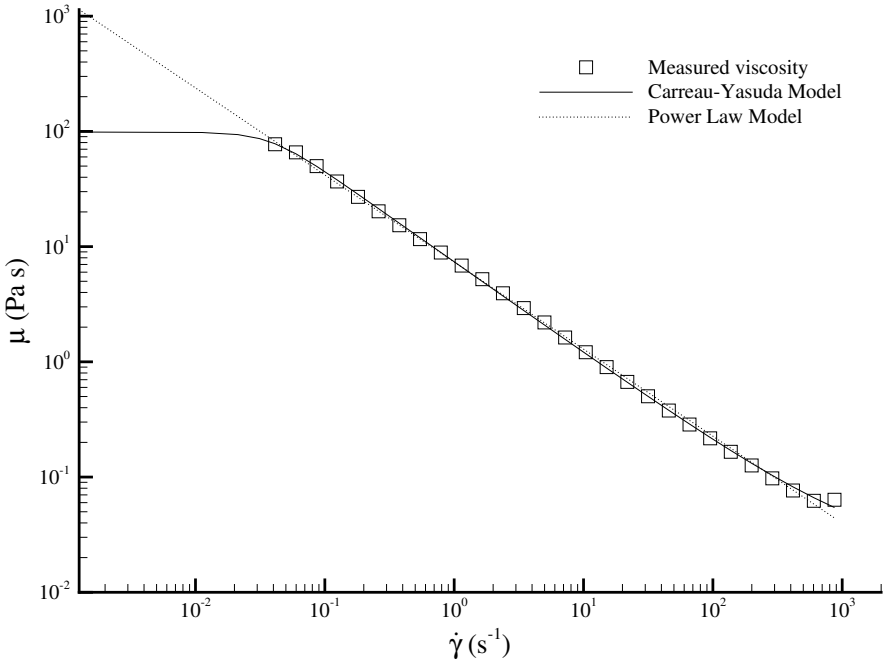

Figure 4.31. Viscosity of the 0.80 wt% PAA solution and viscosity models fitting.

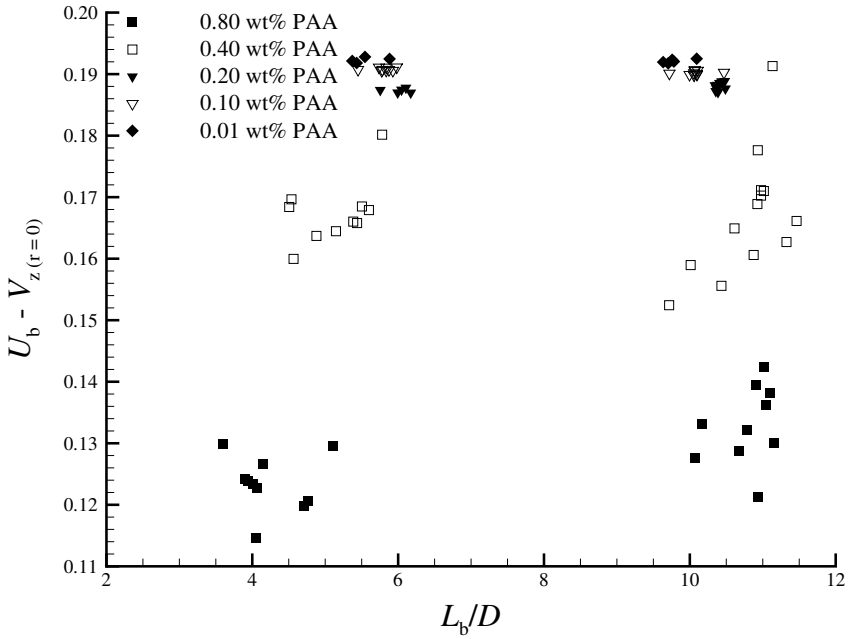

Figure 4.32. Representation of the bubble velocity subtracted by the liquid velocity far ahead from the bubble at $r = 0$ as a function of the dimensionless bubble length for bubbles rising in PAA solutions.

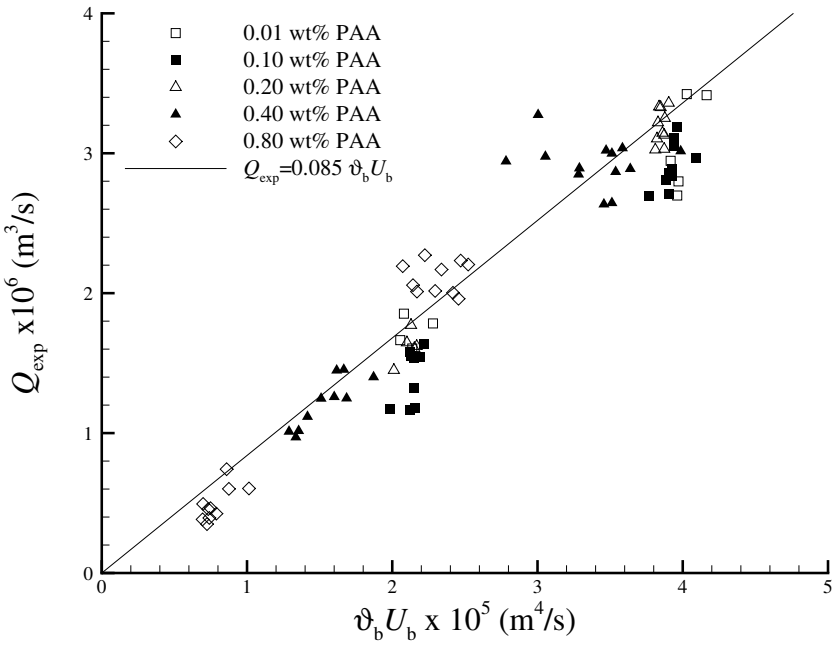

Figure 4.33. Experimental liquid flow rates ahead of the Taylor bubbles, as a function of $\vartheta_b \cdot U_\mathrm{b}$.

solutions, the relation between the liquid flow rate ahead of the bubble and the bubble volume is still valid. In Figure 4.33, the liquid flow rates ahead of the bubble are plotted against $\vartheta_\mathrm{b} \cdot U_\mathrm{b}$.

As shown in §3.3.3, the relation should be linear and with a constant of proportionality given by $(\rho g)/(P_{atm} + \rho g h) = 0.085\,\mathrm{m}^{-1}$, which is represented by a line in Figure 4.33. As this figure shows, the experimental results are in good agreement with the expected values.

4.3.4 Flow around the nose of Taylor bubble

The flow around the Taylor bubble nose presents no significant differences relative to that described for the CMC solutions. In Figure 4.34, the velocity fields around the nose of Taylor bubbles rising in 0.01 and 0.80 wt% PAA solutions are represented. As can be seen from these diagrams, the flow pattern around the nose of Taylor bubbles rising in different PAA solutions is qualitatively the same. There are only small differences in the bubble shape and velocity magnitudes. To illustrate the similar behaviour even in the limit viscosities, the dimensionless axial and radial velocity profiles at $z = 0$ are presented in Figures 4.35 and 4.36 respectively, and compared with those found in the 0.10 wt% CMC

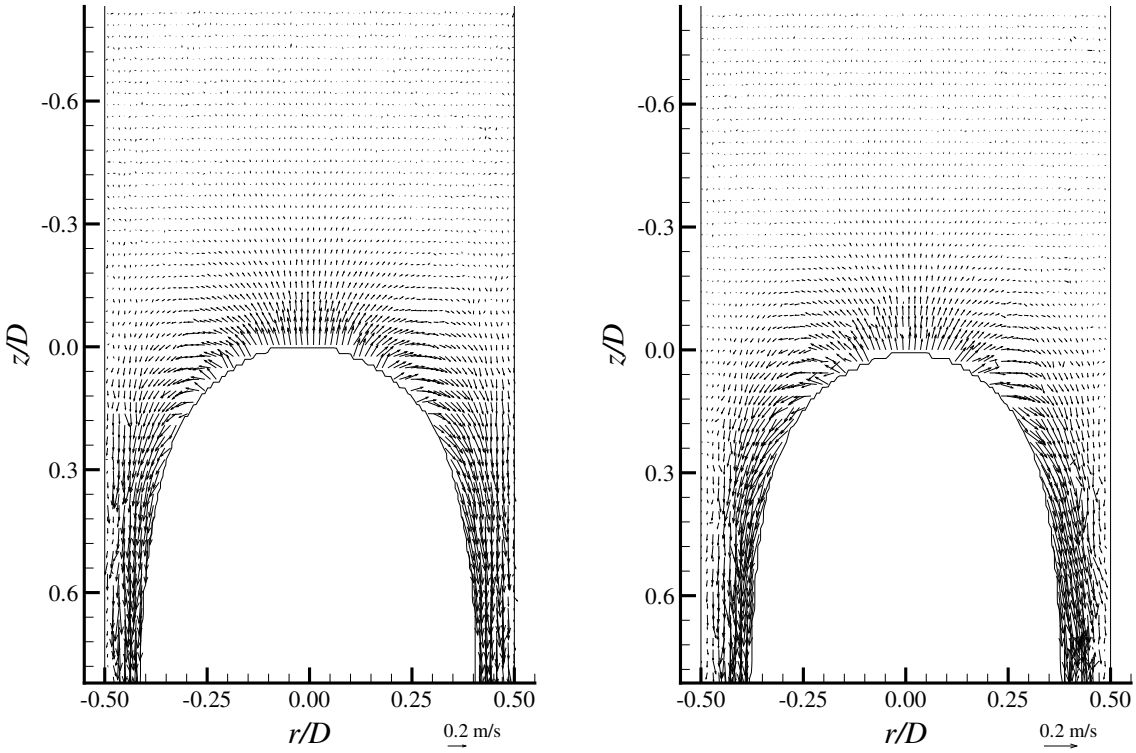

Figure 4.34. Flow fields around the nose of Taylor bubbles rising in (a) 0.01 wt% PAA and (b) 0.80 wt% PAA solutions, in a fixed frame of reference.

solution.

The distance for which the flow is disturbed by the passage of the bubble is also similar to that found in the CMC solutions. Figure 4.37 shows the dimensionless axial velocity profile at $r/D = 0$, ahead of bubbles rising in 0.01 and 0.80 wt% PAA solutions. From this figure it can be seen that the liquid starts to be disturbed by the bubble passage at around $0.7D$ ahead of the bubble nose.

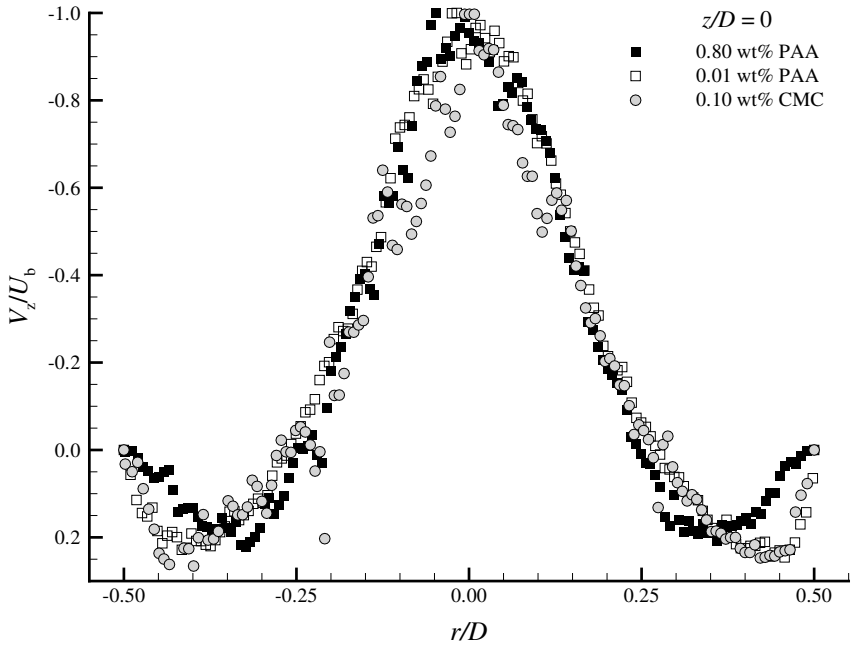

Figure 4.35. Axial dimensionless velocity profile at $z = 0$ for bubbles rising in 0.01 and 0.80 wt% PAA and 0.10 wt% CMC solutions.

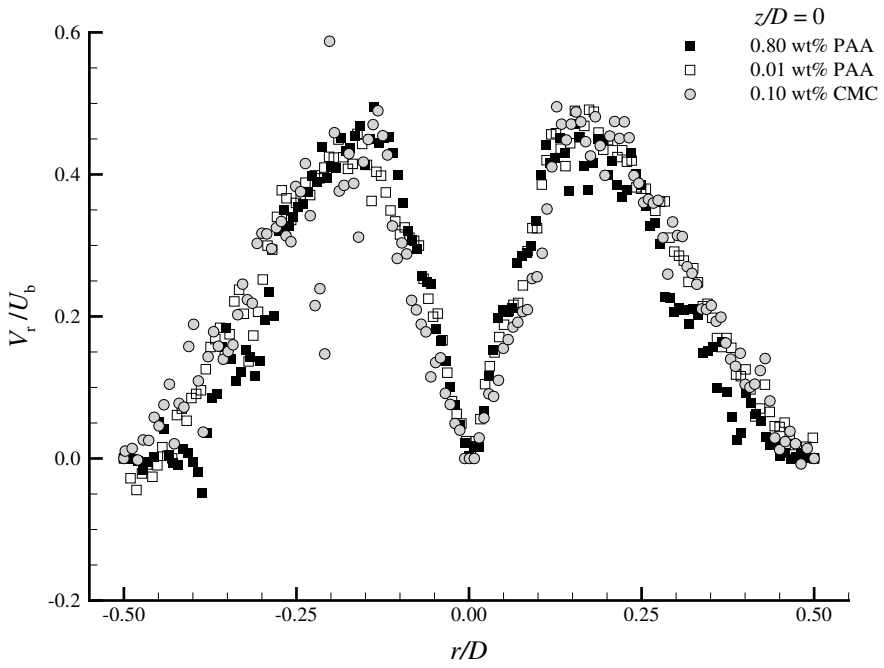

Figure 4.36. Radial dimensionless velocity profile at $z = 0$ for bubbles rising in 0.01 and 0.80 wt% PAA and 0.10 wt% CMC solutions.

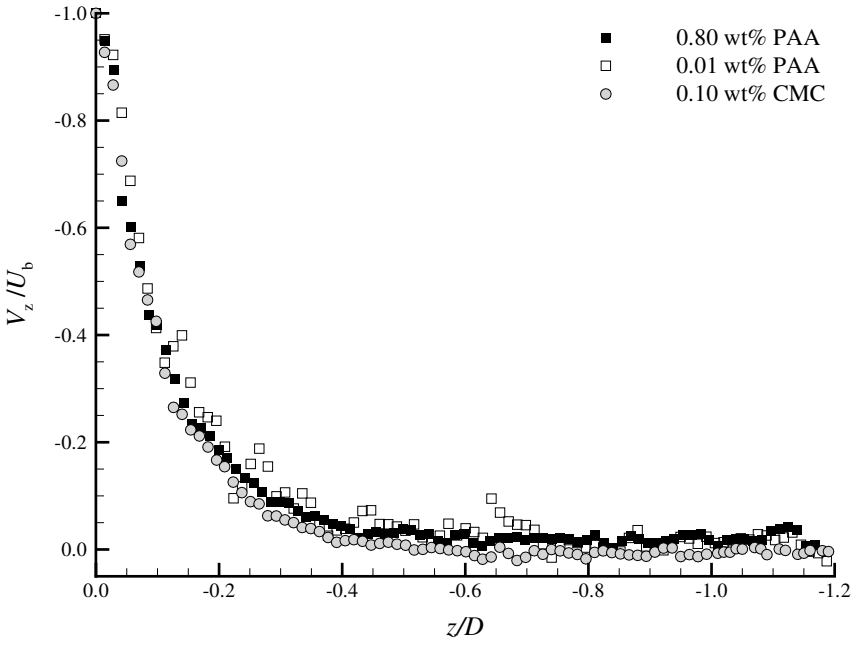

Figure 4.37. Axial dimensionless velocity profile at $r/D = 0$ ahead of bubbles rising in 0.01 and 0.80 wt% PAA solutions.

4.3.5 Liquid film

The liquid film was only analysed for the solutions up to a concentration of 0.20 wt% PAA. As mentioned in §4.3.2, for the 0.40 and 0.80 wt% PAA solutions the bubble velocity, and therefore the liquid film velocity, is very dependent on the fluid history and a study on a larger number of bubbles within the same conditions should be performed.

The liquid film analysis was performed with the longer bubbles studied for each solution in order to have fully-developed velocity profiles. No instabilities were found in the liquid film. The average length and velocity of the bubbles studied are presented in Table 4.6.

Table 4.6. Average length and velocity of the bubbles rising in PAA solutions in which the liquid film was analysed.

PAA wt%	L_b/D	U_b (m/s)
0.01	9.6	0.198
0.10	10.0	0.198
0.20	10.3	0.196

As described in §3.3.5, a study was performed to find the distance from the bubble nose at which the liquid film velocity profile stabilises. In Figure 4.38, the axial velocity at a fixed radial position versus the distance to the bubble nose is plotted for the 0.01 wt% PAA solution. It is observed that in this solution, as expected from the bubble shape, the liquid film around the Taylor bubbles does not stabilise even for the longest bubbles studied. The velocity keeps increasing up to the end of the liquid film and a higher bubble volume was needed to have a stabilised film. Higher bubble volumes were not possible with the available experimental setup. The same analysis was made for the 0.10 and 0.20 wt% PAA solutions, which are presented in Figures 4.39 and 4.40 respectively.

In the 0.10 and 0.20 wt% PAA solutions, the liquid film velocity increases up to the distance at which the bubble radius stabilises. The approximate axial distances to the nose at which the liquid film stabilises are presented in Table 4.7.

The average developed velocity profiles between z_{stable} and the end of the liquid film were determined for the 0.10 and 0.20 wt% PAA solutions. The film thicknesses are 1.8 and 1.9 mm respectively, which are in the range between the values found for the 0.10 and 0.30 wt% CMC solutions.

The average developed liquid film profiles were determined from more than 600 individual velocity profiles. The standard deviations of the window displacement were between

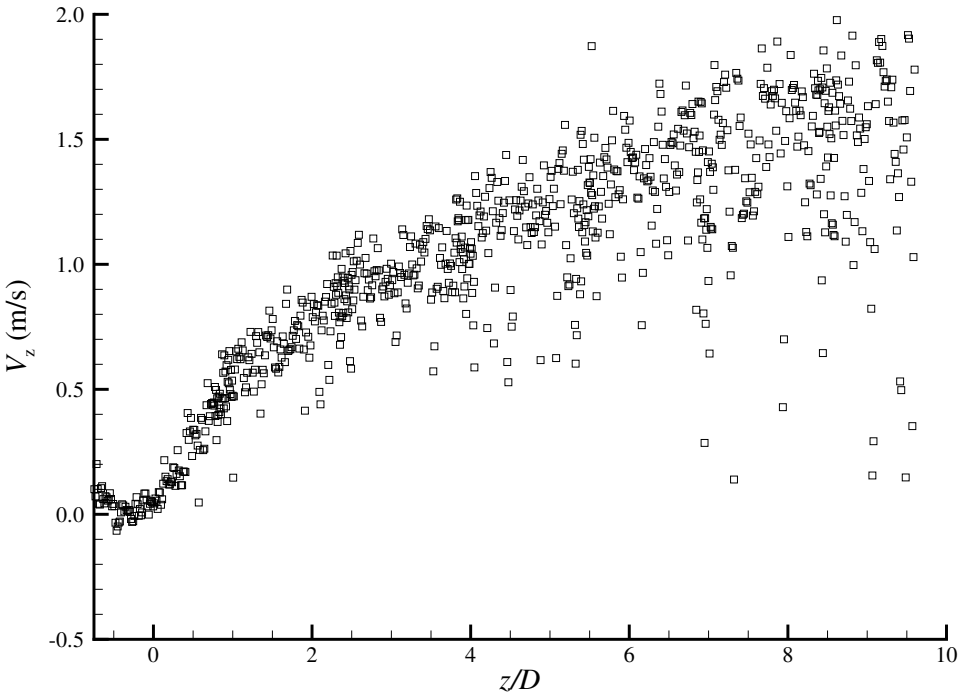

Figure 4.38. Axial velocity at $r/D = 0.47$ versus the distance to the bubble nose, for the 0.01 wt% PAA solution.

Table 4.7. Approximate distance to the bubble nose from which the liquid film is fully developed, z_{stable}, for the PAA solutions.

PAA wt%	z_{stable}/D
0.01	>10
0.10	8.0
0.20	6.0

0.8 and 1.0 pixels (corresponding to about 15% of the liquid velocity), on the same order of the data scattering found in the CMC film velocity profiles. These profiles are represented in Figure 4.41. As explained in §3.3.5, a mask with null velocity was used in the column wall, and another in the bubble interface with the maximum liquid film velocity. As expected, for the less concentrated solutions the velocities are higher and the liquid film is thinner.

The same mass balance performed in the CMC solutions was made for the PAA solutions, to compare the flow rates ahead of the bubble (Q_{A}) and in the liquid film (Q_{B}) in

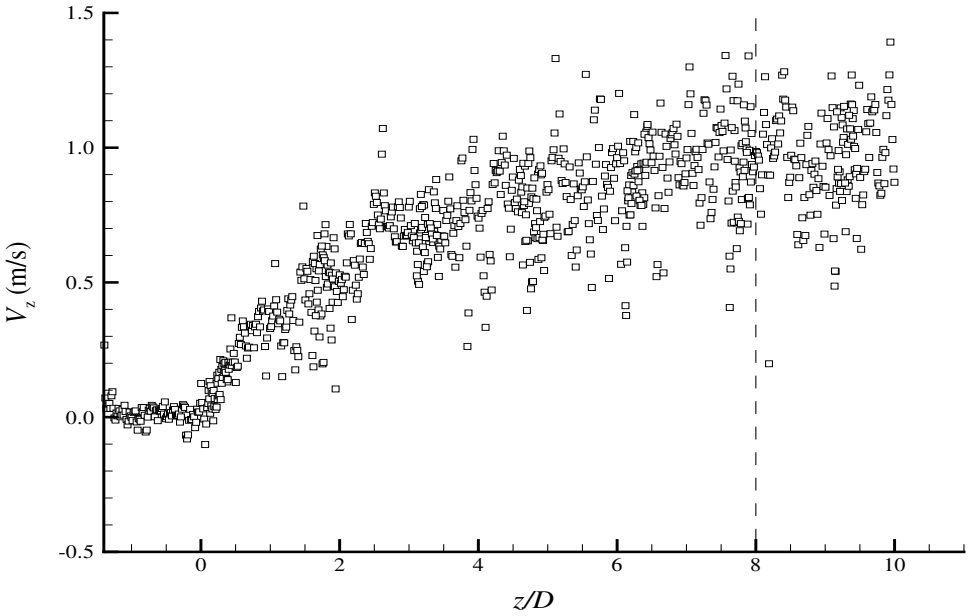

Figure 4.39. Axial velocity at $r/D = 0.47$ versus the distance to the bubble nose, for the 0.10 wt% PAA solution.

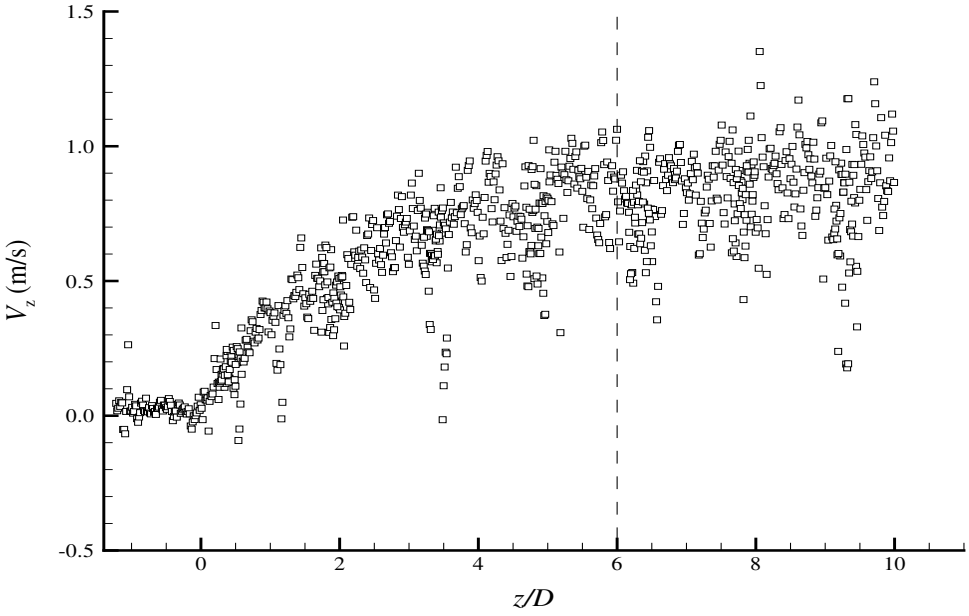

Figure 4.40. Axial velocity at $r/D = 0.47$ versus the distance to the bubble nose, for the 0.20 wt% PAA solution.

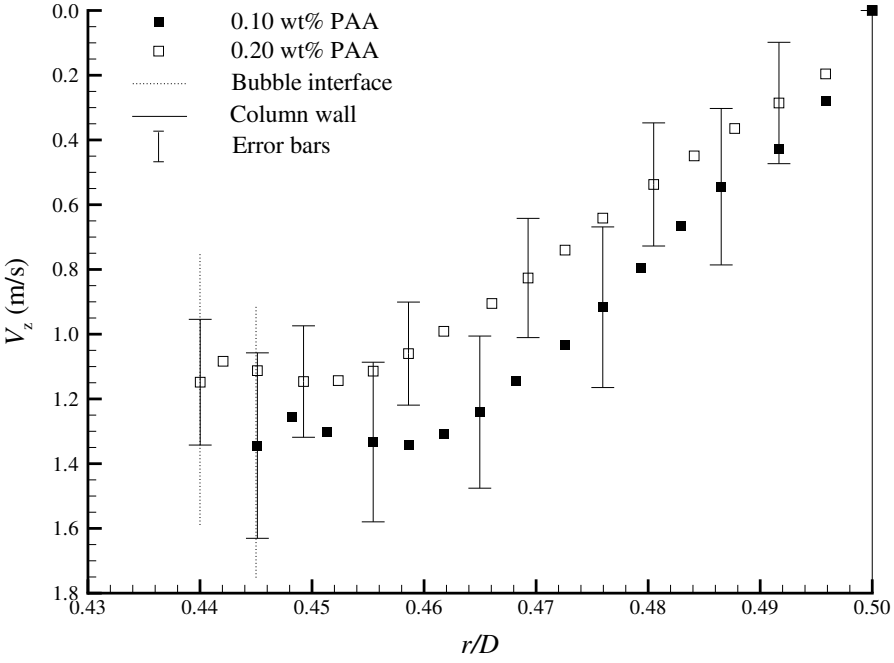

Figure 4.41. Average developed velocity profiles around the Taylor bubbles rising in the 0.10 and 0.20 wt% PAA solutions.

a frame of reference moving with the bubble (equations 3.15 and 3.16). In Table 4.8 the average flow rates for each solution and the respective difference in percentages are presented. As seen from the values in this table, the differences between Q_A and Q_B are higher

Table 4.8. Comparison between flow rates ahead of the bubble (Q_A) and in the liquid film (Q_B) in a frame of reference moving with the bubble.

PAA wt%	$Q_A \times 10^4 (m^3/s)$	$Q_B \times 10^4 (m^3/s)$	$(Q_B - Q_A)/Q_A\%$
0.10	1.56	1.83	14.6
0.20	1.55	1.68	7.8

than those in the CMC solutions. The most probable reason is a deviation of the column vertical alignment. A slight deviation causes an asymmetric flow around the bubble, but in the integration of the average liquid film profile a symmetric flow is assumed.

Since the experimental film flow rates are higher than expected a deviation from the theoretical ones should be observed. In Figure 4.42 the theoretical film velocity profiles determined from equations 3.17–3.20 are compared with the experimental ones. As seen

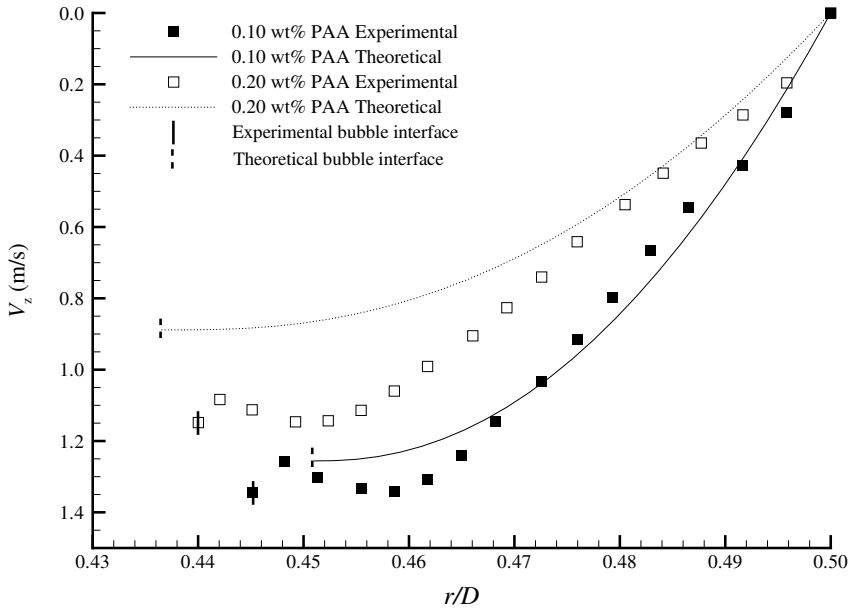

Figure 4.42. Comparison between experimental and theoretical film velocity profiles around bubbles rising in 0.10 and 0.20 wt% PAA solutions.

from this figure, the theoretical velocity profile for the 0.10 wt% PAA solution is very close to the experimental one, apart from a different film thickness. In the 0.20 wt% PAA film velocity profile, the difference is not only in the film thickness but also in the velocity magnitude.

To show the effect of the fluid history on the liquid film around bubbles rising in the 0.40 and 0.80 wt% PAA solutions, two average velocity profiles in bubbles of the same length rising in 0.40 wt% PAA solution are represented in Figure 4.43. This figure shows that, despite having the same length, due to different fluid history the bubbles have a different velocity, which affects the velocity profile in the liquid film. As seen from the plot in Figure 4.43, the higher velocity bubble presents higher liquid velocities in the film. A difference between the flow rates Q_A (eq.3.15) and Q_B (eq.3.16) in the order of 10% was once more observed, confirming that the column could not be perfectly vertical. In the 0.80 wt% PAA solution, not only was the bubble velocity more dependent on the fluid history but a clear asymmetry was observed between the film thickness on opposite sides of the bubble (paper plane), as is shown in Figure 4.44. The fact that the asymmetry has no preferential side indicates that this bubble behaviour could be related with the fluid

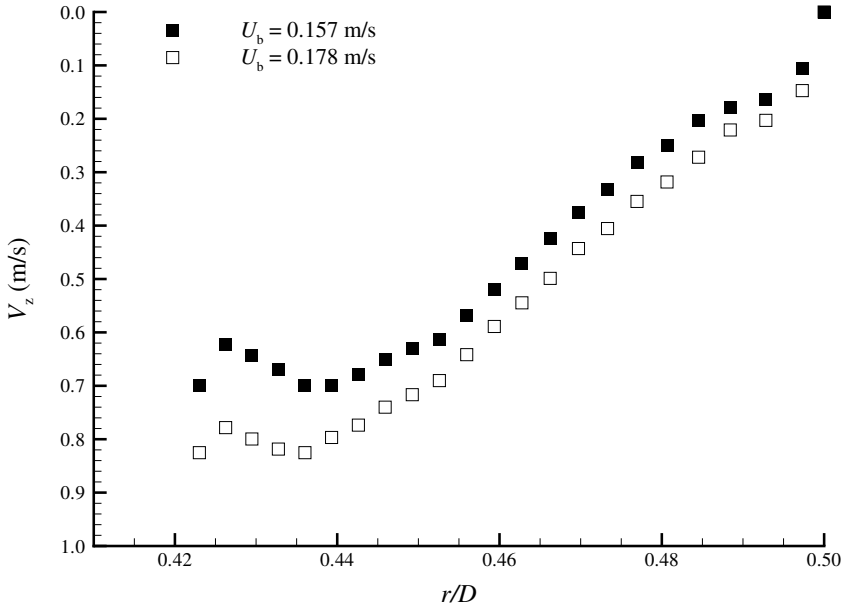

Figure 4.43. Average liquid film velocity profile around two bubbles with a 10.4D length rising in 0.40 wt% PAA solution.

history, since a non-homogeneous viscosity field might be created after the passage of the bubbles.

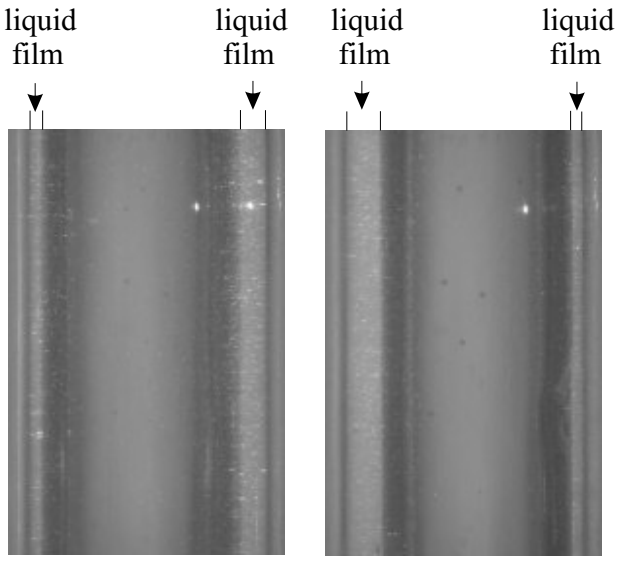

Figure 4.44. Asymmetric flow around two different Taylor bubbles rising in 0.80 wt% PAA solution.

4.3.6 Bubble wake

As seen from the CMC results, the flow around the nose and in the liquid film is very similar between the different solutions, despite some differences in velocity magnitudes. The ultimate objective of this investigation is the coalescence phenomena between Taylor bubbles rising in non-Newtonian liquids, and for this end the feature of most interest is the flow pattern in the wake of bubbles rising in different solutions.

The visualisation studies with PAA polymer solutions already showed a different flow pattern from those observed in the CMC solutions and in Newtonian liquids. The characterisation of these flow patterns using the PIV/ST technique is presented in the next sections.

0.01 wt% PAA

In the visualisation studies, it was observed that the trailing edge of the Taylor bubbles rising in the 0.01 wt% PAA solution oscillated three-dimensionally and small bubbles were trapped in the wake. Despite the strong oscillations, coloured liquid was seen in the wake but no defined recirculation regions were observed.

In Figure 4.45, some examples of PIV images showing the trailing edge of bubbles rising in a 0.01 wt% PAA solution are represented. From these images, the similarity between the PIV experiments and the visualisation studies is evident, and it is possible to observe the trailing edge in different positions plus some bubbles trapped in the wake.

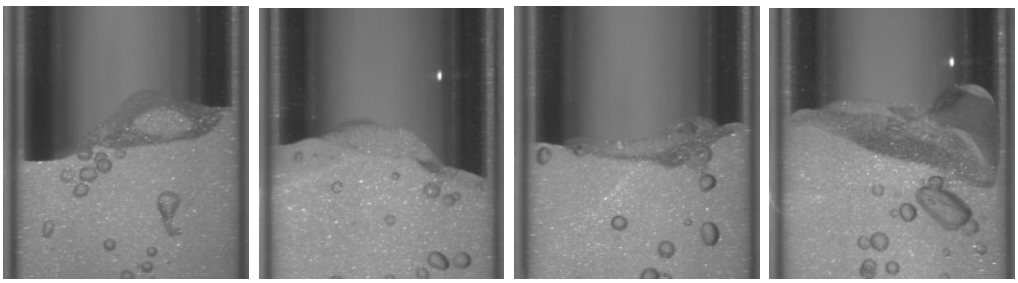

Figure 4.45. Trailing edge images (PIV/ST) of Taylor bubbles rising in a 0.01 wt% PAA solution.

The transport of liquid in the wake can only be confirmed by the wake flow fields. In Figure 4.46, the flow field in the wake region close to the bubble trailing edge is represented at four random instants.

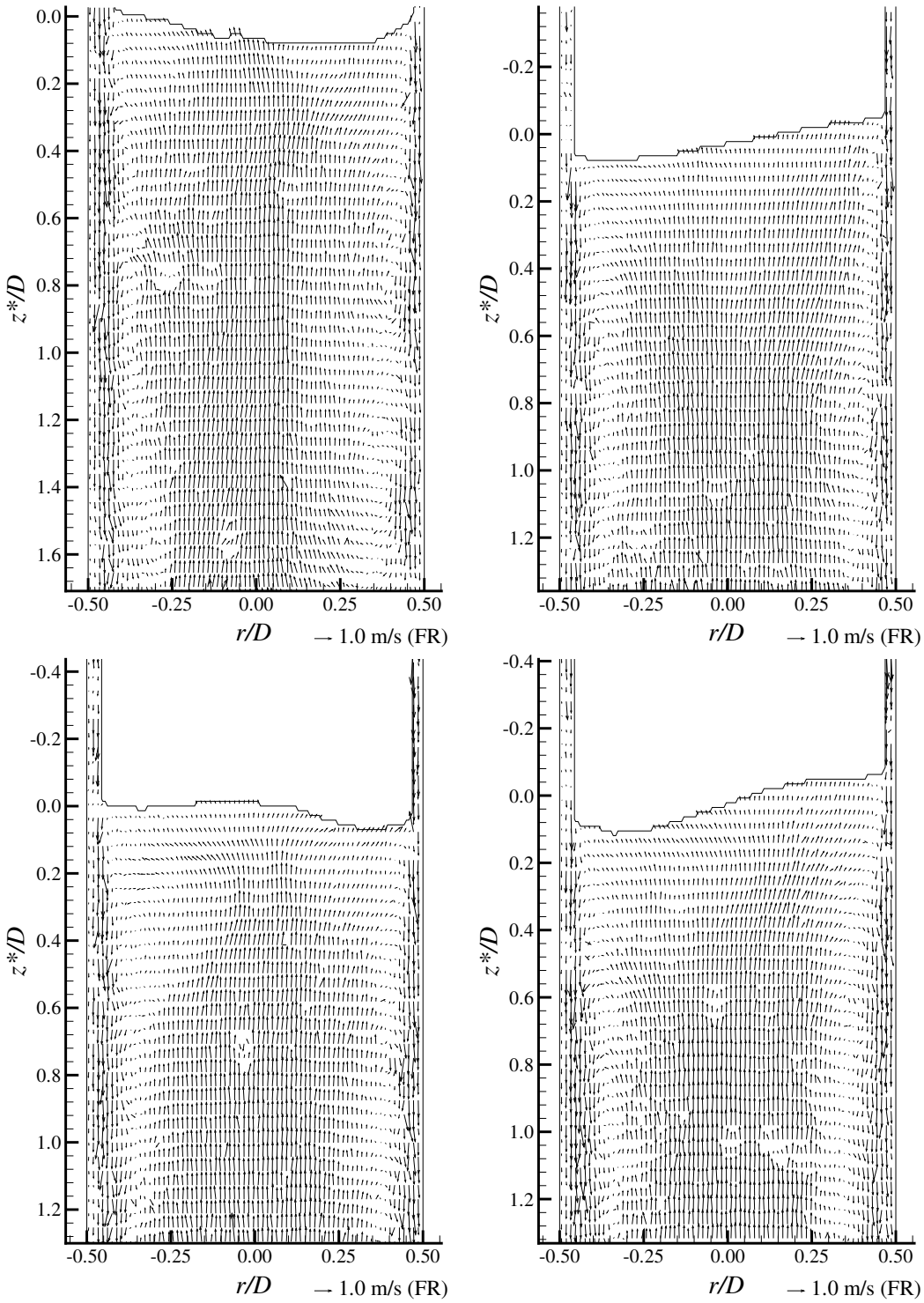

Figure 4.46. Flow fields in the upper wake region of Taylor bubbles rising in a 0.01 wt% PAA solution; fixed frame of reference.

These flow fields show that despite the oscillation of the bubble trailing edge, the flow does not present the random recirculation structures seen in the less concentrated CMC solution, which is ten times more concentrated in mass than this PAA solution. In fact, in the 0.01 wt% PAA solution the flow fields with different trailing edge orientations have a very similar pattern, apart from the region close to the bubble trailing edge and the disturbance caused by small bubbles in the wake. In all cases, a central region with high upward velocity (approximately 4 times the bubble velocity) is observed, and near the wall the falling film maintains its thickness and high velocity magnitude for a longer distance than those observed in CMC solutions.

Due to the long wake lengths it was not possible to capture the complete wake flow field in the same image at a reasonable resolution. The flow fields acquired in the subsequent instants are represented in Figure 4.47, showing the lower region of the wake. The flow fields in this figure show that the described pattern is maintained up to a distance of about $2D$ from the bubble trailing edge. Only then is the liquid film expansion observed, although asymmetric in some cases and having a high velocity magnitude for more than $2.8D$. At $2.8D$ from the bubble trailing edge an upward velocity magnitude greater than the Taylor bubble velocity is also seen around the axis. This is in accordance with the $3D$ wake lengths observed in the visualisation studies.

The upward velocity magnitude in the central region of the wake is four times higher than the bubble velocity, which implies that the fluid must be in recirculation. Some of the downward liquid flowing in the high radial positions should be fluid belonging to a long wake recirculation region. The recirculations are better seen in a frame of reference moving with the bubble. Due to the high liquid velocities the velocity field does not present a significant change from the fixed frame of reference, but the streamlines can give some information about the recirculation in the wake, as is represented in Figure 4.48 with a moving frame of reference. This figure shows that the streamlines in the falling film are practically vertical up to $2D$ from the trailing edge. In the central region of the wake, liquid is moving in an elongated recirculation region, enclosing some smaller vortex structures closer to the liquid film. The elongated recirculation regions usually extend up to $2.2 - 2.6D$, where the liquid film reattaches. This analysis is qualitative, since the flow is three-dimensional and the streamlines are plotted in a two-dimensional plane.

To have an idea of the effect of the oscillations in the wake flow, in Figure 4.49 four instantaneous axial (a) and radial (b) velocity profiles at $z* = 0.8D$ are represented.

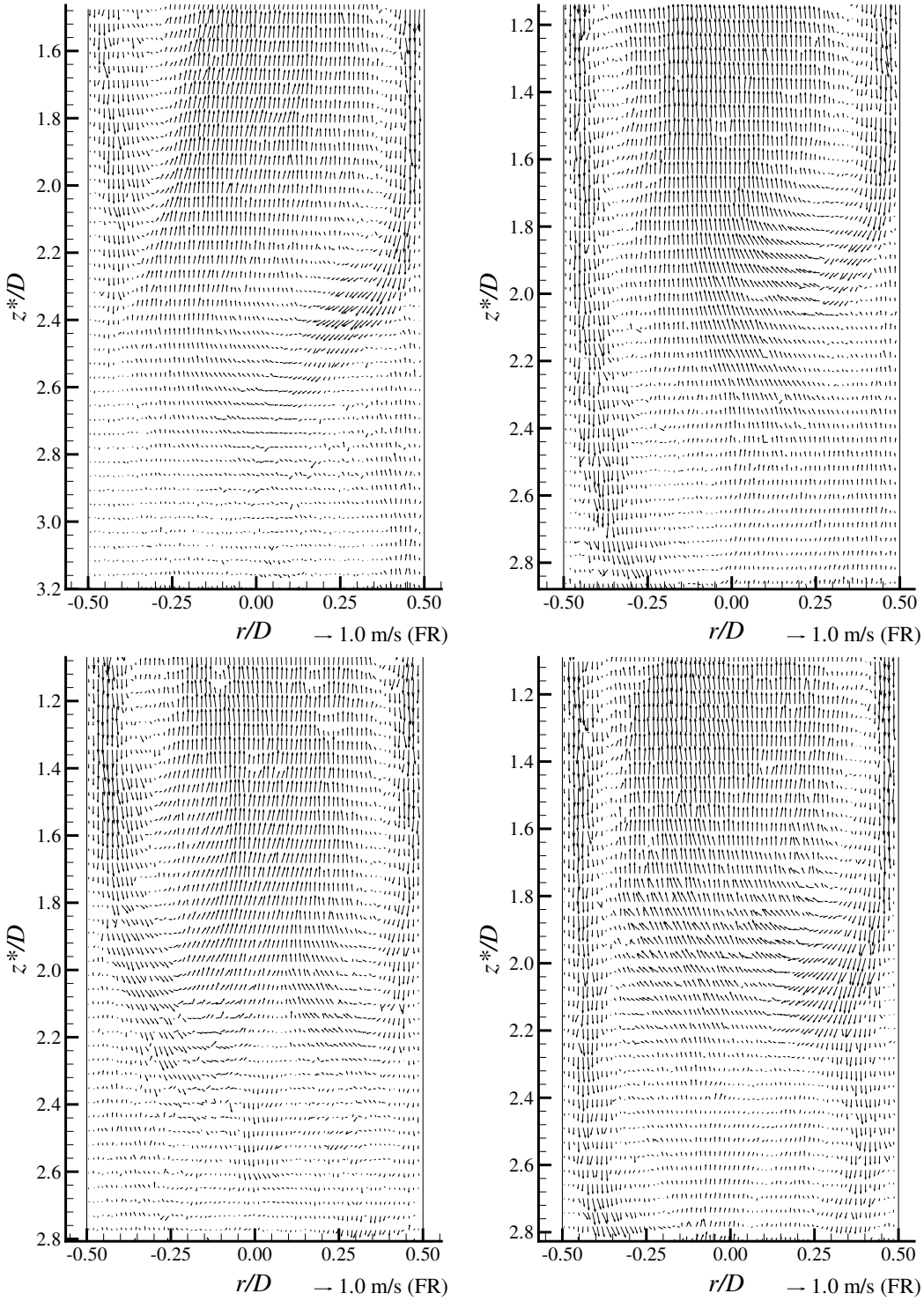

Figure 4.47. Flow fields in the lower region of the wake of Taylor bubbles rising in a 0.01 wt% PAA solution; fixed frame of reference.

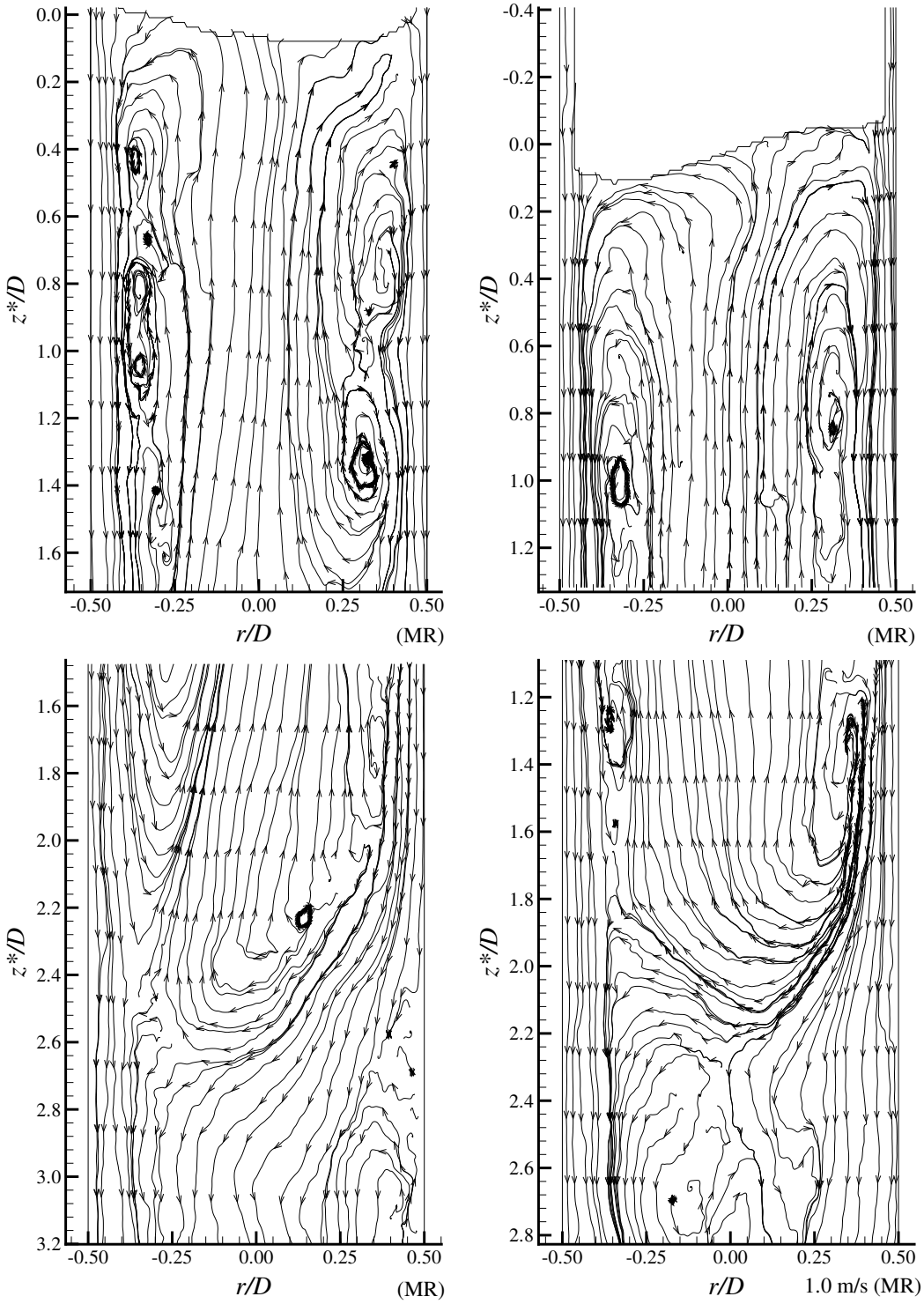

Figure 4.48. Instantaneous liquid trajectories in the wake of Taylor bubbles rising in a 0.01 wt% PAA solution; frame of reference moving with the bubble.

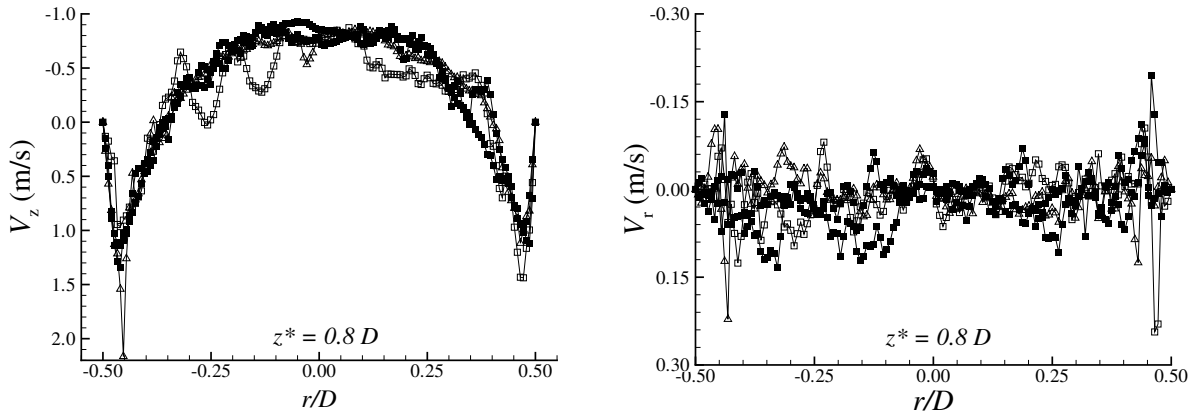

(a) Instantaneous axial velocity profiles (b) Instantaneous radial velocity profiles

Figure 4.49. Instantaneous velocity profiles at $z* = 0.8D$ in the wakes of Taylor bubbles rising in a 0.01 wt% PAA solution.

Although there are oscillations in the liquid velocity, they are less intense than in the 0.10 wt% CMC solution and the pattern is similar between all the instantaneous velocity profiles. In the axial velocity profiles a high velocity magnitude is observed, both in the downward liquid film and in the upward flow in the central region of the wake. The radial velocities also present some oscillations, with a lower amplitude than those observed in the 0.10 wt% CMC solution, and always around a zero value, indicating that the flow in this region is mainly in the axial direction.

Following the wake flow description and according to the same methodology applied for the CMC solutions, average velocity profiles were determined at different distances from the bubble trailing edge. Due to the presence of very small bubbles in most of the PAA solutions the synchronisation mode described in §2.2.2 and referred to as **Synchronous Mode** was not used, since these bubbles cause triggering of the laser pulse at undesired instants, making it difficult to obtain reproducible results. Average profiles were then obtained from images of the wake region acquired in the normal mode. In the 0.01 wt% PAA solution, ten images with the desired conditions were available. To test whether this number of images was sufficient to find meaningful average values, the average velocity and standard deviation at a fixed point were plotted in Figure 4.50 as a function of the number of images analysed. As seen in this figure, the average velocity values seem to stabilise after about 6 images, so ten images should be enough to be representative of the average velocity field.

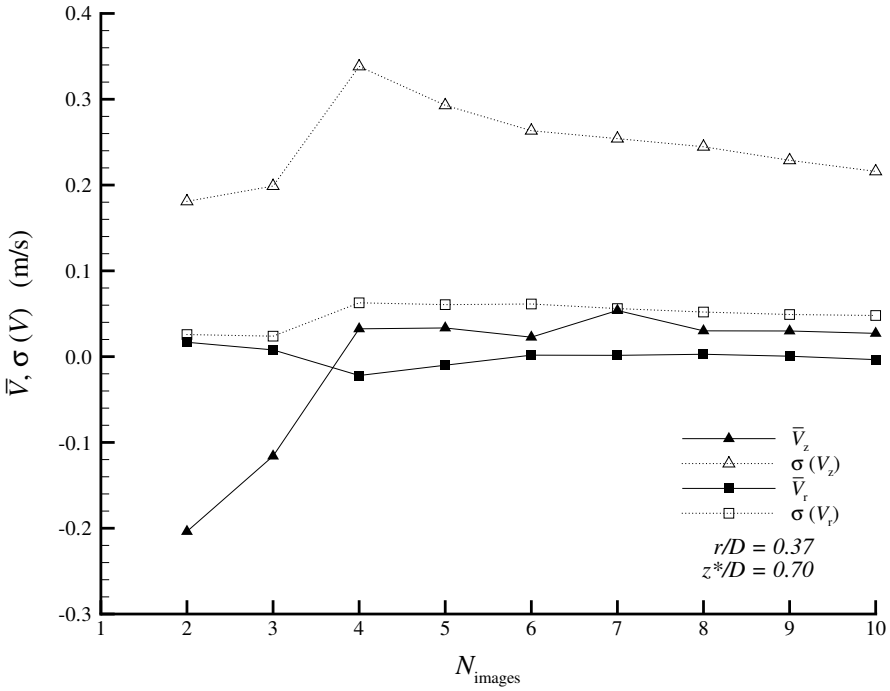

Figure 4.50. Average velocity components and respective standard deviations at fixed coordinates, as a function of the number of images analysed in the wake of Taylor bubbles rising in a 0.01 wt% PAA solution.

The average axial velocity profiles and standard deviation at different distances from the bubble trailing edge are represented in Figure 4.51 for the 0.01 wt% PAA solution. These profiles confirm the flow pattern already described, with a central upward-moving region and a high velocity magnitude film moving downward near the wall. This general behaviour is not very different from those found in the CMC solutions. The main difference is seen in the extension of this flow pattern.

From the velocity profiles presented in Figure 4.51, an increase is seen in the upward liquid velocity from the region close to the trailing edge up to $z* = 0.6D$, where the liquid velocity is three times higher than the bubble velocity. The falling film velocity at this point is around 1.0 m/s. This axial velocity profile at $z* = 0.6D$ is maintained practically unchanged up to $z* = 1.6D$. Only then is a smooth decrease in velocity magnitude observed, both in the central region and in the liquid film up to around $z* = 2.8D$, where the flow inversion occurs. After that point the liquid moves downwards in the axis and upwards away from the axis with very low velocity magnitude, tending to stagnate, apart from disturbances caused by the passage of small bubbles. The standard deviation of the

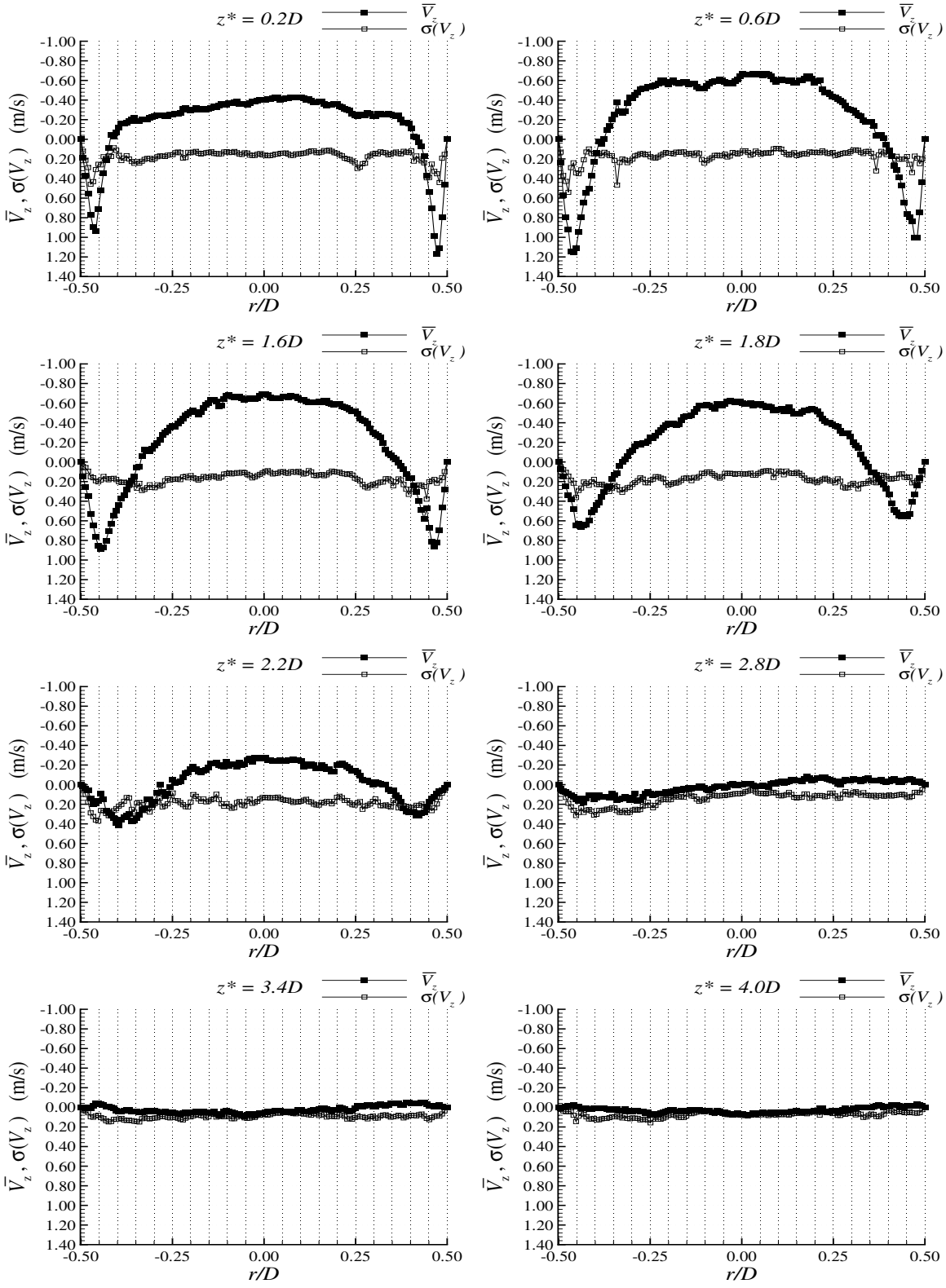

Figure 4.51. Average axial velocity profiles (fixed frame of reference) and standard deviation at different distances from the bubble trailing edge, of bubbles rising in a 0.01 wt% PAA solution.

axial velocity is higher near the falling film, similar to the pattern found in the CMC solutions but with lower magnitude than in the 0.10 wt% CMC solution.

The average radial velocity profiles at different distances from the bubble trailing edge are presented in Figure 4.52 These profiles show a pattern similar to those found in the CMC solutions, but now in a longer recirculation region. Close to the bubble trailing edge the radial velocities are positive, meaning that the fluid is moving from the axis to the outer region, which corresponds to the upper part of the recirculation region. The magnitude of the radial velocity decreases up to about $z* = 1.2D$, where the radial velocity is around zero in the central region and in the falling film, which should correspond to the centre of the principal recirculation region. From this point there is an inversion of the velocity direction, which now starts to move into the axis of the column. The radial velocities tend to be negative, although some positive velocity regions are present due to some flow asymmetries in the bottom region of the wake, and also due to the smaller recirculation regions observed in Figure 4.48. The radial velocity in the direction of the axis reaches its maximum at around $z* = 2.0D$, with a smooth magnitude reduction from there on. In the lower region of the wake, the oscillation of the fluid is responsible for the increase of the standard deviation and for the asymmetries found in this region.

In Figure 4.53, the average flow field in the wake of Taylor bubbles rising in a 0.01 wt% PAA solution is represented. From this figure, a much longer wake than those found in the CMC solutions is clear, with the liquid film expanding very smoothly, maintaining a high velocity magnitude for a long distance.

The axial velocity profile at $r = 0$ in function of the distance to the bubble trailing edge is represented in Figure 4.54. In this plot the wake length is confirmed to be between 2.2 and $2.4D$, since it is the region where the liquid film has the bubble velocity magnitude in a fixed frame of reference, corresponding to a zero velocity in a frame of reference moving with the bubble. The upward velocity magnitude is almost four times the bubble velocity, much higher than that found in the CMC solutions, and maintains a magnitude around the maximum value from $z* = 0.6D$ to $z* = 1.6D$. After this point, the pattern is similar to those found in the less concentrated CMC solutions. The velocity magnitude decreases and changes direction, starting to flow downwards after the liquid film reattachment. Like in the 0.10 wt% CMC solution, little bubbles rising behind the Taylor bubble cause small disturbances in the liquid velocity, not allowing stagnation of the fluid even at several column diameters from the Taylor bubble trailing edge. From the acquired images, there

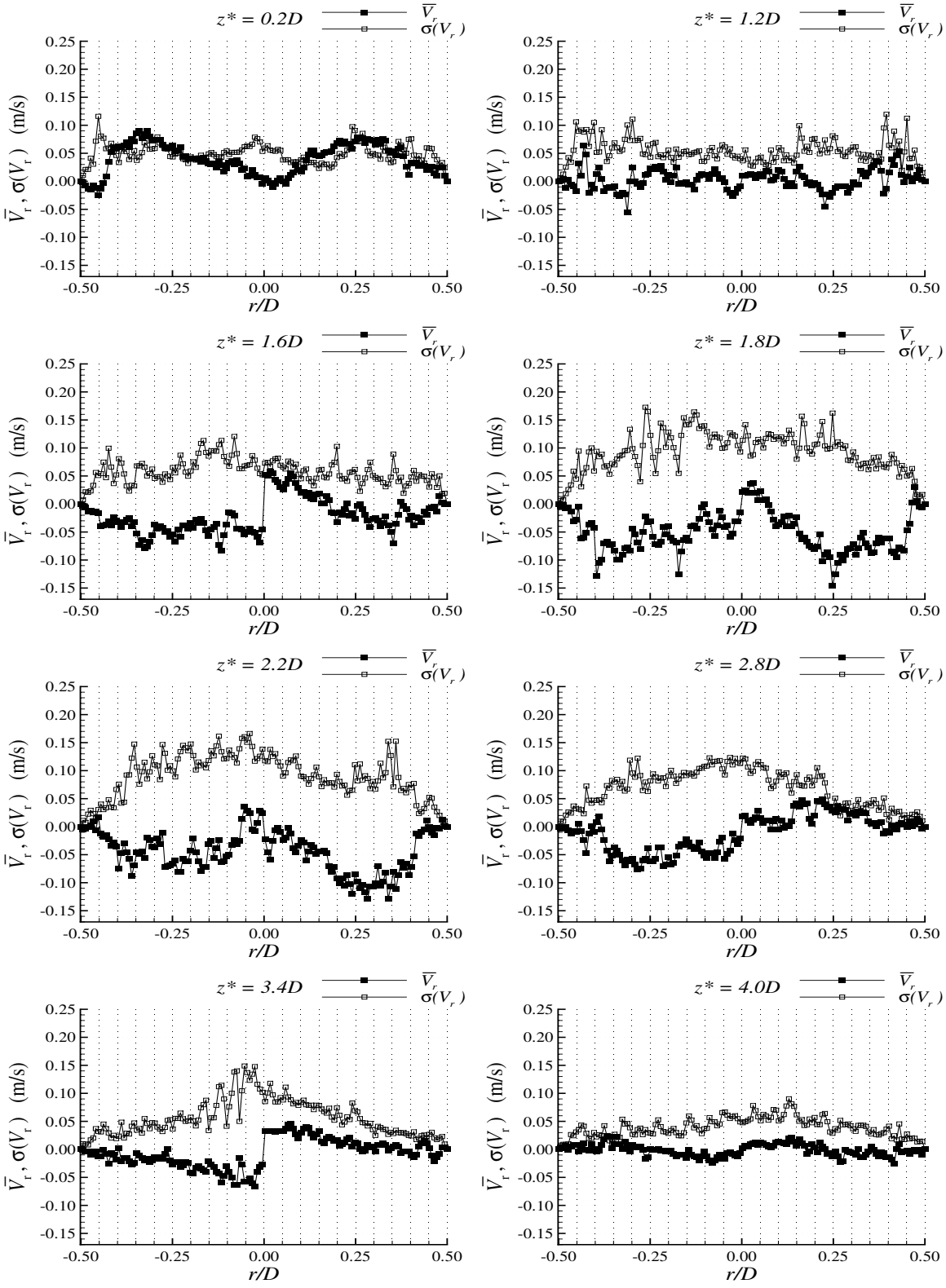

Figure 4.52. Average radial velocity profiles (fixed frame of reference) and standard deviation at different distances from the bubble trailing edge of bubbles rising in a 0.01 wt% PAA solution.

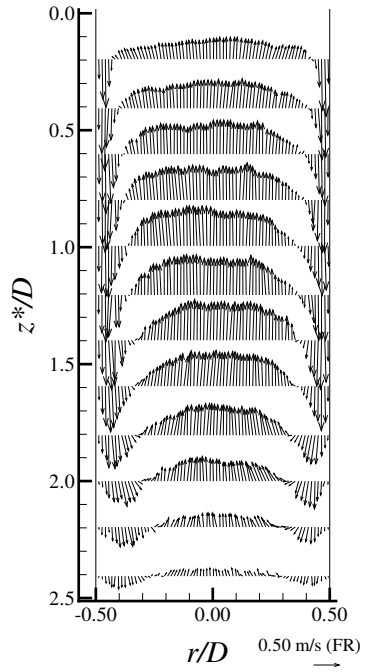

Figure 4.53. Average flow field in the wakes of Taylor bubbles ($L_b = 9.6D$) rising in a 0.01 wt% PAA solutions, obtained from the average velocity profiles.

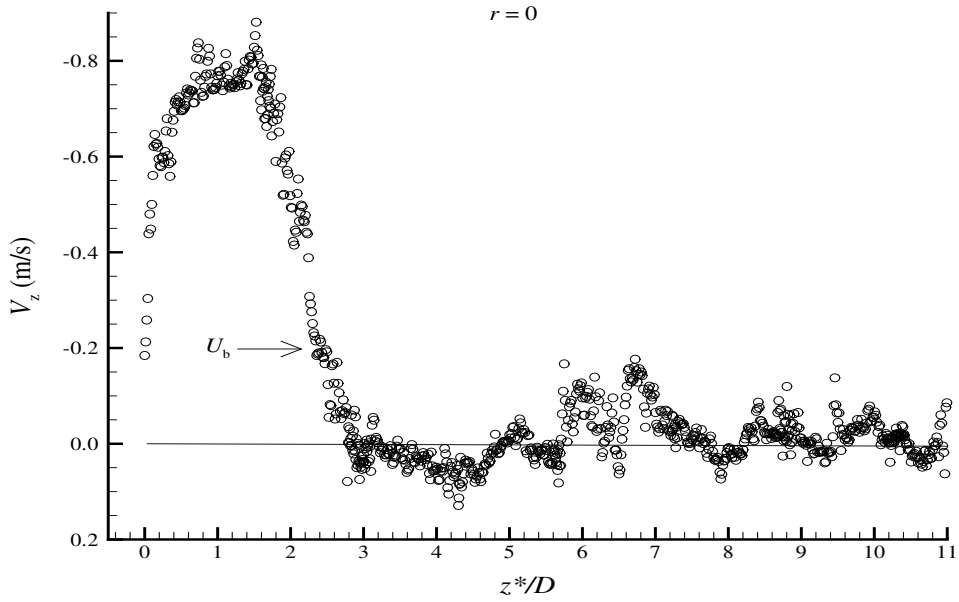

Figure 4.54. Instantaneous axial velocity profile (fixed frame of reference) at $r = 0$ as a function of $z*/D$ behind a Taylor bubble rising in a 0.01 wt% PAA solution.

are small bubbles rising behind the Taylor bubble at distances over $20D$ from the bubble trailing edge.

0.10 wt% PAA

In the visualisation studies of the wake behind Taylor bubbles rising in a 0.10 wt% PAA solution, the flow pattern was different from the previous solution. An elongated recirculation region was perceptible in the upper part of the wake, while in the lower part, a tail with wavy movement was visible. In the central region of the column, coloured liquid was moving upwards for up to $6D$ from the bubble trailing edge. The oscillations of the bubble trailing edge had very low amplitude and frequency.

Examples of the bubble trailing edge position obtained from the PIV images are represented in Figure 4.55. The behaviour of the bubble trailing edge in the PIV studies is similar to the one found in the visualisation studies. A few small bubbles were seen trapped in the recirculation region but not behind the bubble wake.

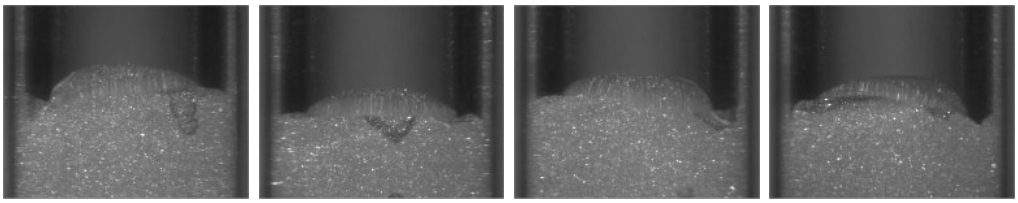

Figure 4.55. Trailing edge images (PIV/ST) of Taylor bubbles rising in a 0.10 wt% PAA solution.

As in the previous solution, the flow field of the complete wake could not be obtained in a single PIV image. In the following figures, flow fields obtained from consecutive images of two bubbles (left and right) are presented. In these flow fields a pattern similar to the one described in the visualisation studies is seen. In the upper region of the wake, liquid is flowing up with practically no radial velocity. The upward velocity magnitude is between two and three times the bubble velocity. The falling film maintains approximately the same thickness in this region, apart from some instabilities created by interaction with the downward recirculating liquid.

In the lower region of the wake there is a waving movement of the fluid flowing up in the axis of the tube, starting around $z* = 2.4D$ and decreasing in oscillation amplitude up to $8D$ from the bubble trailing edge. There is still liquid moving upwards at longer distances,

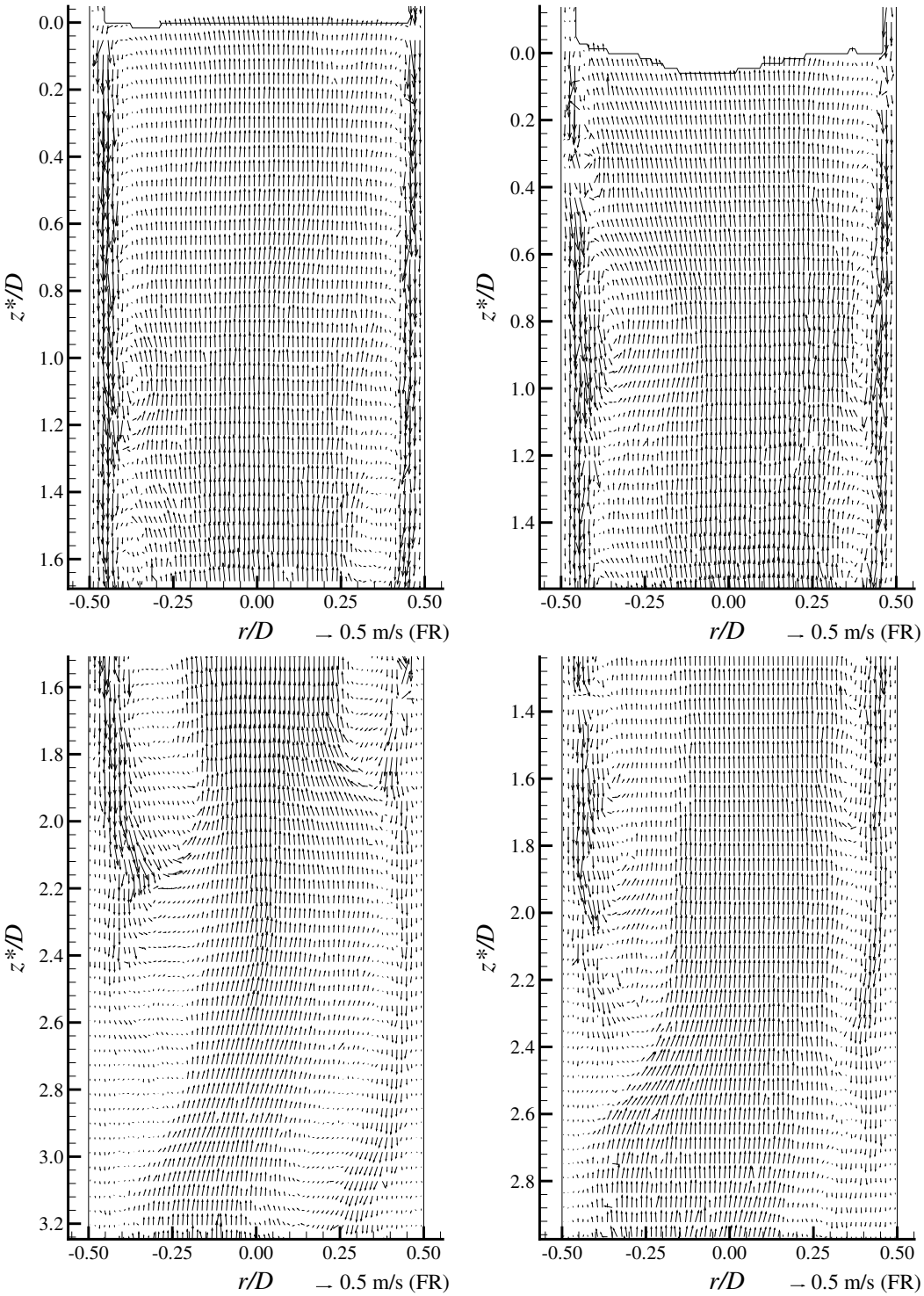

Figure 4.56. Flow fields in the wake of two Taylor bubbles (left and right) rising in a 0.10 wt% PAA solution (continues).

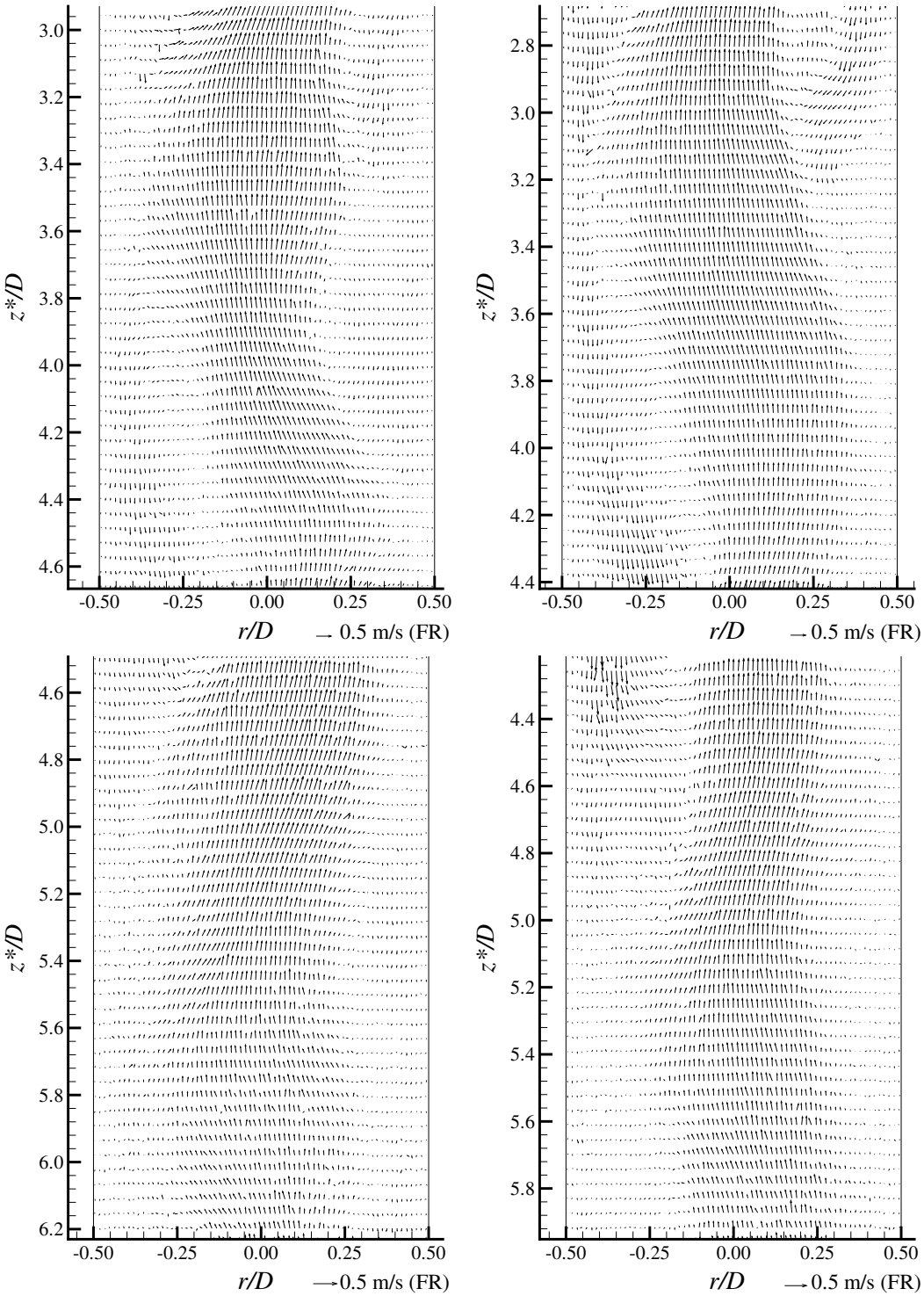

Figure 4.56. (continuation) Flow fields in the wake of two Taylor bubbles rising in a 0.10 wt% PAA solution (continues).

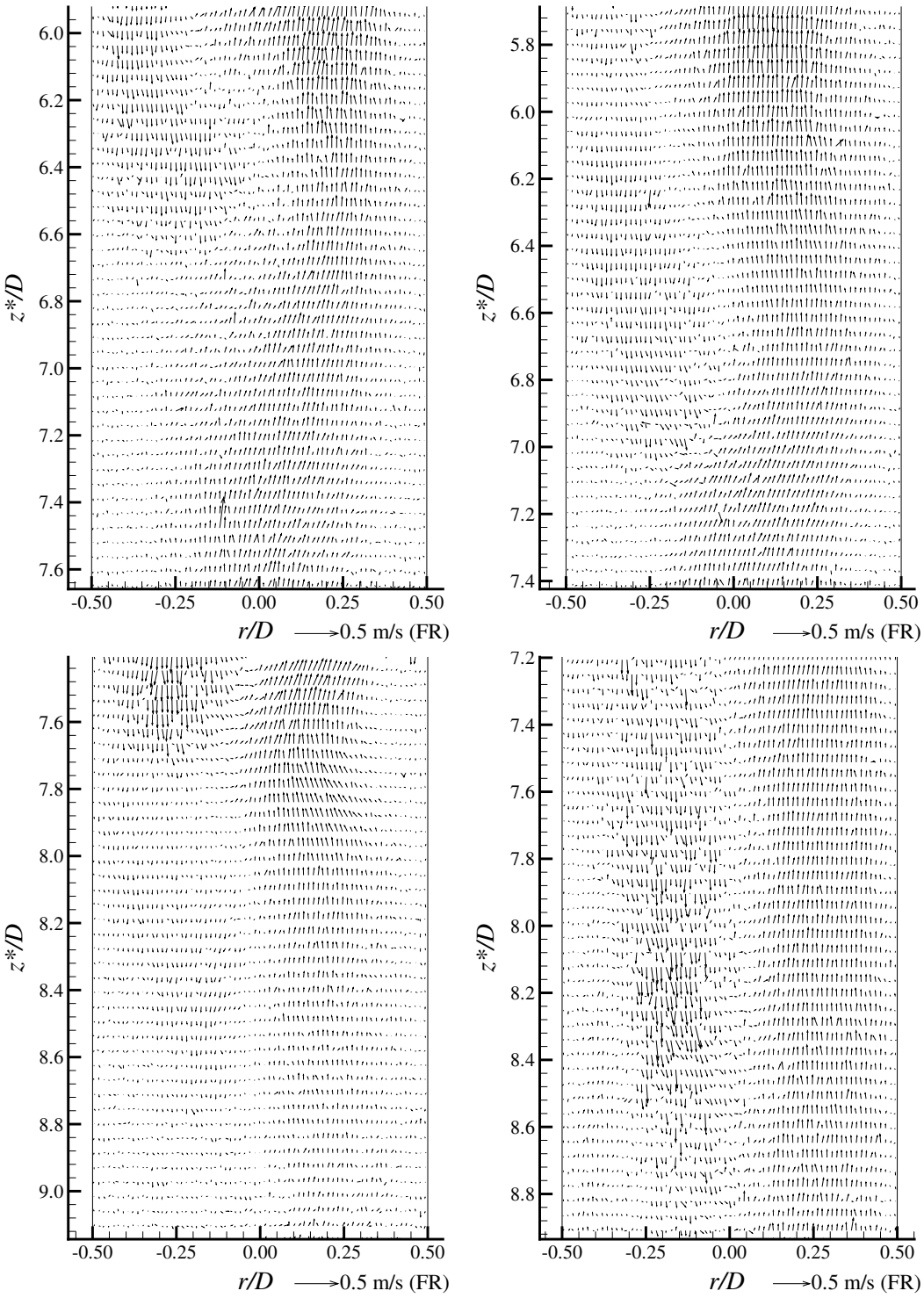

Figure 4.56. (continuation) Flow fields in the wake of two Taylor bubbles rising in a 0.10 wt% PAA solution.

but with no oscillations. Since the images relative to the same bubble were acquired at a frequency of 4.11 Hz, the liquid at the same distance from the bubble trailing edge might have a different velocity direction in consecutive images due to the waving movement. The upward liquid velocity magnitude also decreases in this region, only reaching the bubble velocity around $z* = 5.2D$, which can be considered as the wake length according to the criteria adopted in this work. After this point there is liquid still moving upwards, although slower than the bubble. At $8D$ from the bubble trailing edge its magnitude is still half that of the bubble velocity. This flow pattern indicates that the liquid in the axis of the column is continuously being stretched by the extensional stresses, which is in accordance with the visualisation studies, where an upward coloured liquid movement was perceptible in the axis of the column up to at least $6D$ from the bubble trailing edge.

From this flow pattern it seems that the liquid film extends only up to $z* = 2.4D$. After this point there is liquid flowing downwards away from the axis, but only due to the oscillating upward central flow and not due to the momentum acquired by the liquid when flowing around the bubble.

The images acquired with a longer time gap between PIV frames show that there is still an upward liquid movement at $12D$ from the bubble trailing edge, and although only having a velocity magnitude around one tenth of the bubble velocity this movement should still affect the velocity of a following bubble.

The streamlines of the liquid in the upper region of the wake of a Taylor bubble rising in a 0.10 wt% PAA solution are represented in Figure 4.57. In this region, an elongated vortex is seen with smaller vortexes inside, which were also visible in the visualisation studies.

After $z* = 2.4D$, the waving flow becomes three-dimensional and the streamlines on the plane lose accuracy. Even so, in Figure 4.58 (frame of reference attached to the bubble), the flow fields in the lower region of the wake are represented. An upward liquid movement in the axis of the column is seen up to $z* = 5.2D$. For longer distances the liquid velocity is lower than the bubble velocity, and so a downward movement is seen relative to the bubble, despite being stretched and moving upwards in a fixed frame of reference.

Average velocity profiles at different distances from the bubble trailing edge were determined from ten images. In Figure 4.59, the average axial velocity profiles are presented. Similar to the previous solution, there is an upward central liquid flow surrounded by a falling liquid film, which maintains approximately the same profile for a very long dis-

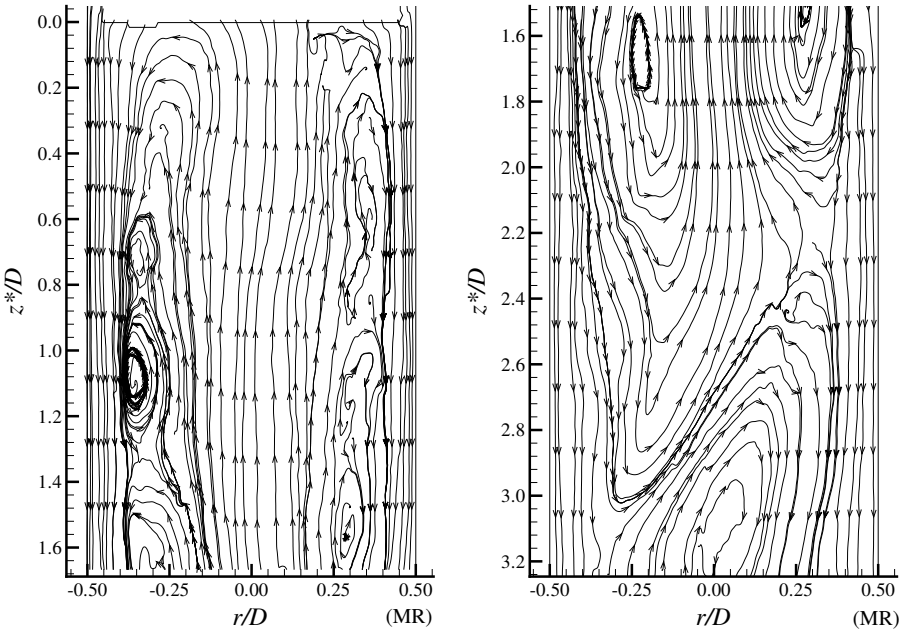

Figure 4.57. Instantaneous streamlines in the upper region of the wake of a Taylor bubble rising in a 0.10 wt% PAA solution, in a frame of reference moving with the bubble.

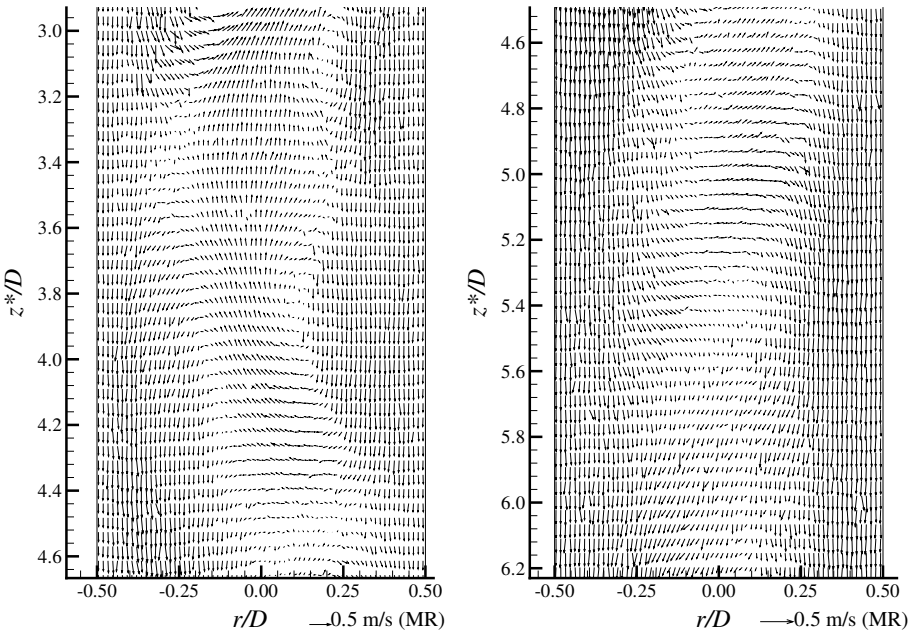

Figure 4.58. Flow fields in the lower region of the wake of a Taylor bubble rising in a 0.10 wt% PAA solution, in a frame of reference moving with the bubble.

tance. The maximum upward velocity (around $2.5 \cdot U_\mathrm{b}$) occurs between $1D$ and $2D$ from the bubble trailing edge and then slowly decreases. The downward liquid film maintains a high velocity magnitude and smoothly increases in thickness with distance from the bubble trailing edge. After the liquid film expansion ($z* > 2.4D$), the velocity profile pattern is the same even at $8D$ from the bubble trailing edge, with decreasing velocity magnitude and slight asymmetry due to the oscillations in the lower region of the wake.

The radial velocity profiles, represented in Figure 4.60, show that the flow is mainly axial, since the radial velocity magnitudes are not higher than 0.03 m/s, which is lower than those seen in previous solutions. In the upper region of the wake it is seen the outward liquid flow (positive velocities) corresponding to the upper region of the elongated recirculation region. An inversion occurs around $z* = 1.6D$, and in the lower regions the radial velocity tends to be practically null, apart from the oscillations that induce some punctual asymmetries.

The average velocity field behind Taylor bubbles rising in a 0.10 wt% PAA solution is represented in Figure 4.61, where the extension of the wake can be observed. This figure shows the upward liquid movement region in the axis of the column is several diameters long, with decreasing velocity magnitude. This flow pattern suggests that the fluid in the central region is being stretched due to the action of strong extensional stresses.

The instantaneous axial velocity profile in the axis of the column in function of the distance to the bubble trailing edge is represented in Figure 4.62. This plot shows that within the studied solutions the longest region with upward liquid flow is behind a Taylor bubble rising in a 0.10 wt% PAA solution, except for the cases where a train of small bubbles was formed. In the 0.10 wt% PAA solution the subsequent downward liquid movement corresponding to the liquid film reattachment is not seen. The upward liquid movement decreases its magnitude over a distance of about $12D$ from the bubble trailing edge, to where it practically stagnates. This means that within this distance the velocity of a following bubble should be affected.

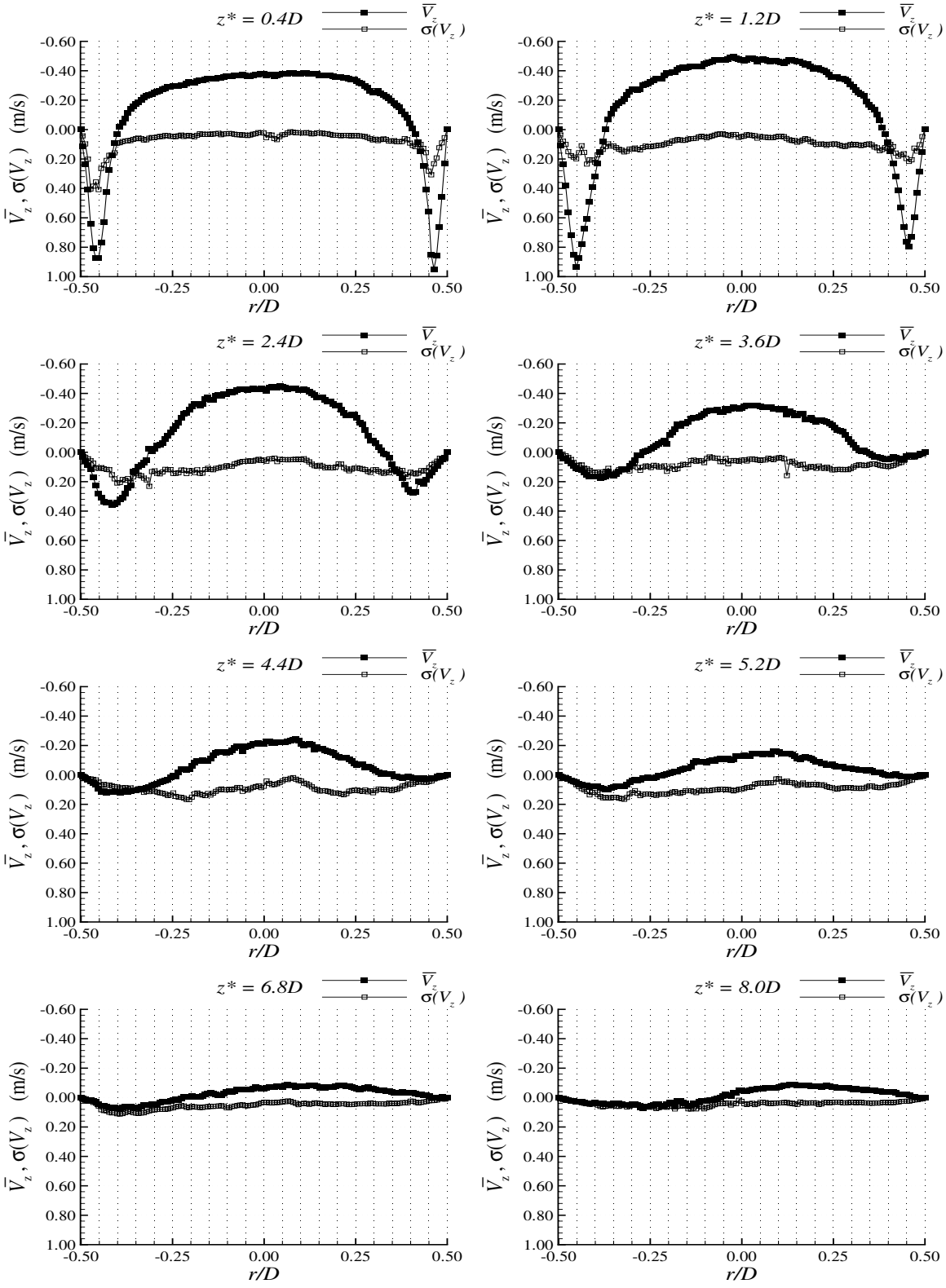

Figure 4.59. Average axial velocity profiles (fixed frame of reference) and standard deviation at different distances from the bubble trailing edge of bubbles rising in a 0.10 wt% PAA solution.

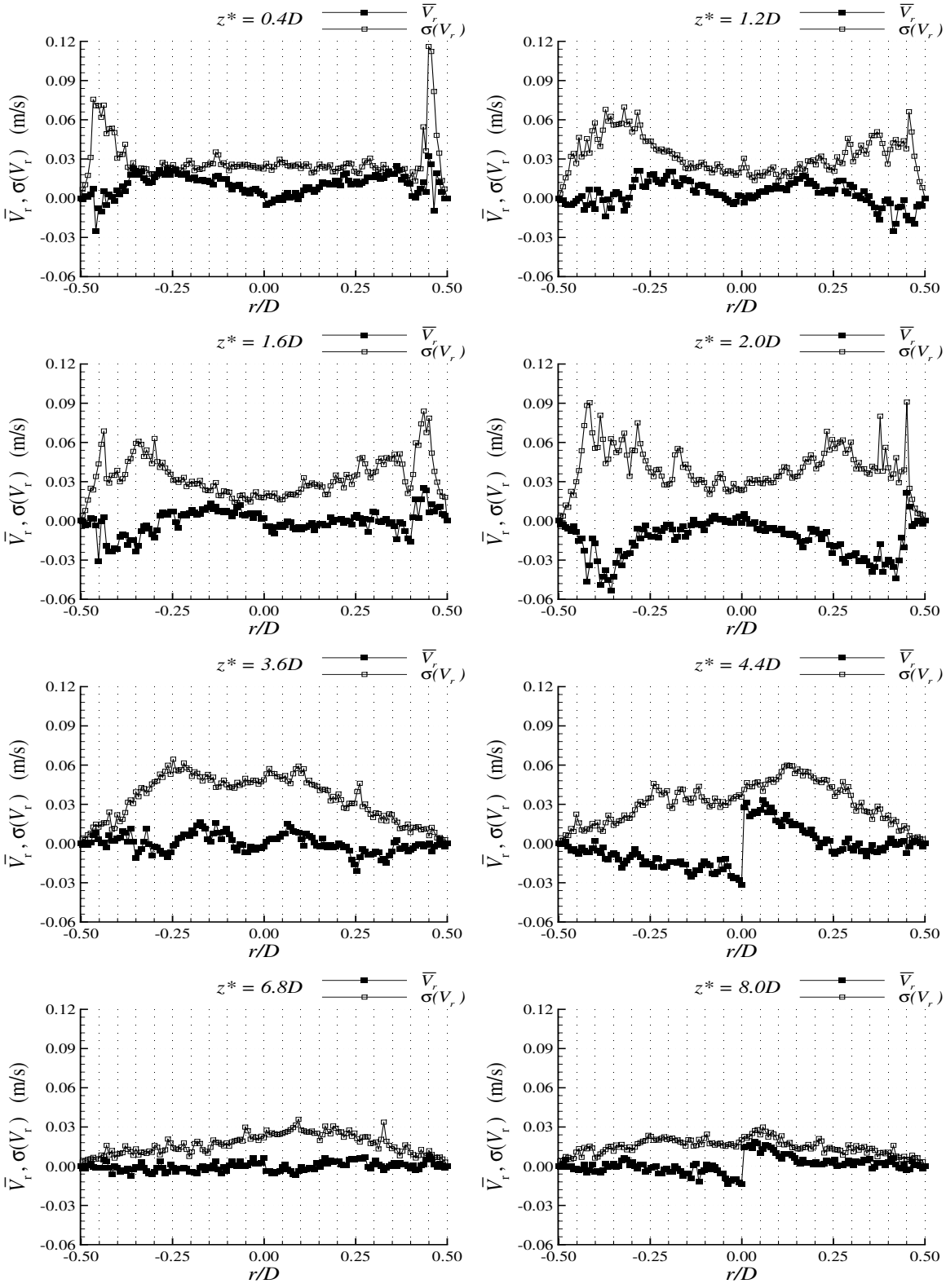

Figure 4.60. Average radial velocity profiles (fixed frame of reference) and standard deviation at different distances from the bubble trailing edge of bubbles rising in a 0.10 wt% PAA solution.

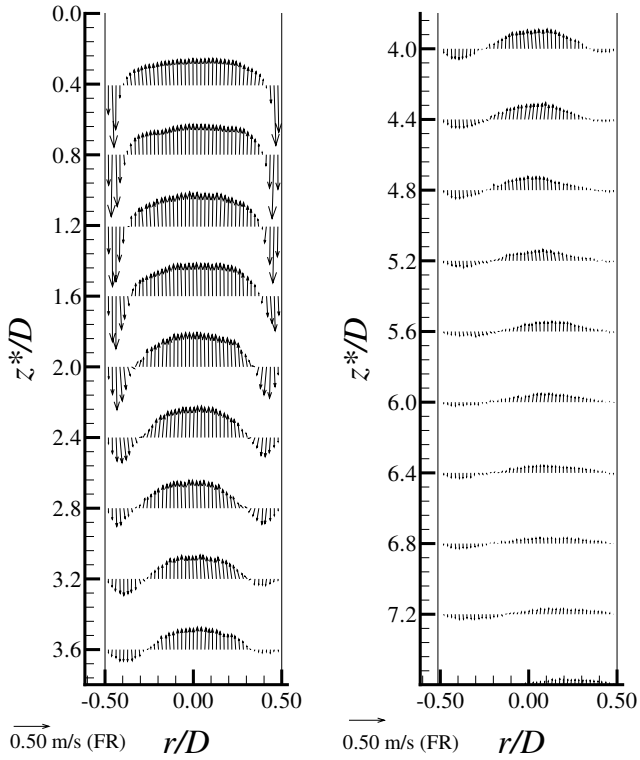

Figure 4.61. Average flow field in the wakes of Taylor bubbles ($L_b = 10D$) rising in a 0.10 wt% PAA solution, obtained from the average velocity profiles.

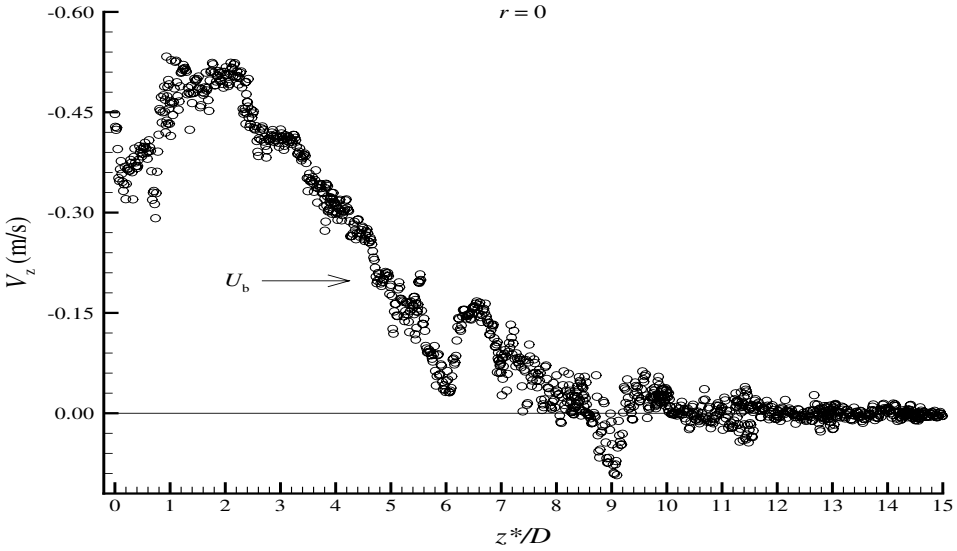

Figure 4.62. Instantaneous axial velocity profile (fixed frame of reference) at $r = 0$ in function of $z*/D$ behind a Taylor bubble rising in a 0.10 wt% PAA solution.

0.20 wt% PAA

In the 0.20 wt% PAA solution, the visualisation studies showed that fluid history starts to have an effect on the flow pattern in the wake of Taylor bubbles. Despite a very stable trailing edge in the first bubbles after leaving the liquid at rest for some time, there was no coloured liquid in the wakes. After the first bubbles a region of coloured liquid was seen, practically stagnant relative to the bubble and surrounded by the downward liquid film. In the axis of the column an upward liquid movement was seen, similar to the previous solution but shorter in length.

In Figure 4.63, instantaneous trailing edge positions obtained in the PIV experiments are presented. This figure shows that despite non-symmetric positions of the bubble trailing

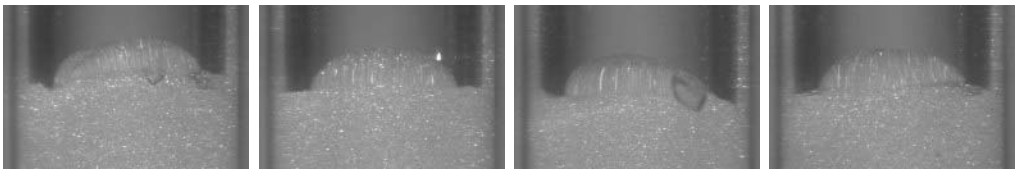

Figure 4.63. Trailing edge images (PIV/ST) of Taylor bubbles rising in a 0.20 wt% PAA solution.

edge, there are only small differences in the positions at different instants.

Instantaneous flow fields behind Taylor bubbles rising in 0.20 wt% PAA solution are represented in Figure 4.64. As expected from the visualisation studies, in the central region of the wake the velocity magnitude is not so high as in the previous solutions. The upward central liquid has a velocity magnitude around 1.0-1.5 times the bubble velocity up to $z* = 1.5D$. After this distance the fluid continues to move upwards in a central region, but with decreasing velocity magnitude as the distance from the bubble trailing edge increases. In Figure 4.65, this upward central flow is clearly seen by increasing the vector scale.

As was already mentioned, the flow fields in a frame of reference moving with the bubble allow a better perception of the low velocity magnitude of the liquid in the wake relative to the bubble, as shown in Figure 4.66. This portion of liquid flowing at approximately the bubble velocity extends up to $z* = 1.6D$. Around this distance there is an almost imperceptible liquid film expansion surrounding a central liquid region which moves upwards with a velocity magnitude lower than the bubble velocity, similar to the 0.10 wt% PAA solution.

The streamlines in the wake of the Taylor bubbles are represented in Figure 4.67. The

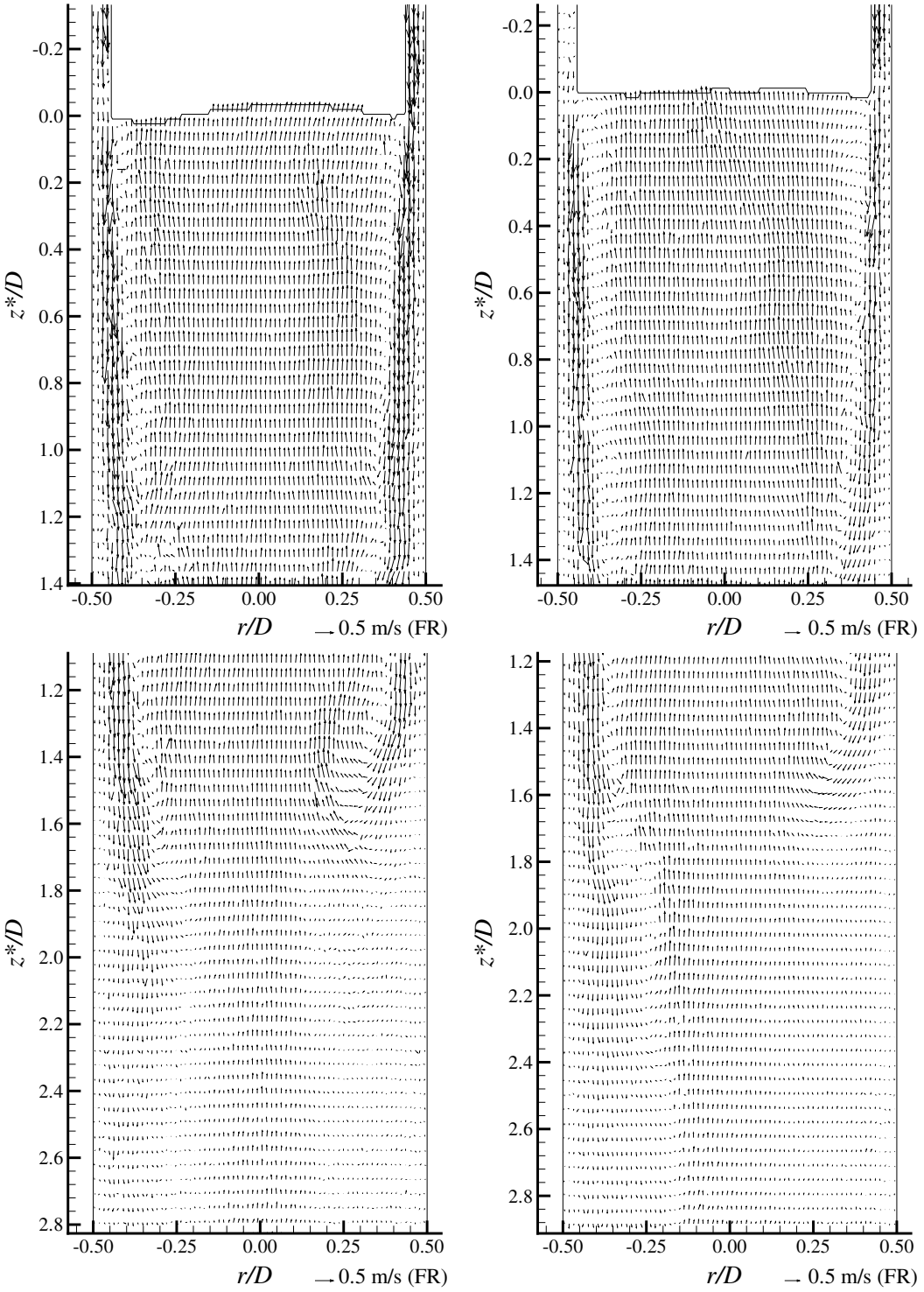

Figure 4.64. Flow fields in the wake of Taylor bubbles rising in a 0.20 wt% PAA solution; fixed frame of reference.

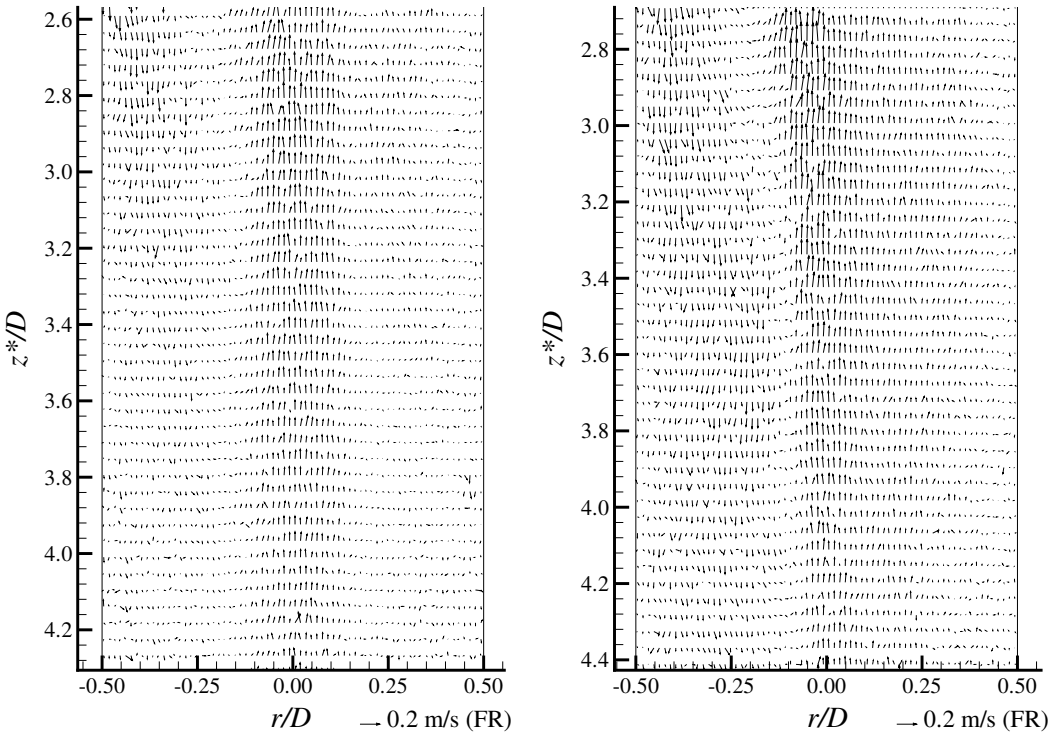

Figure 4.65. Flow fields in the far wake of Taylor bubbles rising in a 0.20 wt% PAA solution; fixed frame of reference.

low velocity magnitudes do not allow a good definition of the streamlines, but it is clear that the patterns differ from bubble to bubble. There is, however, a tendency for the formation of small recirculation regions close to the falling liquid film inside the longer recirculation region. The streamlines in the liquid film are practically vertical up to $z* = 1.6D$, showing that, similar to the previous PAA solutions, its expansion is retarded when compared with the CMC solutions.

Average liquid velocity profiles were obtained from ten bubbles of the same length ($L_\mathrm{b} = 10.3D$). The axial velocity profiles are represented in Figure 4.68 The plots in this figure show that the velocity profile is practically uniform (with $1.5U_\mathrm{b}$ velocity magnitude) in the central region up to $1.4D$ from the bubble trailing edge. The liquid film maintains practically the same thickness and velocity magnitude in the upper region. After $z* = 1.4D$, the liquid film smoothly expands. From there on, there is liquid in the axis that is being stretched while moving upwards. This upward flow is responsible for the downward flow away from the axis. While this pattern is maintained for a long distance, the velocity magnitude decreases as the distance from the bubble trailing edge increases. The standard

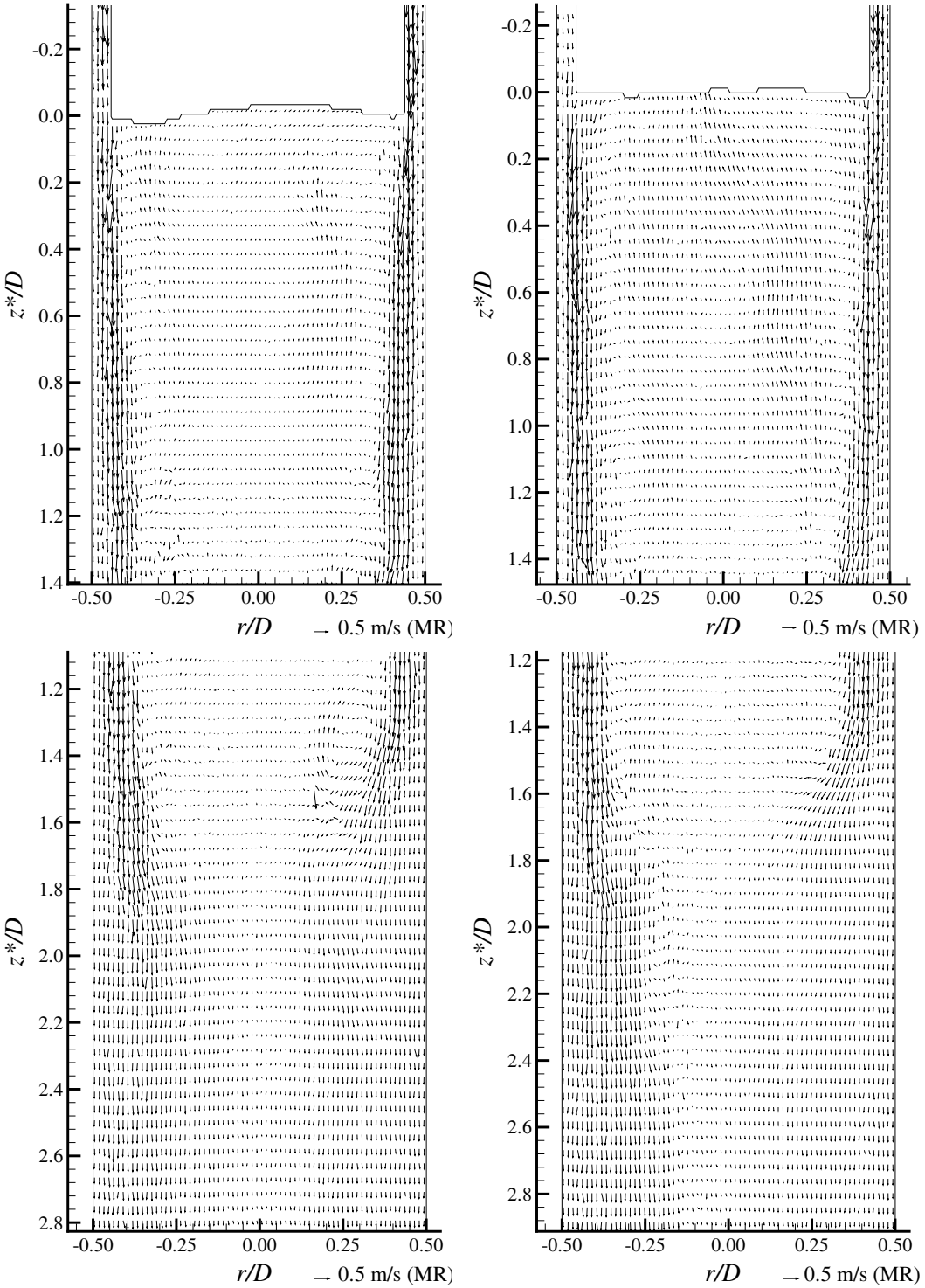

Figure 4.66. Flow fields in the wake of Taylor bubbles rising in a 0.20 wt% PAA solution; frame of reference moving with the bubble.

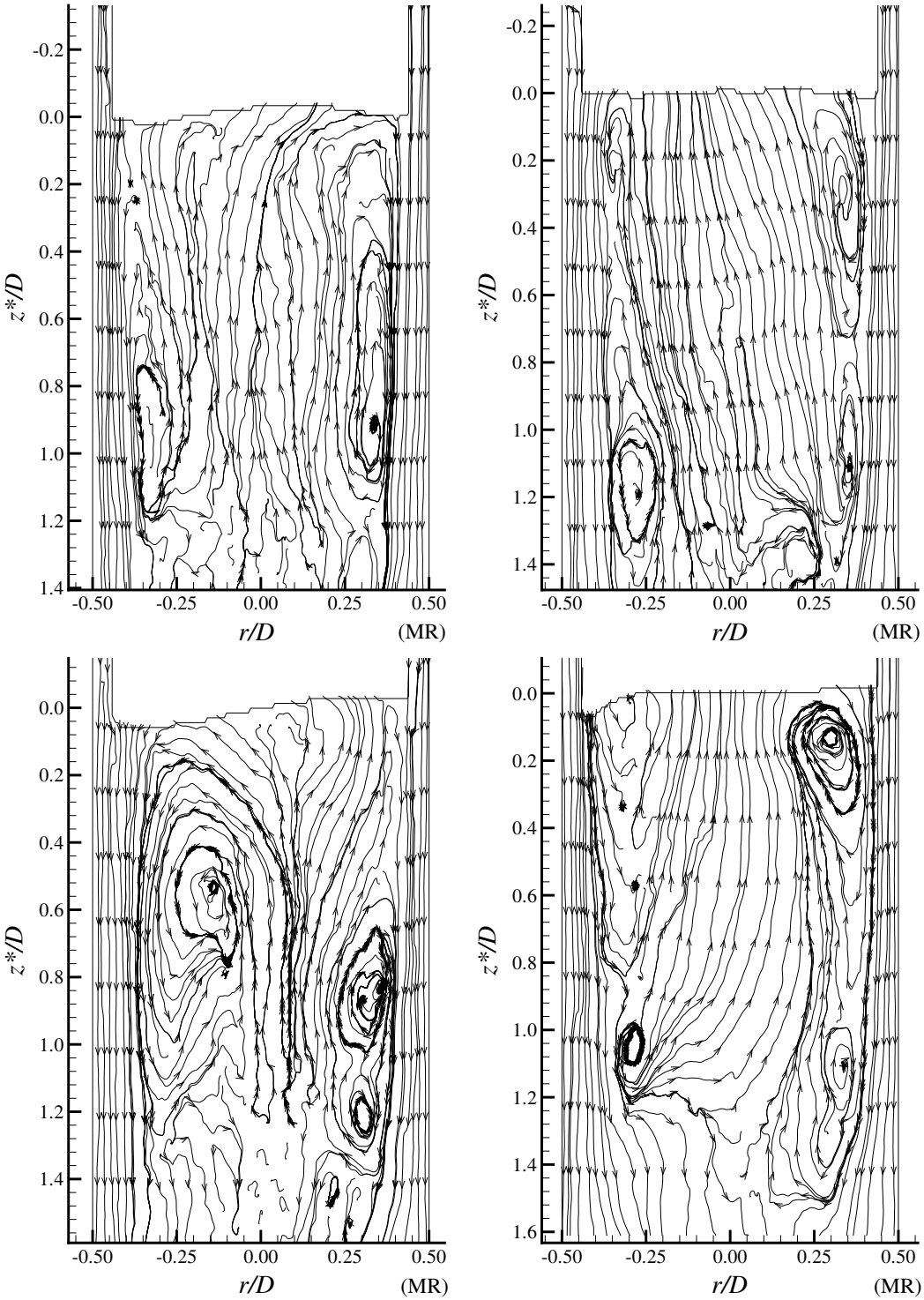

Figure 4.67. Instantaneous streamlines in the wake of Taylor bubbles rising in a 0.20 wt% PAA solution; frame of reference moving with the bubble.

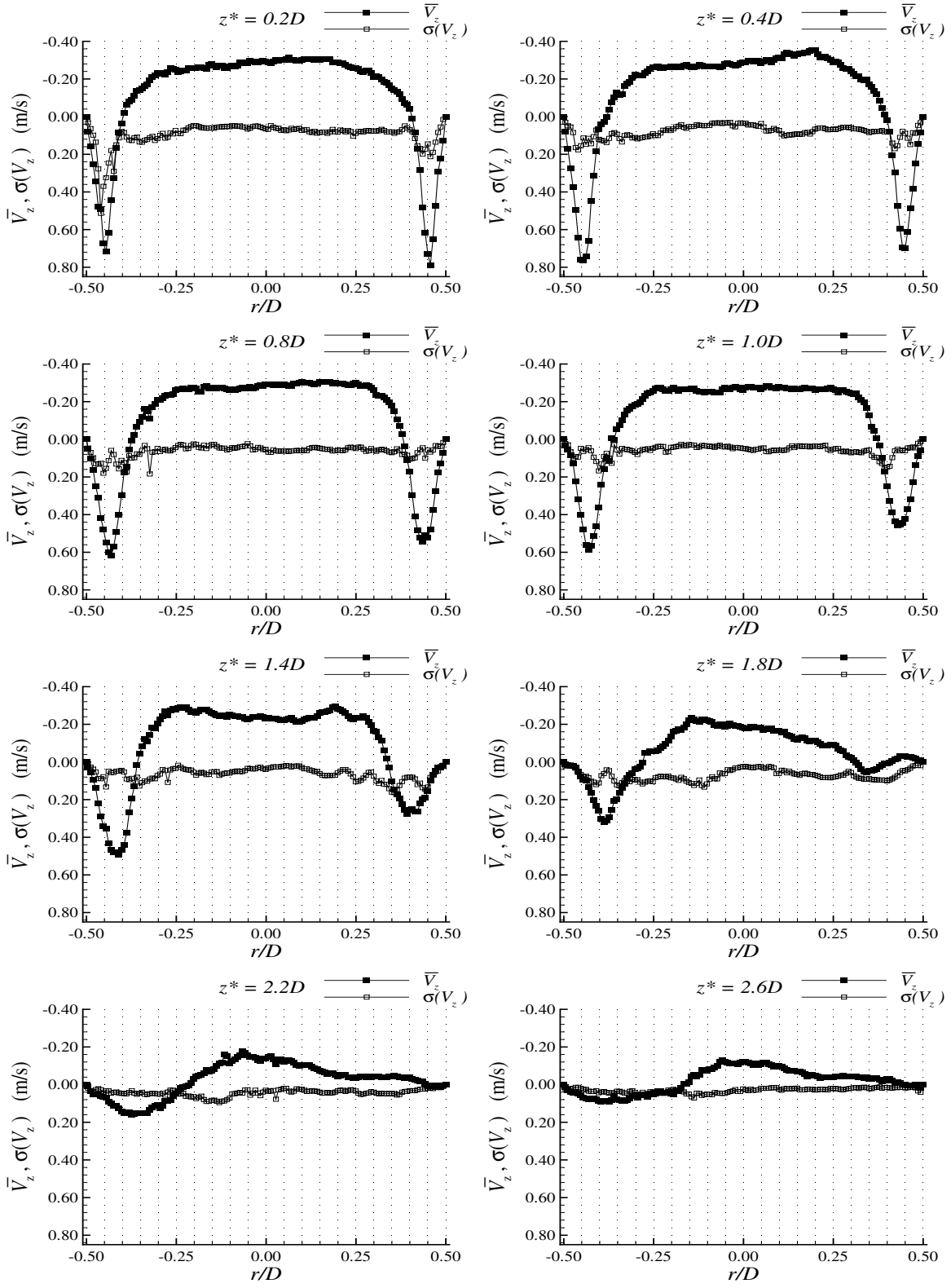

Figure 4.68. Average axial velocity profiles (fixed frame of reference) and standard deviation at different distances from the bubble trailing edge of bubbles rising in a 0.20 wt% PAA solution.

deviation on the axial velocity is similar to that in the previous solution, keeping to values below 0.10 m/s in the central region and having a maximum in the region where the liquid film contacts with the downward recirculating liquid.

The radial velocity profiles at the same distances from the bubble trailing edge are represented in Figure 4.69. As expected from the velocity fields, the radial velocity magnitude is very low in the upper region of the wake. In fact, it is close to the experimental error in these measurements (0.02 m/s) in practically the whole wake. It is only measurable in the region where the liquid film expands, between $1.2D$ and $1.8D$ from the bubble trailing edge, and even there it has a maximum amplitude of only 0.05 m/s.

These velocity profiles confirm that the flow in the wakes of Taylor bubbles rising in a 0.20 wt% PAA solution is mainly in the axial direction, as shown in the average flow field presented in Figure 4.70.

The instantaneous axial velocity profile at $r = 0$ as a function of the distance to the bubble trailing edge is represented in Figure 4.71. This figure shows that the maximum upward liquid velocity is around 1.5 times the bubble velocity and occurs between $z* = 0$ and $z* = 1.2D$. The velocity magnitude decreases after this region, reaching the bubble velocity magnitude at around $z* = 1.8D$ but keeping its upward direction up to $6D$ from the bubble trailing edge. After $z* = 6D$, there appears to be a slight downward liquid movement with a velocity magnitude identical to the experimental error. Although the upward liquid movement region is shorter than in the 0.10 wt% PAA solution, it is still much higher than in the CMC solutions, which should lead to long interaction distances between consecutive bubbles rising in a column.

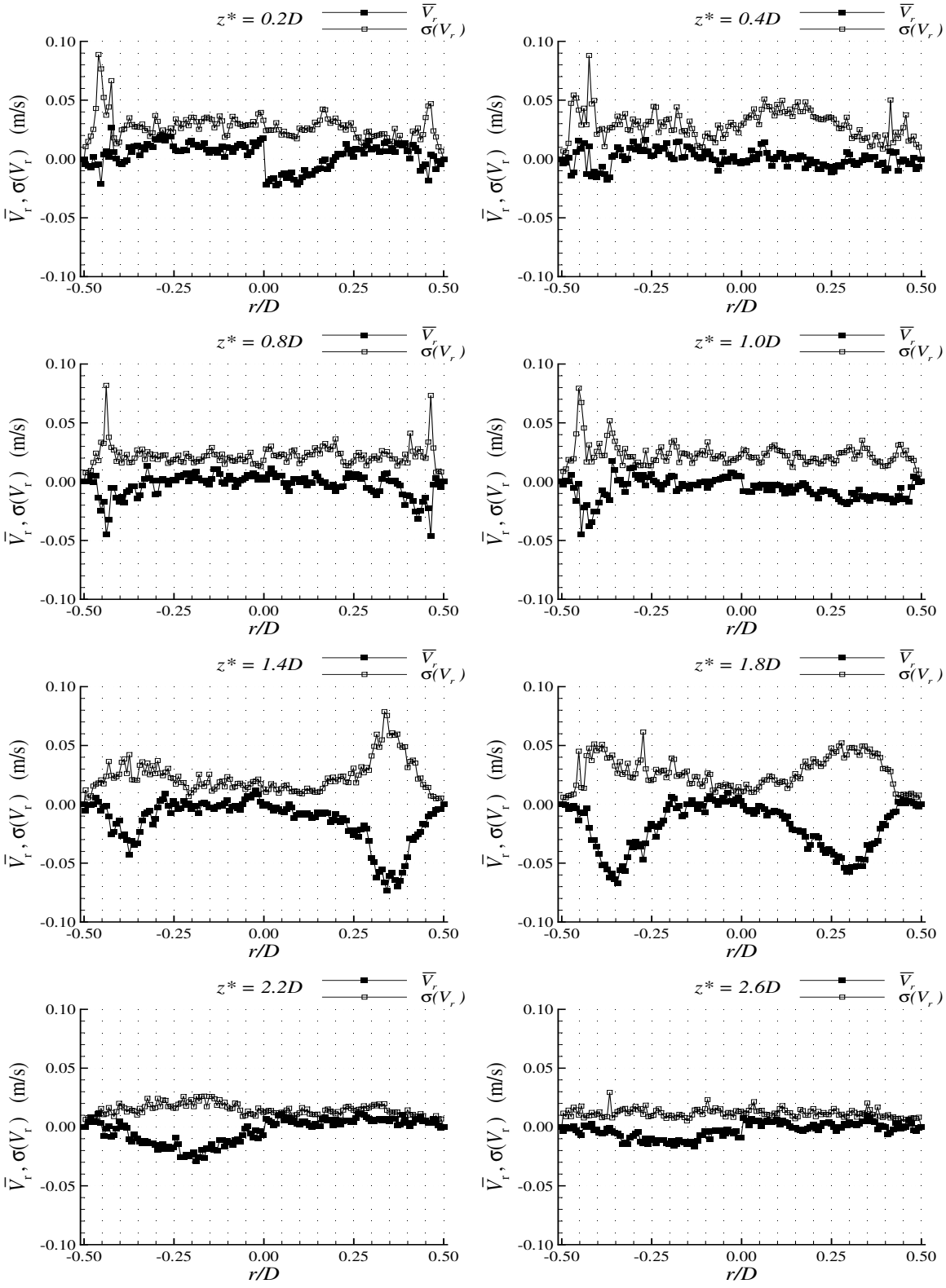

Figure 4.69. Average radial velocity profiles (fixed frame of reference) and standard deviation at different distances from the trailing edge of bubbles rising in a 0.20 wt% PAA solution.

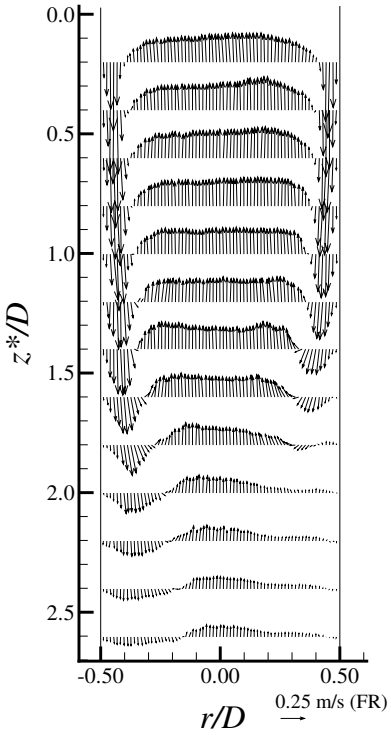

Figure 4.70. Average flow field in the wake of Taylor bubbles ($L_b = 10.3D$) rising in a 0.20 wt% PAA solutions, obtained from the average velocity profiles.

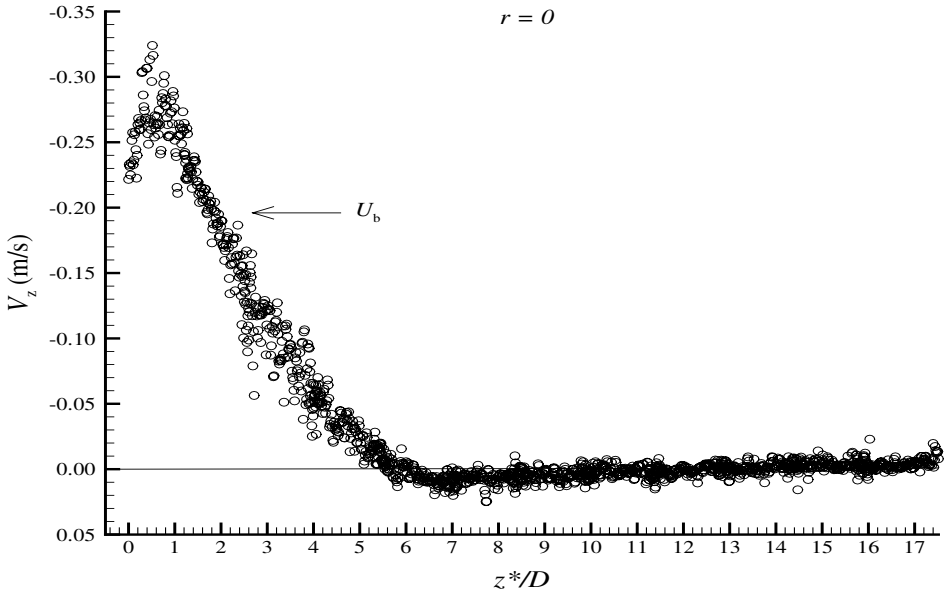

Figure 4.71. Instantaneous axial velocity profile (fixed frame of reference) at $r = 0$ in function of $z*/D$ behind a Taylor bubble rising in a 0.20 wt% PAA solution.

0.40 wt% PAA

The visualisation studies with the 0.40 wt% PAA solution showed that there was no coloured liquid transported in the wake and that the fluid history had a strong effect on the bubble velocity. In the wake, the movement of a small bubble seemed to indicate a practically stagnant region close to the bubble trailing edge followed, by a downward liquid movement.

In the PIV results, as explained in §4.3.2, the effect of the fluid history could not be eliminated. In bubbles of the same length, velocity differences of 20% were found. The time between injected bubbles was approximately the same, but to completely eliminate the effect of the fluid history the time between consecutive bubbles should be much higher. Nevertheless, individual Taylor bubbles were studied and the most relevant results are Presented here.

In Figure 4.72, some examples of the trailing edge of bubbles rising in a 0.40 wt% PAA solution are presented. This figure shows that the bubble trailing edge presents some

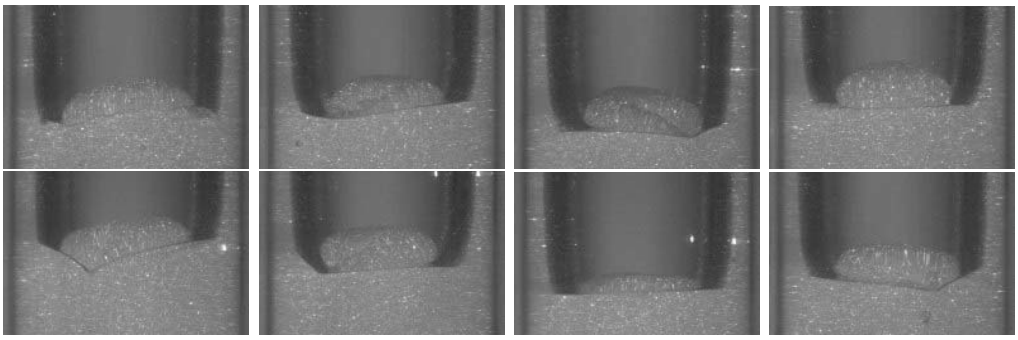

Figure 4.72. Trailing edge images (PIV/ST) of Taylor bubbles rising in a 0.40 wt% PAA solution.

slight differences from bubble to bubble. During the rise of the bubbles some oscillations of the bubble body were seen in the radial direction, causing slight asymmetries in the flow around the bubble. Due to this behaviour, the flow field behind different Taylor bubbles was also asymmetric in most cases.

In Figure 4.73, an instantaneous velocity field in the wake of a Taylor bubble rising in 0.40 wt% PAA solution is represented. This is one of the few symmetric flow patterns found. From the velocity field it is clear that this is a negative wake, similar to those found in the 0.80 and 1.00 wt% CMC solutions, despite the differences in the bubble trailing

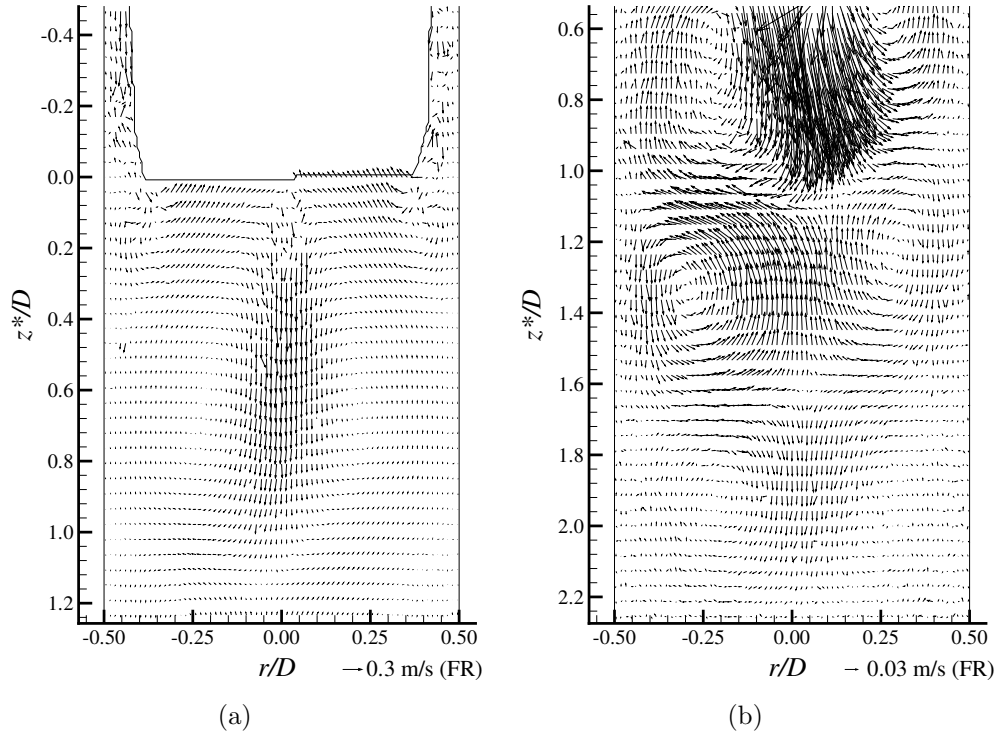

Figure 4.73. Flow field in the wake of a Taylor bubble (U_b=0.142 m/s) rising in a 0.40 wt% PAA solution; fixed frame of reference.

edge shape. The erroneous vectors in the liquid film are due to the long time gap between frames in order to obtain the low wake velocities. By increasing the vector length, Figure 4.73(b), three recirculation regions are clearly seen, with inversion of the flow direction and decreasing velocity magnitude. In the upper recirculation region, the downward velocity magnitude is about twice the bubble velocity, while in the lower one it is about one tenth of the bubble velocity magnitude.

However, this flow pattern was not frequently found. Due to the aforementioned asymmetries in the liquid film around the bubble, the most common wake flow pattern is slightly asymmetric, as shown in Figure 4.74.

Very often a negative wake is not seen in the measurement plane. Figure 4.75 shows two examples of very asymmetric flow fields in the wake of Taylor bubbles rising in a 0.40 wt% PAA solution, where negative wakes are not present. In these flow fields it is clear that the fluid coming from the liquid film has different velocity magnitude on both sides of the plane, creating a large recirculation region behind the Taylor bubble.

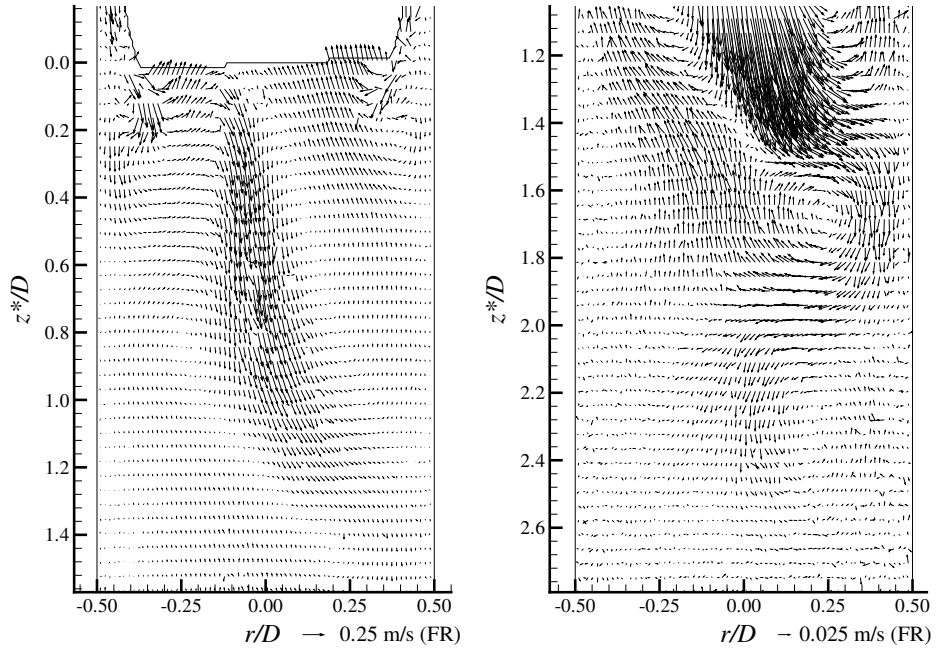

Figure 4.74. Slightly asymmetric flow field in the wake of a Taylor bubble (U_b=0.167 m/s) rising in a 0.40 wt% PAA solution; fixed frame of reference.

As seen from the flow fields presented here, different flow patterns were found behind the bubbles rising in 0.40 wt% PAA solution, which had no apparent correlation with the bubble velocity. The reasons, as already mentioned, could be related to the fluid history and a possible non-homogeneity of the solution. Nevertheless, as seen in the flow fields of Figure 4.73 and 4.74, when there is symmetry in the flow around the Taylor bubble, a negative wake should be expected behind the Taylor bubble.

Since an insufficient number of bubbles with the same velocity and length was obtained to have statistically meaningful average velocity profiles, instantaneous profiles obtained from a practically symmetric negative wake are presented. Figure 4.76 shows the axial velocity profiles at different distances from the bubble trailing edge. From these profiles, the negative wake is clearly seen by the central downward flow close to the bubble trailing edge. The velocity magnitude decreases as the distance from the trailing edge increases and some inversions in the flow direction occur. The second recirculation region starts between $z* = 1.0D$ and $z* = 1.2D$, with an upward liquid flow around the axis. A second inversion of the flow occurs after $1.6D$ from the bubble trailing edge (third recirculation region). Despite the low velocity magnitude, another inversion is seen around $z* = 2.2D$

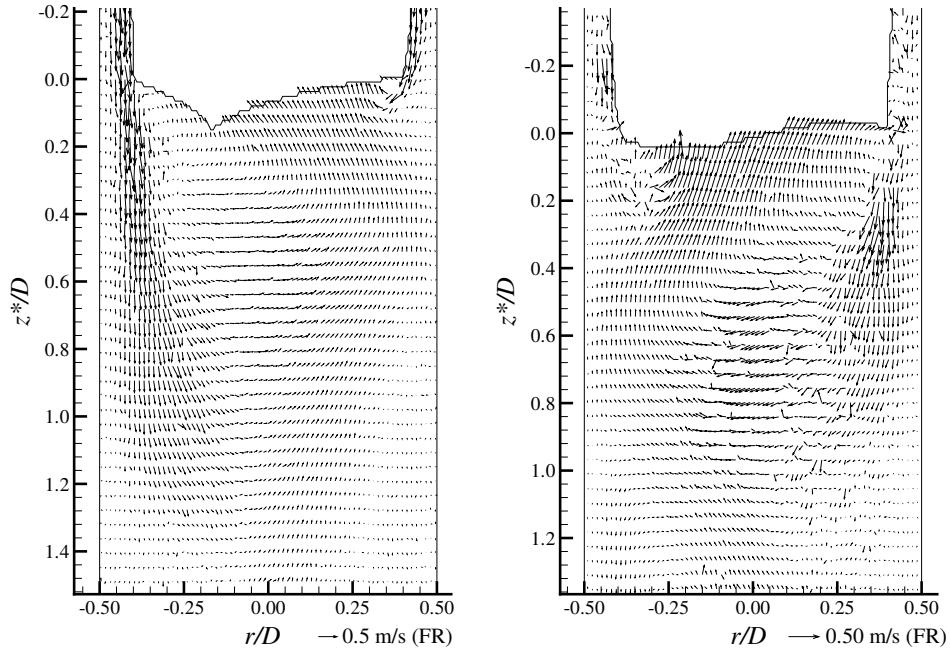

Figure 4.75. Flow field in the wake of Taylor bubbles ($U_\mathrm{b} = 0.158\,\mathrm{m/s}$) rising in a 0.40 wt% PAA solution; fixed frame of reference.

(fourth recirculation region). With the used time between frames, at least four recirculation regions were detected behind the Taylor bubble, with decreasing velocity magnitude and alternating rotational direction.

The instantaneous radial velocity profiles in the negative wake behind a Taylor bubble rising in 0.40 wt% PAA solution are represented in Figure 4.77. Remembering that negative radial velocities are those in the direction of the axis of the column, the change in the fluid rotational direction is also perceptible in the radial velocity profiles. It is, however, impossible to detect the passage of consecutive recirculation regions since the radial velocity profiles in the lower part of a recirculation region are similar to those in the upper part of the following recirculation.

In the first recirculation region, between $z* = 0$ and $z* = 0.5D$, the fluid is moving towards axis of the column, and from $z* = 0.5D$ to $z* = 1.0D$ the fluid is moving outwards. The opposite occurs in the second recirculation, which moves away from the axis in the upper region and towards the axis in the lower region. The third recirculation region moves in the same direction of the first one, but below $z* = 2.5D$ the velocity magnitudes are

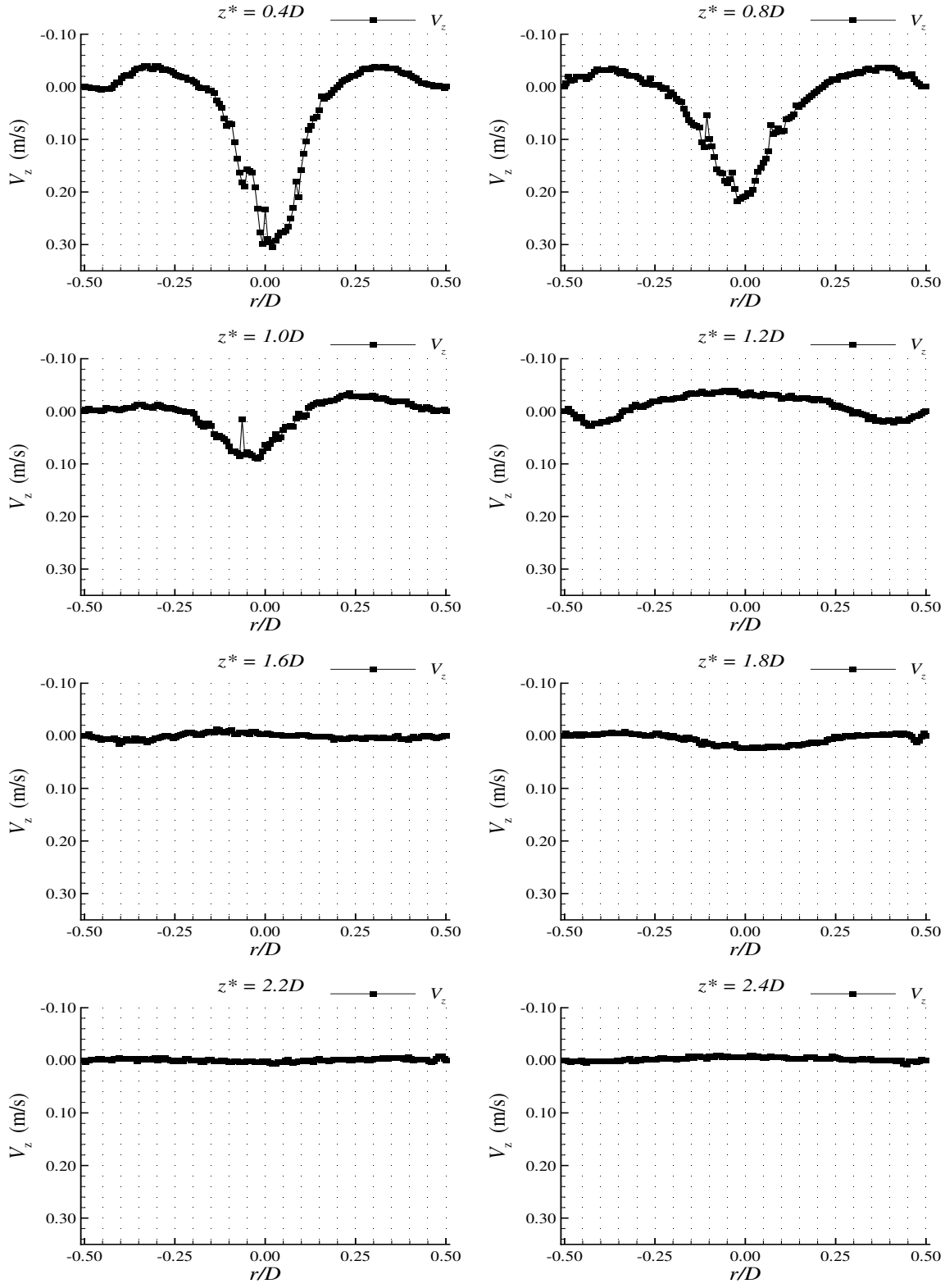

Figure 4.76. Instantaneous axial velocity profiles (fixed frame of reference) at different distances from the trailing edge of a bubble rising in a 0.40 wt% PAA solution.

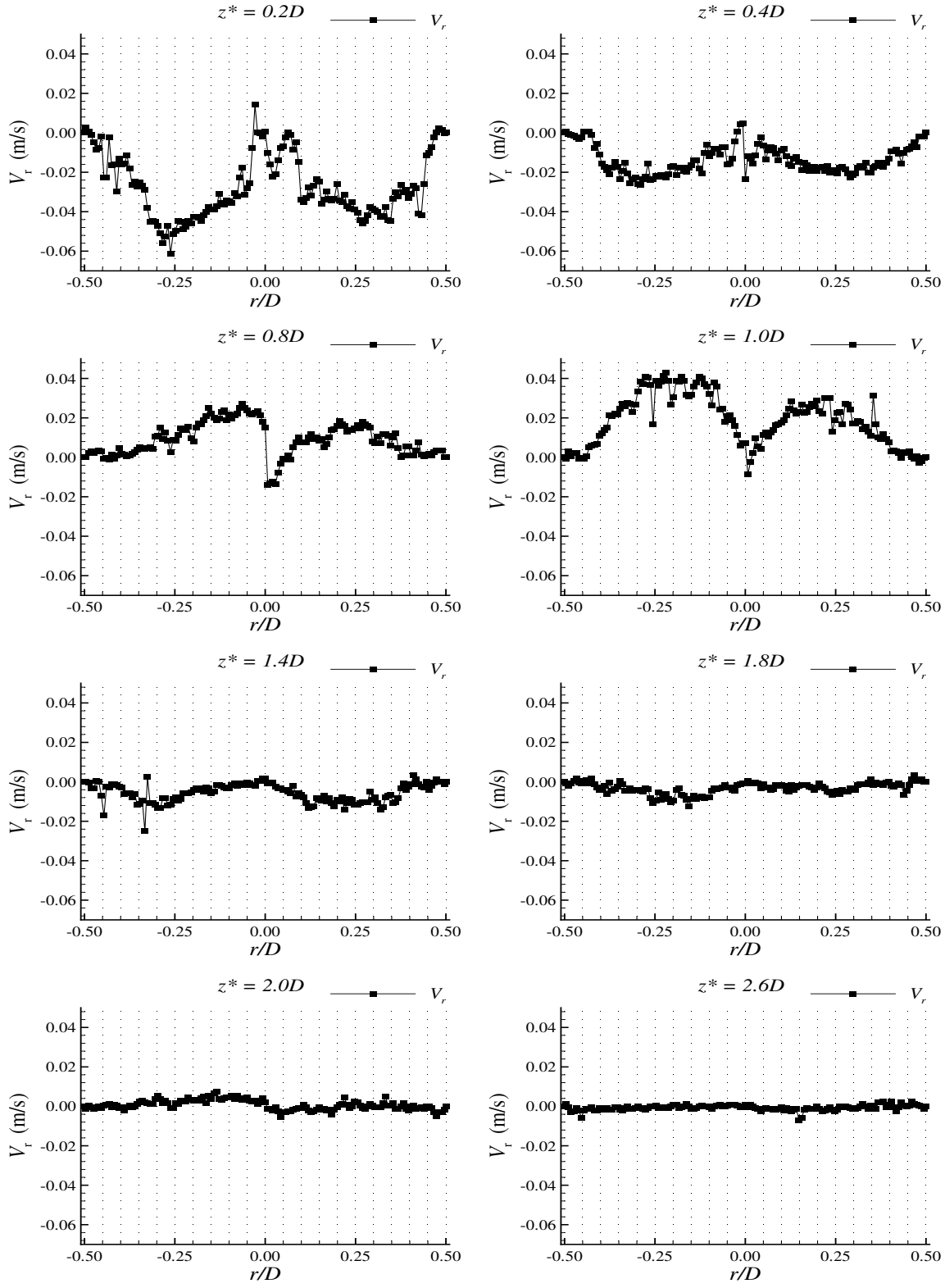

Figure 4.77. Instantaneous radial velocity profiles (fixed frame of reference) at different distances from the trailing edge of a bubble rising in a 0.40 wt% PAA solution.

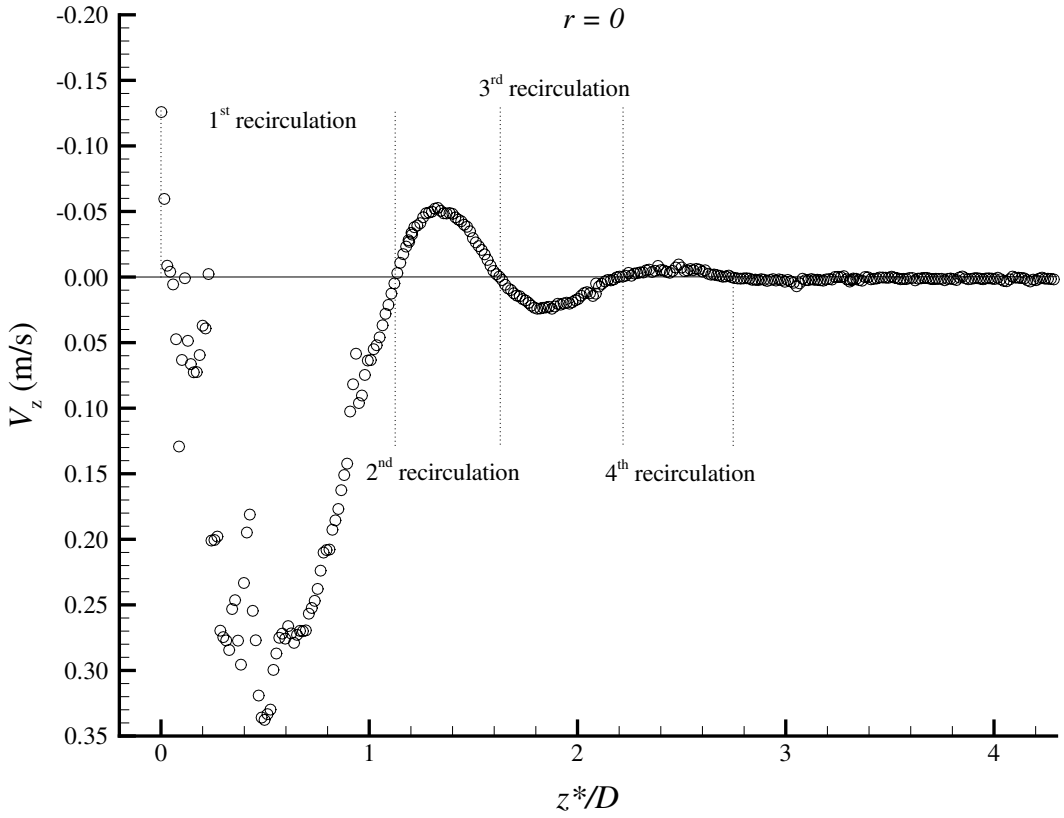

Figure 4.78. Instantaneous axial velocity profile (fixed frame of reference) at $r = 0$ in function of $z*/D$ behind a Taylor bubble rising in a 0.40 wt% PAA solution.

already negligible.

From the plot of the axial velocity at $r = 0$, Figure 4.78, four recirculation regions are clearly seen, starting with a downward flow with more than twice the bubble velocity magnitude. The flow direction is then inverted sequentially with decreasing velocity magnitude.

As mentioned before, this Figure represents a rare, practically symmetric flow behind a Taylor bubble rising in a 0.40 wt% PAA solution. Asymmetric flows were seen frequently, as described in previous figures, but what caused them was not conclusively identified. In the 0.80 wt% PAA solution, these asymmetries were even more evident, as described in the next section.

0.80 wt% PAA

In the visualisation studies with a 0.80 wt% PAA solution, the bubble trailing edge presented a lachrymal shape, similar to those found in the 0.80 and 1.00 wt% CMC solutions. No coloured liquid was seen in the wake.

In the PIV/ST studies, the bubble did not exhibit the same behaviour. The lower experimental temperature and the larger volume of solution prepared might have led to a higher viscosity and more difficulties in obtaining an homogeneous solution. Therefore, the flow around bubbles rising in 0.80 wt% PAA solution tended to be very asymmetric, with the bubble rising the column close to the column wall, with no preferred side. The velocity of bubbles having the same length varied more than 30%.

Some examples of images of the trailing edge of bubbles rising in a 0.80 wt% PAA solution are presented in Figure 4.79 As seen from this figure, the trailing edge always

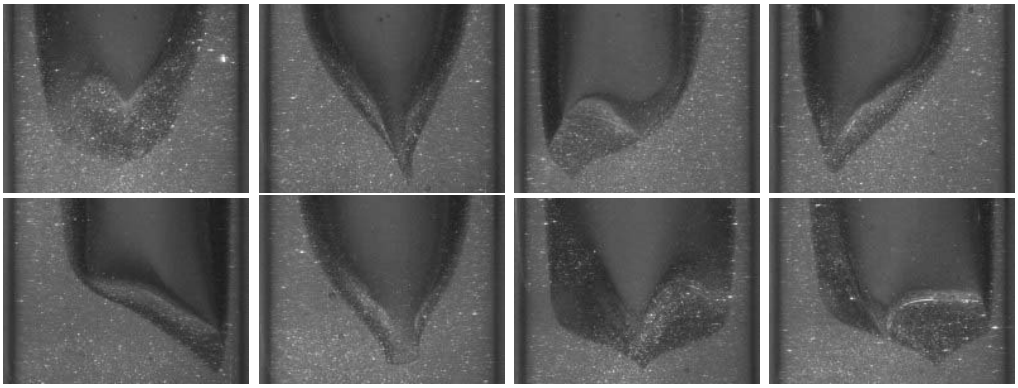

Figure 4.79. Trailing edge images (PIV/ST) of Taylor bubbles rising in a 0.80 wt% PAA solution.

presents an asymmetric shape, with no preferential orientation. However, during the rise of a single bubble, the trailing edge shape does not change much. It maintains an almost stable position in one of the orientations presented in Figure 4.80.

The flow field behind Taylor bubbles rising in a 0.80 wt% PAA solution is then dependent on the trailing edge position. Since it is not axi-symmetric, the velocity field projection on the measurement plane presents different patterns. In Figure 4.80, two examples of the flow field obtained behind Taylor bubbles rising in a 0.80 wt% PAA solution are represented. Since the Taylor bubble rises close to the column wall, the falling liquid film is not axi-symmetric and the velocity is higher in the plane region, where the liquid film thick-

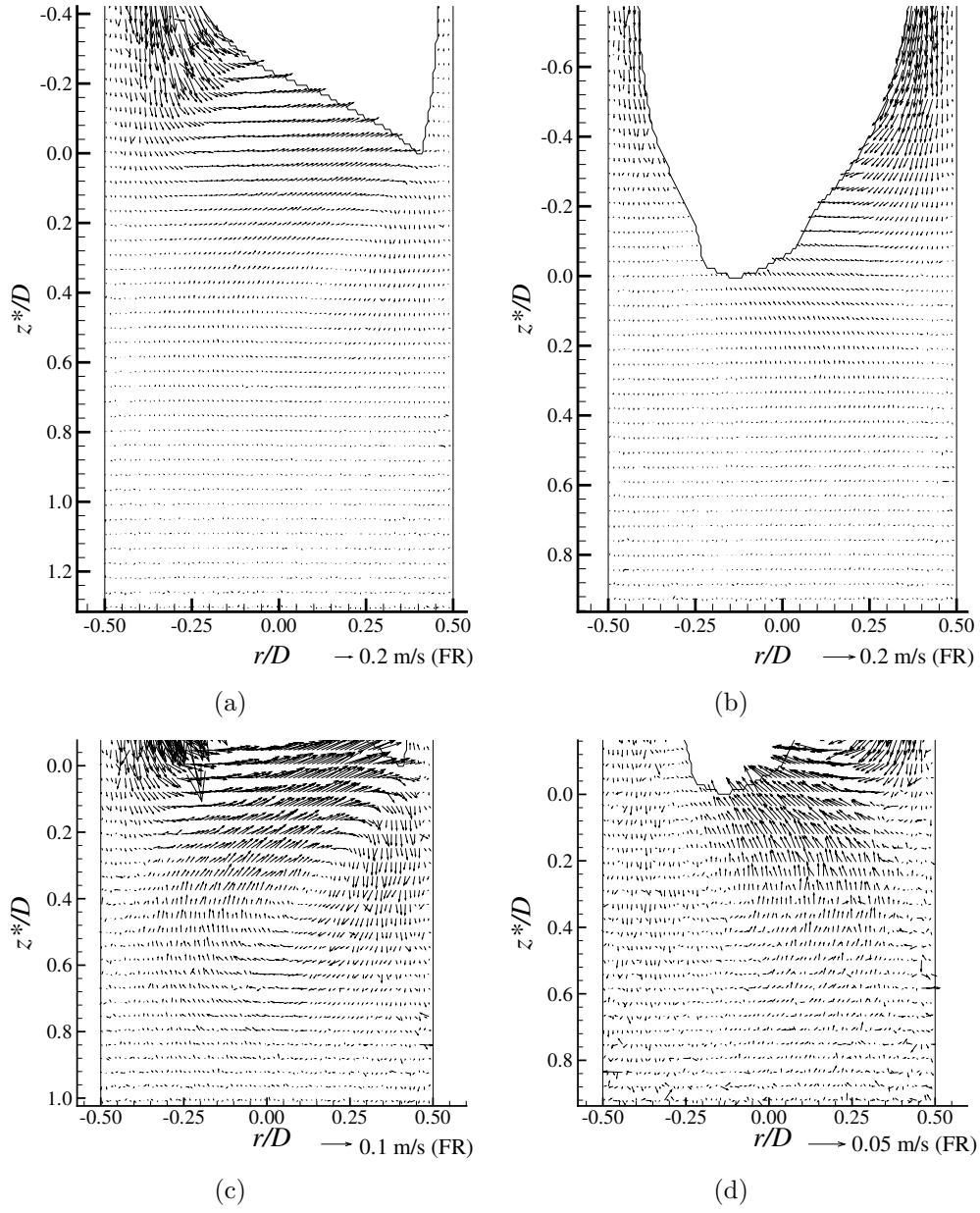

Figure 4.80. Flow field in the wake of Taylor bubbles rising in a 0.80 wt% PAA solution; fixed frame of reference.

ness is also higher. When the liquid film reaches the bubble trailing edge it gains radial velocity to occupy the space left by the bubble. The liquid can move from left to right (Figure 4.80(a)), in the opposite direction (Figure 4.80(b)), or in any other direction out of the measurement plane, depending on the three-dimensional orientation of the trailing

edge. In Figures 4.80(c) and 4.80(d), the increased vector scale allows, as before, a clear perception of recirculation regions below the trailing edge, induced by the radial movement of the liquid coming from the falling film. This rotational movement is similar to those found in the negative wakes, but there the flow around the bubble is symmetric, and an axi-symmetric rotational movement is created. The velocity magnitude of the liquid in the recirculation region is only around 20% of the bubble velocity and after $z* = 0.8D$, the fluid is practically stagnant.

Other trailing edge orientations induce the fluid rotational movement in planes that are out of the measurement plane. The three-dimensional flow field has then, a different pattern in the two dimensional measurement plane, as shown in Figure 4.81. In Figure

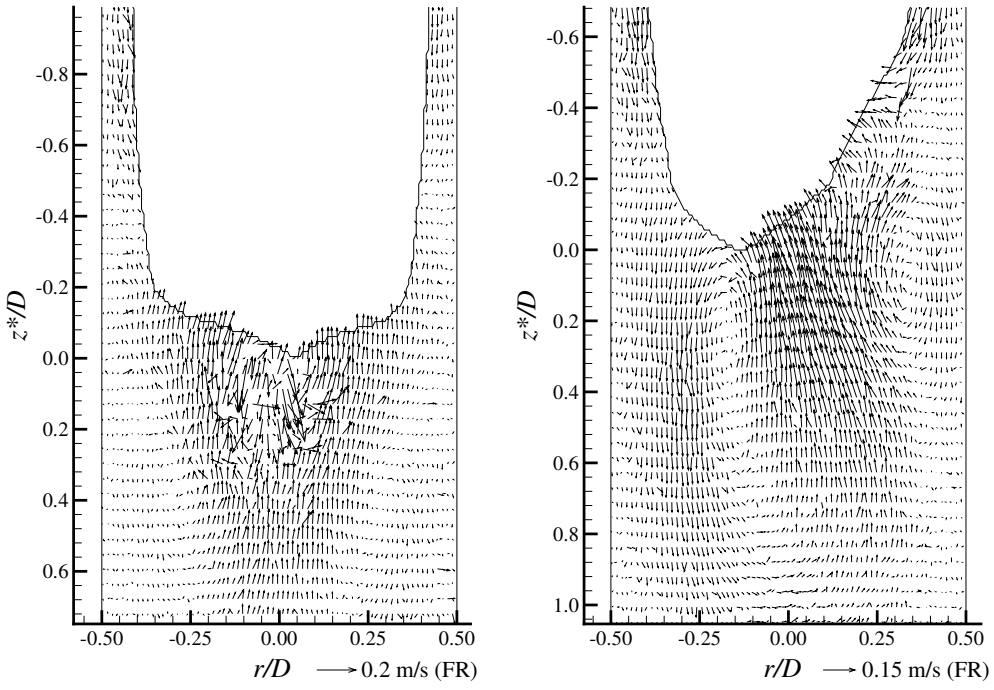

Figure 4.81. Flow field in the wake of Taylor bubbles rising in a 0.80 wt% PAA solution; fixed frame of reference.

4.81(a), the rotational movement direction appears to be perpendicular to the measurement plane. In its projection, only the upward liquid movement is seen, and it approximately corresponds to a plane perpendicular to those represented in Figures 4.80(c) or 4.80(d), crossing those planes at $r = 0$. An intermediate orientation is represented in Figure 4.81,

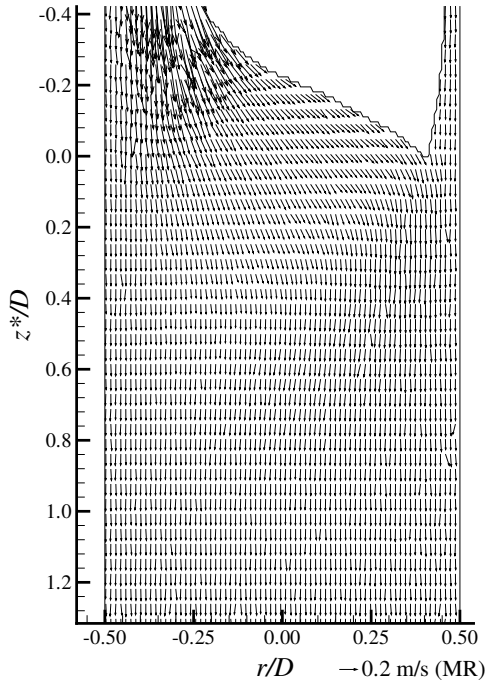

Figure 4.82. Flow field in the wake of a Taylor bubble rising in a 0.80 wt% PAA solution; frame of reference moving with the bubble.

where the rotational movement is perceptible, although in an oblique plane relative to the measurement plane. Due to the different bubble velocity, trailing edge orientations and the absence of a symmetric wake flow, average velocity profiles are meaningless.

The wake flow field in a frame of reference moving with the bubble is represented in Figure 4.82. In a moving frame of reference it is seen that the liquid simply follows the bubble shape, and no recirculation regions are perceptible due to their low velocity magnitude. After $z* = 0.8D$, the bubble disturbance on the flow is already imperceptible.

4.3.7 Summary of bubble wakes in PAA solutions

Similar to the CMC solutions, a comparison between the flow in the wakes of Taylor bubbles rising in the PAA solutions studied is now presented.

In Figure 4.83, the axial velocity profiles at $r = 0$ behind the Taylor bubbles are represented. This figure is elucidative of the long region behind the wakes where the flow is disturbed. In the 0.01 wt% PAA solution, the upward velocity magnitude behind the trailing edge is higher than those observed in the CMC solutions. The velocity magnitude

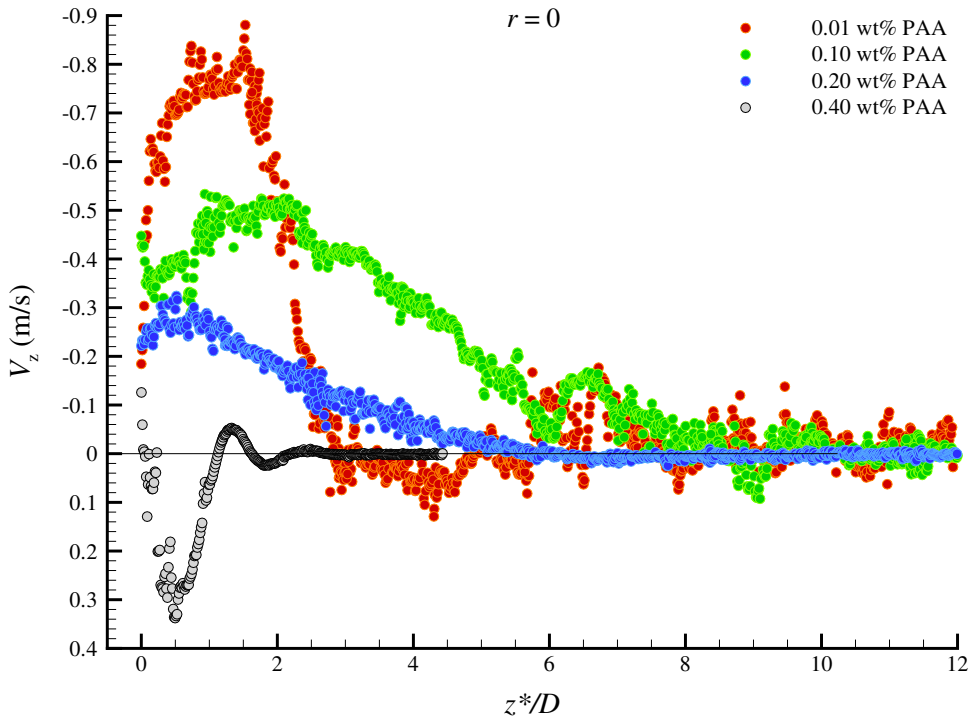

Figure 4.83. Axial velocity profile at $r = 0$ behind Taylor bubbles rising in PAA solutions.

decreases up to around $3.0D$ from the bubble trailing edge, where the liquid film reattaches (in a fixed frame of reference). A downward liquid flow is seen until $z* = 6D$, before the disturbance caused by a train of small bubbles rising behind the Taylor bubble (up to $20D$ from the bubble trailing edge). The distance at which the liquid stagnates is then dependent on the amount of small bubbles. The 0.10 wt% PAA solution is where the longest region of upward central liquid flow behind the Taylor bubble is seen. The upward velocity magnitude is not so high as in the 0.01 wt% PAA solution, but the decrease in velocity is smoother. There is liquid moving upwards in the axis of the column to around $9.0D$ from the bubble trailing edge. In the 0.20 wt% PAA solution, the behaviour is similar, although the upward velocity magnitude is now closer to the bubble velocity. There is also a smooth decrease in the velocity magnitude up to $z* = 6.0D$, after which the fluid slowly stagnates. This smooth velocity decrease observed behind the Taylor bubbles rising in 0.10 and 0.20 wt% PAA solution occurs due to the continuous stretching of the fluid in the axis of the column. The high extensional and shear viscosity allows the fluid to be stretched without breaking. The liquid coming from the falling film flows for a long

distance under high velocity gradients, and therefore under high shear rates, which lowers its shear viscosity by more than one order of magnitude.

In the 0.40 wt% PAA solution, the higher shear viscosity and elasticity induce a negative wake behind the Taylor bubbles, if the flow around the bubbles is symmetric. At least four recirculation regions are perceptible in the flow field.

The plot in Figure 4.83 is virtually enough to understand the flow patterns behind the Taylor bubbles. Nevertheless, the axial velocity profiles at $z* = 0.4D$ from the bubble trailing edge are represented in Figure 4.84 for the PAA solutions. This figure shows that

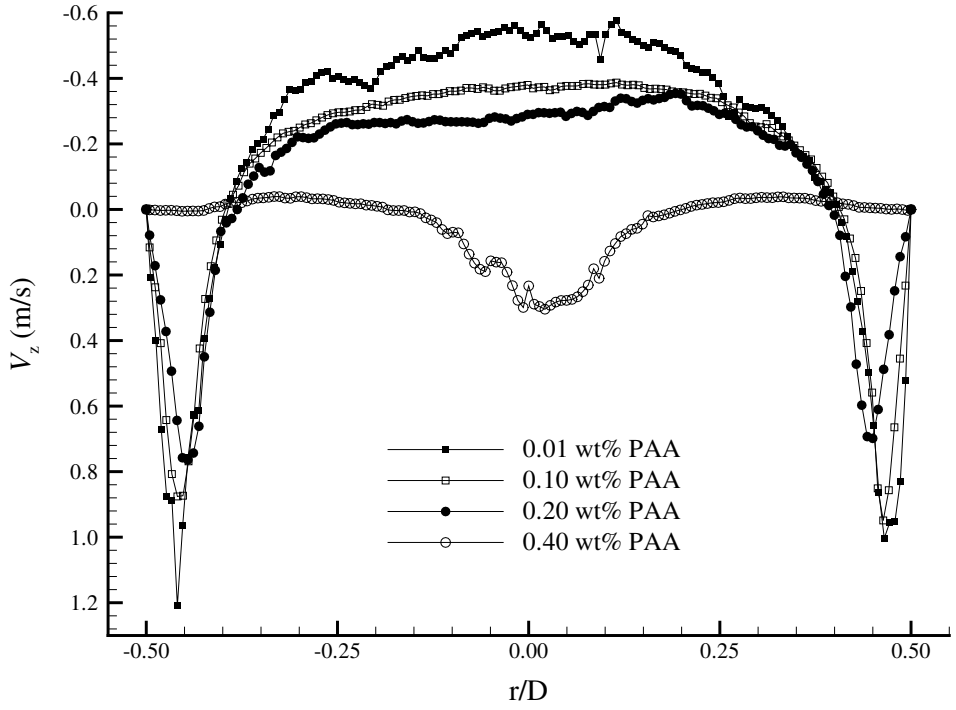

Figure 4.84. Axial velocity profile at $z* = 0.4D$ in the wake of Taylor bubbles rising in PAA solutions.

the velocity profiles are very similar in the wakes where upward liquid flow is seen, varying only slightly in the velocity magnitude. In the 0.40 wt% PAA solution, the negative wake is easily distinguishable by the positive (downward) axial velocity component in the axis of the column.

In the PAA solutions, only in the 0.01 wt% solution can a wake length be defined. This is around $2.3D$ from the trailing edge, which is the region where the liquid film reattaches

in a frame of reference moving with the bubble. In the 0.10 and 0.20 wt% PAA solutions the reattachment of the liquid film is not observed. We can, however, estimate the wake length as the distance from the trailing edge to where the upward velocity magnitude equals the bubble velocity, which is around $z* = 5D$ and $z* = 1.8D$ for the 0.10 and 0.20 wt% PAA solutions, respectively.

After analysing the flow around individual Taylor bubbles rising in several CMC and PAA solutions, coalescence studies between two Taylor bubbles were performed in selected solutions to see the relation between the wake flow patterns and the distance behyond which the bubbles do not interact. The results are shown in the following chapter.

Chapter 5

Study of bubble coalescence

Abstract

This chapter presents the results obtained in the coalescence studies. A study was performed with pairs of Taylor bubbles rising in stagnant liquid to observe the effect of the leading bubble on the behaviour of the following one. The results are interpreted and related to the previously described flow fields around individual Taylor bubbles.

The aim of this thesis is to investigate the occurrence of Taylor bubble coalescence in non-Newtonian fluids and to explore the mechanisms which influence this phenomenon. After describing the flow field around individual Taylor bubbles, an experimental study was performed with pairs of bubbles rising in stagnant liquid to observe what effect the leading bubble has on the following one. The experimental setup and procedure is described below.

5.1 Experimental setup

The study consisted of injecting pairs of Taylor bubbles at different instants and analysing any interaction during their rise. It was performed in a vertical acrylic column, with a height of 7 m and a 32 mm internal diameter.

Two lateral tubes connected at the bottom of the main column, as shown in Figure 5.1, worked as the bubble injection system. In each injection tube, two globe valves (V_A and V_B) facilitated the launch of a Taylor bubble; opening the upper valve released the air trapped between the valves into the main column. For each solution, studies were made

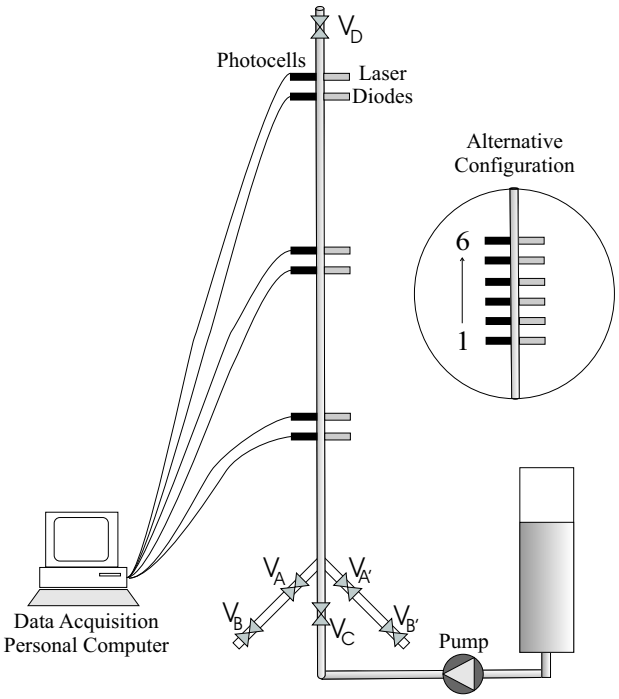

Figure 5.1. Experimental setup used in the coalescence studies.

with the column open to the atmosphere on top, and with the column closed on top (valve V_D).

The bubble velocity was determined with the technique described in §2.2.7, using six sets of laser diodes/photocells. The laser diodes/photocells were mounted with two different configurations, as represented in Figure 5.1. First, pairs of laser diodes/photocells were placed at three distant positions, to determine the bubble velocity variation along the column and bubble interaction at long distances. After checking the distance above which there is no interaction between the bubbles, the laser diodes were placed according to the alternative configuration shown in Figure 5.1, with the six sets of laser diodes/photocells placed closer and equal distant to each other to analyse the bubbles interaction during coalescence (short distances between bubbles).

The signals of the photocells were acquired with a Data Acquisition Personal Computer and an example of the signals obtained in each configuration is presented in Figure 5.2. In this figure, the signals were shifted vertically for better visualisation. In case (a), pairs of laser diodes/photocells were placed near the bottom of the column (PC_1, PC_2), in the middle (PC_3, PC_4) and close to the top (PC_5, PC_6). The passage of the two Taylor bubbles

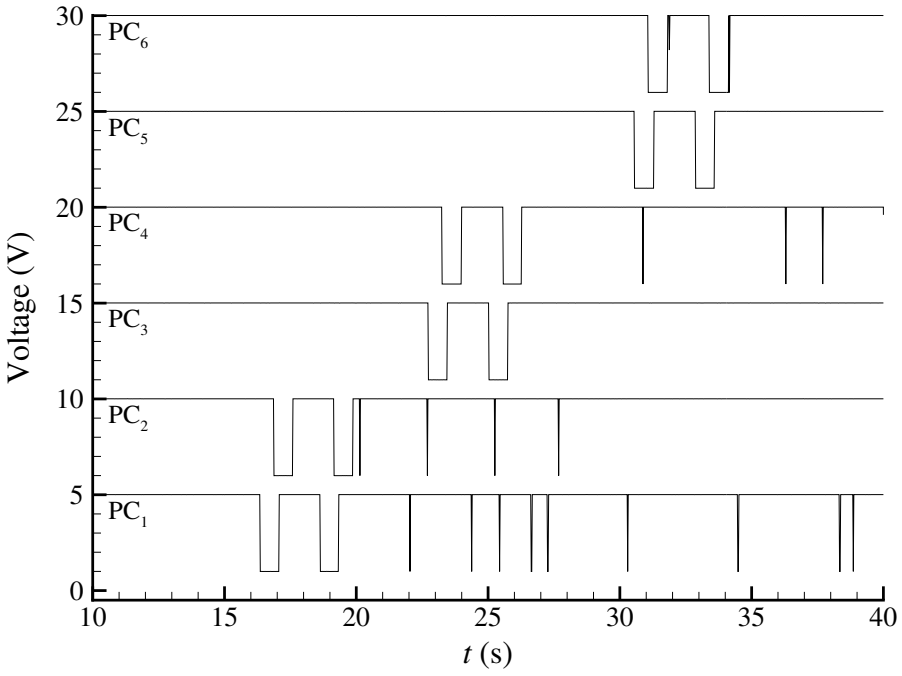

(a)

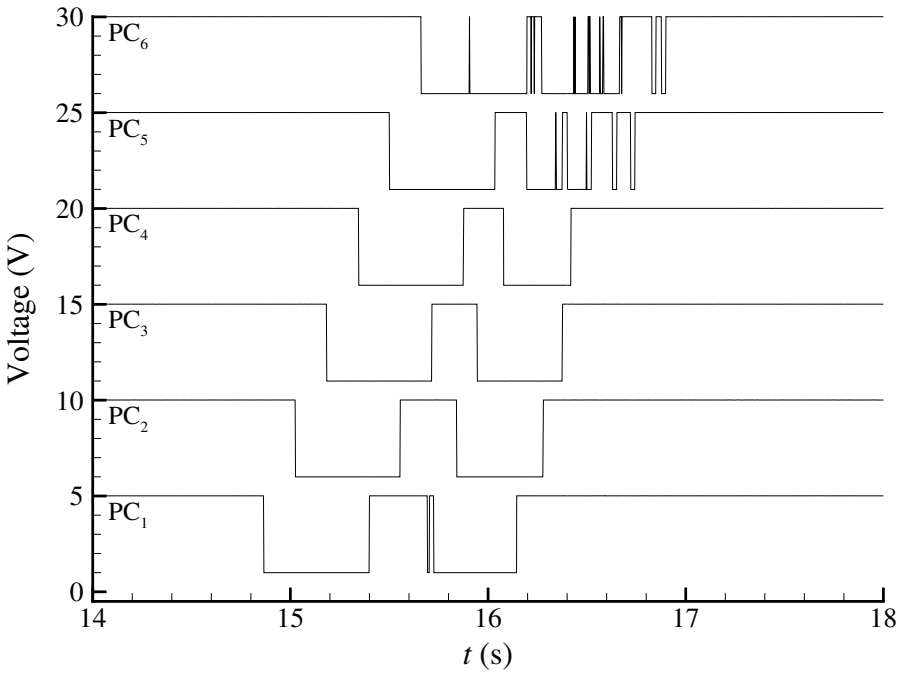

(b)

Figure 5.2. Signals obtained from the photocells (PC) in original (a) and alternative (b) configurations; ascending number of photocell according to ascending position in the column. Signals were shifted according to the expression: $PC_i = V * 4/5 + 5 * i - 4$.

Table 5.1. Experimental conditions in the coalescence studies with CMC solutions.

CMC wt%	T^oC	$\overline{L}_b/D$
0.10	18.1	4.8
0.30	18.1	4.8
0.40	21.1	3.5
0.80	22.6	4.4

is clearly seen by the large downward steps in the output signal of each photocell (Figure 5.2(a)). In this example, the bubbles kept approximately the same distance between them along the column. The short peaks after the Taylor bubbles are caused by the presence of small bubbles behind the wakes, as shown in previous chapters for the less viscous solutions.

To study coalescence in more detail, the alternative configuration was used; placing the six sets of laser diodes/photocells equally separated in the same region. One example of the signal acquired with this configuration is represented in Figure 5.2(b). In this example, the approach of the second bubble is clearly seen by the decreasing time lag between the downward steps as the bubbles pass through the photocells. The peaks seen in the voltage of the last photocells are due to oscillations in the nose of the second bubble when entering the wake of the leading one and to the presence of small bubbles.

From the acquired signals it is possible to determine the bubble velocity, the bubble length and the distance between consecutive bubbles, l_s. This distance is that between the second bubble nose and the first bubble trailing edge. According to the coordinate system used in the PIV results, the bubble velocity is negative. The results of this study on the interaction of Taylor bubbles rising in CMC solutions are presented in the next section.

5.2 Coalescence of Taylor bubbles rising in CMC solutions

After describing the flow field around individual Taylor bubbles rising in CMC solutions, the study of the coalescence of pairs of Taylor bubbles rising in stagnant CMC solutions was performed on selected cases, covering the different flow patterns seen in the PIV results. The experimental conditions are presented in Table 5.1, where the bubble lengths were determined from the photocells signals. The bubble volume was determined by the length

of the injection tubes at the bottom of the column (Figure 5.1). For the less concentrated solutions the average bubble length was below the minimum length to have a developed liquid film, but as seen from the PIV results in the wakes of 0.10 wt% CMC, this only affects the trailing edge oscillation, amplitude and frequency. The wake flow pattern is practically the same for long and short bubbles.

5.2.1 0.10 wt% CMC solution

In the 0.10 wt% CMC solution, the PIV and visualisation studies showed a wake flow pattern with high velocity magnitudes and oscillations. The low viscosity and the detachment of vortex structures imply a long distance until the fluid stagnates after the passage of a Taylor bubble. The presence of small bubbles behind the wake induce an upward liquid flow around the axis of the column, contributing to a very long region with liquid in movement.

In the coalescence studies, preliminary experiments were performed with single Taylor bubbles to compare how having the column open or closed on top affects bubble velocity and length. In Figure 5.3, the results obtained with the column open are presented. As expected, during the rise along the column the decrease in hydrostatic pressure is responsible for gas expansion and the consequent increase of bubble length. The length of a single bubble may increase up to 20% between the lower and upper measurement positions. The bubble volume change rate varies with the bubble progress along the column (§3.3.3 - Eq.3.12) and thus, both the liquid velocity profile ahead of the bubble and the bubble velocity suffer slight changes. However, by determining the effect of the bubble volume expansion rate on the bubble velocity, it is found that the variation of the bubble velocity between those locations is around the uncertainty on the bubble velocity measurement, 0.002 m/s. This is the reason why the bubble velocity variation along the column is not perceptible in these experiments.

If the column is completely closed the gas is not free to expand, and so the bubble length is expected to be constant along the column. Figure 5.4, shows the bubble velocity and length variation along the column when the top valve is closed. Here, both the bubble velocity and length remain practically constant during the rise in the column. The higher scattering on the bubble length is due to the oscillation of the bubble trailing edge in this solution. It is, however, evident that the bubble velocity is higher when the column is open

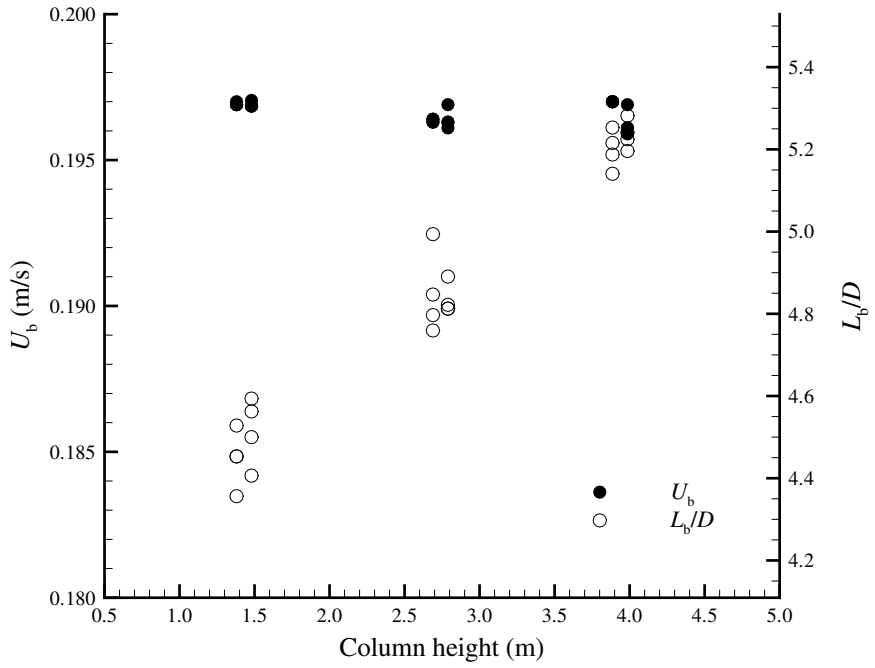

Figure 5.3. Representation of length and velocity of single bubbles rising in a column open on top, filled with 0.10 wt% CMC solution.

to the atmosphere, due to the influence of the liquid flow ahead of the bubble induced by the gas expansion.

After checking the behaviour of a single bubble rising along the column, studies were made with two consecutive bubbles rising in the column with different distances between them. When the column is open on the top, the liquid ahead of the first bubble is moving at a flow rate resulting from the sum of both bubbles' volume expansion. The liquid between the bubbles is only moving at a flow rate resulting from the volume expansion rate of the second bubble. Disregarding the wake flow pattern, this fact would always induce a higher velocity on the first bubble relative to the second bubble and the tendency would be to increase the distance between them. For this reason, the study was focused on the interaction between bubbles with the column closed on the top.

In Figure 5.5, the distance between the second bubble nose and the bottom of the first bubble (distance between two consecutive bubbles), l_s, is represented in a dimensionless form as a function of the bubble locations in the column. Since the distance between the bubbles is only determined when the second bubble nose reaches the laser diodes, the column height in the plots refers to the location of the second bubble nose in the column.

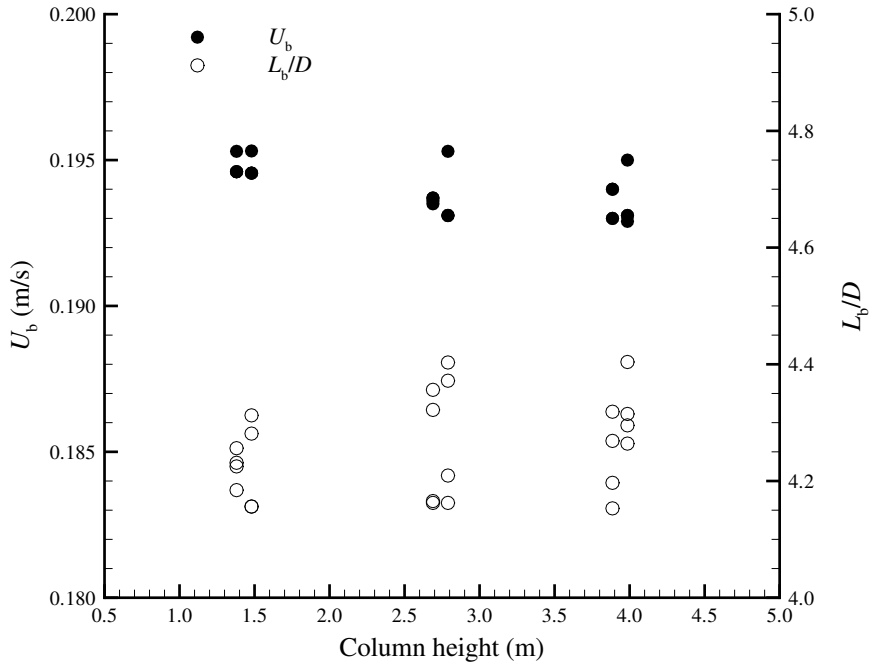

Figure 5.4. Representation of length and velocity of single bubbles rising in a column closed on top, filled with 0.10 wt% CMC solution.

Each line in Figure 5.5 corresponds to a pair of Taylor bubbles. From this figure, it is

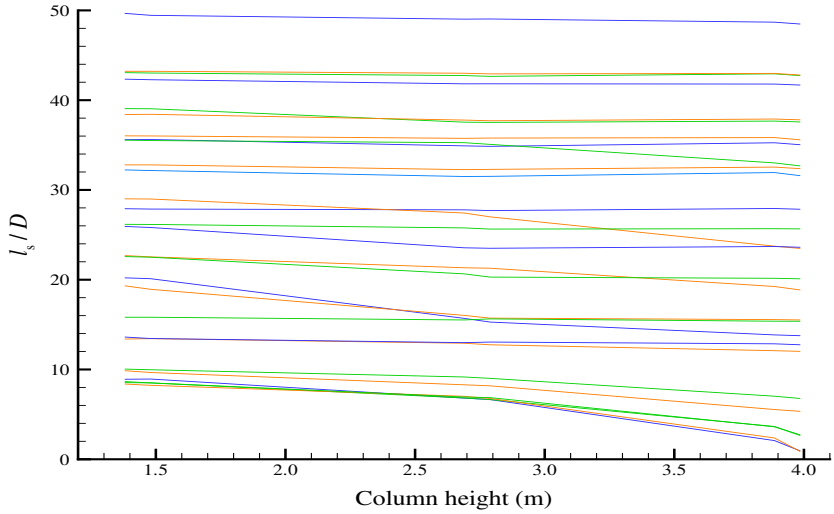

Figure 5.5. Distance between consecutive bubbles, l_s/D, rising in a 0.10 wt% CMC solution, as a function of the second bubble nose position in the column.

seen that when the distance between the bubbles is below $10D$, the distance between them tends to decrease, meaning that the second bubble is flowing faster than the first bubble. What's more, due to the influence of small bubbles in the wake of the first Taylor bubble, even at distances up to $40D$ some interaction is seen between the bubbles.

After the determination of the distance below which the bubbles would coalesce, the photocells were placed closer together (alternative configuration of Figure 5.1), to analyse the interaction between bubbles at shorter distances. In Figure 5.6, the ratio between the trailing bubble velocity, U_{T}, and the leading bubble velocity, U_{L}, is represented as function of the distance between them. Values higher than 1 mean that the second bubble velocity is higher than the leading bubble velocity and so they are approaching each other. For

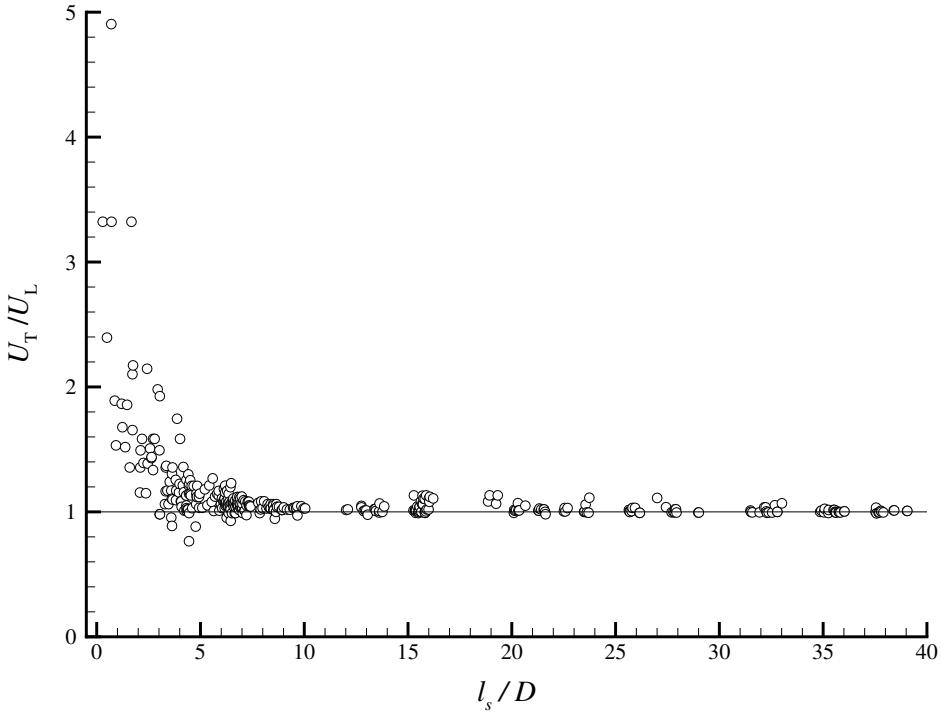

Figure 5.6. Ratio between the velocities of consecutive bubbles as a function of the distance between them, when rising in a 0.10 wt% CMC solution.

distances above $20D$, the bubbles velocity is the same in general. Between $l_{\mathrm{s}} = 10D$ and $l_{\mathrm{s}} = 20D$, there begin to be some cases where the second bubble velocity increases, mainly due to the presence of small bubbles. Below $l_{\mathrm{s}} = 10D$, there is a clear influence of the leading bubble wake. Due to the liquid velocity oscillations along the cross-section of the

column, there is a large scattering in the data of the second bubble velocity. There are even cases where the second bubble velocity decreases relative to the leading one, since the second bubble nose can encounter a downward liquid flow in the region where the liquid film of the first bubble reattaches. From this figure, despite the effect of the small bubbles, the influence of the first bubble wake on the second bubble velocity is negligible above $l_s = 10D$.

To relate the coalescence studies with the PIV results, in Figure 5.7 an instantaneous profile of the axial velocity component in the axis of the column behind a Taylor bubble is represented as a function of the distance to the bubble trailing edge simultaneously with the velocity of a trailing bubble as a function of the distance between bubbles. The higher

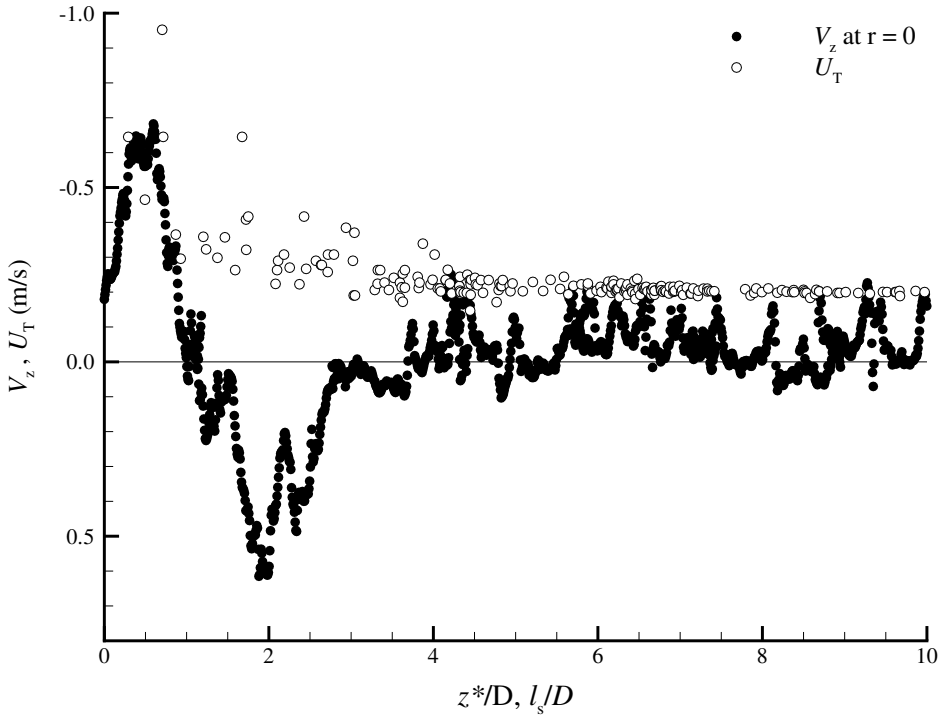

Figure 5.7. Comparison between the trailing bubble velocity and the axial liquid velocity at $r = 0$ in the wake of Taylor bubbles rising in 0.10 wt% CMC solution.

scattering of the trailing bubble velocity data is clearly related with the presence of the bubble in the region of higher liquid velocity oscillations, i.e., in the wake of the preceding bubble. Although there is a downward flow in the central region of the wake, the general tendency of the trailing bubble velocity is still to increase. This is explained by the velocity

profiles in the wake that show an upward liquid flow away from the axis. This affects the trailing bubble velocity, and its nose oscillates when approaching the leading bubble, as it seeks the least resistant displacement (maximum upward liquid velocity).

5.2.2 0.30 wt% CMC solution

In the 0.30 wt% CMC solution, the visualisation and PIV studies showed a wake flow pattern which was also time dependent, although with less oscillations than in the 0.10 wt% CMC solution. Behind the bubble, although small bubbles were seen, they were not so frequent as in the previous solution.

The distance between pairs of consecutive bubbles during the rise along the column is represented in Figure 5.8. The lower velocity oscillations, higher viscosity and the practical

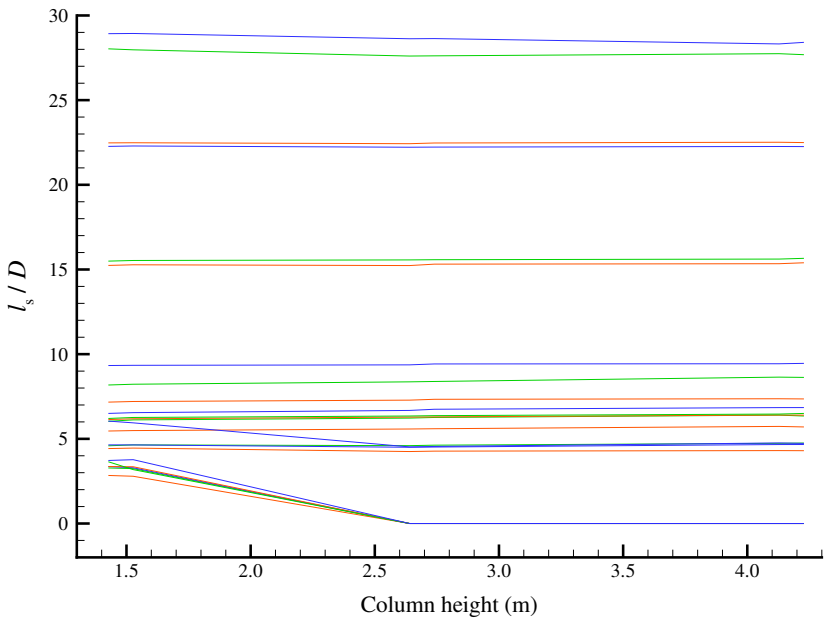

Figure 5.8. Distance between consecutive bubbles, l_s/D, rising in a 0.30 wt% CMC solution, as a function of the trailing bubble nose position in the column.

absence of small bubbles behind the Taylor bubble induce stagnation of the fluid in a shorter distance than in the 0.10 wt% CMC solution. Figure 5.8 shows that there is no interaction between the bubbles if they are separated by more than $4D$. For distances below this value, the bubbles always coalesce before reaching the top of the column.

The ratio between the trailing and leading bubble velocities is represented in Figure 5.9 for bubbles rising in a 0.30 wt% CMC solution, as a function of the distance between bubbles. This figure confirms that the second bubble velocity is only affected when the distance to the leading bubble is less than $4D$.

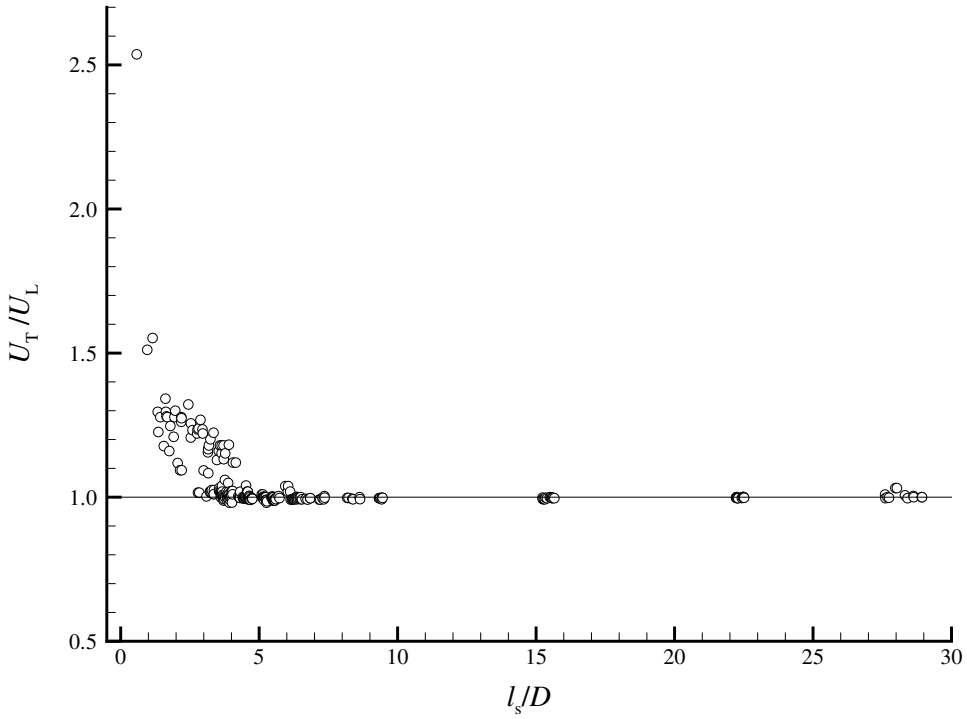

Figure 5.9. Ratio between the velocity of consecutive bubbles as a function of the distance between them, when rising in a 0.30 wt% CMC solution.

This behaviour is easily understood, when the second bubble velocity is compared with the axial component of the liquid velocity in the axis of the column obtained in the PIV measurements, as shown in Figure 5.10. As seen from the liquid axial velocity profile, at distances above $z* = 4D$ the liquid is practically stagnant, which means that the second bubble is flowing in the same conditions as the first bubble; its velocity is not affected and the bubbles do not interact. For distances below $4D$, the liquid is in movement and the velocity of the trailing bubble is affected. Between $z* = 1.5D$ and $z* = 4D$, the liquid flow in the axis of the column is in the downward direction, so the bubble nose tries to deviate from the axis and flow closer to the column walls where the liquid flows in the upward direction. This bubble nose oscillation is responsible for the data scattering in that region.

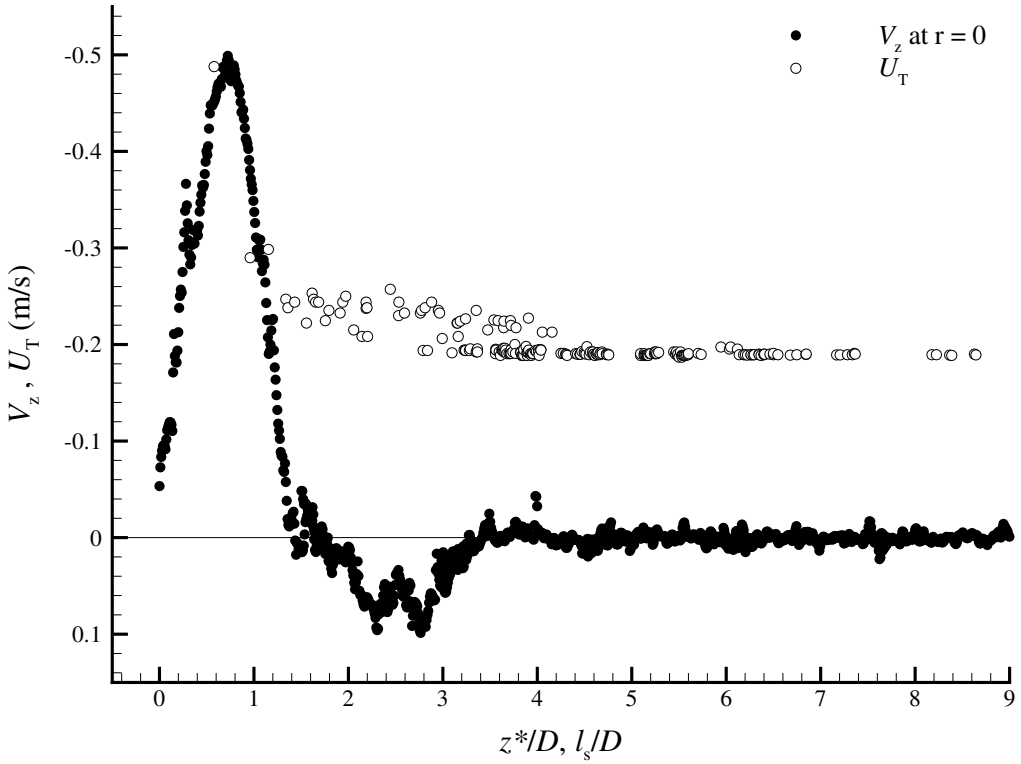

Figure 5.10. Comparison between the trailing bubble velocity and the axial liquid velocity at $r = 0$ in the wake of Taylor bubbles rising in 0.30 wt% CMC solution.

The region where the second bubble velocity suffers the highest acceleration is, however, between $z* = 0.5$ and $z* = 1.5D$, when the liquid is flowing upwards with a higher and increasing velocity magnitude. Below $z* = 0.5D$, despite the absence of data, a trailing bubble deceleration relative to its maximum velocity at $z* = 0.5D$ is expected from the liquid velocity profile.

5.2.3 0.40 wt% CMC solution

In the 0.40 wt% CMC solution, the wake flow pattern found in the visualisation and PIV studies showed a closed recirculation wake behind the Taylor bubbles, with a shorter length than in the previous solutions.

Due to the shorter wake length and higher viscosity, it was expected that the maximum bubble interaction distance would be shorter than in the 0.10 and 0.30 wt% CMC solutions.

The distance between consecutive bubbles as they rise in the column filled with 0.40 wt%

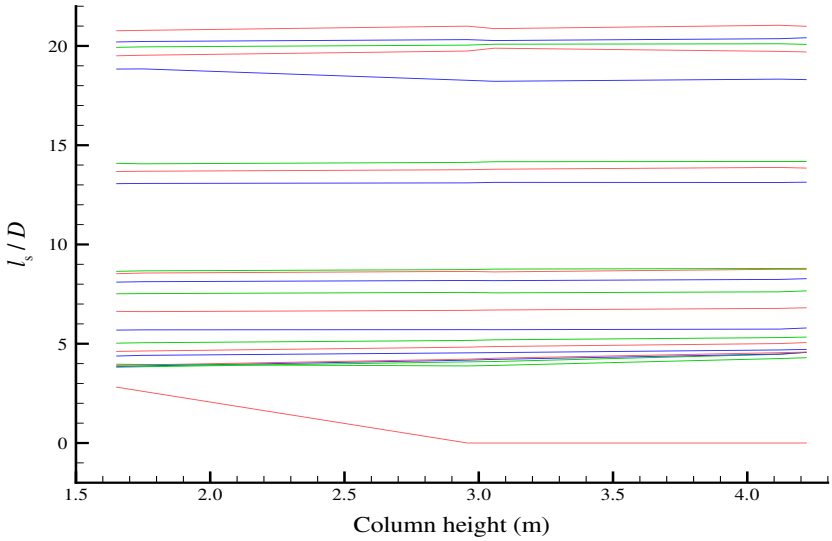

Figure 5.11. Distance between consecutive bubbles, l_s/D, rising in a 0.40 wt% CMC solution, as a function of the trailing bubble nose position in the column.

CMC solution, is represented in Figure 5.11. Like the behaviour in the 0.30 wt% CMC solution, no interaction is seen between bubbles when the distance between them is higher than $4D$.

The ratio between the velocities of the bubbles is represented in Figure 5.12 as a function of the distance between bubbles. The influence of the leading bubble wake on the second bubble velocity is very similar to that found in the 0.30 wt% CMC solution. It seems, however, that the distance above which there is no interaction is slightly shorter for the 0.40 wt% CMC solution.

The comparison between the second bubble velocity and the axial liquid velocity at $r = 0$ obtained from the PIV results is represented in Figure 5.13. There is a lot of similarity between the results obtained in this solution and in the 0.30 wt% CMC solution, although due to the lower velocity magnitudes the effect on the second bubble velocity is less accentuated in the 0.40 wt% CMC solution, especially in the region of downward liquid flow in the axis of the column. Once more, the higher data dispersion is seen when the trailing bubble reaches the downward liquid flow of the leading bubble wake, due to the nose oscillations searching for the point with higher upward velocity. At very short distances to the leading bubble, a slight deceleration of the trailing bubble is expected, from the liquid velocity profile.

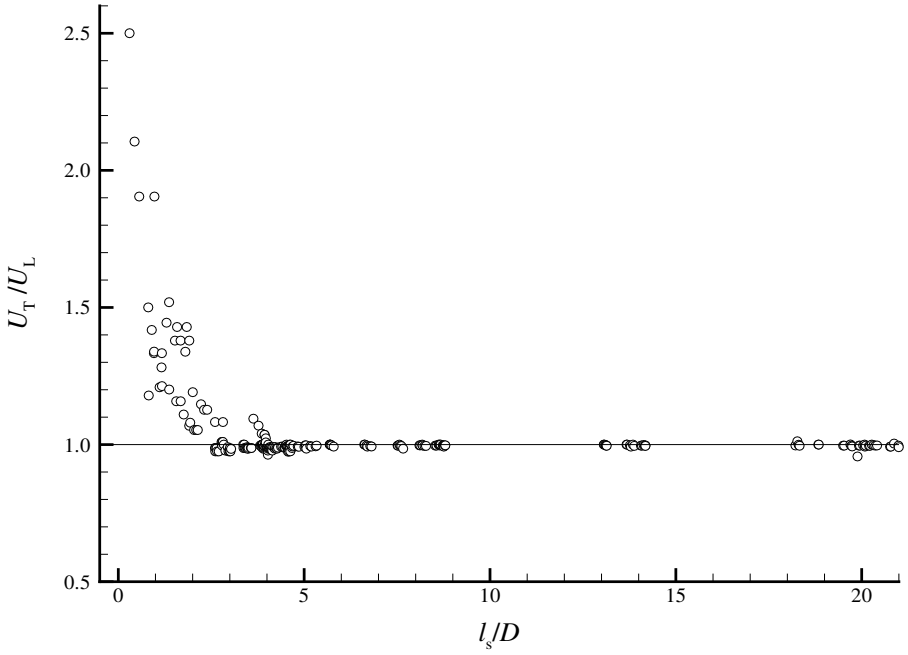

Figure 5.12. Ratio between the velocities of consecutive bubbles as a function of the distance between them, when rising in a 0.40 wt% CMC solution.

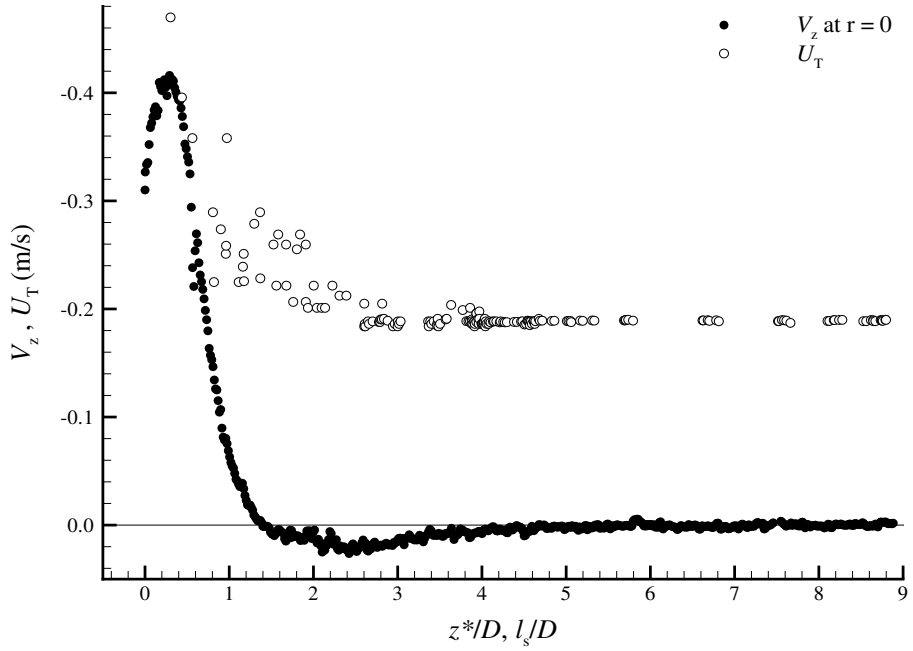

Figure 5.13. Comparison between the trailing bubble velocity and the axial liquid velocity at $r = 0$ in the wake of Taylor bubbles rising in 0.40 wt% CMC solution.

5.2.4 0.80 wt% CMC solution

In the PIV studies with the 0.80 wt% CMC solution, a negative wake behind the Taylor bubble was found. From those results, coalescence between two Taylor bubbles was not expected. The only doubt was whether the small velocity amplitude upward flow away from the axis would be enough to allow the trailing bubble to catch the leading one.

The distance between two bubbles rising in a 0.80 wt% CMC solution is represented in Figure 5.14 as a function of the trailing bubble nose location in the column. This figure

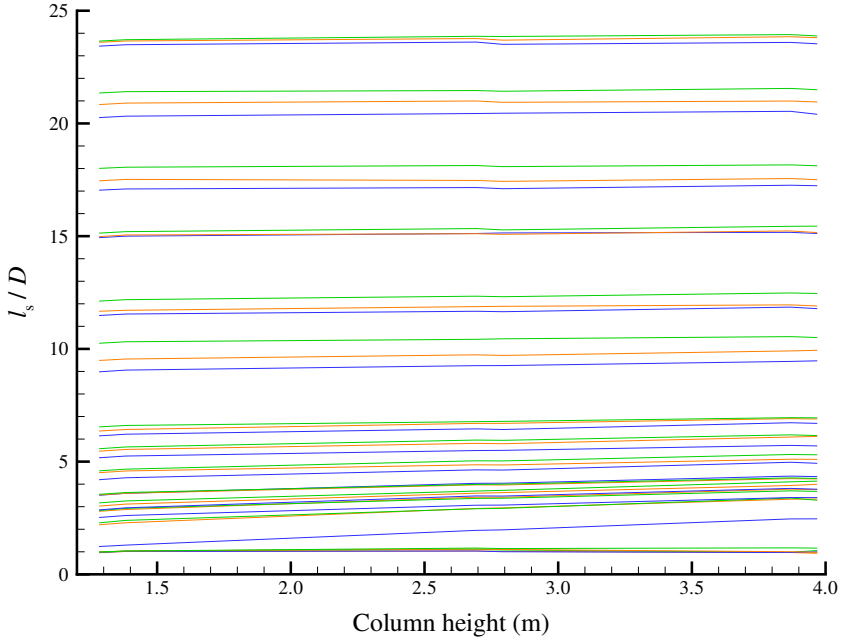

Figure 5.14. Distance between consecutive bubbles, l_s/D, rising in a 0.80 wt% CMC solution, as a function of the trailing bubble nose position in the column.

shows that even with only $1D$ separating the bubbles, coalescence does not occur. For distances up to $5D$ there is even a tendency for the bubbles to separate. This means that the downward liquid flow in the negative wake is determinant, creating a barrier to the trailing bubble, which does not allow it to approach the leading one.

The ratio between the velocities of the bubbles is represented in Figure 5.15 as a function of the distance between bubbles. As this figure shows, the values of the bubble velocities are always very close to each other, independently of the distance between them. The short range scale allows, however, a decrease to be perceived in the second bubble velocity between $l_s = 2D$ and $l_s = 5D$. For higher distances, the ratio between the bubble velocities

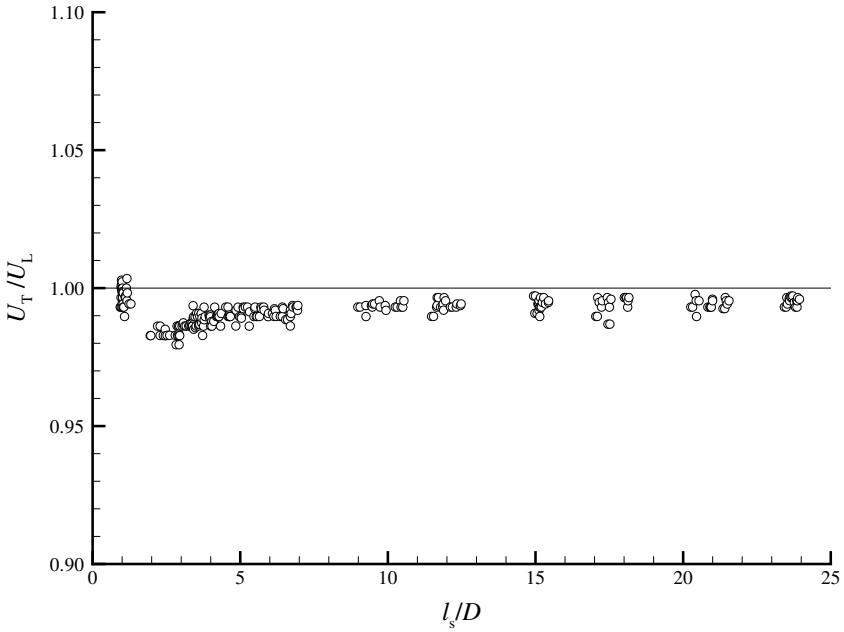

Figure 5.15. Ratio between velocities of consecutive bubbles as a function of the distance between them, when rising in a 0.80 wt% CMC solution.

is practically constant, and slightly below 1. The only region where the bubble velocity values are equal is around $l_s = 1D$. There are two regions where no data is available: below $l_s = 1D$ and between $l_s = 1.5D$ and $l_s = 2D$.

The comparison between the trailing bubble velocity and the axial liquid velocity obtained from the PIV studies is represented in Figure 5.16, which allows a visual rendering of the coalescence results.

As described in the PIV results (§3.3.6), behind Taylor bubbles rising in a 0.80 wt% CMC solution, there is a negative wake close to the bubble trailing edge. At least one recirculation region is seen after the main region, with inverted rotational direction. The fact that there are no data available in the coalescence studies for distances below $1D$ between bubbles is due to the central downward flow in the negative wake. As shown in Figure 5.16, this downward flow extends around $z* = 1D$ and does not allow the second bubble to approach. The absence of data between $l_s = 1.5D$ and $l_s = 2.0D$ is explained by the central upward flow of the secondary recirculation region, which impels the second bubble nose up to the region between the recirculations. So when the second bubble reaches this region it gets blocked, maintaining a fixed distance to the leading bubble.

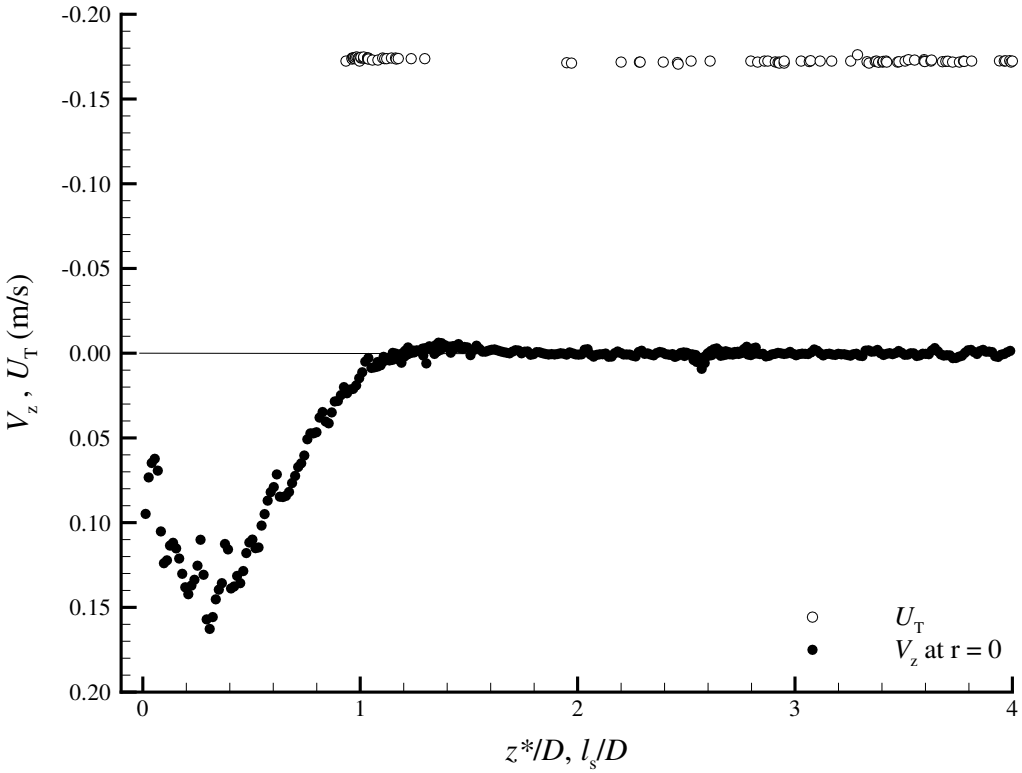

Figure 5.16. Comparison between the trailing bubble velocity and the axial liquid velocity at $r = 0$ in the wake of Taylor bubbles rising in 0.80 wt% CMC solution.

5.3 Coalescence of Taylor bubbles rising in PAA solutions

The coalescence of Taylor bubbles rising in PAA solutions was studied using the same procedure applied to the CMC solutions. The experimental temperature and average bubble lengths covered with the PAA solutions are presented in Table 5.2.

Table 5.2. Experimental conditions in the coalescence studies with PAA solutions.

PAA wt%	T^oC	$\overline{L}_b/D$
0.10	21.4	4.5
0.20	20.0	4.5

From the PIV experiments, only two PAA solutions were chosen to perform coalescence studies on. As was the case in the 0.10 wt% CMC solution, in the 0.01 wt% PAA solution

it was expected that bubble interaction is mainly driven by the amount of small bubbles ascending behind the leading bubble. For concentrations above 0.20 wt% PAA, there are a lot of tiny bubbles suspended in the liquid, which were formed during its preparation, and these create difficulties for using the photocells technique because they induce a large amount of small peaks in the acquired data signal.

5.3.1 0.10 wt% PAA solution

In the PIV and visualisation studies, the wake length of the 0.10 wt% PAA solution was higher than those in the CMC solutions. A long tail with upward central flow behind the Taylor bubble was seen (up to $z* = 10D$ and more), which should be responsible for a longer interaction distance between two consecutive bubbles.

The distance between two consecutive bubbles rising in a column filled with a 0.10 wt% PAA solution is represented in Figure 5.17. As seen from this figure, the distance between

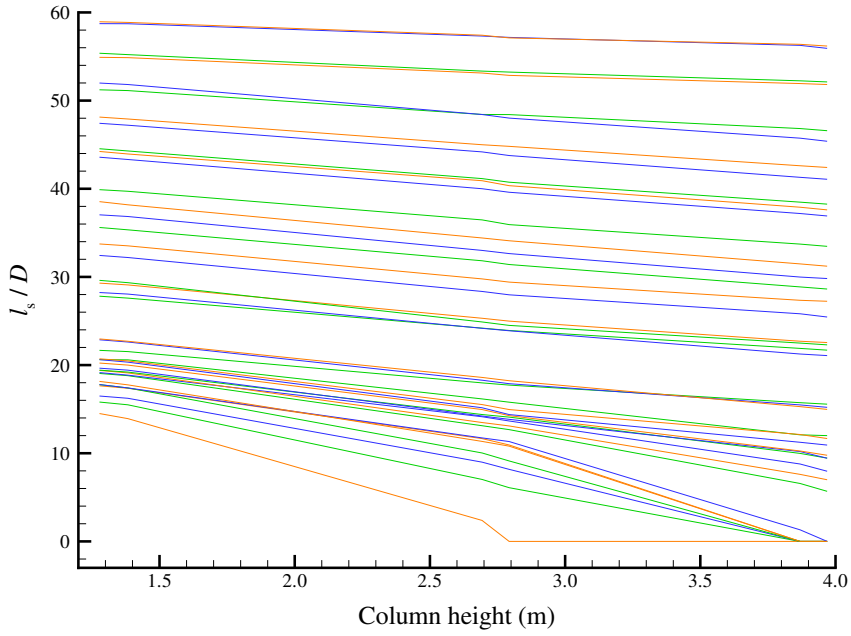

Figure 5.17. Distance between consecutive bubbles, l_s/D, rising in a 0.10 wt% PAA solution, as a function of the trailing bubble nose position in the column.

two consecutive bubbles always decreases, even when they are separated by $60D$. From the PIV measurements, at those distances the liquid is stagnant. This shows that despite the long wake length there is another factor that determines the trailing bubble velocity, which

is related with the relaxation time of the fluid. After the passage of the first bubble there is a decrease in the viscosity of the liquid, which has been subject to high shear rates during the flow around the bubble. Due to the long relaxation time of the PAA solutions, the viscosity of the liquid ahead of the trailing bubble is always less than ahead of the leading bubble, unless the time gap between them is longer than the relaxation time. This justifies the fact that, even for very long distances between the bubbles, the trailing bubble moves faster than the leading one. The wake influence is noticed for distances between bubbles below $10D$, where the decrease in the bubble distance is more significant. Funfschilling and Li (2001) also describe the effect of the temporarily reduced viscosity on the interaction between small bubbles rising consecutively in PAA solutions.

The ratio between the velocities of the bubbles is represented in Figure 5.18, as a function of the distance between bubbles. As expected from Figure 5.17, the ratio between

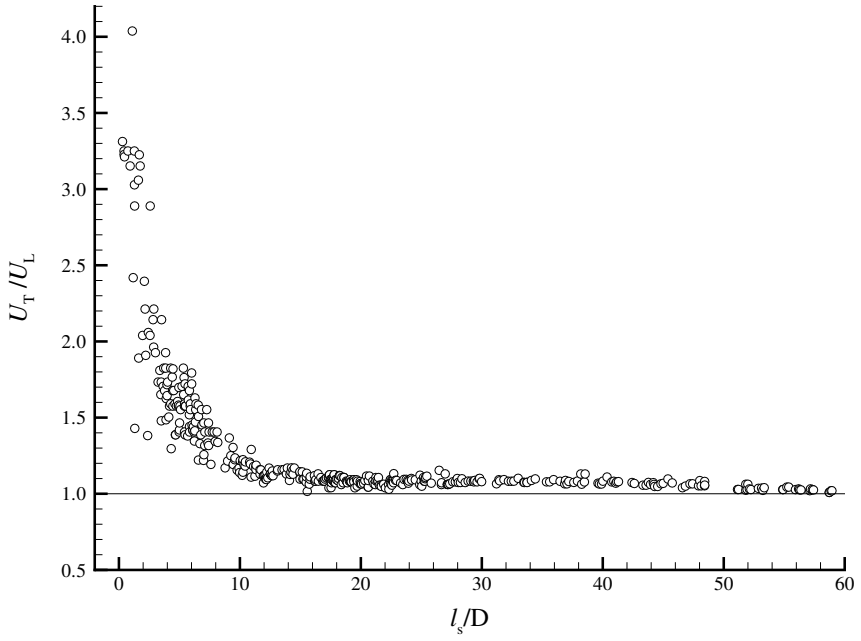

Figure 5.18. Ratio between velocities of consecutive bubbles as a function of the distance between them, when rising in a 0.10 wt% PAA solution.

the two bubble velocities is always higher than one. Only at a distance of $60D$ is there a tendency for the trailing bubble velocity to be close to the leading bubble velocity. Since the leading bubble velocity is about 0.191 m/s, this means that $60D$ corresponds to a time gap of around 10 s between the bubbles. In the rheological characterisation of the

liquids, the 0.10 wt% PAA solution relaxation time was not conclusively determined, but 10 s should be a good estimate.

As these last figures demonstrate, at long distances between bubbles the trailing bubble velocity is dependent on the fluid relaxation time. The influence of the wake flow pattern at shorter distances is seen in Figure 5.19, where the trailing bubble velocity is compared with the axial liquid velocity obtained from the PIV studies. From this figure it is clear

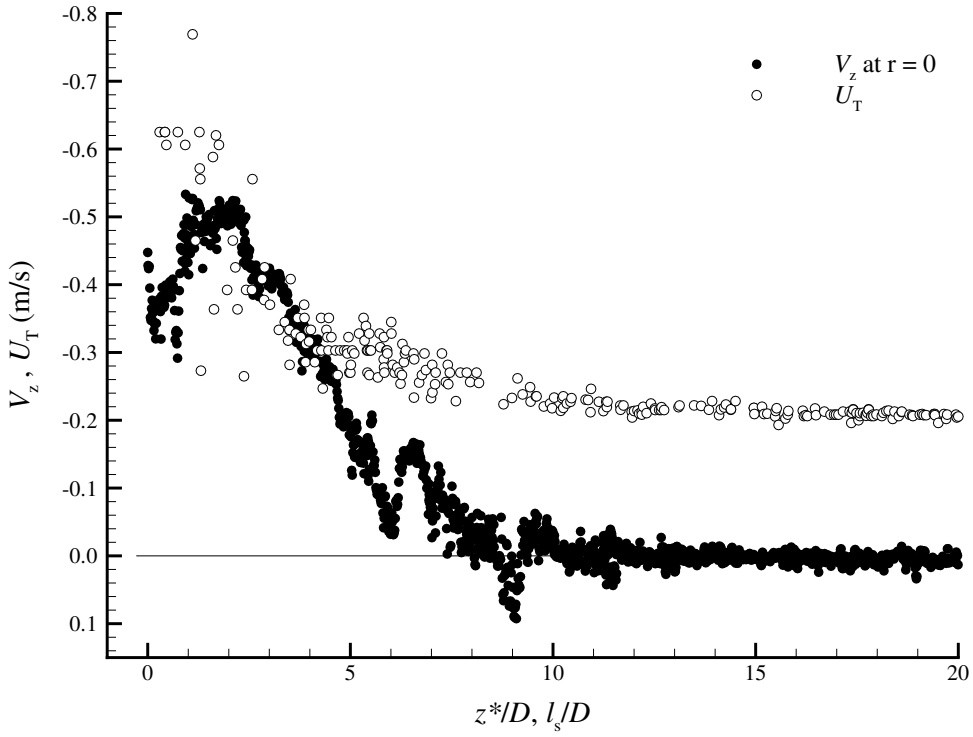

Figure 5.19. Comparison between the trailing bubble velocity and the axial liquid velocity at $r = 0$ in the wake of Taylor bubbles rising in 0.10 wt% PAA solution.

that the increase in the trailing bubble velocity for distances below $10D$ is related with the upward central liquid flow behind the Taylor bubbles, which was observed in the PIV studies. These results confirm that, besides the effect of the relaxation time, the wake flow pattern by itself is also responsible for a longer bubble interaction distance relative to the one observed in the CMC solutions.

5.3.2 0.20 wt% PAA solution

The 0.20 wt% PAA visualisation and PIV studies showed a wake flow pattern with a first region of fluid moving at practically the bubble velocity, followed by an upward central flow, similar to that found in the 0.10 wt% PAA solution but with a shorter length.

The variation of the distance between two bubbles rising simultaneously in a column filled with a 0.20 wt% PAA solution is represented in Figure 5.20 as a function of the trailing bubble nose position in the column. This figure shows that similar to the previous

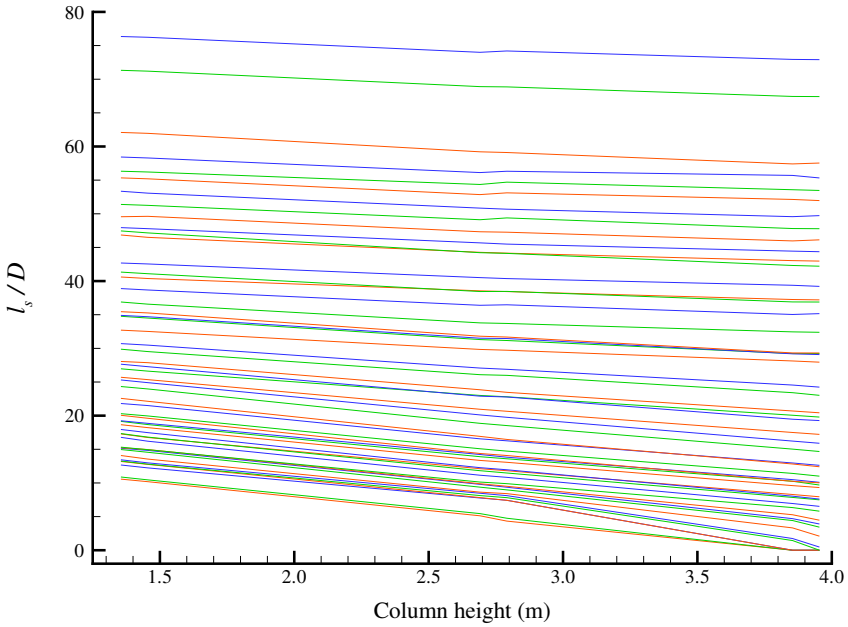

Figure 5.20. Distance between consecutive bubbles, l_s/D, rising in a 0.20 wt% PAA solution, as a function of the position in the column.

solution, the high relaxation time is responsible for a lower liquid viscosity ahead of the trailing bubble, and consequently a higher bubble velocity. This leads to a decreasing distance between bubbles during their rise, at least for distances up to $250D$. This distance corresponds to a time gap between bubbles of more than 40 s, but is still below the relaxation time of this solution, around 175 s (from rheological data). Only in bubbles with a time gap longer than this should no interaction be expected.

In Figure 5.21, the ratio between the velocities of the bubbles is represented as a function of the distance between bubbles. Once again, this ratio is higher than one, in general. There is an increase of the trailing bubble velocity between $l_s = 10D$ and $l_s = 20D$, but the largest

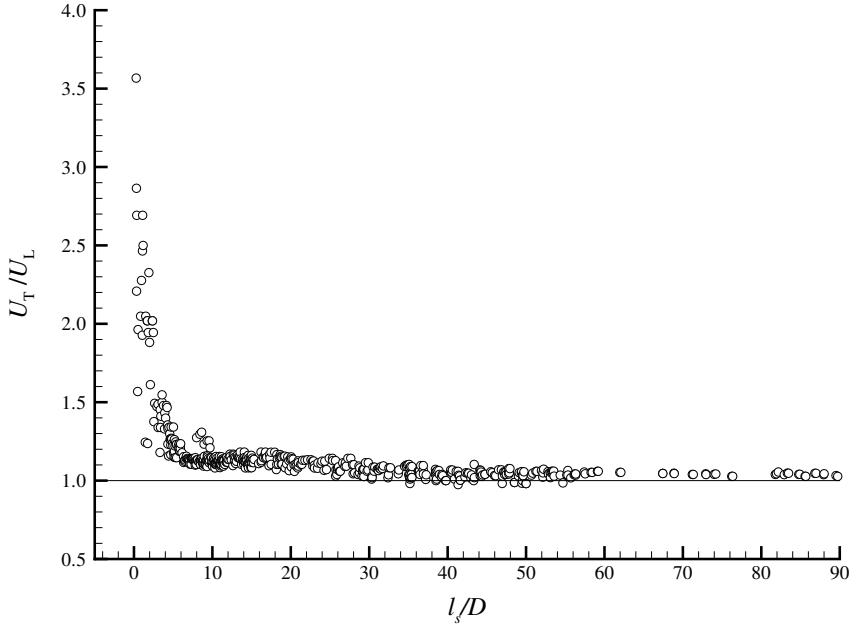

Figure 5.21. Ratio between the velocities of consecutive bubbles as a function of the distance between them, when rising in a 0.20 wt% PAA solution.

increase happens below $l_s = 6D$.

In Figure 5.22, the comparison between the trailing bubble velocity and the axial component of the liquid velocity in the axis of the column, obtained from the PIV experiments is made. Once again, the relation between the axial liquid velocity and the second bubble velocity is evident. The upward liquid velocity now extends only up to $6D$ from the bubble trailing edge, the distance below which there is a practically identical increase in the second bubble velocity. The term identical means that the bubble velocity increases at the same rate as the liquid velocity in the column axis.

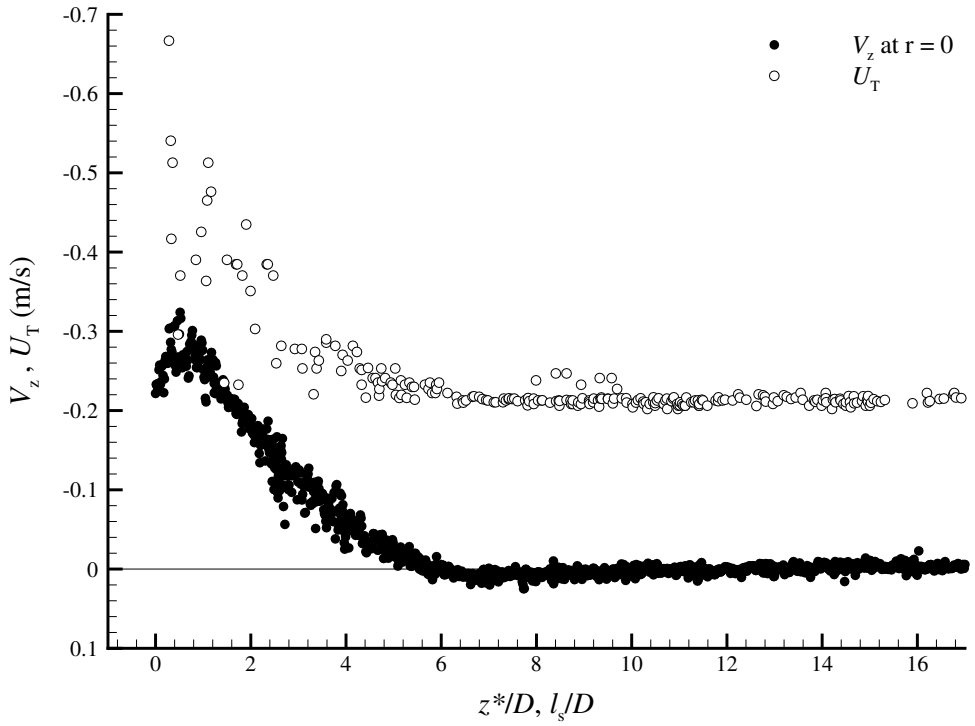

Figure 5.22. Comparison between the trailing bubble velocity and the axial liquid velocity at $r = 0$ in the wake of Taylor bubbles rising in 0.20 wt% PAA solution.

5.4 Summary of coalescence studies

The coalescence studies presented earlier showed that the distance above which there is no interaction between two consecutive bubbles is strongly dependent on the liquid rheology.

In the CMC solutions, where the liquid relaxation time is very short, the trailing bubble velocity is mainly dependent on the wake flow pattern. In Figure 5.23, the ratio between the velocities of two consecutive bubbles rising in the different CMC solutions is represented as a function of the distance between bubbles. Correlations from Moissis and Griffith (1962) for a solid bubble in water and from Pinto and Campos (1996) for Newtonian liquids with different viscosities are also presented. This figure puts into evidence the effect of the liquid rheology on the bubble interaction. In the 0.10 wt% CMC solution, the trailing bubble velocity is mainly affected by the presence of a long train of small bubbles rising behind the leading Taylor bubble, their influence extending for a distance of several column diameters.

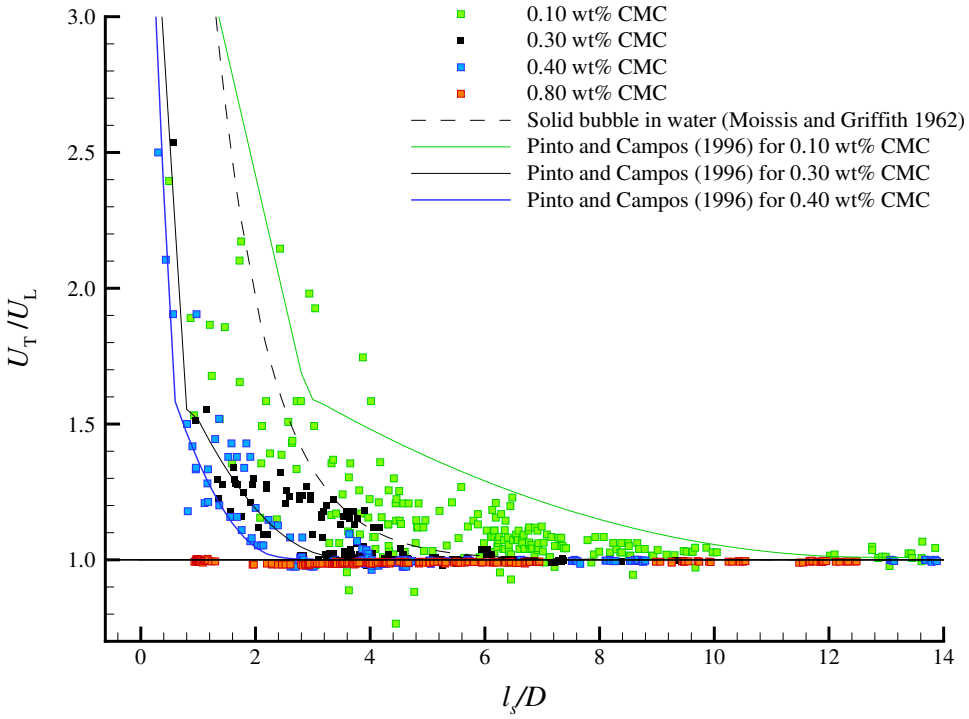

Figure 5.23. Representation of the ratio between the velocities of consecutive bubbles rising in CMC solutions as a function of the distance between bubbles and comparison with data from literature.

The increase of polymer concentration, and subsequently of the liquid viscosity, promotes liquid stagnation in a shorter distance after the passage of a Taylor bubble. In the 0.30 and 0.40 wt% CMC solutions, liquid is recirculating in a closed region in the Taylor bubbles wake. The longer wake in the 0.30 wt% CMC solution is responsible for a longer interaction distance between two consecutive bubbles.

For the more concentrated solutions, there is no liquid in the wake rising with the bubble, and a negative wake appears. In the 0.80 wt% CMC solution, due to a fast stagnation of the liquid behind the Taylor bubbles, the main effect on the trailing bubble velocity is the downward central liquid movement behind the leading bubble, which does not allow the trailing bubble to get closer than $1D$.

The correlation of Moissis and Griffith (1962) (eq. 1.6) describing interaction between solid bubbles in water is also represented, being similar to the results for the less concentrated CMC solution. The correlations found by Pinto and Campos (1996) (eq. 1.7-1.11) for pairs of bubbles rising in stagnant liquids with different viscosities was also adapted to

the present study. The dimensionless number $(gD^3)^{1/2}\rho_l/\mu$ was determined for the CMC solutions by using the viscosity at the characteristic shear rate, $\dot{\gamma} = U_\mathrm{b}/D$. Despite an overestimate of the trailing bubble velocity for the less concentrated solution, the predictions are close to the experimental results for the 0.30 and 0.40 wt% CMC solutions.

In the PAA solutions, due to the high relaxation times the passage of the first bubble causes a decrease of the liquid viscosity, which takes some time to recover its initial value. If, by velocity conversion, the distance between two consecutive bubbles corresponds to a time gap below the relaxation time of the liquid, the trailing bubble will always flow in a less viscous liquid and its velocity will be higher than the velocity of the leading bubble, despite the fact that both are flowing in stagnant liquid. Figure 5.24 shows the ratio between the velocities of two consecutive bubbles rising in PAA solutions as a function of the distance between bubbles. The ratio between bubble velocities is greater than 1 for several column

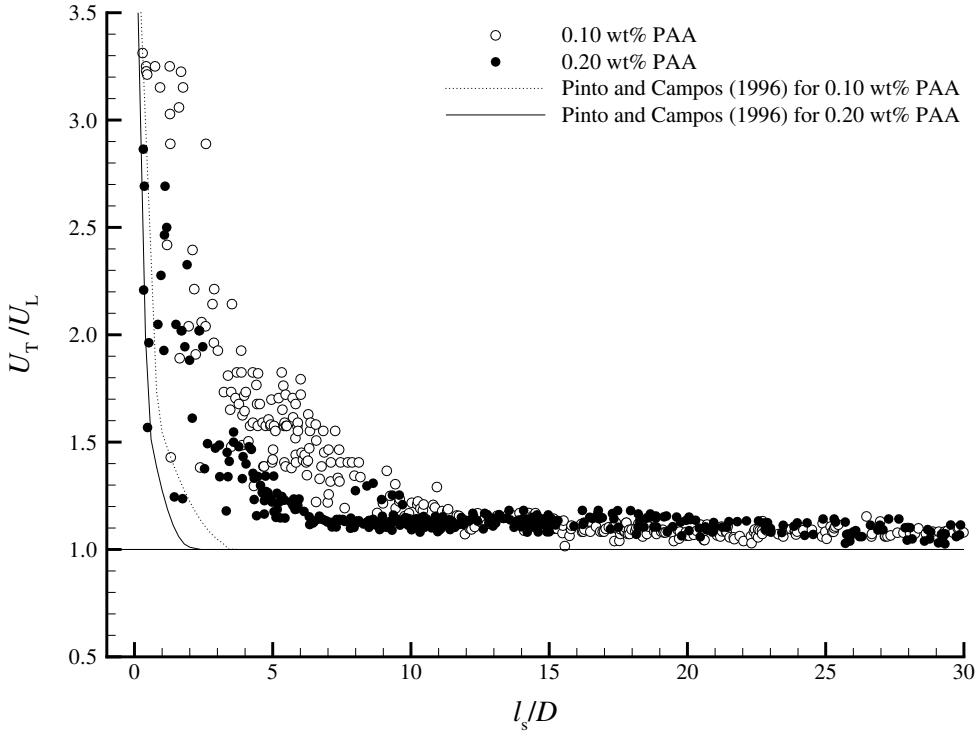

Figure 5.24. Ratio between velocities of consecutive bubbles rising in PAA solutions as a function of the distance between bubbles.

diameters distance. Despite the stagnation of the liquid at a certain distance below the leading bubble, the reduced viscosity induces a higher velocity on the trailing bubble. At

shorter distances, the tail in the wake of the leading bubble (which induces an upward liquid flow in the axis of the column) is responsible for a greater increase in the trailing bubble velocity. The different tail lengths determine the different distances at which the liquid velocity effect overlaps the relaxation time effect. The correlations of Pinto and Campos (1996) are unable to predict the bubble interaction in the PAA solutions here, since besides the wake effects on the flow, there are elastic effects which induce a different flow pattern and impose a liquid viscosity dependent on the fluid history.

As seen from the coalescence results, the information obtained in the PIV experiments is essential to understanding the different ways in which bubbles interact.

Chapter 6

Conclusions and suggestions for future work

Abstract

This chapter concludes this dissertation by summarising the most relevant conclusions of the work and giving some recommendations for future study.

6.1 Conclusions

This thesis investigated slug flow in non-Newtonian liquids. The fluids used in this work were solutions with different weight percentages of two polymers: Carboxymethylcellulose (CMC) and Polyacrylamide (PAA).

A study of the flow around individual Taylor bubbles was done first. As no previous information was found in the literature on the conditions studied, preliminary visualisation studies were performed. These showed that the wake flow pattern behind Taylor bubbles is strongly dependent on the properties of the liquid. In the CMC solutions, the wake flow was observed to change with lower to higher solution concentrations: from a highly unstable three-dimensional flow, through an intermediate transition stage, to finally reaching a stable axisymmetric flow with closed recirculations. In the higher concentration solutions a change in the bubble trailing edge shape was observed, taking the form of a two-dimensional cusp.

In the PAA solutions, the visualisation studies also showed that the trailing edge ins-

tabilities decrease with increasing polymer concentration. The wake flow patterns were, however, different from those observed in the CMC solutions, consisting of an upper region of liquid in recirculation rising with the bubble and a central region of liquid being stretched. This stretched liquid is seen moving upwards even at long distances from the bubble trailing edge. In the higher concentration solutions, a change was also observed on the trailing edge shape, similar to that in the CMC solutions.

After the visualisation studies, the complete flow field around individual Taylor bubbles was studied using Particle Image Velocimetry (PIV) and shadowgraphy, covering the most relevant conditions. The results showed very similar behaviour in the flow pattern around the nose of the bubbles. Average velocity profiles were determined in the liquid film, and an increase in film thickness with a decrease in the average velocity was observed as the polymer concentrations increased. The velocity profiles were validated by a mass balance between a cross-section ahead of the bubble and in the liquid film (frame of reference attached to the bubble). In the wake region, the flow patterns seen in the visualisation studies were confirmed by the instantaneous velocity fields obtained. In the higher concentration solutions where the trailing edge becomes a two-dimensional cusp shape, a negative wake was found and characterised. The wake flow patterns were described and quantified by several average axial and radial velocity profiles, at different distances from the bubble trailing edge. The extent of the flow disturbances caused by the passage of a Taylor bubble were also described.

The final objective of this work was coalescence studies, investigating the interaction between two consecutive Taylor bubbles rising in some of the studied solutions. The variation of the trailing bubble velocity with the distance to the leading bubble was analysed and related with the wake flow fields obtained in the PIV experiments. The results showed that the liquid velocity in the wake of a leading bubble has a clear influence on the velocity of the trailing one. In the presence of a negative wake no coalescence between bubbles was observed. Another interesting fact was that in the PAA solutions, when the bubble were separated by shorter times than the long relaxation time of these fluids, the velocity of the trailing bubble was always higher than the velocity of the leading one. This is due to the decrease in the liquid viscosity caused by the passage of the first bubble, which has insufficient time to recover its initial value before the passage of the second bubble.

One intention of this work was to extend the research of slug flow to non-Newtonian liquids. The results obtained reveal new and interesting features, which can be used to

improve the models of slug flow by enlarging their range of applicability.

6.2 Suggestions for future work

The present work contributes to the understanding of slug flow phenomena in non-Newtonian liquids. For future work and a better description of the influence of the different non-Newtonian properties of the liquids on the slug flow, it would be interesting to perform studies with Boger fluids; fluids with a negligible viscosity variation but with different elastic properties. This would isolate the effect of the elastic properties on the flow pattern around the bubbles and add to understanding the physical phenomena that induce differences in the flow patterns relative to Newtonian fluids.

The consequences of the relaxation time of the liquids also needs more detailed analysis. If an accurate viscosity variation with time and shear rate can be determined, the current models that exist for slug flow might be easily adapted to viscoelastic fluids. The measurement of the extensional viscosity could also explain the flow patterns found in the wakes of bubbles rising in PAA solutions.

As a continuation of the present work, it would also be interesting to apply PIV in continuous slug flow, to understand the changes in the flow pattern between two consecutive bubbles and to have more detailed information on the flow field during the bubbles coalescence. A higher frequency camera will be required in order to capture the evolution of the transient flow field.

Concerning the experimental techniques, improvements in the PIV image processing would benefit the final results, especially close to the interfaces. Different definitions of boundary conditions, such as setting the velocity gradient or different velocities along the interface could help the image processing in these regions. Another difficulty of the PIV processing is that when the liquid velocity has different orders of magnitude in the same field of view, a different time between frames has to be chosen in order to accurately quantify the different liquid velocities. This means that the results of both regions are not acquired at the same instant, which is a problem in unsteady flows. A way to overcome this problem would be to acquire for example three consecutive frames, with different time lags between them. The different velocity magnitudes could then be obtained from processing the first two or last two frames at practically the same instant.

Another improvement could be made by applying Particle Tracking Velocimetry (PTV),

a technique very similar to PIV but where the displacement of individual particles is determined instead of the window displacement. This technique has, however, a more complicated post-processing of the images and needs some particular experimental conditions to be applied. For the non-axisymmetric flows, the application of 3-D PIV could also give some crucial information about the flow patterns, although it might be difficult to implement due to optical distortion.

Appendix A

Polymer characteristics

In this appendix, some properties of the polymers used in this work are presented.

A.1 Carboxymethylcellulose (CMC)

The CMC polymer used in this work was the BLANOSE® Cellulose Gum, which is the sodium salt of Carboxymethylcellulose. This polymer was obtained from Hercules, with the reference CMC 7H4C, with a molecular weight around 3000000 kg/kmol.

It is commonly used as an additive in petroleum, paper, cosmetics and pharmaceutical industries. In food products it is identified as E-466, by the European Commission.

It is produced by reacting alkali cellulose with sodium monochloroacetate under rigidly controlled conditions. The idealised unit structure of CMC, with a cellulose degree of substitution equal to 1 is represented in Figure A.1

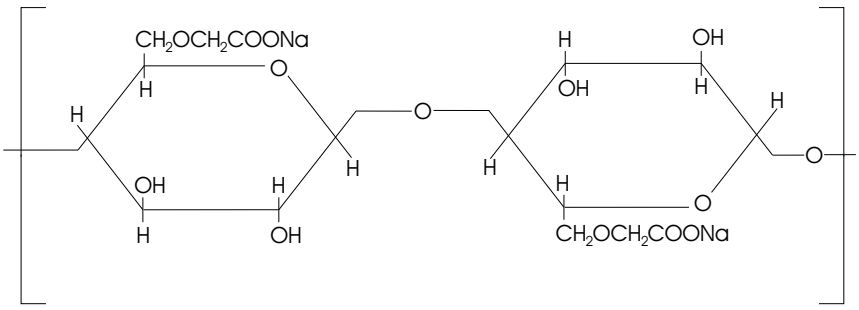

Figure A.1. Chemical structure of the CMC polymer, with a cellulose degree of substitution equal to 1.

Some specifications of BLANOSE® Cellulose Gum are presented in Table A.1.

Table A.1. Some specifications of BLANOSE® Cellulose Gum.

Physical state	granular powder
Colour	white to off-white
Odor	odorless
Specific gravity	1.59
Percent volatile	negligible at 20^{o}C
Solubility in water	limited by viscosity
Browning temperature	226^{o}C
Charring temperature	252^{o}C
Purity, CMC content on dry basis, %	99.5 min
(NaCl + Na glycolate), %	0.5 max.
Na glycolate, %	0.4 max
Moisture content as packed, %	8 max.
Bulk density, g/cm^3	0.55-1.00
Solution pH, at 2%	7.5
Surface tension, 1% solution, dynes/cm at 25^oC	71
Specific gravity, 2% solution	1.0068
Refractive index, 2% solution	1.336

In the preparation of solutions, CMC particles have a tendency to agglomerate, or lump, when first added to water. To obtain homogeneous solutions easily, CMC should be added to the vortex of vigorously agitated water. The rate of addition must be slow enough to permit the particles to separate and their surfaces to become individually wetted, but it should be fast enough to minimise viscosity buildup of the aqueous phase while the gum is being added.

When a polymer is dispersed in a solvent, the degree of disaggregation, i.e., separation of polymer molecules, is affected by the:

- chemical composition of the polymer
- solvating power of the solvent
- shear history of the resulting solution

When preparing solutions, the same procedure, polymer and water sources should be used, to obtain reproducible results.

The CMC solutions have shear thinning or pseudoplastic behaviour, i.e., the solution viscosity decreases with increasing shear rate.

Effect of temperature

Viscosity of CMC solutions decreases with increasing temperature. Under normal conditions, the effect of temperature is reversible, so temperature variation has no permanent effect on viscosity. However, long periods of heating at high temperatures will degrade CMC and permanently reduce its viscosity.

Effect of pH

CMC solutions maintain their normal viscosity over a wide pH range. In general, CMC solutions exhibit their maximum viscosity and best stability at pH 7 to 9. Above pH 10, a slight decrease in viscosity is observed. Below pH 4, the less soluble free acid carboxymethylcellulose predominates and viscosity may increase significantly.

Stability

CMC is subject to microbiological attack and chemical degradation. However, corrective measures can be taken to prevent both from occurring.

Although CMC is more resistant to microbiological attack than many other water-soluble gums, its solutions are not immune. Heat treatment can be used to destroy many micro-organisms while having little effect on CMC properties. Heating for 30 min at 80^{o}C, or for 1 min at 100^{o}C, is generally sufficient.

When solutions are stored, a preservative should be added to prevent viscosity degradation. If cellulases (hydrolic, viscosity-destroying enzymes) have been introduced by microbial action, even in trace amounts, addition of most preservatives will not prevent degradation; therefore, it is important to preserve solutions as soon as possible after preparation.

Under certain conditions, solutions of CMC are susceptible to chemical degradation. Permanent loss of viscosity can occur, resulting from scission of the long-chain molecules. Such viscosity loss is accelerated by increasing the temperature and/or lowering the pH. An oxidative type of degradation occurs under alkaline conditions in the presence of oxygen. The rate of viscosity loss is also increased by heat and/or ultraviolet light.

Oscillatory tests

During the rheologic characterisation of the fluids, small-amplitude oscillatory tests were performed. In these tests, the cone of the rheometer undergoes small amplitude sinusoidal oscillations with frequency ω. For polymeric materials, the shear stress response oscillates with frequency ω but is not in phase with the shear strain. Assuming that the shear strain amplitude, γ_0 is sufficiently small so that the shear stress varies linearly with strain:

$$\tau_{yx} = -G'(\omega)\gamma_0 \sin(\omega t) - G''(\omega)\gamma_0 \cos(\omega t) \tag{A.1}$$

where G' is known as the storage modulus and G'' the loss modulus. The first gives information about the elastic character of the fluid or the energy storage that takes place and the latter tells about the viscous character of the fluid or the energy dissipation that occurs in flow (Bird *et al.*, 1987).

In the following figures, the storage and loss modulus are presented as a function of the oscillation frequency for the CMC solutions. The strain amplitude was set to 0.05, after a strain sweep test at constant frequency to check the maximum strain amplitude for which there was no change in the polymer structure.

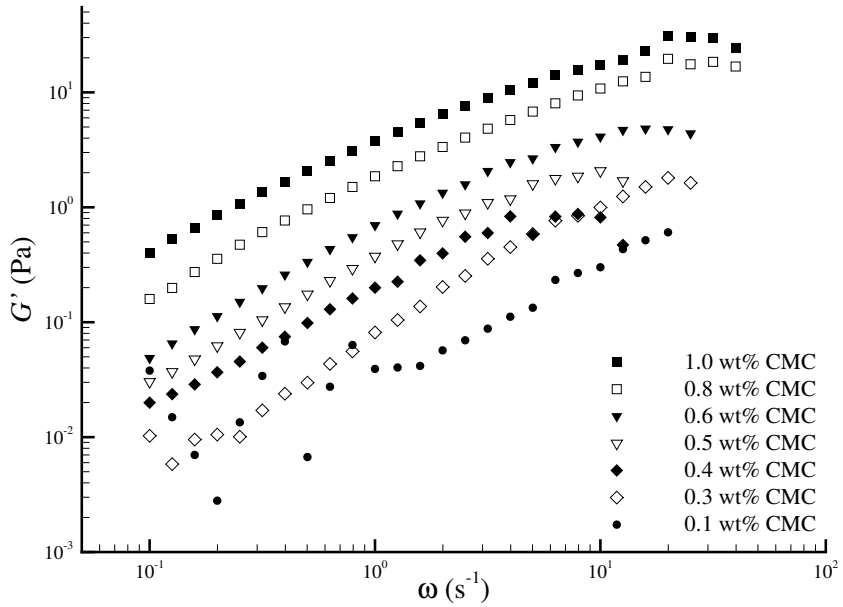

Figure A.2. Storage modulus, G', as a function of oscillation frequency, ω, for the CMC solutions studied; strain rate equal to 0.05.

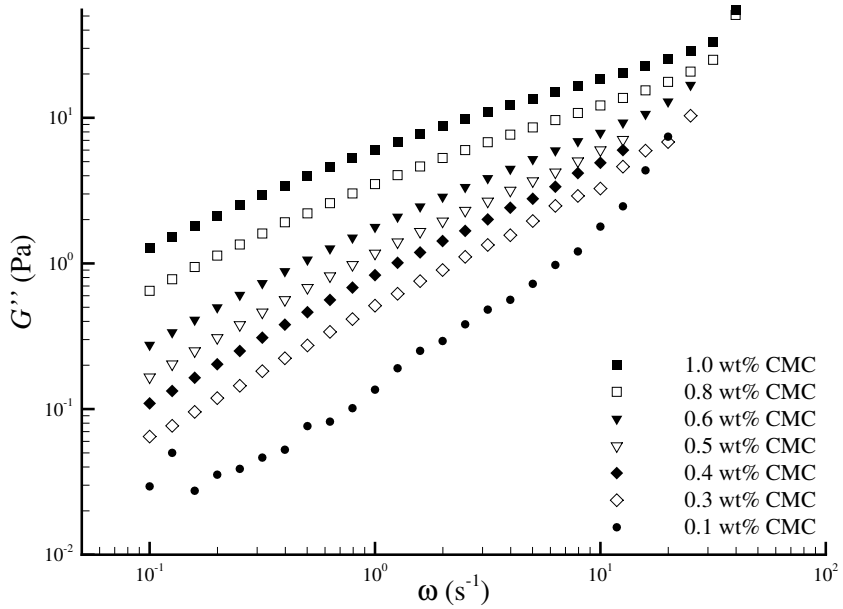

Figure A.3. Loss modulus, G'', as a function of oscillation frequency, ω, for the CMC solutions studied; strain rate equal to 0.05.

A.2 Polyacrylamide (PAA)

The polyacrylamide polymer used in this work was the Separan AP30, produced by SNF Floerger. This polymer behaves as an anionic poly-electrolyte in neutral or alkaline solutions. In acid solutions, the ionisation is repressed and the macromolecule assumes a non-ionised form. The rheology of PAA solutions is, therefore, highly dependent on pH.

The information given by the manufacturer is not so detailed as for the CMC polymer. The chemical structure of the polyacrylamide polymer is represented in Figure A.4.

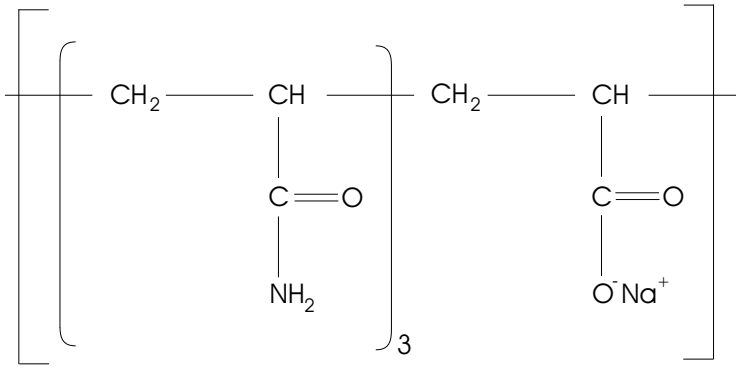

Figure A.4. Chemical structure of the PAA polymer.

Polyacrylamide is a copolymer of acrylamide and acrylic acid (normally supplied as sodium salt) that is sufficiently cross-linked to render it insoluble in water but which retains its hydrophilic nature. It can therefore absorb a very large amount of water, swelling proportionately as it does so. The amount of water that can be absorbed is typically around 400 times the weight of polymer if the water is completely free of solutes, decreasing quite markedly as the level of solute(s) increases.

Polyacrylamide is a condensation polymer with an unusual and useful property. The structure of polyacrylamide is similar to that of polyethylene, but having a hydrogen on every other carbon replaced by an amide group. The molecule is composed of repeating -CH2-CH(CONH2)- units. The amide groups allow for linking between polymer strands. The -CONH2 group from one molecule can react with the same group of another molecule, forming a link between them with the structure -CONHCO-. This produces a network of polymer chains, rather like a tiny sponge. The free, unlinked amide groups, because they contain -NH2 groups, can form hydrogen bonds with water. This gives the tiny cross linked sponges a great affinity for water. Polyacrylamide can absorb many times its mass in

water. This property is useful in a variety of applications, such as in diapers and in potting soil. The polyacrylamide will release the absorbed water if a substance that interferes with hydrogen bonding is added. Ionic substances, such as salt, cause polyacrylamide to release its absorbed water.

Some specifications of the polyacrylamide polymer are presented in Table A.2

Table A.2. Some specifications of polyacrylamide polymer.

Physical state	granular powder
Colour	white or faint yellow
Molecular weight, kg/kmol	18000000-23000000
Density, g/cm^3	1.122
Free monomer %	< 0.5
Surface tension, 1% solution, dynes/cm at 25^oC	72
Refractive index, 1% solution	1.335

Polyacrylamide polymer is widely used in oil drilling, mill running, coal washing, metallurgy, paper making, textiles, sugar refinement, medicine, environmental protection, building materials and agricultural production.

Oscillatory tests

The oscillatory tests were also done with the PAA solutions. The respective storage and loss modules are represented in the following figures, as a function of the oscillation frequency. The values of the 1.00 wt% CMC solution are also presented for a better comparison.

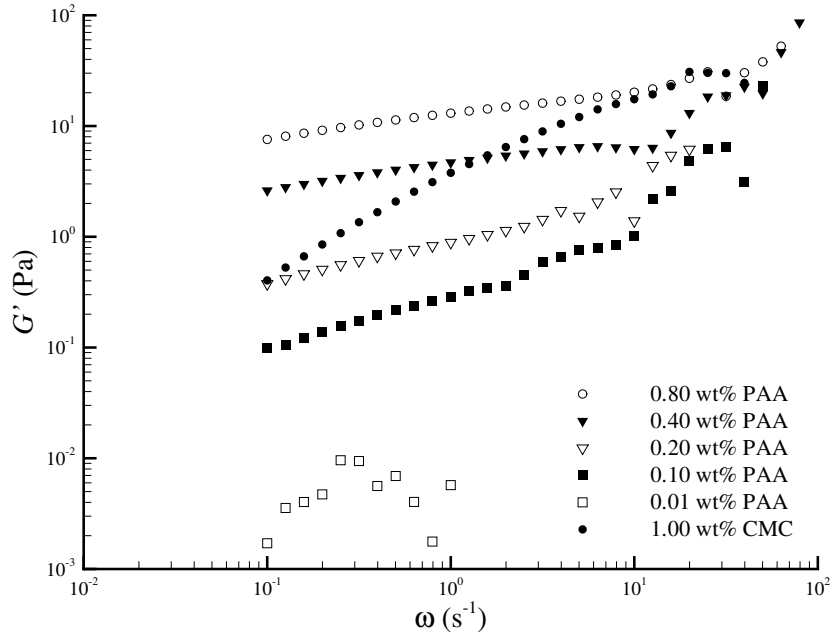

Figure A.5. Storage modulus, G', as a function of oscillation frequency, ω, for the PAA solutions studied; strain rate equal to 0.05.

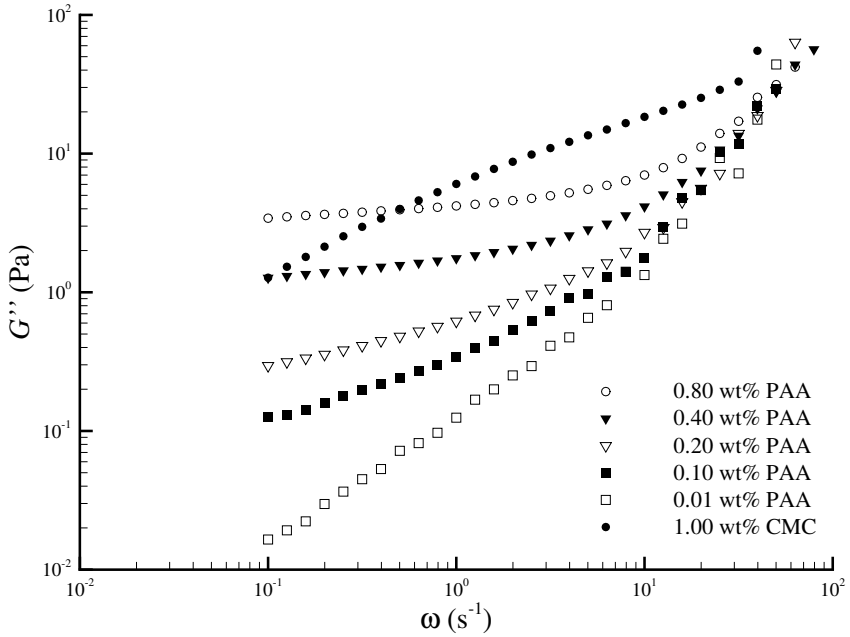

Figure A.6. Loss modulus, G'', as a function of oscillation frequency, ω, for the PAA solutions studied; strain rate equal to 0.05.

Appendix B

Error analysis

Every experimental measurement has an associated uncertainty due to instrument resolution and operator accuracy. The evaluation of the uncertainty for the most relevant quantities determined in this work, was made according to the general procedure: if one quantity X, is determined based on a formula containing other quantities, x_i, $X = f(x_1, x_2, ..., x_n)$, the uncertainty associated with X, δX, can be estimated through the uncertainties of the different quantities:

$$(\delta X)^2 = \left(\frac{\partial X}{\partial x_1} \cdot \delta x_1\right)^2 + \left(\frac{\partial X}{\partial x_2} \cdot \delta x_2\right)^2 + ... + \left(\frac{\partial X}{\partial x_n} \cdot \delta x_n\right)^2 \tag{B.1}$$

The uncertainty of measured quantities is normally assumed as half of the resolution of the measurement instrument. Higher values can be attributed when the measurement has a certain subjectivity. According to this procedure, the uncertainty associated with the most relevant quantities presented in this work is estimated in the next sections.

B.1 Taylor bubble velocity

The Taylor bubble velocity was one of the most important parameters in this study and was measured in all the experiments, although with different methods.

Visualisation studies

In the visualisation studies, the Taylor bubble velocity was measured by determining its displacement from the acquired images and dividing it by the time interval between images:

$$U_{\mathrm{b}} = \frac{\Delta z(m)}{\Delta t(s)} = \frac{\Delta pixels}{VC(\frac{pixels}{mm}) \cdot N_{images} \cdot \Delta t_{\mathrm{i}}(\frac{s}{image}) \cdot 1000(\frac{mm}{m})} \tag{B.2}$$

As the number of elapsed images and the conversion from millimetres to metres contain no uncertainty, the bubble velocity uncertainty is given by:

$$(\delta U_{\mathrm{b}})^2 = \left(\frac{\partial U_{\mathrm{b}}}{\partial \Delta pixels} \cdot \delta \Delta pixels\right)^2 + \left(\frac{\partial U_{\mathrm{b}}}{\partial VC} \cdot \delta VC\right)^2 + \left(\frac{\partial U_{\mathrm{b}}}{\partial \Delta t_{\mathrm{i}}} \cdot \delta \Delta t_{\mathrm{i}}\right)^2 \tag{B.3}$$

For the uncertainty on the pixels displacement, a maximum of 2 pixels can be estimated if the images are sharp, however, there is a certain subjectivity in this value due to reflections at the bubble interface. Concerning the uncertainty on the time between images, it is assumed that the electronically imposed 25 Hz camera frequency has a negligible associated error, so the 0.04 s between images has an estimated uncertainty equal to half of the exposure time of the images. In most cases, a 1/2000 s exposure time was used, so an uncertainty of $2.5 \times 10^{-4}\, s$ is assumed. The vertical calibration, VC(pixels/mm), is determined from $VC = \Delta pixels/distance$. Its uncertainty can be determined by applying equation B.1, assuming that the uncertainty in the distance between the ruler marks is negligible and that the pixels distance has an uncertainty of 1 pixel. If so, $\delta VC = 0.15$ pixels/mm for a typical distance of 50 mm between ruler marks.

According to these assumptions, typical values for the related quantities and uncertainties are presented in Table B.1, for the measurement of the bubble velocity from the visualisation images. From this table, the uncertainty of the velocity can be estimated as 0.001 m/s. Taking the uncertainties of the different quantities, the three terms in equation B.3 were compared, the bubble velocity uncertainty being mainly affected by the first term. The contribution of the last term is negligible.

Since the uncertainties of the measured quantities are practically constant, the effect of the number of images used, and so the displacement of the bubble, was checked. Figure B.1 shows the decrease of the bubble velocity uncertainty with increasing number of images used. The maximum number of images where the bubble nose appeared, which was between 5 and 7 images, was used in this work.

Table B.1. Uncertainties associated with the measurement of Taylor bubble velocity from visualisation images.

Variable	X	δX	units
VC	11.0	0.15	pixels/mm
Δpixels	430	2	pixels
Δt_i	0.04	0.00025	s/images
N_{images}	5	-	images
U_{b}	0.1954	0.00091	m/s

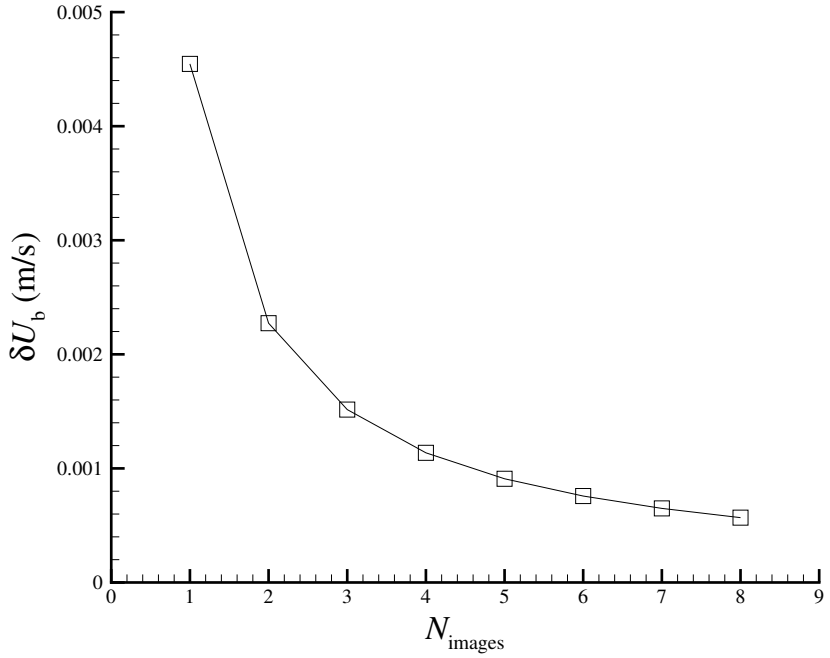

Figure B.1. Variation of the bubble velocity uncertainty with the number of images used to determine the bubble displacement.

PIV and coalescence studies

In the PIV and coalescence experiments, the bubble velocity was determined by a different method, since in the PIV the camera frequency was too low to always acquire at least two images containing the nose of the bubble. In the coalescence studies no camera was used. These experiments used the signal given by pairs of photocells/laser diodes placed along the column.

The bubble velocity was determined by dividing the distance between the photocells

by the time lag between the signals: $U_{\mathrm{b}} = \Delta z(\mathrm{m})/\Delta t_{\mathrm{pc}}(\mathrm{s})$. According to equation B.1, the uncertainty on the bubble velocity is then given by

$$(\delta U_{\mathrm{b}})^2 = (\frac{1}{\Delta t_{\mathrm{pc}}} \cdot \delta\Delta z)^2 + (-\frac{\Delta z}{\Delta t_{\mathrm{pc}}^2} \cdot \delta\Delta t_{\mathrm{pc}})^2 \tag{B.4}$$

The distance between photocells was measured with a ruler with 1 mm of resolution. An uncertainty of 0.5 mm should be estimated but a value of 1.0 mm is more convenient due to possible misalignments on the photocells horizontality. Concerning the uncertainty in the time lag between the voltage signals of the photocells, different values are attributed depending on the experiments. In the PIV experiments, the signals were acquired and read directly from an oscilloscope. The acquisition frequency was adjusted according to bubble lengths and velocities in order to acquire the complete signal in the oscilloscope monitor. It was normally set to 200 Hz, only being set to 100 Hz for the higher viscosity solutions where the bubble velocity was lower, inducing a longer signal. In the coalescence studies, the signals were acquired from a data acquisition interface installed in a personal computer. The acquisition frequency could be set by the user, up to 1000 Hz.

Figure B.2 shows the bubble velocity uncertainty as a function of the distance between photocells and of the acquisition frequency, for a typical value of 0.195 m/s. According to this figure, the uncertainty of the bubble velocity is mainly dependent on the distance between the photocells. In the PIV measurements the photocells were separated by a fixed distance of 0.25 m. As seen from this figure, the difference between using 100 Hz and 200 Hz does not change (significantly) the uncertainty of the bubble velocity, staying close to 0.001 m/s (the same from the visualisation studies). However, in the coalescence studies, shorter distances between photocells had to be used. When studying the bubbles interaction along the full column, each pair of photocells were separated by 0.10 m, which increased the bubble velocity uncertainty to about 0.002 m/s. While studying the trailing bubble velocity before coalescence, the six photocells were closer to each other, separated by 0.03 m. This significantly increases the uncertainty on the measured bubble velocity to about 0.006 m/s. The oscillations of the trailing bubble nose while approaching the leading bubble wake, are the main cause of the scattering found in the velocity data.

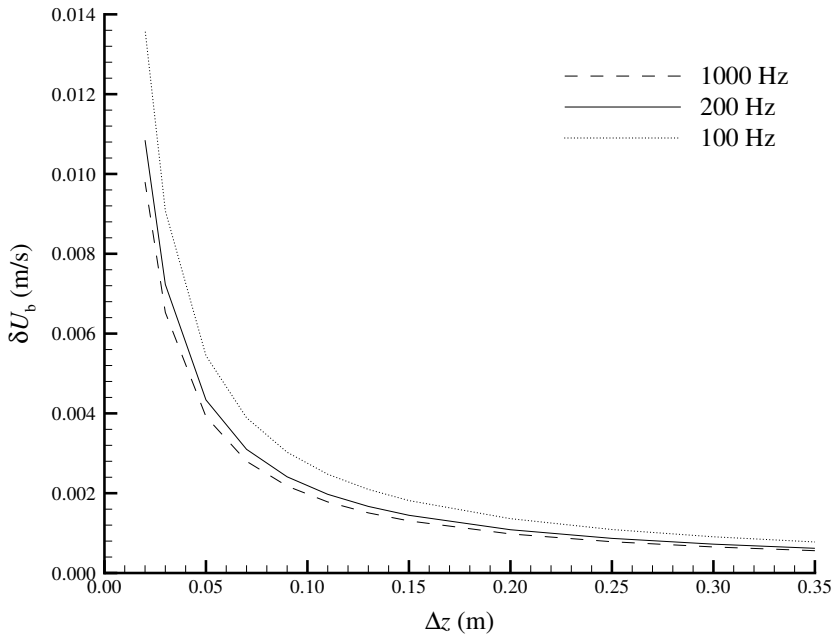

Figure B.2. Variation of bubble velocity uncertainty with the distance between photocells and the acquisition frequency.

B.2 Taylor bubble length

Once again, the bubble length was determined by different methods, after the determination of the bubble velocity.

Visualisation studies

In the visualisation studies, the bubble length was determined by summing the distance between the nose and the bottom in two different frames with the distance travelled by the bubble, assuming a constant velocity:

$$L_{\mathrm{b}} = \frac{\Delta pixels}{1000(\frac{\mathrm{mm}}{\mathrm{m}}) \cdot VC(\frac{\mathrm{pixels}}{\mathrm{mm}})} + U_{\mathrm{b}}(\mathrm{m/s}) \cdot N_{images} \cdot \Delta t_{\mathrm{i}}(\frac{s}{images}) \tag{B.5}$$

By applying equation B.1, with the uncertainties referred to in the previous section, and for typical values of $\Delta pixels = 450$ and $N_{images} = 15$, an uncertainty of 0.001 m ($0.03D$) is obtained for a bubble length of 0.160 m ($5D$).

This error is only reasonable when the bubble trailing edge is stable. In the cases where

Table B.2. Uncertainty associated with the liquid velocities in the PIV measurements.

Δt_f (µs)	2000	1000	500	150
δV (m/s)	0.002	0.004	0.009	0.03

it oscillates, the bubble length has a higher associated uncertainty.

PIV and coalescence studies

In the PIV and coalescence studies, the bubble length was also determined by multiplying the bubble velocity by the time duration of the photocells signal: $L_\mathrm{b} = U_\mathrm{b} \cdot \Delta t$.

With this method, according to equation B.1 and to the aforementioned acquisition frequencies, an uncertainty of around 0.001 m is also obtained. This is also the uncertainty associated with the distance between consecutive bubbles in the coalescence studies, since the formula is similar to that used for the bubble length, but with a different time gap. Once again, these errors are only an estimate, and only valid when there are no oscillations in the bubble nose and trailing edge.

B.3 Liquid velocity (PIV)

The liquid velocities obtained in the PIV measurements are determined dividing the window displacement, converted to metres, by the time gap between the PIV frames in seconds:

$$V(\mathrm{m/s}) = \frac{\Delta p}{\Delta t_\mathrm{f}(s) \cdot PIVC(\frac{pixels}{m})} \tag{B.6}$$

The maximum uncertainty on the window displacement, in pixels, was estimated to be 0.2 pixels (except in the liquid film where an uncertainty of 0.8 pixels was obtained).

The calibration was done by dividing the distance in pixels by the known distance of a millimetric ruler image inside the column. For a typical distance of 0.050 m in the calibration image corresponding to a distance of 1100 ± 2 pixels, the calibration factor can be estimated as 22000±7 pixels/m.

Disregarding the uncertainty associated with the time between the pulses, which is several orders of magnitude lower than the time gap itself, the application of equation B.1 gives the velocity uncertainties presented in Table B.2

From this table it is seen that since the uncertainty on the window displacement is fixed, it is obvious that the absolute uncertainty on the measured velocity increases with shorter times between frames. However, the velocity also increases in the same proportion, so the relative error is the same for a given pixel displacement. There are, naturally, different relative errors in a given velocity field, being less relevant for the higher velocities.

B.4 PIV distances and locations

Concerning the locations of the velocity vectors; since the final vector field resolution is of 5 pixels, the uncertainty on their location is estimated as 2.5 pixels, which is about 1/10 of a millimetre ($0.003D$). This is also the order of magnitude of the uncertainty estimated for the distances measured directly from the PIV images, such as the bubble radius or the liquid film thickness, since an uncertainty of 2 pixels is commonly accepted.

Appendix C

Optical distortion

In this appendix an analysis is made of the optical distortion in the experiments where Taylor bubble images were obtained.

It is assumed that the light travels in straight lines and its velocity is dependent on the propagation medium. The light velocity in a vacuum is about $3 * 10^8$ m/s, and the ratio between this value and the velocity in a certain medium gives the refractive index, n_{i}, of that medium (Möller, 1988). The different light velocity in two different mediums causes a deflection in light rays that pass through the interface. This phenomenon is called refraction and is illustrated in Figure C.1. The quantitative relationship between angles θ_1 and θ_2 is given by Snell's law:

$$n_1 \sin(\theta_1) = n_2 \sin(\theta_2) \tag{C.1}$$

Qualitatively, when the ray passes into a higher refractive index medium it deflects towards a line perpendicular to the interface, and when passes into a lower refractive index medium the opposite occurs. The greater the difference in the refractive index the greater the deviation is. This law is valid below a certain angle, above which only reflection occurs.

In Figure C.1 the light passes through a plane parallel plate, medium 2, surrounded by medium 1. Although the incident and the emergent rays are parallel, they are displaced, which induces an image that does not correspond to the correct position of the real object to an observer.

In Table C.1 the refractive indexes of the materials used in the experiments are presented.

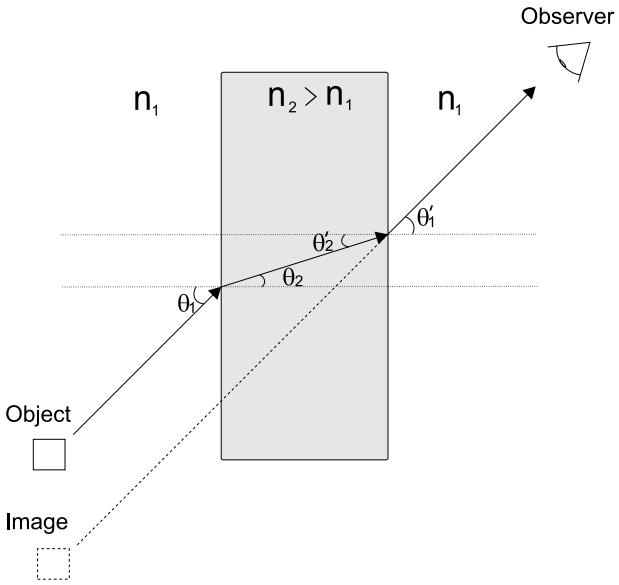

Figure C.1. Refraction of a light ray when passing a plane interface.

Table C.1. Refractive index of perspex and polymer solutions used.

Material	Refractive Index
Air	1.001
Water	1.333
2.0 wt% CMC	1.336
1.0 wt% PAA	1.335
Perspex	1.490

The differences in the refractive indexes of the liquids are negligible. The main difference occurs in the air/perspex interface. Figure C.2 represents the differences between the incident and the emergent rays in the air/perspex and perspex/liquid interfaces, according to Snell's law.

Light refraction occurs in the Taylor bubble experiments where light rays pass through different interfaces between the camera and the central plane of the column. In Figure C.3 it can be seen that between the camera and the central plane of the column there are 4 interfaces: a) air/perspex interface in the front face of the box, b) perspex/liquid interface inside the box, c) liquid/perspex interface in the outer diameter of the column and d) perspex/liquid interface in the inner diameter of the column.

Figure C.4 shows a finger extended inside the optical box half-filled with liquid. In the

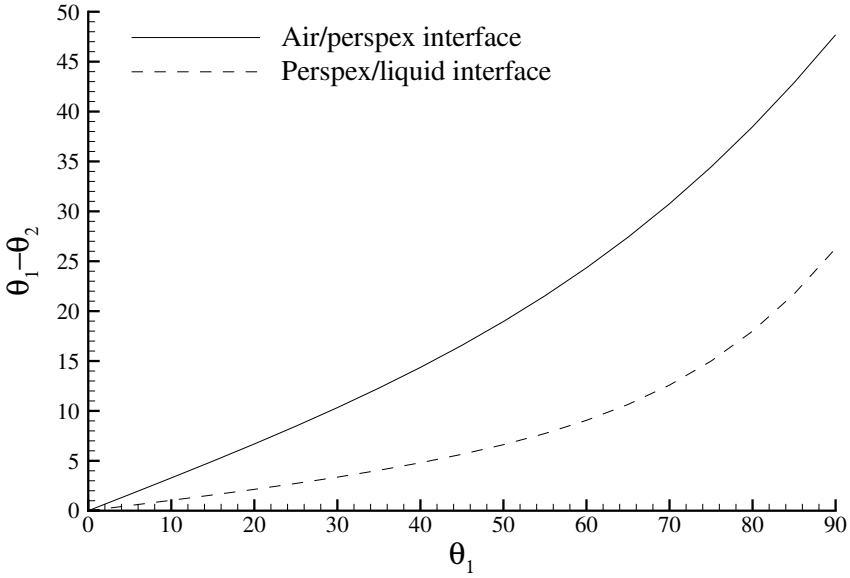

Figure C.2. Difference between incident and emergent light rays in the air/perspex and perspex/liquid interfaces. θ_1 and θ_2 are the angles shown in Figure C.1

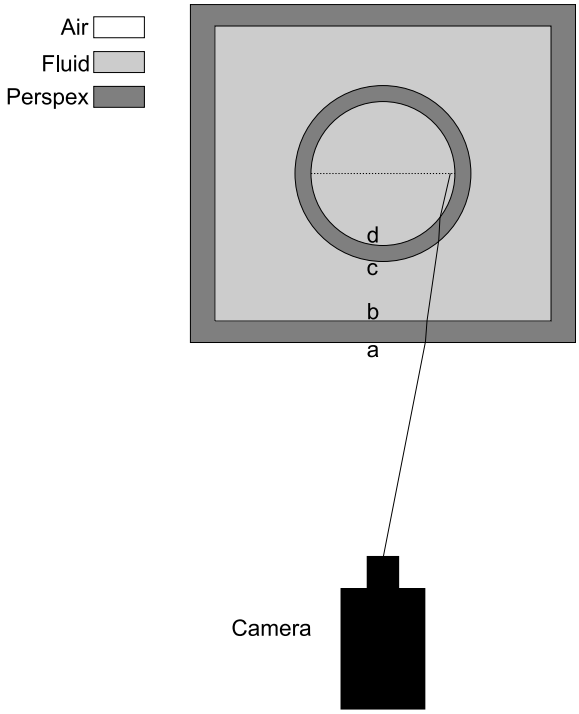

Figure C.3. Sketch of the deflection of light rays in the experimental setup.

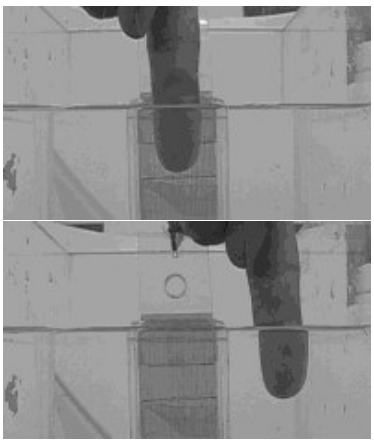

Figure C.4. Optical distortion that occurs in the half empty optical box, front face.

optical box face plane there is some distortion due to the difference between the refractive indexes of air, liquid and perspex. In the centre of the image (Figure C.4 up), there is no visible distortion between a finger out of the water (above the horizontal line) and immersed in water, since the incident angle is close to zero (camera placed perpendicular to the front face of the optical box). As the finger moves away from the centre of the image (Figure C.4 below), the incident angle is higher and the image becomes distorted.

After passing the optical box faces, the rays reach the external curved surface of the column. In this face the incident angle can become very high as the distance from the axis of the column increases, leading to higher ray deflections.

A test was done in order to check the effect of the box in the reduction of the optical distortion. Very thin equally-spaced lines were printed and placed inside the column (in a central plane perpendicular to the camera). Images taken with and without the optical box are presented in Figure C.5. In the upper image, taken without the optical box, the lines

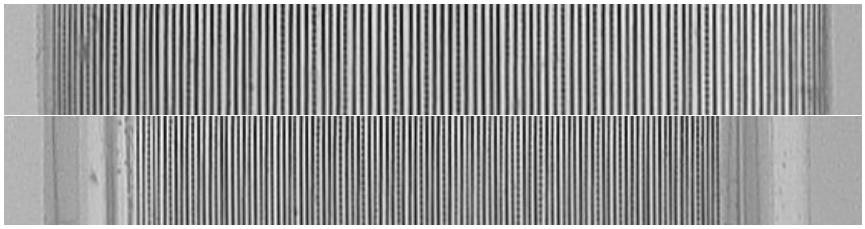

Figure C.5. Images of equally-spaced lines in a vertical plane containing the axis of the column without (upper image) and with(lower image)the optical box.

are distorted, becoming closer to each other as the distance from the axis increases. With the optical box, the distance between the lines appears constant and the inner face of the column is clearly visible. An image analysis was made to check the distance between the lines. In Figure C.6 the distances between the lines with and without the optical box are represented. From this figure the importance of the optical box is evident, as the distortion

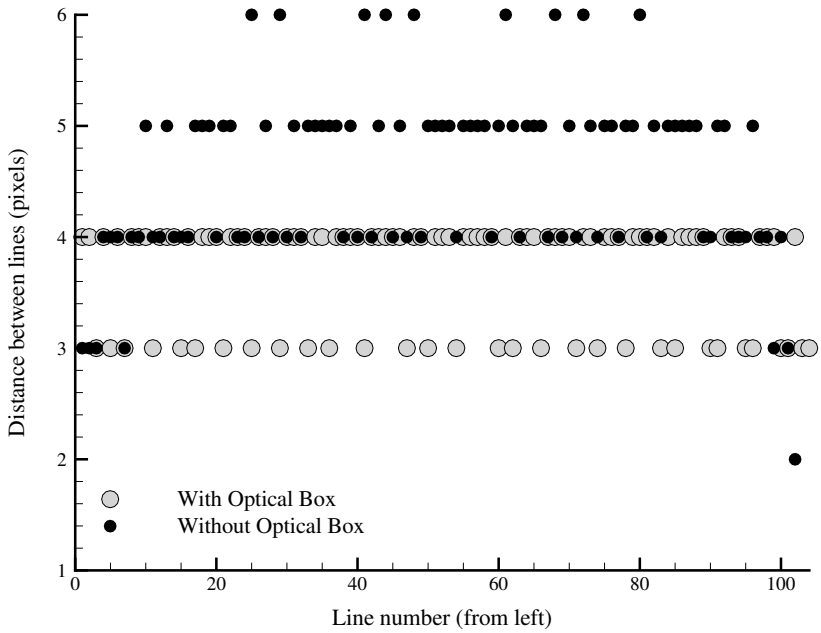

Figure C.6. Distance between consecutive lines, from left to right, with and without the optical box.

is clearly reduced. Without the optical box the distance between the lines is higher in the axis of the column and decreases with increasing radial position, while with the optical box, the distance appears to remain almost constant. This test demonstrates the importance of the optical box, but due to the low camera resolution and position errors in the printed lines the distortion can not be quantified.

The quantification of the optical distortion was made by ray tracing, i.e., by analysing the trajectory of the rays crossing the different interfaces, knowing the materials refractive index and dimensions. In the experiments the camera was located approximately 0.25 m from the front optical box face. For the ray tracing, it was considered that the image was acquired from a single point. In Figure C.7 the ray deflections predicted by Snell's law with and without the optical box are represented. From this Figure it is possible to understand

the distortions observed in Figure C.5. Without the box the column is surrounded by air,

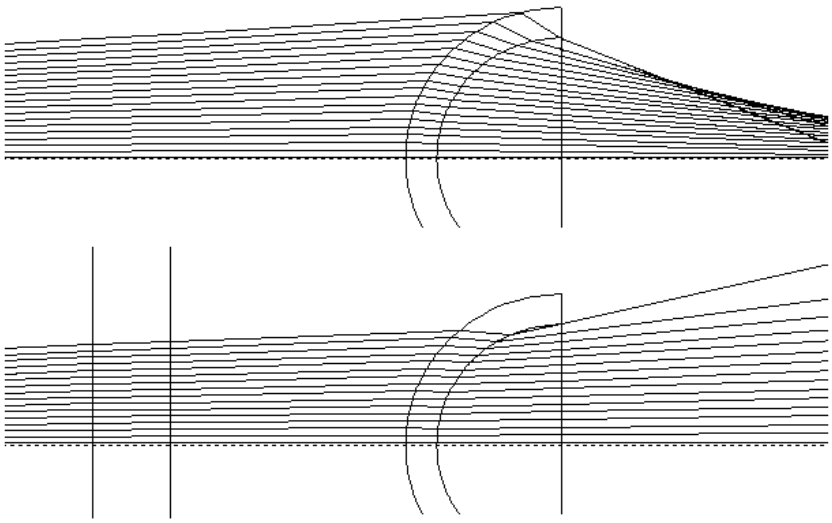

Figure C.7. Prediction of the path of the light rays in the actual setup, without (up) and with (down) the optical box, according to Snell's law.

and due to the higher difference between the refractive indexes the rays suffer a higher deviation in the outer column face. With the optical box, the inner and outer column faces are in contact with the same liquid. Therefore the ray deflection is not so high, and even for the higher radial position the deflections in the inner and outer column faces tend to compensate each other, so the point where the ray intercepts the central plane of the column is practically a continuation of the initial ray direction.

The optical distortion can be quantified by comparing the coordinates of the light rays in the front face of the optical box (which are seen by the camera), with the correspondent coordinates in the central plane of the column (the real positions). If no distortion is present, the ratio between these coordinates should be constant, and the constant value would be consequence of the different distances to the camera. In Figure C.8 vertical lines are plotted in the radial positions where the light rays intercept the central plane of the column and the box front face, and the ratio between these radial positions is shown. In Figure C.8 it is seen that the radial positions in the box front face are reduced, relative to the corresponding coordinates in the central plane of the column, and more importantly, the ratio between them is not constant over the column width. Although the difference is not considerable, there is a decrease of this ratio for higher values of the

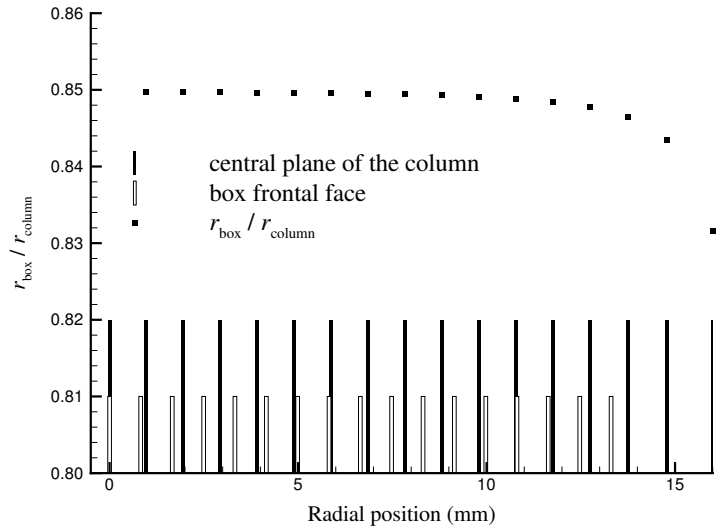

Figure C.8. Radial position of light rays in the optical box front face, their corresponding position in the central plane of the column and the ratio between them.

radial position. This fact shows that the calibrated images have a certain error in the radial positions. The calibration is made by assuming that the maximum radial position in the box front face corresponds to the column radius and then the radial positions are obtained proportionally, as if there was no distortion. The error in the radial position can be determined by comparing the real value with the one read in the calibrated images. Table C.2 presents the real radial position in the central plane of the column, the radial position in the box front face, the radial position after calibration, and the difference between this value and the real one.

From these values, it is possible to correct the radial positions in the calibrated images from the real positions in the central plane of the column.

In order to check the distortion in the vertical direction a similar procedure was performed. Although the rays were still deflected due to the different refractive indexes, the ratio between the image coordinates and the actual coordinates is constant so the vertical error in the calibrated images can be ignored.

Table C.2. Radial position in the central plane of the column, in the optical box front face, radial position in images and error, all in mm.

r_{column}	r_{box}	r_{image}	$error$
16.00	13.50	16.00	0.00
14.80	12.66	15.00	0.20
13.77	11.81	14.00	0.23
12.77	10.97	13.00	0.23
11.78	10.12	11.99	0.21
10.79	9.28	10.99	0.20
9.81	8.44	9.99	0.18
8.78	7.55	8.95	0.17
7.84	6.75	7.99	0.15
6.96	5.99	7.10	0.14
5.88	5.06	5.99	0.11
4.90	4.22	4.99	0.09
3.92	3.37	4.00	0.08
2.94	2.53	3.00	0.06
1.96	1.69	2.00	0.04
0.98	0.84	1.00	0.02
0.00	0.00	0.00	0.00

C.1 Laser diodes

In the PIV and coalescence studies, laser diodes were used to measure Taylor bubble velocity and length. Pairs of laser diodes were placed in the horizontal position, aimed at photocells on the opposite side of the column. The bubble transit causes a deflection in the laser ray, which produces a severe drop in the photocell signal. Knowing the accurate distance between the photocells, the bubble velocity and length can be determined by comparing the time delay between the signal drop and the duration of this drop respectively. As explained earlier, if the light ray intercepts a perpendicular surface it is not deflected. Therefore, if the laser diode is placed perpendicular to the column wall it would not be deflected in the bubble region where the radius is constant, only in the bubble nose. However, if the laser ray is slightly deviated from the axis of the column it is deflected, even in the constant radius region of the bubble because the incident angle is different from zero. These two configurations are represented in Figure C.9.

The bubble passing causes a deviation of about 1 mm from the plane crossing the axis of the column. This is enough to deflect the laser ray from the photocell and does

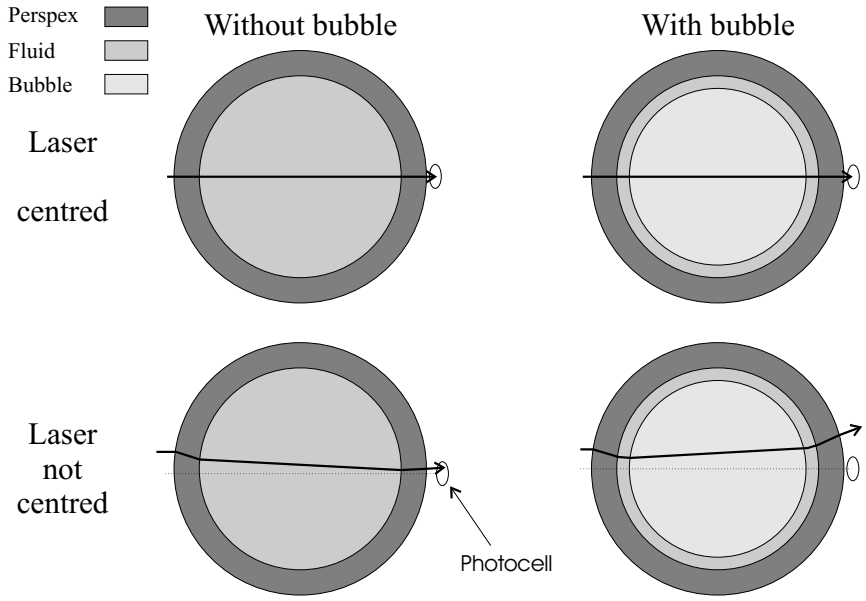

Figure C.9. Trajectory of laser ray through the column at different positions, with and without the presence of the bubble.

not introduce any significant error to the bubble measurements since the ray still passes practically in the axis of the column when no bubble is present. The deviation was the same for every laser diode, so the bubble nose detection point was the same in all cases.

Appendix D

Matlab programs

In this appendix the most relevant Matlab programs created in this work are listed, with a brief description of their function.

D.1 Splitrotvarios

This program does batch processing of the original PIV images, by splitting them into two individual frames, then rotating them 90^o to place the column in the vertical direction and correct the burned pixels. For each bubble several images were acquired. To use this program, the PIV images should be named as `CCPPPBB_IIII.tif`, where `CC` refers to the polymer concentration (08 to 0.80 wt%), `PPP` to the polymer (CMC or PAA), `BB` to the bubble number and `IIII` to the image number. The final result are two frames, with filenames `CCPPPBB_IIIa.tif` and `CCPPPBB_IIIb.tif`. The use of only three digits for the frame number and the letters `a` and `b` to identify the frames has to do with the way that the code WIDIM reads the files. The `splitrotvarios` program is listed below.

```
slug=  [26 26 27 28]; imagem=[18 19 20 20]; root='08paa';
%Lines cut (when image croped in SENSICONTROL)
uplines=2; downlines=4; nimages=length(slug);
for i=1:nimages
    messg=['Processing image ',num2str(i),' out of ',num2str(nimages)];
    disp(messg)
    if imagem(i)>9
        zeros='_00';
    else
        zeros='_000';
```

```
    end
    if imagem(i)>99
        zeros='_0';
    end
filename=[root,num2str(slug(i)),zeros,num2str(imagem(i)),'.tif'];
% READ IMAGE
    A=imread(filename);
% SPLIT IMAGE IN TWO PARTS
    [alin,acol]=size(A);
   A1=A(1:alin/2,1:acol);
   A2=A(alin/2+1:alin,1:acol);
%   Burned pixels
    X1 = [194 195 196 ];
    Y1 = [825 826 829 ];
    Y2 = [832 832 832 ];
    X2 = [20 40 60 ];
%Y1=Y1-32*uplines;
%Y2=Y2-32*uplines;
   for br=1:3
       if Y2(br)>0
            if Y1(br)< (1024-32*(uplines+downlines))
                if Y1(br)<1
                   Y1(br)=1;
                end
                if Y2(br)>(1024-32*(uplines+downlines))
                   Y2(br)=(1024-32*(uplines+downlines)) ;
                end
          A1(Y1(br):Y2(br),X1(br))=A1(Y1(br):Y2(br),X2(br));
          A2(Y1(br):Y2(br),X1(br))=A2(Y1(br):Y2(br),X2(br));
            end
       end
   end
   A1=rot90(A1);
   A2=rot90(A2);
   if imagem(i)>9
        zeros='_0';
    else
        zeros='_00';
    end
    if imagem(i)>99
        zeros='_';
    end
   filename1=[root,num2str(slug(i)),zeros,num2str(imagem(i)),'a.tif'];
   filename2=[root,num2str(slug(i)),zeros,num2str(imagem(i)),'b.tif'];
% WRITE IMAGES
```

```
   imwrite(A1,filename1);
   imwrite(A2,filename2);
end
 disp('spliting done')
```

D.2 Shadow

This program uses a PIV image and a background reference image to create a binary image: 0 for the gas phase and 1 for the liquid phase. It also determines the coordinates of the gas-liquid interface, and stores them in a file.

```
clear all
% Reads the image and stores in variable "a"
slug='01cmc_064a';          %bubble image
background='01cmcref.tif'; %background reference image
temp=[slug,'.tif'] a=imread(temp); a=im2double(a);

back=imread(background); back=im2double(back);

%Median filter to remove particles
size=11;       %dimension of the neighborhood cell
a=medfilt2(a,[size size]); back=medfilt2(back,[size size]);

%Subtract the background image to the original
dif=((back-a)*50);

%Binarize the image according to threshold
treshval=0.2; final=dif>treshval;
%imwrite(final,'binarized.tif')

%See if upper or lower line of the image contain the bubble
[m,n]=size(final); minu=n; maxu=1; mind=n; maxd=1; for col=1:n;
        if final(1,col)==1;
            if col<minu
                minu=col ;
            end;
            if col>maxu
                maxu=col ;
            end;
        end
        if final(m,col)==1
            if col<mind
                mind=col ;
```

```
            end;
            if col>maxd
                maxd=line ;
            end;

        end;
end; final(1,minu:maxu)=1; final(m,mind:maxd)=1;

% Fill the interior of the bubble
final=bwfill(final,'holes'); final2=final<0.5; figure
imshow(final2) title('FINAL IMAGE') temp=[slug,'shadow.tif']
imwrite(final2,temp)

%Apply filter to obtain derivative of intensity - Find edges

horizontal edges h=[ 0 -1 0
                     0  2 0
                     0 -1 0];
hedge=filter2(h,final);

vertical edges v=[0 0 0
                 -1 2 -1
                  0 0 0];

vedge=filter2(v,final);

totaledge=max(hedge,vedge); totaledge=totaledge>0.5; figure
imshow(totaledge) title('Edges')

%Save matrix with shape coordinates

[x y]=find(totaledge==1); z=[x y]; file=[slug, '.dat'] save file z
-ASCII
```

D.3 Tecconvshadow

This program converts the original window displacement obtained from WIDIM into velocities in m/s. It also creates the dimensionless radial and axial coordinates, taking into account the optical distortion in the radial direction. A new variable is introduced in the file corresponding to the bubble shadow.

```
clear all;
%*****************  IMAGE PARAMETERS *********************
```

```
calib=22.2     % calibration in pixels/mm
dt=2005        % time between PIV frames, in micro-seconds
root='08paa'   % root of the filename
maskmin=63     %the X pixel corresponding to the left column wall
maskmax=774    %the X pixel corresponding to the right column wall

%*********************************************************************
slug=  [43 46 57 57 57 57 57 57 57 ] %different slug numbers to process
imagem=[18 23 15 16 17 18 19 20 21 ] %images to process
shadow=imagem

nimages=length(slug);

for i =1:nimages
    messg=['Processing image ',num2str(i),' out of ',num2str(nimages)];
    disp(messg)
    if imagem(i)>9
        zeros='_0';
    else
        zeros='_00';
    end
    if imagem(i)>99
        zeros='_';
    end
    filenamein=[root,num2str(slug(i)),zeros,num2str(imagem(i)), '.plt'];
    shimage=[root,num2str(slug(i)),zeros,num2str(imagem(i)),'ash.tif']
if uslug==0
    suf='c'
else

    suf='cs'
end if ~strcmp(shimage,'')
    suf=[suf,'im']
end
filenameout=[root,num2str(slug(i)),zeros,num2str(imagem(i)),suf,'.plt'];

%--------- Load the shadow image ------
if ~strcmp(shimage,'') disp(['reading ' shimage])
    Z=imread(shimage);
    Z=rot90(Z,2);
    Z=fliplr(Z);
    Z=im2double(Z);
    Z=medfilt2(Z,[11 11]);
end
```

```
%---------- LOAD TECPLOT FILE --------
disp('OPEN TECPLOT FILES ');

   disp(['reading ' filenamein])

    fid=fopen(filenamein,'r');
    [line1,count]=fscanf(fid,'%s',[1,1]);
    [line2,count]=fscanf(fid,'%s',[1,1]);
    [line31,count]=fscanf(fid,'%s',[1,1]);
    [line32,count]=fscanf(fid,'%s',[1,1]);
    %[line33,count]=fscanf(fid,'%s',[1,1]);
    stri=fscanf(fid,'%s',[1,1]);
    strj=fscanf(fid,'%s',[1,1]);
    eval([stri ';']);
    eval([strj ';']);

    col=6;
    lin=I*J;

    [A,count]=fscanf(fid,'%g',[col,lin]);
    fclose(fid);

    % construct matrix of X, Y, U, V similar to image

    for j=1:J
        X(j,1:I)=A(1,(j-1)*I+1:j*I);
        Y(j,1:I)=A(2,(j-1)*I+1:j*I);
        U(j,1:I)=A(3,(j-1)*I+1:j*I);
        V(j,1:I)=A(4,(j-1)*I+1:j*I);
        SN(j,1:I)=A(5,(j-1)*I+1:j*I);
        IN(j,1:I)=A(6,(j-1)*I+1:j*I);
    end
    SH=IN;
    for i=1:I
        for j=1:J
    %*** Convert window displacement to velocities in m/s (positive downwards)****
    U(j,i)=U(j,i)*1000/(calib*dt);
    V(j,i)=-V(j,i)*1000/(calib*dt);

    %*** Creates SH variable with zeros inside slug and in column and 1 outside ***
    if ~strcmp(shimage,'')
    SH(j,i)=Z(round(Y(j,i)),round(X(j,i)));
    end

    %*** Convert coordenates to r/D and z/D ***
```

```
    X(j,i)=(X(j,i)-(maskmax+maskmin)/2)/(maskmax-maskmin)  ;
    Y(j,i)=(1280-Y(j,i))/(maskmax-maskmin);
             end
    end

    %*** Corrects the radial coordinates due to optical distortion ***

    original=X(1,1:I)
    original=original'
    coluna=[-0.5
-0.499989879 -0.489124419 -0.479694963 -0.470911924 -0.462473363
-0.454262677 -0.446182827 -0.438197862 -0.430281964 -0.398994548
-0.368027877 -0.337204013 -0.306450513 -0.27432555 -0.24505928
-0.217570308 -0.183749349 -0.153111384 -0.122481135 -0.091856263
-0.061235445 -0.030617116 0 0.030617116 0.061235445 0.091856263
0.122481135 0.153111384 0.183749349 0.217570308 0.24505928
0.27432555 0.306450513 0.337204013 0.368027877 0.398994548
0.430281964 0.438197862 0.446182827 0.454262677 0.462473363
0.470911924 0.479694963 0.489124419 0.499989879 0.5 0.9];

image=[-0.5 -0.499990182 -0.492163011 -0.484336542 -0.476510601
-0.468678538 -0.460861233 -0.453037459 -0.445214492 -0.43739378
-0.406102805 -0.374829183 -0.343567016 -0.312308955 -0.279617023
-0.249812977 -0.221807115 -0.187339915 -0.156109974 -0.124883749
-0.093660204 -0.062438952 -0.031219121 0 0.031219121 0.062438952
0.093660204 0.124883749 0.156109974 0.187339915 0.221807115
0.249812977 0.279617023 0.312308955 0.343567016 0.374829183
0.406102805 0.43739378 0.445214492 0.453037459 0.460861233
0.468678538 0.476510601 0.484336542 0.492163011 0.499990182 0.5
0.9];

np=size(original); n=size(coluna) for i=1:np(1) orig=original(i);

ncima=find(image>orig) ncima=ncima(1)
    if ncima==n(1)
        corr(i)=orig
elseif ncima==n(1)-1
        corr(i)=0.5
elseif ncima==1
        corr(i)=orig
elseif ncima==2
        corr(i)=-0.5
else
    corr(i)=coluna(ncima-1)+(coluna(ncima)-coluna(ncima-1))/&
    &(image(ncima)-image(ncima-1))*(orig-image(ncima-1))
```

```
end end
    %Reconstruct the tecplot file
    for j=1:J
        A(1,(j-1)*I+1:j*I)=X(j,1:I);
        A(2,(j-1)*I+1:j*I)=Y(j,1:I);
        A(3,(j-1)*I+1:j*I)=U(j,1:I);
        A(4,(j-1)*I+1:j*I)=V(j,1:I);
        A(5,(j-1)*I+1:j*I)=SN(j,1:I);
        A(6,(j-1)*I+1:j*I)=SH(j,1:I);
    end
    %Write the file
disp(['writing ' filenameout]) fid=fopen(filenameout,'w');
fprintf(fid,'%s\n','TITLE="TecplotShadow"');
fprintf(fid,'%s\n','VARIABLES="r/D","z/D","U","V","SN","IM"');
fprintf(fid,'%s%i%s%i\n','ZONE T="Velocity_Shadow", I=',I,', J=',J);
fprintf(fid,'%8.5f %8.5f %8.5f %8.5f %8.5f %8.5f \n',A);
fclose(fid);

clear A X Y U V SN IN Z
end
```

D.4 Average

This program determines the average of several variables along the axial direction at different radial positions. It was used to determine the average velocity profiles in the stabilised liquid film region.

```
clear all;

root='01paa' % image filename root
slug=  [65 66 67 68 69] %bubbles to be analysed
imagem=[16 14 14 13 12] %images of bubbles
nimages=length(slug); filenameout=[root,'desviosfilmeconv.dat'];

for i = 1:nimages messg=['Processing image ',num2str(i),' out of
',num2str(nimages)];
    disp(messg)
    if imagem(i)>9
        zeros='_0';
    else
        zeros='_00';
    end
    if imagem(i)>99
```

```
        zeros='_';
    end
    filenamein=[root,num2str(slug(i)),zeros,num2str(imagem(i)), 'im.plt'];

%---------- LOAD DATA FILE --------
disp('OPEN DATA FILES ');
   disp(['reading ' filenamein])
    fid=fopen(filenamein,'r');

    [line1,count]=fscanf(fid,'%s',[1,1]);
    [line2,count]=fscanf(fid,'%s',[1,1]);
    [line31,count]=fscanf(fid,'%s',[1,1]);
    [line32,count]=fscanf(fid,'%s',[1,1]);
    stri=fscanf(fid,'%s',[1,1]);
    strj=fscanf(fid,'%s',[1,1]);
    eval([stri ';']);
    eval([strj ';']);
    col=6;
    lin=I*J;
    [A,count]=fscanf(fid,'%g',[col,lin]);
    fclose(fid);
 % construct matrix of X, Y, U, V similar to image

    for j=1:J
        X(j,1:I)=A(1,(j-1)*I+1:j*I);
        Y(j,1:I)=A(2,(j-1)*I+1:j*I);
        U(j,1:I)=A(3,(j-1)*I+1:j*I);
        V(j,1:I)=A(4,(j-1)*I+1:j*I);
        SN(j,1:I)=A(5,(j-1)*I+1:j*I);
        SH(j,1:I)=A(6,(j-1)*I+1:j*I);
    end
    VV(1+(i-1)*J:i*J,1:I)=V;
    UU(1+(i-1)*J:i*J,1:I)=U;
end
     RD=mean(X);
     VelV=mean(VV);
     stdV=std(VV,0,1);
     VelU=mean(UU);
     stdU=std(UU,0,1);
RD=RD'; VelV=VelV'; stdV=stdV'; VelU=VelU'; stdU=stdU';
     z=[RD VelU stdU VelV stdV ];
     save(filenameout,'z','-ascii');
```

D.5 WakeAverage

This program was used to determine average flow fields in the wakes of the bubbles. The position of the bubble trailing edge must be individually determined and placed in variable `linhazero` .

```
clear all;

root='02paa' slug=   [16 17 18 19 20 46 47 48 50] imagem= [11 13
13 13 12 10 12 13 12]

linhazero=[112 99 104 112 113 96 89 110 115]

nimages=length(slug); linhas=min(linhazero); for i =1:nimages
    messg=['Processing image ',num2str(i),' out of ',num2str(nimages)];
    disp(messg)
    if imagem(i)>9
        zeros='_0';
    else
        zeros='_00';
    end
    if imagem(i)>99
        zeros='_';
    end
    filenamein=[root,num2str(slug(i)),zeros,num2str(imagem(i)), 'cim.plt'];

%---------- LOAD TECPLOT FILE --------
disp('OPEN TECPLOT FILES ');
   disp(['reading ' filenamein])
    fid=fopen(filenamein,'r');
    [line1,count]=fscanf(fid,'%s',[1,1]);
    [line2,count]=fscanf(fid,'%s',[1,1]);
    [line31,count]=fscanf(fid,'%s',[1,1]);
    [line32,count]=fscanf(fid,'%s',[1,1]);
    stri=fscanf(fid,'%s',[1,1]);
    strj=fscanf(fid,'%s',[1,1]);
    eval([stri ';']);
    eval([strj ';']);
    col=6;
    lin=I*J;
    [A,count]=fscanf(fid,'%g',[col,lin]);
    fclose(fid);

    % construct matrix of X, Y, U, V similar to image
```

```
    for j=1:J
        X(j,1:I)=A(1,(j-1)*I+1:j*I);
        Y(j,1:I)=A(2,(j-1)*I+1:j*I);
        U(j,1:I)=A(3,(j-1)*I+1:j*I);
        V(j,1:I)=A(4,(j-1)*I+1:j*I);
       %SN(j,1:I)=A(5,(j-1)*I+1:j*I);
       %IN(j,1:I)=A(6,(j-1)*I+1:j*I);
    end
   todasV(i,1:linhas,:)=V(linhazero(i)-linhas+1:linhazero(i),:);
   todasU(i,1:linhas,:)=U(linhazero(i)-linhas+1:linhazero(i),:);
end for steps=2:nimages
   Xfinal(1:linhas,:)=X(linhazero(i)-linhas+1:linhazero(i),:);
   Yfinal(1:linhas,:)=Y(J-linhas+1:J,:);
   Umedia=mean(todasU(1:steps,:,:));
   Vmedia=mean(todasV(1:steps,:,:));
   stdU=std(todasU(1:steps,:,:));
   stdV=std(todasV(1:steps,:,:));
   Ufinal(:,:)=Umedia(1,:,:);
   Vfinal(:,:)=Vmedia(1,:,:);
   stdUfinal(:,:)=stdU(1,:,:);
   stdVfinal(:,:)=stdV(1,:,:);
%Reconstruct the tecplot file
    for j=1:linhas
        A(1,(j-1)*I+1:j*I)=Xfinal(j,1:I);
        A(2,(j-1)*I+1:j*I)=Yfinal(j,1:I);
        A(3,(j-1)*I+1:j*I)=Ufinal(j,1:I);
        A(4,(j-1)*I+1:j*I)=Vfinal(j,1:I);
        A(5,(j-1)*I+1:j*I)=stdUfinal(j,1:I);
        A(6,(j-1)*I+1:j*I)=stdVfinal(j,1:I);
    end
    %extrair pontos%
    Vi=137;
    Vj=42;
    Ui=137;
    Uj=42;
    pontov(steps-1,:)=[steps Xfinal(Vj,Vi) Yfinal(Vj,Vi)&
    &Vfinal(Vj,Vi) stdVfinal(Vj,Vi)];
    pontou(steps-1,:)=[steps Xfinal(Uj,Ui) Yfinal(Uj,Ui)&
    &Ufinal(Uj,Ui) stdUfinal(Uj,Ui)];
%Write the file
filenameout=[root,'wakeav',num2str(steps),'.plt']; disp(['writing
' filenameout]) fid=fopen(filenameout,'w');
fprintf(fid,'%s\n','TITLE="TecplotShadow"');
fprintf(fid,'%s\n','VARIABLES="r/D","z/D","Umean","Vmean","stdU","stdV"');
fprintf(fid,'%s%i%s%i\n','ZONE T="WakeAverage", I=',I,', J=',linhas);
```

```
fprintf(fid,'%8.5f %8.5f %8.5f %8.5f %8.5f %8.5f \n',A);
fclose(fid); end

filev=[root,'pontoV.dat']; fileu=[root,'pontoU.dat'];
disp(['writing ' filev]) save(filev,'pontov','-ascii');
disp(['writing ' fileu]) save(fileu,'pontou','-ascii');
disp(['Inicio:',num2str(fix(ci(4))),'h',num2str(fix(ci(5))),'m']);
cf=clock;
disp(['FIM:',num2str(fix(cf(4))),'h',num2str(fix(cf(5))),'m']);
clear all
```

Bibliography

Acharya, A., Mashelkar, R. A., Ulbrecht, J., 1977. Mechanics of bubble motion and deformation in non-newtonian media. Chemical Engineering Science 32, 863–872.

Acharya, A., Ulbrecht, J. J., 1978. Note on the influence of viscoelasticity on the coalescence rate of bubbles and drops. AIChE J. 24, 348–351.

Adrian, R. J., 1991. Particle-imaging techniques for experimental fluid mechanics. Ann. Rev. Fluid Mech. 22, 261–304.

Adrian, R. J., July 2004. Twenty years of particle image velocimetry. 12th International Symposium on Applications of Laser Techniques to Fluid Mechanics, Lisbon, Lisbon.

Ahmad, W. R., DeJesus, J. M., Kawaji, M., 1998. Falling film hydrodynamics in slug flow. Chemical Engineering Science 53 (1), 123–130.

Arigo, M. T., McKinley, G. H., 1998. An experimental investigation of negative wakes behind spheres settling in a shear-thinning viscoelastic fluid. Rheol. Acta 37, 307–327.

Astarita, G., Apuzzo, G., 1965. Motion of gas bubbles in non-newtonian liquids. AIChE J. 11, 815–820.

Bhavaraju, S. M., Mashelkar, R. A., Blanch, H. W., 1978. Bubble motion and mass transfer in non-newtonian fluids. AIChE J. 24 (6), 1063–1076.

Bird, R. B., Armstrong, R. C., Hassager, O., 1987. Dynamics of Polymeric Liquids, 2nd Edition. Vol. 1 - Fluid Dynamics. Wiley-Interscience Publication.

Brown, R. A. S., 1965. The mechanics of large gas bubbles in tubes. i. bubble velocities in stagnant liquids. Can. J. Chem. Engng. 43, 217–223.

Brücker, C., 2000. PIV in two-phase flows. lecture series 2000-01, particle image velocimetry and associated techniques. von Karman Institute for Fluid Dynamics (ed. M. L. Riethmuller) Lecture Series 2000-01.

Brujan, E. A., 1999. A first-order model for bubble dynamics in a compressible viscoelastic liquid. J. Non-Newtonian Fluid Mechanics 84, 83–103.

Bugg, J., Saad, G. A., 2002. The velocity field around a taylor bubble rising in a stagnant viscous fluid: Numerical and experimental results. Int. J. Multiphase Flow 28, 791–803.

Bugg, J. D., Mack, K., Rezkallah, K. S., 1998. A numerical model of taylor bubbles rising through stagnant liquids in vertical tubes. Int. J. Multiphase Flow 24 (2), 271–281.

Campos, J. B. L. M., Guedes de Carvalho, J. R. F., 1988. An experimental study of the wake of gas slugs rising in liquids. J. Fluid Mechanics 196, 27–37.

Carew, P. S., Thomas, N. H., Johnson, A. B., 1995. A physical based correlation for the effects of power law rheology and inclination on slug bubble rise velocity. Int. J. Multiphase Flow 21 (6), 1091–1106.

Clarke, A., Issa, R. I., 1997. A numerical model of slug flow in vertical pipe tubes. Computers & Fluids 26, 395–415.

Clift, R., Graze, J. R., Sollazzo, V., 1974. Continuous slug flow in vertical tubes. J. Heat Transfer 96 (3), 371–376.

Collins, R., 1965. A simple model of the plane gas bubble in a finite liquid. J. Fluid Mechanics 22(4), 763–771.

Collins, R., 1966. A second approximation for the velocity of a large gas bubble rising in an infinite liquid. J. Fluid Mechanics 25 (2), 469–480.

Collins, R., DeMoraes, F., Davidson, J. F., 1978. The motion of a large gas bubble rising through liquid flowing in a tube. J. Fluid Mechanics 89, 497–514.

Coutanceau, M., Hajjam, M., 1982. Viscoelastic effect on the behaviour of an air bubble rising axially in a tube. Applied Scientific Research 38, 199–207.

Davidson, J. F., Harrison, D., 1963. Fluidised Particles. Cambridge University Press.

Davies, R. M., Taylor, G. I., 1950. The mechanics of large bubbles rising through extended liquids and through liquid tubes. Proc. R. Soc. London Ser. A 200, 375–390.

De Kee, D., Chan Man Fong, C. F., 2002. Bubble shape in non-newtonian fluids. J. of Applied Mechanics 69, 703–705.

DeJesus, J. D., Ahmad, W., Kawaji, M., 1995. Experimental study of flow structure in vertical slug flow. Advances in Multiphase Flow , 105–118.

Dekée, D., Carreau, P. J., Mordarski, J., 1986. Bubble velocity and coalescence in viscoelastic liquids. Chemical Engineering Science 41, 2273–2283.

Delfos, R., Rops, C. M., Kockx, J. P., Nieuwstadt, F. T. M., 2001. Measurement of the recoalescence flux into the rear of a taylor bubble. Physics of Fluids 13, 1141–1150.

Dias, I., Riethmuller, M. L., 1998. PIV in two-phase flows: Simultaneous bubble sizing and liquid velocity measurements. In: Springer-Verlag (Ed.), Bound Volume of Selected Papers of the "9th Symposium on Laser Techniques Applied to Fluid Mechanics.

Dukler, A. E., Maron, D. M., Brauner, N., 1985. A physical model for predicting the minimum stable slug length. Chemical Engineering Science 40, 1379–1385.

Dumitrescu, D. T., 1943. Strömung an einer luftblase im senkrechten rohr. Z. Angew. Math. Mech 23, 139–139.

Elperin, T., Fominykh, A., 1995. Two models of fluid flow and mass transfer at the trailing edge of a gas slug. Int. J. Heat Mass Transfer 38 (18), 3341–3347.

Fabre, J., Liné, A., 1992. Modeling of two-phase slug flow. Annu. Rev. Fluid Mech. , 21–46.

Fernandes, R. C., Semiat, R., Dukler, A. E., 1983. Hydrodynamic model for gas-liquid slug flow in vertical tubes. AIChE J. 29, 981–989.

Filla, M., Donsi, G., Crescitell, S., 1979. Tecniche sperimentali per lo studio della scia di bolle. ICP Rivista Industria Chimica 10.

Fulford, G. D., 1964. The flow of liquids in thin films. Adv. Chem. Eng. 5, 151–236.

Funfschilling, D., Li, H. Z., 2001. Flow of non-newtonian fluids around bubbles: PIV measurements and birefringe visualisation. Chemical Engineering Science 56, 1137–1141.

Gouriet, J. B., Stitou, A., Riethmuller, M. L., September 17-19 2001. Practical implications of camera resolution and peak locking in actual measurements. 4th International Symposium on Particle Image Velocimetry, Göttingen.

Gui, L., Lindken, R., Merzkirch, W., 1996. Phase-separated PIV measurements in two phase flow by applying a digital mask technique. ERCOFTAC Bulletin 30, 45–48.

Harlen, O. G., 2002. The negative wake behind a sphere sedimenting through a viscoelastic fluid. J. Non-Newtonian Fluid Mechanics 108, 411–430.

Hasanein, H. A., Tudose, G. T., Wong, S., Malik, M., Esaki, S., Kawaji, M., 1996. Slug flow experiments and computer simulation of slug length distribution in vertical pipes. AIChE Symposium Series 92 (310), 211–219.

Hassager, O., 1979. Negative wake behind bubbles in non-newtonian liquids. Nature 279, 402–403.

Hassan, Y. A., Blanchat, T. K., Jr, C. H. S., Canaan, R. E., 1992. Simultaneous velocity measurements of both components of a two-phase flow using particle image velocimetry. Int. J. Multiphase Flow 18 (3), 371–395.

Hassan, Y. A., Philip, O. G., Schmidl, W. G., 1993. Bubble colapse velocity measurements using a particle image velocimetry technique with fluorescent tracers. ASME FED 172, 85–92.

Herrera-Velarde, J. R., Zenit, R., Chehata, D., Mena, B., 2003. The flow of non-newtonian fluids around bubbles and its connection to the jump discontinuity. J. Non-Newtonian Fluid Mechanics 111, 199–209.

Joseph, D. D., Feng, J., 1995. The negative wake in a second-order fluid. J. Non-Newtonian Fluid Mechanics 57, 313–320.

Kamışlı, F., 2003. Free coating of a non-newtonian liquid onto walls of a vertical and inclined tube. Chemical Engineering and Processing 42, 569–581.

Keane, R. D., Adrian, R. J., 1990. Optimization of particle image velocimeters. part i: Double pulsed systems. Meas. Sci. Technol. 1, 1202–1215.

Layzer, D., 1955. On the instability of superimposed fluids in a gravitational field. J. Astrophys. 122, 1.

Leal, L. G., Skoog, J., Acrivos, A., 1971. On the motion of gas bubbles in a viscoelastic liquid. The Canadian Journal of Chemical Engineering 49, 569–575.

Leider, P. J., Bird, R., 1974. Squeezing flow between parallel disks. i. theoretical analysis. Ind. Eng. Chem. Fundam. 13, 336.

Li, H. Z., Frank, X., Funfschilling, D., Mouline, Y., 2001. Towards the understanding of bubble interactions and coalescence in non-newtonian fluids: A cognitive approach. Chemical Engineering Science 56, 6419–6425.

Li, H. Z., Mouline, Y., Choplin, L., 1997a. Rheological simulation of in-line bubble interactions. AIChE J. 43 (1), 265–267.

Li, H. Z., Mouline, Y., Choplin, L., Midoux, N., 1997b. Chaotic bubble coalescence in non-newtonian fluids. Int. J. Multiphase Flow 23, 713–723.

Li, H. Z., Mouline, Y., Funfschilling, D., Marchal, P., Choplin, L., Midoux, N., 1998. Evidence for in-line bubble interactions in non-newtonian fluids. Chemical Engineering Science 53 (12), 2219–2230.

Lindken, R., Merzkirch, W., 2002. A novel PIV technique for measurements in multi-phase flows and its application to two-phase bubbly flows. Experiments in Fluids 33, 814–825.

Liu, Y. J., Liao, T. Y., Joseph, D. D., 1995. A two-dimensional cusp at the trailing edge of an air bubble rising in a viscoelastic liquid. J. Fluid Mechanics 304, 321–342.

Mao, Z. S., Dukler, A., 1990. The motion of taylor bubbles in vertical tubes.: I. a numerical simulation for the shape and rise velocity of taylor bubbles in stagnant and flowing liquid. J. Comp. Phys. 91, 132–160.

Margaritis, A., Bokkel, D. W. T., Karamanev, D. G., 1999. Bubble rise velocities and drag coefficients in non-newtonian polysaccharide solutions. Biotechnology and Bioengineering 64 (3), 257–266.

Maxworthy, T., 1967. A note on the existence of wakes behind large rising bubbles. J. Fluid Mechanics 27 (2), 367–368.

Moissis, R., Griffith, P., 1962. Entrance effects in a two-phase slug flow. J. Heat Transfer, Trans. ASME, Series C 2, 29–39.

Möller, K. D., 1988. Optics. University Science Books, Calf.

Nickens, H. V., Yannitell, D. W., 1987. The effects of surface tension and viscosity on the rise velocity of a large gas bubble in a closed, vertical liquid-filled tube. Int. J. Multiphase Flow 13 (1), 57–69.

Nicklin, D. J., Wilkes, J. O., Davidson, J. F., 1962. Two-phase flow in vertical tubes. Trans. Inst. Chem. Engrs 40, 61.

Nogueira, S., 2005. Hydrodynamic characterisation of gas-liquid slug flow: Numerical and experimental investigation. Ph.D. thesis, Faculdade de Engenharia da Universidade do Porto.

Nogueira, S., Dias, I., Pinto, A. M. F. R., Riethmuller, M. L., 2000. Liquid PIV measurements around a single gas slug rising through stagnant liquid in vertical pipes. In: Bound Volume of Selected Papers of the "10th Symposium on Laser Techniques Applied to Fluid Dynamics". Springer.

Nogueira, S., Sousa, R. G., Pinto, A. M. F. R., Riethmuller, M. L., Campos, J. B. L. M., 2003. Simultaneous PIV and shadowgraphy in slug flow: A solution for optical problems. Experiments in Fluids 35, 598–609.

Otten, L., Fayed, A. S., 1976. Pressure drop and drag reduction in two-phase non-newtonian slug flow. The Canadian Journal of Chemical Engineering 54, 111–114.

Philip, O. G., Schmidl, W. D., Hassan, Y. A., 1994. Development of a high speed particle image velocimetry technique using fluorescent tracers to study steam bubble collapse. Nuclear Engineering and Design 149, 375–385.

Pinheiro, M. N. C., Pinto, A. M. F. R., Campos, J. B. L. M., 2000. Gas hold-up in aerated slugging columns. Trans IChemE 78, 1139–1146.

Pinto, A. M. F. R., Campos, J. B. L. M., 1996. Coalescence of two gas slugs rising in a vertical column of liquid. Chemical Engineering Science 51, 45–54.

Pinto, A. M. F. R., Pinheiro, M. N. C., Campos, J. B. L., 2001a. On the interaction of taylor bubbles rising in two-phase co-current slug flow in vertical columns: Turbulent wakes. Experiments in Fluids 31, 643–652.

Pinto, A. M. F. R., Pinheiro, M. N. C., Campos, J. B. L. M., 1998. Coalescence of two gas slugs rising in a co-current flowing liquid in vertical tubes. Chemical Engineering Science 53, 2973–2983.

Pinto, A. M. F. R., Pinheiro, M. N. C., Campos, J. B. L. M., Nogueira, S., 2001b. On the transition from laminar to turbulent regime in vertical upward two-phase slug flow. 5th Experimental heat transfer, fluid mechanics and thermodynamics .

Polonsky, S., Shemer, L., Barnea, D., 1999. The relation between the taylor bubble motion and the velocity field ahead of it. Int. J. Multiphase Flow 25, 957–975.

Richardson, S., 1968. Two-dimensional bubbles in slow viscous flows. J. Fluid Mechanics 33, 476–493.

Rodrigue, D., Kee, D. D., Fong, C. F. C. M., 1998. Bubble velocities: Further developments on the jump discontinuity. J. Non-Newtonian Fluid Mechanics 79, 45–55.

Rodrigue, D., Kee, D. D., Fong, C. F. C. M., 1999. The slow motion of a single gas bubble in a non-newtonian fluid containing surfactants. J. Non-Newtonian Fluid Mechanics 86, 211–227.

Rosehart, R. G., Rhodes, E., Scott, D. S., 1975. Studies of gas-liquid (non-newtonian) slug flow: Void fraction meter, void fraction and slug characteristics. The Chemical Engineering J. 10, 57–64.

Rosehart, R. G., Scott, D. S., Rhodes, E., 1972. Gas-liquid slug flow with drag-reducing polymer solutions. AIChE J. 18 (4), 744–750.

Scarano, F., 2000a. Advances in iterative multigrid PIV image processing. Experiments in Fluids Suppl., S51–S60.

Scarano, F., March 2000b. Particle image velocimetry - development and application, investigation of coherent structures in turbulent shear flows. Ph.D. thesis, Universita degli Studi di Napoli (UniNa).

Scarano, F., Riethmuller, M. L., 1999. Iterative multigrid approach in PIV image processing with discrete window offset. Experiments in Fluids 26, 513–523.

Schram, C., 2001. Technical note - BMI series 5000 nd: YAG laser - model PVL 400/TS, serial number b19373. Tech. rep., von Karman Institute for Fluid Dynamics.

Shemer, L., Barnea, D., 1987. Visualization of the instantaneous velocity profiles in gas-liquid slug flow. PhysicoChemical Hydrodynamics 8, 243–253.

Sotiriadis, A. A., Thorpe, R. B., 2005. Liquid re-circulation in turbulent vertical pipe flow behind a cylindrical bluff body and a ventilated cavity attached to a sparger. Chemical Engineering Science 60, 981–994.

Sousa, J. T. V., França, F. A., Nakagawa, E. Y., Laje, A. C. V. M., 1996. Estudo experimental do movimento relativo de bolhas alongadas em tubo inclinado, nas misturas bifásicas ar-água e ar-dispersão de goma xantana. In: Congresso Brasileiro de Engenharia Norte-Nordeste, 1996.

Taitel, Y., Barnea, D., Dukler, A., 1980. Modelling flow pattern transitions for steady upward gas-liquid flow in vertical tubes. AIChE J. 3, 345–354.

Talvy, C. A., Shemer, L., Barnea, D., 2000. On the interaction between two consecutive elongated bubbles in a vertical pipe. Int. J. Multiphase Flow 26, 1905–1923.

Terasaka, K., Tsuge, H., 2003. Gas holdup for slug bubble flow of viscous liquids having a yield stress in bubble columns. Chemical Engineering Science 58, 513–517.

Ting, R. Y., 1975. Viscoelastic effect of polymers on single bubble dynamics. AIChE J. 21 (4), 810–813.

Tokuhiro, A., Maekawa, M., Iizuka, K., Hishida, K., Maeda, M., 1998. Turbulent flow past a bubble and an ellipsoid using shadow-image and PIV techniques. Int. J. Multiphase Flow 24, 1383–1406.

Tsuei, L., Savaş, Ö., 2000. Treatment of interfaces in particle image velocimetry. Experiments in Fluids 29, 203–214.

Tudose, E. T., Kawaji, M., 1999. Experimental investigation of taylor bubble acceleration mechanism in slug flow. Chemical Engineering Science 54, 5761–5775.

van Hout, R., Barnea, D., Shemer, L., 2002a. Translational velocities of elongated bubbles in continuous slug flow. Int. J. Multiphase Flow 28, 1333–1350.

van Hout, R., Gulitski, A., Barnea, D., Shemer, L., 2002b. Experimental investigation of the velocity field induced by a taylor bubble rising in stagnant water. Int. J. Multiphase Flow 28, 579–596.

Vatai, G., Tetik, M. N., 1987. Gas hold-up in bubble columns with non-newtonian liquids. Chemical Engineering Science 42, 166–169.

Wagner, A. J., 2000. Simulation of a cusped bubble rising in a viscoelastic fluid with a new numerical method. Computer Physics Communications 129, 227–232.

White, E. T., Beardmore, R. H., 1962. The velocity of rise of single cylindrical air bubbles through liquids contained in vertical tubes. Chemical Engineering Science 17, 351–361.

Zukoski, E. E., 1966. Influence of viscosity, surface tension, and inclination angle on motion of long bubbles in closed tubes. J. Fluid Mechanics 25 (4), 821–837.